

DYNAMIC ANALYSIS OF TRANSPORT PHENOMENA
IN DIRECTIONAL SOLIDIFICATION
OF BINARY ALLOYS

by

DO HYUN KIM

B. S., Seoul National University

(1979)

M. S., Korea Advanced Institute of Science and Technology

(1981)

Submitted to the Department of Chemical Engineering

in partial fulfillment of the requirements

for the degree of

DOCTOR OF SCIENCE

at the

MASSACHUSETTS INSTITUTE OF TECHNOLOGY

February, 1990

©Massachusetts Institute of Technology

Signature of Author _____

Department of Chemical Engineering

February 2, 1990

Certified by _____

Robert A. Brown

Professor, Department of Chemical Engineering

Thesis Supervisor

Accepted by _____

William M. Deen

Professor, Department of Chemical Engineering

Chemical Engineering Graduate Officer

Vol. 1
MASSACHUSETTS INSTITUTE
OF TECHNOLOGY

MAR 28 1990

LIBRARIES

ASST. DIR.

To my parents.

To have knowledge,
you must have reverence for the LORD.
(Proverbs 1:7, GNB)

DYNAMIC ANALYSIS OF TRANSPORT PHENOMENA
IN DIRECTIONAL SOLIDIFICATION
OF BINARY ALLOYS

by
DO HYUN KIM

Submitted to the Department of Chemical Engineering
on February 2, 1990 in partial fulfillment of the
requirements for the Degree of Doctor of Science in
Chemical Engineering

ABSTRACT

The goal of the research in this thesis is to extend the understanding of the physics involved in the directional solidification of semiconductor and optoelectronic crystals grown in vertical Bridgman and gradient freeze systems. The specific objectives focus on the investigation of convection in the melt during growth of dilute or nondilute binary alloys and its effect on species transport and axial and radial segregation of impurities and dopants. These objectives have been met by constructing detailed pseudo-steady-state and transient models describing the crystal growth process; the models include the shape of the melt/crystal interface, convection, heat and solute transfer in the melt, heat conduction in the crystal and ampoule, and radiative exchange between the furnace and the ampoule. The transient analyses presented in this study are meaningful because these are the first time-dependent simulations of crystals growth in the closed ampoule of the vertical Bridgman growth system, which account for these effects simultaneously.

Robust numerical algorithms for solution of these complex moving-boundary problems were constructed for the transient model by systematic implementation of finite element discretizations and implicit time integration methods for the resulting differential-algebraic set of equations. A modified Newton's method, coupled with frontal elimination methods for linear systems, was effective in solving the large set of nonlinear algebraic equations that arise at each time step.

The effect of a vertically-aligned magnetic field on the convection in the melt and solute segregation in the crystal has been analyzed using the pseudo-steady-state model in the limit of zero magnetic Reynolds number. Steady cellular convection driven by radial temperature gradients causes good axial and radial mixing without a magnetic field. A weak magnetic field decreases the intensity of convection and the effectiveness of this mixing. The radial nonuniformity in composition is greatest at an intermediate field strength. Stronger fields suppress flow recirculation completely and lead to uniform solute segregation across the crystal and to diffusion-controlled segregation. Predictions are made for the growth of Ga-doped Ge in the vertical Bridgman system at MIT.

For the growth of nondilute HgCdTe crystals, a strong cellular motion exists near the interface, but flow away from it is damped by the stabilizing dependence of the melt density on the heavier component HgTe of the pseudobinary mixture, which is rejected

at the interface. Increasing the composition of CdTe lowers the melt density far from the interface and further damps the melt motion, but causes the formation of additional vertically stacked cells in the melt. Multiple steady-state flows and flow hysteresis are predicted. Large radial segregation is predicted and is caused by the incomplete solute mixing adjacent to the interface, as has been observed in experimental studies. The prediction of solute mixing only in a region adjacent to the interface suggests a model for axial segregation that couples a small well-mixed region there to diffusion-controlled axial transport elsewhere. The axial segregation predicted by this model is qualitatively similar to the diffusion-controlled growth and agrees with experimental observation and with the numerical simulations.

The transient simulations were used to study convection and segregation in both dilute and nondilute alloy systems. In the well designed vertical Bridgman furnace at MIT, almost steady-state temperature and flow fields are reached near the melt/crystal interface shortly after the beginning of the ampoule translation. Solute concentration in the crystal increases without reaching a constant value even without convection in the melt because of the finite length of the ampoule. Nevertheless, the radial segregation and effective segregation coefficient reach constant values after the initial transient. These observations justify the use of the pseudo-steady-state analysis for the same MIT system. Comparisons between our calculations and experiments by Wang [PhD Thesis (1984)] in the MIT system demonstrated the accuracy of the model and solution algorithm for predictions of transients in the growth process.

Simulations of the growth of gallium arsenide in a small-scale gradient freeze system changed with time throughout the simulation because of the large latent heat of solidification which leads to continuous changes in the temperature field. The pseudo-steady-state model cannot describe this growth system.

Transient analysis of the growth of HgCdTe alloy in the vertical Bridgman growth system has demonstrated the transition of flow structure caused by the development of the solute diffusion layer next to the interface. The flow field damped by this concentration gradient maintains the structure of two axially-stacked toroidal cells, but with much lower flow intensity. The calculated solute segregation corresponds to almost one-dimensional, diffusion-controlled growth. Large radial temperature gradients and the coupling of the melting point with concentration leads to large deflections of the melt/crystal interface. The solute mixing by the flow cell near the interface was not enough to reduce the concentration variations along the interface and large radial solute variations exist. The radial segregation is set by the interface deflection. The dependence of β_t of HgCdTe melt on temperature and composition leads to the instability in the convection near the interface. This instability, combined with sideways diffusive instability in the bulk, resulted in the secondary flow cells between the upper and lower flow cells. The concentration field is not affected by the variation of β_t because of the weak convection level.

Thesis Supervisor: Dr. Robert A. Brown
Title: Professor of Chemical Engineering

ACKNOWLEDGEMENT

First of all, I would like to express the deepest gratitude to my advisor, Professor Robert A. Brown, for his excellent guidance and endless enthusiasm throughout this study. He showed me what is research and what is teaching. I feel truly privileged to have had the opportunity to work with him. I would also like to thank the members of my thesis committee: Professor Robert C. Armstrong and Professor T. Alan Hatton of the Department of Chemical Engineering and Dr. Michael J. Wargo of the Department of Materials Science and Engineering for their valuable input.

I would like to acknowledge the support to the author provided by the Department of Chemical Engineering, MIT in the form of Michelin Fellowship and by the Materials Processing Center, MIT in the form of Graduate Award. This work and author's Research Assistantship was funded by the National Aeronautics and Space Administration (NASA).

Thanks are due to all my colleagues in our group, including Jeff Derby, Jeff Atherton, Jacques Duranceau, Mark Bennett, Phil Sackinger, Paul Thomas (author of PLOT), Sanjay Patnaik, N. Ramprasad, Howard Covert, Tom Kinney, Angelo Kyrlidis, Dimitri Maroudas, Costas Tsiveriotis and Reza Mehrabi, for making pleasant air in 66-256 and stimulating discussions. Special thanks are to fellow students in ChemE, including Glen, Hyung Jae, Shin-Gyoo, Sung Min, Jonghun, Jae-Sung and Chun-Hyuk who made for an enjoyable stay at MIT and helped finishing this thesis. Thanks are also due Ms. Arline Benford, who cared for my arrangements to see Professor Brown.

I want express my thanks to all members of my extended family: To my mother- and father-in-law, Hyung Bin Kang and Chang Kyun Chu, and my sister- and brother-

in-laws, I give thanks for their encouragements and support during my study. And most of all, I wish to thank to my parents, Shinae Lee and Sang Chul Kim. My late father inspired me to study at MIT, when I was young. My mother supported me by prayer when I was weak in soul and body, together with my grandmother, Young Eui Kim.

Finally, I wish to give very special thanks to my wife, Yoon Kyung Chu, who has shared all those good and bad times with me throughout this study. Without her love, understanding and prayer, this work could not be completed. Many thanks to my daughter, Nayoung, who deserves the right to play with daddy more often from now on.

Contents

Abstract	3
Acknowledgement	5
1 Introduction	30
1.1 Crystal Growth	30
1.1.1 Semiconductor Materials	36
1.1.2 Melt Crystal Growth Systems	38
1.2 Transport Phenomena in Directional Solidification	44
1.2.1 Basic Transport Processes	44
1.2.2 Melt Convection	51
1.2.3 Effect of Melt Convection on Solute Segregation	67
1.3 Previous Models for Vertical Bridgman Process	73
1.3.1 Experimental Modelling	73
1.3.2 Theoretical Modelling	78
1.4 Thesis Direction	88
1.4.1 Objectives and Approach	88

1.4.2	Structure of Thesis	89
2	Modelling of Directional Solidification	92
2.1	Introduction	92
2.2	Pseudo-Steady-State Model	96
2.2.1	Modelling Assumptions	96
2.2.2	Governing Equations and Boundary Conditions	101
2.3	Transient Model	105
2.3.1	Modelling Assumptions	106
2.3.2	Governing Equations and Boundary Conditions	107
3	Numerical Formulation	112
3.1	Finite Element Method	113
3.2	Formulation of Pseudo-Steady-State Model	125
3.2.1	Introduction	125
3.2.2	Discretization by the Galerkin Finite Element Method	128
3.2.3	Algebraic Solution by Newton-Raphson Method	138
3.2.4	Continuation of Solution in Parameter Space	141
3.2.5	Test of Petrov-Galerkin Methods	145
3.3	Formulation of Transient Model	162
3.3.1	Introduction	162
3.3.2	Spatial Discretization	163

3.3.3	Time Integration	171
3.3.4	Algebraic Solution with Quasi-Newton Iterations	175
3.3.5	Example of Time-Dependent Calculation	176
4	Effect of Vertical Magnetic Field	196
4.1	Introduction	196
4.2	Action of the Magnetic Fields	202
4.3	Pseudo-Steady-State Model For Magnetic Vertical Bridgman Process . .	205
4.4	Growth of Gallium-doped Germanium with a Magnetic Field	209
4.4.1	Vertical Bridgman Growth System	211
4.4.2	Constant Gradient Furnace	223
4.5	Asymptotic Analysis for High Magnetic Fields	230
4.6	Discussion	238
5	Convection and Segregation in Vertical Bridgman Growth of Nondilute Alloy Semiconductors	241
5.1	Introduction	241
5.2	Pseudo-Steady-State Model of Vertical Bridgman Growth of HgCdTe . .	249
5.3	Analysis of Flow Structure and Radial Segregation	255
5.3.1	Effect of Solutal Field on Flow	255
5.3.2	Flow Structure with Solute Damping	267
5.3.3	Effect of Growth Rate	269
5.3.4	Effect of Microgravity	272

5.4	Axial Segregation Model	276
5.5	Discussion	282
6	Transient Analysis of the Growth of Dilute Binary Alloy in a Vertical Bridgman Process and Gradient Freeze Furnace	287
6.1	Introduction	287
6.2	Transient Model for Vertical Bridgman Growth Process and Gradient Freeze Growth Process	295
6.3	Growth of Gallium-doped Germanium in MIT Vertical Bridgman Heat- pipe Furnace	298
6.3.1	Thermal Boundary Conditions	298
6.3.2	Temperature Fields and Growth Velocity	305
6.3.3	Flow Fields	312
6.3.4	Solute Fields	320
6.3.5	Comparison with Experimental Measurements	328
6.4	Growth of Selenium-doped Gallium Arsenide in GTE Gradient Freeze Furnace	334
6.4.1	Furnace Temperature Profile	334
6.4.2	Temperature Fields and Growth Velocity	339
6.4.3	Flow Fields	346
6.4.4	Solute Fields	349
6.4.5	Effect of Ampoule	354
6.5	Discussion	365

7	Transient Analysis of the Growth of Nondilute Binary Alloy Crystal in a Vertical Bridgman Growth System.	368
7.1	Introduction	368
7.2	Thermophysical Properties	378
7.2.1	Phase Diagram	378
7.2.2	Variation of Thermophysical Properties	381
7.3	Flow Structure and Solute Segregation	391
7.3.1	Temperature Fields and Growth Velocity	396
7.3.2	Flow Fields	403
7.3.3	Solute Fields	410
7.4	The Effect of Variable Coefficient of Thermal Expansion	420
7.5	Conclusions	428
8	Conclusions	430
8.1	Steady State Analysis	430
8.2	Transient Analysis	433
8.3	Suggestions for the Future Work	436
9	Bibliography	441
	Biographical Note	480

List of Figures

1.1	Relation between the normalized production cost per chip of different size and the diameter of silicon wafers (Shimura,1989).	33
1.2	Size trends for crystal and wafer (Larrabee,1985).	34
1.3	Factors affecting device performance along the path of device fabrication.	35
1.4	Thermal conductivities and critical resolved shear stress of common semiconductor materials (Brown, 1988).	39
1.5	Commonly used systems for melt crystal growth of electronic materials	42
1.6	Temperature, solute concentration, and density profile in one-dimensional directional solidification of a binary alloy.	45
1.7	Idealized phase diagram for binary alloys.	47
1.8	Solute composition profile along the crystal without convection in the melt.	50
1.9	Solute composition profile along the crystal with complete mixing in the melt.	52
1.10	Three-dimensional scheme for representation of flow states.	54
1.11	(a) Model configuration with isothermal top, bottom and wall temperature. (b) Types of different crystal growth techniques according to the model configuration.	56

1.12	Schematic of prototypical vertical Bridgman crystal growth system. . . .	57
1.13	The effect of Ra_s and k on the role of solute field in thermosolutal convection.	59
1.14	The variation of macroscopic interface shape with composition (Burden <i>et al.</i> , 1973).	61
1.15	Temperature fluctuations for various magnetic field strength (Kim, 1982).	64
1.16	Solute concentration profile of InSb crystals grown in space and on earth (Witt <i>et al.</i> , 1975).	66
1.17	Effect of convection on Δc and k_{eff} in directional solidification.	69
1.18	Striation patterns of Te-doped InSb crystal grown in destabilizing vertical Bridgman system (Kim <i>et al.</i> , 1972).	74
1.19	Stability diagram for flow patterns and transitions from laminar to unsteady convection (shaded area) for $h/d = 1$ in water in terms of Ra_t and Ra_w (Müller <i>et al.</i> , 1987).	76
1.20	Sample flow fields, isotherms and solute fields for the growth of GaGe in idealized vertical Bridgman system (Chang and Brown, 1983a).	85
1.21	Sample flow fields and solute fields for the growth of GaGe in Wang's system with boron nitride ampoule (Adornato and Brown, 1987a). . . .	87
2.1	Schematic diagram of the heat pipe Bridgman-Stockbarger growth system (Wang, 1984).	94
2.2	Schematic diagram of the crucible used for growth in the heat-pipe Bridgman-Stockbarger growth system (Wang, 1984).	95
2.3	A prototypical vertical Bridgman-Stockbarger crystal growth system. . .	97

3.1	Lagrangian linear and quadratic basis functions defined on a unit element.	118
3.2	Isoparametric mapping of a biquadratic element.	122
3.3	Finite element meshes for the analysis of vertical Bridgman crystal growth.	129
3.4	A solution family with bifurcation and limit points in the parameter space.	142
3.5	One-dimensional composition profiles computed using the Petrov-Galerkin methods with essential boundary conditions: (L) for bilinear elements and (Q) for biquadratic elements.	149
3.6	Effect of circulation rate on the solute field calculated using the Petrov-Galerkin methods: Essential solute boundary conditions(I).	151
3.7	Effect of circulation rate on the solute field calculated using the Petrov-Galerkin methods: Essential solute boundary conditions(II).	152
3.8	One-dimensional composition profiles computed using the Petrov-Galerkin methods with mixed boundary conditions.	154
3.9	The accuracy of the Petrov-Galerkin methods measured in terms of the interfacial solute balance.	155
3.10	Effect of flow circulation rate on the solute field calculated using the Petrov-Galerkin methods: Mixed solute boundary conditions(I).	156
3.11	Effect of circulation rate on the solute field calculated using the Petrov-Galerkin methods: Mixed solute boundary conditions(II).	157
3.12	Interfacial solute balance computed using the Petrov-Galerkin methods with the mixed boundary conditions.	159
3.13	Comparison of the accuracy of the Petrov-Galerkin method developed by Heinrich <i>et al.</i> (1977) using regular and transformed concentration variables.	161

3.14	Convergence of a typical iteration of nonlinear equations using the quasi-Newton method.	177
3.15	Finite element meshes in the vertical ampoule generated during the transient simulation of the test problem.	179
3.16	History of the time step size generated by the fully-implicit time integration.	182
3.17	History of the elapsed time generated by the fully-implicit time integration.	184
3.18	Sample time-dependent temperature fields for growth of GaGe in the vertical Bridgman system.	185
3.19	Sample time-dependent solute fields for growth of GaGe in the vertical Bridgman furnace.	186
3.20	Crystal growth rate computed from the time derivative of the interface location.	188
3.21	Axial composition profile in the crystal grown under microgravity conditions.	189
3.22	Time-dependent evolution of the error in the solute balance in the melt.	192
3.23	Three finite element meshes used for the calculations presented in Table 3.5.	193
4.1	Schematic drawing of the effect of flow intensity on the effective segregation coefficient and the percentage radial segregation in a directional solidification system.	198
4.2	Diagrams of the models for Bridgman-Stockbarger and constant gradient directional solidification furnaces.	201

4.3	Contours of temperatures, stream function and concentration for growth in the vertical Bridgman furnace with $Ra_t = 1 \times 10^5$. Streamlines are spaced at equal intervals between the maximum (or minimum) values for the cells and zero.	213
4.4	Comparison of the temperature fields for growth in the vertical Bridgman furnace with $Ra_t = 0$ and 1×10^5	215
4.5	Sample flow fields for growth of GaGe in the vertical Bridgman furnace with increasing magnetic field strength, as measured by Ha ; $Ra_t = 1 \times 10^5$	216
4.6	Sample flow fields for growth of GaGe in the vertical Bridgman furnace with increasing convection driving force, as measured by Ra_t ; $Ha = 500$	217
4.7	Maximum values of stream function in the upper and lower flow cells as a function of Ra_t and Ha for growth of GaGe in the vertical Bridgman furnace.	219
4.8	Sample concentration fields for gallium solute in the vertical Bridgman system; results are for different values of Ha and $Ra_t = 1 \times 10^5$	220
4.9	Sample concentration fields for gallium solute in the vertical Bridgman system; results are for different values of Ra_t and $Ha = 500$	221
4.10	Percentage radial segregation as a function of thermal Rayleigh number and Hartmann numbers for growth of GaGe in the vertical Bridgman system. The solid dot (●) corresponds to experimental measurement of Wang (1984).	222
4.11	Effective segregation coefficient computed from Eq. (4.1) in the vertical Bridgman system; The solid dot (●) corresponds to experimental measurement of Wang (1984).	224

4.12	Contours of temperatures, stream function and concentration for growth in the constant gradient furnace with $Ra_t = 1.25 \times 10^4$. Streamlines are spaced at equal intervals between the maximum, and minimum, values for the cells and zero.	226
4.13	Sample melt flow fields for growth in vertical Bridgman system; results are for different values of Ha and $Ra_t = 1.25 \times 10^4$	227
4.14	Maximum values of stream function in the single toroidal cell plotted as a function of Ra_t and Ha for growth of GaGe in the constant gradient furnace.	228
4.15	Sample concentration fields for gallium solute in constant gradient furnace; results are for different values of Ha and $Ra_t = 1.25 \times 10^4$	229
4.16	Percentage radial segregation as a function of thermal Rayleigh number and Hartmann number for growth of GaGe in the constant gradient system.	231
4.17	Effective segregation coefficient computed from Eq. (4.1) plotted as a function of Ra_t and Ha for growth of GaGe in the constant gradient furnace.	232
4.18	The simplified directional solidification system considered in the asymptotic analysis of flow with large magnetic fields. A qualitative picture of regions of the flow as expected for high Ha is included.	233
4.19	Variation of flow intensity with increasing Hartmann number predicted by finite element analysis rescaled as $\Psi_{max} \sim Ha^{-2}$, as determined from asymptotic analysis in the limit $Ha \gg 1$	239
5.1	Phase diagram of pseudobinary HgCdTe (Szofran and Lehoczky, 1981).	244
5.2	Schematic of prototypical vertical Bridgman crystal growth system. . . .	247

5.3	Sample isotherms, stream function and solute contours for thermophysical properties of HgCdTe listed in Tables 5.1 and 5.2, except that $Ra_s = 0$. Streamlines are spaced at equal intervals between maximum (or minimum) for flow cells and zero.	257
5.4	Flow intensity for lower flow cell (Ψ_{max}) as a function of solutal Rayleigh number Ra_s . All other parameters are fixed at the values listed in Tables 5.1 and 5.2.	259
5.5	Radial segregation Δc as a function of solutal Rayleigh number Ra_s . All other parameters are fixed at the values listed in Tables 5.1 and 5.2. . .	260
5.6	Streamlines and isoconcentration contours for calculations with decreasing Ra_s up to the first limiting value $Ra_s^{(1)} \approx -1.57 \times 10^4$; $Ra_t = 2 \times 10^4$.	262
5.7	Streamlines and isoconcentration contours for three flow states that coexist at $Ra_s = -1.5 \times 10^4$ with all other parameters held fixed.	264
5.8	Streamlines and isoconcentration contours for calculations with decreasing Ra_s from the second limiting value $Ra_s^{(2)} \approx -1.27 \times 10^4$; $Ra_t = 2 \times 10^4$.	265
5.9	Variation of dimensionless concentration of CdTe along the melt/crystal interface for varying Ra_s with $Ra_t = 2 \times 10^4$	266
5.10	Variation of melt/crystal interface shapes for varying Ra_s with $Ra_t = 2 \times 10^4$	268
5.11	Dependence of the circulation rate in the upper flow cell on the modified solutal Rayleigh number Ra_s^* . Results are shown that were obtained with increasing Ra_s (--) and with increasing the dimensionless crystal growth rate Pe (- -).	270
5.12	Radial variation of the axial velocity near the ampoule wall in the scaled variables predicted by the analysis of the thermosolutal boundary-layer. Results for increasing Ra_s show convergence to the boundary-layer scaling.	271

5.13	Streamlines and isoconcentration contours for calculations with varying crystal growth rate Pe ; $Ra_t = 2 \times 10^4$ and $Ra_s = -2 \times 10^4$	273
5.14	Flow intensity for lower flow cell Ψ_{max} as a function of solutal Rayleigh number Ra_s for varying values of Ra_t . All parameters are fixed at the values listed in Tables 5.1 and 5.2.	274
5.15	Radial segregation Δc as a function of solutal Rayleigh number Ra_s for varying values of Ra_t . All parameters are fixed at the values listed in Tables 5.1 and 5.2.	275
5.16	Schematic of one-dimensional model of axial segregation. The crystal is assumed to be separated from a bulk of diffusion-controlled melt by a region of thickness δ with intense convection.	277
5.17	Comparison of predictions for the axial composition variation in the crystal for the approximate solution with the complete solution of Smith <i>et al.</i> (1955) for $\delta = 0$ and a dilute alloy ($m = 0$).	281
5.18	Variation of the axial composition in the crystal predicted by the one-dimensional model with the extent of the mixing zone adjacent to the interface. The profiles vary between diffusion-controlled growth for $\delta \ll 1$ to growth from a well-mixed melt for $\delta \sim 1$; $m = 0.27$	283
5.19	Comparison of the axial composition variation in the crystal predicted with increasing the extent of the mixing zone ($\delta = 0.1, Pe_m = 9.2$) or increasing the diffusion coefficient of the solute by a factor of two ($\delta = 0, Pe_m = 4.6$); the result for diffusion-controlled growth corresponds to $\delta = 0$ and $Pe_m = 9.2$	284
6.1	Schematic diagrams of the prototypical models for the (a) MIT vertical Bridgman crystal growth system and (b) GTE gradient freeze growth system.	292

6.2	Schematic diagrams of the crucibles used for growth in (a) MIT vertical Bridgman growth system and (b) GTE gradient freeze growth system.	293
6.3	Typical furnace temperature profiles for (a) MIT vertical Bridgman furnace system and (b) GTE gradient freeze furnace system.	296
6.4	Comparison of axial temperature profiles along the center of a graphite rod predicted by finite element analysis and measured by Wang (1984).	304
6.5	Sample finite element mesh used for the transient calculations for the MIT vertical Bridgman system.	306
6.6	Sample temperature fields for growth of GaGe in MIT furnace with thermal Rayleigh number of (a) $Ra_t = 0$ and (b) $Ra_t = 2 \times 10^5$	307
6.7	Transient growth rate of GaGe crystal for several values of thermal Rayleigh numbers, Ra_t	308
6.8	Transient interface deflection for several values of thermal Rayleigh numbers, Ra_t	309
6.9	Growth rate transients for step change in ampoule translation rate; comparison is shown to the correlation of Fu and Wilcox (1981).	311
6.10	Sample flow fields for growth of GaGe in MIT system with boron nitride ampoule: $Ra_t = 2 \times 10^2$	313
6.11	Sample flow fields for growth of GaGe in MIT system with boron nitride ampoule: $Ra_t = 2 \times 10^3$	314
6.12	Sample flow fields for growth of GaGe in MIT system with boron nitride ampoule: $Ra_t = 2 \times 10^4$	315
6.13	Sample flow fields for growth of GaGe in MIT system with boron nitride ampoule: $Ra_t = 2 \times 10^5$	316

6.14	Time histories of the maximum values of the stream function in the upper and lower flow cells as a function of Ra_t for growth of GaGe in MIT system.	318
6.15	Maximum values of the stream function in the upper and lower flow cells as a function of Ra_t for fraction solidified $f = 0$ and 0.6 .	319
6.16	Sample gallium concentration fields for growth of GaGe in MIT system. $Ra_t = 0$ and $V_g = 4\mu\text{m}/\text{sec}$.	321
6.17	Sample gallium concentration fields for growth of GaGe in MIT system. $Ra_t = 2 \times 10^2$ and $V_g = 4\mu\text{m}/\text{sec}$.	322
6.18	Sample gallium concentration fields for growth of GaGe in MIT system. $Ra_t = 2 \times 10^3$ and $V_g = 4\mu\text{m}/\text{sec}$.	323
6.19	Sample gallium concentration fields for growth of GaGe in MIT system. $Ra_t = 2 \times 10^4$ and $V_g = 4\mu\text{m}/\text{sec}$.	324
6.20	Sample gallium concentration fields for growth of GaGe in MIT system. $Ra_t = 2 \times 10^5$ and $V_g = 4\mu\text{m}/\text{sec}$.	325
6.21	Simulations of GaGe crystal growth at the ampoule translation rate of $4\mu\text{m}/\text{sec}$ and several values of thermal Rayleigh numbers; (a) axial segregation profile, (b) radial segregation, and (c) effective segregation coefficient in the crystal.	327
6.22	Comparison of computed transient growth rate of GaGe crystal with experimental data by Wang (1984) for the case of a step change in ampoule translation rate from $2\mu\text{m}/\text{sec}$ to $4\mu\text{m}/\text{sec}$: $Ra_t = 2 \times 10^5$.	329
6.23	Comparison of computed transient interface deflection during the growth of GaGe crystal with experimental data by Wang (1984) for the case of step change in ampoule translation rate from $2\mu\text{m}/\text{sec}$ to $4\mu\text{m}/\text{sec}$; $Ra_t = 2 \times 10^5$.	331

6.24	Comparison of computed axial segregation profile in GaGe crystal with experimental data by Wang (1984) for the case of step change in ampoule translation rate from 2 $\mu\text{m}/\text{sec}$ to 4 $\mu\text{m}/\text{sec}$: $Ra_t = 2 \times 10^5$	332
6.25	Comparison of computed transient (a) radial segregation and (b) effective segregation coefficient during the growth of GaGe crystal with experimental data by Wang (1984) for the case of step change in ampoule translation rate from 2 $\mu\text{m}/\text{sec}$ to 4 $\mu\text{m}/\text{sec}$: $Ra_t = 2 \times 10^5$	333
6.26	Furnace temperature data from GTE experiment.	338
6.27	Refined transient furnace temperature profiles based on initial and final temperature profiles.	340
6.28	Furnace temperature profiles used in the numerical model created by analytical expressions.	341
6.29	Sample mesh used for the analysis of GaAs growth in GTE furnace. . .	343
6.30	Sample transient temperature fields for growth of GaAs in GTE furnace: $Ra_t = 0$ and $Ra_t = 1.2 \times 10^5$	344
6.31	Comparison of temperature fields obtained from the transient calculation and steady-state calculation for the stationary furnace temperature profile.	345
6.32	Transient growth rate of selenium-doped GaAs crystal and interface deflection as predicted for several values of thermal Rayleigh numbers. . .	347
6.33	Sample flow fields for growth of GaAs in GTE system with pyrolytic boron nitride ampoule: $Ra_t = 1.2 \times 10^3$ and $Ra_t = 1.2 \times 10^5$	348
6.34	History of the maximum values of the stream function in the flow cell for the growth of selenium-doped GaAs in GTE system for $1.2 \times 10^3 < Ra_t < 1.2 \times 10^5$	350

6.35	Sample selenium concentration fields computed for growth of GaAs in GTE system: $Ra_t = 1.2 \times 10^3$ and $Ra_t = 1.2 \times 10^5$	351
6.36	Simulation of selenium-doped GaAs crystal growth in the GTE growth system; (a) axial segregation profile, (b) radial segregation, and (c) effective segregation coefficient in the crystal for several values of thermal Rayleigh numbers.	353
6.37	Sample transient temperature fields for growth of GaAs in GTE furnace for the cases of (a) anisotropic and (b) isotropic thermal conductivity of ampoule material: $Ra_t = 1.2 \times 10^5$	355
6.38	Sample transient temperature fields for growth of GaAs in GTE furnace for the cases of (a) thick and (b) thin ampoule wall: $Ra_t = 1.2 \times 10^5$. . .	356
6.39	Transient growth rate of GaAs crystal and interface deflection for the isotropic ampoule and three thicknesses of the anisotropic ampoule. . .	358
6.40	Sample flow fields for growth of GaAs in GTE furnace system for the cases of (a) anisotropic and (b) isotropic thermal conductivity of ampoule material: $Ra_t = 1.2 \times 10^5$	359
6.41	Sample flow fields for growth of GaAs in GTE furnace system for the cases of (a) thick and (b) thin ampoule wall: $Ra_t = 1.2 \times 10^5$	360
6.42	History of the maximum value of the stream function in the flow cell for the growth of selenium-doped GaAs in GTE system for different ampoule designs: $Ra_t = 1.2 \times 10^5$	361
6.43	Sample selenium concentration distributions computed for growth of selenium-doped GaAs in GTE furnace system for the cases of (a) anisotropic and (b) isotropic thermal conductivity of ampoule material: $Ra_t = 1.2 \times 10^5$	362

6.44	Sample selenium concentration distributions computed for growth of selenium-doped GaAs in GTE furnace system for the cases of (a) thick and (b) thin ampoule wall: $Ra_t = 1.2 \times 10^5$	363
6.45	Simulation of selenium-doped GaAs crystal growth in the GTE growth system; (a) axial segregation profile, (b) radial segregation, and (c) effective segregation coefficient in the crystal for different ampoule design: $Ra_t = 1.2 \times 10^5$	364
6.46	Comparison of axial segregation profiles in the crystal obtained from transient analysis and modified Scheil equation for $Ra_t = 1.2 \times 10^5$	366
7.1	Bridgman-Stockbarger crystal growth furnace assembly (Szofran and Lehoczky, 1984).	374
7.2	Profiles for furnace temperature and Biot number used in the modelling of Bridgman growth system.	376
7.3	Schematic diagram of vertical Bridgman crystal growth system used in model calculation.	377
7.4	The pseudobinary phase diagram for CdTe–HgTe alloy system. Symbols (o) denote median values within 90 % confidence limits, as suggested by Brice <i>et al.</i> (1986).	380
7.5	Comparison of equilibrium distribution coefficient values from the diagram and the formulae. Symbols (o) denote values of k from the phase diagram of Brice <i>et al.</i> (1986).	382
7.6	Thermal diffusivity of $Hg_{1-x}Cd_xTe$ (Holland and Taylor, 1983).	383
7.7	Density for liquid $Hg_{1-x}Cd_xTe$. Circles (o) denote experimental measurements by Chandra and Holland (1983).	385

7.8	Contours of $\text{Hg}_{1-x}\text{Cd}_x\text{Te}$ melt density in the possible ranges of temperature and composition in the crystal growth system.	386
7.9	Coefficients of thermal expansion for $\text{Hg}_{1-x}\text{Cd}_x\text{Te}$ for selected compositions.	387
7.10	Coefficients of solutal expansion for $\text{Hg}_{1-x}\text{Cd}_x\text{Te}$ for selected compositions.	388
7.11	Range of Ra_t under the condition imposed in the model.	390
7.12	Sample finite element meshes used for the transient calculations for the growth of HgCdTe in vertical Bridgman system.	395
7.13	Sample temperature fields for growth of HgCdTe in vertical Bridgman growth: with $\bar{\kappa}a_t = 0$	397
7.14	Time histories of the melting point temperature at the midpoint of interface for several gravitational force level.	398
7.15	Sample temperature fields for growth of HgCdTe in vertical Bridgman growth: $Ra_t = 1 \times 10^4$	400
7.16	Transient growth rate of HgCdTe crystal for several pairs of the thermal Rayleigh number, Ra_t and solutal Rayleigh number, Ra_s	401
7.17	Transient interface deflections of HgCdTe crystal in vertical Bridgman growth system for several pairs of the thermal Rayleigh number, Ra_t and solutal Rayleigh number, Ra_s	402
7.18	Sample flow fields for growth of HgCdTe crystal in the vertical Bridgman furnace: $(Ra_t, Ra_s) = (1.0 \times 10^4, -8.5 \times 10^3)$	404
7.19	Sample flow fields for growth of HgCdTe crystal in the vertical Bridgman furnace: $(Ra_t, Ra_s) = (1.0 \times 10^5, -8.5 \times 10^4)$	406
7.20	(I) Sample flow fields for growth of HgCdTe crystal showing the transition in flow structure: $(Ra_t, Ra_s) = (1.0 \times 10^5, -8.5 \times 10^4)$	407

7.21 (II) Sample flow fields for growth of HgCdTe crystal showing the transition in flow structure: $(Ra_t, Ra_s) = (1.0 \times 10^5, -8.5 \times 10^4)$	408
7.22 Time histories of the maximum absolute stream function values in each flow cell for growth of HgCdTe crystal at the conditions of $(Ra_t, Ra_s) = (1.0 \times 10^4, -8.5 \times 10^3)$ and $(1.0 \times 10^5, -8.5 \times 10^4)$	409
7.23 Sample CdTe concentration fields for growth of HgCdTe in vertical Bridgman growth system: $Ra_t = Ra_s = 0$	411
7.24 Sample CdTe concentration fields for growth of HgCdTe in vertical Bridgman growth system: $(Ra_t, Ra_s) = (1.0 \times 10^4, -8.5 \times 10^3)$	412
7.25 Sample CdTe concentration fields for growth of HgCdTe in vertical Bridgman growth system: $(Ra_t, Ra_s) = (1.0 \times 10^5, -8.5 \times 10^4)$	413
7.26 Sample CdTe concentration fields for growth of HgCdTe in vertical Bridgman growth system during the early period: $(Ra_t, Ra_s) = (1.0 \times 10^5, -8.5 \times 10^4)$	415
7.27 Axial segregation profile of CdTe in the crystal. Comparison is made with the cases of diffusion-controlled growth and complete mixing in the melt.	416
7.28 Time histories of the radial segregation and effective segregation coefficient for growth of HgCdTe in vertical Bridgman growth system.	418
7.29 Sample flow fields for growth of HgCdTe crystal in the vertical Bridgman furnace calculated with variable β_t . Gravity acceleration is 0.1 of terrestrial condition.	422
7.30 Time histories of the maximum absolute stream function values in each flow cell for growth of HgCdTe crystal at $Ra_s = -8.5 \times 10^3$: $Ra_t = 1.0 \times 10^4$ for constant β_t and Ra_t does not have a single value for variable β_t	423

7.31	Transient interface deflections for growth of HgCdTe in vertical Bridgman growth system at $Ra_s = -8.5 \times 10^3$: $Ra_t = 1.0 \times 10^4$ for constant β_t and Ra_t does not have a single value for variable β_t	425
7.32	Sample CdTe concentration fields for growth of HgCdTe in vertical Bridgman growth system calculated with variable β_t . Gravity acceleration is 0.1 of terrestrial conditions.	426
7.33	Histories of radial segregation and effective segregation coefficient for growth of HgCdTe in vertical Bridgman growth system at $Ra_s = -8.5 \times 10^3$: $Ra_t = 1.0 \times 10^4$ for constant β_t and Ra_t does not have a single value for variable β_t	427

List of Tables

1.1	The use of crystals in semiconductor devices	32
1.2	Features of IC chips of various degree of integration (Lawrence and Huff,1982).	32
1.3	Characteristics of crystals grown by various methods (Brice, 1986). . . .	40
1.4	Classification of previous theoretical models for vertical Bridgman growth.	79
2.1	Dimensionless groups.	103
3.1	Two-dimensional Lagrangian bilinear and biquadratic interpolating functions.	120
3.2	Thermophysical properties of germanium.	180
3.3	Parameters for furnace design and processing conditions.	180
3.4	Dimensionless groups and characteristic values for modelling gallium-doped germanium crystal growth by the vertical Bridgman method. . .	181
3.5	Results of mesh refinement for the solution at $t = 0$ and the meshes displayed in Figure 3.23.	194
4.1	Dimensionless groups and their characteristic values appropriate for gallium-doped germanium crystal growth.	207

4.2	Thermophysical properties of germanium.	210
4.3	Design parameters for vertical Bridgman and constant gradient furnace	212
4.4	Dimensionless groups and characteristic values for gallium-doped germanium crystal growth in constant gradient furnace for asymptotic analysis.	235
5.1	Definitions of dimensionless groups that appear in analysis of thermosolutal convection of HgCdTe crystal growth; characteristic values computed from the thermophysical properties of HgCdTe are also shown.	251
5.2	Thermophysical property data used in analysis of HgCdTe growth. . . .	254
5.3	Thermophysical data for ampoule and system geometry.	256
6.1	Thermophysical properties of germanium.	299
6.2	Design parameters for MIT vertical Bridgman furnace	300
6.3	Dimensionless groups and characteristic values appropriate for gallium-doped germanium crystal growth in MIT furnace.	301
6.4	Thermophysical properties of gallium arsenide.	335
6.5	Design parameters for GTE gradient freeze furnace.	336
6.6	Dimensionless groups and characteristic values appropriate for selenium-doped gallium arsenide crystal growth in GTE furnace.	337
7.1	Thermophysical property data used in analysis of HgCdTe growth. . . .	392
7.2	Thermophysical data for ampoule and system geometry.	393
7.3	Definitions of dimensionless groups that appear in analysis of thermosolutal convection of HgCdTe crystal growth; characteristic values computed from the thermophysical properties of HgCdTe are also shown.	394

Chapter 1

Introduction

1.1 Crystal Growth

Crystal growth is a process where disordered atoms in a fluid phase join together to form a solid phase with ordered structure. Usually, it is preferable to form single crystals, with atoms aligned on specific crystallographic planes, rather than polycrystalline materials. While some single crystals are used for mechanical components (*e.g.* turbine blades, bearings, abrasive and cutting tools) or for jewellery (*e.g.* gem-quality diamond, cubic zirconia, ruby and sapphire), the central role of single crystals has been and will almost certainly continue to be in microelectronics and optoelectronics technology. Examples of the use of single crystals of various materials in major semiconductor devices are shown in Table 1.1 (Brice,1986).

The directions crystal growth research and technology relevant to semiconductor devices have been summed into three categories (Hoselitz,1968;Laudise,1974). First, crystal growth processes are being applied to newer materials that are more difficult to produce. When solid-state physicists find a new candidate material for advanced device applications, the engineering application is often limited by crystal growth process. In 1950's, the transition from Ge to Si which caused a revolution in semiconductor device capabilities was dependent on crystal growers learning how to produce crystals of more

reactive and higher melting point Si. The successful growth of single crystal GaAs, which is considered a next generation material, is plagued by problems of stoichiometry control and excess crystallographic defects in the lattice.

A second trend in semiconductor single crystal growth is toward the growth of larger sized crystals. Since IC (Integrated Circuit) chips are produced batchwise, the diameter of wafers used for device fabrication significantly affects the productivity and the production cost. The effect of the diameter of wafers on the production cost is shown in Figure 1.1 for the chips of various size. Production costs are normalized with the production cost of 6×6 mm chips on 100 mm-diameter silicon wafers. It is clear that wafers of larger diameter produce IC chips with less cost and the advantage becomes more evident with the increase of IC chip size, which is the trend of VLSI/ULSI¹ circuitry. The trends of diameter for Si crystals and wafers is plotted in Figure 1.2 for the last two decades. Currently, 6-in. material is being used. It is generally believed that 8-in. wafers will be in commercial use in the 1990s. The main problems that must be overcome in the growth of larger size crystal are the increased level of buoyancy-driven convection, nonuniform distribution of dopants in the crystal and more strict temperature control needed to keep defects at a low level.

Next, the demand for semiconductor single crystal with higher compositional and structural uniformity will increase. The chemical and structural quality of crystal has been and continues to be the rate determining step to advances in semiconductor devices and systems. Improvements in device characteristics, such as speed, sensitivity, power handling capacity, can be directly traced to improvements of the single crystal characteristics (Gatos, 1982). Factors affecting device performances are depicted in Figure 1.3 beginning from crystal growth processes. As an example, it was found that not only charge carrier concentration, but also the diffusion length and the lifetime of excess carriers are quantitatively related to the dopant concentration in silicon (Chi and Gatos, 1979). Also, the stoichiometry in compound semiconductors has been shown to affect the dislocation density of GaAs crystal (Ogawa, 1988) and energy bandgap of

¹VLSI/ULSI refers to the degree of circuit integration according to the number of device components per chip. See Table 1.2 for more detail.

USAGE	MATERIALS
Electrical diodes	Si, Ge
Photo-diodes	Si, GaAs, $Cd_xHg_{1-x}Te$
Transistors	Si, GaAs
Thyristors	Si
Photoconductive devices	Si, $Cd_xHg_{1-x}Te$
Integrated circuits	Si, GaAs
Light-emitting devices	GaAs, $Sn_xPb_{1-x}Te$
Radiation detectors	Si, Ge, CdTe
Strain gauges	Si
Hall effect magnetometers	InSb

Table 1.1: The use of crystals in semiconductor devices

Parameter	ULSI	VLSI	LSI	MSI
Components/chip	10^7-10^9	10^5-10^7	10^3-10^5	10^2-10^3
Chip Area (mm^2)	50-100	25-50	10-25	10

ULSI = Ultra Large Scale Integration

VLSI = Very Large Scale Integration

LSI = Large Scale Integration

MSI = Medium Scale Integration

Table 1.2: Features of IC chips of various degree of integration (Lawrence and Huff, 1982).

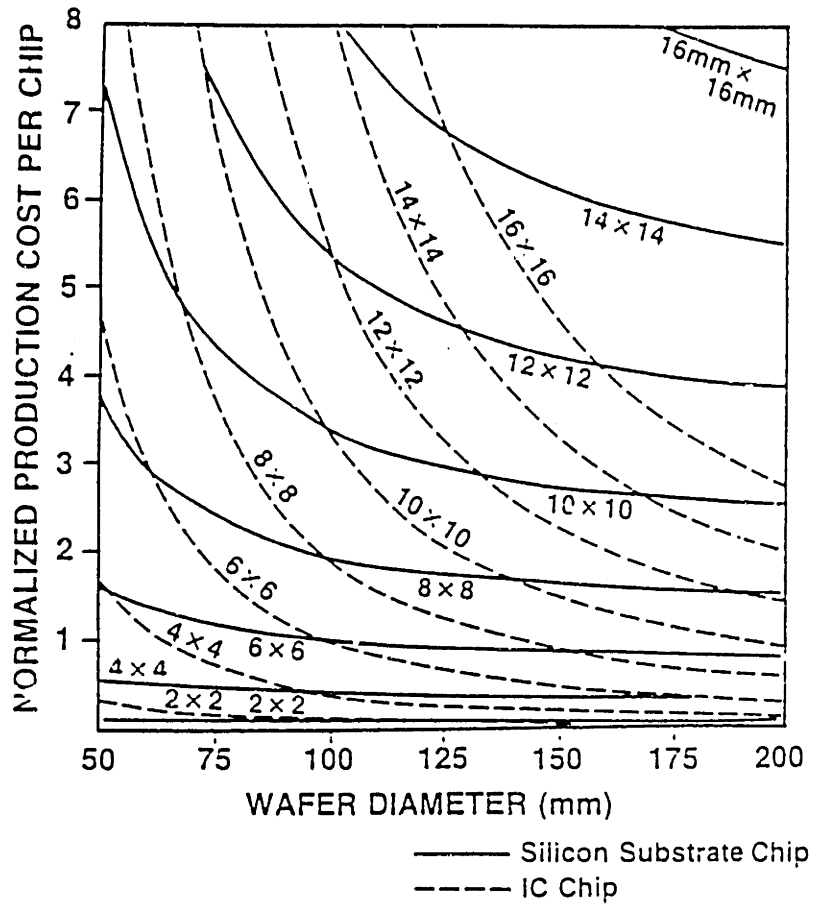


Figure 1.1: Relation between the normalized production cost per chip of different size and the diameter of silicon wafers (Shimura,1989).

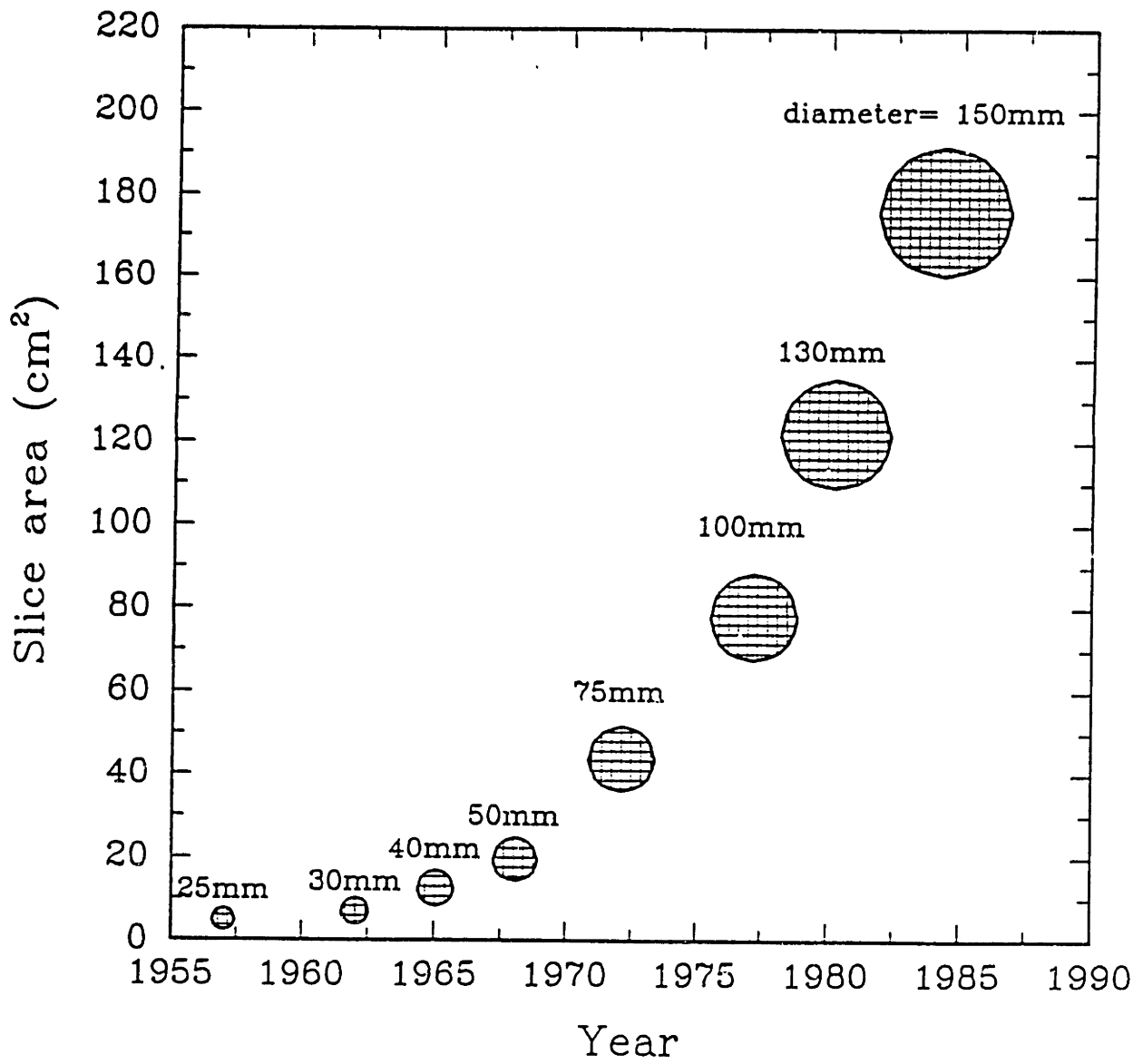


Figure 1.2: Size trends for crystal and wafer (Larrabee,1985).

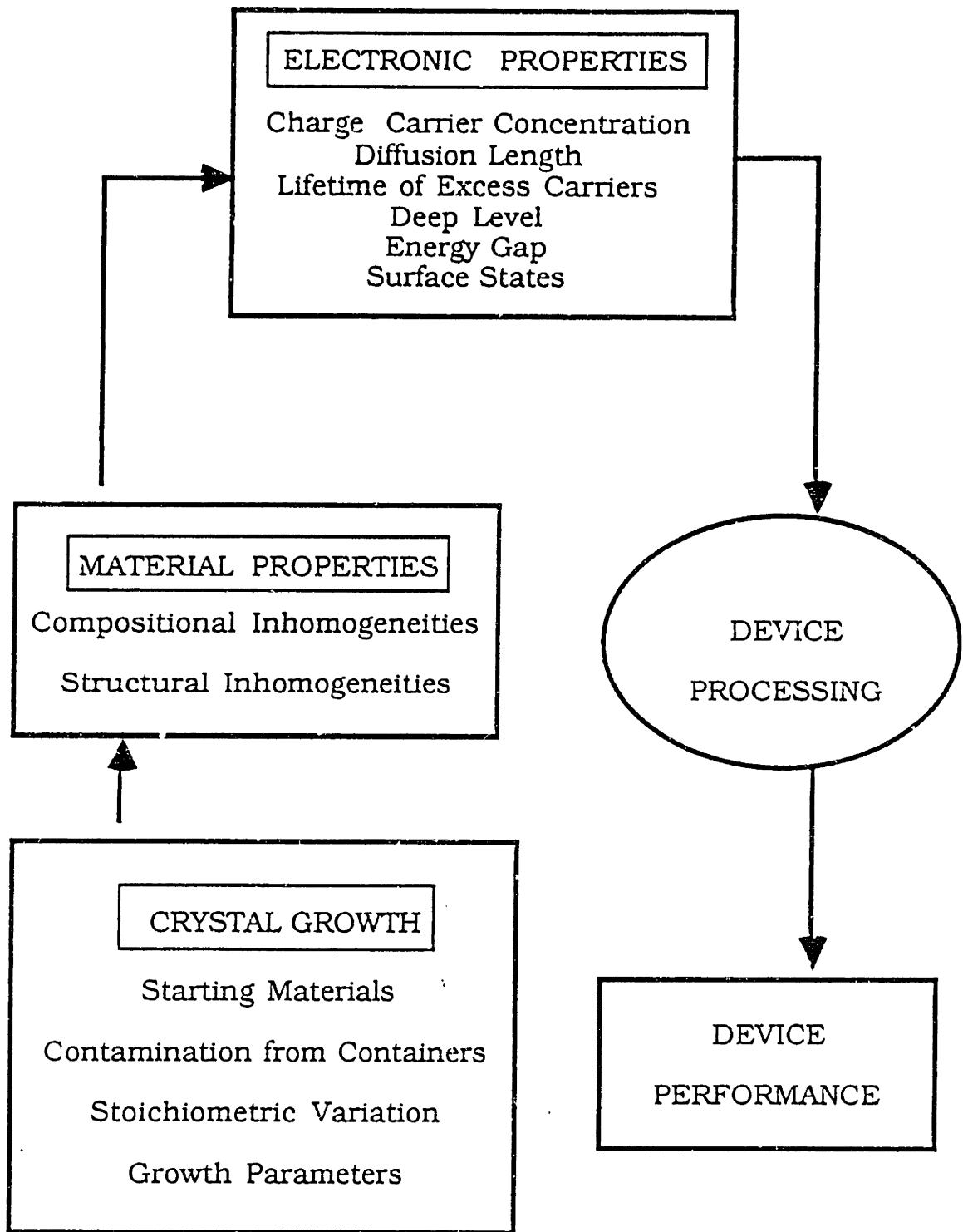


Figure 1.3: Factors affecting device performance along the path of device fabrication.

$\text{Hg}_{1-x}\text{Cd}_x\text{Te}$ crystals (Long, 1968). The compositional and structural homogeneities of large semiconductor crystals grown from the melt are strongly governed by coupled heat and mass transfer and melt flow during crystal growth. For typical semiconductor materials, the solute distribution in the melt, which ultimately determines the compositional homogeneity in the crystal through thermodynamic relation at the interface, is highly dependent on convection in the melt because of low solute diffusivities. Investigations of the mechanisms of convection in the melt and its influence on spatial segregation in the crystal has been the subject of vigorous research, both theoretically and experimentally, in the last decade. However, the effect of processing variables on structural inhomogeneity has not been developed so well as the effect of convection on compositional inhomogeneity because the link between microscopic variations in the structure of the crystal and macroscopic processing conditions is missing (Brown, 1988).

1.1.1 Semiconductor Materials

Since the invention of the transistor by Bardeen and Brattain at Bell Laboratories in 1947 and the first semiconductor integrated circuit (IC) by Kilby at Texas Instruments ten years later, several semiconductor materials have been developed for use in electronic and optoelectronic devices. Originally, germanium (Ge) was used as a semiconductor material for solid-state electronic devices (Teal, 1976). However, the narrow bandgap (0.66eV), which causes considerable leakage currents above 90 °C, and the inability to provide a stable passivation layer caused germanium to yield to silicon (Si) as the most popular semiconductor material. The ability of silicon to accommodate surface passivation by forming silicon dioxide enabled the basic technologies, including the process for doping and defining intricate patterns (Shimura, 1989). Silicon has other advantages including that it is entirely nontoxic and it is available at low cost, since Si is second abundant element on the earth next to oxygen. Electronic-grade silicon can be obtained at less than one-tenth the cost of germanium (Wolf and Tauber, 1986).

However, silicon is not an optimum choice in every respect. For example, compound semiconductors such as gallium arsenide (GaAs) has higher electron mobilities

than silicon, enabling reduced parasitic gate-source resistance and improved frequency response. As a result, gallium arsenide has advantages over silicon in conventional high-speed devices by a factor of 3–4 in speed (Dilorenzo, 1978). A more serious disadvantage of silicon is that it cannot be used in optoelectronic devices because of its indirect bandgap. Again, the direct bandgap of gallium arsenide makes it a useful material for light emitting devices. In spite of the several disadvantages of silicon, the impact of compound semiconductors has been limited to areas where the unique properties of compound semiconductors allow functions that cannot be performed by silicon. These areas include transferred electron devices, light-emitting diodes, lasers, and infrared detectors (Ghandhi, 1983).

Next to gallium arsenide, mercury cadmium telluride ($\text{Hg}_{1-x}\text{Cd}_x\text{Te}$) is one of the most thoroughly studied compound semiconductors. Its alloy system is being developed for many infrared detector applications because its properties are uniquely suited to both the detection of infrared radiation and the requirements for fabricating junction devices. Mercury telluride (HgTe) and cadmium telluride (CdTe) are completely miscible in all proportions and form a direct bandgap semiconductors, for which the spectral response of HgCdTe can be compositionally tuned between 0.8 and 50 μm by varying the mole fraction of CdTe to tailor a detector for optimum performance at a given wavelength (Lehoczky and Szofran, 1982).

From the theory of continuum thermoelasticity, dislocations in the crystal are believed to be created by thermal stress when its magnitude exceeds the critical resolved shear stress (CRSS) evaluated in the slip directions for the crystal (Tsivinsky, 1979). Since thermal stress is caused by the thermal gradient in the crystal, which is inversely proportional to thermal conductivity, CRSS and thermal conductivities play important roles in determining the level of difficulty for growing perfect crystal. Thermal conductivities of several semiconductor materials are plotted against the appropriate values of the critical resolved shear stress (CRSS) in Figure 1.4 to show the trend in the *degree of difficulty* of crystal growth. Semiconductor materials with low thermal conductivity and low CRSS are more difficult to grow because the driving force for dislocation generation,

represented by thermal gradient. is large and the resistance to dislocation formation, represented by CRSS, is small.

The modelling of crystal growth in multicomponent systems can be divided into dilute and nondilute systems. In dilute systems, like gallium-doped germanium (GaGe) or selenium-doped gallium arsenide (GaAs), the dopant concentration is small¹ enough to neglect the dependence of thermophysical properties on dopant concentration. This implies that the equilibrium distribution coefficient (k) and melting point temperature (T_m) are constant and that convection driven by density gradients caused by composition variation can be neglected. On the contrary, in nondilute systems thermophysical properties are strongly dependent on the composition. Examples of nondilute systems are the 5-atom% silicon in germanium grown at the Centre d'Etudes Nucléaires de Grenoble (Rouzaud *et al.*, 1985), lead-tin telluride with tin-lead ratios as high as 3:7 on a mole basis, grown by Bourret at MIT (Bourret *et al.*, 1984), and mercury cadmium telluride with mercury-cadmium ratio of 8:2, grown by Lehoczky's group (Szofran and Lehoczky, 1981). In these systems, the variation of melting point temperature and equilibrium distribution coefficient with composition must be accounted for quantitative numerical modelling.

1.1.2 Melt Crystal Growth Systems

Growth methods used for the production of semiconductor materials are classified into melt growth, vapor growth, solution growth and solid growth, according to the phase adjacent to the growing crystal. Small growth rates are typical of vapor and solution growth, which are mainly used for the deposition of thin film to the substrate material. The crystals grown by solid growth technique show low purity and coarse crystalline perfection and are not appropriate for substrate material. Only the melt growth method is currently used for the production of substrate material. Qualitative characteristics of each growth method are listed in Table 1.3.

¹0(10⁻⁵) for the case of gallium-doped germanium (Adornato and Brown, 1987a)

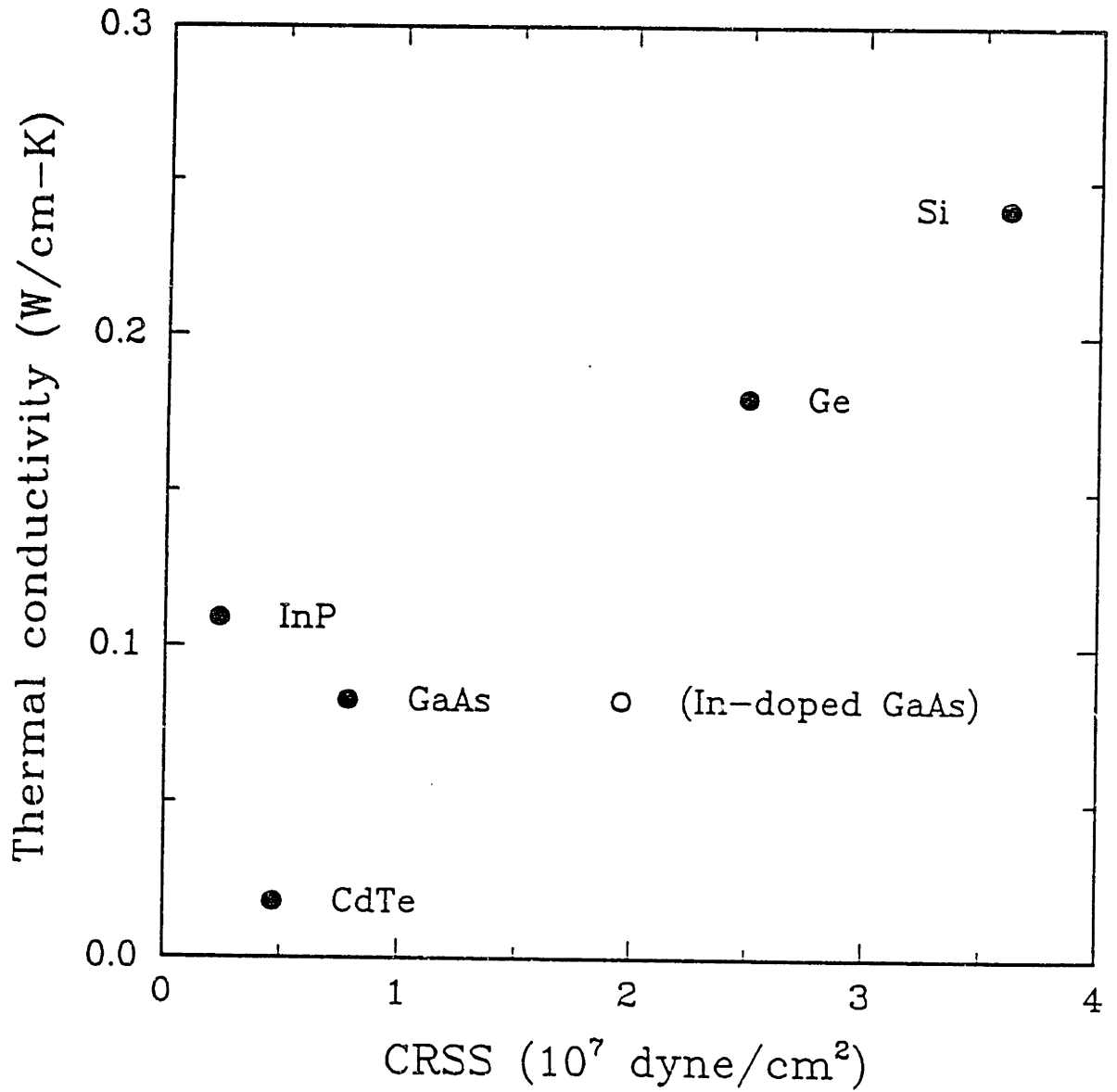


Figure 1.4: Thermal conductivities and critical resolved shear stress of common semiconductor materials (Brown, 1988).

Method	Purity	Perfection	Growth rate
<u>Melt</u>			
Czochralski	Good	Excellent	Very large
Bridgman	Good	Fair	Large
Floating zone	Excellent	Good	Very large
<u>Solution</u>			
All types ¹	Good ²	Good	Small
<u>Vapor</u>			
Sublimation	Good	Good	Small
CVD ³	Fair	Good	Small
Sputtering	Fair	Fair	Very small
<u>Solid</u>			
All types	Bad	Bad	Large

¹ Including hydrothermal growth

² Depends on solvent

³ Chemical Vapor Deposition

Table 1.3: Characteristics of crystals grown by various methods (Brice, 1986).

Examples of melt growth methods are the Bridgman method, the floating zone method (FZ) and the Czochralski method (CZ); each are shown schematically in Figure 1.5. They represent normal freezing technique, zone melting and crystal pulling, according to the classification of Flemings (1974). Alternatively, these methods can be classified into confined and meniscus-defined crystal systems, depending on the presence of a melt/ambient surface (Brown, 1988).

The vertical Bridgman growth system has been studied most intensively, either by theoretical analyses or by experiments, because the simple furnace system and the confined growth environment allows the precise control of thermal field necessary for solidification. We will focus on this system to analyze the convection in the melt and its effect on the segregation in the crystal.

The vertical Bridgman growth or Bridgman-Stockbarger method was named after Bridgman, who grew metal crystals with this variation of directional solidification (Bridgman, 1925). The furnace is composed of isothermal hot and cold zones separated by an insulated region designed to create a constant axial temperature gradient in the melt and crystal adjacent to the solidification interface. The charge and the single crystal seed are loaded into a closed ampoule, melted and resolidified by translating the furnace temperature profile relative to the ampoule: either by furnace or ampoule motion. Translation rates are mostly in the range of 1 to 30 mm/h to prevent constitutional supercooling (Brice, 1986). The use of an ampoule permits the shaping of the crystal and the sealing of the growing system.

The vertical Bridgman method can be operated in configurations that are *stabilizing* or *destabilizing* with respect to thermal convection depending on the position of melt and crystal relative to the direction of gravity. The stabilizing mode (bottom seeding) refers to the configuration of melt above crystal and the destabilizing mode (top seeding) has melt below the crystal. The stabilizing configuration has been the focus of our research because it allows steady, axisymmetric convection and is the most used system for confined crystal growth.

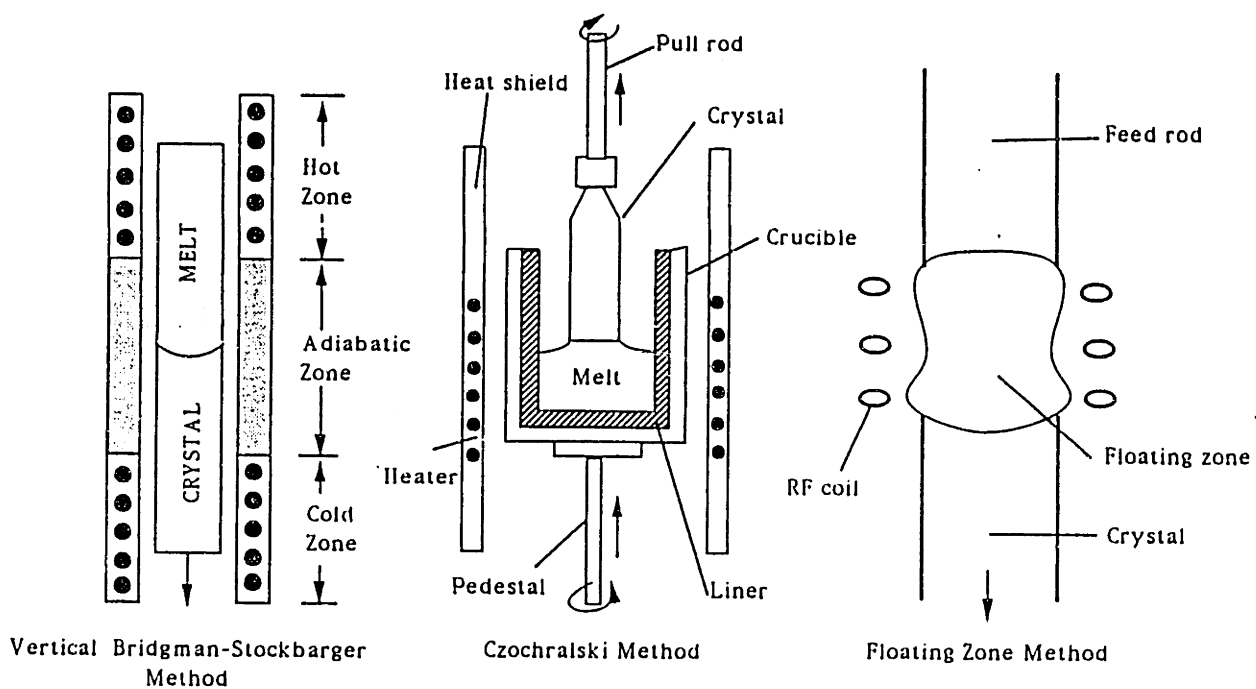


Figure 1.5: Commonly used systems for melt crystal growth of electronic materials

The vertical Bridgman method has received recent attentions for the growth of III-V (GaAs, InP) and II-VI (CdTe, HgCdTe) electronic and optoelectronic materials. These materials are not easily grown by the Czochralski method because the high thermal stress that develops during the Czochralski growth leads to excessive defects in the crystal or the high vapor pressure of the melt requires confinement to maintain stoichiometry. The confinement in a crucible does not necessarily lead to the high thermal stress in the crystal because new atomic layer created on a planar solid/liquid interface is not more constrained by crucible walls than by a radial temperature gradient (Horowitz and Horowitz, 1989). Previous works show that GaP, InP and GaAs crystals of better quality can be produced by the vertical Bridgman process compared to the Czochralski method (Gault *et al.*, 1986; Monberg *et al.*, 1987, 1988; Clemans and Conway, 1988), if a planar interface is maintained during the growth. To minimize the effect of crucible, crucible material with a thermal conductivity at least comparable with or lower than that of growing material is desirable. To reduce the strain and to facilitate the removal of crystal after solidification, the crucible material should be chosen so that the crystal material does not adhere to the crucible.

If the transport of heat is controlled by reducing heater power in time instead of translating ampoule through furnace, the technique is specially referred to as the *gradient freeze method*. Temperature control is easier with this technique by using multizone heater in the furnace. Temperature gradients in the range of 0.2 to 0.4 °C/cm can be reproducibly generated leading to very limited convective flow, negligible stress and strong control over the solid/liquid interface shape (Parsey and Thiel, 1987).

A variant of the vertical Bridgman growth system with horizontal configuration is called the *horizontal Bridgman technique*. Crystal is grown in an open ampoule or boat which adds melt/ambient meniscus to the growth system. The open configuration facilitates the control of the vapor pressure of volatile component (for example, arsenic in GaAs growth) necessary to maintain the stoichiometry of the melt. Surface tension force at the free surface is important to the melt convection in the space processing because surface tension is independent of the gravity level.

1.2 Transport Phenomena in Directional Solidification

1.2.1 Basic Transport Processes

In crystal growth, the transport of momentum and species in the melt and transport of heat in the melt, crystal, crucible and furnace are complicated by the phase change at the solidification front. When convection in the melt is unimportant, as in the idealized case of diffusion-controlled growth, profiles of passive scalars (temperature, solute concentration) in the directional solidification system can be represented schematically as shown in Figure 1.6.

Temperature profile in the melt and crystal is almost linear except that the gradient is changed at the interface due to different thermal conductivities of each phase. However, several factors determine the detailed temperature field, such as thermophysical properties of various materials comprising the system, growth rate through latent heat release at the solidification front and the design of heat delivery system from furnace to melt and crystal through ampoule. In a confined growth system, convection in the melt is caused by the translation of the ampoule through the furnace and by buoyancy force due to temperature and concentration gradient. The details of the convection pattern is determined by heat transfer in the system and by the orientation of the melt and crystal with respect to gravity. More on the convection in the melt is discussed in the later Section.

The mechanism of heat transfer in each phase are: (i) conduction and convection in the melt, (ii) conduction in the solid, and (iii) conduction, convection and radiation between furnace and ampoule. The goal of design of heat delivery systems in melt crystal growth is minimizing the convective effect to accomplish diffusion-controlled growth for compositional homogeneity and growing the crystal with flat interface for structural homogeneity. This Section focuses on species transport for solutes that form ideal solutions in the melt and single-phase crystalline solids.

The transport of solute is governed by convection and diffusion in the melt and

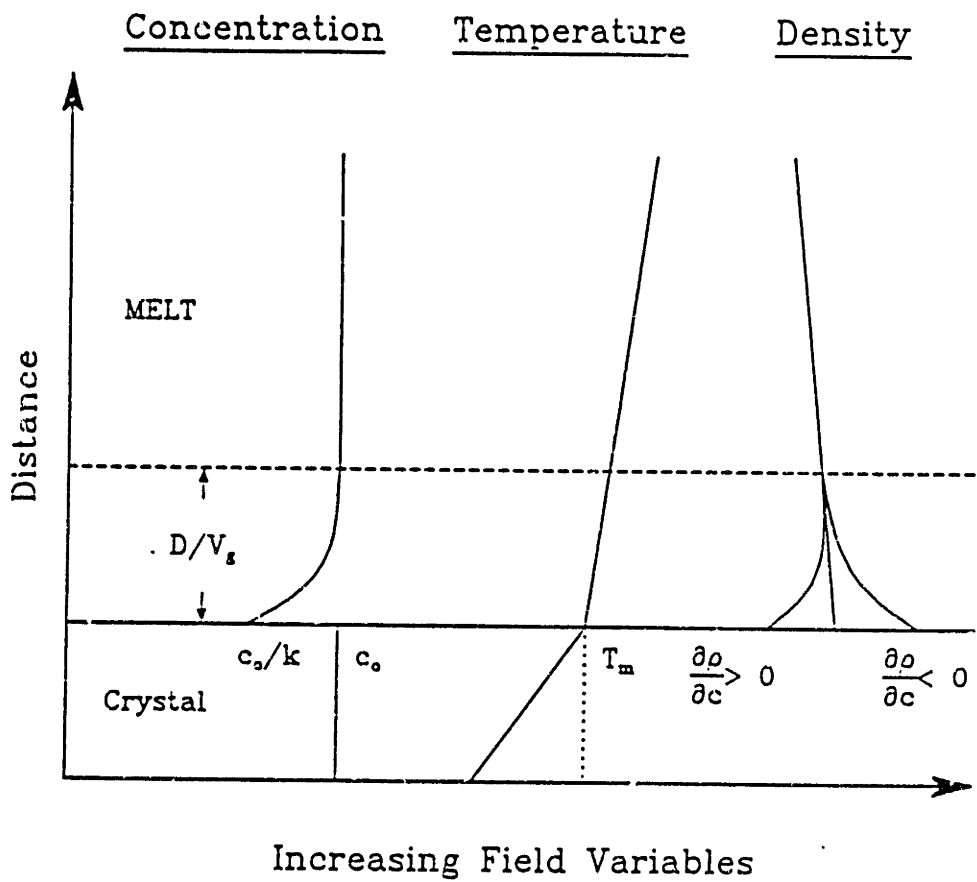


Figure 1.6: Temperature, solute concentration, and density profile in one-dimensional directional solidification of a binary alloy.

the boundary condition at the interface which is characteristic of crystal growth. This boundary condition originates from the equilibrium relationship of solute across the interface, which is represented by equilibrium distribution coefficient, k . Equilibrium distribution coefficient is determined from the phase diagram where the liquidus T_l and solidus T_s temperature is described as a function of concentration. Then, the solute composition of melt and solid in equilibrium are related by

$$\bar{c}_l = \bar{c}_s / k \quad (1.1)$$

The phase diagram with constant k are shown in Figure 1.7 for the cases of k greater and less than unity. (The symbol tilde (\sim) is used throughout this thesis to denote dimensional variables; the absence of it corresponds to a dimensionless formulation.)

The behaviour of solute transport is illustrated by the limiting case of diffusion-controlled growth where the effect of convection is negligible (Tiller *et al.*, 1953). If the crystal is sufficiently long, steady-state is reached and the concentration far from the interface remains nearly constant as c_o . With the coordinate system fixed to the moving interface, the solute transport in the melt is given by the differential equation as

$$D \frac{\partial^2 \bar{c}}{\partial \bar{z}^2} + V_g \frac{\partial \bar{c}}{\partial \bar{z}} = 0 \quad (1.2)$$

where \bar{z} is distance from interface, D is diffusion coefficient of solute in the melt and V_g is rate of movement of interface. The requirement of solute conservation at the interface provides the boundary condition for Eq. (1.2):

$$-D \left(\frac{\partial \bar{c}}{\partial \bar{z}} \right)_{\bar{z}=0} = V_g (1 - k) \bar{c} |_{\bar{z}=0} \quad (1.3)$$

where k is the equilibrium distribution coefficient defined by Eq. (1.1). The solution to Eq. (1.2) with constant far-field concentration c_o is

$$\bar{c}(\bar{z}) = c_o \left[1 + \frac{1 - k}{k} \exp(-V_g \bar{z} / D) \right] \quad (1.4)$$

Exponential solute boundary layer is predicted due to the rejection ($k < 1$) or incorporation ($k > 1$) of solute at the interface. The characteristic e -folding distance is on

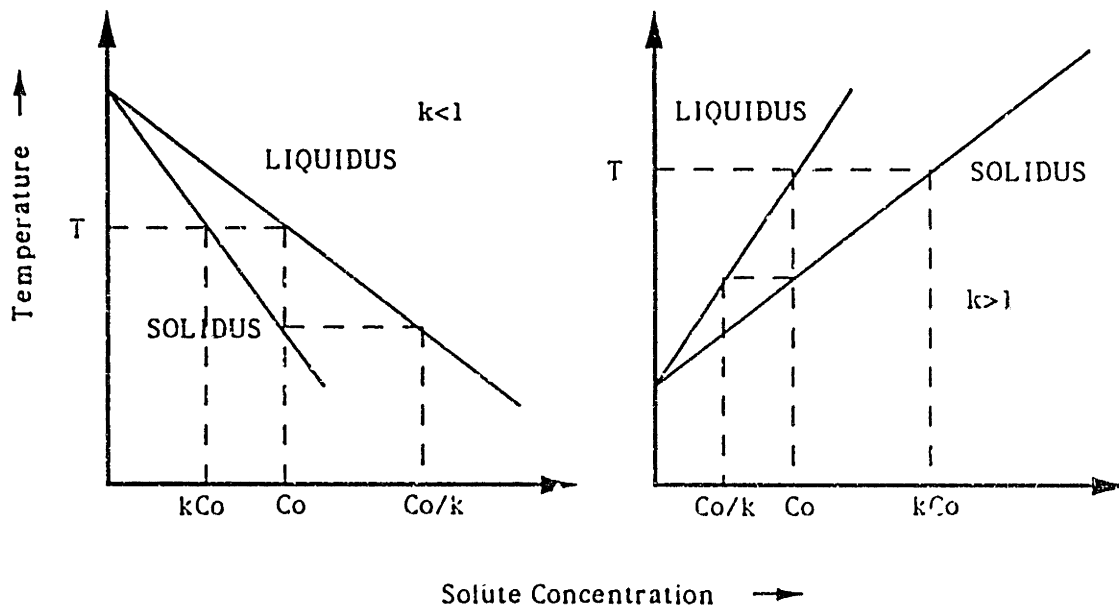


Figure 1.7: Idealized phase diagram for binary alloys.

the order of D/V_g and depends only on D and V_g . Equation (1.4) applies in many real cases of single crystal growth even in the presence of some convection (Flemings, 1974).

Analysis of transients in directional solidification is complicated by the interaction between heat transfer, the melt/crystal interface shape, and solute transport. We examine two limiting case of no mixing and complete mixing in the melt with respect to the efficiency of mixing. In these two cases, the diffusion in the crystal is neglected because diffusion of solute in the crystal is much slower than in the melt.

No Mixing in the Melt

Smith *et al.* (1955) analyzed the one-dimensional, diffusion-controlled growth without convection in the melt. The growth rate is assumed to be equal to the ampoule translation rate because the thermal diffusion is much faster than solute diffusion.

Conservation of solute in the melt leads to the following equation which is the same as Eq. (1.2) except the accumulation term on the left hand side.

$$\frac{\partial \bar{c}}{\partial \bar{t}} = D \frac{\partial^2 \bar{c}}{\partial \bar{z}^2} + V_g \frac{\partial \bar{c}}{\partial \bar{z}} \quad (1.5)$$

where \bar{z} is the coordinate system along crystal, with $\bar{z} = 0$ at melt/solid interface. The diffusivity of solute in the melt is D and V_g is the growth velocity. This equation cannot be solved analytically for the whole domain of melt with finite length. We focus on the solution for the initial transient. Smith *et al.* (1955) introduced the infinite-melt assumption to solve the initial transient, with following boundary conditions:

$$\bar{c} = c_o \quad \text{at } \bar{z} = \infty \quad \text{for all } \bar{t}, \quad (1.6)$$

$$\bar{c} = c_o \quad \text{at } \bar{t} = 0 \quad \text{for all } \bar{z} > 0, \quad (1.7)$$

$$\frac{\partial \bar{c}}{\partial \bar{z}} + \frac{V_g}{D}(1 - k)\bar{c} = 0 \quad \text{at } \bar{z} = 0 \quad \text{for all } \bar{t} \quad (1.8)$$

The boundary condition given by Eq. (1.8) expresses the conservation of solute across

the interface at all times. They derived the concentration profile in the crystal as

$$\frac{\bar{c}_s(\bar{x})}{c_o} = \frac{1}{2} \left\{ 1 + \operatorname{erf} \left(\frac{\sqrt{(V_g/D)\bar{x}}}{2} \right) \right. \quad (1.9)$$

$$\left. + (2k - 1) \exp[-k(1 - k)(V_g/D)\bar{x}] \operatorname{erfc} \left(\frac{(2k - 1)}{2} \sqrt{(V_g/D)\bar{x}} \right) \right\}$$

where \bar{x} ($= V_g \bar{t}$) is a distance solidified in the crystal. For small values of k , this reduces to (Tiller *et al.*, 1953; Pohl, 1954)

$$\bar{c}_s = c_o \{ k + (1 - k) \{ 1 - \exp[-k(V_g/D)\bar{x}] \} \} \quad (1.10)$$

Concentration profile in the crystal are plotted in Figure 1.8 according to Eq. (1.9) for several values of k . Solute concentration in the crystal approaches gradually to its steady-state value ($\bar{c}_s = c_o$) as solidification proceeds. The distance \bar{x} to reach the steady-state value depends on D/V_g and k . From Eq. (1.10), the characteristic distance for the length of this transient is $D/V_g k$. This limiting case was successfully verified to be valid in the microgravity environment (Witt *et al.*, 1978) and in the presence of vertical magnetic field (Matthiesen *et al.*, 1987).

Recently, Verhoeven *et al.* (1988) numerically solved the same equation set (Eqs. (1.5)–(1.8)). They determined the ranges of growth velocity and equilibrium distribution coefficient for which the transient solution obtained by Smith *et al.* (1955) is valid.

Complete Mixing in the Melt

When the convection in the melt is intense enough to provide a complete mixing, the solute concentration is assumed to be uniform throughout the melt. In the solidification of melt in an ampoule with length L and initial composition c_o , solute conservation equation in the melt is written as

$$d[(L - \bar{z})\bar{c}_l] + \bar{c}_s d\bar{z} = 0 \quad (1.11)$$

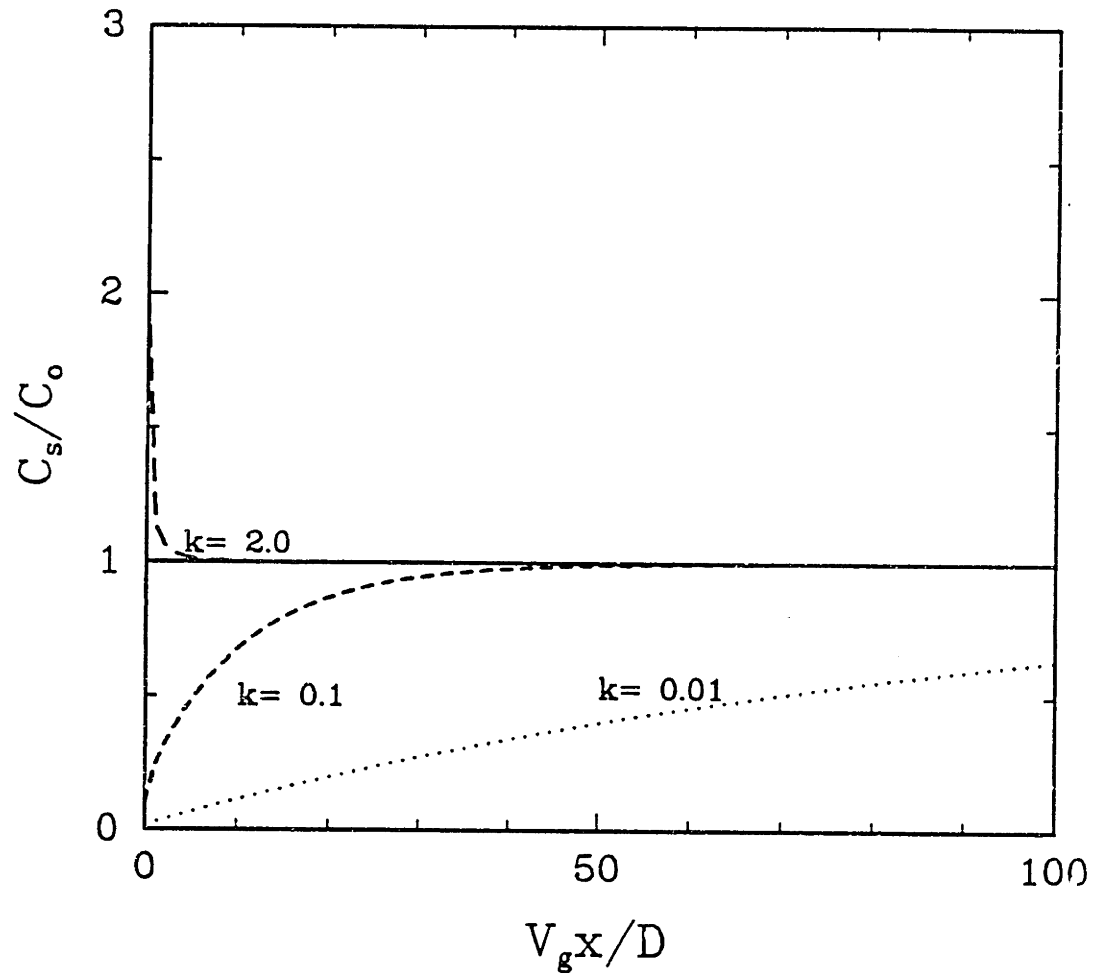


Figure 1.8: Solute composition profile along the crystal without convection in the melt.

where \bar{z} is a length of crystal solidified. In this equation, the amount of solute incorporated to the crystal balances the change of concentration in the remaining melt. With the definition of $\bar{c}_l = \bar{c}_s/k$, Eq. (1.11) can be rearranged to give

$$\frac{d\bar{c}_s}{d\bar{z}} = \frac{(1-k)\bar{c}_s}{L-\bar{z}} \quad (1.12)$$

Integrating Eq. (1.12) from $\bar{z} = 0$ to \bar{z} with initial condition of $\bar{c}_s = kc_o$ gives

$$\bar{c}_s(\bar{z}) = kc_o(1-f)^{(k-1)} \quad (1.13)$$

where $f = \bar{z}/L$ is a fraction solidified. This problem has been analyzed by Gulliver (1922), Scheil (1942) and Phann (1952), leading to the basically same equation as Eq. (1.13), which is termed the *Scheil equation*, or the *nonequilibrium lever rule*. Segregation profiles computed with Eq. (1.13) for several values of k are plotted in Figure 1.9 as a function of fraction solidified. This equation closely describes solute redistribution in the crystal under a wide range of experimental conditions on earth (Witt *et al.*, 1978; Wang, 1984).

In the growth of nondilute alloy, the melting point temperature depends on the local concentration at the interface following the liquidus curve in the phase diagram. Then the solidification interface is coupled to the solute and temperature field leading to the longer initial transient. This problem has been analyzed numerically for the one dimensional system (Bourret *et al.*, 1985; Derby and Brown, 1986).

1.2.2 Melt Convection

Thermosolutal Convection

The typical high temperature environment for melt growth of semiconductor materials leads to thermal buoyancy driven convection in earth-bound system. For the growth of nondilute alloy system, convection is driven by the density variations due to solute gradient in the melt.

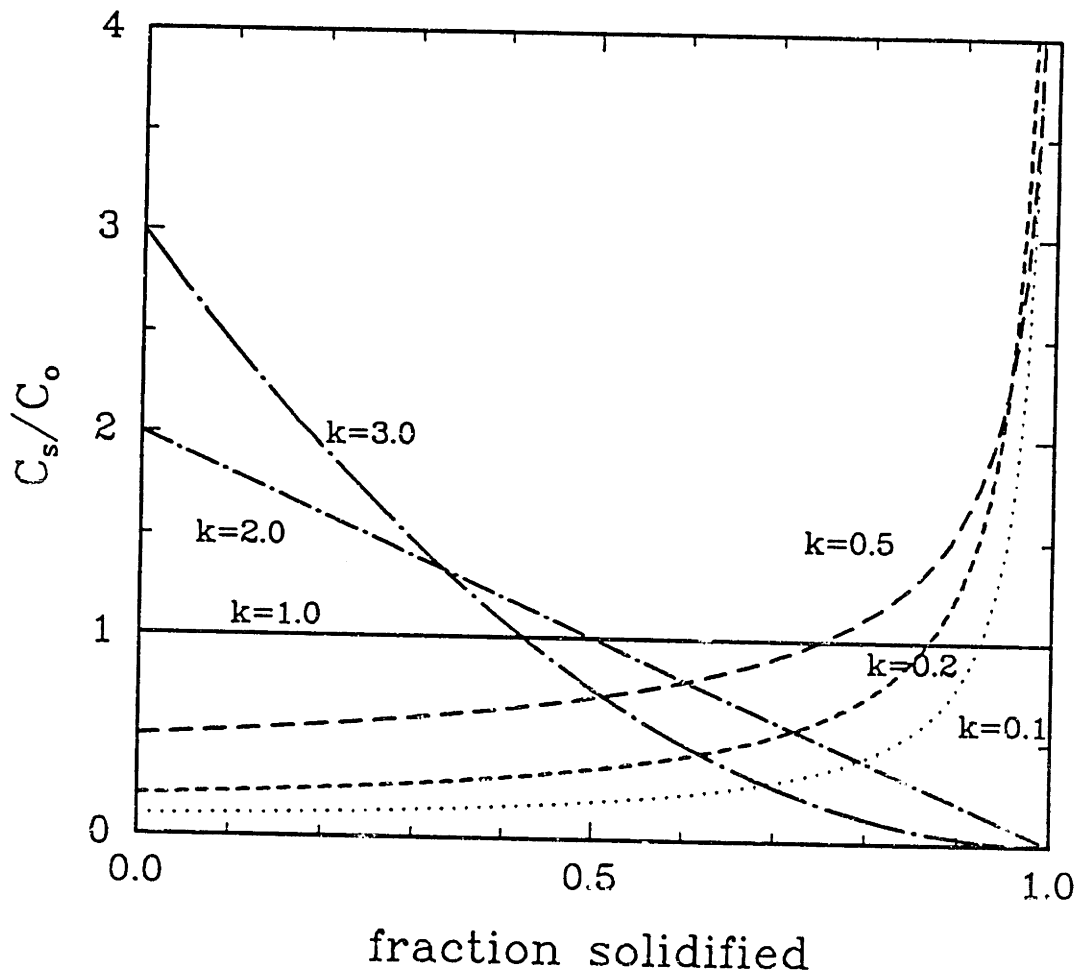


Figure 1.9: Solute composition profile along the crystal with complete mixing in the melt.

Thermal convection in directional solidification can be divided into stable and unstable configurations according to the direction of temperature gradient. These configurations correspond to the bottom seeding and top seeding, respectively, which differ in the location of seed crystal with respect to the melt and determine the direction of crystal growth. In a stable growth configuration, density in the melt is decreasing with the height, stabilizing the thermal convection. When the temperature gradient is perfectly aligned with gravity, convection is not caused by the thermal field. In an unstable growth configuration, buoyancy-driven convection begins at a critical value of thermal Rayleigh number as an instability of a static fluid layer heated from below (Chandrasekhar, 1961; Drazin and Reid, 1981).

In an unstable configuration, convection is characterized by three dimensionless numbers: the thermal Rayleigh number Ra_t , Prandtl number Pr and aspect ratio (h/d) (The definitions of dimensionless groups are in Chapter 2). Series of flow transitions from static fluid to turbulence through steady convection and unsteady periodic convection can be described in three-dimensional coordinate system, as shown in Figure 1.10. In the plane of Ra_t - Pr , the experimental results of Krishnamurti(1973) are drawn in the limit of small aspect ratio ($h/d \ll 1$). For the growth of specific material, Prandtl number is constant and the course of crystal growth run can be represented in a plane Ra_t versus (h/d).

In the typical crystal growth, temperature gradient in the melt is not unidirectional due to the complex heat transfer mechanism, which makes it difficult to interpret the convection in the melt in terms of simple one dimensional model. This limitation leads to the two-Rayleigh-number model of convection suggested by Müller *et al.* (1987) which allows the lateral heat exchange in the melt. In this model, additional parameter of wall Rayleigh number, Ra_w , similar to a Rayleigh number based on lateral temperature gradient (Gill, 1974; Hurle *et al.*, 1974) was introduced to account for the lateral component of driving force. The model system is shown in Figure 1.11(a), where T_a (top temperature), T_b (bottom temperature) and T_w (wall temperature) are constant. Thermal Rayleigh number, Ra_t , and wall Rayleigh number, Ra_w , are defined, based on ($T_b - T_a$)

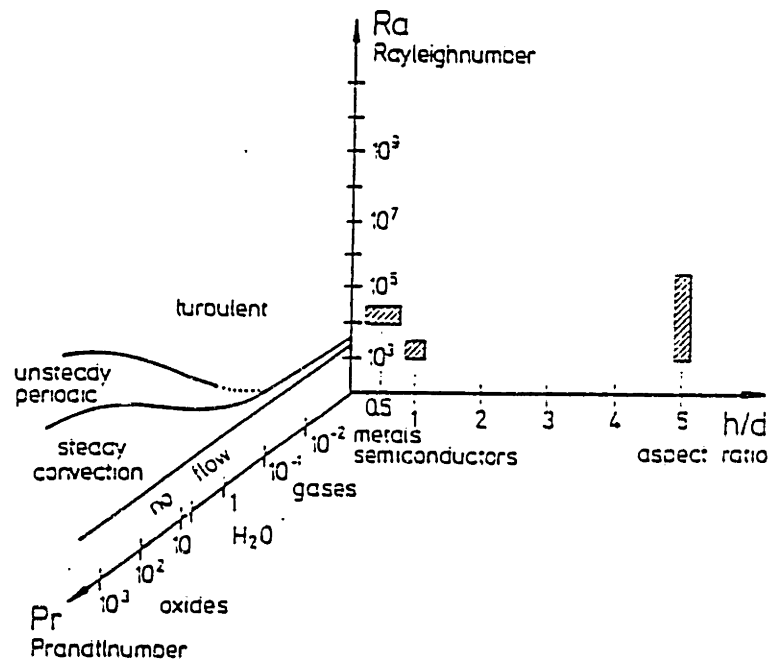


Figure 1.10: Three-dimensional scheme for representation of flow states.

and $(T_w - (T_a + T_b)/2)$ respectively as

$$Ra_t = \frac{g\beta_t h^3 (T_b - T_a)}{\alpha\nu} \quad (1.14)$$

$$Ra_w = \frac{g\beta_t 2h^4 \{T_w - (T_a + T_b)/2\}/d}{\alpha\nu} \quad (1.15)$$

Depending on the relative magnitudes and signs of Ra_t and Ra_w , several different crystal growth techniques can be represented in Ra_t - Ra_w plane, as shown in Figure 1.11(b). The limitation of this model in representing the flow state with (Ra_t, Ra_w) is that it does not consider the temperature variations along the wall, which occur in practice. Several reviews have been published describing the thermal buoyancy-driven convection in general (Gebhart *et al.*, 1988) and in crystal growth systems (Hurle, 1972; Carruthers, 1977; Pimputkar and Ostrach, 1981; Langlois, 1985).

In the Bridgman growth of a pure component melt or dilute binary alloy with the stabilizing configuration, convection is driven by the radial temperature gradients caused by the different thermal conductivities of the melt, crystal and ampoule near the interface and by other thermal imperfections in the system. The calculations of Chang and Brown (1983b) demonstrated the strong effect of the difference in thermal conductivities between melt and crystal on the direction and intensity of thermal convection in the melt. The analysis of convection and segregation in the vertical Bridgman system by Adornato and Brown (1987a) included heat transfer through the ampoule in calculation of the temperature and showed the generic structure for the axisymmetric flow driven by radial temperature gradients in the melt. This flow structure is summarized below.

The flow field is composed of two distinct toroidal roll cells stacked axially in the ampoule. These cells are driven by different sets of radial temperature gradients. Near the melt/crystal interface, the mismatch in the thermal conductivities of the melt, crystal and ampoule drives flow which is up along the center of the ampoule when the solidification interface is convex with respect to the melt, as it is drawn in Figure 1.12. Large radial temperature gradients are also caused by the mismatch in thermal boundary conditions at the junction of the hot zone with the insulation region of the furnace. These

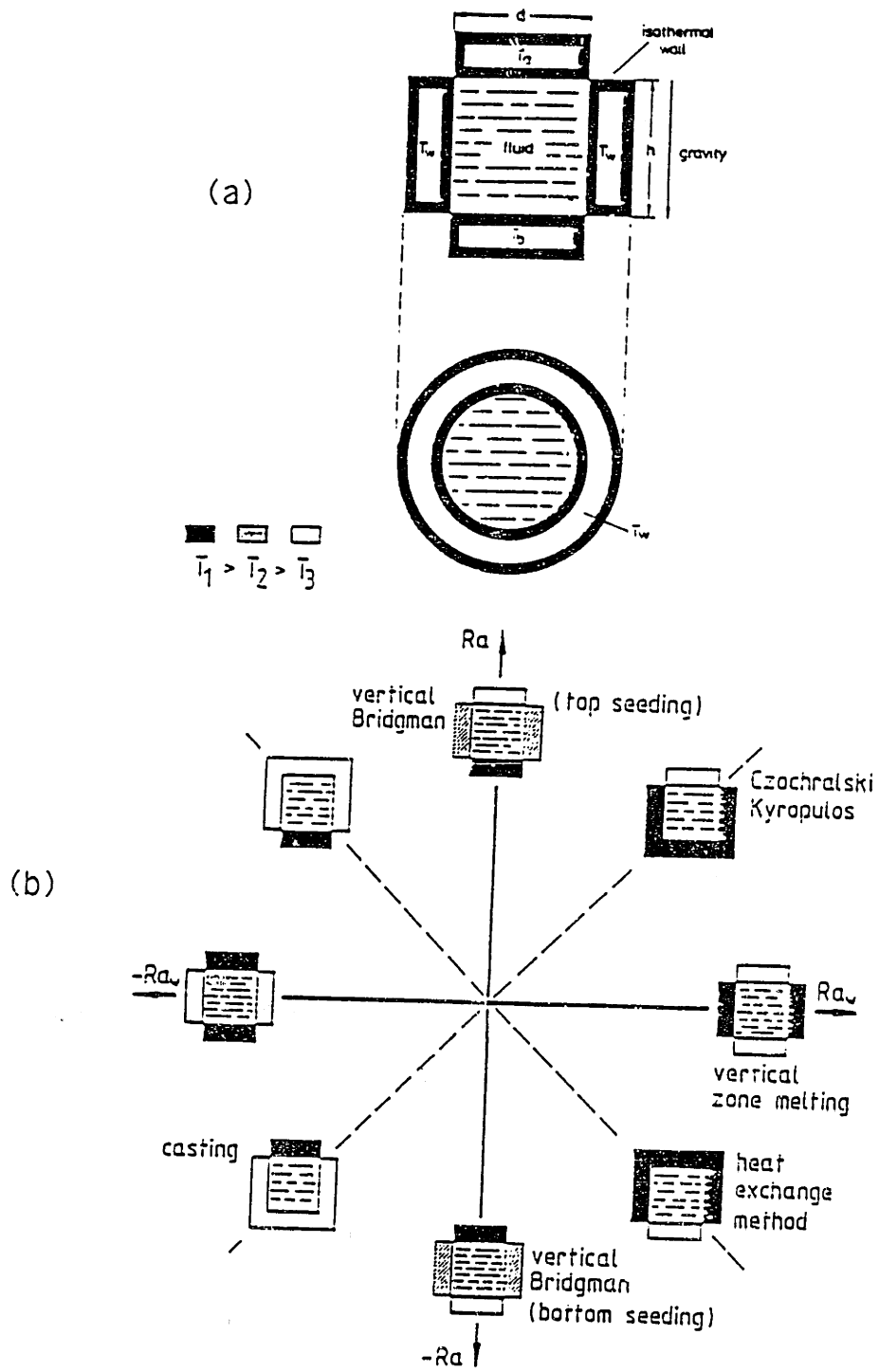


Figure 1.11: (a) Model configuration with isothermal top, bottom and wall temperature. (b) Types of different crystal growth techniques according to the model configuration.

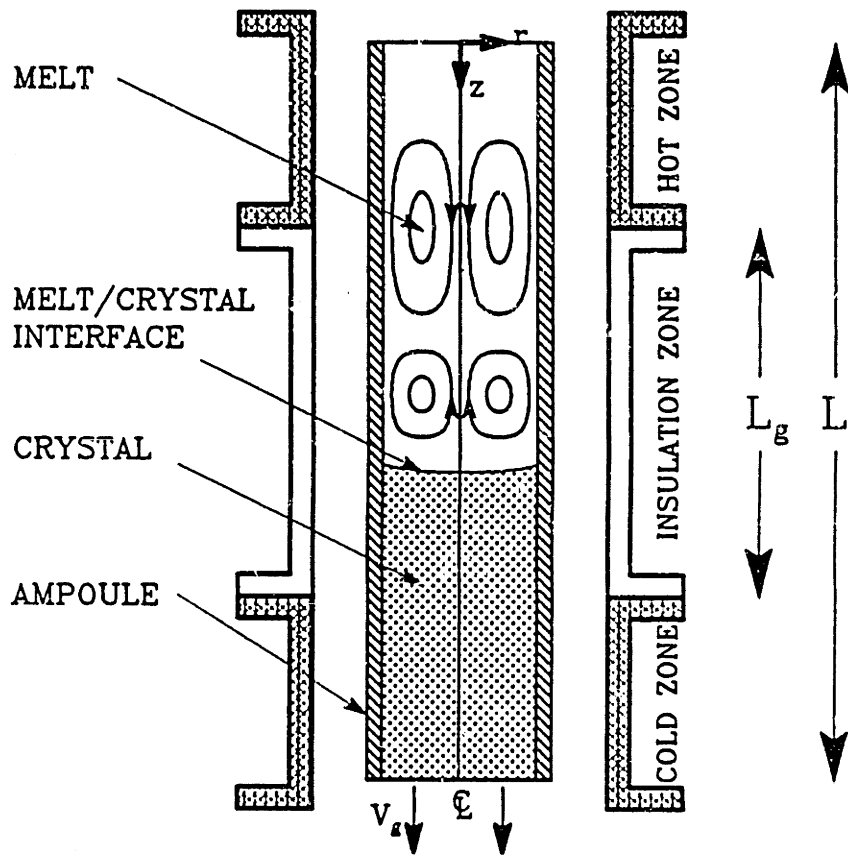


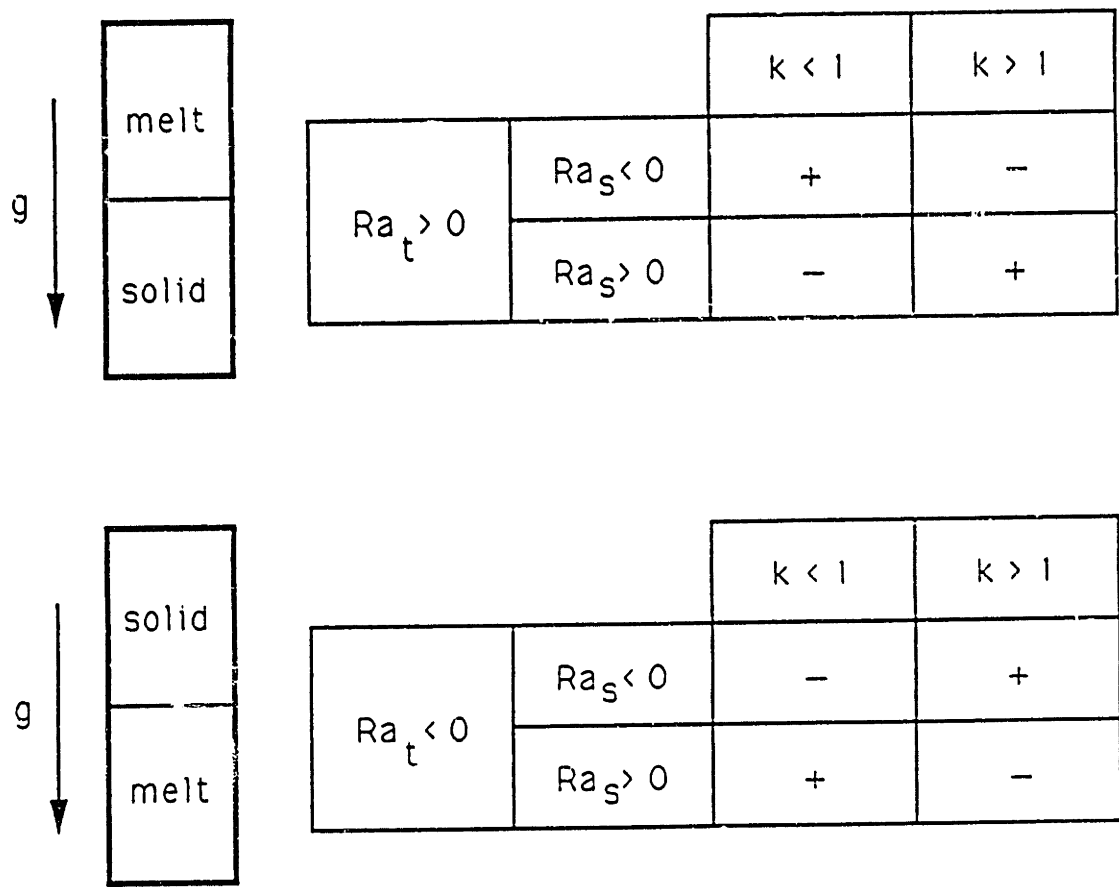
Figure 1.12: Schematic of prototypical vertical Bridgman crystal growth system.

gradients lead to an upper toroidal cell in which melt moves upward along the sidewall and down along the axis of the ampoule. This flow cell is not present in directional solidification systems where the axial temperature gradient is established by tailoring the heater design in such a way that the radial temperature gradient is of the same sign all along the ampoule.

When a fluid layer with more than one diffusing components is perturbed, flow instabilities may arise even when the total density of the fluid decreases with height (Turner, 1973; Stern, 1960). Motions due to such instabilities are variously known as multicomponent convection, double-diffusive convection, thermohaline convection or thermosolutal convection. The basic physical aspect of this type of convection (Turner, 1973, 1985) and its relevance to crystal growing process (Hurle, 1983; Brown, 1987) have been extensively reviewed. In thermosolutal convection during the crystal growth, solute field stabilizes or destabilizes the thermal buoyancy-driven convection depending on the sign of solutal Rayleigh number and the magnitude of equilibrium distribution coefficient with respect to one. The relationship is summarized in Figure 1.13, where Ra_s is based on $\Delta T (= T_{top} - T_{bottom})$ and the sign of Ra_s is the same as the sign of the coefficient of solutal expansion, β_s . Examples of stabilizing solute field in thermally stable configuration (melt above solid) are systems of GeSi and HgCdTe, for which k is greater than 1 and Ra_s is negative. Destabilizing solute field is observed in the system of PbSn, for which k is less than 1 and Ra_s is negative. In the pseudo-binary representation of HgCdTe, the less dense component CdTe is preferentially partitioned into the crystal so that the axial density gradient is stably stratified when the crystal is below the melt. The diffusion-controlled solute transport observed along the growth axis (Lehoczky and Szofran, 1982) is consistent with the idea that this density profile retards buoyancy-driven convection.

Effects of Melt Convection on the Interface Morphology

For low Prandtl number melt of semiconductor materials, solute field is more affected by the flow field near the interface, leading to the local variations in the conditions which



+ : Solute field is destabilizing.
 - : Solute field is stabilizing.

Figure 1.13: The effect of Ra_s and k on the role of solute field in thermosolutal convection.

determine the morphological stability of the interface. The first work which quantified the effect of solute field on the interface shape was done by Chalmers and coworkers (Rutter and Chalmers, 1953; Tiller *et al.*, 1953) in investigating the formation of cellular structure at the interface during normal freezing and zone melting. They termed the phenomena which result in the cellular structure as *constitutional supercooling* with the word *constitutional* indicating that supercooling arises from a change in composition, not temperature. Since then, the morphological stability of the melt/crystal interface during the directional solidification of a binary alloy at constant velocity was treated by Mullins and Sekerka (1963, 1964; Sekerka, 1965, 1967, 1968) in the absence of fluid flow in the melt. The topic of morphological instability and dendrite formation is well documented in the book by Kurz and Fisher (1984).

Experimentally, Burden *et al.* (1973) have reported macroscopic changes in the interface shape due to convective flow induced by density differences during directional solidification. They controlled the flow field by changing the composition of Al-Cu alloys (0.5 to 10 wt% Cu in Al) for the same growth rate (8.3×10^{-4} cm/sec) and temperature gradient (60°C/cm). Their result is shown in Figure 1.14 as a function of Al-Cu composition. Chang and Wilcox (1974a) have observed the breakdown of solid/liquid interface as affected by radial heat flow and convection pattern during zone melting of naphthalene. McCartney and Hunt (1981) have shown that by selecting a composition of the ternary Al-Mg-Si system to minimize the dependence of liquid density on composition, the interface curvature effects could be minimized due to the reduced level of convection. For dilute binary alloy of Ga-doped Ge, thermal convection driven hardly influences the morphological stability (Holmes and Gatos, 1981a).

Only recently, rigorous analysis using linear stability analysis (Coriell and Sekerka, 1981; Hurle *et al.*, 1982; Coriell *et al.*, 1984) or weakly nonlinear analysis (Jenkins, 1985) have dealt with the effect of convection on the morphological stability of binary alloys. Review for the interaction of flow with the interface can be available elsewhere (Glicksman *et al.*, 1986).

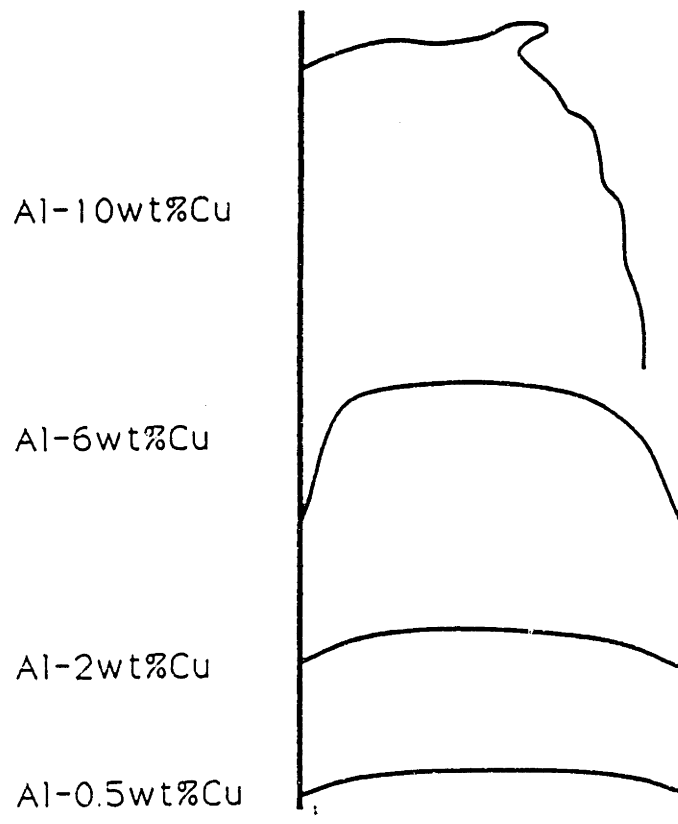


Figure 1.14: The variation of macroscopic interface shape with composition (Burden *et al.*, 1973).

Reduction of Melt Convection

Growth with the unidirectional convection is most desirable because of the axial uniformity of crystal that results when no mixing is present. These conditions are not easily achieved in practice and several attempts have been made to reduce the convection level, including the improvement of furnace design, the growth in a low gravity environment and the application of vertical magnetic field to the growth system. Solutal effect in the growth of a nondilute alloy can be advantageous in achieving the unidirectional convection by the stabilizing density gradient which solute field provides.

Improved design or operation In principle, the vertically stabilizing Bridgman method with bottom seeding can minimize convection in the melt, because the axial temperature gradient in the system does not drive the thermal convection. In the real system, radial temperature gradients exist because of the thermal conductivity differences between melt, crystal and ampoule and other thermal imperfections in the crystal growth system. This radial temperature gradients cause instability in the flow field and drive the thermal convection in the melt. The requirement of pure axial temperature gradient in the vertical Bridgman growth system for the minimum convection and the flat interface could not be fulfilled in the past as discussed by Wang *et al.* (1984). Müller (1984) has reported the success in obtaining a flat interface and diffusion-controlled axial segregation profile by insulate the sidewall of ampoule in vertical Bridgman configuration.

Magnetic field The effect of magnetic field on the fluid flow in electrically conducting fluid was treated comprehensively by Chandrasekhar (1961) and Shercliff (1965). When the induced magnetic field is small compared to the imposed magnetic field such as the case for small magnetic Reynolds number, the strength of magnetic field remains steady in time. The interaction of flow field and magnetic field results in Lorentz force which inhibits the flow across the magnetic flux lines and reduces the convection level. First experimental applications of magnetic field to the crystal growth process were to

suppress the time-dependent fluctuations in horizontal Bridgman configurations (Hurle, 1966,1967; Utech and Flemings, 1966,1967).

Kim (1982) has grown InSb crystal by the vertically destabilizing Bridgman technique using a transverse magnetic field. The temperature fluctuations near melt/solid interface were measured during the increase of magnetic field strength from 0 to 1.69 kG. Temperature fluctuations shown in Figure 1.15 manifests the transition of flow states with the increase of magnetic field strength. Above the critical value of 1.69 KG, temperature fluctuation is completely suppressed, verifying the effect of magnetic field on the time-dependent convection in the melt.

Contrary to the case of vertically destabilizing Bridgman method, transverse magnetic field applied to vertically stabilizing Bridgman method was reported to degrade the uniformity of crystal (Müller, 1988). The change of flow configuration from axisymmetric to nonaxisymmetric caused unsteady convection, leading to the striations in the crystal.

Vertical magnetic field aligned with the growth axis does not provide nonaxisymmetric boundary condition and its application to Czochralski growth technique showed the consistent results in the growth of Si (Hoshikawa 1982; Hirata *et al.*, 1984; Kim and Smetana, 1985; Hirata and Inoue, 1985), GaAs (Osaka and Hoshikawa, 1984) and InP (Ozawa *et al.*, 1987; Hofmann *et al.*, 1988). Typically, magnetic field above 2 kG successfully suppressed the temperature fluctuations and corresponding striations caused by time-dependent convection. However, the regular patterns of striation which can be correlated to the crystal rotation were not suppressed with the application of magnetic field.

Recently, magnetic field has been proven to be beneficial in reducing the level of steady convection, thus accomplishing the diffusion-controlled growth of single crystal in the vertically stabilizing Bridgman method (Matthiesen *et al.*, 1987).

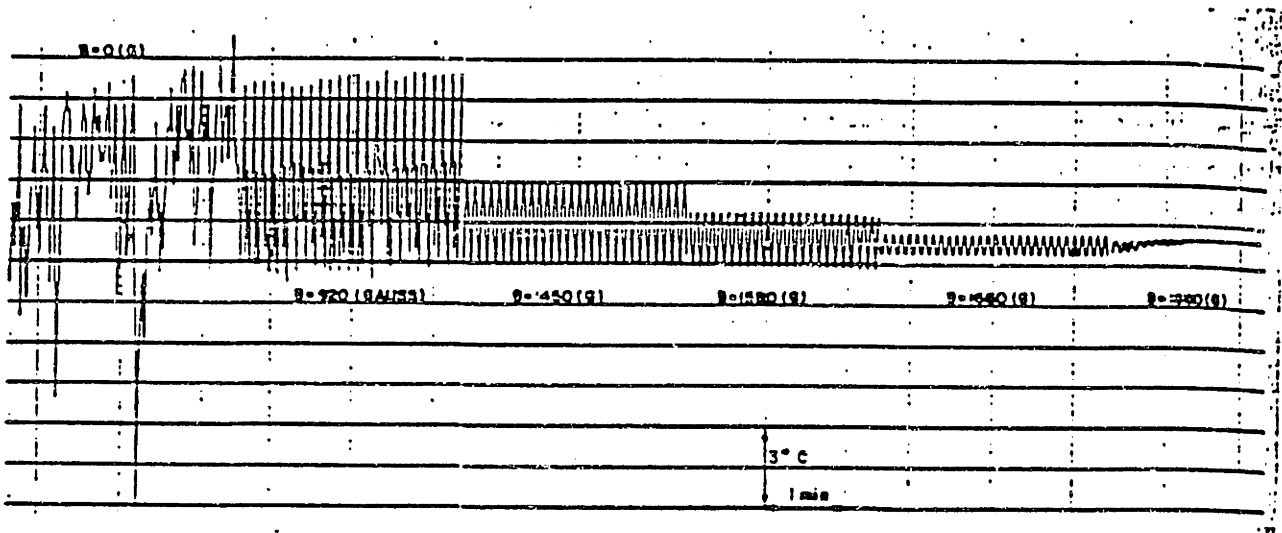


Figure 1.15: Temperature fluctuations for various magnetic field strength (Kim, 1982).

Microgravity Since the buoyancy force due to the density gradient is directly proportional to the level of gravity, several attempts have been made to grow crystal in reduced gravity environment to minimize the convection effect. Semiconductor crystal growth experiments were carried out in the Skylab (1973–74) and in the Apollo-Soyuz (1975) missions.

In the Skylab mission (Witt *et al.*, 1975) cylindrical InSb single crystal was grown during the flight in the space. The space-grown segment of crystal revealed no microsegregation and the solute concentration profile demonstrated the steady and diffusion-controlled growth, as shown in Figure 1.16. In the Apollo-Soyuz mission (Witt *et al.*, 1978), germanium crystals were grown in the space, demonstrating the diffusion-controlled segregation profile with negligible convection effect.

Although some space experiments of crystal growth gave quite promising results, several problems have been revealed in the space processing of materials (Gatos, 1982; Hurle, 1983). First, as reduced gravity suppresses buoyancy convective flow, the role of surface tension-driven flow becomes more important in the presence of free surface such as in the floating-zone method, horizontal boat method or Czochralski method. Next, the interaction between the flow field and melt/crystal interface becomes stronger. Under the terrestrial condition, the buoyancy convection is in general so strong that the energies associated with it are much greater than those associated with deformation of melt/crystal interface (Gibbs-Thomson effect). However, in space where the buoyancy flows are extremely weak, these two energies may become comparable leading to the stronger coupling between the morphological stability and convective stability.

Control of the convection motivates our first goal, that is to analyze the growth conditions necessary for optimum design of growth systems with moderate convection level. Convection and solute segregation under the influence of body forces other than gravity are studied by considering the application of a vertical magnetic field to Bridgman growth systems of differing design. The role of solute field in the growth of nondilute binary alloy is studied for the HgCdTe system. These two works are conducted by modifying the pseudo steady-state model (PSSM) developed previously (Chang, 1983;

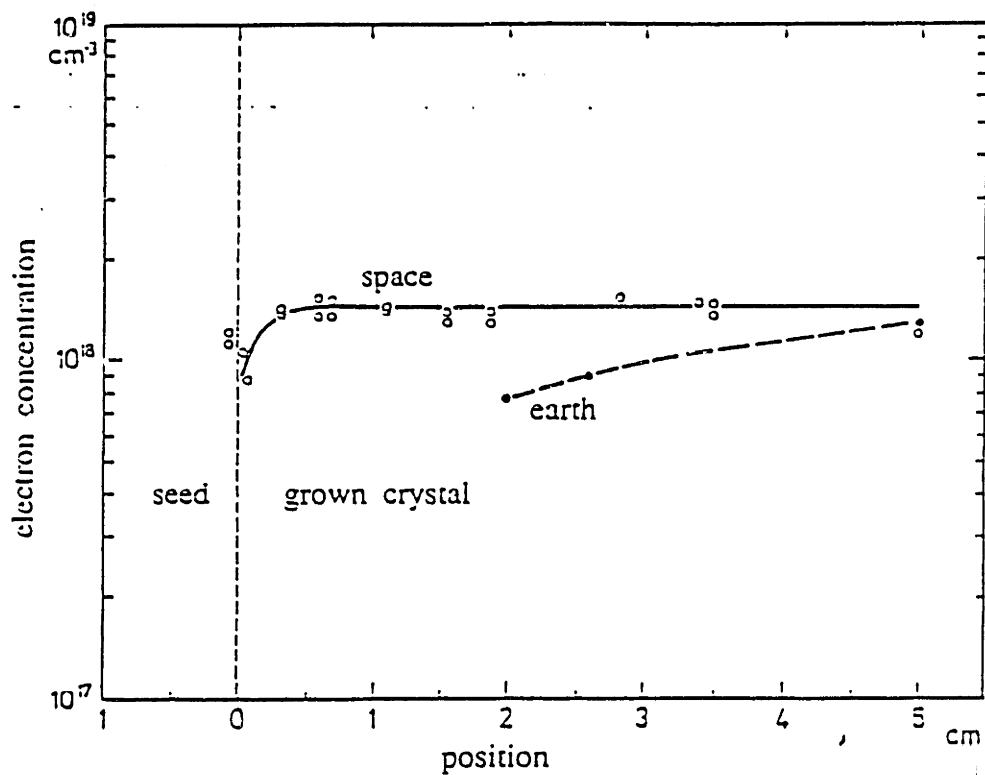


Figure 1.16: Solute concentration profile of InSb crystals grown in space and on earth (Witt *et al.*, 1975).

Adornato, 1987).

1.2.3 Effect of Melt Convection on Solute Segregation

Convection in the melt causes mixing and change the structure of solute diffusion layer near the melt/crystal interface. This alteration of solute field changes the rate of solute incorporation into the crystal, influencing the axial and radial profiles of solute concentration in the crystal. The detailed segregation profiles are set by the structure and intensity of the flow in the melt. Before discussing the effect of convection in different flow regimes, we define two parameters representing the radial and axial segregation in the crystal.

Parameters for Radial and Axial Segregation

The degree of nonuniformity of solute distribution in radial direction is termed *percentage radial segregation* and defined as the maximum difference in the concentration across the crystal divided by the local average value, $\langle \bar{c} \rangle_I$:

$$\Delta C(\%) = \frac{(\bar{c}_{s,max} - \bar{c}_{s,min})}{\langle \bar{c}_s \rangle_I} \times 100 \quad (1.16)$$

$$= \frac{(\bar{c}_{max} - \bar{c}_{min})_{intf}}{\langle \bar{c} \rangle_I} \times 100 \quad (1.17)$$

When the diffusion in the crystal is negligible, radial solute distribution on the melt side of interface is preserved in the crystal. Equation (1.16) is used for the characterization of crystal in the experiment. We use Eq. (1.17) in the numerical simulation from the information of solute field in the melt.

Coriell and Sekerka (1979) analytically analyzed the lateral segregation caused by the interface curvature, giving the radial segregation as

$$\Delta C(\%) \sim |1 - k| \Delta \bar{H} \frac{V_g(t)}{D} \times 100 \quad (1.18)$$

where $\Delta\bar{h}$ is the maximum difference in the interface location along the interface. They obtained a reasonable agreement with the experimental data of Witt *et al.* (1978) in growing Ga-doped Ge. They extended the analysis for radial segregation to a case with large departures from planarity by analytical and numerical method (Coriell *et al.*, 1981). Carlson *et al.* (1982) confirmed the analysis by Coriell and his coworkers by finite element method, again under the assumption of no convection. Recently, Brattkus and Davis (1988) analyzed the radial segregation in the growth of nondilute binary alloy. They contended that radial segregation cannot be calculated solely from the knowledge of interface shape. This is true for the growth of nondilute alloys in the presence of convection, because of the complex coupling of flow field, solute field and interface shape.

The effect of convection on the axial segregation of solute in the crystal is represented by the *effective distribution coefficient* k_{eff} , which is defined as the ratio of concentration in the crystal at the interface to the bulk concentration in the melt (Burton *et al.*, 1953):

$$k_{eff} = \frac{\langle \bar{c}_s \rangle_I}{\langle\langle \bar{c} \rangle\rangle} = k \frac{\langle \bar{c} \rangle_I}{\langle\langle \bar{c} \rangle\rangle} \quad (1.19)$$

where $\langle\langle \bar{c} \rangle\rangle$ is the volume averaged concentration in the melt.

Effect of Melt Convection

The effect of convection on the axial segregation k_{eff} defined in Eq. (1.19) and radial segregation Δc defined in Eq. (1.17) is schematically described in Figure 1.17 in terms of driving force of convection. When the driving force is small, only unidirectional convection due to solidification is present and solute transport is diffusion-controlled. In this flow regime, solute distribution at the interface is radially uniform resulting $\Delta C = 0$ for planar interface. If the melt is sufficiently long and the concentration far away from the interface remains constant, solute concentration in the crystal is the same as the far-field concentration in the melt leading to steady-state growth. Then, k_{eff} approaches unity as indicated by Eq. (1.19). In the real growth, ΔC has some finite

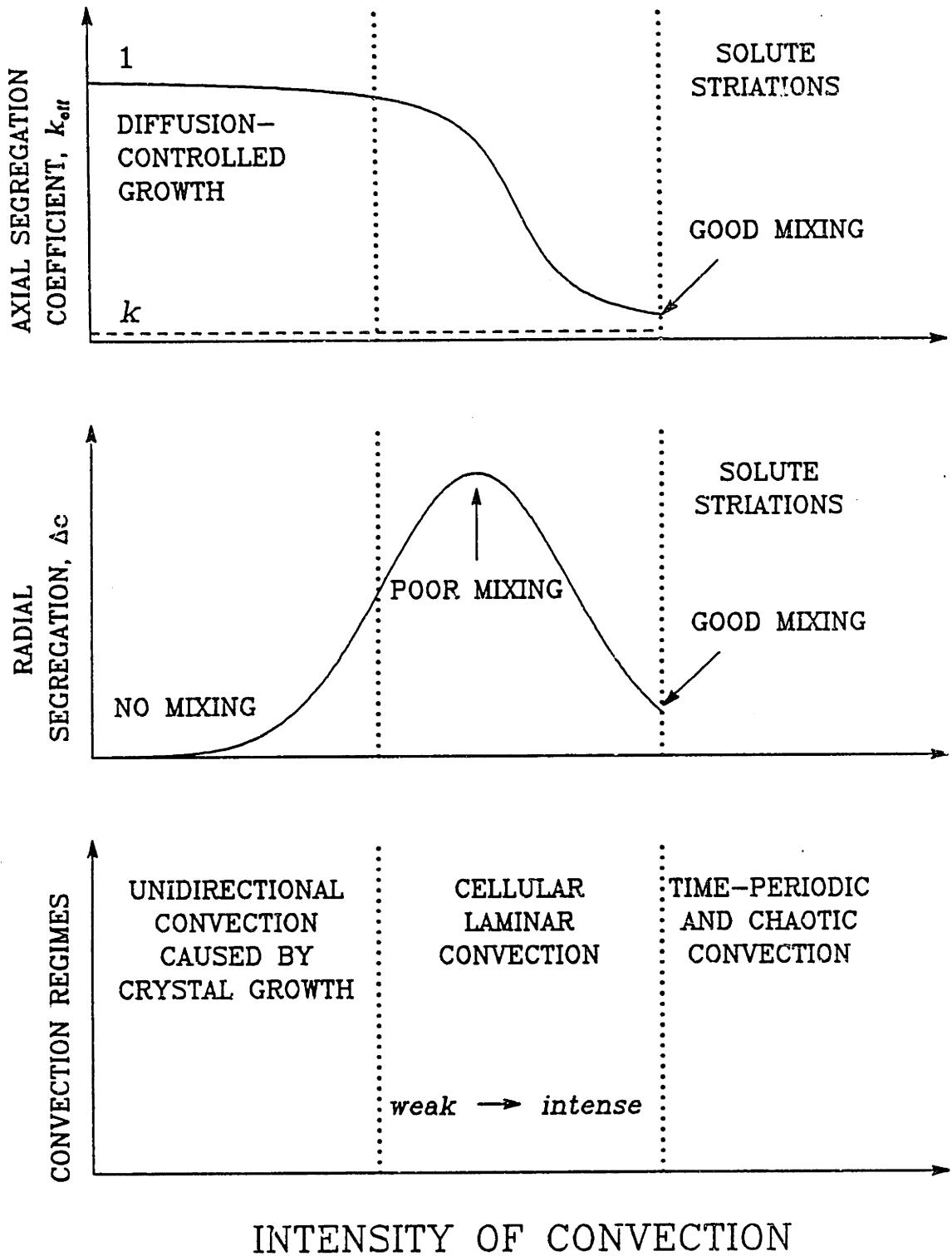


Figure 1.17: Effect of convection on Δc and k_{eff} in directional solidification.

value and k_{eff} deviates from unity due to the curvature of interface and finite length of the melt. With the increase of the driving force for convection, cellular convection dominates in the melt. When this convection is weak, flow field near the interface only distorts the composition profile leading to high radial segregation. Further increase of driving force results well-mixed region near the interface, causing the radial segregation to decrease again. Radial segregation shows the maximum value at some intermediate level of convection. This has been demonstrated in small-scale floating zone where convection is driven by rotating the feed rod and crystal (Harriott and Brown, 1984) and in vertical Bridgman system where convection is driven by thermal gradient and can be damped by stabilizing solute field (Adornato and Brown, 1987a). The relative magnitude of radial segregation in the limit of no mixing and good mixing depends on the curvature of the interface and the attainable intensity of convection under the real situation. With the introduction of convection, k_{eff} decreases monotonically to approach k depending on the level of convection. In the limit of good mixing, $\langle \bar{c} \rangle_I$ is close to $\langle \bar{c} \rangle$ and k_{eff} is close to k as predicted from Eq. (1.19). Beyond the critical value of driving force, flow becomes time-periodic or chaotic which causes fluctuations in the field of velocity, temperature and solute. These fluctuations leave its traces in the crystal in the form of striations, which is also an evidence for fluctuating ΔC and k_{eff} . More will be discussed on the striations later in this Section.

Although k_{eff} is useful to measure the role of convection in axial segregation, the definition of k_{eff} (Eq. (1.19)) contains a bulk concentration in the melt, which is not directly measurable. One way of obtaining k_{eff} from composition profile in the crystal is using the normal freezing expression with a dynamic equilibrium where k_{eff} is assumed constant. Equation (1.13) is rewritten in terms of k_{eff} as

$$\bar{c}_s(\bar{z}) = k_{eff} c_o (1 - f)^{(k_{eff}-1)} \quad (1.20)$$

where f is a fraction solidified.

Burton *et al.* (1953) first related the convection in the melt and k_{eff} in terms of hypothetical stagnant film thickness. Stagnant film model (Nernst, 1904) assumes a

thin layer on the solid surface, inside of which mass transfer is by diffusion only and its rate determines overall reaction rate in heterogeneous reaction. Likewise, stagnation film model adapted to the crystal growth system assumes a thin boundary layer near the melt/crystal interface. Inside this boundary layer, solute transport is by diffusion only and melt flow is uniaxial due to solidification. Outside the boundary layer is assumed to be a well-mixed region due to convection. If the concentration in the bulk remains constant as c_o , the steady-state composition profile in the boundary layer can be obtained by solving Eqs. (1.2) and (1.3) with the boundary condition

$$\bar{c}(\bar{\delta}) = c_o \quad (1.21)$$

This yields

$$\bar{c}(\bar{z}) = c_o \frac{k + (1 - k) \exp(-V_g \bar{z}/D)}{k + (1 - k) \exp(-V_g \bar{\delta}/D)} \quad (1.22)$$

The effective segregation coefficient k_{eff} can be obtained from the definition of k_{eff} , Eq. (1.19), and solute concentration profile, Eq. (1.22), in terms of the stagnation film thickness as

$$k_{eff} = \frac{k}{k + (1 - k) \exp(-V_g \bar{\delta}/D)} \quad (1.23)$$

The concept of stagnation film is good for understanding the role of convection in the axial segregation. However, it has limitations in practical use. First, it needs a additional correlations to relate the stagnant film thickness and intensity of convection. For simple geometry, such as rotating disk or flat plate, correlation for δ can be obtained from asymptotic analysis, similarity transform, boundary-layer analysis or experiments: some of them are referred in the review by Wilcox (1969). However, crystal growth system has so complex geometry and boundary conditions that it does not allow a simple correlation. Stagnation film model assumes only one well-mixed region outside the boundary layer, which is not valid where more than one flow cells exist. With the multicellular flow, the well-mixed regions of almost uniform concentration center around each cell and communicate with its neighbors by diffusion through thin internal layers, which complicates the direct application of stagnation film model. Examples

of multicellular flow were observed in the numerical simulations (Carlson *et al.*, 1984; Adornato and Brown, 1987a; Heinrich, 1988) and in the experimental models (Müller *et al.*, 1984; Neugebauer and Wilcox, 1988) for vertical Bridgman growth system.

We have discussed the effect of steady laminar convection on the axial and radial segregations in the macroscale, that is over the scale of crystal length or diameter. As the driving force for buoyancy-driven flow is increased, a point is reached at which the motion becomes time periodic. Further increase in driving force results in more complex time-dependent behaviour until the flow becomes completely chaotic. The periodic or chaotic time-dependent flow causes the oscillations in the temperature and solute field near the interface, leading to the solute segregation in the crystal in a much smaller length scale. This segregation in microscale takes the form of striations, that is oscillations in the solute concentration which are either periodically or irregularly distributed along the growth direction in the crystal. This form of inhomogeneity is more deleterious for the production of integrated circuit devices than macrosegregation.

Ueda (1961) was one of the first to relate the period of resistivity striations in germanium single crystals grown horizontally to the temperature oscillations in the melt in front of the interface. The striations and temperature fluctuations have been observed primarily during the horizontal Bridgman and the Czochralski growth, because the temperature field can easily destabilize the flow field (Morizane *et al.*, 1966; Witt *et al.*, 1966, 1973; Cockayne and Gates, 1967; Carruthers and Witt, 1975; Murgai *et al.*, 1976; Miller *et al.*, 1978). They are also observed in the crystal grown by the vertical Bridgman technique with top seeding, because of the destabilizing thermal gradient (Kim *et al.*, 1972, 1978). In the vertical Bridgman growth with bottom seeding, thermal gradients are not destabilizing and so neither temperature fluctuations in the melt or striations in the crystal have been observed (Witt *et al.*, 1978; Wang, 1984). In Section 1.2.2 we discussed that the thermal convection is driven by the radial temperature gradient in the vertically stabilizing Bridgman system. Very large radial temperature gradient drives the chaotic convection in the melt, leading to the striations in the crystal even in the the stabilizing Bridgman growth (Holmes and Gatos; 1981b).

In the growth of Ga-doped Ge by the vertically destabilizing Bridgman method, Kim *et al.* (1978) related the intensity of striations along the crystal axis to the depth of melt. Destabilizing temperature gradients were kept nearly constant during the growth. They found that turbulent aperiodic striations occurred when the melt was deep (2.4 to 1.8 cm), followed by a transition to periodic small-amplitude striations at intermediate melt depths (1.8 to 1.2 cm), and striation-free uniform growth thereafter (1.2 to 0 cm). Within one experiment, three different flow regimes could be identified. Since the Rayleigh number depends on the fourth power of the melt depth for the constant temperature gradient, the Rayleigh number decreased rapidly from the initial to final stage of crystal growth experiment. During the experiment, Ra_t was varied from 5×10^5 to 0. When Ra_t was less than 2×10^4 , flow field was stabilized. The results are shown in Figure 1.18 for the the growth of Te-doped InSb with different melt depths (Kim *et al.*, 1972).

1.3 Previous Models for Vertical Bridgman Process

In the vertical Bridgman method, field variables (velocity, pressure, temperature, and concentration) show transients due to the steady decrease of the length of the melt with crystal growth and the displacement of the ampoule in the furnace. The transient nature of the Bridgman growth of crystal motivates our second goal, the development of transient model describing the process and its solution algorithm.

For the construction of the transient model, we review the previous works on the modeling of vertical Bridgman growth system. We describe the works on the experimental model before we discuss the theoretical modelling.

1.3.1 Experimental Modelling

In the experimental modelling, proper materials and process conditions are selected so that similar magnitudes of characteristic dimensionless groups as in the modelled growth

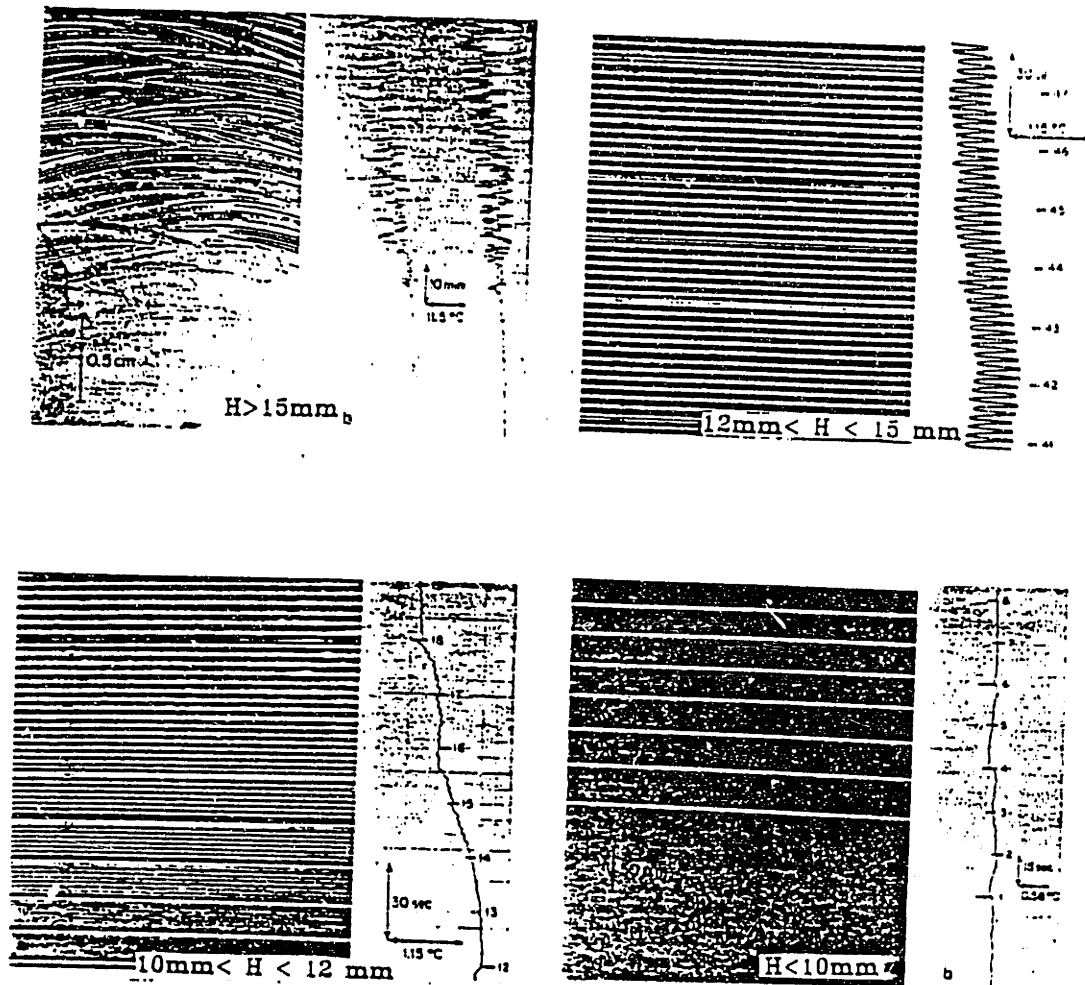


Figure 1.18: Striation patterns of Te-doped InSb crystal grown in destabilizing vertical Bridgman system (Kim *et al.*, 1972).

system are obtained. It is used most for the simulation of flow field, because the flow pattern is hard to observe in the high temperature environment of real crystal growth.

Müller *et al.* (1984) performed an experimental investigation into buoyancy-driven convection in closed vertical cylinders heated from below using water ($Pr = 6.7$) and gallium ($Pr \simeq 2 \times 10^{-2}$) to provide the visual insight of flow patterns in vertically destabilizing Bridgman crystal growth system. The hydrodynamic state was described by three dimensionless numbers, the thermal Rayleigh number Ra_t , the aspect ratio (height/diameter) h/d and the Prandtl number Pr . The value of critical Rayleigh number Ra^{c1} for the onset of convection was obtained experimentally for $0.5 \leq h/d \leq 5$ and shown to be in good agreement with the theoretical predictions by Charlson and Sani (1971). The flow pattern showed axial symmetry for $h/d = 0.5$ and nonaxial symmetry for $1 \leq h/d \leq 5$. They also showed that occurrence of doping striations in Te-doped GaSb crystals grown in the same configuration was very well correlated to the unsteady flow regime.

Müller *et al.* (1987) presented experimental results for thermal buoyancy-driven convection in a experimental model that can be extrapolated to various vertical melt crystal growth configurations. The model consists of a vertical cylinder with the top, bottom and side walls forming three independent, isothermal boundaries as shown in Figure 1.11. The hydrodynamic state in this model was described by four dimensionless groups: the aspect ratio (height/diameter) h/d , the Prandtl number Pr , the vertical Rayleigh number Ra_t and a wall Rayleigh number Ra_w . Flow patterns as well as transitions from steady to unsteady convection were studied as a function of Ra_t and Ra_w , which are defined in Eqs. (1.14) and (1.15). Prandtl number and aspect ratio were fixed to 6.7 (water) and 1 respectively. Under the constant Pr and h/d , stability diagram for flow pattern and transition to unsteady convection were obtained, as shown in Figure 1.19. where positive Ra_t corresponds to cold top and hot bottom while positive Ra_w is corresponding to hotter surrounding than the core of the fluid. The vertically stabilizing Bridgman system is located near negative Ra_t axis with Ra_w depending on the thermal characteristics of the system.

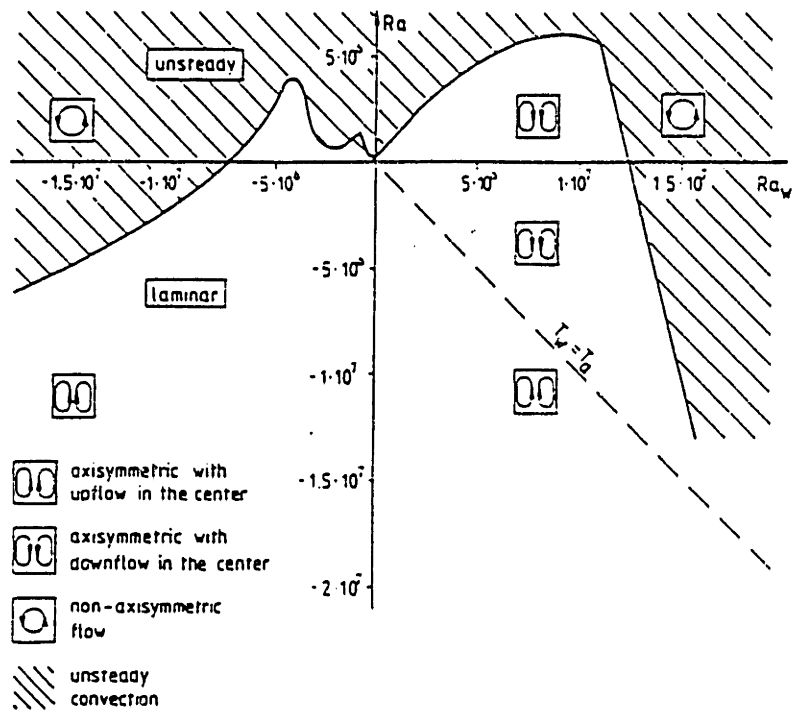


Figure 1.19: Stability diagram for flow patterns and transitions from laminar to unsteady convection (shaded area) for $h/d = 1$ in water in terms of Ra_t and Ra_w (Müller *et al.*, 1987).

Woods and Huppert (1988) studied the segregation of composition in the solid grown by cooling a supereutectic melt, aqueous sodium carbonate solution, from below. When the composition of melt is greater than eutectic, it is called supereutectic. The melt at the solid/liquid interface can have low density even though it is cold. Destabilizing density gradient drives intense solutal convection, leading to the compositionally stratified solid. This case is similar to PbSn system, in that light component is rejected at the interface and the resulting solute field is destabilizing.

Schaefer and Coriell (1984) observed the convective flow fields and solid/liquid interface shape during the solidification of a transparent material, succinonitrile-ethanol, which has similar Prandtl number to oxide materials. The convection due to the radial temperature gradients in the crystal growth apparatus caused solute transport so that macroscopic depression developed in the solid/liquid interface.

In an effort to simulate a thermosolutal convection in a horizontal Bridgman growth configuration, there have been several experimental investigations of thermosolutal convection in shallow enclosures with horizontal temperature and solute gradients.

Ostrach (1983) reported a three-layer structured thermosolutal convection using an electrolyte solution of copper sulfate acid ($\text{H}_2\text{SO}_4 + \text{CuSO}_4 + \text{H}_2\text{O}$) in a shallow cavity with differentially heated vertical end walls. In his experiment the thermal and solutal buoyancy forces were imposed in either opposing or augmenting senses.

Jiang et al. (1988) investigated a thermosolutal convection by opposed thermal and solutal buoyancy forces in a low aspect ratio rectangular system by electrochemical method. They identified three flow regimes as a function of buoyancy ratio (solutal/thermal), classified as multi-layer, secondary cell and mixed flow structures. The multi-layer flow was found to be a quasi-steady process, while the secondary cell flow was unsteady due to a thermosolutal instability.

Lee et al. (1988) carried out experiments in rectangular enclosures of aspect ratio 0.2 and 2.0, for the steady-state thermosolutal convection of a salt-water solution with an osmotic system. Unicell flow and multi-layer flow patterns were observed depending

on the relative magnitude of the buoyancy ratio.

Thompson and Szekely (1988) conducted an experiment where a double-diffusive liquid is solidified beginning from a vertical wall in a rectangular box. The experiment provided a visual picture of the role of double-diffusion in producing a vertical stratification of composition and density in an initially homogeneous liquid during solidification. The development of horizontally oriented convection cells in the stratified liquid was correlated with the magnitude of the destabilizing lateral temperature gradients across the liquid region.

1.3.2 Theoretical Modelling

We summarize in Table 1.4 the major theoretical models for the vertical Bridgman growth developed by previous researchers. These works are classified according to the equations solved for in each analysis. The number of spatial dimensions and the inclusion of time in the analysis are specified with the solution method, whether it is analytical or numerical.

Most theoretical research for the Bridgman growth system has been limited to the steady-state analysis, which is based on assumptions valid for the region of steady solidification in a sufficiently long ampoule. One or more aspects of the transport processes, such as heat transfer, convective flow and solute segregation, in the Bridgman growth system have been previously analyzed using steady-state assumption.

Transient analysis of the directional solidification system has been confined to one-dimensional analysis focusing on the single aspect of transport processes, either heat or solute transfer, in the absence of convection in the melt. In some analyses the time-dependent solute diffusion equations have been solved by taking the growth rate transients into accounts (Calyton *et al.*, 1982; Favier, 1980; Bourret *et al.*, 1985; Derby and Brown, 1986)

Energy	1D steady-state	Naumann (1982a) ^A , Ravishankar and Fu (1983) ^A , Jasinski <i>et al.</i> (1983,1984) ^A
	2D steady-state	Chang and Wilcox (1974) ^A , Sen and Wilcox (1975) ^N , Fu and Wilcox (1980) ^N , Naumann (1982b) ^A , Chiu and Carlson (1983) ^N , Naumann and Lehoczky (1983) ^A , Huang <i>et al.</i> (1983) ^N , Jasinski and Witt (1985) ^N , Taghavi and Duval (1989) ^A
	1D transient	Clyne (1980) ^N , Fu and Wilcox (1981) ^N , Sukanek (1982a,b) ^A
	2D transient	Borisov <i>et al.</i> (1982) ^N
Solute	1D transient	Pohl (1954) ^A , Smith <i>et al.</i> (1955) ^A , Hulme (1955) ^A , Memelink (1956) ^A , Clayton <i>et al.</i> (1982) ^N , Verhoeven (1988) ^N , Kobayashi (1988) ^A
	2D steady-state	Coriell and Sekerka (1979) ^A , Coriell <i>et al.</i> (1981) ^{A,N} , Carlson <i>et al.</i> (1982) ^N
Energy and solute	1D transient	Favier (1980) ^N , Bourret <i>et al.</i> (1985) ^N , Derby and Brown (1986) ^N
Energy and flow	2D steady-state	Chang and Brown (1983a,1984) ^N , Müller <i>et al.</i> (1984,1987) ^N , Carlson <i>et al.</i> (1984) ^N , Arnold <i>et al.</i> (1989) ^N
Energy, flow, and solute	2D steady-state	Chang and Brown (1983b) ^N , Adornato and Brown (1987a,b) ^N
	2D transient	This work

A: analytical method, N: numerical method

Table 1.4: Classification of previous theoretical models for vertical Bridgman growth.

Thermal Modelling

In the vertical Bridgman-Stockbarger crystal growth system shown in Figure 1.5, heater and cooler provide the necessary temperature gradient for solidification. Between the heater and cooler, gradient zone or adiabatic zone can be located to control the shape and location of melt/crystal interface. Because of the simplicity and its relevance for semiconductor material, almost every thermal modelling assumed that conduction is the only mechanism for heat transfer in the melt.

Davis (1972) calculated analytically for the first time the one-dimensional axial temperature distributions around the gradient region for a charge directionally solidifying within a Bridgman-type three zone furnace. He solved the steady-state conduction equation in the liquid and solid including the heat transfer from the furnace and latent heat of solidification at the interface.

Chang and Wilcox (1974b) solved analytically the steady-state differential equation for temperature in an infinitely long solid cylindrical rod in a two zone furnace configuration. The differential equation included conductive and convective heat transfer, where convection was due to the growth velocity only. They investigated the effect of heater and cooler temperature, growth velocity, latent heat release and finite charge length on the location and shape of interface. The importance of the insulation zone between the heater and cooler was identified to decrease the dependence of the interface shape on its position in the furnace, which was later verified by numerical calculation by Fu and Wilcox (1980).

Sen and Wilcox (1975) studied the effect of ampoule thermal conductivity on the interface shape and position within a two zone configuration. The steady-state heat conduction equation was solved using a finite difference method. They concluded that the thermal conductivity of the ampoule should be close to that of the charge to reduce the radial heat transfer.

Bartholomew and Hellowell (1980) added the effect of radiation explicitly where the quantity of radiant heat was modified by a view factor taking account of the geom-

etry of the system.

Jones *et al.* (1982, 1984) used an electric analogue to model the heat transfer between the furnace and the charge, where conduction and radiation was described as a resistor network. They noted the importance of thermal boundary conditions at the bottom of the ampoule especially in the early stage of solidification.

Naumann (1982a) developed a one-dimensional analytical expression for the temperature distribution in a solidifying rod in the three-zone Bridgman-Stockbarger configuration. The analysis included the translation effects, finite charge lengths in the hot zone and the use of booster heater in the gradient zone to increase the axial gradients at the interface. This analysis was extended to two-dimensional case using hybrid analytical/numerical method (Naumann, 1982b). In an application of his analysis to HgCdTe system, he found that the use of insulation zone can adversely affect the interface shape if the melt and crystal thermal conductivities are significantly different and the ampoule carries the bulk of heat flux (Naumann and Lehoczky, 1983).

Jasinski *et al.* (1983, 1984) performed a similar analysis as Naumann (1982a,b), but included the radial heat flux in the one- and two-dimensional models by defining an effective Biot number. They also defined the minimum length of the charge in the hot and cold zones for which the ampoule translation rate equals the growth rate at the interface. Their model was further extended to account for the Peltier effect at the interface (Jasinski and Witt, 1985).

Ravishankar and Fu (1983) performed a parametric study using a one-dimensional heat transfer model. The effect of parameters naturally occurring during nondimensionalization on the temperature gradient and interface location was investigated and compared with experimental results of MnBi/Bi eutectic system.

Chin and Carlson (1983) first applied the finite element method to the analysis of heat transfer in Bridgman crystal growth system, which was also used by Huang *et al.* (1983) to investigate the effect of different thermal conductivities between the melt and crystal.

Cheng et al. (1985) investigated the behavior of the melt/crystal interface shape during Bridgman growth of CsCdCl_3 , model material for CdTe, by finite element analysis. The result showed that the convexity displayed a sharp maximum in a region where the temperature gradient decreased sharply and the high translation rate increased the concavity of interface.

Dakhoul et al. (1988) analyzed numerically the effect of growth parameters on the thermal distribution during a Bridgman-Stockbarger type crystal growth of HgCdTe alloys. In the analysis, the dependence of thermal conductivity on the temperature and concentration was explicitly specified from empirical data. Concentration profile in the melt was assumed to follow that of diffusion-controlled growth. The interface shape was shown to be concave or convex depending on the cooling temperature. The inclusion of the compositional dependence of melting point increased the interface curvature significantly as compared to the isothermal melting point.

When the translation rate of ampoule is abruptly changed, there is a transient period when the crystal growth rate differs from the translation rate, as shown by **Wang et al. (1984)** who measured the growth rate by interface Peltier demarcation.

Clyne (1980b) computed the transient ratio of the crystal growth rate to the translation rate of the ampoule in the directional solidification using a simple conduction model and obtained a good agreement with experimentally measured growth rate (Clyne, 1980a) in the initial transient of solidification of aluminum.

Fu and Wilcox (1981) characterized the transients caused by a step change in the translation rate by solving a one-dimensional heat transfer model with finite difference technique. The growth rate or interface location was correlated to an exponential function in terms of the Biot number, the latent heat and the length of insulation zone. They further extended their analysis to include a linear or fluctuating change in the translation rate of ampoule (Fu and Wilcox, 1982). Their analysis was verified in the experiment where current induced demarcation was used to determine the microscopic growth rate in MnBi/Bi eutectic (Fu et al., 1982).

Sukanek (1982a, 1982b) used a perturbation technique to study the effect of finite charge lengths on the deviation of the crystal growth rate from the translation rate of ampoule in a three zone Bridgman-Stockbarger system. As a result, he obtained a criteria for the critical length of the ampoule above which the steady-state growth rate can be achieved for the cases of slow translation and moderate translation, respectively.

Borisov *et al.* (1982) solved numerically using enthalpy method for the two-dimensional time-dependent temperature fields in a single crystal of copper and aluminum grown by Bridgman method. With their model, it was possible to track the interface shape with time which showed the radial variation of crystal growth rate. With the same model, they also investigated the effect of furnace temperature change on the interface shape and location (Warchol and Modrzejewski, 1986).

Convection and Segregation

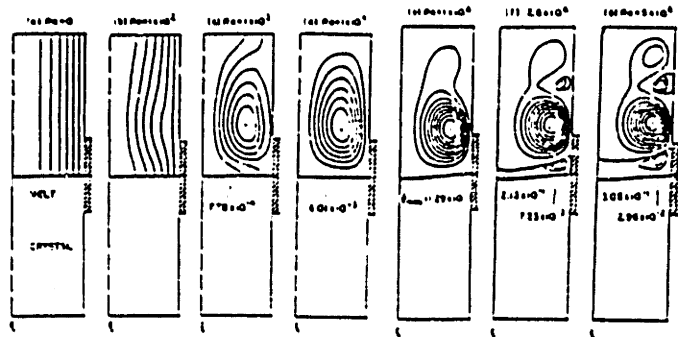
Clayton *et al.* (1982) developed the one-dimensional model for solute redistribution for the growth of HgCdTe crystal. Their model accounted for the variations in melting point and equilibrium distribution coefficient with composition. However, they assumed the constant temperature gradient throughout the melt and crystal so that heat transfer characteristics of Bridgman configuration was oversimplified. Nevertheless, the result was shown to be in good agreement with experimental data demonstrating the segregation profile of diffusion-controlled growth.

Bouret *et al.* (1984,1985) performed similar analysis as Clayton *et al.* (1982) but employed the realistic furnace temperature profile and heat transfer between furnace and the charge. In these studies, heat transfer was modelled in one-dimension with fin approximation and only growth-induced convection was assumed to be present in the melt. This latter assumption is valid practically either in reduced gravity environment or in the small-scale terrestrial experiments with a highly stabilizing solute field. Detailed numerical scheme can be found elsewhere (Derby and Brown, 1986).

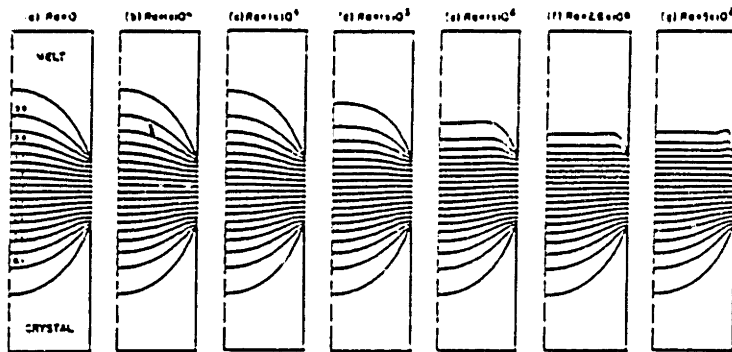
Chang and Brown (1983a) first examined the flow field induced by radial tem-

perature gradients in an idealized Bridgman-Stockbarger system where furnace temperatures were imposed directly on the melt and crystal in the absence of the ampoule with perfectly insulating region between the hot and cold region. The complete solutions of steady-state velocity, temperature, concentration and melt/solid interface shape were computed with Boussinesq approximation in the momentum equation. Pseudo-steady-state was taken for solute field, where solute of given concentration enters the ampoule with the melt from the top and the crystal is pulled away from the bottom with the concentration which preserve solute balance in the melt. The analysis was based on finite-element/Newton algorithm, which solves the field variables and interface shape simultaneously. This algorithm was shown to be more efficient than successive iterations for decoupled field variables and interface shape (Chang and Brown, 1983b). The results are shown in Figure 1.20 for flow, temperature and concentration field. Conduction dominates the heat transfer in the melt because of the low Prandtl number for typical semiconductor materials as shown in the temperature field. The toroidal flow cells are driven by the radial temperature gradient due to the sudden change of thermal boundary conditions at the junction of hot and insulating zone. Isoconcentration curves in the solute field shows the typical transition from diffusion-controlled growth to a well-mixed core in the melt with the maximum radial segregation at the intermediate level of convection, as described schematically in Figure 1.17. They also compared the flow fields in the vertically destabilized Bridgman system with that of Rayleigh-Bénard problem using computer-aided bifurcation analysis. Results showed that the introduction of imperfection due to the boundary condition appropriate to Bridgman system modified flow structure in the melt (Chang and Brown, 1984).

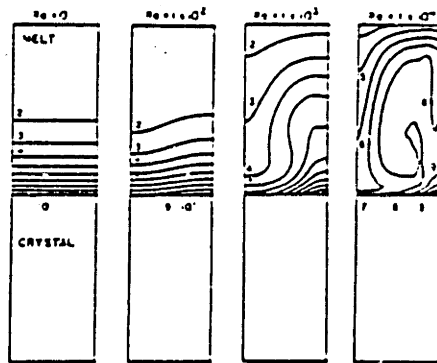
Carlson *et al.* (1984) studied thermally driven flows which occur during stabilized vertical Bridgman crystal growth of single component fluid using finite element method. They simplified the modelling by specifying the isothermal interface shape as parabolic. In their result, a single cell flow was observed when the interface was convex as viewed from the melt. A concave interface caused multiple counterrotating cells. They also identified the importance of radial temperature gradient for the flow and examined the effect of the insulation thickness and heat transfer from the furnace to the charge on



(a) Flow Field



(b) Temperature Field



(c) Solute Field

Figure 1.20: Sample flow fields, isotherms and solute fields for the growth of GaGe in idealized vertical Bridgman system (Chang and Brown, 1983a).

the flow pattern.

Adornato and Brown (1987a) extended the analysis by **Chang and Brown (1983a)** with boundary conditions closer to experiments by including the ampoule and heat transfer between ampoule and furnace in thermal modelling. Nondilute binary alloy system was also analyzed through the linearized phase diagram. To facilitate the computation of solute field for highly convective case Petrov-Galerkin finite element method was used, where the weighting functions poses the different form from basis functions (**Adornato and Brown, 1987b**). Numerical analysis was performed for the growth of gallium-doped germanium and nondilute germanium-silicon alloys in the Bridgman-Stockbarger furnace of **Wang (1984)** and in the constant gradient furnace of **Rouzaud *et al.* (1985)**. In **Wang's** furnace, heat pipes were used to maintain the constant temperature in the hot and cold zone while in the constant gradient zone furnace temperature profile was almost linear by use of tapered graphite heater. When the ampoule was included, it caused a radial temperature gradient near the interface due to the different thermal conductivities of the melt, crystal and ampoule, which drove another flow cell near the interface in addition to the one near the junction of hot zone and gradient zone, as described in Figure 1.21(a). Corresponding solute field showed the characteristic profile of diffusion-controlled growth at low Rayleigh number. Even at this low convection level, radial segregation could be detected because of the curvature of the interface. At high level of convection, two well-mixed core of nearly uniform composition were formed within the flow cells separated by the internal layers.

Oreper and Szekely (1984) numerically analyzed the effect of imposed magnetic field on the convection in Bridgman-Stockbarger crystal growth system. Although the role of magnetic field in suppressing the convection was clearly described, modelling the Bridgman growth system itself was not faithful to the real situation. Transport equations were solved only in the melt with flat interface and the partition of solute between the melt and the crystal at the interface was not taken into account.

Camel and Favier (1986) investigated the influence of convective transport on the macrosegregation in Bridgman crystal growth system by order-of-magnitude analysis of

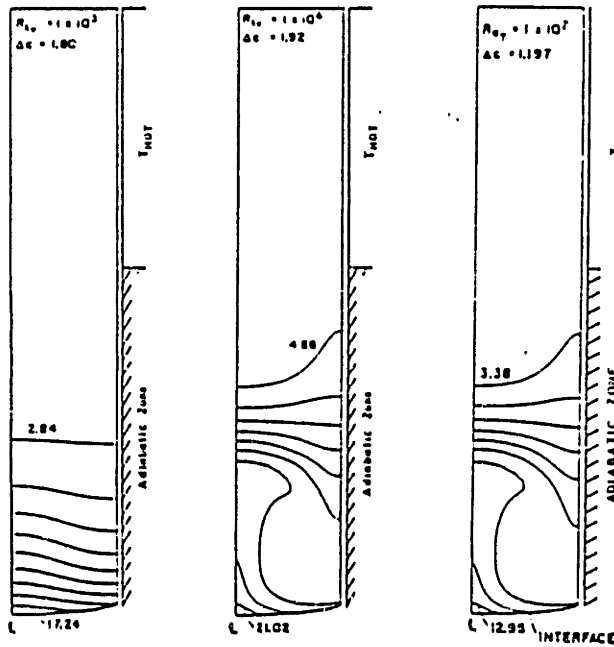
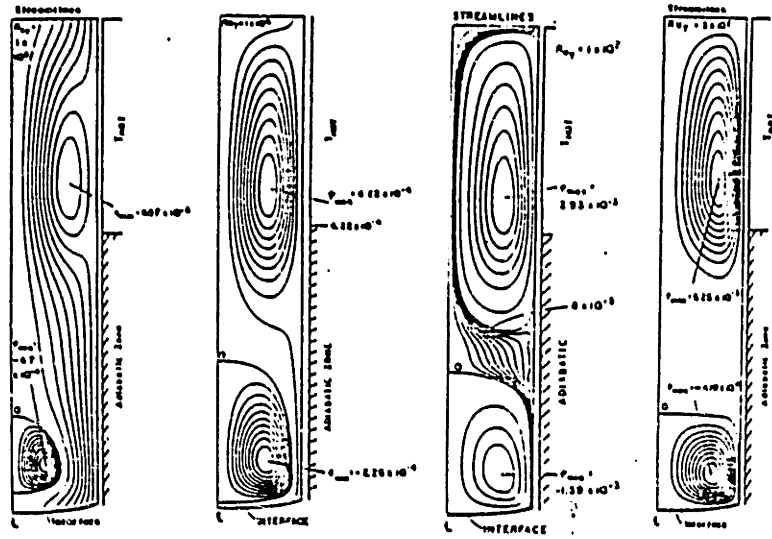


Figure 1.21: Sample flow fields and solute fields for the growth of GaGe in Wang's system with boron nitride ampoule (Adornato and Brown, 1987a).

the set of balance equations for momentum and solute in the melt and at the interface. The different solute transport regimes were defined on the $Gr-Pe_s$ plane, where Gr is a Grashof number and Pe_s is a Peclet number of solute transport. They also obtained the scaling for radial segregation and effective segregation coefficient in terms of Gr and Pe_s .

Crochet *et al.* (1983,1985) developed the two-dimensional numerical simulations to represent the thermomechanical behaviour of semiconductor melts in horizontal Bridgman growth system. These computer models were based on time-dependent finite-difference and finite-element codes in a geometry of rectangular box. At moderate Rayleigh numbers, steady flow fields with multiple cells in a horizontal direction was observed. Above a critical Rayleigh number, these steady solutions were replaced by oscillatory melt convection, as suggested by earlier experimental studies (Hurle *et al.*, 1974) in the horizontal Bridgman configuration. Thermal oscillations due to the oscillatory convection caused periodic freezing and remelting at the interface, which may be the probable explanation for the observed striations. Detailed numerical schemes can be found in a series of works by this group (Crochet *et al.*, 1987; Dupont *et al.*, 1987; Wouters *et al.*, 1987) including the extension to three-dimensional case. Throughout these analyses, solute field was not considered as a part of solution preventing the analysis of convection effect on the solute transport. Since the thermal boundary conditions on both sidewalls were specifying the constant temperatures, interface was fixed spatially except due to the oscillatory convective motion.

1.4 Thesis Direction

1.4.1 Objectives and Approach

The goal of this research is to extend the understanding of the physics involved in the directional solidification process, especially during the growth of crystal in the vertical Bridgman system. The specific objectives have been the investigation of convection in

the growth of dilute or nondilute binary alloys and its effect on the species transport and axial and radial segregation. These objectives have been met by constructing a comprehensive pseudo-steady-state and transient models describing the crystal growth process, including convection, heat and solute transfer in the melt and heat conduction in the crystal and ampoule. Finite element analysis has been developed for solution of both steady-state and transient models.

Our approach is the numerical simulation by pseudo-steady-state and time-dependent model describing the temperature, flow and solute fields in two-dimensional axisymmetric growth system. This approach enables us to analyze the steady-state and time-dependent interaction of field variables during the growth of crystal. Convection and solute segregation under the influence of body forces other than gravity are studied by considering the application of a vertical magnetic field to Bridgman growth systems of differing design. The role of solute field in the growth of nondilute binary alloy is studied for the HgCdTe system. These two works are conducted by modifying the pseudo-steady-state model (PSSM) developed previously (Chang, 1983; Adornato, 1987). The experimental system of Wang (1984) at MIT for the growth of dilute Ga-doped Ge is simulated numerically using the transient model to demonstrate the accuracy and robustness. The growth of Se-doped GaAs in the furnace at GTE (Arnold *et al.*, 1989) is also analyzed with the transient model. The growth of nondilute alloy is studied for the growth of pseudobinary HgCdTe alloy in the vertical Bridgman system at NASA (Szofran and Lehoczky, 1984) including the complete phase diagram of the alloy in the calculation.

1.4.2 Structure of Thesis

The models for the crystal growth in the vertical Bridgman system are described in Chapter 2 in terms of mathematical statements of the governing equations and boundary conditions along with modelling assumptions, for both pseudo-steady-state and transient model.

Numerical methodologies for spatial and temporal discretization will be discussed in Chapter 3. A brief outline of finite element method will be presented with some discussions about the comparison of Bubnov- and Petrov-Galerkin finite element methods. The numerical scheme to solve the nonlinear algebraic systems of equations resulting from finite element discretization and time-integration scheme will also be examined. The numerical algorithm for solution of the transient model is tested through calculations for the vertical Bridgman growth system used by Wang (1984) without convection.

In Chapter 4, the effect of vertical magnetic field on the convective transport is analyzed in the crystal growth system at MIT (Wang, 1984) and at the Centre d'Etudes Nucléaires de Grenoble, France (Rouzaud *et al.*, 1985). The flow structure at high magnetic field strength is analyzed asymptotically for the comparison with numerical analysis.

Inclusion of solutal effect on the convective transport in the growth of nondilute HgCdTe alloy system is investigated in Chapter 5. Phase diagram is taken into account for the melting point in a linearized form. Momentum boundary layer near the wall is analyzed following Hart's (1971) analysis, when the solute field stabilizes the thermal buoyancy-driven flow. Simple one-dimensional analysis of axial redistribution of solute is developed for the growth of HgCdTe.

The analyses in Chapter 4 and 5 use the pseudo-steady-state model previously developed by Chang (1983) and Adornato (1987) and modified in this research. The results of the transient analysis of growth of gallium doped germanium in the heat pipe furnace by Wang (1984) is described in Chapter 6. The calculated temperature profile is compared with the experimental data for a stationary graphite rod inserted in the furnace. The results are also compared with experimental data in terms of the crystal growth rates and axial segregation in the crystal. Also, the growth of selenium doped gallium arsenide in the gradient freeze growth system by GTE (Gustafson *et al.*, 1986) is simulated numerically to help characterize the growth experiment to be performed in space.

In Chapter 7, transient numerical analysis is done to simulate the growth of nondilute pseudobinary HgCdTe in the Bridgman-type system used by Space Science Laboratory of NASA Marshall Space Flight Center (Szofran and Lehoczky, 1984). For the accuracy of the model, full phase diagram is included in terms of variation of melting point and equilibrium distribution coefficient with composition. Among the thermophysical properties, the dependence of the coefficient of thermal expansion β_t on the temperature and composition is considered in the model, because it can change sign along the axial direction in the melt which adds additional driving force for convection.

Finally, conclusion and some issues which may supplement this work is set forth in Chapter 8.

Chapter 2

Modelling of Directional Solidification

2.1 Introduction

It is worthwhile to begin with the elements of the modelling process before mathematical model of specific process is made. The initial step, and driving force, is the definition of phenomena with proper boundary conditions and initial conditions. In this step several assumptions are introduced to simplify the process while maintaining key features involved. Boundary conditions and initial conditions are selected that they are feasible for mathematical representation. The next step involves the numerical representation usually in the form of differential equations of physical phenomena and boundary and/or initial conditions defined in the former step. The characteristic length scale, time scale and scales for other variables are introduced during nondimensionalization at this stage. It is in the next step to devise a numerical scheme to solve the resulting differential equations from the former step. Generally, this step can be divided into two small steps. First is for discretizing the continuous variables into discrete variables in space and time, yielding a algebraic set of equations out of differential equations. Then these algebraic equations are solved with the aid of a certain iterative scheme or direct

solver, depending on the nonlinearity of equations. Finally, results are obtained and compared with experiment, the actual process or intuition. At this point the modeller either accepts the results as having reached the required standard or makes some modifications in his model. Because the numerical model should be firmly grounded on the actual process or experiment, it will be helpful to examine the growth system and the procedure used in the experiment by Wang (1984).

A heat pipe operated Bridgman-Stockbarger growth system was designed and constructed to control the temperature fields in the melt and the growing crystal. A schematic diagram of the three-zone furnaces described in Figure 2.1 shows two vertically aligned annular heat pipes separated by layers of insulating material. Sodium-filled inconel heat pipes were used to obtain radially symmetric, isothermal furnace zones operated in the temperature range from 570°C to 1100°C in vacuum and inert atmosphere. An axial temperature gradient developed in the insulating zone can be varied by changing the temperature of either heat pipe or by changing the length or axial and radial thermal conductivity of the insulating zone. Thus, this insulating zone can also be called as the *gradient control zone*. The gradient control zone can be structured to function as an *adiabatic* zone which does not allow for heat transfer between the furnace and the charge within the gradient zone and as a *diabatic* zone which enhances heat transfer within the gradient zone, depending on the combinational use of Al₂O₃ and Inconel 600.

The typical procedure for crystal growth follows (Wang, 1984). A <111> germanium seed crystal approximately 8 cm long and a pre-cast germanium charge (~ 100 g) are loaded into the boron nitride cylinder (1.36 cm i.d., 1.9 cm o.d. and 30.5 cm in length) shown in Figure 2.2. Gallium is added to achieve a melt concentration of approximately 5×10^{19} gallium atoms/cm³. The crucible is positioned within the furnace so as to place the top of the germanium seed near the top of the gradient control zone to insure back-melting of the seed. Because of the small distance (1 mm) between the crucible and furnace wall, the alignment of the crucible is critical for thermal symmetry. The chamber is evacuated to 0.4 torr and the heat pipes were heated at a rate not exceeding

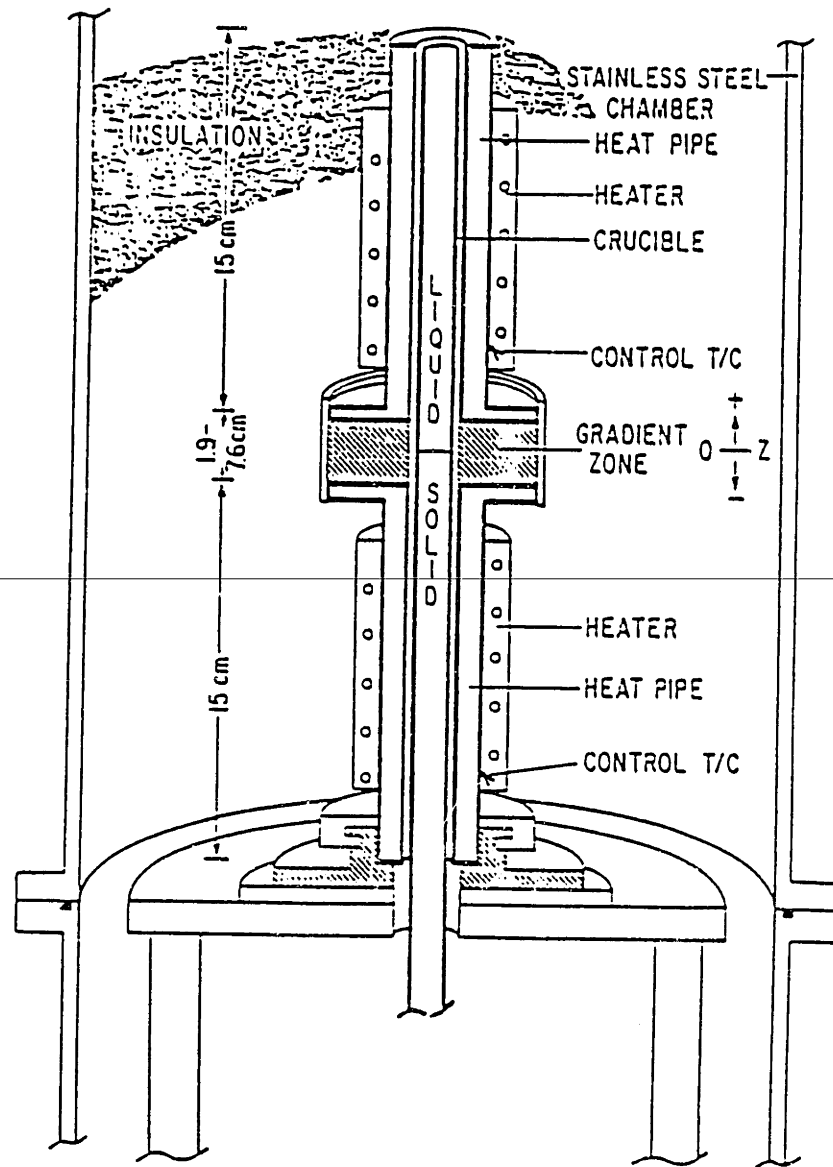


Figure 2.1: Schematic diagram of the heat pipe Bridgman-Stockbarger growth system (Wang, 1984).

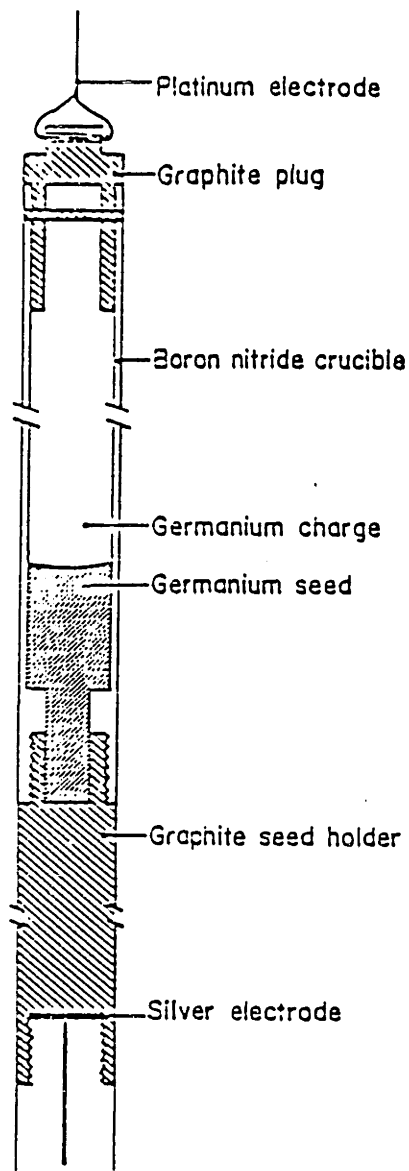


Figure 2.2: Schematic diagram of the crucible used for growth in the heat-pipe Bridgman-Stockbarger growth system (Wang, 1984).

8°C/min until 500°C is reached, because a faster heating rate can cause internal stresses in the heat pipe. The temperature of each heat pipe is increased at $\sim 4^\circ\text{C}/\text{min}$ to the desired value. After the temperature set point of each heat pipe is stabilized, the system is thermally equilibrated for 30 minutes. The germanium crystals are grown at constant crucible lowering rates of either 2 or 4 $\mu\text{m}/\text{sec}$. The grown crystals range from 11 to 21 cm in length.

2.2 Pseudo-Steady-State Model

The pseudo-steady-state model (PSSM) of directional solidification (Chang,1983; Adornato,1986) takes the approach of simultaneously determining axisymmetric convection and solute transport in the melt, heat transfer in melt, crystal, and ampoule and the melt/solid interface shape. A prototypical vertical Bridgman-Stockbarger crystal growth system is illustrated in Figure 2.3

2.2.1 Modelling Assumptions

The finite length of a real ampoule in a Bridgman growth system causes the transport phenomena in this system to be transient for any nonzero translation rate, through the steady decrease of the melt volume. These transients are slow for the growth rates typical for semiconductor materials. The pseudo-steady-state model has been generated by replacing the unsteady problem with a pseudo-steady-state process viewed from a stationary reference frame and described in the cylindrical polar coordinate system shown in Figure 2.3. Thus, the description neglects transients in the field variables (velocity, pressure, temperature and concentration) caused by the steady decrease of the volume of the melt and the displacement of the ampoule in the furnace. The translation of the ampoule through the furnace is accounted for by supplying melt to the ampoule at the top ($\bar{z} = 0$) with uniform velocity V_m and composition c_o and removing crystal from the bottom of the ampoule at the same average composition and growth rate V_g

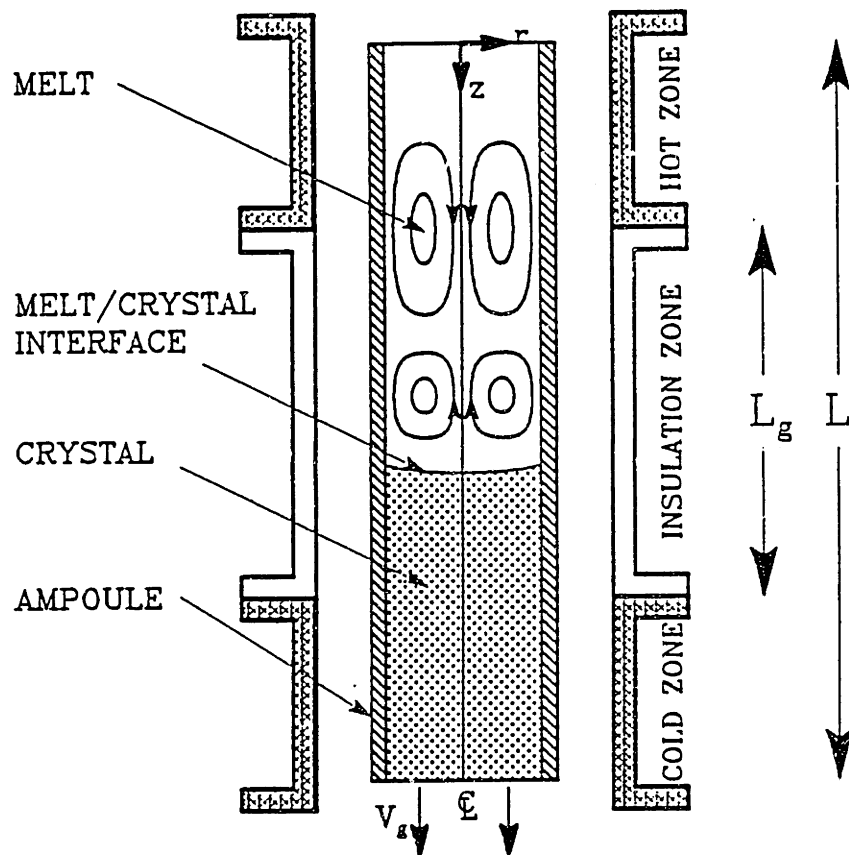


Figure 2.3: A prototypical vertical Bridgman-Stockbarger crystal growth system.

determined to conserve mass:

$$V_g = V_c = V_m(\rho_m/\rho_c). \quad (2.1)$$

Since the pseudo-steady-state model does not include the ends of ampoule, end effects cannot be taken into account. Fortunately, thermal end effects are negligible for sufficiently long ampoules (Sukanek, 1982a, 1982b; Jasinski *et al.*, 1983).

The major assumptions and approximations of the pseudo-steady-state model are:

1. The field variables are axisymmetric. This assumption allows for a two-dimensional model and is a reasonable approximation to the vertically stabilizing Bridgman system. The assumption of axisymmetry may eliminate the possibility of three-dimensional nature of field variables in a destabilized growth system as indicated by recent works (Müller *et al.*, 1984; Potts and Wilcox, 1986; Neugebauer and Wilcox, 1988).
2. The melt is assumed to be a Boussinesq fluid (Turner, 1973). A linear change in density due to variations in temperature and concentration affects only the buoyancy term in the Navier-Stokes equation. Elsewhere, the density is approximated as a constant. Under the conditions appropriate for the growth of germanium crystal in the experiment by Wang (1984), $\Delta\rho/\rho$ is about 1 %, which justifies this assumption.
3. When the density of the melt changes, on solidification it induces the flow near the interface. Mathematically, this implies an aphysical jump in the velocity at the ampoule wall and introduces a singularity at the tri-junction of melt, crystal and ampoule. Analysis of a similar singularity for liquid/liquid/solid contact lines has demonstrated the necessity of allowing the fluid to slip in a small region near the contact line (Huh and Scriven, 1971; Dussan, 1979). For typical semiconductor material, this density change is small (~ 3 % for germanium). Therefore, densities in both phases are assumed to be same throughout the analysis, *i.e.* $\rho_m = \rho_s$.
4. The pseudo-steady-state model simulates the crystal growth process in the region where the crystal growth rate is the same as lowering rate of ampoule. Al-

though the growth rate was shown to be transient at all times in the conventional Bridgman-Stockbarger growth system (Wang *et al.*, 1984), it was also demonstrated that growth rate reached the steady lowering rate of the ampoule after the initial transient period in carefully designed heat pipe furnaces (Wang, 1984).

5. The time scale for solute redistribution in the melt is assumed to be small compared with the growth rate. Solute is transported in the melt both by convection along streamlines and by diffusion across solute gradients where each mechanism occurs on different time scales. Rhines and Young (1983) argued that the first stage of solute redistribution is due to the rapid convection followed by the much slower diffusion process. Intense convection and steep solute gradients prevail in the vertical Bridgman growth process; this assumption seems reasonable.
6. Perfect thermal contact at the melt/ampoule and crystal/ampoule interfaces is assumed, so that the conductive heat fluxes at these boundaries are equal on both sides. The effect of imperfect thermal contact on the interface shape has been discussed recently by Holland (1989).
7. Ampoule and furnace temperature are not very different at a specific axial location so that the radiative contribution can be linearized, as was done by Jasinski *et al.* (1983).
8. Heat transfer in the crystal consists only of conduction and convection. This is valid for systems where bulk radiative transfer is not important. However, recent investigations revealed that internal radiation can affect the temperature distribution and convection pattern appreciably for semitransparent materials (Matsushima and Viskanta, 1988).
9. The thermal conductivities of all the phases including melt, crystal and crucible are assumed to be isotropic. For melts, the assumption of isotropic thermal conductivity is quite reasonable. However, the thermal conductivity in the crystal can be anisotropic depending on the crystallographic orientations (Carslaw and Jaeger, 1959). Because of the difficulty of making accurate measurements on con-

duction of heat, little accurate information is available for the conductivity tensor for specific crystals.

10. The kinetics of the melt/solid phase transformation is assumed to be infinitely fast since the time scale for the solidification reaction is much smaller than that for heat transfer. Also, supercooling at the melt/solid interface is excluded, so that the melt/solid interface shape follows the melting point in the system. In addition, it is assumed that the surface free energy does not affect the interface shape.
11. The solidification front is assumed to be smooth on the length scale used in this analysis. The existence of a mushy region is neglected as in an analysis by Thomson and Szekely (1988). Although there are ways to include the mushy zone in the analysis of solidification (Bennon and Incropera, 1988; Salcudean and Abdullah, 1988; Poulikakos and Cao, 1989), there has been no evidence for mushy zone for the growth of semiconductor materials in the stabilized vertical Bridgman system.
12. No cross-coupling is assumed to be present between heat and mass transfer, such as the Soret and Dufour effects. These effects are only coupled through the dependence of density on the temperature and composition.
13. As has been indicated by several authors (Jasinski *et al.*, 1984; Jasinski and Witt, 1985), the presence of crucible and the difference in thermal conductivities of melt, crystal and crucible introduce the singular behavior at the tri-junction of melt, solid and crucible. This singularity is due to the fact that temperature gradient at the melt/solid interface suffers a sudden change while the temperature gradient in the crucible does not. Kuiken (1988) analyzed this singular behavior to find that the singularity is weakly logarithmic. In the PSSM, no attention has been paid to this singularity in developing finite element method.
14. The crucible is assumed to be inert to the melt. When the crucible is highly reactive, surface reaction terms on the crucible wall should be accounted.

2.2.2 Governing Equations and Boundary Conditions

The physical configuration of the mathematical model for vertical Bridgman growth system is shown schematically in Figure 2.3. The distinguished phases are melt, crystal and ampoule, each of which is characterized by different thermophysical properties. The axisymmetric cylindrical coordinate system (r, z) is placed so that $r = 0$ coincides with the axis of crucible and $z = 0$ is located at the top of the ampoule.

Variables are put in dimensionless form by scaling lengths with the radius of the crystal, velocity $\tilde{\mathbf{v}}(r, z)$ with ν/R_c , pressure $\tilde{p}(r, z)$ with $\tilde{\rho}_m \nu^2/R_c^2$ and composition $\tilde{c}(\tilde{r}, \tilde{z})$ with the inlet concentration c_o , where ν is the kinematic viscosity in the melt and ρ_m is a melt density. The dimensionless concentration and temperature are defined as

$$S(r, z) \equiv c(r, z) - 1 \quad (2.2)$$

$$\theta(r, z) \equiv \frac{T(r, z) - T_{cold}}{T_{hot} - T_{cold}} \quad (2.3)$$

where T_{hot} and T_{cold} are the dimensional temperatures in the hot and cold zones, respectively.

In a nondilute binary alloy, convection in the melt is driven by density variations due to both temperature and composition. The dependence of density on these variables is expressed by the linear relation

$$\tilde{\rho} = \rho_o [1 - \beta_t(T - T_o) - \beta_s(\tilde{c} - c_o)] \quad (2.4)$$

where the reference density is that of the melt at the temperature T_o and composition c_o . The coefficients of thermal and solutal expansion are defined as $\beta_t \equiv -(1/\tilde{\rho})(\partial\tilde{\rho}/\partial T)_{\tilde{p},\tilde{c}}$ and $\beta_s \equiv (1/\tilde{\rho})(\partial\tilde{\rho}/\partial\tilde{c})_{\tilde{p},T}$, respectively. Equation (2.4) is written in terms of dimensionless variables as

$$\Delta\rho \left(\frac{gR_c^3}{\nu^2} \right) \equiv (\rho - 1) \left(\frac{gR_c^3}{\nu^2} \right) = \frac{1}{Pr} \{ Ra_s S - Ra_t (\theta - 1) \} \quad (2.5)$$

where ρ is the dimensionless density ($\tilde{\rho}/\rho_o$) and Pr , Ra_t and Ra_s are the Prandtl number,

thermal and solutal Rayleigh numbers, respectively. These and other dimensionless groups are listed in Table 2.1.

Under the assumptions described above, the two-dimensional axisymmetric forms of the steady-state equations of motion, continuity, and transport of heat and solute in the melt are (Bird *et al.*, 1960):

$$\nabla \cdot \mathbf{v} = 0 \quad (2.6)$$

$$\mathbf{v} \cdot \nabla \mathbf{v} = -\nabla p + \nabla^2 \mathbf{v} - \frac{1}{Pr} \{ Ra_s S - Ra_t (\theta - 1) \} \mathbf{e}_z \quad (2.7)$$

$$Pr \mathbf{v} \cdot \nabla \theta = \nabla^2 \theta \quad (2.8)$$

$$Sc \mathbf{v} \cdot \nabla S = \nabla^2 S \quad (2.9)$$

where Sc is Schmidt number and ∇ is the gradient operator.

The energy equations in the crystal and ampoule are

$$Pe \mathbf{e}_z \cdot \nabla \theta = \gamma_c \nabla^2 \theta \quad (2.10)$$

$$Pe \mathbf{e}_z \cdot \nabla \theta = \gamma_a \nabla^2 \theta \quad (2.11)$$

where Pe is dimensionless growth rate or Peclet number and $\gamma_c \equiv \alpha_c / \alpha_m$ and $\gamma_a \equiv \alpha_a / \alpha_m$ are ratios of the thermal diffusivities of each phase to the value for the melt.

The boundary condition that is distinguished to determine the melt/crystal interface shape is the equilibrium condition described as

$$\theta(r, H(r)) = \theta_m(S) = \theta_m^0 + m(S + 1 - 1/k) \quad (2.12)$$

where θ_m^0 is the melting temperature of the alloy with concentration $1/k$ and dimensionless slope m is obtained from the binary phase diagram by approximating a curve with a straight line. It has been shown that iterative schemes using the equilibrium condition to determine interface shape are more accurate and efficient than methods based on the balance of heat flux (Ettouney and Brown, 1983). The location of the melt/crystal interface is described by $z = H(r)$, $0 \leq r \leq 1$. The unit vectors normal \mathbf{N} and tangential

Dimensionless Groups	Definition
thermal Rayleigh number	$Ra_t \equiv \frac{\beta_t g \Delta T R_c^3}{\alpha_m \nu}$
solulal Rayleigh number	$Ra_s \equiv \frac{\beta_s g c_o R_c^3}{\alpha_m \nu}$
Peclet number	$Pe \equiv \frac{V_g R_c}{\alpha_m}$
Prandtl number	$Pr \equiv \frac{\nu}{\alpha_m}$
Schmidt number	$Sc \equiv \frac{\nu}{D}$
Stefan number	$St \equiv \frac{\Delta H_f}{C_{pm} \Delta T}$

Table 2.1: Dimensionless groups.

\mathbf{t} to the surface are written as

$$\mathbf{N} = \frac{\mathbf{e}_z - H_r \mathbf{e}_r}{\sqrt{1 + H_r^2}}, \quad \mathbf{t} = \frac{\mathbf{e}_r + H_r \mathbf{e}_z}{\sqrt{1 + H_r^2}} \quad (2.13)$$

where $H_r \equiv dH/dr$ and $(\mathbf{e}_r, \mathbf{e}_z)$ are the unit vectors in axisymmetric cylindrical coordinates.

The interfacial temperature and solute fields are related to the corresponding values in the bulk melt by the balances

$$[\mathbf{N} \cdot \nabla \theta]_m - K_c [\mathbf{N} \cdot \nabla \theta]_c = St Pe (\mathbf{N} \cdot \mathbf{e}_z) \quad (2.14)$$

$$[\mathbf{N} \cdot \nabla S] = \frac{Pe Sc}{Pr} (\mathbf{N} \cdot \mathbf{e}_z) (1 - k) (S + 1) \quad (2.15)$$

where St is the Stefan number, k is the equilibrium distribution coefficient, and $K_c \equiv k_c/k_m$ is the ratio of thermal conductivities between crystal and melt. The product $(Pe Sc/Pr)$ is the Peclet number for solute transfer which is the dimensionless growth velocity based on the solute diffusivity. It is used to describe the effect of growth on solute transport.

The boundary conditions on the velocity field at the interface are

$$\mathbf{v} \cdot \mathbf{t} = \frac{Pe}{Pr} (\mathbf{e}_z \cdot \mathbf{t}), \quad \sigma (\mathbf{v} \cdot \mathbf{N}) = \frac{Pe}{Pr} (\mathbf{e}_z \cdot \mathbf{N}) \quad (2.16)$$

where $\sigma \equiv \rho_c/\rho_m$. The top and sidewall of the ampoule are assumed to be no-slip surfaces so that $v_r = 0$ and $v_z = Pe/Pr$ are essential boundary conditions there.

The top of the melt is taken as the fictitious inlet where the Danckwerts boundary condition (Danckwerts, 1955) is set:

$$\frac{\partial S}{\partial z} = \frac{Pe Sc}{Pr} S \quad \text{for } 0 \leq r \leq 1, z = 0. \quad (2.17)$$

With this boundary condition, the solute entering the top of the ampoule balances the solute transported by convection and diffusion in the melt. Equation (2.17) introduces a

discontinuity in concentration at the inlet boundary. Nevertheless, it is more reasonable approximation than assuming the constant concentration at this boundary.

Thermal boundary conditions are specified along the ampoule wall according to the heat transfer condition

$$\left[\frac{\partial \theta}{\partial r} \right]_a = Bi(z) [\theta_\infty(z) - \theta] \quad (2.18)$$

where $Bi(z)$ is a dimensionless heat transfer coefficient ($Bi = h_a R_c / k_a$) defined to include radiative, conductive, and convective transport between the ampoule and the furnace, and $\theta_\infty(z)$ is the temperature distribution of the furnace wall. The particular profiles of $Bi(z)$ and $\theta_\infty(z)$ depend on the design of the furnace and should be determined accordingly. The top and bottom of the domain of interest do not coincide with the real top and bottom of the ampoule. The temperature on these boundaries are assumed to be that of hot and cold zone, *i.e.* $\theta = 1$ at $z = 0$ and $\theta = 0$ at $z = 1$. These conditions have little influence on the calculations when the ampoule is sufficiently long.

The axis of the cylinder is taken as a line of symmetry for all field variables,

$$v_r = \frac{\partial v_z}{\partial r} = \frac{\partial \theta}{\partial r} = \frac{\partial S}{\partial r} \text{ at } r = 0 \quad (2.19)$$

which is consistent with the assumption of axisymmetric fields.

2.3 Transient Model

The finite length of a real ampoule in a Bridgman growth system causes the transport phenomena in this system to be transient for any nonzero translation rate through the steady decrease of the melt volume. This should be reflected in the quantitative model so that it can describe or predict the transport phenomena occurring in the system as accurately as possible.

2.3.1 Modelling Assumptions

Major assumptions and approximations for the pseudo-steady-state model are still valid except the followings:

1. The Melt and crystal are enclosed in the ampoule and there is neither source nor sink of material. That is, the melt, crystal and ampoule form a closed system with respect to mass transfer and an open system with respect to heat transfer.
2. The ampoule has finite length so that the melt volume changes in time with solidification as the ampoule translates through the furnace. Accordingly, all the field variables (velocity, pressure, temperature and concentration) and interface shape and location exhibit transient behavior.
3. In practice the space occupied by melt and crystal in the ampoule expands or shrinks depending upon the density change on solidification. However, in this transient model melt and crystal fill the ampoule completely, leaving no free surface at the top of the melt. Therefore, there is no necessity to consider surface-driven convection in the melt. This is consistent with the approximation of equal densities of melt and crystal.
4. Remelting or back-melting is not accounted in the growth process. It would be necessary to solve the solute equation in the crystal to account for the remelting of the crystal.
5. The thickness of the ampoule at the top and bottom is assumed to be very thin. The error generated by this assumption is negligible when the temperature at the top and bottom of ampoule is equilibrated with the furnace temperature.
6. Because of the translation of the ampoule, it is more efficient to fix the coordinate system to the ampoule. Thus, the translation of the ampoule is accounted for by the time-dependent change of profiles of furnace temperature and heat transfer coefficients between the furnace and the ampoule with respect to this coordinate system.

2.3.2 Governing Equations and Boundary Conditions

The physical configuration of the time-dependent model for the vertical Bridgman growth system is shown schematically in Figure 2.3. The axisymmetric cylindrical coordinate system (r, z) is placed so that the origin of coordinate is located at the axis of ampoule top, as shown in Figure 2.3.

The scales used for the nondimensionalization are the same as for PSSM, except that time is scaled with momentum diffusion time, R_c^2/ν . There are several possible choices of time scale: the thermal diffusion time, solute diffusion time, momentum diffusion time and ampoule translation rate. Among these, momentum diffusion time was chosen following the analysis of thermal convection by Gresho *et al.* (1980a).

The magnitudes of these time scales are compared for the growth of Ga-doped Ge in the vertical Bridgman system used by Wang (1984). With the kinematic viscosity $\nu = 0.0013$ and thermal diffusivity $\alpha = 0.20$ for the molten germanium, the solute diffusivity of Ga in Ge $D = 2.1 \times 10^{-4}$, and the translation rate $V_g = 4\mu\text{m}/\text{sec}$ of ampoule $R_c = 0.68$ cm, the characteristic times are

$$\text{for momentum diffusion} \quad t_m = \frac{R_c^2}{\nu} = 355.2 \text{ sec}$$

$$\text{for heat conduction} \quad t_h = \frac{R_c^2}{\alpha} = 2.3 \text{ sec}$$

$$\text{for solute diffusion} \quad t_s = \frac{R_c^2}{D} = 2199 \text{ sec}$$

$$\text{for ampoule translation} \quad t_a = \frac{R_c}{V_g} = 1699 \text{ sec}$$

The ratio of these time scales to the momentum diffusion time are represented in terms of dimensionless groups as

$$\frac{t_h}{t_m} = \frac{\nu}{\alpha} = Pr = \mathcal{O}(10^{-3} - 10^{-2})$$

$$\frac{t_s}{t_m} = \frac{\nu}{D} = Sc = \mathcal{O}(10)$$

$$\frac{t_a}{t_m} = \frac{\nu}{V_g R_c} = \frac{Pr}{Pe} = \mathcal{O}(1 - 10) \quad (2.20)$$

where the orders of magnitude are for the typical semiconductor materials. From these comparisons, we expect that the selection of momentum diffusion time for nondimensionalizing the time in transient model neglects the transient in heat conduction which occurs on a much smaller time scale. The calculated temperature fields from transient model will not differ much from the results of steady-state calculation. However, the transients in the flow and solute fields will be described well enough with this selection of time scale.

Using the assumptions listed above and in the PSSM, the time-dependent field equations in the melt are written as

$$\nabla \cdot \mathbf{v} = 0 \quad (2.21)$$

$$\frac{\partial \mathbf{v}}{\partial \tau} + \mathbf{v} \cdot \nabla \mathbf{v} = -\nabla p + \nabla^2 \mathbf{v} + \frac{1}{Pr} (Ra_s S - Ra_t \theta) \mathbf{e}_z \quad (2.22)$$

$$Pr \left(\frac{\partial \theta}{\partial \tau} + \mathbf{v} \cdot \nabla \theta \right) = \nabla^2 \theta \quad (2.23)$$

$$Sc \left(\frac{\partial S}{\partial \tau} + \mathbf{v} \cdot \nabla S \right) = \nabla^2 S \quad (2.24)$$

where the dimensionless groups are define in Table 2.1.

The energy equations in the crystal and ampoule are

$$Pr \left(\frac{\partial \theta}{\partial \tau} \right) = \gamma_c \nabla^2 \theta \quad (2.25)$$

$$Pr \left(\frac{\partial \theta}{\partial \tau} \right) = \gamma_a \nabla^2 \theta \quad (2.26)$$

where $\gamma_c \equiv \alpha_c / \alpha_m$ and $\gamma_a \equiv \alpha_a / \alpha_m$ are ratios of the thermal diffusivities of each phase to the value for the melt.

In the transient model, the distinguished boundary condition to determine the in-

interface shape and location is the same equilibrium condition described in the pseudo-steady-state model.

For the coordinate system which moves with the ampoule translation rate V_g , boundary conditions at the interface are different from those used in PSSM. The temperature and solute fields are subject to the following balances.

$$[\mathbf{N} \cdot \nabla \theta]_m - K_c [\mathbf{N} \cdot \nabla \theta]_c = -St Pr \frac{\partial H}{\partial \tau} (\mathbf{N} \cdot \mathbf{e}_z) \quad (2.27)$$

$$[\mathbf{N} \cdot \nabla S] = -Sc \frac{\partial H}{\partial \tau} (\mathbf{N} \cdot \mathbf{e}_z) (1 - k)(S + 1) \quad (2.28)$$

where $\partial H / \partial \tau (\mathbf{N} \cdot \mathbf{e}_z)$ is the normal component of interface velocity.

The boundary condition on the velocity field at the interface and on the inside wall of the ampoule becomes

$$\begin{aligned} \mathbf{v} = \mathbf{0} \quad & \text{for } 0 \leq r \leq 1, z = 0, H(r, \tau) \\ & \text{and } r = 1, 0 \leq z \leq H(1, \tau) \end{aligned} \quad (2.29)$$

to satisfy the no-slip condition.

Thermal boundary condition is also dependent on time as the ampoule translates.

$$\left[\frac{\partial \theta}{\partial r} \right]_a = Bi(z, \tau) [\theta_\infty(z, \tau) - \theta(r, z, \tau)] \quad (2.30)$$

where $Bi(z, \tau)$ and $\theta_\infty(z, \tau)$ are functions of time and determined from the characteristics of furnace design.

Another boundary conditions assumed here is that the surfaces of the ampoule are not a source or sink for the solute, so that the fluxes there are zero:

$$\left[\frac{\partial S}{\partial z} \right]_{z=0} = \left[\frac{\partial S}{\partial r} \right]_{r=1} = 0 \quad (2.31)$$

As mentioned in a previous subsection, the boundary conditions for heat transfer at the top and bottom of the ampoule are not easily defined. Most of the previous

works employed the Newton's cooling-law boundary conditions (Kreith, 1958) with the magnitude of heat transfer coefficient depending on those in hot and cold zone (Sen and Wilcox, 1975; Sukanek, 1982a, 1982b; Chin and Carlson, 1983). The insulated ends were also use in the analysis (Bourret *et al.*, 1985; Derby and Brown, 1986). In the present model, the temperature on this boundaries are assumed to be that of furnace at the same axial location. Because the furnace temperature profile is time-dependent, the top and bottom temperature of the ampoule also varies with time.

$$\theta(r, z, \tau) = \theta_{\infty}(z, \tau) \quad \text{for } 0 \leq r \leq \Lambda_a, z = 0, L/R_c \quad (2.32)$$

where $\Lambda_a \equiv R_a/R_c$; R_a and R_c are radii of ampoule and crystal respectively.

The axis of the cylinder is taken as a line of symmetry for all field variables as in PSSM.

$$v_r = \frac{\partial v_z}{\partial r} = \frac{\partial \theta}{\partial r} = \frac{\partial S}{\partial r} \quad \text{at } r = 0 \quad (2.33)$$

which is consistent with the assumption of axisymmetric fields.

The specification of the moving-boundary problem is completed by setting the initial velocity, solute and temperature profiles and interface location at $\tau = 0$. These initial conditions are obtained from steady-state calculations of velocity and temperature field in the absence of ampoule translation. The initial condition for the solute field specifies a uniform concentration throughout the melt.

The transient model developed here is based on the vertical Bridgman growth system used in the experiments by Wang (1984). However, the application of this model is not restricted to Wang's system and is extended to various kinds of confined growth systems where the crystal is grown vertically in a gravitational field or in any direction under zero gravity condition, such as the conventional Bridgman growth system (Wang, 1984), constant gradient furnace (Rouzaud *et al.*, 1985), a vertical gradient freeze growth system (Gustafson *et al.*, 1986; Gault *et al.*; 1986; Monberg *et al.*, 1987,1988; Clemans and Conway, 1988).

The experimental system of Wang (1984) at MIT for the growth of dilute Ga-doped

Ge is simulated in Chpter 6, along with the growth of Se-doped GaAs in the furnace at GTE (Arnold *et al.*, 1989). The growth of pseudobinary HgCdTe alloy in the vertical Bridgman system at NASA (Szofran and Lehoczky, 1984) is analyzed in Chapter 7.

Chapter 3

Numerical Formulation

Detailed analysis for optimization of the design and control of crystal growth systems requires efficient and accurate numerical methods for solution of the complex free- and moving-boundary problems that describe solidification including thermosolutal convection and transport of solute. The set of governing equations in Chapter 2 defines such a nonlinear free-boundary problem for the pseudo-steady-state model and a moving-boundary problem for the transient model.

A Galerkin finite element method coupled with the Newton iteration scheme has been developed previously for the simultaneous computation of the field variables and interface shape for steady-state solidification problems (Chang and Brown, 1983a,b,1984; Adornato and Brown, 1987a,b). In this chapter, the numerical method based on Galerkin finite element method, Newton iteration and implicit time integration is developed for the transient model described in Chapter 2.

The general concepts of the finite element method are outlined in Section 3.1 and followed in Sections 3.2 and 3.3 by the specific applications to the pseudo-steady-state and transient models, respectively. These Sections include the details of the approximation methods for the field and interface variables, the discretization schemes for the partial differential equations, and the solution method for the resultant nonlinear

algebraic equation and differential equation sets.

3.1 Finite Element Method

The *finite element method*, which was first devised for structural analysis (Zienkiewicz, 1971), has become recognized as an effective tool for analysis of a wide range of physical problems. Among these are problems in the field of fluid mechanics and heat and mass transport, which are discussed extensively in a series of books, *Finite Elements in Fluids* (Gallagher *et al.*, 1975a, 1975b, 1978, 1982, 1984, 1985, 1988) and in the journal, *International Journal for Numerical Methods in Fluids*. Special emphasis has been placed on the finite element solution of Navier-Stokes equations by Thomasset (1981), Girault and Raviart (1986) and Cuvelier *et al.* (1986). General background is available in the books by Zienkiewicz (1977), Chung (1978), Irons and Ahmad (1980), Huebner and Thornton (1982), Rao (1982), Fletcher (1984) and Schwarz (1988). Along with the empirical success of finite element method for solving these physical problems, mathematical theory has been developed to describe the computational accuracy of the finite element approximations (Strang and Fix, 1973; Whiteman, 1973–1987; Oden and Carey, 1982).

The basic philosophy underlying the finite element method is that any continuous variable, such as temperature, pressure, velocity or concentration, can be approximated with low-order polynomial interpolating functions which are defined in a piecewise manner over a finite number of subdomains or elements. The interpolating functions, also called approximation functions, basis functions, shape functions or trial functions, are defined by the values of the variable at a set of nodes. The behavior of the variables within the elements is completely described in terms of these nodal values and the underlying interpolating functions. The nodal values are unknowns in the solution of a partial differential equation and the success of finite element analysis depends on how fast and accurately the nodal values can be computed subject to the equation and boundary conditions. The finite element method formulates the problem in each individual element and then combines the elemental formulation for the solution of the problem in global

domain. This feature reduces a complicated problem to a series of routine operations in each element. This procedure is well suited to the computation with large digital computers.

Concepts of the finite element method began to solidify in 1960's when Melosh (1963) and Jones (1964) recognized that the finite element method was a variant of the Rayleigh-Ritz method and confirmed it as a general technique for solving linear elastic continuum problems. The finite element method received an even broader interpretation when Zienkiewicz and Cheung (1965) reported that it is applicable to all field problems that could be cast into variational form. The applicability of finite element analysis was extended even farther when it was shown that the weighted residual approach could be easily applied when a variational formulation was not available (Szabo and Lee, 1969; Zienkiewicz and Parekh, 1970). Among the various weighted residual methods, the Galerkin method has been proved in practice to be the most powerful technique for the approximation of the solution of differential equations (Finlayson, 1972). Galerkin's method not only encompasses the variational formulation, when such exists, but also goes far beyond, because it can be applied to any well-posed system of differential equations and boundary conditions.

The fundamental idea is briefly described here for the formulation and solution of a boundary-value problem written in operator form as

$$\mathcal{L} \{ \mathbf{u}(\mathbf{x}) \} = \mathbf{f}(\mathbf{x}), \quad (3.1)$$

where \mathcal{L} is a differential operator, $\mathbf{u}(\mathbf{x})$ is the function of independent variable \mathbf{x} and $\mathbf{f}(\mathbf{x})$ is the nonhomogeneous forcing function. In Galerkin's method (Galerkin, 1915) $\mathbf{u}(\mathbf{x})$ is approximated within a finite-dimensional subspace of the original function space by

$$\mathbf{u}(\mathbf{x}) \cong \hat{\mathbf{u}}(\mathbf{x}) = \sum N^i(\mathbf{x}) a_i = \mathbf{N}(\mathbf{x}) \mathbf{a}, \quad (3.2)$$

where \mathbf{u} represents the solution to the continuum problem, $\hat{\mathbf{u}}$ is the approximation to \mathbf{u} in the discretized problem, \mathbf{N} is a vector of interpolating functions and \mathbf{a} is the vector of scalar coefficients. The coefficients are determined so as to minimize the error of the

discrete solution $\hat{\mathbf{u}}$. This is done by forcing each of the inner products of Eq. (3.1) and weighting functions to be zero ,i.e.

$$\langle \mathcal{L}(\mathbf{u}) - \mathbf{f}, \mathbf{w} \rangle = 0, \quad (3.3)$$

where $\langle \cdot, \cdot \rangle$ is the appropriate inner product in the function space and \mathbf{w} is a set of arbitrary weighting functions the number of which is equal to that of unknowns. The boundary conditions on \mathbf{u} are accounted for either by adding constraints or by integrating by parts and replacing the relevant term with boundary conditions. If Eq. (3.3) holds for all \mathbf{w} , then the boundary-value problem, Eq. (3.1), with corresponding boundary conditions are satisfied in a *weak* sense (Strang and Fix, 1973); the resulting form of Eq. (3.3) is called the *weal form*. When the weighting functions are chosen to be the same as interpolating functions, that is , $w_i = N_i$ for $i = 1, \dots, N$, Eq. (3.3) is called the Bubnov-Galerkin method or simply the Galerkin finite element method. Otherwise, the residual formulation (3.3) is called the Petrov-Galerkin method, which will be examined briefly in the next Section.

The behaviour of the field variables in the solution domain is described by the nodal values and interpolating functions in the finite element method, and the efficiency and accuracy of the Galerkin finite element method depends on the choice of the functions. The interpolating functions are defined in such a way that, as the finite element mesh is refined, the approximate Galerkin solution converges to the exact solution. Sufficient condition for the convergence requirement is that the elements should be *compatible* and *complete* (Hughes, 1987). The compatibility and completeness are discussed below.

The requirement of *compatibility* means that the interpolating functions should be smooth (i.e. at least C^1) on each element interior, Ω^e , and continuous across each element boundary, $\partial\Omega^e$. When at most first derivatives appear in the integrands of weighted residual as is the case for the present study, finite elements constructed from the interpolating functions which satisfy above conditions are C^0 -elements. If the integrands involve derivatives of order m , the compatibility condition is strengthened so that the interpolating functions should be of class C^{m-1} . The elements which satisfy the compatibility requirement are called *conforming* elements.

We are interested in the second-order boundary value problem for which the first derivatives appears in the integrands of weighted residual equations. In this case, the concept of *completeness* requires that the element interpolating function is capable of exactly representing an arbitrary linear polynomial when the nodal degrees of freedom are assigned values in accordance with it. For problems involving m th derivatives in the integrands, completeness should be strengthened to m th-order polynomials. For convergence, the completeness is stronger requirement than compatibility and *patch test* has been proposed to ensure the global completeness of nonconforming finite elements (Bazeley *et al.*, 1965; Irons *et al.*, 1970; Strang and Fix, 1973).

The *weak* form of the boundary value problem and the finite element solutions and their derivatives must have certain integrability properties. Functions which have these properties are the elements of *Sobolev spaces of functions* defined as

$$H^k = H^k(\Omega) = \{w | w \in L_2; w_{,x} \in L_2; \dots; w_{, \underbrace{x \dots x}_{k \text{ times}}} \in L_2\}, \quad (3.4)$$

where

$$L_2 = L_2(\Omega) = \{w | \int_{\Omega} w^2 dx < \infty\}. \quad (3.5)$$

The Sobolev space of degree k , denoted by H^k , consists of functions that have square-integrable derivatives through order k . Details about the Sobolev spaces, which are most important in the numerical solution of the elliptic boundary value problems, are available in the book by Marti (1986). The smoothness and continuity of functions in each Sobolev space is provided by the *Sobolev imbedding theorems* (Oden and Reddy, 1976), which states that $H^s \subset C^k$ if Ω is a bounded domain in \mathcal{R}^n and $s > n/2 + k$. In the finite element analysis, the solutions are approximated as linear combinations of the interpolating functions in each element and it follows that interpolating functions are also elements of the Sobolev spaces. In the present study the highest derivatives are first order and functions in $H^1(\Omega)$ are required. These have the first derivatives with finite norm. To be more specific, the admissible functions are H_E^1 , where subscript E denotes that the essential boundary condition is satisfied, as discussed at length by Strang and Fix (1973).

The advantages of locally defined piecewise polynomials as a interpolating functions were first identified by Courant (1943) and by Prager and Synge (1960). Piecewise interpolating functions are defined over a few elements, outside of which the functions are zero. For example, the solution $u(x)$ of a one-dimensional elliptic problem is represented in a given element by

$$u(x) = \sum_{i=1}^N \alpha_i \tilde{N}^i(x), \quad (3.6)$$

where the coefficients $\{\alpha_i\}$ are the unknown nodal values, $\{\tilde{N}^i(x)\}$ is the set of one-dimensional interpolating functions and N is the total number of nodes in the domain. The discussion here concentrates on Lagrangian interpolating functions.

In each element, the interpolating functions can be represented in terms of local coordinate system ξ ($-1 \leq \xi \leq 1$) which has a linear relationship with the global coordinate:

$$u(x) = \sum_{j=1}^{N_b} \alpha_j \tilde{N}^j(\xi), \quad (3.7)$$

where N_b is the number of interpolating functions necessary for each element and depends on the order of interpolating functions: 2 for linear, 3 for quadratic, 4 for cubic interpolating functions. The forms of interpolating functions are given in Figure 3.1. Linear and quadratic basis functions are Lagrangian polynomials and the values of the coefficients represent the solution values $u(x)$ at the nodes of the element.

For Lagrangian polynomial interpolating functions, the transformation of global coordinate to the local coordinate system is done with the *isoparametric transformation*:

$$x = \sum_{j=1}^{N_b} x_j \tilde{N}^j(\xi), \quad (3.8)$$

where x is the original coordinate and the set $\{x_j\}$ are the positions of the nodes for each element.

With the isoparametric transformation, the evaluation of the derivatives and the integration using the inner product require the use of the chain rule and the computation

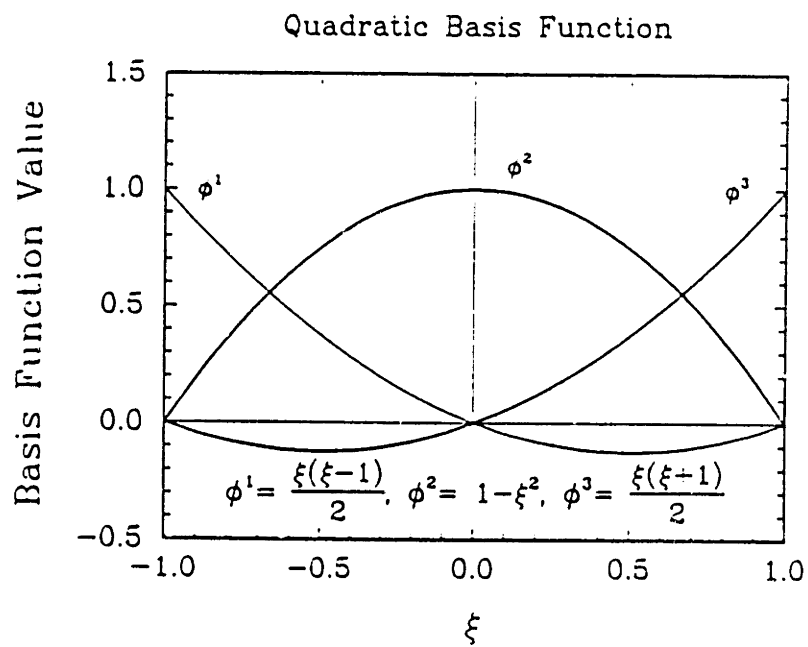
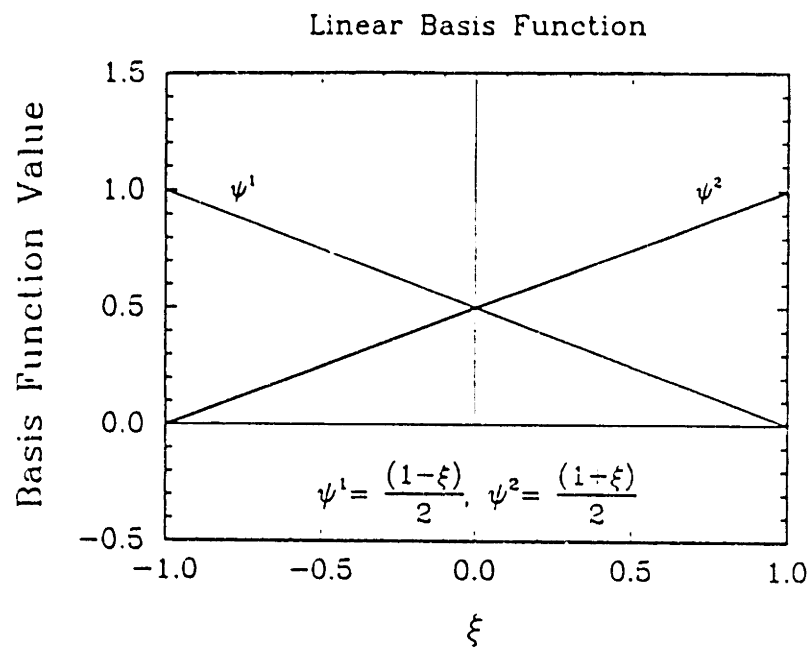


Figure 3.1: Lagrangian linear and quadratic basis functions defined on a unit element.

of the elemental Jacobian, because the interpolating functions are expressed in terms of the local coordinate ξ rather than in terms of x . For example,

$$\frac{du}{dx} = \sum_{j=1}^{N_b} \frac{d\tilde{N}^j}{dx} u_j = \det(J)^{-1} \sum_{j=1}^{N_b} \frac{d\tilde{N}^j}{d\xi} u_j, \quad (3.9)$$

where J is a elemental Jacobian and is $(dx/d\xi)$ in one dimension. The value of $\det(J)$ is $h_e/2$ for linear interpolation and for the special case of quadratic interpolation for which the middle node set at the mid-point of two corner nodes; h_e is the length of the one-dimensional element.

In a similar manner, a two-dimensional function $u(x, y)$ is approximated as

$$u(x, y) = \sum_{i=1}^N \alpha_i N^i(x, y) \quad (3.10)$$

where the coefficients $\{\alpha_i\}$ are the unknown nodal values, $\{N^i(x, y)\}$ is the set of two-dimensional interpolating functions and N is the total number of nodes in the domain.

In each element, the elements of global coordinate (x, y) are mapped into the unit element expressed in the (ξ, η) coordinate system $(-1 \leq \xi \leq 1, -1 \leq \eta \leq 1)$ with elemental interpolating functions

$$u(x, y) = \sum_{i=j}^{N_b} \alpha_j N^j(\xi, \eta). \quad (3.11)$$

The elemental interpolating functions $\{N^j(\xi, \eta)\}$ are constructed as the tensor products of the corresponding one-dimensional interpolating functions (Schwarz, 1988). The functional forms of the two-dimensional interpolating functions are listed in Table 3.1, where the bilinear and biquadratic interpolating functions are expressed as ψ and ϕ , respectively and \checkmark denotes the one-dimensional interpolating functions.

The nodes in the $\xi - \eta$ plane are mapped into corresponding nodes in the $x - y$ plane

Two-dimensional Basis Functions	Tensor Products	Polynomial Forms
Bilinear		
$\psi^1(\xi, \eta)$	$\bar{\psi}^1(\xi)\bar{\psi}^1(\eta)$	$(1 - \xi)(1 - \eta)/4$
$\psi^2(\xi, \eta)$	$\bar{\psi}^2(\xi)\bar{\psi}^1(\eta)$	$(1 + \xi)(1 - \eta)/4$
$\psi^3(\xi, \eta)$	$\bar{\psi}^1(\xi)\bar{\psi}^2(\eta)$	$(1 - \xi)(1 + \eta)/4$
$\psi^4(\xi, \eta)$	$\bar{\psi}^2(\xi)\bar{\psi}^2(\eta)$	$(1 + \xi)(1 + \eta)/4$
Biquadratic		
$\phi^1(\xi, \eta)$	$\bar{\phi}^1(\xi)\bar{\phi}^1(\eta)$	$\xi(\xi - 1)\eta(\eta - 1)/4$
$\phi^2(\xi, \eta)$	$\bar{\phi}^2(\xi)\bar{\phi}^1(\eta)$	$(1 - \xi^2)\eta(\eta - 1)/2$
$\phi^3(\xi, \eta)$	$\bar{\phi}^3(\xi)\bar{\phi}^1(\eta)$	$\xi(\xi + 1)\eta(\eta - 1)/4$
$\phi^4(\xi, \eta)$	$\bar{\phi}^1(\xi)\bar{\phi}^2(\eta)$	$\xi(\xi - 1)(1 - \eta^2)/2$
$\phi^5(\xi, \eta)$	$\bar{\phi}^2(\xi)\bar{\phi}^2(\eta)$	$(1 - \xi^2)(1 - \eta^2)$
$\phi^6(\xi, \eta)$	$\bar{\phi}^3(\xi)\bar{\phi}^2(\eta)$	$\xi(\xi + 1)(1 - \eta^2)/2$
$\phi^7(\xi, \eta)$	$\bar{\phi}^1(\xi)\bar{\phi}^3(\eta)$	$\xi(\xi - 1)\eta(\eta + 1)/4$
$\phi^8(\xi, \eta)$	$\bar{\phi}^2(\xi)\bar{\phi}^3(\eta)$	$(1 - \xi^2)\eta(\eta + 1)/2$
$\phi^9(\xi, \eta)$	$\bar{\phi}^3(\xi)\bar{\phi}^3(\eta)$	$\xi(1 + \xi)\eta(\eta + 1)/4$

Table 3.1: Two-dimensional Lagrangian bilinear and biquadratic interpolating functions.

by the *isoparametric* transformation:

$$x = \sum_{j=1}^{N_b} x_j N^j(\xi, \eta) \quad (3.12)$$

$$y = \sum_{j=1}^{N_b} y_j N^j(\xi, \eta) \quad (3.13)$$

where the (x_i, y_i) are the locations of the nodes in the elements. Curve-sided elements formulated in such a way that the functional representation of field variables and its curved boundaries are expressed by interpolating functions of the same order are called *isoparametric elements*. In contrast to isoparametric elements, *subparametric elements* are defined as elements whose geometry is described by a polynomial of order lower than the one used for the field variables and *superparametric elements* as those whose geometry is described by a higher-order polynomial (Huebner and Thornton, 1982). An example of an isoparametric mapping is shown in Figure 3.2. An important consideration in the construction of curved elements is preservation of the continuity conditions in the global coordinate system. In this regard, useful guidelines are suggested by Zienkiewicz *et al.* (1969).

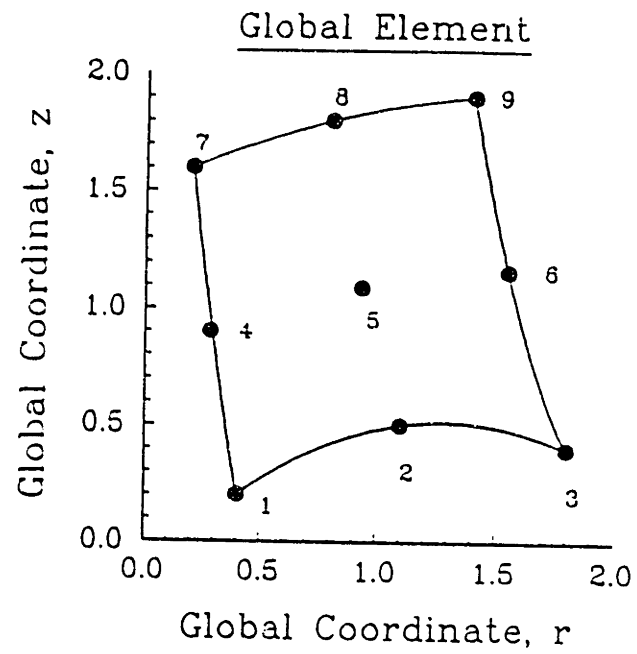
As discussed for the one-dimensional element, the isoparametric transformation of the field variables in two dimensions requires the evaluation of the element Jacobian. In two dimensions, this is

$$\frac{\partial u}{\partial x} = \frac{\partial u}{\partial \xi} \frac{\partial \xi}{\partial x} + \frac{\partial u}{\partial \eta} \frac{\partial \eta}{\partial x} \quad (3.14)$$

$$\frac{\partial u}{\partial y} = \frac{\partial u}{\partial \xi} \frac{\partial \xi}{\partial y} + \frac{\partial u}{\partial \eta} \frac{\partial \eta}{\partial y} \quad (3.15)$$

Unfortunately, the partial derivatives of ξ and η with respect to x and y are not directly available and the inverse of Eq. (3.14) must be written as

$$\frac{\partial u}{\partial \xi} = \frac{\partial u}{\partial x} \frac{\partial x}{\partial \xi} + \frac{\partial u}{\partial y} \frac{\partial y}{\partial \xi} \quad (3.16)$$



Isoparametric Mapping

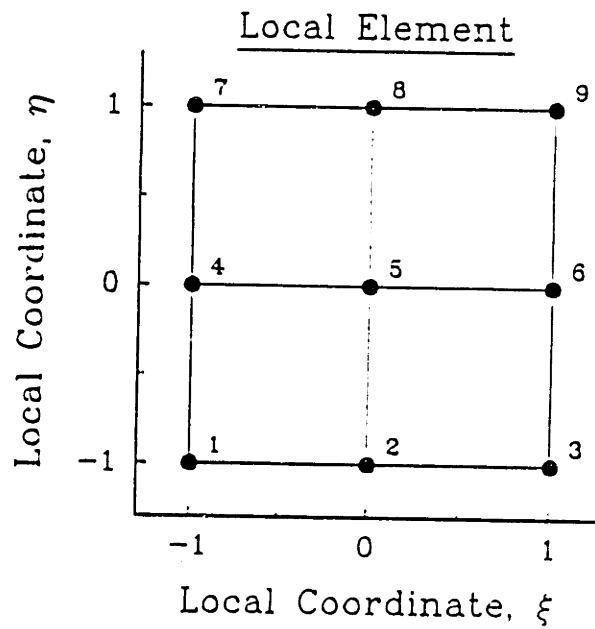


Figure 3.2: Isoparametric mapping of a biquadratic element.

$$\frac{\partial u}{\partial \eta} = \frac{\partial u}{\partial x} \frac{\partial x}{\partial \eta} + \frac{\partial u}{\partial y} \frac{\partial y}{\partial \eta}, \quad (3.17)$$

or

$$\begin{bmatrix} \partial u / \partial \xi \\ \partial u / \partial \eta \end{bmatrix} = [\mathbf{J}] \begin{bmatrix} \partial u / \partial x \\ \partial u / \partial y \end{bmatrix} \quad (3.18)$$

where $[\mathbf{J}]$ is the elemental Jacobian matrix and has components

$$[\mathbf{J}] = \begin{bmatrix} \partial x / \partial \xi & \partial y / \partial \xi \\ \partial x / \partial \eta & \partial y / \partial \eta \end{bmatrix} = \begin{bmatrix} \sum \partial N^i / \partial \xi x^i & \sum \partial N^i / \partial \xi y^i \\ \sum \partial N^i / \partial \eta x^i & \sum \partial N^i / \partial \eta y^i \end{bmatrix} \quad (3.19)$$

Then, Eq. (3.14) is written as

$$\begin{bmatrix} \partial u / \partial x \\ \partial u / \partial y \end{bmatrix} = [\mathbf{J}]^{-1} \begin{bmatrix} \partial u / \partial \xi \\ \partial u / \partial \eta \end{bmatrix} \quad (3.20)$$

The isoparametric mapping is invertible between the global and local elements if the determinant of the element Jacobian does not change sign over each element. This condition is satisfied if the quadrilateral element in the global domain is convex (Carey and Oden, 1983).

In the analysis of solidification problems, it is crucial to approximate accurately the location and shape of curved free- and moving-boundaries and the conditions imposed along these boundaries. Biquadratic elements with the isoparametric mapping are preferred to bilinear approximations. The other advantages of using the higher-order interpolating functions will be the higher *order of convergence* or *order of accuracy* for a given mesh size (Strang and Fix, 1973) and the requirement of less elements for a given level of accuracy (Brown, 1979).

Before going to the next Section, a comparison of the finite element method (FEM) and the finite difference method (FDM) will somewhat justify the use of the FEM in this work. The finite difference method has long been a driving force in computational

studies of transport phenomena since its beginning early in this century (Richardson, 1910; Roache, 1976). In spite of the more complex formulation, the FEM provides better features as a numerical tool in several respects:

1. The standard nine-point FDM is analogous to FEM if linear approximations are used in the FEM for problems with essential boundary conditions (Arakawa, 1966; Jespersen, 1974).
2. The FEM satisfies Neumann boundary conditions through the weak form as derived from the variational approach, which contributes toward a better conservation of field variables throughout the domain. This is not true of the FDM (Crandall, 1956).
3. Irregular boundaries are troublesome in the FDM and have lead to the use of coordinate transformations for solutions of transformed equations on a regular mesh (Thompson *et al.*, 1974). On the other hand, the FEM approximates the irregular boundaries in a self-consistent manner, accounting for the degree of the interpolating functions and mesh refinement.
4. Rigorous mathematical error estimates are available in the FEM (Strang and Fix, 1972), and help determine the number of elements and select the degree of interpolating functions needed to obtain a given level of accuracy.
5. The element-by-element formulation makes the FEM suitable to the numerical algorithms which take advantage of today's digital computer structure. Especially, many aspects of the FEM (for example, generation of the elemental arrays and iterative solution of global equations) are well suited to parallel computation (Noor *et al.*, 1983). These features have lead to the development of the *Finite Element Machine*, which is a computer with multiple processors operating in parallel and is designed to optimize the finite element computations Storaasli *et al.*, 1982; Adams, 1982).

3.2 Formulation of Pseudo-Steady-State Model

3.2.1 Introduction

The solution technique for the pseudo-steady-state model presented here was originally developed by Ettouney (1983), Chang (1983) and Adornato (1986) for the edge-defined film-fed crystal growth and vertical Bridgman crystal growth system. The distinguished feature of modelling transport phenomena in the crystal growth system is that it involves the phase change at the interface and it is crucial to representing the interface shape and location accurately as a part of solution to a free-boundary problem. Conservation equations written in terms of field variables (velocity, pressure, concentration in the melt and temperature in both phases) are coupled to the location of the melt/solid interface through the conditions at the phase boundary. For the boundary conditions associated with the melt/solid interface, essential boundary conditions and natural boundary conditions are used: the former specifies both melt and solid temperature along the interface equal to the equilibrium melting point of material and the latter balances the net energy flux by conduction through the interface with the latent heat released by solidification. Although both conditions must be satisfied simultaneously along the interface, one condition is used as a boundary condition for the energy balances and the other condition is *distinguished* for determining the shape of the interface.

The choice of *distinguished* condition for determining free surface strongly influences the rate of the convergence (Silliman and Scriven, 1980) and accuracy of a numerical solution (Ettouney and Brown, 1983) to a free-boundary problems. Ettouney and Brown (1983) found that the methods which employ melting point isotherm as a *distinguished* condition to determine interface location and use energy flux condition as boundary condition for the energy balance were more accurate and efficient than formulations based on the interfacial energy balance as a *distinguished* condition in their finite element analysis of heat transfer in edge-defined film-fed crystal growth system.

Analysis by Chang and Brown (1983a,b) used the isoparametric finite element rep-

representations of the velocity, pressure, temperature and solute fields with a consistent polynomial approximations to the melt/solid interface. Velocities, temperature and solute fields were approximated by expansions of Lagrangian biquadratic polynomials and the pressure in the melt was approximated by continuous bilinear polynomials. Galerkin's method was employed to reduce the partial differential equations to nonlinear algebraic equations and Newton's method coupled with direct Gaussian elimination was used to solve the algebraic system. When the Newton's method was not employed to solve the interface shape and field variables simultaneously, the calculation of the field variables and interface shape were decoupled into successive steps.

Traditional numerical schemes for the solution of free-boundary problems iterate between the calculation of the field variables for the assumed interface shape and procedure for updating the location of the interface (Bonnerot and Jamet, 1974; Kroeger and Ostrach, 1974; Duda *et al.*, 1975; Sparrow *et al.*, 1977; Saitoh, 1978; Ramachandran, 1982; Lesaint and Touzani, 1989). In calculating field variables, one of the interfacial boundary conditions mentioned above must be relaxed. Then, this relaxed condition is used to update a new location of the interface. On the other hand, Newton's method calculates the field variables and interface shape simultaneously by setting the interface location to be unknown and employing either boundary condition at the interface as a equation for this unknown interface location in building Jacobian matrix. When the equations for the field variables are nonlinear, Ettouney and Brown (1983) demonstrated that Newton's method used less computation time than the conventional schemes. This increase in computational efficiency was due to the well-known quadratic convergence rate of Newton's method compared with the linear convergence of the conventional successive approximation scheme (Ortega and Rheinboldt, 1970). The efficiency of the Isotherm/Newton method over successive approximation scheme for the free-boundary problem was also demonstrated by Chang and Brown (1983b) in the analysis of convection during vertical Bridgman crystal growth process. In view of the linear convergence rate of successive iteration scheme and the quadratic convergence rate of Newton's method, the efficiency of the Newton iteration scheme increases when the number of unknowns goes up, because the distinguished boundary condition adds only one extra

equation to the problem and the computational load in every iteration is almost same in either case.

Besides yielding more rapid convergence to the solutions of the discrete equation sets, Newton's method allows implementation of the continuation methods for tracking solutions in parameter space (Kubiček, 1976; Brown *et al.*, 1980) and of numerical techniques for detecting multiple solutions (Keller, 1977; Ur and Brown, 1982) and for determining solution stability with respect to small perturbations (Yamaguchi *et al.*, 1984).

The Galerkin finite element method is known to be stable and convergent for elliptic equations (Strang and Fix, 1973). However, this method is notoriously unstable for hyperbolic and nearly-hyperbolic equations such as convection-diffusion equation (Christie *et al.*, 1976, Brooks and Hughes, 1982). An example of convection-diffusion equation is written as

$$\nabla \cdot (k \nabla T) - \mathbf{V} \cdot \nabla T = 0$$

which is typical of convective heat transport problems. This equation is mathematically elliptic but with high velocity it can behave like hyperbolic equation because of the hyperbolicity of the convection operator. In many instances, these numerical instabilities of the Galerkin finite element method result in the oscillations in the solution field. The difficulties in the numerical solution of convection-diffusion equations are evident when steep gradients of the field variables within the boundary layer develop as the parameters multiplied to the convection terms increase so that the convection terms dominate over the diffusion terms. In this case, the loss of ellipticity due to the dominant convection term causes the numerical instabilities in the form of oscillations.

With the mesh refinement, the Galerkin approximations are improved to the extent so that the boundary layer of the field variables are adequately resolved and the oscillations are removed as the ellipticity of the equation in the elemental level is recovered. However, the extremely fine meshes that are needed to resolve the field variables adequately enough to stabilize the Galerkin approximation for complicated two- and three-dimensional flow problems are quite costly using present supercomputers, espe-

cially in the context of the Newton algorithm, which requires solution of large sets of linear equations. Alternatively, the Petrov-Galerkin method can be used to alleviate the oscillations in under-refined Galerkin or centered-difference schemes. The algorithm and discussion are available in the literature, as are the criticisms (Gresho and Lee, 1979; Leonard, 1979) inherent to any methods that purposely introduce artificial diffusivity into the approximations and lose the accuracy. Finite element methods for solving convection-dominated problems can be classified according to the formalism used to introduce artificial diffusivity into the Galerkin formulation. Methods based on modification of the numerical quadrature (Hughes, 1978), on direct introduction of an artificial diffusivity to increase the diffusivity (Hughes and Brooks, 1982; Kelly *et al.*, 1980) and on modification of the weighting function in the weighted residual method known as the Petrov-Galerkin method (Christie *et al.*, 1976; Heinrich and Zienkiewicz, 1977; Brooks and Hughes, 1982; Donea *et al.*, 1985) have been proposed. Some of these schemes will be tested in Section 3.2.5 for a convection-diffusion model which is analogous to the problems that arise in the analysis of crystal growth systems.

3.2.2 Discretization by the Galerkin Finite Element Method

The pseudo-steady-state problem defined in Chapter 2 is reduced to a finite-dimensional set of nonlinear residual equations by approximating velocities, pressure, temperature and the shape of the melt/solid interface in terms of expansions of finite element interpolating functions and unknown coefficients, and applying the Galerkin method for which the weighting functions are identical to the interpolating functions. A mesh is formed of quadrilateral elements by subdividing the domains which cover the melt, crystal and crucible. The shape of melt/solid interface is approximated by one-dimensional edges of the quadrilateral elements, so that the interfaces always coincide with the element boundaries. Sample meshes are shown in Figure 3.3 for the vertically stabilized Bridgman crystal growth system. Because of the possible formation of the thin boundary layers of solute and momentum in the melt, finer meshes are used in the melt region than in the crystal and ampoule where only heat transfer equations are solved.

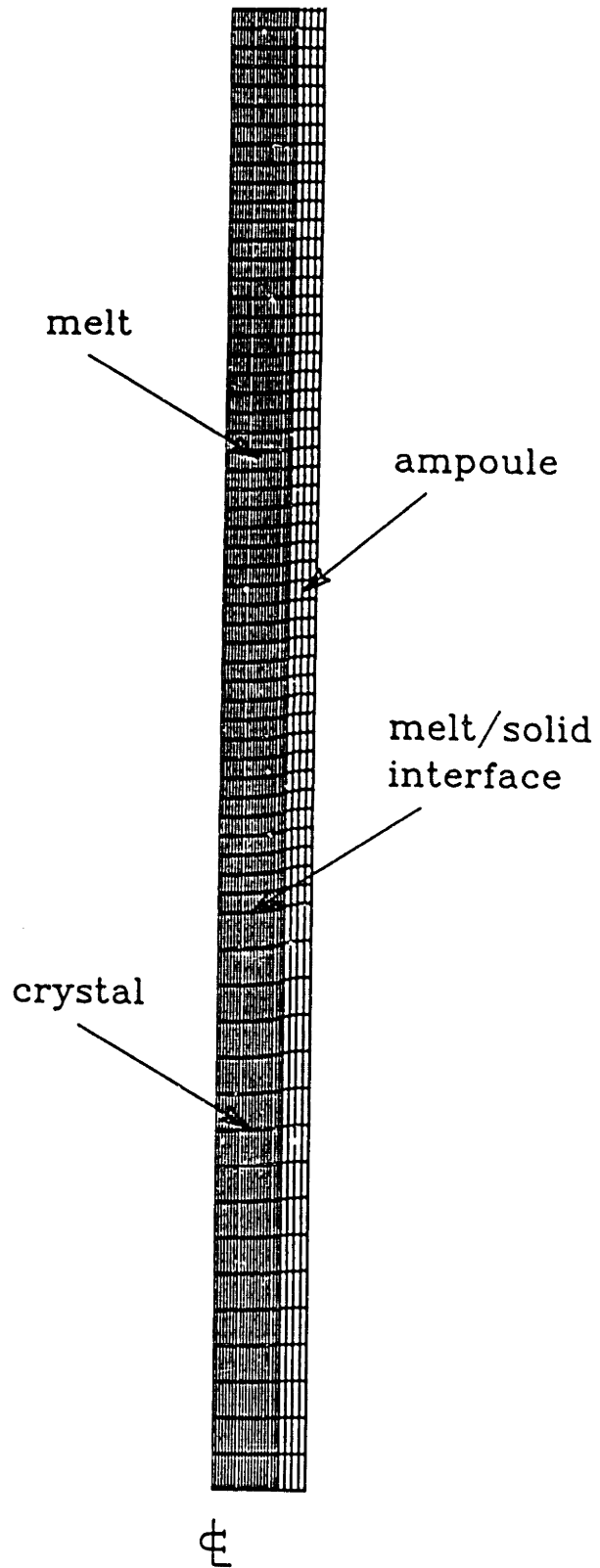


Figure 3.3: Finite element meshes for the analysis of vertical Bridgman crystal growth.

Mesh

The isoparametric mapping consistent with the Lagrangian biquadratic interpolating functions is used to transform each element in the cylindrical coordinate system (r, z) to local coordinate system (ξ, η) , which spans $(-1 \leq \xi \leq 1, -1 \leq \eta \leq 1)$, as

$$r = \sum_{i=1}^9 r^{(i)} \phi^i(\xi, \eta), \quad z = \sum_{i=1}^9 z^{(i)} \phi^i(\xi, \eta) \quad (3.21)$$

where $\{r^{(i)}, z^{(i)}\}$ are the locations of the nodes in the global coordinate system and $\{\phi^i(\xi, \eta)\}$ are biquadratic Lagrangian interpolating functions.

Approximating Functions

The field variables are discretized using a mixture of finite element interpolating functions. The velocity and concentration in the melt and temperature in all phases are approximated by nine-node Lagrangian biquadratic functions ($\phi^i \in Q_2$) as

$$\mathbf{v}(r, z) = \sum_{i=1}^{N_m} \begin{bmatrix} v_r^{(i)} \\ v_z^{(i)} \end{bmatrix} \phi^i(r, z), \quad (3.22)$$

$$S(r, z) = \sum_{i=1}^{N_m} S^{(i)} \phi^i(r, z) \quad (3.23)$$

$$\theta(r, z) = \sum_{i=1}^N \theta^{(i)} \phi^i(r, z) \quad (3.24)$$

where N_m is the number of nodes in the melt and N is the total number of nodes in all phases. The coefficients $v_r^{(i)}$, $v_z^{(i)}$, $S^{(i)}$ and $\theta^{(i)}$ are the nodal values of the velocity, concentration and temperature that are to be computed.

The dynamic pressure in the melt is approximated by discontinuous piecewise-linear interpolating functions (P_1) defined at the centroid node of each element in the local

coordinate system as

$$p(r, z) = \sum_{i=1}^3 p^{(i)} \psi^i(\xi, \eta) \quad (3.25)$$

where the linear basis functions $\psi^i(\xi, \eta)$ are

$$\begin{aligned} \psi^1(\xi, \eta) &= 1 \\ \psi^2(\xi, \eta) &= \xi \\ \psi^3(\xi, \eta) &= \eta \end{aligned} \quad (3.26)$$

In Eq. (3.25), $p^{(1)}$ represent the value of dynamic pressure at the centroid node while $p^{(2)}$ and $p^{(3)}$ denote the pressure gradient in the radial and axial direction respectively. This formulation of the pressure field show the discontinuity across the element because pressure is not formulated in terms of nodal values at the boundaries. Since there are no pressure derivatives in the weak formulation of momentum equations (Eq. (3.39), discontinuous approximations for pressure field are allowed if only they are square-integrable, i.e., $p \in L_2(\Omega)$.

The interpolating functions for velocity and pressure must be selected carefully to yield a stable and convergent algorithm. The importance of this choice was noted empirically by many researchers (Hood and Taylor, 1974; Nickell *et al.*, 1974; Yamada *et al.*, 1975; Gartling and Becker, 1976; Kawahara *et al.*, 1976; Huyakorn *et al.*, 1978) who all selected mixture of interpolating functions for velocity and for pressure.

A mathematical theory for the finite element method with mixture of interpolating functions has been developed during the last two decades. The key is featured in the *Babuška-Brezzi stability condition* which was proposed and studied for linear elliptic problems and their approximations by Babuška (Babuška, 1971, 1973; Babuška and Aziz, 1972) and by Brezzi (1974). The main idea is that one cannot mix together arbitrary an approximation of velocity with any approximation of pressure. The same condition was first derived in an alternative but equivalent form by Ladyzhenskaya (1969) and it is also called *LBB condition*.

Most of our problems for momentum transport are solution of the Navier-Stokes equation. But, when the solution of the mathematical problem is unique, the methods applicable for the Stokes equations have been proved to converge for the Navier-Stokes equation and the error estimates for the Stokes approximation yield the same order of accuracy for the Navier-Stokes equations (Jamet and Raviart, 1974; Thomasset, 1981).

We shall consider a Stokes problem in a bounded domain Ω of \mathcal{R}^2 . We look for $\mathbf{u} \in V$ and $p \in L_2(\Omega)$ such that for a given $\mathbf{f} \in L_2(\Omega)$

$$-\nabla^2 \mathbf{u} + \nabla p = \mathbf{f}$$

$$\nabla \cdot \mathbf{u} = 0$$

$$\mathbf{u}|_{\partial\Omega} = 0$$

where $V = H_0^1 \times H_0^1$ and

$$H_0^1 = \{u | u \in L_2(\Omega), \nabla u \in L_2(\Omega) \times L_2(\Omega), u|_{\partial\Omega} = 0\}$$

The equivalent weak formulation of the Stokes problem is

$$\int_{\Omega} \{\nabla \mathbf{u} \cdot \nabla \mathbf{v} - p \nabla \cdot \mathbf{v} - \mathbf{f} \cdot \mathbf{v}\} d\Omega = 0 \quad \forall \mathbf{v} \in V \quad (3.27)$$

$$\int_{\Omega} q \nabla \cdot \mathbf{u} d\Omega = 0 \quad \forall q \in L_2(\Omega) \quad (3.28)$$

where \mathbf{v} is the weighting functions for the momentum equation and q is the weighting function for the continuity equation.

The incompressibility condition plays the role of a linear constraint in a constrained optimization problem:

$$\min_{\mathbf{v} \in V} \int_{\Omega} \{|\nabla \mathbf{v}|^2 - \mathbf{f} \cdot \mathbf{v}\} d\Omega \quad (3.29)$$

Then, Eqs. (3.27) and (3.28) are the same as the equilibrium equations of the saddle point problem for (\mathbf{u}, p) :

$$\min_{\mathbf{v} \in V} \max_{q \in L_2(\Omega)} \int_{\Omega} \{|\nabla \mathbf{v}|^2 + q \nabla \cdot \mathbf{v} - \mathbf{f} \cdot \mathbf{v}\} d\Omega \quad (3.30)$$

where the pressure is considered as a *Lagrange multiplier* associated to the linear constraint, $\nabla \cdot \mathbf{v} = 0$. These equivalences lead to the derivation of the Babuška-Brezzi condition for convergence from the discrete formulation of the equation: there must exist a constant k independent of mesh such that (Fortin, 1981)

$$\sup_{\mathbf{v}_h \in V_h} \frac{\int_{\Omega} q_h \nabla \cdot \mathbf{v}_h d\Omega}{\|\mathbf{v}_h\|_V} \geq k \|q_h\|_{L_2(\Omega)/\mathcal{R}} \quad \forall q_h \in Q_h \quad (3.31)$$

where V_h and Q_h are the finite element approximations of V and $L_2(\Omega)$ respectively and

$$\|q\|_{L_2(\Omega)/\mathcal{R}} = \inf_{c \in \mathcal{R}} \|q + c\|_{L_2(\Omega)}$$

is a quotient norm, because p is only defined up to an additive constants. The condition (3.31) implies that the discrete pressure p_h must belong to the same class of functions as $\nabla_h \mathbf{u}_h$. The violation of this condition leads to the *spurious modes* in the pressure.

The LBB condition is rather abstract and to establish whether or not this condition is satisfied for elements of interest is not a trivial task. However, several combinations of velocity and pressure elements have been shown to be stable and convergent by satisfying the LBB condition (Bercovier and Pironneau, 1979; Fortin, 1981; Fortin and Fortin, 1985a,b). Biquadratic velocity-linear discontinuous pressure element (Q_2 - P_1) and biquadratic velocity-continuous bilinear pressure element (Q_2 - Q_1) are most widely used combinations which satisfy the LBB condition. For both mixture of elements, the rate of convergence is *optimal* and is $\mathcal{O}(h^2)$ measured in the L_2 norm (Fortin and Fortin, 1985b).

Several previous works (Sani *et al.*, 1981; Engelman *et al.*, 1982; Kheshgi and Scriven, 1984; Pelletier *et al.*, 1989; Sackinger *et al.*; 1989) empirically support the use of (Q_2 - P_1) formulation over (Q_2 - Q_1) formulation. The (Q_2 - Q_1) formulation yields less exact mass balances over each element because of the fewer incompressibility constraints it introduces relative to momentum constraints (Hughes, 1987).

Free Surface

For implementation of the isotherm/Newton scheme (Ettouney and Brown, 1983) it is necessary to express the location of each node within the element as a function of interface location, because the number of elements in each phase are fixed and elements are deformed by the change of the interface location during the iterations. The simplest case is a uniform mesh throughout both phases connected by the interface whose shape is not deviated excessively from planarity, so that its location is a single-valued function of a radial coordinate system, *i.e.* $z = H(r)$. Then, the initial locations of the nodes are unchanged radially and only the axial locations are coupled with the interface location :

$$\text{melt: } r_i = (i - 1)/(N_r - 1) \quad z_j = (j - 1)H(r_i)/(N_{z,m} - 1) \quad (3.32)$$

$$\text{solid: } r_i = (i - 1)/(N_r - 1) \quad z_j = H(r_i) + (j - N_{z,m})\{L/R_c - H(r_i)\}/N_{z,s} \quad (3.33)$$

where N_r is the number of node radially and $N_{z,m}$ and $N_{z,s}$ are the number of nodes axially in the melt and solid respectively. Grading the mesh near any boundary will modify above expressions.

The shape of the melt/solid interface is approximated by one-dimensional quadratic Lagrangian polynomials $\{\check{\phi}(\tau)\}$ which are consistent with the sides of the biquadratic elements used for velocity, temperature and concentration and isoparametric mapping for the coordinate system. The interface shape $H(r)$ is expressed as

$$H(r) = \sum_{i=1}^{N_I} H^{(i)} \check{\phi}^i(r) \quad (3.34)$$

where N_I is the number of nodes along the interface.

Weak Forms

The weak forms of the field equations are obtained by applying Galerkin's method to the equations in Section 2.2.2. The weak form of the continuity equation is formed using

the interpolating function for pressure as a weighting function, *i.e.*

$$\int_{D_m} \psi^i (\nabla \cdot \mathbf{v}) dV = 0, \quad (3.35)$$

where $i = 1, \dots, N_p$ which is identical to $3N_{E,m}$ because there are three unknowns of pressure for each element.

The Galerkin method is applied to the momentum equation (Eq.(2.7)) to yield residual equations for the velocity in the melt as

$$\int_{D_m} \phi^i \{ \mathbf{v} \cdot \nabla \mathbf{v} + \nabla p - \nabla^2 \mathbf{v} - \frac{1}{Pr} [Ra_s S - Ra_t (\theta - 1)] \mathbf{e}_z \} dV = 0 \quad (3.36)$$

where $i = 1, \dots, N_m$ and the $\{\phi^i\}$ represent the weighting functions that are identical to velocity interpolating functions multiplied by the unit vectors ($\mathbf{e}_r, \mathbf{e}_z$) for the corresponding velocity components. Therefore, Eq. (3.36) has a total of $2N_m$ residual equations for the velocity in the melt.

In a similar manner, the residual equations associated with the solute balance in the melt and energy balance in all phases are expressed as

$$\int_{D_m} \phi^i (Sc \mathbf{v} \cdot \nabla S - \nabla^2 S) dV = 0 \quad (3.37)$$

$$\int_{D_m} \phi^i (Pr \mathbf{v} \cdot \nabla \theta_m - \nabla^2 \theta_m) dV + \int_{D_k} \phi^i (Pe \mathbf{e}_z \cdot \nabla \theta_k - \gamma_k \nabla^2 \theta_k) dV = 0 \quad (3.38)$$

where $i = 1, \dots, N$ represent the residual equation for each node and $k = \text{sanda}$ denotes the crystal and ampoule, respectively.

The final forms of the residual equation set is derived by integrating Eqs. (3.36)–(3.38) by parts and applying the divergence theorem (Mase, 1970) so that the boundary conditions on field variables at the fictitious inlet, melt/solid interface and along the ampoule wall are incorporated into boundary integrals that appear. Another advantage of the finite element method is that the energy and solute balances at the interface are automatically incorporated during the formulation of weak form. The weak form of the

field equations are

$$\int_{D_m} \phi^i \mathbf{v} \cdot \nabla \mathbf{v} - (\nabla \cdot \phi^i) p + \nabla \phi^i \cdot \nabla \mathbf{v} - \frac{\phi^i}{Pr} [Ra_s S - Ra_t(\theta - 1)] \mathbf{e}_z dV = 0 \quad (3.39)$$

$$\begin{aligned} & \int_{D_m} Sc \phi^i \mathbf{v} \cdot \nabla S + \nabla \phi^i \cdot \nabla S dV + \int_{\partial D_e} \check{\phi}^i Pe_m S dS \\ & - \int_{\partial D_I} \check{\phi}^i Pe_m (\mathbf{N} \cdot \mathbf{e}_z) (S + 1)(1 - k) dS = 0 \end{aligned} \quad (3.40)$$

$$\begin{aligned} & \int_{D_m} Pr \phi^i \mathbf{v} \cdot \nabla \theta_m - \nabla \theta_m \cdot \nabla \theta_m dV + \int_{D_k} \phi^i Pe \mathbf{e}_z \cdot \nabla \theta_k - \gamma_k \nabla \phi^i \cdot \nabla \theta_k dV \\ & - \int_{\partial D_I} \check{\phi}^i St Pe (\mathbf{N} \cdot \mathbf{e}_z) dS - \int_{\partial D_w} \check{\phi}^i Bi (\theta_\infty - \theta) dS = 0 \end{aligned} \quad (3.41)$$

where ∂D_e , ∂D_I and ∂D_w denote the boundaries at the inlet, at the interface and at the outer surface of the ampoule, respectively. Note that the pressure term in Eq. (3.39) has been integrated by parts. This is due to the selection of piecewise linear interpolating functions for pressure field. If it is not integrated by parts, pressure is expressed only by $p^{(2)}$ and $p^{(3)}$ in Eq. (3.25) and there is no way to obtain $p^{(1)}$. Only the gradients of pressure are important in the momentum equation, so that it is necessary to specify a datum level of the pressure. Thus, one of the pressure unknowns is set arbitrarily as a datum pressure by replacing the first residual equation derived from Eq. (3.35) with the condition

$$p(0, 0) = 0. \quad (3.42)$$

The residual equations for the interface location are formed by applying the Galerkin's method to melting point constraint (Eq. (2.12)) evaluated along the melt-solid interface as

$$\int_{\partial D_I} \check{\phi}_i(r) [\theta(r, H(r)) - \theta_m(S)] dS = 0 \quad (3.43)$$

where the differential unit of arc-length along the interface dS is

$$dS \equiv \sqrt{1 + H_r^2} dr \quad (3.44)$$

This Isotherm formulation has been used successfully in the finite element analysis of solidification during edge-defined film-fed process (Ettouney and Brown, 1983; Thomas *et al.*, 1986), vertical Bridgman process (Chang and Brown, 1983a,b,1984; Adornato and Brown, 1987a.b), Czochralski method (Derby *et al.*, 1985,1987; Sackinger *et al.*, 1989) and in the analysis of interface morphology in directional solidification (Ungar *et al.*, 1988).

The flow pattern is most easily understood in terms of contours of the stream function. The stream function is computed as a post-processing step using velocity data from the finite element solution. In the axisymmetric cylindrical coordinate system the velocities are expressed in terms of the Stokes stream function $\Psi(r, z)$ (Bird *et al.*, 1960) as

$$v_r \equiv \frac{1}{r} \frac{\partial \Psi}{\partial z} \quad (3.45)$$

$$v_z \equiv -\frac{1}{r} \frac{\partial \Psi}{\partial r}. \quad (3.46)$$

From the condition for irrotational flow ($\nabla \times \mathbf{v} = 0$), the second-order equation for the stream function is derived as

$$\begin{aligned} \frac{\partial v_r}{\partial z} - \frac{\partial v_z}{\partial r} - \frac{1}{r} \frac{\partial^2 \Psi}{\partial r^2} + \frac{1}{r^2} \frac{\partial \Psi}{\partial r} - \frac{1}{r} \frac{\partial^2 \Psi}{\partial z^2} = \\ \frac{\partial v_r}{\partial z} - \frac{\partial v_z}{\partial r} - \nabla^2(\Psi/r) + \frac{1}{r^2}(\Psi/r) = 0 \end{aligned} \quad (3.47)$$

The stream function $\Psi(r, z)$ is discretized using the same biquadratic Lagrangian interpolating functions used for the velocity field:

$$\Psi(r, z) = \sum_{i=1}^{N_m} \Psi^{(i)} \phi^i(r, z). \quad (3.48)$$

Residual equations for the stream function are formed by applying Galerkin's method to Eq. (3.47) to yield

$$\int_{D_m} \phi^i \left(\frac{\partial v_r}{\partial z} - \frac{\partial v_z}{\partial r} \right) dV - \int_{D_m} \nabla \phi^i \cdot \nabla(\Psi/r) + \frac{1}{r^2} \phi^i(\Psi/r) dV = 0 \quad (3.49)$$

The residual equations are reduced to a set of algebraic equations by numerical integration. Widely used numerical integration techniques are grouped into Newton-Cotes formula and Gauss-Legendre quadrature rules. The former methods use the equally spaced sampling points, while the latter scheme optimizes the positions of the sampling points. In the integration of finite element matrices, a subroutine is called to evaluate the values of integrand at given points, and these points may be anywhere on the element. No additional difficulties arise if the sampling points are not equally spaced. Therefore, for finite element analysis it is common to use the Gauss-Legendre integration scheme over Newton-Cotes formulas (Stroud and Secrest, 1966; Irons, 1971; Zienkiewicz *et al.*, 1971). The advantage of the Gauss-Legendre quadrature is that it requires less sampling points than Newton-Cotes formula for the same level of accuracy. In one dimension, we can integrate exactly a polynomial of order at most $(2n - 1)$ using n sampling points by Gauss-Legendre quadrature, while $2n$ sampling points are needed for the same polynomial by Newton-Cotes formula. In this work, nine-point (3×3) Gaussian quadrature is used to calculate the area integrals and three-point quadrature for all line integrals within each element.

3.2.3 Algebraic Solution by Newton-Raphson Method

The set of nonlinear algebraic equations has been formulated in the previous section. The nonlinearities originate from the dependence of thermophysical properties on the temperature and composition, from the convective transport terms in the momentum, energy and solute equations and, most influentially, from the implicit coupling of residual equations with the interface shape through the dependence of the finite element interpolating functions and the Galerkin integrals on the interface location. These nonlinearities force the employment of the appropriate iterative solution of the equations. Since the overall performance of the numerical technique depends strongly on the choice of the iteration scheme, especially in the complex free- and moving-boundary problems, its selection cannot be over-emphasized. The advantage of the Newton-Raphson method in the finite element analysis of solidification problem relevant to the crystal growth

system has been demonstrated several times previously (Ettouney, 1983; Chang, 1983; Adornato, 1986; Derby, 1986; Sackinger, 1989); these results lead to the adoption of Newton's method in this study.

The entire set of algebraic equations is represented by the vector equation

$$\mathbf{R}(\mathbf{x}; \lambda) = \mathbf{0} \quad (3.50)$$

where \mathbf{x} is the vector of unknown coefficients associated with field variables and interface location, $\mathbf{x}^T = (\mathbf{v}_r^T, \mathbf{v}_z^T, \mathbf{p}^T, \theta^T, \mathbf{S}^T, \mathbf{H}^T)$, and the vector λ represents the parameters in the problem. Successive approximations are calculated for all unknowns simultaneously using the Newton-Raphson iteration scheme. Given an initial guess for the solution $\mathbf{x}^{(0)}$, a correction vector $\delta^{(k)}$ for the k -th iteration is computed as

$$\mathbf{x}^{(k+1)} - \mathbf{x}^{(k)} \equiv \delta^{(k)} \equiv \mathbf{J}^{-1}(\mathbf{x}^{(k)})\mathbf{R}(\mathbf{x}^{(k)}; \lambda) \quad (3.51)$$

where elements of the Jacobian matrix $J_{ij} \equiv \partial R_i / \partial x_j$ represent the sensitivity of the residual equation set with respect to the unknowns. All contributions to the Jacobian matrix are expressed analytically as functions of the unknowns $\mathbf{x}^{(k)}$. Analytical expression of the elements in the Jacobian matrix are documented in the literature (Chang, 1983) for the similar problem.

In Newton's method with unknown interface location, the terms of sensitivity of field equations to the location of interface are required in the Jacobian matrix. The simple way to obtain these terms is transformation of the original solidification problem to fixed meshes so that melt and solid regions have fixed boundaries and differentiation in the transformed domain. This transformation technique was applied first by Landau (1950) for one-dimensional and later by others (Spaid *et al.*, 1971; Duda *et al.*, 1975; Saitoh, 1978) to two-dimensional Stefan problems where the interface shape was a function of a single spatial coordinate. These applications of transformation methods all solve the the nonlinear equation set by successive iteration between the interface shape and the temperature field. Ettouney and Brown (1983) implemented the Newton's method in solving the entire free-boundary problem in transformed coordinates. Solution of the

free-boundary problem in the original coordinate system has the additional complexity of requiring the generation of a new, and generally irregular, grid at each iteration. Accordingly, the calculation of the Jacobian elements which express the sensitivity of field equations to the unknown interface location becomes complex, too. In analyzing a viscous flow with a meniscus, Saito and Scriven (1981) employed Galerkin's method in the original coordinate system while the residuals and elements of the Jacobian matrix were calculated in the transformed coordinates that correspond to the standard isoparametric mapping for each element (Bathe and Wilson, 1976). Chang (1983) have shown these two approaches in obtaining the Jacobian matrix elements are equivalent in the analysis of convective flow near the melt/solid interface.

In the finite element method, the interpolating functions and weighting functions have *local support*, i.e. they are zero outside a few number of adjacent elements. As a result, the Jacobian matrix \mathbf{J} is sparse and banded, i.e. most of its components are zero and the nonzero components are located within a small band around the diagonal. This structure enables the efficient use of storage and solution algorithm in solving the linear equation sets resulting from Newton's method. For the small system of equations with truly banded Jacobian matrices, a simple *band solver* can be used. In the present study of solidification system, simple band solver cannot be used because the number of unknowns are huge (up to 30,000 to 40,000) and the field equations are coupled with the interface shape resulting the arrow-type structure of Jacobian matrix. The correction vector in Eq. (3.51) is computed using the frontal method originally developed by Irons (1970) and modified by Hood (1976, 1977). The frontal method stores only a part of the Jacobian matrix in core for pivoting and elimination by formulating the components of Jacobian matrix and residual equations generated from *frontal elements*. The reduction in storage requirements allows to solve much larger equation sets by frontal method than by traditional band solvers or matrix solvers. Additional advantage is that the frontal method does not require the stringent node numbering scheme as is used for the band solver.

A typical finite element mesh used in the calculations for the pseudo-steady-state

model contained 20 radial element in the melt and crystal and 4 elements radially across the ampoule. The axial approximation was composed of 48 elements in the melt and 16 elements in the crystal. This mesh resulted in 24,085 nonlinear algebraic equations which required 90 seconds on the CRAY XMP for a single Newton iteration; convergence was achieved in fewer than 6 iterations. The global accuracy of the computation was checked by the solute balance at the melt/solid interface expressed as

$$\frac{\int_0^1 c(r, H(r)) \sqrt{1 + H_r^2} r \, dr}{\int_0^1 \sqrt{1 + H_r^2} r \, dr} \equiv \langle c \rangle_I = \frac{1}{k} \quad (3.52)$$

3.2.4 Continuation of Solution in Parameter Space

Partial differential equations for the field variables in Section 2.2.2 or their weak forms (Eq. (3.39) – Eq. (3.41)) are nonlinear and multiple solutions are possible with *exchange of stability* at the critical points. Bifurcation points and limit points are the examples of such critical points in the parameter space as shown in Figure 3.1. These critical points are identified in the parameter space by computing the determinant of the Jacobian matrix. Classical perturbation methods are well known for analysis of both limit and bifurcation points and have been adapted by several researchers (Keller, 1977; Rheinboldt, 1978; Brown *et al.*, 1980; Ungar and Brown, 1982; Yamaguchi *et al.*, 1984) for implementation in numerical algorithms. These algorithms enables to track solutions in the multi-dimensional parameter space, which is the only consistent way of understanding the complex physics involved in multi-component solidification.

Analytic Continuation

Sequences of solutions to Eq. (3.50) are generated in parameter space by incrementally changing a parameter of interest while fixing other parameters. From a set of field variables and interface shape, \mathbf{x}_o , that satisfy Eq. (3.50) for $\lambda = \lambda_o$, an initial guess ($\mathbf{x}^{(0)}$) for the parameter values $\lambda = \lambda_o + \Delta\lambda$, where $\Delta\lambda$ is small, is constructed by analytic continuation based on Taylor-series expansion (Kubiček, 1976; Wacker, 1978;

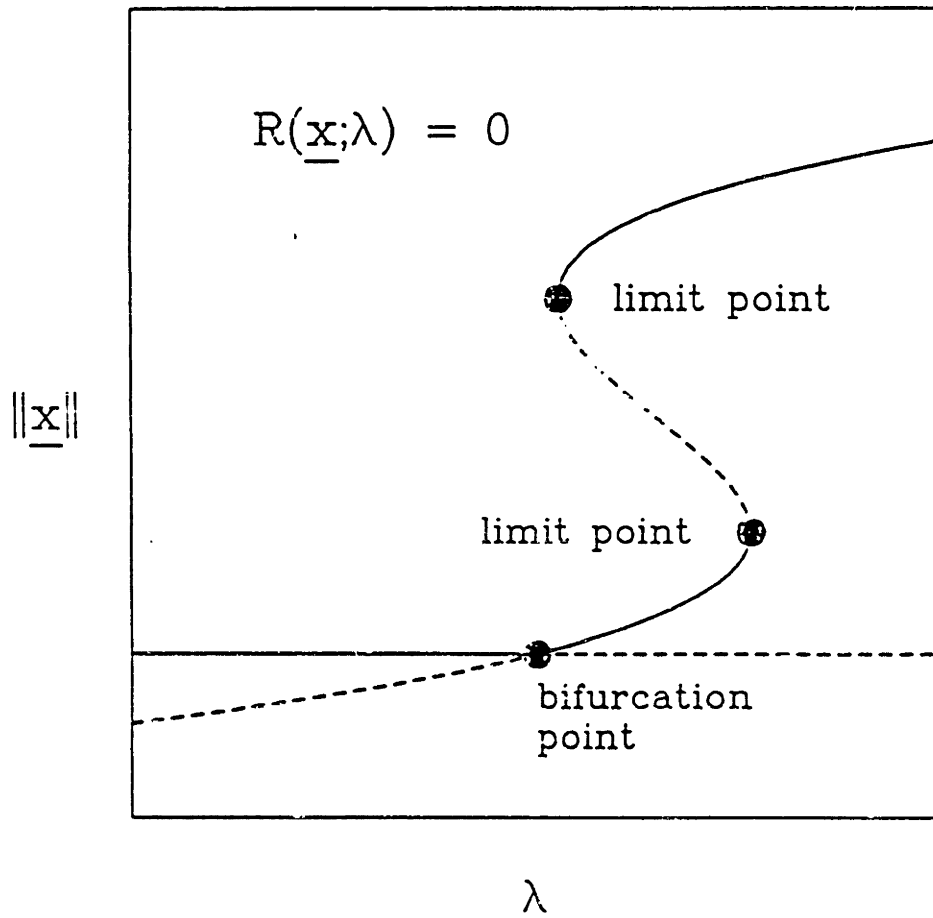


Figure 3.4: A solution family with bifurcation and limit points in the parameter space.

Brown *et al.*, 1980) as

$$\mathbf{x}^{(0)}(\lambda_o + \Delta\lambda) = \mathbf{x}_o + \mathbf{x}_\lambda \cdot \Delta\lambda \quad (3.53)$$

where \mathbf{x}_λ denotes the vector of differential change caused by the parameter λ . This vector is calculated from the solutions of the linear equation set

$$\mathbf{J}(\mathbf{x}_o) \cdot \mathbf{x}_\lambda + \left(\frac{\partial \mathbf{R}}{\partial \lambda} \right)_{\lambda_o} = \mathbf{0}, \quad (3.54)$$

with the Jacobian matrix previously evaluated in obtaining \mathbf{x}_o .

The continuation method defined by Eq. (3.53) leads to an essentially predictor-corrector scheme; the new solution is predicted by Eq. (3.53) and then corrected by subsequent Newton iterations. When the Newton iteration has converged, the new Jacobian is ready for use in the next predictor step. This continuation method has been primarily used in this study to track the solution families with respect to the Rayleigh number.

Arc-length Continuation

Continuation methods have been extended to cope with the pathologies cases by non-linear systems, where the Jacobian matrix is singular at limit points (Simpson, 1975; Keller, 1977). Because of the singularity of the Jacobian matrix the analytical continuation method fails there. Arc-length continuation method will track solution families around limit points (Keller, 1977). In most cases, imperfections in the physical system break the bifurcation and limit points are more frequently encountered. The arc-length continuation method is employed in this study to track the steady-state solution family with respect to solutal Rayleigh number.

The arc-length of the solution, s , is defined as the length of arc along the solution curve from an arbitrarily chosen starting point. The vector function $\mathbf{x}(s)$ is a single-valued function even if $\mathbf{x}(\lambda)$ has multiple solutions caused by limit points. An augmented equation is used with the parameter s to solve for unknowns (\mathbf{x}, λ) along the solution

curve. The augmented system of equation is

$$\begin{aligned}\mathbf{R}(\mathbf{x}, \lambda; s) &= \mathbf{0} \\ N(\mathbf{x}, \lambda; s) &= 0\end{aligned}\tag{3.55}$$

where one of the several choices for $N(\mathbf{x}, \lambda; s)$ (Yamaguchi *et al.*, 1984) is

$$N(\mathbf{x}, \lambda; s) \equiv (s_1 - s_0)^2 - \|\mathbf{x}(s_1) - \mathbf{x}(s_0)\|^2 - [\lambda(s_1) - \lambda(s_0)]^2,\tag{3.56}$$

which prescribes the distance measured from the point $[\mathbf{x}(s_0), \lambda(s_0)]$ to the point $[\mathbf{x}(s_1), \lambda(s_1)]$. Solution curves are computed by varying s . The predictor step for $(s_1 + \Delta s)$ is similar to the analytic continuation procedure described above with the definition of s (Eq. (3.56)) included:

$$\begin{aligned}\mathbf{x}(s_1 + \Delta s) &= \mathbf{x}(s_1) + \mathbf{x}_s \Delta s \\ \lambda(s_1 + \Delta s) &= \lambda(s_1) + \lambda_s \Delta s\end{aligned}\tag{3.57}$$

where $(\mathbf{x}_s, \lambda_s)$ denotes the vector of differential changes in \mathbf{x} and λ caused by the parameter s . This vector is calculated from the solutions of the linear equations with the Jacobian matrix previously evaluated in obtaining $(\mathbf{x}(s_1))$, *i.e.*

$$\begin{bmatrix} \mathbf{J} & \mathbf{R}_\lambda \\ N_{\mathbf{x}} & N_\lambda \end{bmatrix} \begin{bmatrix} \mathbf{x}_s \\ \lambda_s \end{bmatrix} = \begin{bmatrix} \mathbf{R}_s \\ N_s \end{bmatrix} = \begin{bmatrix} \mathbf{0} \\ 2(s_1 - s_0) \end{bmatrix}\tag{3.58}$$

The prediction $(\mathbf{x}(s_1 + \Delta s), \lambda(s_1 + \Delta s))$ are corrected in the subsequent Newton iteration using the augmented Jacobian matrix as

$$\hat{\mathbf{J}}(\mathbf{x}^{(k)}, \lambda^{(k)}) \hat{\delta}^{(k+1)} = -\hat{\mathbf{R}}^{(k)}(\mathbf{x}^{(k)}, \lambda^{(k)})\tag{3.59}$$

where $\hat{\mathbf{J}}$, $\hat{\delta}^{(k+1)}$ and $\hat{\mathbf{R}}^{(k)}$ denote augmented matrix, correction vector and residual, respectively, defined by

$$\hat{\mathbf{J}} = \begin{bmatrix} \mathbf{J} & \mathbf{R}_\lambda \\ N_{\mathbf{x}} & N_\lambda \end{bmatrix}, \quad \hat{\delta}^{(k+1)} = \begin{bmatrix} \Delta \mathbf{x}^{(k+1)} \\ \Delta \lambda^{(k+1)} \end{bmatrix}, \quad \hat{\mathbf{R}}^{(k)} = \begin{bmatrix} \mathbf{R}^{(k)} \\ N^{(k)} \end{bmatrix}.\tag{3.60}$$

3.2.5 Test of Petrov-Galerkin Methods

Various Petrov-Galerkin finite element methods have been proposed to overcome the spurious node-to-node oscillations or *wiggles* which arise in the Galerkin formulation of convection-dominated transport problems. In this Section, the performance of three representative Petrov-Galerkin schemes are compared here with the standard Galerkin method with bilinear or biquadratic interpolating functions for the solution of convection-diffusion problem that is typical of those arising in crystal growth systems.

The model problem is for the melt region in the steady growth system. In this model, the steady-state solute transport equation in a rectangular coordinate system with a origin located at the inlet is

$$\nabla^2 C - Pe \mathbf{v} \cdot \nabla C = 0 \quad (3.61)$$

where $Pe = V_g R_c / D$ is a Peclet number based on the solute transport, V_g is a growth velocity and R_c is a half width of the crystal plate. Variables are put in dimensionless form by scaling lengths with the half width of the crystal R_c , velocity \mathbf{v} with V_g and composition C with the inlet concentration c_o . By assuming a flat melt/solid interface, the two-dimensional domain covering half-width of melt is rectangular with $y = 0$ and $y = H$ corresponding to the top of the melt and a flat interface, respectively. The form of the flow field is assumed to approximate the cell structure of flow in the crystal growth system and to include the component of growth velocity, as expressed by the stream function

$$\Psi = -V_c \{1 - (2x - 1)^2\}^2 \{1 - (2y/H - 1)^2\}^2 - x \quad (3.62)$$

where V_c scales the intensity of the flow circulation. This representation of the flow field satisfies the no-slip and symmetry boundary conditions at the boundaries, *i.e.*

$$\begin{aligned} v_x &= 0 & \text{at all boundaries,} \\ v_y &= 0 & \text{at } x = 0 \text{ and } x = 1, \\ v_y &= 1 & \text{at } y = 0 \text{ and } y = H \end{aligned} \quad (3.63)$$

For the solute field we are imposing two kinds of boundary conditions at the top and at the interface: Dirichlet-type and Robin-type boundary conditions, which are

$$\begin{aligned} \text{(I) Dirichlet } C = 1 \quad \text{at } y = 0, \\ C = 1/k \quad \text{at } y = H \end{aligned} \quad (3.64)$$

$$\begin{aligned} \text{(II) Robin } \partial C/\partial y = Pe(C - 1) \quad \text{at } y = 0, \\ \partial C/\partial y = Pe(1 - k)C \quad \text{at } y = H \end{aligned} \quad (3.65)$$

where k is a equilibrium distribution coefficient. Solute boundary conditions at the interface account for the solute rejection or incorporation depending on the value of k . Additional solute boundary conditions are specified to satisfy the condition of symmetry at $x = 0$ and no-flux condition at $x = 1$.

$$\frac{\partial C}{\partial x} = 0 \quad \text{at } x = 0 \text{ and } x = 1 \quad (3.66)$$

In the present study, k is assumed to be 0.1 to approximate the segregation of gallium from germanium and the aspect ratio H is set to 3.

The Galerkin formulation of Eq. (3.61) with bilinear interpolating function and uniaxial velocity field ($V_c = 0$) yields the linear algebraic equation for the arbitrary nodal point m as

$$\left(1 + \frac{\pi}{2}\right) C_{m-1} - 2C_m + \left(1 - \frac{\pi}{2}\right) C_{m+1} = 0 \quad (3.67)$$

where $\pi \equiv V_g h/D$ is a elemental Peclet number based on element size h . The exact solution for this difference equation is

$$C_m = A + B \left(\frac{1 + \pi/2}{1 - \pi/2}\right)^m, \quad (3.68)$$

where constants A and B are to be determined from the boundary conditions. The solution displays an oscillatory behaviour when π is greater than 2. These oscillations are caused by the central-difference-type approximations of standard Galerkin method which gives equal weight to both ends of the element. Petrov-Galerkin methods (Christie

et al., 1976; Heinrich and Zienkiewicz, 1977; Brooks and Hughes, 1982; Donea *et al.*, 1985) weight contributions from upstream nodes more heavily than those from downstreams by modifying the Galerkin weighting functions. This is essentially the finite element analog of the upwind difference schemes (Spalding, 1972) used in finite difference method.

Heinrich and Zienkiewicz (1977) (hereafter referred to as HZ) modified the weighting function by adding the portion of cubic modifying function to the quadratic Galerkin weighting function, *i.e.*

$$w^i(\xi) = \phi^i(\xi) + \beta F(\xi) \quad (3.69)$$

Their choice of the modifying function $F(x)$ is quite arbitrary, satisfying

1. $F(\xi) = 0$ at $\xi = -1, 0, 1$.
2. $F(\xi)$ is positive for $-1 \leq \xi \leq 0$ and negative for $0 \leq \xi \leq 1$.
3. $-1 \leq F(\xi) \leq 1$

in the local coordinate system within the element. The value of β was obtained separately for middle and corner node in one-dimensional analysis by matching the nodal solutions from the finite element analysis to the exact solutions and extended the result to two-dimension in a similar procedure to tensor product generation.

In the following two Petrov-Galerkin methods, weighting functions are modified based on the concept of *artificial diffusion*. Artificial diffusion method (Hughes and Brooks, 1979; Kelly *et al.*, 1980) is one of the basic techniques utilized to achieve the upwind effect in finite element method, along with *quadrature technique* and Petrov-Galerkin method. In this scheme, artificial diffusion is added to the physical diffusion and a conventional Galerkin finite element discretization is employed. The proper amount of the artificial diffusion is determined in one dimension to give the exact nodal solutions to the convection-dominated transport equations. Supporters of the artificial diffusion methods (Hughes and Brooks, 1979) interpret the artificial diffusion as relative to central differences and not to the actual physics of the problem.

Brooks and Hughes (1982) defined streamline upwind/Petrov-Galerkin(SU/PG) weighting function by equating the modification term of weighting function and artificial diffusive term which accounts for upstream effects. In this formulation, the modification of the weighting function is discontinuous and its effect is confined to the element interior without affecting boundary or continuity conditions. Accordingly, the divergence theorem cannot be applied to diffusion term which are weighted by $w^i(\xi)$. The use of linear interpolating function for the field variables prevents the modification of the weighting function from mechanically affecting the diffusion term. It only affects the weighting of convective terms.

The Petrov-Galerkin method proposed by Donea *et al.* (1985) (hereafter referred to as DBS) modified the governing equation by subtracting from the original differential equation the scalar product of its gradient with a vector of free parameters Λ associated with each of the coordinate directions, *i.e.*

$$\nabla^2 C - Pe \mathbf{v} \cdot \nabla C - \Lambda \cdot \nabla(\nabla^2 C - Pe \mathbf{v} \cdot \nabla C) = 0 \quad (3.70)$$

The modified governing equation is subsequently discretized by the standard Galerkin finite element method. This modification is equivalent to the change of weighting function and thus to the Petrov-Galerkin formulation. The resulting artificial diffusivity acts only in the direction of the flow and crosswind diffusion is prevented, as in SU/PG.

The test problem is solved to investigate the influence of boundary conditions, growth velocity and circulation rate on the results of the several Petrov-Galerkin methods. For the calculations, meshes of 10×20 bilinear elements or 5×10 biquadratic elements have been used.

First, the effects of growth velocity on the accuracy of the Petrov-Galerkin methods are shown in Figure 3.5 for the Dirichlet-type essential boundary conditions with corresponding flow field and sample solute field for $Pe = 1$. In this case, the circulation velocity is set to zero corresponding to the unidirectional flow. The exponential composition profiles calculated with the Petrov-Galerkin methods agree with the exact one-dimensional solution even for $Pe = 50$ where the solute boundary layer near the in-

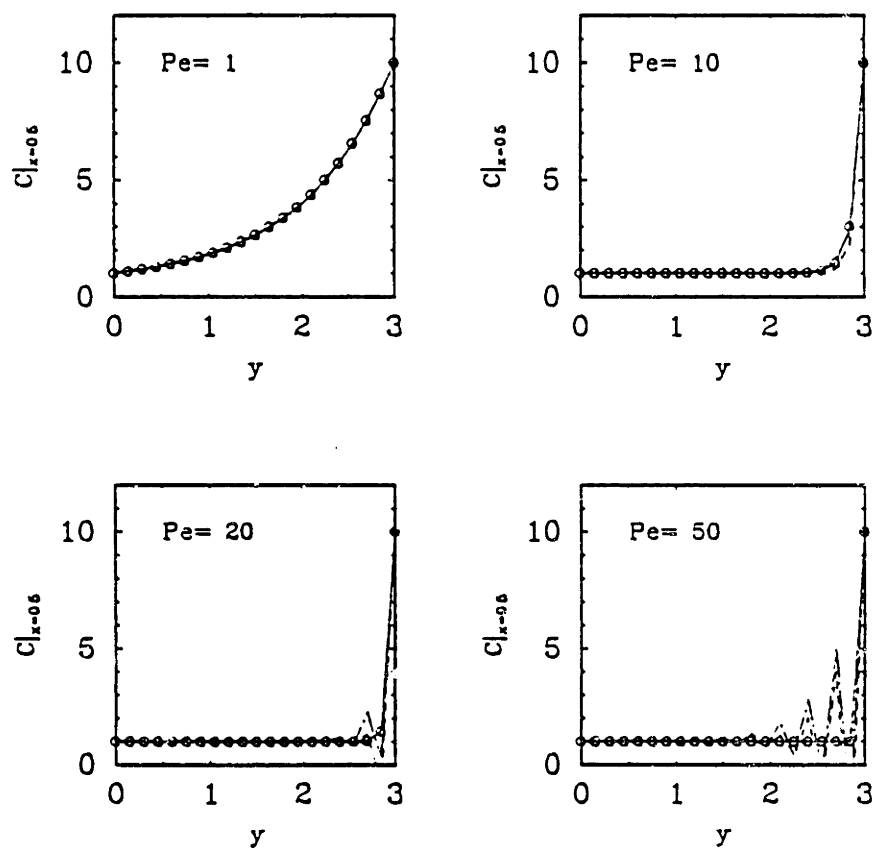
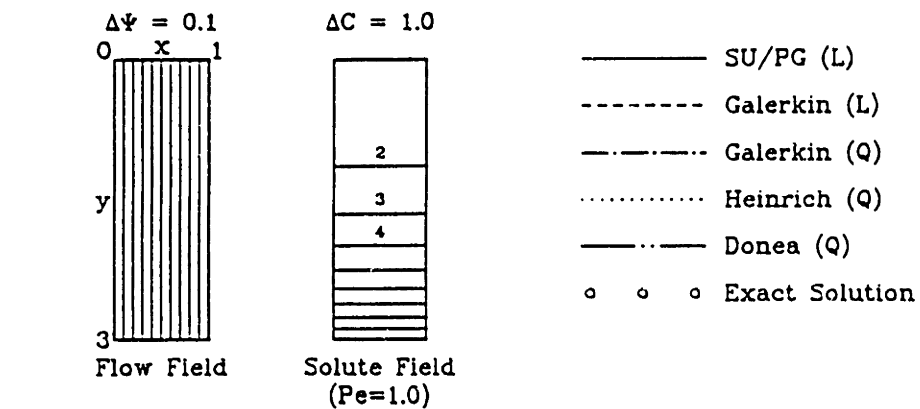


Figure 3.5: One-dimensional composition profiles computed using the Petrov-Galerkin methods with essential boundary conditions: (L) for bilinear elements and (Q) for biquadratic elements.

interface is very thin. On the other hand, the composition profiles computed by standard Galerkin methods begin to show wiggles in the boundary layer at $Pe = 20$ where the currently used number of elements can not resolve the solution structure sufficiently. From the stability condition following Eq. (3.68), the exact value of Pe for the onset of wiggle can be calculated, *i.e.*

$$2 = \pi = \frac{V_g h}{D} = \frac{Pe^c H}{N_{E,y}} \implies Pe^c = 13.33 \quad (3.71)$$

where $N_{E,y}$ is the number of elements in the flow direction.

The introduction of a nonzero circulation rate modified the flow field so that it has a two-dimensional flow cell. The change of flow structure deforms the isoconcentration contours from one-dimensional solute field of diffusion-controlled growth to the typical convection-dominated composition profile. The calculated results are shown in Figure 3.6 and 3.7 to illustrate the effect of circulation rate where Peclet number is given as unity. Comparison of the performance among Petrov-Galerkin methods has been made in terms of axial concentration profiles at the mid-point between the centerline and the outer surface of the melt. The curves represent the same Petrov-Galerkin method used for generating them as in Figure 3.5, though they are not distinguished readily from one another in the plots due to the almost same accuracy. Flow fields and solute fields are also shown as a function of circulation rate, where solute fields have been calculated by the DBS scheme. When $V_c = 1$, the solute field does not deviate much from one-dimensional profile and all the curves calculated by different Petrov-Galerkin methods superimpose on one curve. Above $V_c = 5$ solute boundary layers are formed near the top of the melt and melt/solid interface where the essential boundary conditions are specified and the region of uniform concentration broaden with the increase of V_c . Every method gives the nearly same solution for V_c as high as 100. Thus, all the Galerkin methods tested here give the accurate results for the convection-dominated problem with essential boundary conditions except the standard Galerkin methods which give wiggles near the solute boundary layer when the elemental Peclet number exceeds the critical value for numerical stability.

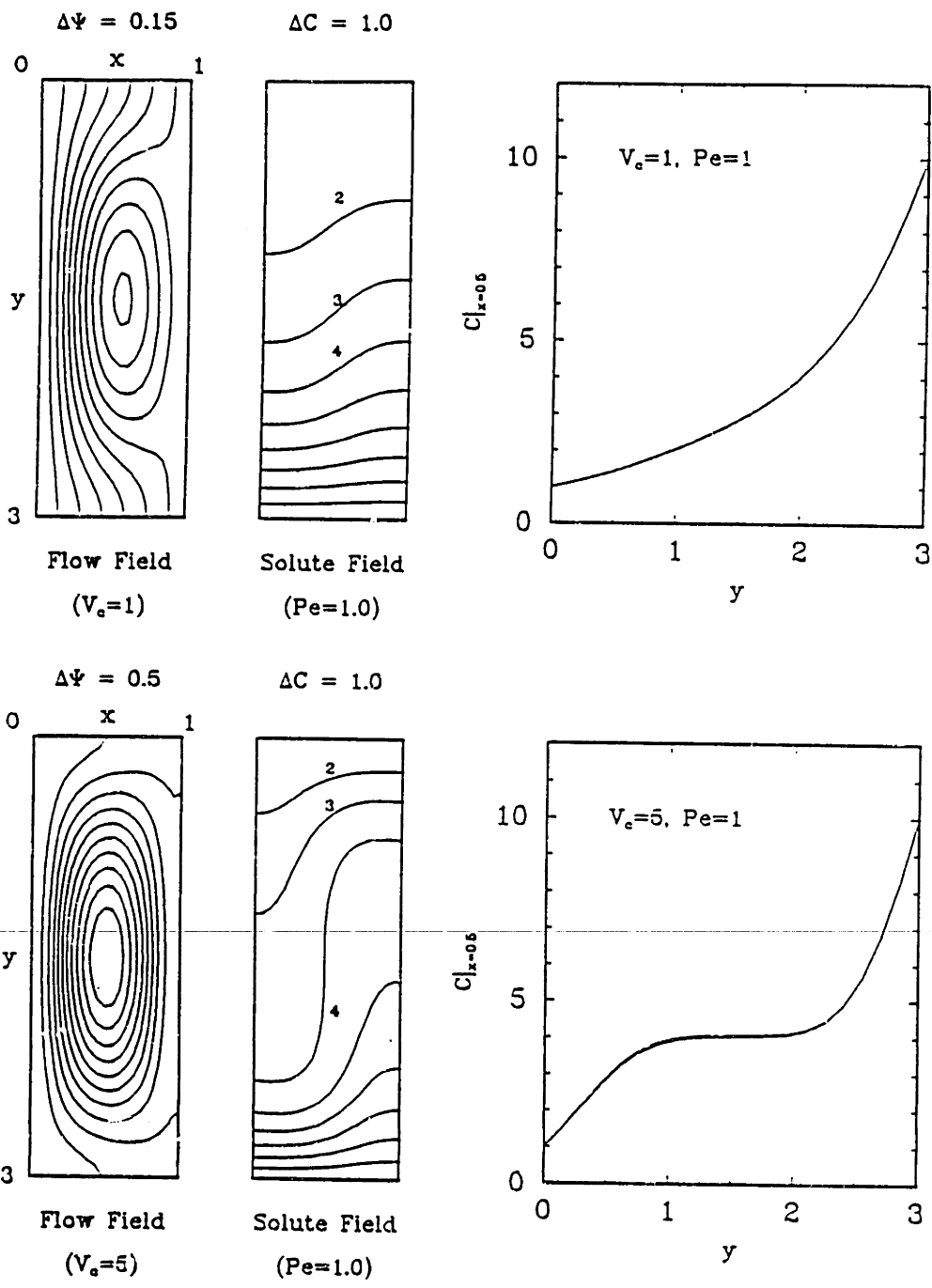


Figure 3.6: Effect of circulation rate on the solute field calculated using the Petrov-Galerkin methods: Essential solute boundary conditions(I).

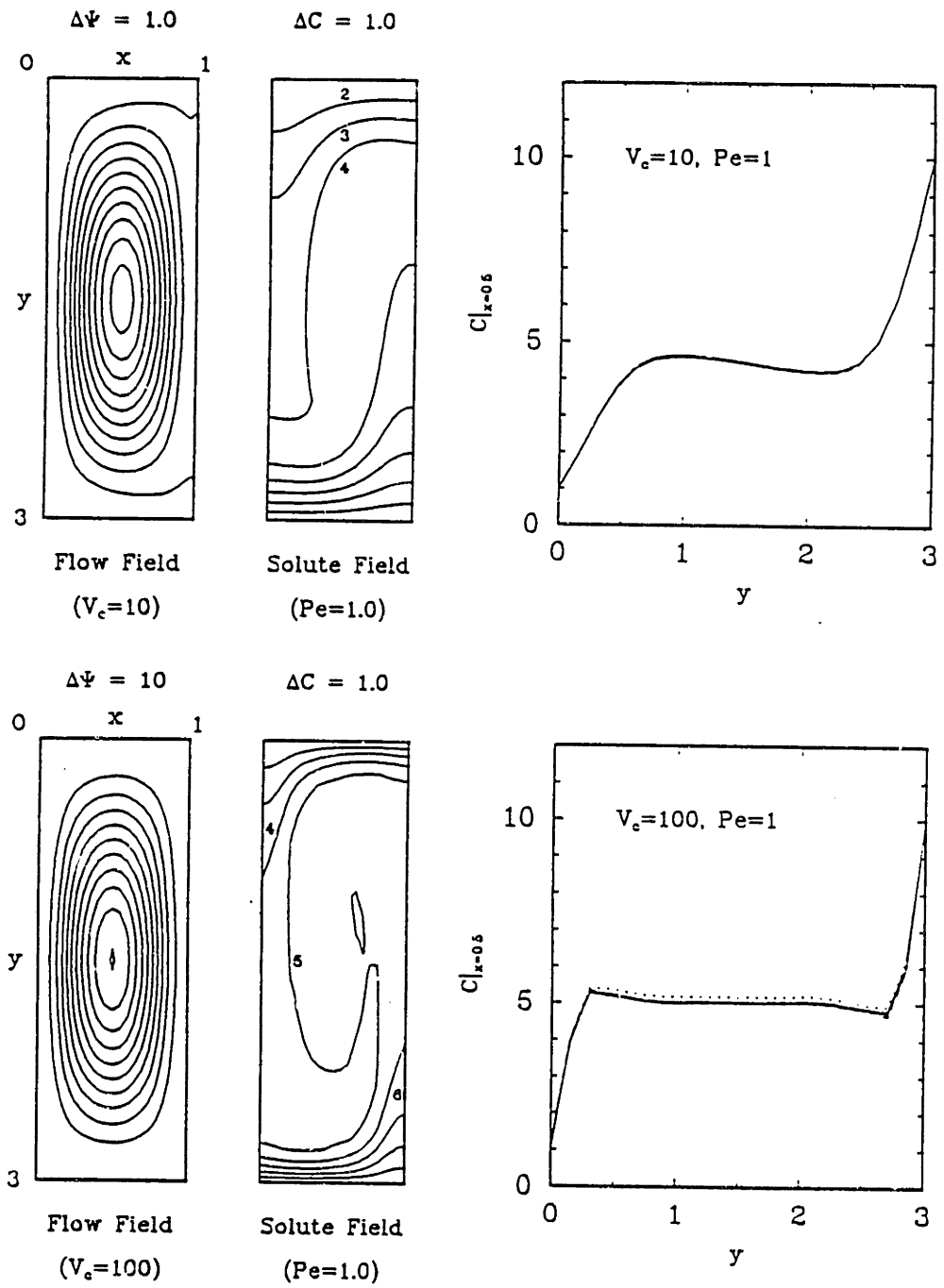


Figure 3.7: Effect of circulation rate on the solute field calculated using the Petrov-Galerkin methods: Essential solute boundary conditions(II).

The convection-dominated problem with the Robin boundary conditions has been tested with the same Petrov-Galerkin methods. This problem is more demanding than the previous problem because the Robin boundary condition is applied weakly in the finite element method while the essential boundary conditions can be applied exactly.

The effect of growth velocity on the solution of the one-dimensional problem ($V_c = 0$) is similar to that in the previous problem with essential boundary conditions: the onset of wiggles is observed in the Galerkin formulation beyond Pe^c . In this problem, the concentration at the interface ($y = H = 3$) deviates as high as 20 from the exact value ($1/k = 10$) when calculated by HZ. The reason for this behaviour is that the upwind corrections are forced to vanish at nodal points and the Robin conditions are not equally weighted in this scheme, leading to the erroneous results in the solution at the boundaries. These results are shown in Figures 3.8 and 3.9. The results with Galerkin method give an accurate interface concentration. Among Petrov-Galerkin methods, only SU/PG gives an accurate boundary value; the solutions computed with HZ and DBS begin to deviate from the exact value for V_c greater than 5.

All the methods give nearly the same results shown in Figure 3.10, if the circulation rate V_c is small and the axial concentration profile is almost one-dimensional. Increasing V_c to 5 gives solutions that are grouped following the order of elements. Further increase of V_c separates the solution by HZ from others and this becomes more severe when V_c is large, as shown in Figure 3.11. In the same manner as the one-dimensional problem (*i.e.* $V_c = 0$), the accuracy of the method can be measured by comparing the average concentration along the interface with the exact value ($1/k = 10$). This exact value of average concentration which is independent of circulation rate or growth velocity can be derived from the solute balance at the interface and velocity boundary conditions used in the problem. Integral equation for the solute balance is

$$\int_D (\nabla^2 C - Pe \mathbf{v} \cdot \nabla C) dV = 0$$

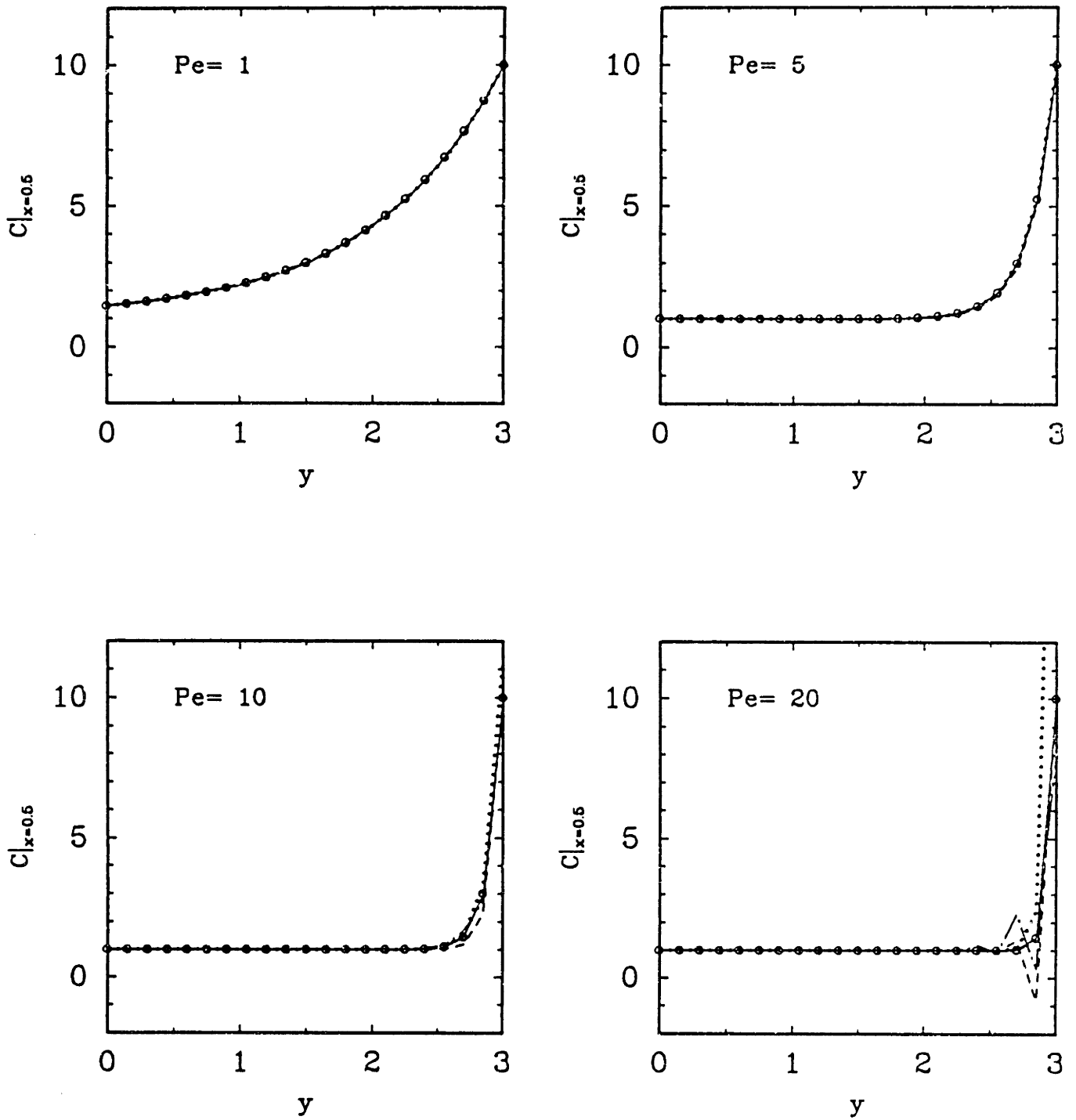


Figure 3.8: One-dimensional composition profiles computed using the Petrov-Galerkin methods with mixed boundary conditions.

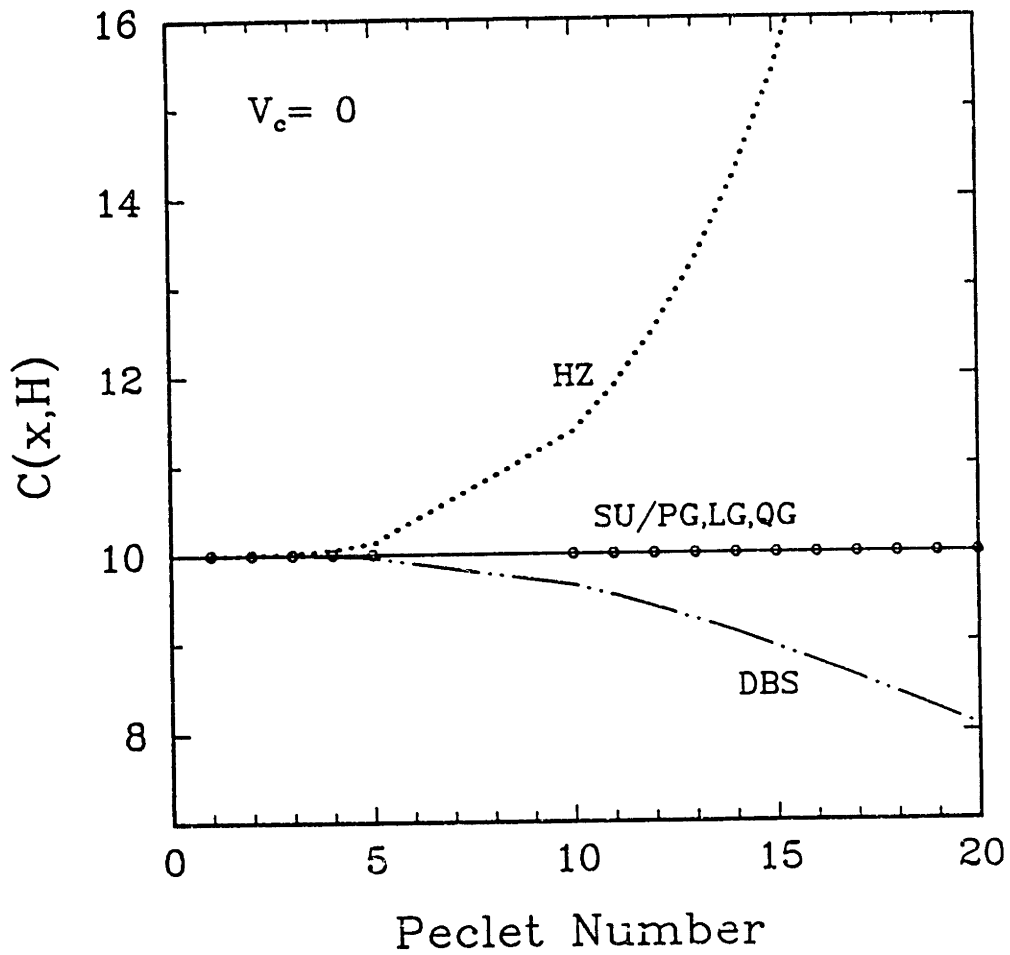


Figure 3.9: The accuracy of the Petrov-Galerkin methods measured in terms of the interfacial solute balance.

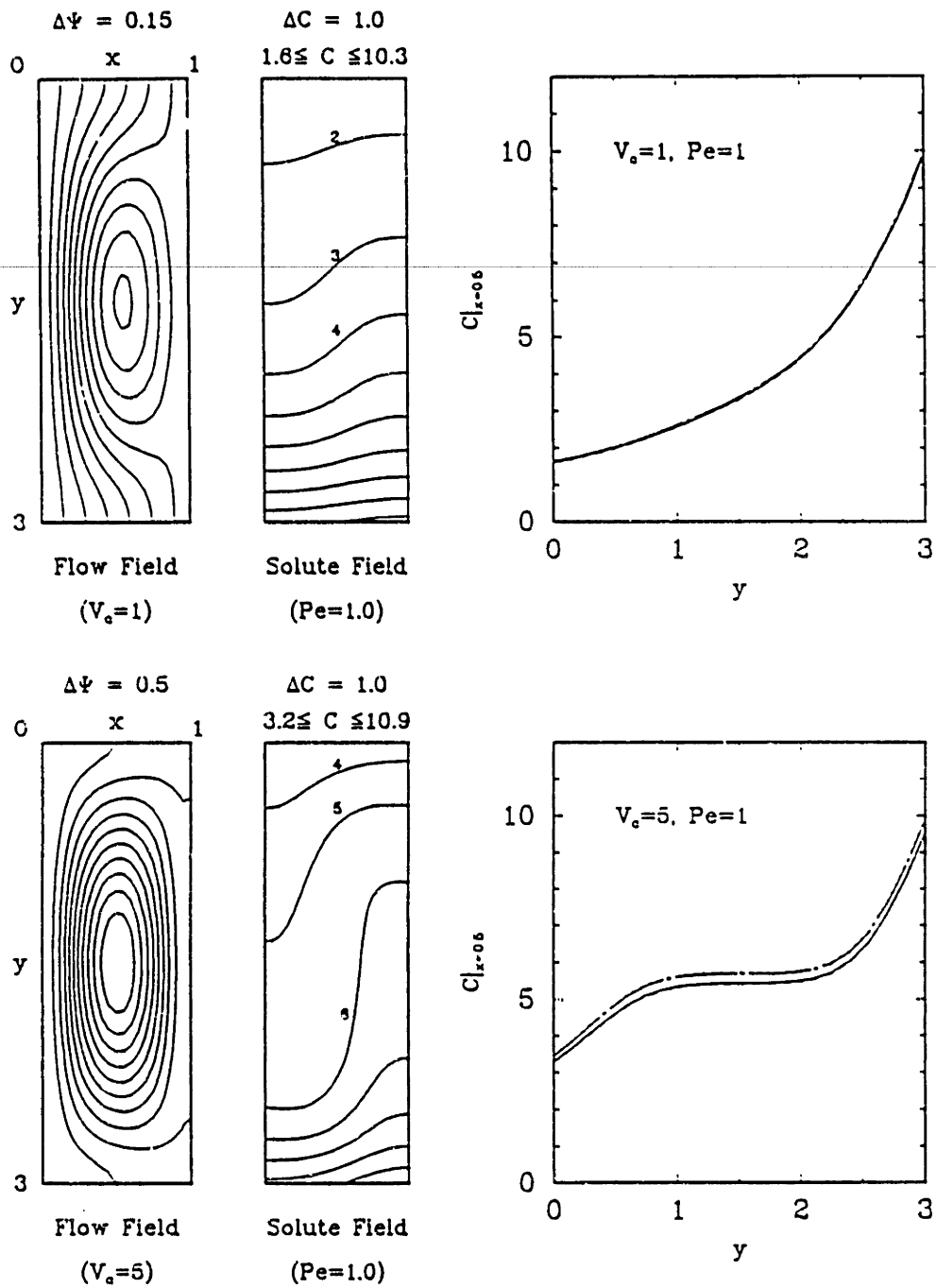


Figure 3.10: Effect of flow circulation rate on the solute field calculated using the Petrov-Galerkin methods: Mixed solute boundary conditions(I).

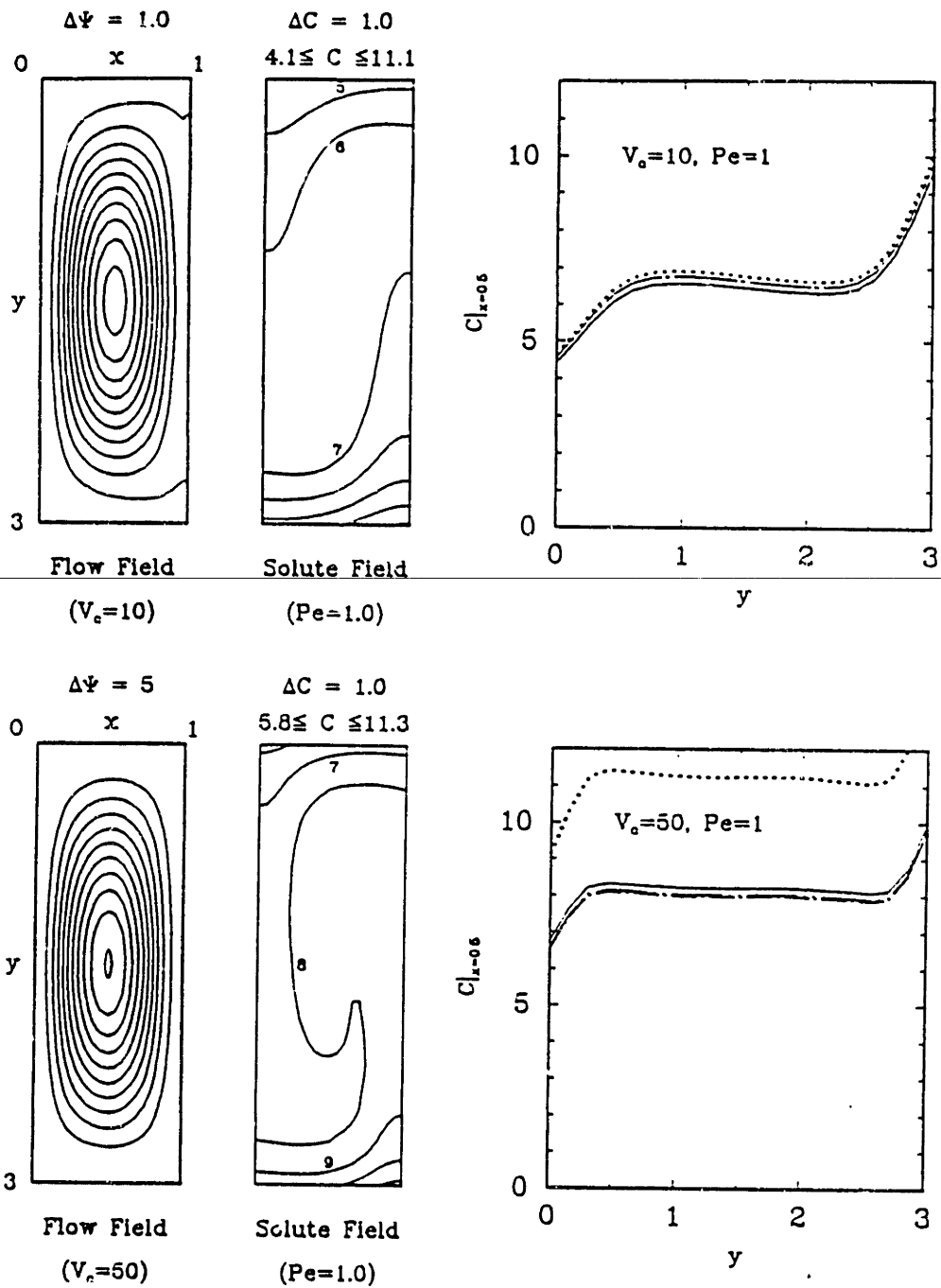


Figure 3.11: Effect of circulation rate on the solute field calculated using the Petrov-Galerkin methods: Mixed solute boundary conditions(II).

Applying the divergence theorem gives

$$\int_{\partial D} \mathbf{n} \cdot \nabla C - Pe \mathbf{n} \cdot (\mathbf{v}C) \, dS = 0$$

Since the sidewall cannot be penetrated by the solute, contribution for the surface integral come only from the inlet and interface.

$$\begin{aligned} & \int_{\partial D_i} \mathbf{n} \cdot \nabla C - Pe \mathbf{n} \cdot (\mathbf{v}C) \, dS \\ & + \int_{\partial D_I} \mathbf{n} \cdot \nabla C - Pe \mathbf{n} \cdot (\mathbf{v}C) \, dS = 0 \end{aligned}$$

where ∂D_i and ∂D_I denote the boundaries at the inlet and at the interface, respectively.

Applying the Robin boundary condition at the inlet and interface gives

$$\begin{aligned} & \int_{\partial D_i} -Pe(C - 1) + Pe v_y C \, dS \\ & + \int_{\partial D_I} PeC(1 - k) - Pe v_y C \, dS = 0 \end{aligned}$$

Axial velocity component at the inlet and interface v_y is 1 from the stream function in Eq (3.62), which simplifies the equation as

$$\int_{\partial D_i} 1 \, dS - \int_{\partial D_I} kC \, dS = 0$$

From this relation, the exact value of the average concentration at the interface is gives as

$$\int_{\partial D_I} C \, dS = \frac{1}{k}$$

The average concentration at the interface are shown in Figure 3.12 as a function of V_c for constant Pe of unity. As expected, methods using biquadratic interpolating functions generally show better accuracy than those using bilinear elements except the method of HZ.

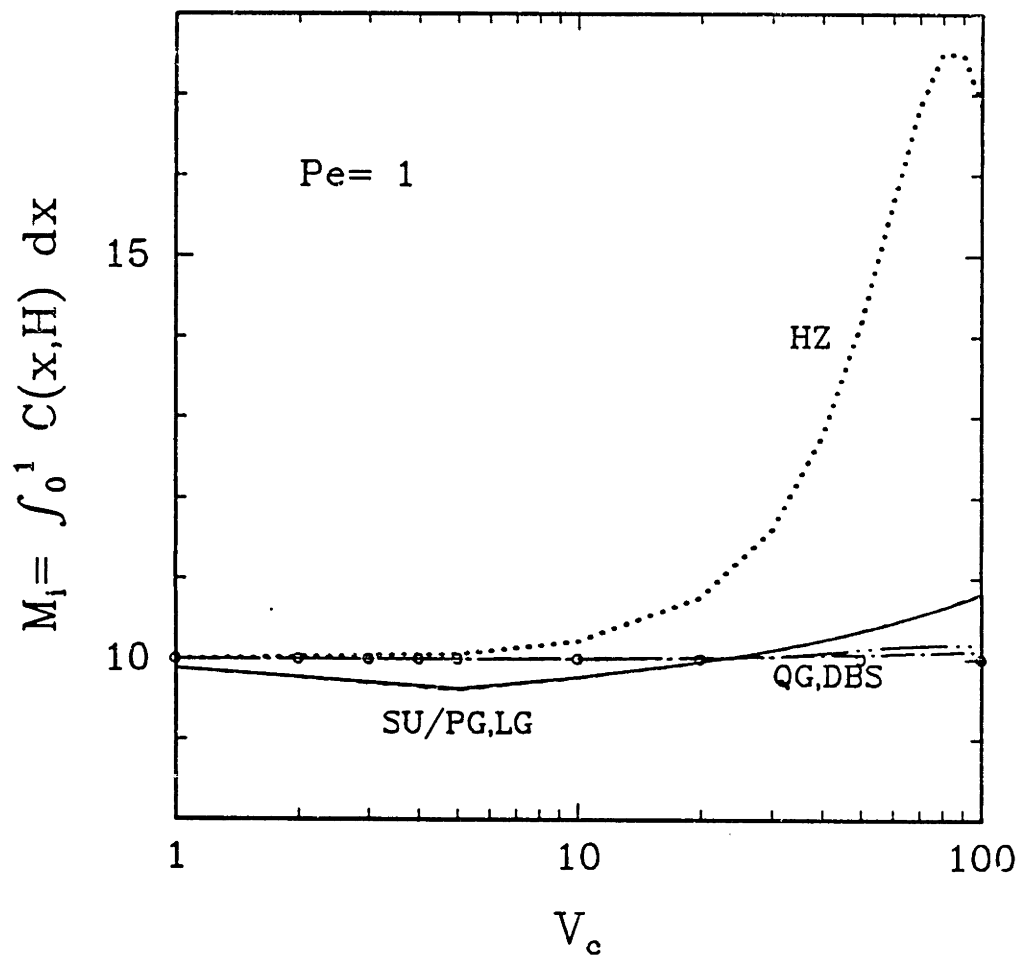


Figure 3.12: Interfacial solute balance computed using the Petrov-Galerkin methods with the mixed boundary conditions.

One reason for the failure of HZ is that the interfacial source term in the weak form of the solute balance is not changed as the elemental Peclet number is increased because the modifying function $F(\xi)$ used to form the Petrov-Galerkin weighting function (Eq. (3.69)) vanishes along all element boundaries. One remedy is to remove the source term from the boundary condition by defining a new concentration variable as the difference between C and one-dimensional concentration field C_u :

$$C_u \equiv 1 + \frac{1-k}{k} \exp[Pe(y-H)] \quad (3.72)$$

In terms of the new concentration variable, $\hat{C} \equiv C - C_u$, new source terms appear in the area integrals instead of in the boundary integrals, leading the source terms all affected by the modified weighting functions. The results calculated with the new concentration variables are shown in Figure 3.13. For unidirectional flow, introducing the new concentration variable definitely improves the accuracy of the interfacial solute balance as expected because the solute field is one-dimensional and there is no contribution from the boundary integral expressed with new concentration variables. When the flow cell is present, the modified HZ still improves the accuracy of the interfacial solute balance but fails to give the solution within the accepted range of error. Similar behaviour of the Petrov-Galerkin method by HZ has been previously observed for the more detailed simulation of vertical Bridgman crystal growth system (Adornato and Brown, 1987b). One way to cure this failure is to refine the mesh simultaneously until it gives the accurate solute balance, but this approach substantially reduces the merits of the Petrov-Galerkin method over the standard Galerkin scheme.

The test of three representative Petrov-Galerkin methods for the convection-dominated transport problem can be summarized as follows. First, all the Petrov-Galerkin methods tested gave correct results for the the problem with essential boundary conditions. When mixed boundary conditions were used, HZ resulted an inaccurate interfacial solute balance at high convection levels regardless of whether the convection results from the high growth rate or high circulation rate. Introduction of a new concentration variable to remove the source terms from the boundary integral did not help much when the mesh is coarse. The method proposed by DBS generated inaccurate

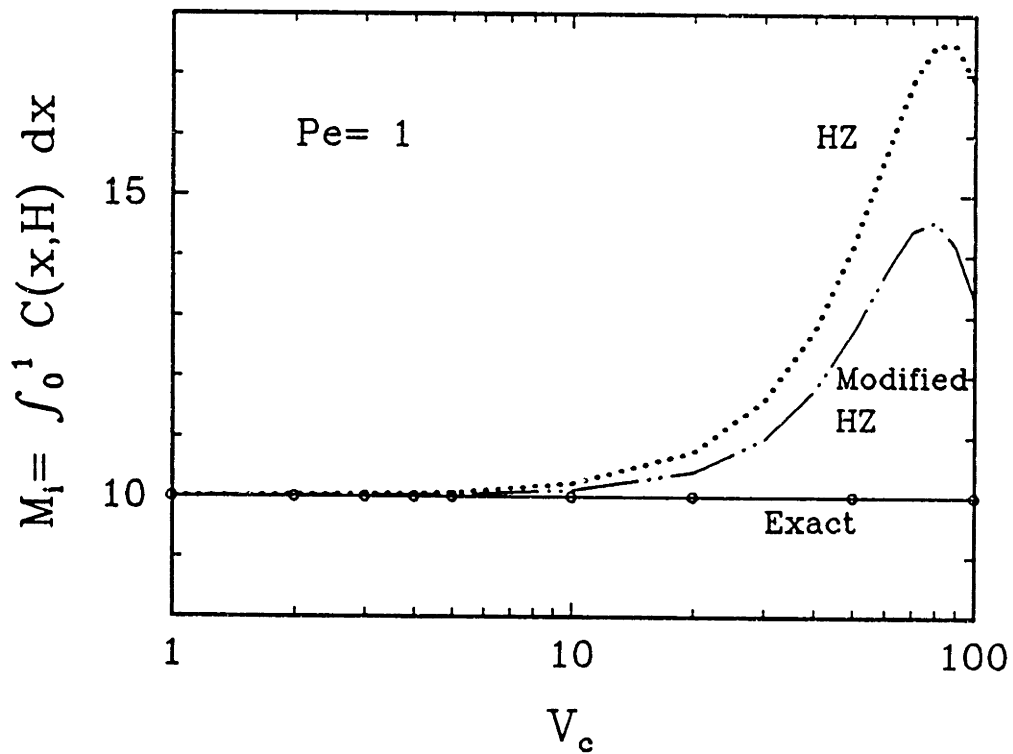
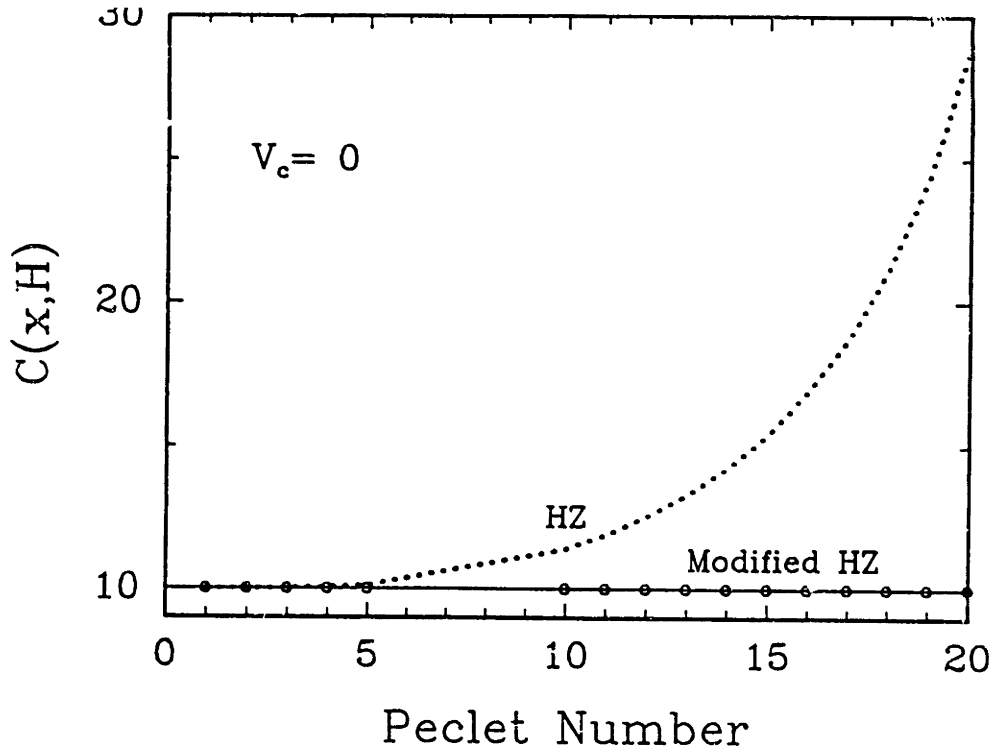


Figure 3.13: Comparison of the accuracy of the Petrov-Galerkin method developed by Heinrich *et al.* (1977) using regular and transformed concentration variables.

solute balances only for the high growth rate.

Although the Petrov-Galerkin solutions were always smooth, no advantage of the Petrov-Galerkin (HZ, DBS) formulation over conventional Galerkin method is obvious for the test problem with high convection level, because the predicted concentration fields lack the accuracy. Only the SU/PG formulation gave the consistent wiggle-free solutions with reasonable accuracy. However, the advantage of higher-order element are sacrificed in this formulation.

3.3 Formulation of Transient Model

3.3.1 Introduction

Transport processes in the vertical Bridgman system are inherently transient because of the steady decrease of the melt volume in a finite length ampoule. No transient description of the vertical Bridgman growth system has been available that includes melt flow, temperature and solute field in the presence of moving melt/solid interface and a description of heat transfer through the ampoule and furnace.

This section describes the development of a robust finite element method for the transient model of the vertical Bridgman growth system developed in Section 2.3. The numerical techniques presented here are novel because of the methodology used to handle the complex moving-boundaries and the disparate time scales associated with the transport of the various field variables. Our strategy is to develop a consistent spatial discretization of the entire set of differential equations describing momentum, heat and solute transport taking explicit account of the moving-boundary. This discretization is the basis for developing time integration algorithms for transient simulations. The numerical formulation of discrete system of equations is described in Section 3.3.2.

Although a Galerkin finite element method similar to that employed in the solution of the pseudo-steady-state model is used for spatial discretization, additional complica-

tions arise from the moving mesh which is updated at each time step. The usefulness of the transient model hinges on the accurate and efficient numerical integration of the discrete equation sets. In this study of moving-boundary problems with complex nonlinearities, it is preferable to employ implicit time integration method, which guarantees the numerical stability (Gear, 1971), over explicit algorithm. For the solidification problems with large differences in the time scales for heat and solute transport, the fully implicit time integration was shown to be more efficient than the explicit algorithm in terms of total CPU time (Derby and Brown, 1986) by taking the larger time step size.

The approach taken here is to implement a fully implicit integration method for solving the system of differential-algebraic equations generated by the Galerkin finite element formulation. This integration strategy is described in Section 3.3.3 and parallels the predictor/corrector type implicit time integration method by Gresho *et al.* (1980b), which is equipped with adaptive time-stepping algorithm and has been widely used in the finite element analyses of transport problems (Bixler and Benner, 1985; Keunings, 1986; Wouters *et al.*, 1987; Derby *et al.*, 1987; Ungar *et al.*, 1988). An improved version of Gresho and coworkers' scheme was also suggested by Bixler (1989) for the case where the solution approaches a steady-state.

In the transient model, large systems of nonlinear equations must be solved at each time step. A quasi-Newton iteration algorithm is an extremely effective means of solving these sets and is described in Section 3.3.4.

The applicability of the numerical method developed here for the transient model is demonstrated in Section 3.3.5 by displaying the sample results from the transient simulation of the vertical Bridgman crystal growth system without melt convection, where the solutions can be compared to simple one-dimensional, closed form results.

3.3.2 Spatial Discretization

The spatial discretization of the transient vertical Bridgman model is based on the finite element/Newton method for solving free- and moving-boundary problems arising

in solidification systems (Chang, 1982; Ettouney, 1983; Ungar, 1984; Adornato, 1986; Derby, 1986). The basic concept of discretizing the interface shape and field variables in expansions of appropriate Lagrangean polynomials is the same as in the steady-state formulation. In the transient problem, additional complexity arises from the fact that the basis functions are implicitly time dependent because they are defined by the finite element mesh which deforms in time as the interface translates.

The spatial domain, including melt, crystal and ampoule, is discretized into a finite element mesh which deforms following the movement of the melt/solid interface shape during solidification. Isoparametric biquadratic elements are used because of their accuracy for solving elliptic problems and for approximation of curved boundary shapes (Strang and Fix, 1973; Hughes, 1987).

The shape of the melt/solid interface is approximated by one-dimensional Lagrangian quadratic polynomials $\{\check{\phi}(r(\tau))\}$, which are consistent with the biquadratic elements in the isoparametric mapping for the coordinate system. The interface shape is expressed as

$$H(r, \tau) = \sum_{i=1}^{N_I} H^{(i)}(\tau) \check{\phi}^i(r(\tau)) \quad (3.73)$$

where N_I is the number of nodes along the interface. The coefficients $\{H^{(i)}\}$ are the time-dependent interface locations at the nodes along interface and the interpolating functions $\{\check{\phi}^i\}$ are implicitly time dependent because of the coupling with the moving interface.

The simplest case of uniform mesh was illustrated in the formulation of pseudo-steady-state model in Section 3.2.2. In the present model of confined crystal growth, the radii of melt and crystal are dictated by the dimension of the crucible leading the radial location of the nodes in the element to be time-independent; only the axial locations of the nodes are coupled with the interface shape. Then, time-dependent locations of the nodes in the element $\{r^{(i)}, z^{(i)}\}$ are

$$r^{(i)} = r^{(i)} \text{ and } z^{(i)} = z^{(i)}(H(r^{(i)}, \tau)).$$

The isoparametric mapping consistent with the Lagrangian biquadratic interpolating functions is used to transform each element in the cylindrical coordinate system (r, z) to a local coordinate system (ξ, η) , which spans $(-1 \leq \xi \leq 1, -1 \leq \eta \leq 1)$, as

$$r = \sum_{i=1}^9 r^{(i)} \phi^i(\xi, \eta), \quad z = \sum_{i=1}^9 z^{(i)}(H(r^{(i)}, \tau)) \phi^i(\xi, \eta) \quad (3.74)$$

where $\{\phi^i(\xi, \eta)\}$ are biquadratic Lagrangian interpolating functions. The coupling of the shape and location of each element to the moving interface governs the location of the nine nodes in the element.

The field variables are discretized using mixture of finite element interpolating functions. The velocity and concentration in the melt and temperature in all phases are approximated by biquadratic Lagrangian interpolating functions as

$$\mathbf{v}(r, z, \tau) = \sum_{i=1}^{N_m} \begin{bmatrix} v_r^{(i)}(\tau) \\ v_z^{(i)}(\tau) \end{bmatrix} \phi^i(r(\tau), z(\tau)), \quad (3.75)$$

$$S(r, z, \tau) = \sum_{i=1}^{N_m} S^{(i)}(\tau) \phi^i(r(\tau), z(\tau)) \quad (3.76)$$

$$\theta(r, z, \tau) = \sum_{i=1}^N \theta^{(i)}(\tau) \phi^i(r(\tau), z(\tau)) \quad (3.77)$$

where N_m is the number of nodes in the melt and N is the total number of nodes in all phases. The coefficients $v_r^{(i)}$, $v_z^{(i)}$, $S^{(i)}$ and $\theta^{(i)}$ are time-dependent velocity, concentration and temperature values at node i . The interpolating functions $\{\phi^i\}$ are implicitly time-dependent since they are defined on elements with shapes that change in time following the evolution of interface shape.

The dynamic pressure in the melt is approximated by discontinuous piecewise-linear interpolating functions defined at the centroid node of each element in the local coordinate system as

$$p(r, z, \tau) = \sum_{i=1}^3 p^{(i)} \psi^i(\xi, \eta) \quad (3.78)$$

where the linear basis functions $\psi^i(\xi, \eta)$ are the same as in Eq. (3.26).

The weak forms of the field equations are obtained by applying the Galerkin's method to the equations in Section 2.3.2. The weak form of the continuity equation is formulated using the interpolating function for pressure as a weighting function, *i.e.*

$$\int_{D_m(\tau)} \psi^i (\nabla \cdot \mathbf{v}) dV = 0, \quad (3.79)$$

where $i = 1, \dots, N_p$ which is identical to $3N_{E,m}$ because there are three unknowns of pressure for each element.

The Galerkin method is applied to the momentum equation (Eq. (2.21)) to yield residual equations for the velocity in the melt as

$$\int_{D_m(\tau)} \phi^i \left\{ \frac{\partial \mathbf{v}}{\partial \tau} + \mathbf{v} \cdot \nabla \mathbf{v} + \nabla p - \nabla^2 \mathbf{v} - \frac{1}{Pr} [Ra_s S - Ra_t (\theta - 1)] \mathbf{e}_z \right\} dV = 0 \quad (3.80)$$

where $i = 1, \dots, N_m$ and $\{\phi^i\}$ represent the weighting functions identical to velocity interpolating functions multiplied by the unit vectors ($\mathbf{e}_r, \mathbf{e}_z$) for corresponding velocity field. Therefore, Eq. (3.80) has a total of $2N_m$ residual equations for the velocity in the melt.

In a similar manner, the residual equations associated with the solute balance in the melt and energy balance in all phases are expressed as

$$\int_{D_m(\tau)} \phi^i \left\{ Sc \left(\frac{\partial S}{\partial \tau} + \mathbf{v} \cdot \nabla S \right) - \nabla^2 S \right\} dV = 0 \quad (3.81)$$

$$\begin{aligned} & \int_{D_m(\tau)} \phi^i \left\{ Pr \left(\frac{\partial \theta}{\partial \tau} + \mathbf{v} \cdot \nabla \theta_m \right) - \nabla^2 \theta_m \right\} dV \\ & + \int_{D_k(\tau)} \phi^i \left\{ Pr \left(\frac{\partial \theta}{\partial \tau} \right) - \gamma_k \nabla^2 \theta_k \right\} dV = 0, \end{aligned} \quad (3.82)$$

where $i = 1, \dots, N$ represents the residual equation for each node and $k = s$ and $k = a$ denotes the crystal and ampoule phase, respectively.

The final forms of the residual equations are derived by integrating the diffusive terms in Eqs. (3.80)–(3.82) by parts and applying the divergence theorem (Mase, 1970) and the flux boundary conditions on velocity, temperature and concentration at the end of the ampoule, melt/solid interface and along the ampoule wall, following the same procedure as in steady-state formulation. This yields

$$\int_{D_m(\tau)} \phi^i \frac{\partial \mathbf{v}}{\partial \tau} + \phi^i \mathbf{v} \cdot \nabla \mathbf{v} - (\nabla \cdot \phi^i) p + \nabla \phi^i \cdot \nabla \mathbf{v} - \frac{\phi^i}{Pr} [Ra_s S - Ra_t (\theta - 1)] \mathbf{e}_z dV = 0 \quad (3.83)$$

$$\begin{aligned} & \int_{D_m(\tau)} Sc \phi^i \left(\frac{\partial S}{\partial \tau} + \mathbf{v} \cdot \nabla S \right) + \nabla \phi^i \cdot \nabla S dV \\ & + \int_{\partial D_I} \check{\phi}^i Sc \frac{\partial H}{\partial \tau} (\mathbf{N} \cdot \mathbf{e}_z) (S + 1)(1 - k) dS = 0 \end{aligned} \quad (3.84)$$

$$\begin{aligned} & \int_{D_m(\tau)} Pr \phi^i \left(\frac{\partial \theta_m}{\partial \tau} + \mathbf{v} \cdot \nabla \theta_m \right) - \nabla \phi^i \cdot \nabla \theta_m dV \\ & + \int_{D_k(\tau)} \phi^i Pr \left(\frac{\partial \theta_k}{\partial \tau} \right) - \gamma_k \nabla \phi^i \cdot \nabla \theta_k dV \\ & + \int_{\partial D_I} \check{\phi}^i St Pr \frac{\partial H}{\partial \tau} (\mathbf{N} \cdot \mathbf{e}_z) dS \\ & - \int_{\partial D_w} \check{\phi}^i Bi(z, \tau) [\theta_\infty(z, \tau) - \theta(r, z, \tau)] dS = 0, \end{aligned} \quad (3.85)$$

where ∂D_e , ∂D_I and ∂D_w denote the boundaries at the top of the ampoule, at the interface and at the outer surface of the ampoule, respectively. In an incompressible fluid, the pressure is an implicit variable which instantaneously adjusts itself in such a way that the incompressibility constraint ($\nabla \cdot \mathbf{v} = 0$) remains satisfied. In Eq. (3.83) the pressure term has been integrated by parts, as discussed for the steady-state formulation. The pressure field is only computed up to an arbitrary additive constant, which is set replacing the first residual equation derived in Eq. (3.79) with

$$p(\mathbf{0}, 0) = 0. \quad (3.86)$$

The spatial discretization is completed by substituting finite element approximations for the field variables Eqs. (3.75)–(3.77) into the residual equations Eqs. (3.83)–(3.84).

The analytical expressions of the time-derivatives in the residual equations are not simple because both nodal values and interpolating functions in Eqs. (3.75)–(3.77) are time-dependent. The formulation of the time-derivative is described below for the energy equation. The time-derivative term in Eq. (3.85) is expanded in terms of finite element approximation for temperature as

$$\frac{\partial \theta}{\partial \tau} = \frac{\partial}{\partial \tau} \left(\sum_{j=1}^9 \theta^{(j)} \phi^j \right) = \sum_{j=1}^9 \left(\frac{\partial \theta^{(j)}}{\partial \tau} \phi^j + \theta^{(j)} \frac{\partial \phi^j}{\partial \tau} \right) \quad (3.87)$$

In evaluating the time-derivative $\partial \phi^j / \partial \tau$, we use the procedure developed previously by Lynch and Gray (1980). We suppose the isoparametric mapping from the parent element in global coordinates (r, z) to the isoparametric element in local coordinates (ξ, η) . The value of ϕ^j is invariant with respect to ξ and η and we have

$$\left. \frac{\partial \phi^j}{\partial \tau} \right|_{\xi, \eta} = 0 \quad (3.88)$$

Applying the isoparametric coordinate transformation to ϕ^j gives

$$\left. \frac{\partial \phi^j}{\partial \tau} \right|_{\xi, \eta} = \nabla \phi^j \cdot \left. \frac{\partial \mathbf{x}}{\partial \tau} \right|_{\xi, \eta} + \left. \frac{\partial \phi^j}{\partial \tau} \right|_{\mathbf{x}} = 0 \quad (3.89)$$

where \mathbf{x} is the vector of the global coordinates, $\mathbf{x} \equiv (r, z)$ and $\nabla \equiv (\partial/\partial r)\mathbf{e}_r + (\partial/\partial z)\mathbf{e}_z$ is the gradient operator with respect to the fixed coordinate frame (r, z) . Equation (3.89) reduces to

$$\frac{\partial \phi^j}{\partial \tau} = -\mathbf{V}^e \cdot \nabla \phi^j \quad (3.90)$$

where the *element* velocity vector \mathbf{V}^e measures how each element deforms and is defined by

$$\mathbf{V}^e \equiv \sum_{k=1}^9 \frac{\partial \mathbf{x}^k}{\partial \tau} \phi^k = \sum_{k=1}^9 \mathbf{V}^k \phi^k, \quad (3.91)$$

where $\mathbf{V}^k \equiv \partial \mathbf{x}^k / \partial \tau$ is the velocity of the coordinates of the k th elemental node.

Substituting Eq. (3.90) into Eq. (3.87) yields

$$\frac{\partial \theta}{\partial \tau} = \sum_{j=1}^9 \left[\phi^j \frac{\partial \theta^{(j)}}{\partial \tau} - \mathbf{V}^e \cdot (\theta^{(j)} \nabla \phi^j) \right] = \sum_{j=1}^9 \left(\phi^j \frac{\partial \theta^{(j)}}{\partial \tau} \right) - \mathbf{V}^e \cdot \nabla \theta \quad (3.92)$$

The effect of moving mesh is summarized as the last term in (3.92) which directly links the velocity of the moving melt/solid interface through the functional dependence of mesh on the interface location. This correction in the time derivative of temperature is applied to each velocity component and concentration in the same manner and gives additional terms in the mass matrix described below.

When the mesh of present model system is considered, this correction term is further simplified. As discussed earlier, only the axial locations of the nodes in each element vary in time, coupled with the moving interface. This eliminates the contribution of the r-component in the element velocity, because the radial locations of the nodes are invariant. The element velocity vector reduces to $\mathbf{V}^e = V_z^e$ and the Eq. (3.92) is rewritten as

$$\frac{\partial \theta}{\partial \tau} = \sum_{j=1}^9 \left(\phi^j \frac{\partial \theta^{(j)}}{\partial \tau} \right) - V_z^e \cdot \frac{\partial \theta}{\partial z} \quad (3.93)$$

The residual equations for determining the interface location are formed by applying the Galerkin's method to the melting point constraint (2.12) evaluated along the melt/solid interface as

$$\int_{\partial D_I} \tilde{\phi}_i(r) [\theta(r, H(r)) - \theta_m(S)] dS = 0 \quad (3.94)$$

where the differential unit of arc-length along the interface is defined as

$$dS = \sqrt{1 + H_r^2} dr \quad (3.95)$$

All the discretized equations are assembled into a set of algebraic- differential equations, which is represented in vector form as

$$M^{(i)} \frac{\partial \mathbf{y}^{(i)}}{\partial \tau} = F^{(i)}(\mathbf{y}^{(i)}) \quad (3.96)$$

where $M^{(i)}$ is termed a mass matrix and $y^{(i)}$ represents the vector containing all the unknown coefficients for the field variables and interface shapes. The mass matrix consists of a banded portion arising from the residual equations for field variables (velocity, temperature and concentration) augmented with dense columns and rows caused by the time-derivative correction linked to the moving interface. The mass matrix is singular since there are no explicit time derivatives in the residual equations for the incompressibility constraint (3.79) and melt/solid interface (3.94). The mass matrix can be written as

$$\mathbf{M} = \begin{bmatrix} \mathbf{M}_1 & \mathbf{O}_1 & \mathbf{M}_2 \\ \mathbf{O}_2 & \mathbf{O}_3 & \mathbf{O}_4 \end{bmatrix} \quad (3.97)$$

and the vector of unknowns is ordered as

$$\mathbf{y}^T = (\mathbf{v}_r^T, \mathbf{v}_z^T, \theta^T, \mathbf{S}^T, \mathbf{p}^T, \mathbf{H}^T).$$

For this ordering, \mathbf{M}_1 is a $(4N_m + N_s) \times (4N_m + N_s)$ banded matrix and \mathbf{M}_2 is a $(4N_m + N_s) \times N_I$ dense rectangular matrix. $\mathbf{O}_1((4N_m + N_s) \times 3N_{E,m})$, $\mathbf{O}_2((3N_{E,m} + N_I) \times (4N_m + N_s))$, $\mathbf{O}_3((3N_{E,m} + N_I) \times 3N_{E,m})$ and $\mathbf{O}_4((3N_{E,m} + N_I) \times N_I)$ are all null matrices with appropriate dimensions. The components of \mathbf{M}_1 are

$$M_{1,ij} \equiv \int_{D_k} \alpha \phi^i \phi^j dV \quad (3.98)$$

where k denotes the region, $i, j = 1, \dots, (4N_m + N_s)$ and α 's are dimensionless parameters for corresponding field equations: 1 for momentum, Pr for energy and Sc for solute. The contributions to \mathbf{M}_2 account for the moving mesh and are multiplied to the time derivative of the interface. With the formulation of time-derivatives (3.93) for the present model system, the components of \mathbf{M}_2 are

$$M_{2,ij} \equiv \int_{D_k} \alpha \phi^i \phi^j \frac{\partial z^j}{\partial H(z^j)} \frac{\partial \langle \rangle}{\partial z} dV \quad (3.99)$$

where $i = 1, \dots, (4N_m + N_s)$ and $j = (4N_m + N_s + 3N_{E,m} + 1), \dots, (4N_m + N_s + 3N_{E,m} + N_I)$ with α 's same as for \mathbf{M}_1 . The symbol $\langle \rangle$ denotes the appropriate variable

for corresponding field equations: v_r or v_z for the momentum, θ for the energy and S for the solute equations.

3.3.3 Time Integration

The set of transient equations that result from the Galerkin finite element method are expressed compactly in a vector notation as

$$\underline{\underline{\mathbf{M}}}(\underline{\mathbf{y}}) \frac{\partial \underline{\mathbf{y}}}{\partial \tau} = \underline{\mathbf{F}}(\underline{\mathbf{y}}) \quad (3.100)$$

where $\underline{\mathbf{y}}$ is a vector containig all the unknowns, $\underline{\underline{\mathbf{M}}}$ is a mass matrix in finite element literature and $\underline{\mathbf{F}}$ is the steady-state part of the Galerkin residual equations. The mass matrix $\underline{\underline{\mathbf{M}}}$ is singular since there are no explicit time derivatives in the residual equations for the incompressibility constraint and for the melt/solid interface. The system of equations with singular mass matrix is a differential algebraic set and is particularly difficult to solve numerically since they are infinitely stiff (Gear, 1971; Petzold, 1982). This singularity prevents the use of traditional explicit time integration methods, which would be much faster per time step, but the size of the time steps would be limited severely by the condition for numerical stability. Ungar *et al.* (1988) compared the performance of fully implicit Adams-Moulton algorithm and explicit predictor-corrector algorithm and concluded that the fully implicit scheme was more efficient and accurate in the microscale solidification problem. Another advantage of the implicit integration method is that it allows the larger time steps because the numerical stability constraint does not limit the size of the time step. Derby and Brown (1986) found the fully implicit algorithm was an order-of-magnitude more efficient with respect to the time step size especially for the solidification problems with large differences in the time scales of several transported physical quantities.

Among the fully implicit integration methods, trapezoidal rule with second-order accuracy is preferred to the backward Euler method because of the lower accuracy and dissipative nature of backward Euler scheme. Trapezoidal rule is the two-step

integration method and variously called modified Euler method, Crank-Nicolson method or second-order Adams-Moulton method in the literature. To obtain an trapezoidal rule we use the general formula for multistep implicit method as written by

$$y_{n+1} = y_n + \Delta\tau(1 - \frac{1}{2}\nabla - \frac{1}{12}\nabla^2 - \frac{1}{24}\nabla^3 - \dots)y'_{n+1} \quad (3.101)$$

Truncation of Eq. (3.101) at the second term gives the expression

$$y_{n+1} = y_n + \Delta\tau[y'_{n+1} - \frac{1}{2}(y'_{n+1} - y'_n)] + \mathcal{O}(\Delta\tau^3), \quad (3.102)$$

which is rearranged to yield

$$y'_{n+1} = \frac{2}{\Delta\tau}(y_{n+1} - y_n) - y'_n + \mathcal{O}(\Delta\tau^2), \quad (3.103)$$

that is accurate up to the term proportional to $\mathcal{O}(\Delta\tau^2)$. The vector equation (3.100) is discretized in time by applying trapezoidal rule (3.103) as

$$M(y_{n+1}) \left[y_{n+1} - y_n - \frac{\Delta\tau_n}{2} \left(\frac{\partial y}{\partial \tau} \right)_n \right] - \frac{\Delta\tau_n}{2} F(y_{n+1}) = 0 \quad (3.104)$$

where the subscripts denote the time step and $(\partial y/\partial \tau)_n$ is calculated from a consistent second-order trapezoidal rule expression as

$$\left[\frac{\partial y}{\partial \tau} \right]_n = \frac{2}{\Delta\tau_{n-1}}(y_n - y_{n-1}) - \left(\frac{\partial y}{\partial \tau} \right)_{n-1} \quad (3.105)$$

Since the trapezoidal rule is a two-step integration method which requires information at the previous time step, integration is started with the implicit backward Euler scheme as

$$M(y_{n+1})(y_{n+1} - y_n) - \Delta\tau_n F(y_{n+1}) = 0 \quad (3.106)$$

The system of nonlinear algebraic equations generated at each time step of either (3.104) or (3.106) is solved by a quasi-Newton algorithm which is described in the next

Section. The initial guess for these iterations is constructed from an explicit second-order Adams-Bashforth step using the information from the two previous time steps:

$$y_{n+1}^p \equiv y_n + \frac{\Delta\tau_n}{2} \left[\left(2 + \frac{\Delta\tau_n}{\Delta\tau_{n-1}} \right) \left(\frac{\partial y}{\partial \tau} \right)_n - \frac{\Delta\tau_n}{\Delta\tau_{n-1}} \left(\frac{\partial y}{\partial \tau} \right)_{n-1} \right] \quad (3.107)$$

where the time derivatives of y are determined by Eq. (3.105). In the iterations for the starting backward Euler method, a forward Euler step is used for generating the initial guess, which is consistent with the implicit integration scheme.

$$y_{n+1}^p \equiv y_n + \Delta\tau_n \left(\frac{\partial y}{\partial \tau} \right)_n \quad (3.108)$$

The strategy for varying the step size $\Delta\tau_n$ is based on an estimation of local time truncation error and follows the heuristics proposed by Gresho *et al.* (1980b). As shown in Eq. (3.102), the highest-order term which is neglected in the trapezoidal rule is $\mathcal{O}(\Delta\tau^3)$ and the estimation of local truncation error becomes

$$\Delta y_{n+1} = \frac{y_{n+1} - y_{n+1}^p}{3 \left(1 + \frac{\Delta\tau_{n-1}}{\Delta\tau_n} \right)} + \mathcal{O}(\Delta\tau^4), \quad (3.109)$$

where the predictor y_{n+1}^p of Eq. (3.107) is used. This estimate of the local time truncation error is used to compute the next step size $\Delta\tau_{n+1}$ by setting the local truncation error at the next step to be ε .

In terms of ε which is the only user-specified parameter, the next time step size is computed as

$$\Delta\tau_{n+1} = \Delta\tau_n \left(\frac{\varepsilon}{\|\Delta\mathbf{y}_{n+1}\|} \right)^{\frac{1}{3}}, \quad (3.110)$$

where $\|\mathbf{y}_{n+1}\|$ is the appropriate norm of the local truncation error. In this work, the following weighted root-mean-square norm has been used:

$$\|\mathbf{y}_{n+1}\| = \frac{1}{N} \left[\frac{1}{|v_r|_{max}^2} \sum_{i=1}^{N_u} \Delta v_{r,n+1}^2 + \frac{1}{|v_z|_{max}^2} \sum_{i=1}^{N_v} \Delta v_{z,n+1}^2 \right]$$

$$\left. + \frac{1}{\theta_{max}^2} \sum_{i=1}^{N_t} \Delta \theta_{n+1}^2 + \frac{1}{S_{max}^2} \sum_{i=1}^{N_c} \Delta S_{n+1}^2 + \frac{1}{H_{max}^2} \sum_{i=1}^{N_h} \Delta H_{n+1}^2 \right]^{\frac{1}{2}} \quad (3.111)$$

where $N(= N_u + N_v + N_t + N_c + N_h)$ is the total number of unknowns and each Δy is calculated by Eq. (3.109). The new step size $\Delta \tau_{n+1}$ is accepted if it is greater than the old step size $\Delta \tau_n$ or if it is less than $0.8\Delta \tau_n$. If $0.8\Delta \tau_n < \Delta \tau_{n+1} < \Delta \tau_n$, the step size is unchanged. The parameter ε for the error criterion at the next step was chosen typically as 1×10^{-4} .

The strategy described above is used for varying the size of the time step unless this step size violates following criteria. The first criterion is

$$\frac{\Delta \tau_{n+1}}{\Delta \tau_n} \leq 2 \quad (3.112)$$

Without this criterion, the step size would increase so much that the predictor would be likely to overshoot the solution at τ_{n+2} causing unacceptable error. In the scheme by Gresho *et al.* (1980b) they repeated the calculation at time τ_{n+1} if $\Delta \tau_{n+1} < 0.8\Delta \tau_n$, which makes the programming more complex and requires more memory. To prevent this additional work, we simply set $\Delta \tau_{n+1}$ as $2\Delta \tau_n$ when this criterion is violated. Secondly, the maximum time step size is specified as

$$\Delta \tau_{n+1} \leq \Delta \tau_{max} \quad (3.113)$$

where $\Delta \tau_{max}$ is set according to the time scale of interest. For the dimensionless time based on momentum time scale, $\Delta \tau_{max}$ was usually set to unity.

The third criterion is

$$\Delta \tau_{n+1} > \Delta \tau_{min} \quad (3.114)$$

where dimensionless $\Delta \tau_{min}$ is determined according to the time scale used. When the time step size is too small, trapezoidal rule oscillations are likely to occur and add to the time discretization errors. To damp the oscillations the backward Euler scheme replaces the trapezoidal rule when this criterion is violated.

3.3.4 Algebraic Solution with Quasi-Newton Iterations

Sets of nonlinear algebraic equations are generated at each time step of transient finite element analysis as a result of discretization of field variables and interface shape both in space and time. These nonlinear equation sets are summarized in a vector notation as

$$\hat{\mathbf{F}}(\mathbf{y}) = \mathbf{0} \quad (3.115)$$

where the caret is used to distinguish between residual equations including time discretization and those arising from steady-state analysis. The nonlinearities in the steady-state part of the model equations originate from the dependence of thermo-physical properties on the temperature and composition, from the convective transport terms in the momentum, energy and solute equations and most influentially from the implicit coupling of residual equations with the interface shape through the dependence of the finite element interpolating functions and the Galerkin integrals on the interface location. The last factor for nonlinearity becomes more evident with the moving mesh of the transient analysis. These nonlinearities force the employment of an appropriate iteration scheme in this analysis.

The best known method for the solution of the problem of this kind is Newton's method and modifications of it to improve its computational efficiency. While the second-order or quadratic convergence rate of Newton's method is very attractive, the well-known disadvantage of Newton's method is the requirement of a very good initial guess if the iteration is to converge, especially when the domain of attraction of the solution is small (Powell, 1970; Dennis and Moré, 1977). The most important computational disadvantage is that it needs the Jacobian matrix to be determined for each iteration. This is very costly requirement especially for large and dense matrices. One way to circumvent this problem is using a finite difference approximation to the Jacobian matrix. This approach reduces the cost of evaluating each element in the Jacobian matrix and this reduction can be substantial if the analytic expression of each element is complex. However the number of Jacobian elements to be evaluated still remains the same.

A popular technique for trying to save overall computational effort of the Newton's method is to hold the Jacobian matrix and its decomposition fixed for a given number of iterations, which is called *the quasi-Newton iteration* in the present study. The Jacobian is recomputed only after the previously obtained Jacobian has failed to yield a converged solution in a given number of iterations. This technique is particularly useful when the Jacobian is not changing very rapidly. Brent (1973) has shown that this technique can increase a certain measure of efficiency in spite of the reduced rate of convergence. Other quasi-Newton methods are discussed at length in the work by Dennis and Moré (1977).

An example of convergence for the typical calculation using quasi-Newton method is illustrated in Figure 3.14 for various number of quasi-Newton steps (N_{mod}) between full Newton iterations. Convergence of the iteration was measured in terms of the absolute and relative error criteria between successive iterations as

$$\varepsilon_{\infty} \equiv \max_i |y_{k+1}^{(i)} - y_k^{(i)}| < \varepsilon_{\infty, \text{set}} \quad \text{or} \quad \varepsilon_r \equiv \max_i \left\| \frac{|y_{k+1}^{(i)} - y_k^{(i)}|}{|y_k^{(i)}|} \right\| < \varepsilon_{r, \text{set}} \quad (3.116)$$

where $\varepsilon_{\infty, \text{set}}$ and $\varepsilon_{r, \text{set}}$ are the specified error tolerances for the absolute error and relative error. If either error criterion is satisfied, the iteration stops and the solution is considered to have been computed.

3.3.5 Example of Time-Dependent Calculation

Problem

The numerical algorithm for solution of the transient model is tested through calculations for the growth of gallium-doped germanium crystal in the vertical Bridgman system used by Wang (1984). In the laboratory experiment, the ampoule is held stationary until the temperature field in the melt and the seed crystal equilibrated with the thermal environments. Corresponding flow and solute fields are steady-state with a uniform concentration throughout the melt. Therefore, the initial conditions for the

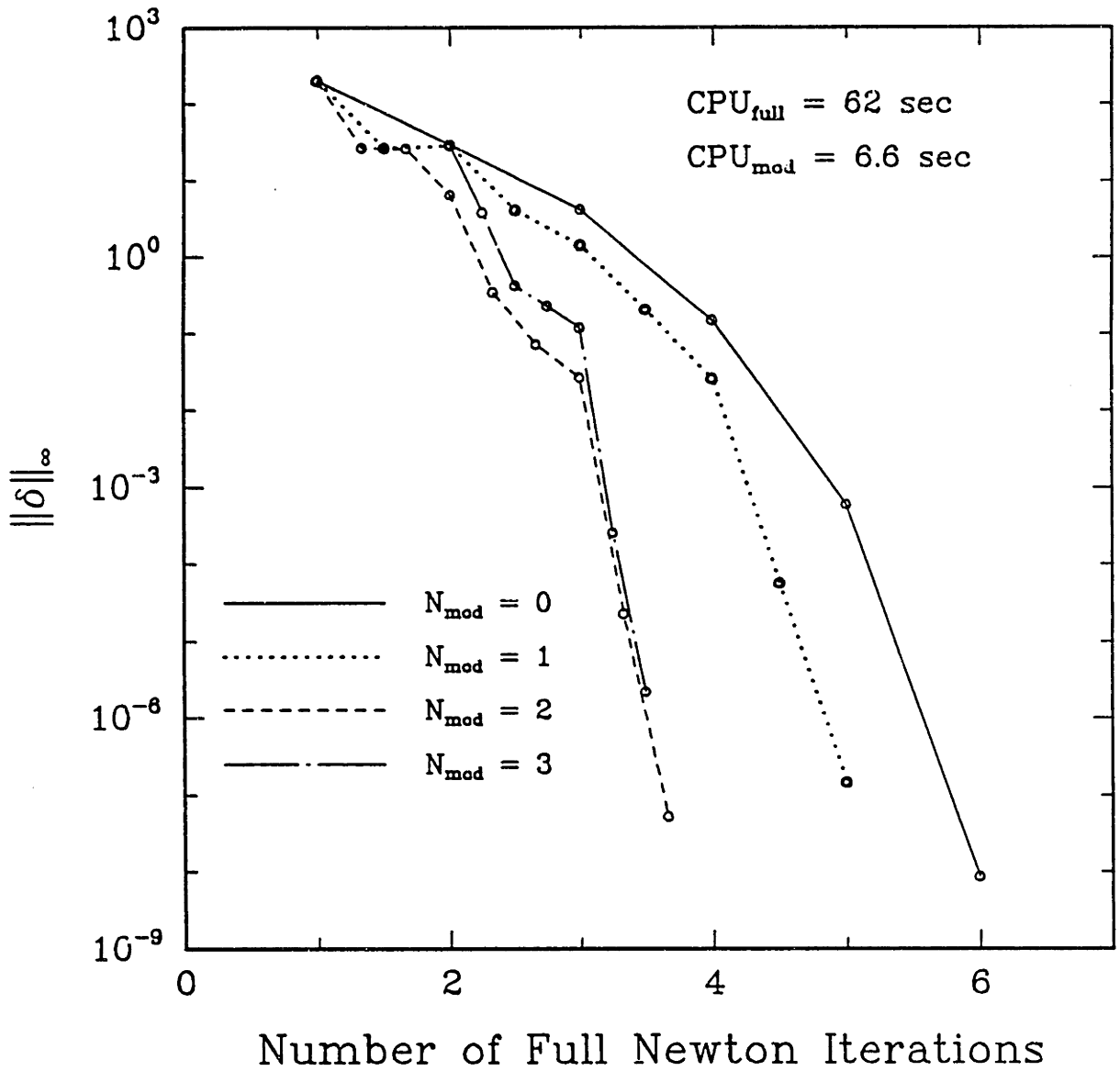


Figure 3.14: Convergence of a typical iteration of nonlinear equations using the quasi-Newton method.

transient integration are the steady-state solution of the field equations in a stationary ampoule. At $t = 0$, the ampoule begins to translate downward in the furnace and solidification starts upward. The transient simulation of the crystal growth process was continued until about half of the melt was solidified. The initial time step was 0.02 and is equal to two percent of viscous time constant (R_c^2/ν). This starting value of Δt comes from the suggestion of Gresho *et al.* (1980b) and the scheme of adaptive time step size described in Section 3.3.3. was employed to adjust Δt for future time step.

The discretization used in the calculation contained 20 radial elements in melt and crystal and 4 elements across the ampoule. The axial approximation was composed of 48 elements in the melt and 16 elements in the crystal. Examples of finite element meshes generated during the simulations are shown in Figure 3.15, where the deformation of mesh with the progress of solidification can be clearly observed.

The thermophysical properties used in this test for gallium-doped germanium are listed in Table 3.2. All properties were assumed to be independent of temperature and the concentration of the gallium is low enough to neglect the solutal buoyancy-driven convection. Test calculations for the growth of GaGe alloy in a boron nitride ampoule were performed without convection, $Ra_t = 0$. This limit of convection-free growth collapses the problem to the solution of a Stefan problem controlled by diffusion equations. This fact will be used later in this Section to estimate the numerical stability bound for Δt .

Parameters corresponding to the test case for this system are tabulated in Table 3.3. From the information on thermophysical properties of GaGe and furnace design, the values of dimensionless groups are listed in Table 3.4.

Results

The time step history is presented in Figure 3.16. to demonstrate the power of implicit time integration method. During the Euler-backward integration scheme was used in the first five time steps, the step size was held constant at 0.02. Then, the time step for the

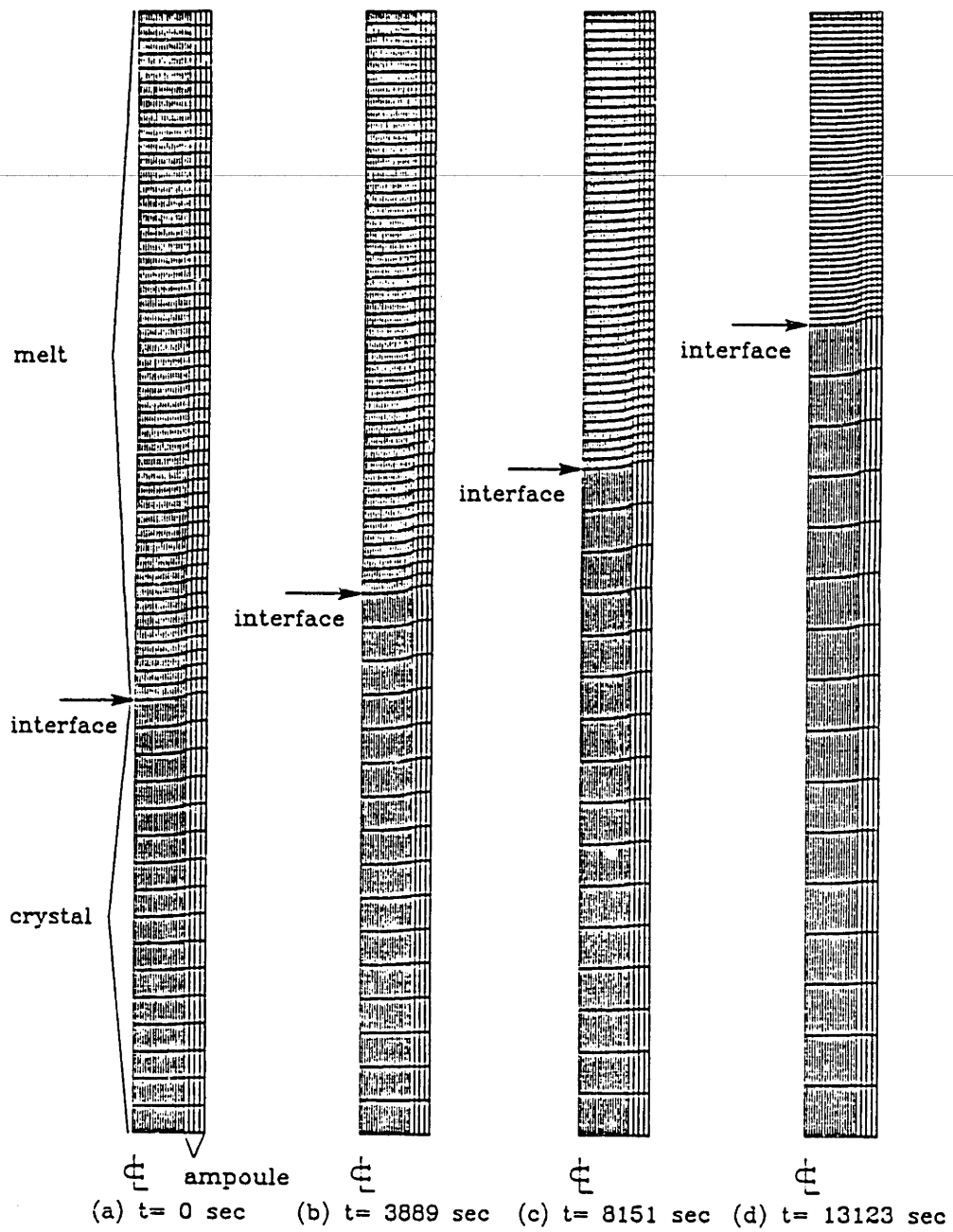


Figure 3.15: Finite element meshes in the vertical ampoule generated during the transient simulation of the rest problem.

Quantity	Symbol (units)	Value
Thermal conductivity of the melt	K_m (W/°C·cm)	0.390
Thermal conductivity of the solid	K_s (W/°C·cm)	0.180
Density of the melt	ρ_m (g/cm ³)	5.480
Density of the solid	ρ_s (g/cm ³)	5.480
Specific heat of the melt	$C_{p,m}$ (J/°C·g)	0.350
Specific heat of the solid	$C_{p,s}$ (J/°C·g)	0.380
Melting temperature	T_m (°C)	937.4
Kinematic viscosity	ν (cm ² /sec)	0.0013
Heat of solidification	ΔH_s (J/g)	460
Thermal expansion coefficient	β_t (°C ⁻¹)	5.0×10^{-4}
Diffusion coefficient of Ga in Ge	D (cm ² /sec)	2.1×10^{-4}
Equilibrium distribution coefficient of Ga	k	0.087

Table 3.2: Thermophysical properties of germanium.

Quantity	Symbol (units)	Value
Ampoule length	L (cm)	15.24
Crystal radius	R_c (cm)	0.680
Ampoule outer radius	R_a (cm)	0.953
Gradient zone length	L_g (cm)	3.810
Temperature difference	$T_h - T_c$ (°C)	340
Growth velocity	V_g ($\mu\text{m}/\text{sec}$)	4.0
Thermal conductivity of ampoule	K_a (W/°C·cm)	0.256
Density of ampoule	ρ_a (g/cm ³)	2.250
Specific heat of ampoule	$C_{p,a}$ (J/°C·g)	1.862

Table 3.3: Parameters for furnace design and processing conditions.

Name	Symbol	Definition	Value
Thermal Rayleigh number	Ra_t	$g\beta_t\Delta TR_c^3/(\alpha_m\nu)$	0
Peclet number	Pe	$V_g R_c/\alpha$	1.34×10^{-3}
Prandtl number	Pr	ν/α_m	6.39×10^{-3}
Schmidt number	Sc	ν/D	6.19
Stefan number	St	$\Delta H_s/C_{p,m}\Delta T$	3.87

Table 3.4: Dimensionless groups and characteristic values for modelling gallium-doped germanium crystal growth by the vertical Bridgman method.

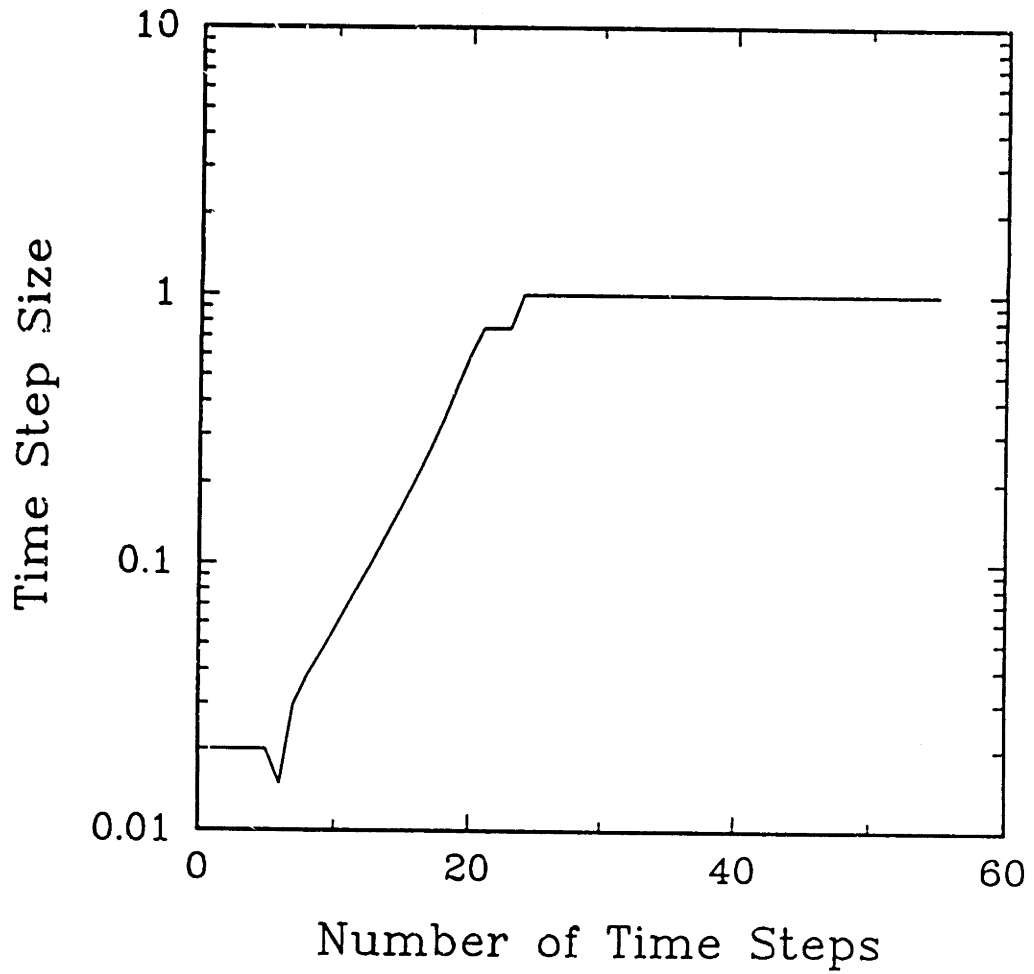


Figure 3.16: History of the time step size generated by the fully-implicit time integration.

trapezoidal time integration grows monotonically until it reaches the preset maximum time step size of unity and remains at the maximum value, because there is no change in the physics that controls the response during this period. However, it is expected that the time step size will decrease as the melt/solid interface approaches the top of the ampoule. The elapsed time corresponding to this time step history is described in Figure 3.17.

The efficiency of the fully-implicit method becomes more clear as we compare these time steps with those which satisfy the stability requirements of an explicit time integration methods. In the test problem, temperature and solute fields determine the size of the time step because velocities are uniformly constant in the melt. The diffusive stability limit for forward-time and centered-space difference approximation in two dimension is on the order of (Roache ,1976)

$$\Delta t \leq \frac{1}{2\alpha} \frac{1}{\Delta x^{-2} + \Delta y^{-2}}, \quad (3.117)$$

where α is an appropriate diffusion coefficient for a field variable of interest: $1/Sc$ for concentration and $1/Pr$ for temperature. For the minimum size of the element $\Delta r \cong 0.05$, the stability limit would be $\Delta t \leq \sim 10^{-2}$ for concentration and $\Delta t \leq \sim 10^{-5}$ for temperature, which we exceed by a factor as high as 100.

The combination of the relatively long gradient zone and the different, but comparable, thermal conductivities of melt, crystal and ampoule leads an interface shape concave to the solid regardless of the position of the ampoule. This concavity results in the radial temperature gradient near the interface so that the fluid at the centerline is hotter than material near the ampoule. Sample temperature fields corresponding to the meshes in Figure 3.15 are shown in Figure 3.18.

Imposing $Ra_t = 0$ excludes cellular convection in the melt and the solute field is almost radially uniform; the unidirectional profile characteristic of diffusion-controlled growth is clearly seen in the solute profiles for dilute gallium in germanium shown in Figure 3.19. The radial segregations in these results is induced only by the interface curvature as discussed by Coriell and Sekerka (1979).

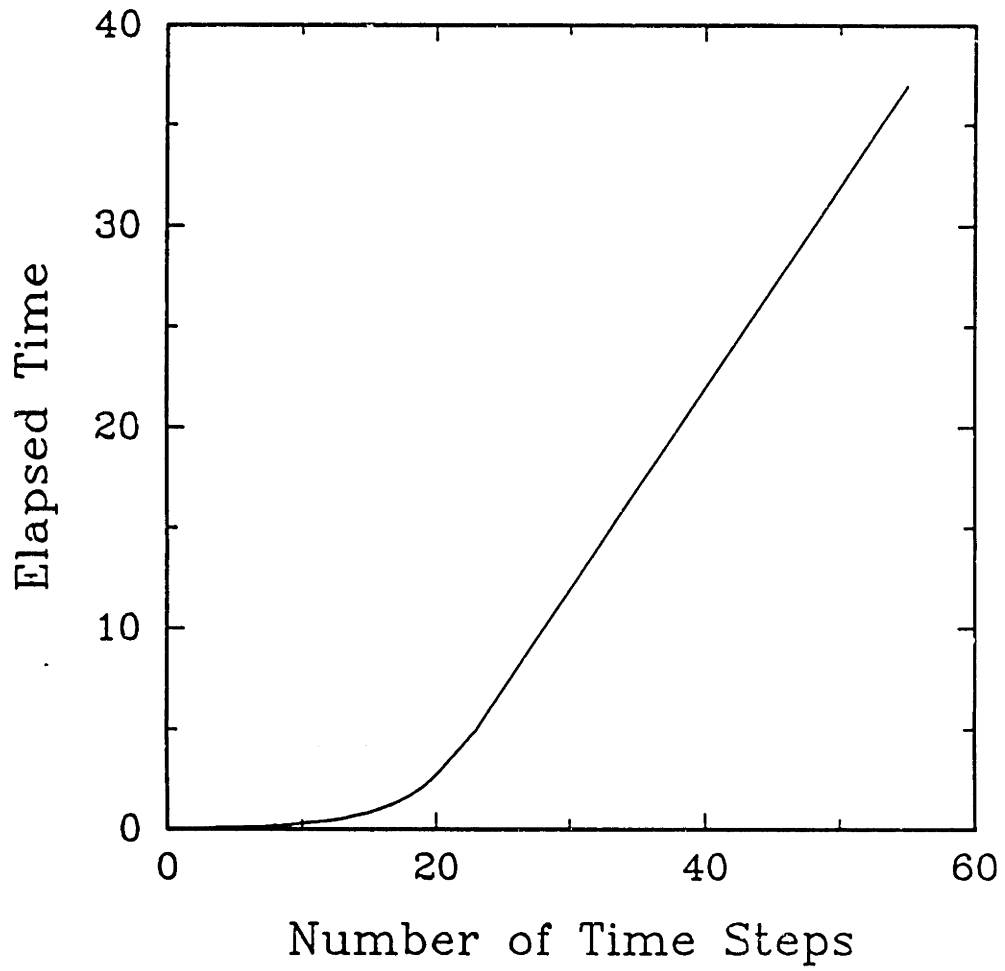


Figure 3.17: History of the elapsed time generated by the fully-implicit time integration.

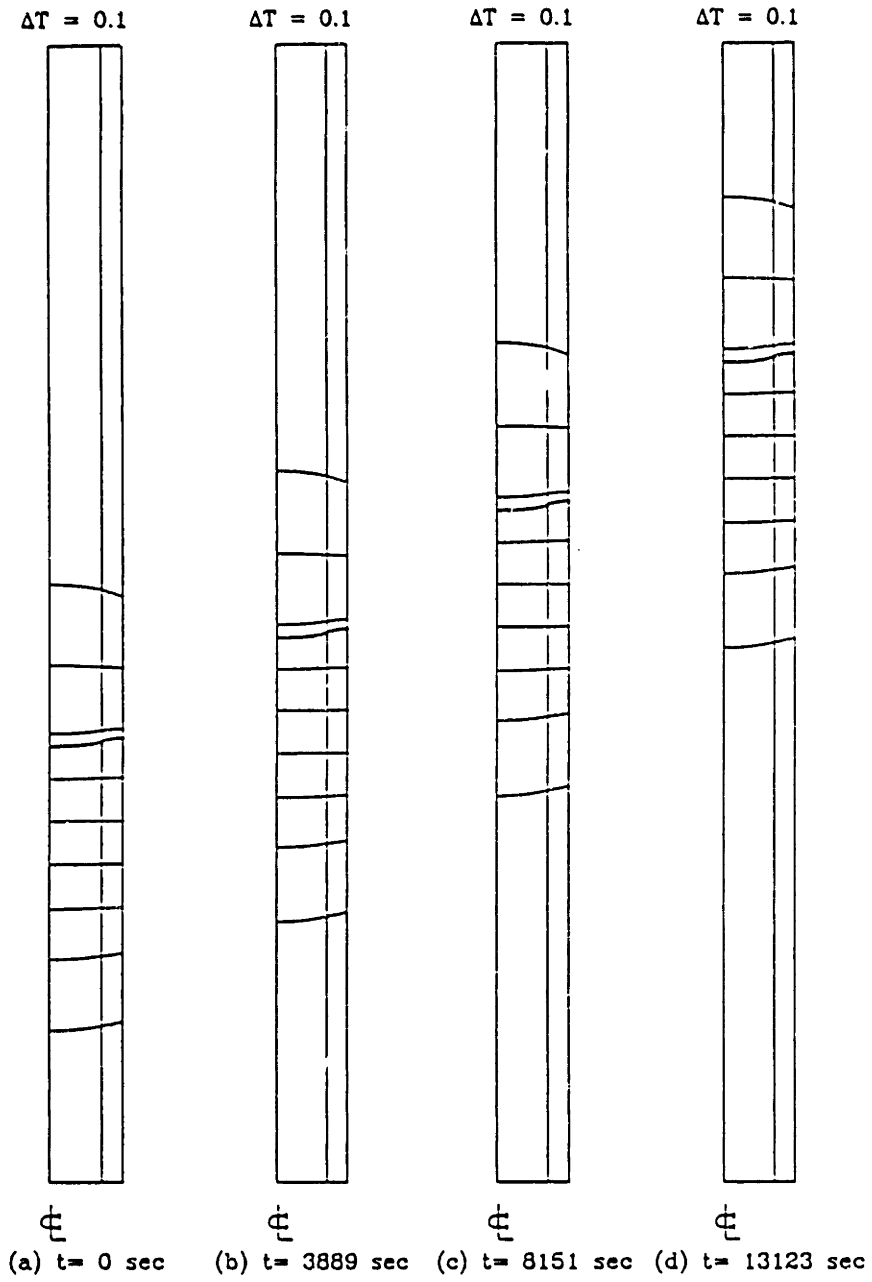


Figure 3.18: Sample time-dependent temperature fields for growth of GaGe in the vertical Bridgman system.

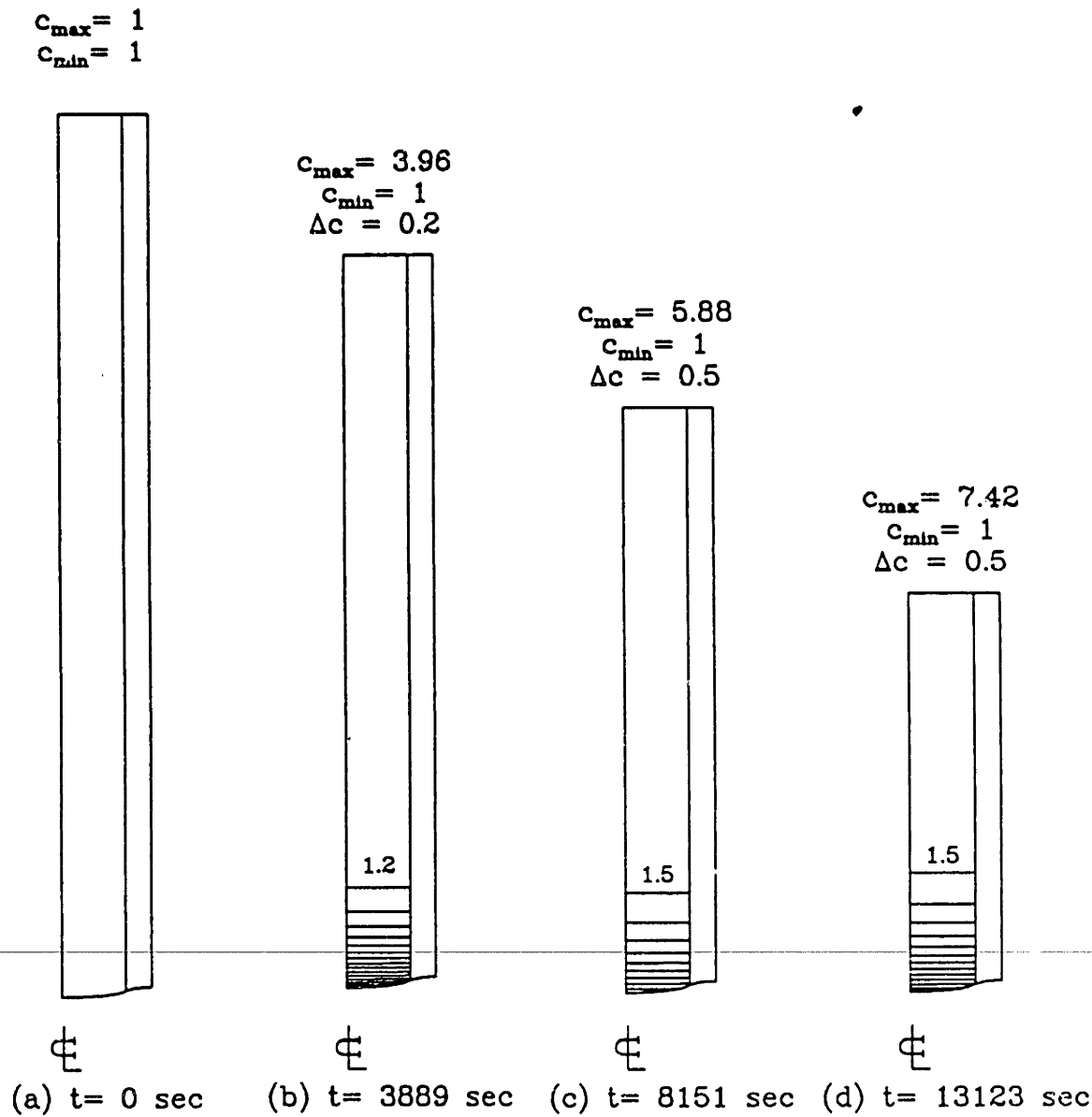


Figure 3.19: Sample time-dependent solute fields for growth of GaGe in the vertical Bridgman furnace.

The growth rate, defined as the advancing rate of the melt/solid interface, is calculated from the time derivatives of the interface location and is shown in Figure 3.20 for an ampoule translation rate of $4 \mu\text{m}/\text{sec}$. The start of ampoule translation can be considered as a special case of sudden change in translation rate, which is accompanied by the transient period where crystal growth rate becomes equilibrated with the ampoule translation rate. Calculated growth rates show an initial exponential profile during this transient period and reach the equilibrium ampoule translation rate, as was observed in one-dimensional calculations (Fu and Wilcox, 1981; Bourret *et al.*, 1985) and in experiments (Fu *et al.*, 1982; Wang *et al.*, 1984).

The composition profile in the grown crystal is of great importance because the uniformity of composition in the crystal is one of the factors that determines crystal quality. The capability of calculating axial solute profiles in the crystal partially justifies the development of transient numerical model. Calculated axial composition profile in the crystal is depicted in Figure 3.21. The solution of the test problem shows a good agreement with the analytical solution by Smith *et al.* (1955) for one-dimensional diffusion-controlled growth.

Accuracy

Checks on the accuracy of the finite element results were performed by examining the species mass balance in the melt. By applying *Reynolds transport theorem* (Whitaker, 1968; Lin and Segel, 1974) to the time-dependent solute equations along with interface flux boundary conditions, we obtain the criterion for the numerical accuracy.

The Reynolds transport theorem has been developed to relate the time derivative of a volume integral to the volume integral of a time derivative, when the surface of the volume moves or deforms. It is written for the scalar function C as

$$\frac{d}{dt} \int_{V(t)} C dV = \int_{V(t)} \frac{\partial C}{\partial t} dV + \int_{S(t)} C \mathbf{w} \cdot \mathbf{n} dS \quad (3.118)$$

where \mathbf{w} is the velocity of each point on the surface of the volume and may be a function

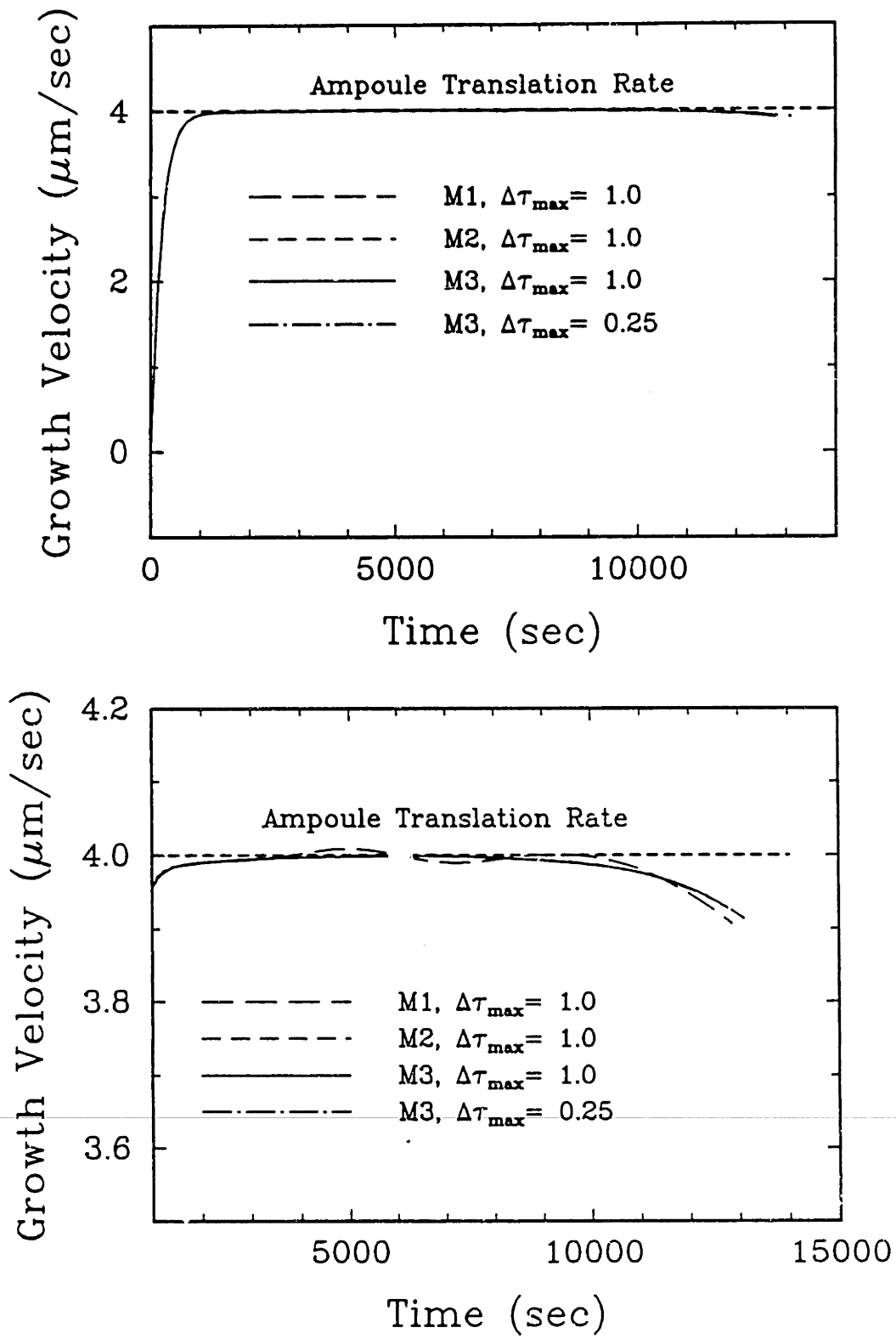


Figure 3.20: Crystal growth rate computed from the time derivative of the interface location.

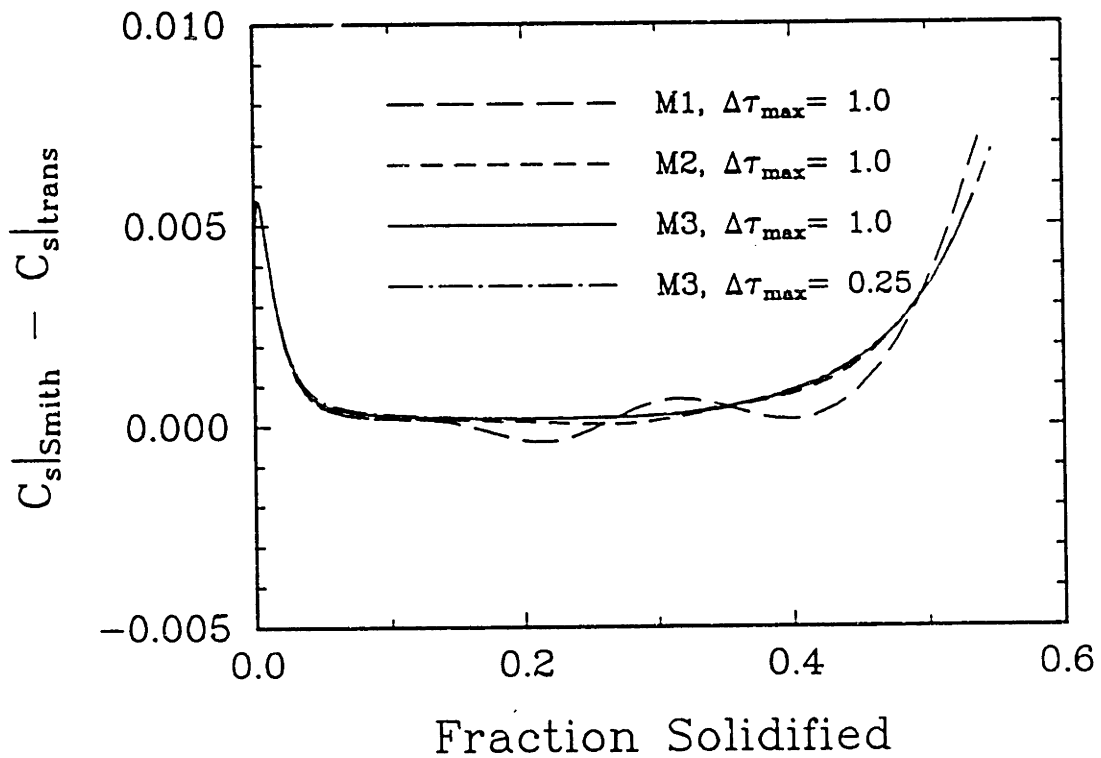
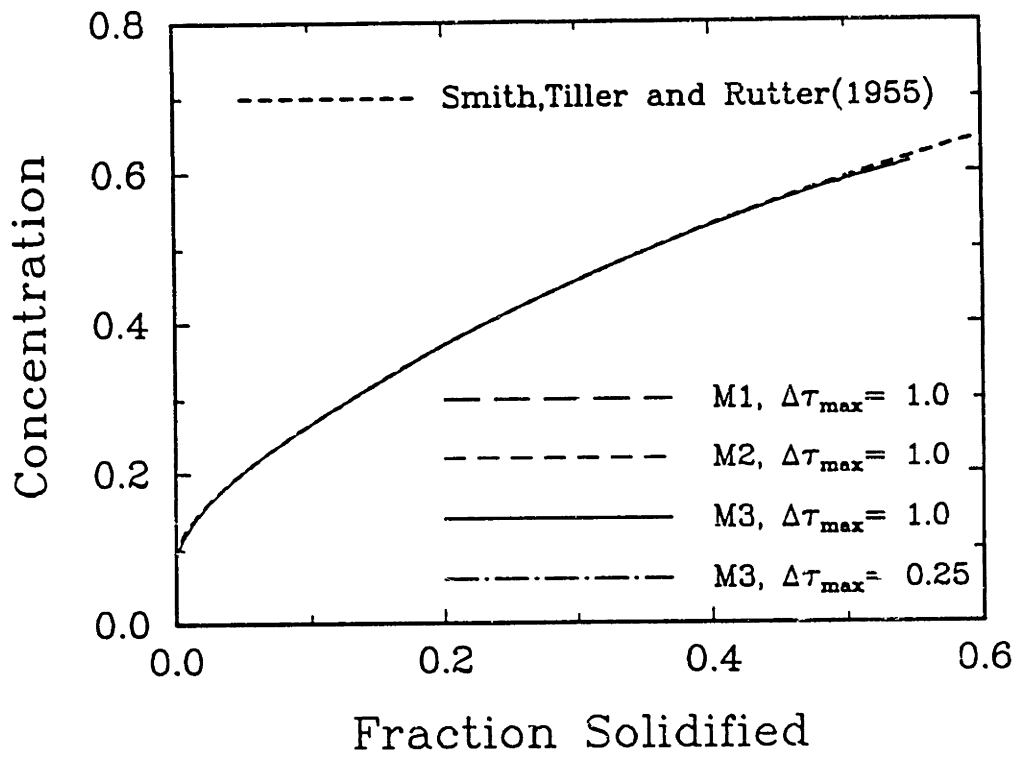


Figure 3.21: Axial composition profile in the crystal grown under microgravity conditions.

of the spatial coordinates and time.

Integral form of the solute equation which governs solute transport in the system is

$$\int_D Sc \left(\frac{\partial C}{\partial t} + \mathbf{v} \cdot \nabla C \right) - \nabla^2 C \, dV = 0 \quad (3.119)$$

Applying the Reynolds transport theorem and divergence theorem to Eq. (3.119) yields

$$\begin{aligned} Sc \frac{d}{dt} \int_D C \, dV - Sc \int_{\partial D_I} C \mathbf{w} \cdot \mathbf{n} \, dS \\ + Sc \int_{\partial D_I} C \mathbf{v} \cdot \mathbf{n} \, dS - \int_{\partial D_I} \nabla C \cdot \mathbf{n} \, dS = 0. \end{aligned} \quad (3.120)$$

When the melt is taken as the domain of the volume integral, the velocity \mathbf{w} is nonzero only along the interface ∂D_I and is equal to the growth velocity $\mathbf{w} = dh/dt \mathbf{e}_z$. Additional conditions along the interface are $\mathbf{v} \cdot \mathbf{n} = 0$ from the no-slip condition and $\nabla C = Sc(-dh/dt) \mathbf{e}_z(1-k)C$ from the flux boundary condition. Unit normal to the interface is given by (Weatherburn, 1927)

$$\mathbf{n} = \frac{\mathbf{e}_z - h_r \mathbf{e}_r}{\sqrt{1 + h_r^2}}$$

where $h_r = dh/dr$. With the relation $dS = \sqrt{1 + h_r^2} r dr$, Eq. (3.120) is rewritten as

$$Sc \left[\frac{d}{dt} \int_D C \, dV - k \int_{\partial D_I} C \frac{dh}{dt} r dr \right] = 0 \quad (3.121)$$

This relation is applied to the discrete time step to give

$$\varepsilon_n \equiv V \ll C \gg|_n - V \ll C \gg|_{n-1} - \int_{\tau_{n-1}}^{\tau_n} kA \langle V_I C \rangle \, dt \quad (3.122)$$

where V and A are volume of the melt and surface area of the interface, respectively. Interface velocity or growth rate is denoted by V_I . Subscripts n and $n-1$ refer to the n -th and $(n-1)$ -th time step. The notations $\ll \gg$ and $\langle \rangle$ are for the volume-averaged

and area-averaged quantities. For an exact balance, ε_n should be zero for n -th time step.

To make this criterion for accuracy more sensible, Eq. (3.122) is reformulated to give

$$\varepsilon_n^* = 1 - \frac{k_{compute}}{k}$$

$$\varepsilon_n^* = 1 - \frac{V \ll C \gg|_n - V \ll C \gg|_{n-1}}{\int_{\tau_{n-1}}^{\tau_n} k A < V_I C > dt} \quad (3.123)$$

The values of ε^* during the transient simulations are plotted against time in Figure 3.22. Throughout the simulation, ε^* remained below three percent, demonstrating the accurate solute conservation for the transient solution calculated by the present numerical model.

Convergence

The accuracy of the transient simulation of the crystal growth processes depends on the accuracy of the spatial discretization of the field variables and interface shapes and on the error associated with the time integration.

Convergence in space. Because no error estimates are available for the free-boundary problem, the error in the finite element discretization can be checked only by mesh refinement. Three finite element meshes shown in Figure 3.23 have been used for this purpose. The interface location and its deflection obtained at $t = 0$ are listed in Table 3.5. In Table 3.5, the error in each solution was estimated by the relative differences with respect to the finest mesh M3, computed as $(M1 - M2)/M3$ and $(M2 - M3)/M3$. These differences in the interface location were less than 0.01 percent and the errors in the computation of the deflection of melt/solid interface were less than one percent. The values show convergence with mesh refinement.

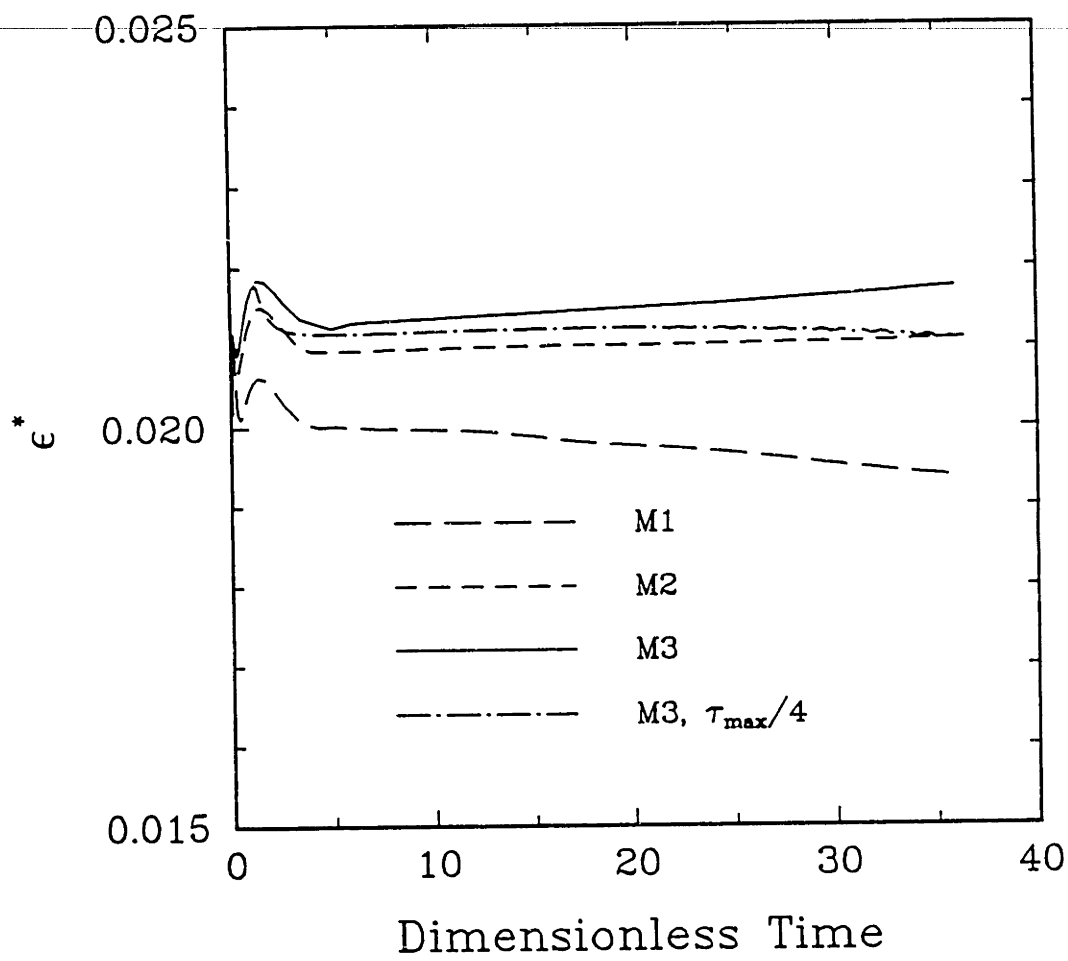


Figure 3.22: Time-dependent evolution of the error in the solute balance in the melt.

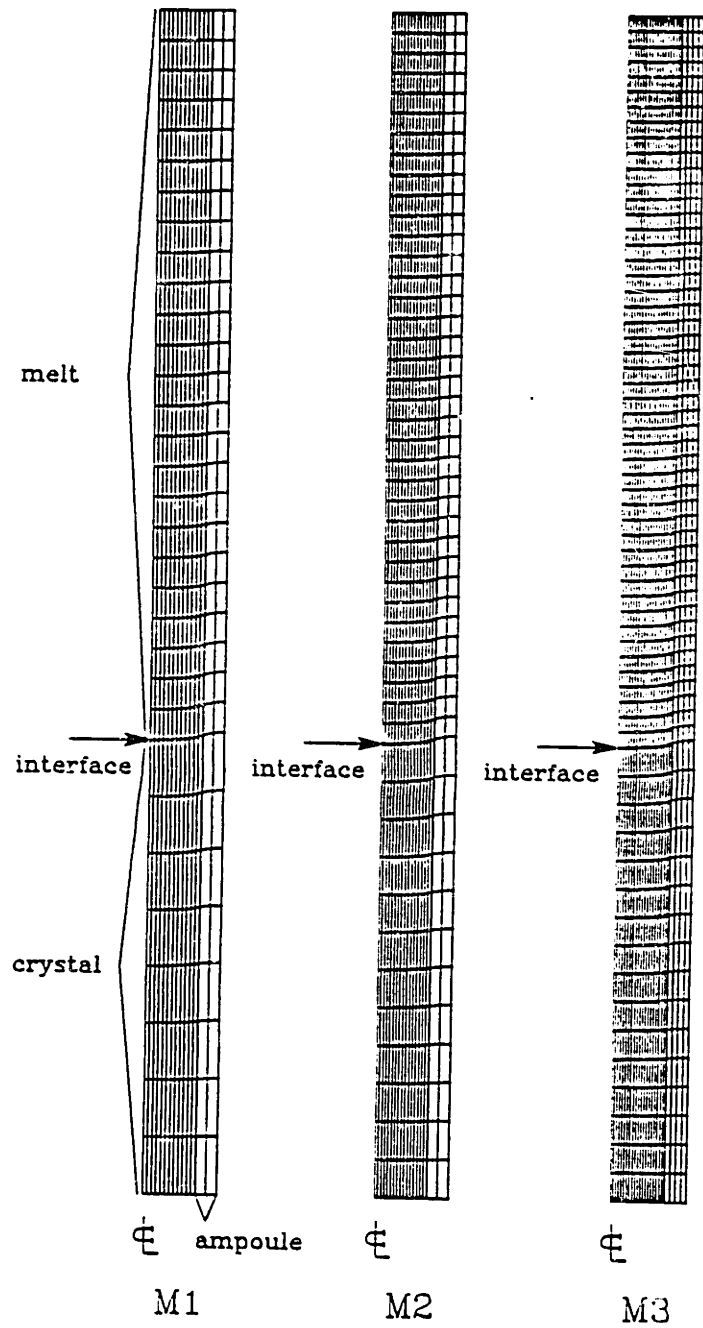


Figure 3.23: Three finite element meshes used for the calculations presented in Table 3.5.

Quantity	M1	M2	M3
Number of radial elements	14	18	24
Number of axial elements (m+s)	24 + 8	36 + 12	48 + 16
Melt/Solid interface, $H(0)$	13.81176	13.81209	13.81206
	(2.17×10^{-6})	(-2.17×10^{-5})	
Deflection of M/S interface,	0.10659	0.10602	0.10558
$\Delta = H(0) - H(1)$	(9.57×10^{-3})	(4.17×10^{-3})	

Table 3.5: Results of mesh refinement for the solution at $t = 0$ and the meshes displayed in Figure 3.23.

Convergence in time. The stability and accuracy of the time integration methods were examined by computing the time dependent growth velocity and solute concentration profile in the crystal. The growth velocities are shown in Figure 3.20 for the three meshes used and for the finest mesh with the maximum time step size reduced by one fourth. When plotted on a large scale, all cases seem to give the same results. But, when the scale of the plot is enlarged, mesh M1 shows slightly oscillating behaviour while other solutions have converged to identical results.

The results shown in Figure 3.21 for the solute segregation in the crystal also looked the same when plotted on the concentration scale covering the whole range of concentration variation. The enlarged view of the profile formed by subtracting the computed solute concentration profile from the analytical solution by Smith *et al.* (1955) displayed small amplitude oscillations for the meshes M1 and M2. The results are converging to the solution with the finest mesh M3. The results are identical for calculations with decreasing maximum time step size, indicating the error in the temporal discretization is small.

This simple test problem satisfactorily demonstrates the capability of the transient model and numerical method developed in the present work. Its extensions to the more complex problems are described in Chapter 6 and 7 for various crystal growth processes with intense thermal and solutal convection.

Chapter 4

Effect of Vertical Magnetic Field

The finite element analysis of vertical Bridgman growth described in Chapter 3 is applied to investigate the effect on convection and solute segregation of a vertically-aligned magnetic field in the limit of zero magnetic Reynolds number. Calculations are presented for growth of a dilute gallium-doped germanium alloy in a vertically stabilized Bridgman-Stockbarger system and in a furnace with a uniform temperature gradient imposed along the ampoule.

4.1 Introduction

In recent years, steady-state magnetic fields have been imposed in melt crystal growth of semiconductor materials to control fluctuations in solute and impurity concentrations caused by chaotic convection in the melt (Chedzey and Hurle, 1966; Utech and Flemings, 1966; Hoshikawa *et al.*, 1980; Kim, 1982; Hoshikawa, 1982). The action of the field is caused by the Lorentz force on the fluid induced by the magnetic field when the melt has high electrical conductivity and the fluid tries to cross the field lines. The presence of the magnetic field decreases the intensity of cellular convection driven by temperature differences and buoyancy forces. Besides eliminating chaotic and time-periodic convection in large-scale systems, sufficiently intense magnetic fields decrease the intensity of

convection to the point that the solute concentration in the crystal is affected in the axial (in the direction of growth) and lateral (perpendicular to it) variations (Series *et al.*, 1985; Matthiesen *et al.*, 1987). The alteration of the laterally averaged axial concentration of oxygen is one of the primary advantages of using magnetic fields in Czochralski growth of silicon (Hoshikawa *et al.*, 1980; Hoshikawa, 1982; Series, 1989a). It is becoming increasingly evident that the lateral uniformity of solute profiles may be adversely influenced by imposed magnetic fields (Oreper and Szekely, 1984; Lin and Benson, 1987).

Recently developed techniques of modulating the strength of magnetic field in time or space add the flexibility in the application of magnetic field to the crystal growth processes. Depending on the properties of materials grown and the design of the furnace, the magnetic field strength can be tailored temporally (Ozawa *et al.*, 1987; Hofmann *et al.*, 1988) and spatially (Hicks *et al.*, 1989; Series, 1989b).

The increase of lateral variations of the composition with decreasing convective mixing is not unexpected. The transition in axial and radial solute segregation from unidirectional crystal growth in the absence of bulk convection to growth with intense laminar mixing is described schematically by the curves shown in Figure 4.1 in terms of the percentage radial segregation Δc , defined as the maximum difference in concentration across the crystal surface measured as a percentage of the local average, and by the effective segregation coefficient k_{eff} defined in Eq. (1.19) of Section 1.2.3 as

$$k_{eff} = k \frac{\langle \bar{c} \rangle_I}{\langle \bar{c} \rangle} \quad (4.1)$$

In directional solidification, diffusion-controlled growth with a planar melt/crystal interface leads to uniform radial distributions of solutes, *i.e.* $\Delta c = 0$. If the melt is sufficiently long that the diffusion layer adjacent to the interface occupies only a small fraction of the total length, k_{eff} is unity in the absence of bulk motion other than the growth velocity V_m . The length of the axial concentration gradient can be controlled, since the scale of the diffusion layer is set by the ratio D/V_m . Curvature of the melt/crystal interface induces lateral solute variation caused by the focusing of the

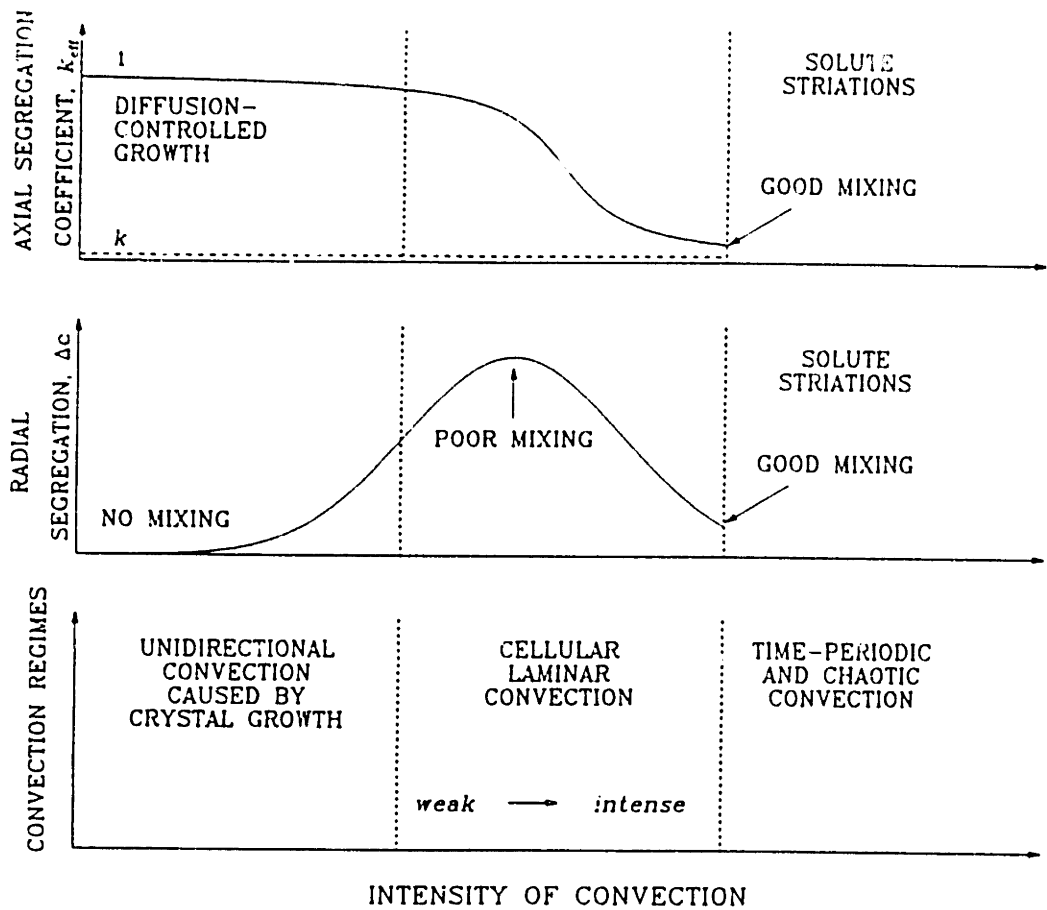


Figure 4.1: Schematic drawing of the effect of flow intensity on the effective segregation coefficient and the percentage radial segregation in a directional solidification system.

diffusion field adjacent to the interface (Coriell and Sekerka, 1979; Coriell *et al.*, 1981).

Weak laminar convection distorts the one-dimensional concentration field and causes the radial and axial segregation indicated on Figure 4.1. When the mixing of a solute by these flow fields is incomplete, the concentration field adjacent to the melt/crystal interface is highly distorted and large amounts of radial segregation exist, even when the axial composition profile indicates diffusion-controlled growth. Harriott and Brown (1984) demonstrated the effect of weak convection caused solely by differential rotation of the feed and crystal rods on radial segregation in small-scale floating zones. Radial segregation caused by weak convection also exists in small-scale crystal growth experiments on earth, in the growth of nondilute binary alloys where the solute field damps convection (Rouzaud *et al.*, 1985), in microgravity experiments in which convection has not been stopped entirely (Witt *et al.*, 1975, 1978), and in experiments with weak magnetic fields (Matthiesen, 1988).

Solute boundary layers form adjacent to the melt/crystal interface when laminar convection leads to intense mixing. Then the radial segregation of solute decreases and the composition of the melt approaches a new bulk value elevated (assuming $k < 1$) by the mixing of the solute rejected at the interface. In systems with very thin solute layers, k_{eff} approaches k and the solute concentration increases steadily along the length of the growing crystal, as described by Scheil (1942). Camel and Favier (1986) have presented an order-of-magnitude analysis for estimating the scalings of both the axial and the radial segregation as a function of driving force for thermal convection in the vertical Bridgman system.

Strong laminar convection is rarely found in the low Prandtl number melts for semiconductor materials. Instead time-periodic and chaotic flows in the melt lead to thermal fluctuations near the interface and induce melting and accelerated crystal growth on the time scale of the fluctuation. The effects of temporal fluctuations in the melt temperature on the axial solute distribution in the crystal are documented in the elucidating directional solidification experiments of Kim *et al.* (1972).

The purpose of this chapter is to present detailed calculations of the action of a magnetic field on convection, segregation, and heat transfer in a realistic model for the vertical Bridgman crystal growth system and to quantify the intensity of the field that is necessary to achieve diffusion-controlled, unidirectional solidification in such systems. The calculations are presented for the furnace and ampoule designs for small-scale experiments used in the experimental studies of Wang (1984) and Rouzaud *et al.* (1985); these two systems are shown schematically in Figure 4.2. Wang's furnace is a classical Bridgman-Stockbarger system with isothermal hot and cold zones separated by an insulated region designed to create a constant axial temperature gradient in the melt and crystal adjacent to the solidification interface. The furnace of Rouzaud *et al.* uses a tapered heating element to establish a nearly linear temperature profile over a length of ampoule approximately 30 times the radius of the furnace. Both furnaces are designed so that the crystal growth rate is equal to the ampoule displacement rate after an initial transient caused by the onset of ampoule motion.

Detailed calculations of the temperature fields, melt flow, and axial and radial segregation patterns for these two furnaces were presented previously (Adornato and Brown, 1987a) for growth of dilute gallium in germanium in both systems without the presence of the magnetic field. Both systems exhibited the transition from diffusion-controlled solute transport to laminar mixing with increasing thermal Rayleigh number. For the conditions of an earthbound experiment, the convection was intense, radial segregation was minimal, and the effective segregation coefficient approached the equilibrium segregation coefficient. The results of this chapter are intended to quantify the levels of imposed magnetic field necessary to damp this convection to the extent that low radial segregation without axial segregation, *i.e.* k_{eff} near unity, is obtained.

Others have modelled the effect of an imposed magnetic field on convection in crystal growth (Oreper and Szekely, 1983, 1984; Langlois and Walker, 1982; Langlois, 1984; Lee *et al.*, 1984; Hjellming and Walker, 1986). Most notably, Mihelčić and Wingerath (1985) have demonstrated the suppression of the temporal fluctuations by an axial magnetic field in Czochralski growth. Langlois and co-workers (Langlois and Walker, 1982;

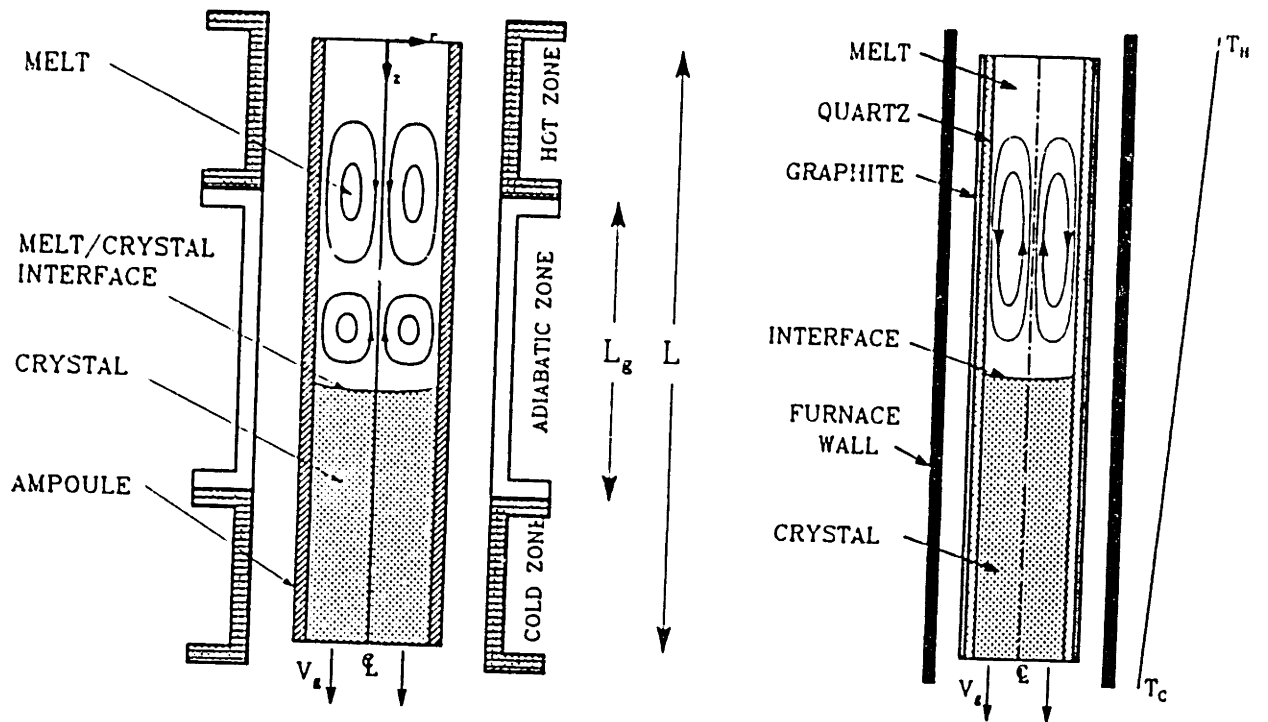


Figure 4.2: Diagrams of the models for Bridgman-Stockbarger and constant gradient directional solidification furnaces.

Langlois, 1984; Lee *et al.*, 1984) have also demonstrated this effect and have computed the effect of moderate magnetic field on oxygen transport in Czochralski growth. Oreper and Szekely (1983) have demonstrated the increased radial nonuniformity of solute incorporation caused by magnetic damping in a prototype system and in the idealized model of the vertical Bridgman-Stockbarger system introduced by Chang and Brown (1983b).

The calculations presented here are refinements to the results of Oreper and Szekely (1984) because the correct thermal boundary conditions are incorporated so that the results are meaningful with respect to actual experiments. We have demonstrated the accuracy of the calculations by the comparison presented by Adornato and Brown (1987a) between the predicted solute segregation and measurements by Wang (1984) without magnetic fields.

The calculations are based on the finite-element Newton method described in Chapter 3 and used by Adornato and Brown (1987a) for the solution of conservation equations and boundary conditions associated with the velocity, pressure, and solute fields in the melt, the temperature in melt, crystal and ampoule, and the shape of the melt/crystal interface.

4.2 Action of the Magnetic Fields

The electrical conductivity of the fluid element and the existence of magnetic field interact in two ways: first, electric currents are generated by the motion of the electrically conducting fluid as it crosses the magnetic flux lines and contribute to the changes of the existing magnetic field; second, the fluid elements carrying currents across the magnetic flux lines cause additional forces acting on the fluid elements. These interactions between the motion of the conductor and the magnetic field form the basis of magnetohydrodynamic (MHD) theory and are the central physics involved in this work.

We assume that a magnetic field is imposed on the furnace so that outside the am-

poule the field is $B_0 \mathbf{e}_z$. The action of the field on the melt, crystal and ampoule is determined by analysis of Maxwell's equations as described in several references (Chandrasekhar, 1961; Shercliff, 1965). Most branches of MHD theory are based on the *quasi-steady approximation* which ignores displacement currents and the effects of variations in the charge density. Without displacement currents, Maxwell's equations are

$$\nabla \times \mathbf{B} = \mu_e \mathbf{J} \quad (\text{Ampère's law}) \quad (4.2)$$

$$\nabla \cdot \mathbf{B} = 0 \quad (4.3)$$

$$\nabla \times \mathbf{E} = -\frac{\partial \mathbf{B}}{\partial t} \quad (\text{Faraday's law}) \quad (4.4)$$

where \mathbf{E} and \mathbf{B} are the intensities of the electric and the magnetic fields, \mathbf{J} is the current density, and μ_e is the magnetic permeability of free space. The magnetic permeability of free space has a value $4\pi \times 10^{-7}$ weber²/joule-meter in the MKSA system.

If the fluid element has a velocity \mathbf{v} , the electric field it will experience is not \mathbf{E} , as measured by the stationary observer, but $\mathbf{E} - \mathbf{v} \times \mathbf{B}$. Then the current is given by

$$\mathbf{J} = \sigma_m (\mathbf{E} - \mathbf{v} \times \mathbf{B}) \quad (\text{Ohm's law}) \quad (4.5)$$

where σ_m is a coefficient of electrical conductivity of the fluid. From Ampère's law, the conservation of charge is deduced as

$$\nabla \cdot \mathbf{J} = 0 \quad (\text{Kirchhoff's first law}) \quad (4.6)$$

Equations (4.2) to (4.6) are the basic equations of the field appropriate for MHD. Through the occurrence of the velocity \mathbf{v} in the expression for \mathbf{J} , the equations account for the effect of fluid motion on the electromagnetic field. The inverse effect of the field on the fluid motions results from the force which the conducting fluid elements experience while traversing the magnetic flux lines. This is the *Lorentz force* given by

$$\mathcal{L} = \mathbf{J} \times \mathbf{B} \quad (4.7)$$

Equations (4.2), (4.4), and (4.5) are combined to eliminate \mathbf{J} and \mathbf{E} and yield

$$\frac{\partial \mathbf{B}}{\partial t} = \nabla \times (\mathbf{v} \times \mathbf{B}) + \frac{1}{\mu_e \sigma_m} \nabla^2 \mathbf{B} \quad (4.8)$$

where $1/\mu_e\sigma_m$ is called a magnetic diffusivity. By nondimensionalizing the above equation, a dimensionless group called *magnetic Reynolds number*, which measure the relative importance of convection to diffusion in modifying the field, is defined as

$$R_m \equiv \mu_e\sigma_m LV^* \quad (4.9)$$

where V^* is the characteristic velocity in the melt and μ_e is the magnetic permeability. In the small-scale crystal growth system for semiconductor materials, the magnetic Reynolds number R_m is much less than unity. The *low- R_m approximation*, which has been used in the analysis of Czochralski growth system under the influence of axial magnetic field (Langlois and Walker, 1982; Mihelčić and Wingerath, 1985). The low- R_m approximation ignores the induced magnetic field entirely and replaces \mathbf{B} by the known field \mathbf{B}_o in all the MHD equations, since the ratio of induced magnetic field to imposed magnetic field is of $\mathcal{O}(R_m)$.

When the ampoule and crystal are moved parallel to the field, the imposed field does not cause a current in these materials. Maxwell's equations admit a simple solution when the ampoule is electrically isolated from the surroundings and the low- R_m approximation is valid. The electric field is everywhere equal to zero ($\mathbf{E} \equiv \mathbf{0}$), the magnetic induction is not distorted by convection in the melt, and the magnetic field is equal to the imposed value ($\mathbf{B} \equiv B_o\mathbf{e}_z$). Then current is expressed as

$$\begin{aligned} \mathbf{J} &= \sigma_m(\mathbf{v} \times \mathbf{B}) \\ &= \sigma_mB_o(\mathbf{v} \times \mathbf{e}_z) \end{aligned} \quad (4.10)$$

The resulting Lorentz body force ($\mathbf{J} \times \mathbf{B}$) in the equations of motion is described by $\mathcal{L} = \sigma_mB_o^2(\mathbf{v} \times \mathbf{e}_z \times \mathbf{e}_z)$.

The action of a uniaxially aligned magnetic field on convection in the melt is most simply demonstrated by considering the equation for momentum conservation written as

$$\frac{D\mathbf{v}}{Dt} = \mathbf{F}_L + \sum \mathbf{F}_i, \quad (4.11)$$

where $\mathbf{F}_L = Ha(\mathbf{v} \times \mathbf{e}_z \times \mathbf{e}_z)$ is the Lorentz force and the \mathbf{F}_i include all other forces (viscous, buoyancy, and pressure) acting on the fluid and D/Dt is the material derivative following the fluid element. Taking the scalar product of Eq. (4.11) with the velocity \mathbf{v} gives the equation of change for the mechanical energy ($v^2 \equiv \mathbf{v} \cdot \mathbf{v} \equiv v_r^2 + v_z^2$) as

$$\frac{1}{2} \frac{D(v^2)}{Dt} - \sum \mathbf{v} \cdot \mathbf{F}_i = \mathbf{v} \cdot \mathbf{F}_L = -Ha^2 v_r^2, \quad (4.12)$$

where only the Lorentz force has been expressed in detail. Neglecting the effects of the other forces, Eq. (4.12) demonstrates that the magnitude of the velocity field in the radial direction must decrease proportionally to the square of the strength of the magnetic field. The axial component of velocity is unaffected by the field except in the coupling of the components through conservation of mass ($\nabla \cdot \mathbf{v} = 0$). Because a uniaxial flow $v_z = Pe/Pr$, where Pe and Pr are the dimensionless growth rate and Prandtl number, is consistent with having no radial flow, the velocity field $(v_r, v_z) = (Pe/Pr, 0)$ almost everywhere in the melt results from a strong field. A more rigorous analysis of the flow structure for $Ha \gg 1$ was first presented by Hjellming and Walker (1986,1987) and a similar analysis is applied to the vertical Bridgman system in Section 4.5.

4.3 Pseudo-Steady-State Model For Magnetic Vertical Bridgman Process

Transport processes in the two directional solidification configurations shown in Figure 4.2 were simulated using the pseudo-steady-state model (PSSM) described in Chapter 2 and 3. The mathematical description of the equations and boundary conditions for convection and species transport are already discussed in Chapter 2; only the parts needed for the discussion of the results are repeated here. The field variables and interface shape are described in terms of the stationary axisymmetric cylindrical polar coordinate system (r, z) shown in Figure 4.2. Variables are put in dimensionless form by scaling lengths with the radius of the crystal R_c , velocity $\mathbf{v}(r, z)$ with the momentum diffusion velocity of the melt ν/R_c , pressure with $\rho\nu^2/R_c$ and the composition with c_o .

The dimensionless concentration and temperature fields are defined as

$$S(r, z) \equiv c(r, z) - 1 \quad (4.13)$$

$$\theta(r, z) \equiv \frac{T(r, z) - T_{cold}}{T_{hot} - T_{cold}} \quad (4.14)$$

where T_{hot} and T_{cold} are the hot and cold set-point temperatures associated with each particular furnace design. These are the values of the hot and cold isothermal zones in the Bridgman furnace and the temperatures at the ends of the constant temperature gradient in the constant gradient furnace. The location of the melt/crystal interface is described by the function $H(r)$ and is computed with the field variables so that the energy balance along the interface and the condition for the melting point isotherm are satisfied.

Axisymmetric convection in the melt is modelled by the Boussinesq equations, which are written in dimensionless form as

$$\nabla \cdot \mathbf{v} = 0 \quad (4.15)$$

$$\begin{aligned} \mathbf{v} \cdot \nabla \mathbf{v} = & -\nabla p + \nabla^2 \mathbf{v} + \frac{1}{Pr} \{ Ra_s S - Ra_t (\theta - 1) \} \mathbf{e}_z \\ & - Ha^2 (\mathbf{v} \times \mathbf{e}_z \times \mathbf{e}_z) \end{aligned} \quad (4.16)$$

$$Pr \mathbf{v} \cdot \nabla \theta = \nabla^2 \theta \quad (4.17)$$

$$Sc \mathbf{v} \cdot \nabla S = \nabla^2 S \quad (4.18)$$

where ∇ is the gradient operator in cylindrical coordinates and the Schmidt (Sc) and Prandtl (Pr) numbers are defined in Table 4.1. The last term on the right side of Eq. (4.15) is the Lorentz force and is the sole modification of this equation set caused by the magnetic field. The Hartmann number $Ha \equiv B_o R_c (\sigma_m / \mu)^{1/2}$ measures the strength of the field relative to the viscous force: for germanium, $Ha = 100$ corresponds to a 3.3 kG field in the small-scale MIT system studied here. The definitions of the thermal and solutal Rayleigh numbers are given in Table 4.1.

The energy equations in the crystal and ampoule are identical to Eqs. (2.10) and (2.11) in Chapter 2. The condition for the interface to correspond to the melting point

Name	Symbol	Definition	Value
Thermal Rayleigh number	Ra_t	$g\beta_t\Delta TR_c^3/(\alpha_m\nu)$	3×10^5 (3.5×10^4) ^{a)}
Solutal Rayleigh number	Ra_s	$g\beta_s c_o R_c^3/(\alpha_m\nu)$	0
Peclet number	Pe	$V_g R_c/\alpha$	1.7×10^{-3} (7.7×10^{-4}) ^{a)}
Prandtl number	Pr	ν/α_m	7.2×10^{-3}
Schmidt number	Sc	ν/D	6.2
Stefan number	St	$\Delta H_s/C_{p,m}\Delta T$	3.9 (3.4) ^{a)}
Hartmann number	Ha	$B_o R_c(\sigma_m/\mu)^{1/2}$	100 ($B_o = 3.3$ kG)

^{a)} For constant gradient furnace

Table 4.1: Dimensionless groups and their characteristic values appropriate for gallium-doped germanium crystal growth.

isotherm for the binary mixture and the solute and energy balances at the melt/crystal interface are given by Eqs. (2.12)–(2.15) there. Equation (2.18) dictates the thermal boundary conditions between the ampoule and the surrounding furnace and is rewritten here as

$$\left[\frac{\partial \theta}{\partial r} \right]_a = Bi(z) [\theta_\infty(z) - \theta] \quad (4.19)$$

where $Bi(z)$ is a dimensionless heat transfer coefficient ($Bi = h_a R_c / k_a$) defined to include radiative, conductive, and convective transport between the ampoule and the furnace, and $\theta_\infty(z)$ is the temperature distribution of the furnace wall.

The changes in the heat transfer coefficient between the three zones of the vertical Bridgman furnace of MIT are modelled by the function

$$Bi(z) = \frac{bi_0}{2} (bi_3 \{1 - \tanh[bi_1(z_c - bi_2 - z)]\} - 1 + \tanh[-bi_1(z_c + bi_2 - z)]) \quad (4.20)$$

where z_c is the location of the mid-plane of gradient zone. The coefficients $\{bi_i\}$ have the following significance: $bi_0 = h_{cold} R_c / k_a$ is the value of Biot number in the cold zone; bi_1 sets the slope of the transition in $Bi(z)$ between the isothermal zones and the adiabatic region; $bi_2 = (L_g / R_c) / 2$ is the half of the dimensionless length of the adiabatic zone; $bi_3 = h_{hot} / h_{cold}$ sets the ratio between the Biot numbers in the hot and cold zone. The furnace wall temperature is modelled by the function

$$\theta_\infty(z) = \frac{1}{2} \{1 + \tanh[\theta_0(z_c - z)]\} \quad (4.21)$$

where θ_0 determines the sharpness of the transition in $\theta_\infty(z)$ between the hot and cold zones. Coefficients for the slopes, bi_2 and θ_0 , are obtained by fitting to the experimental measurements of temperature reported by Wang (1984).

The constant gradient furnace built by the Grenoble group is modelled by using a constant Biot number $Bi = 8$ over the entire length of the ampoule and specifying the

furnace temperature profile in dimensionless form as

$$\theta_{\infty}(z) = 1 - \frac{R_c}{L} z. \quad (4.22)$$

The finite-element method described in Chapter 3 was employed for the solution of transport problem with the imposed magnetic field. The Galerkin weighted residual method described there is used to discretize the partial differential equations. Mixed Lagrangian interpolation of the field variables is employed with a continuous biquadratic representation for velocity, temperature and concentration and a discontinuous linear representation for pressure. The discontinuous pressure approximation gives better approximation to the conservation of mass equation (Eq. 4.15) and allows convergence to higher intensities of convection than were attained with the Petrov-Galerkin method used for the same system by Adornato and Brown (1987a). The mesh of quadrilateral elements used in these calculations had 20 radial elements in melt and crystal and 4 elements across the ampoule; the axial approximation had 48 elements in the melt and 16 elements in the crystal. The nonlinear algebraic equations resulting from this approximation numbered, 24,085 and required 90 seconds on the Cray XMP for a single Newton iteration; three to four iterations were usually sufficient for convergence to the solution of the problem.

4.4 Growth of Gallium-doped Germanium with a Magnetic Field

The values of the thermophysical properties used for modelling the growth of dilute gallium in germanium are compiled in Table 4.2. The calculations assume that the bulk concentration of the gallium is low enough that the effect of the concentration variation on the buoyancy force is minimal and that $Ra_c = 0$ is appropriate. The calculations are presented separately for the two crystal growth systems. In each case, the temperature, flow and concentration fields computed without the field are described first as a reference for the results with increasing field strength. Without the magnetic field the cellular

Quantity	Symbol (units)	Value
Thermal conductivity of the melt	K_m (W/°C·cm)	0.39
Thermal conductivity of the solid	K_s (W/°C·cm)	0.17
Density of the melt	ρ_m (g/cm ³)	5.5
Density of the solid	ρ_s (g/cm ³)	5.5
Specific heat of the melt	$C_{p,m}$ (J/°C·g)	0.39
Specific heat of the solid	$C_{p,s}$ (J/°C·g)	0.39
Melting temperature	T_m (°C)	937.4
Kinematic viscosity	ν (cm ² /sec)	0.0013
Heat of solidification	ΔH_s (J/g)	460
Thermal expansion coefficient	β_t (°C ⁻¹)	5.0×10^{-4}
Diffusion coefficient of Ga in Ge	D (cm ² /sec)	2.1×10^{-4}
Equilibrium distribution coefficient of Ga	k	0.087

Table 4.2: Thermophysical properties of germanium.

convection was so intense that accurate concentration fields in the melt could only be computed for Ra_t up to 1×10^5 in Wang's Bridgman furnace and 1.25×10^4 in the constant gradient furnace, which is very close to the value 3×10^5 and 3.5×10^4 appropriate for crystal growth on earth in the two furnaces. Higher values could be achieved by using more refined mesh.

4.4.1 Vertical Bridgman Growth System

The calculations of convection and segregation are influenced by the design and choice of materials for the ampoule, because of the role of these materials in setting the temperature gradients in the melt. The calculations here are based on the boron nitride ampoule used in the calculations reported in Section 5.1 of reference by Adornato and Brown (1987a) and in the experiments of Wang (1984). The dimensions of the ampoule are listed in Table 4.3. All calculations were performed for a growth velocity of $V_g = 4 \mu\text{m/s}$.

Contour plots of the isotherms, streamlines, and isoconcentration curves are shown in Figure 4.3 for $Ra_t = 1 \times 10^5$ and $Ha = 0$. Streamlines are spaced at equal intervals between zero and the maximum (or minimum) values for each flow cell. The two flow cells evident in this figure are driven by different sets of radial temperature gradients along the ampoule and are due to interactions between the furnace and the ampoule. The differences between the thermal conductivities of the melt ($K_m = 0.39 \text{ W/K}\cdot\text{cm}$), the crystal ($K_s = 0.17 \text{ W/K}\cdot\text{cm}$) and the ampoule ($K_a = 0.26 \text{ W/K}\cdot\text{cm}$) cause the melt/crystal interface to be convex with respect to the melt and results in the temperature decreasing radially adjacent to this phase boundary. These gradients drive a flow that is up along the axis of the ampoule and down along the wall. Because of the slender shape of the melt, the flow is confined to a distance from the melt/crystal interface that is of the same order-of-magnitude as the ampoule radius.

The mismatch in thermal boundary conditions between the adiabatic and hot zones of the furnace causes a second set of radial gradients with the hottest temperature

Parameter	Vertical Bridgman furnace	Constant gradient furnace
Ampoule length, L (cm)	7.6	7.0
Crystal radius, R_c (cm)	0.76	0.35
Ampoule outer radius, R_a (cm)	0.95	0.50 ^{a)} (0.70) ^{b)}
Gradient zone length, L_g (cm)	3.8	-
Temperature difference, $T_h - T_c$ (°C)	300	350
Growth velocity, V_g ($\mu\text{m}/\text{sec}$)	4.0	4.0
Ampoule material	Boron nitride	Quartz/graphite composite
Thermal conductivity of ampoule, K_a (W/°C·cm)	0.26	0.028 ^{a)} (3.26) ^{b)}
Density of ampoule, ρ_a (g/cm ³)	2.0	2.2 ^{a)} (1.5) ^{b)}
Specific heat of ampoule, $C_{p,a}$ (J/°C·g)	1.9	0.77 ^{a)} (2.0) ^{b)}

^{a)} For quartz.

^{b)} For graphite.

Table 4.3: Design parameters for vertical Bridgman and constant gradient furnace

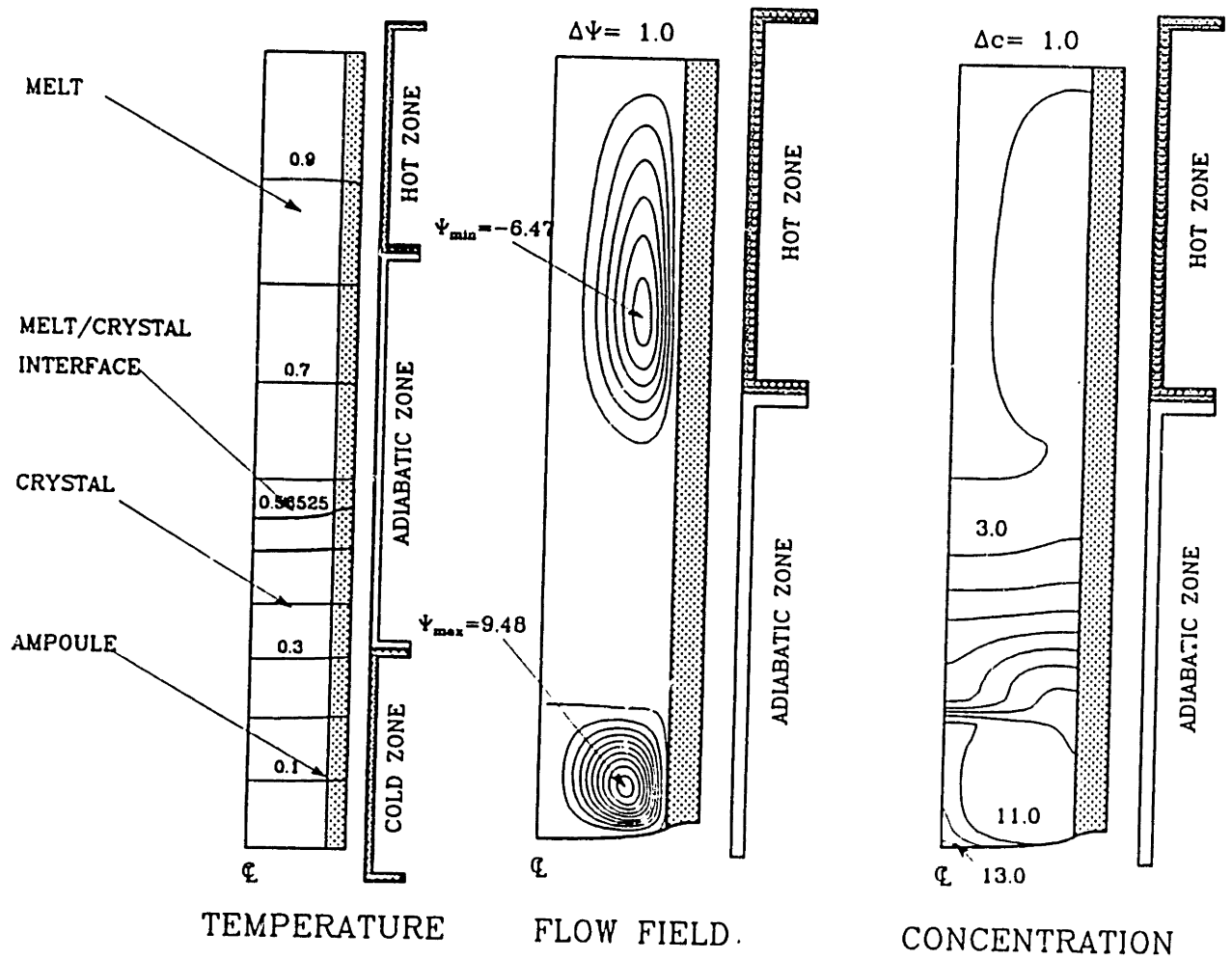


Figure 4.3: Contours of temperatures, stream function and concentration for growth in the vertical Bridgman furnace with $Ra_t = 1 \times 10^5$. Streamlines are spaced at equal intervals between the maximum (or minimum) values for the cells and zero.

located at the ampoule wall. The upper flow cell is driven by this part of the temperature field and moves upward at the wall and downward along the centerline. The spacing between the two flow cells is controlled by the length of the adiabatic zone.

The gallium concentration field in Figure 4.3 shows the effects of the mixing caused by both the top and the bottom flow cells. The radially uniform and exponentially decreasing axial variation of the concentration field expected without bulk convection is distorted in parts of the melt where the flow cells are strong. The concentration above the top of the adiabatic zone is essentially uniform because of the upper cell and because the diffusion layer does not penetrate into this portion of the ampoule, even at $Ra_t = 0$; see Figure 9 in the reference by Adornato and Brown (1987a). The concentration field near the melt/crystal interface is deformed by the lower cell and the first stages of the formation of a region of uniform concentration are evident. Steep axial concentration gradients develop in the region of the ampoule between the two cells.

The temperature field and melt/crystal interface for $Ra_t = 1 \times 10^5$ and $Ha = 0$ are essentially the same as predicted without convection in the melt ($Ra_t = 0$) (see Figure 4.4), because of the low Prandtl number for the melt. Increasing Ha has essentially no effect on these variables.

The effect of increasing the strength of the magnetic field is demonstrated by the flow fields shown in Figure 4.5, where Ra_t is fixed to 1×10^5 . Weak fields ($Ha = 10$) decrease the strength of the flow, but leave its cellular structure unchanged. Magnetic fields are shown to be more effective in reducing the intensity of the lower flow cell near the interface. Stronger fields ($Ha = 100$) decrease the flow strength to the point that the lower flow cell becomes much weaker than the upper cell, which stretches to fill more of the ampoule. Very strong fields ($Ha = 500$) eliminate the lower flow cell entirely and the upper cell occupies most region of the melt in the ampoule. However, this level of magnetic field strength is not sufficient to suppress the cellular convection completely at high Ra_t of 1×10^5 . For lower Ra_t , the same magnetic field strength is effective in suppressing the convection cell completely and leads to unidirectional flow, as argued from the mechanical energy balance (see Figure 4.6).

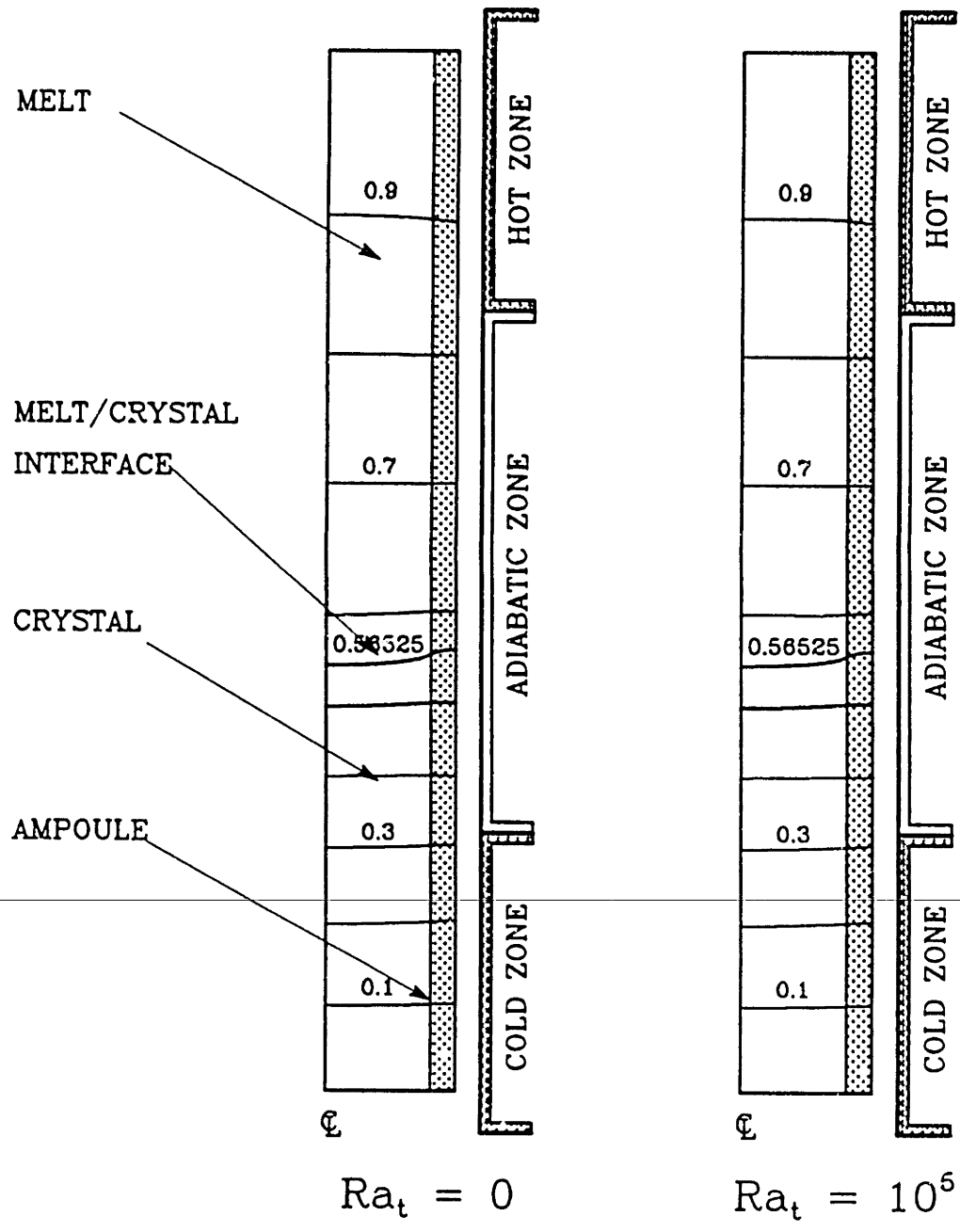


Figure 4.4: Comparison of the temperature fields for growth in the vertical Bridgman furnace with $Ra_t = 0$ and 1×10^5 .

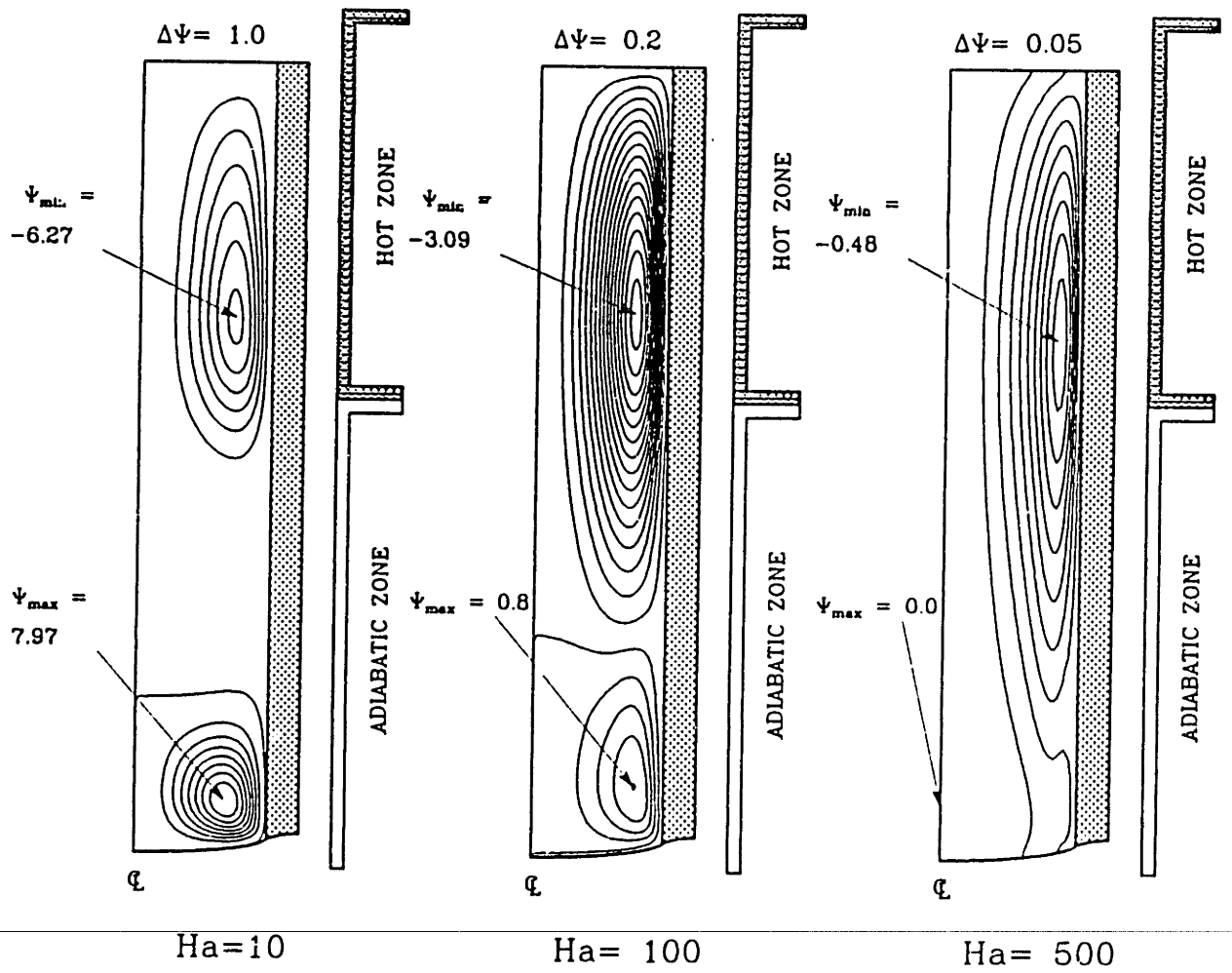


Figure 4.5: Sample flow fields for growth of GaGe in the vertical Bridgman furnace with increasing magnetic field strength, as measured by Ha ; $Ra_t = 1 \times 10^5$.

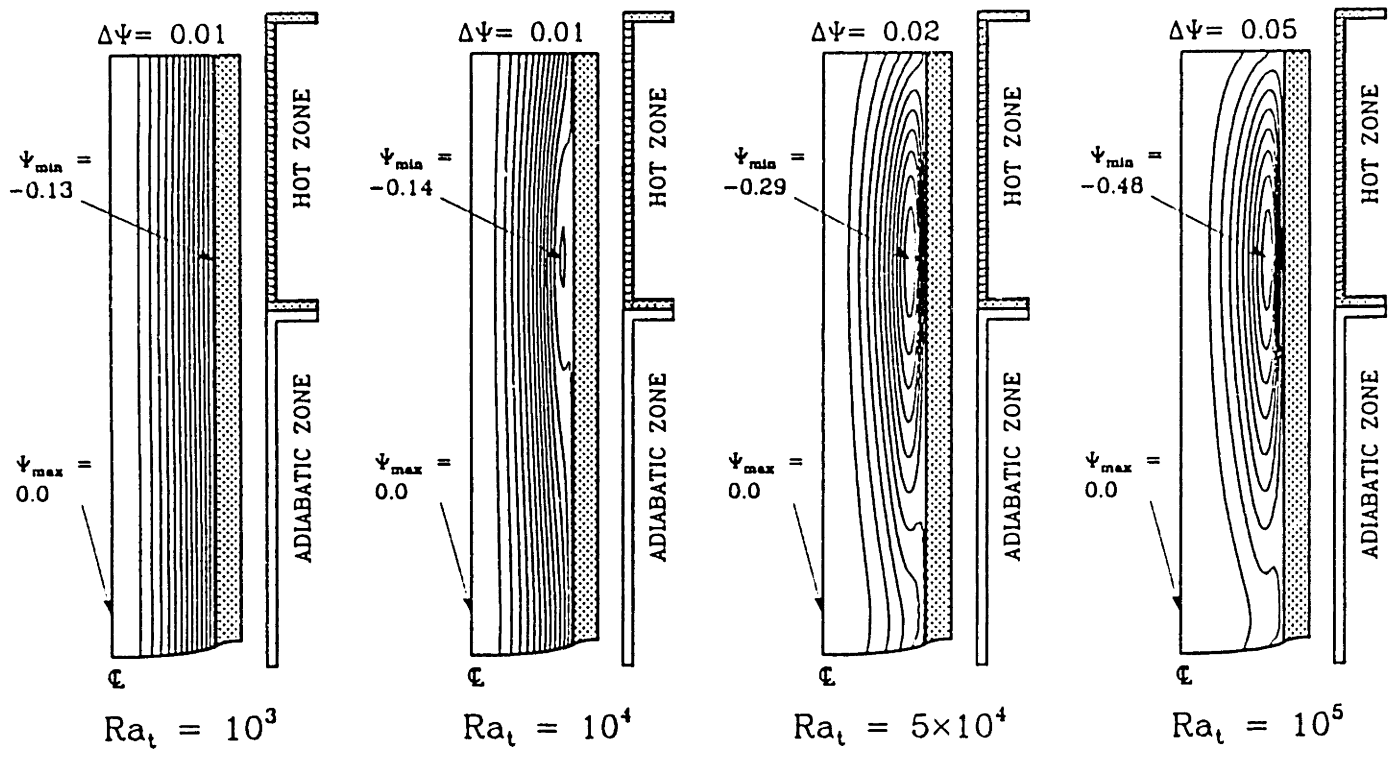


Figure 4.6: Sample flow fields for growth of GaGe in the vertical Bridgman furnace with increasing convection driving force, as measured by Ra_t ; $Ha = 500$.

The flow intensity as measured by the maximum value of the stream function $|\Psi^*|$ is plotted in Figure 4.7 for each flow cell. For low values of Ra_t , the flow is essentially the unidirectional motion caused by crystal growth. Without the magnetic field, the intensity of the upper cell scales linearly with increasing Ra_t for $1 \times 10^2 \leq Ra_t \leq 3 \times 10^3$, indicating that the flow is dominated by a balance of viscous and buoyancy forces. A transition to a weaker dependence of flow intensity on Ra_t occurs for $Ra_t \geq 2 \times 10^3$ and seems to correspond to the formation of boundary layers along the ampoule wall. The lower cell is present for $Ra_t \geq 1 \times 10^2$. Its intensity is a complicated function of Ra_t because of the interactions between this cell and the upper one. Imposing the magnetic field suppresses the lower cell for values of the field strength such that $Ha \geq 100$. The upper cell is still present for high Rayleigh numbers and $Ha = 500$.

The large ratio of solute to thermal diffusivity ($Sc/Pr = \mathcal{O}(10^3)$) makes the solute field much more sensitive to the level of convection than the temperature fields. Solute fields for dilute gallium in germanium are shown in Figure 4.8 as calculated for the flows shown in Figure 4.5. The regions of approximately uniform concentration formed by mixing within the flow cells are still apparent for $Ha = 10$. The weak convection in the lower flow cell shows the characteristic composition field for incomplete mixing at $Ha = 100$. The disappearance of the lower flow cell with increasing Ha leads to the formation of the exponential diffusion layer adjacent to the interface for $Ha = 500$ with weak convective mixing caused only by the upper flow cell.

The influence of the magnetic fields on solute convection is more evident for lower Ra_t , which corresponds to conditions for reduced gravity. Solute fields for gallium in germanium are shown in Figure 4.9 as calculated from the flow fields in Figure 4.6. With the same strength of magnetic field ($Ha = 500$), the exponential diffusion layer becomes more one-dimensional with decreasing Ra_t .

The percentage radial segregation Δc is plotted in Figure 4.10 as a function of Ra_t and Ha ; $V_g = 4 \mu m/s$. The maximum in Δc for $Ra_t = 1 \times 10^3$ with weak magnetic field is similar to the results in the work by Adornato and Brown (1987a). The value of Ra_t for the maximum radial segregation increases as the intensity of the

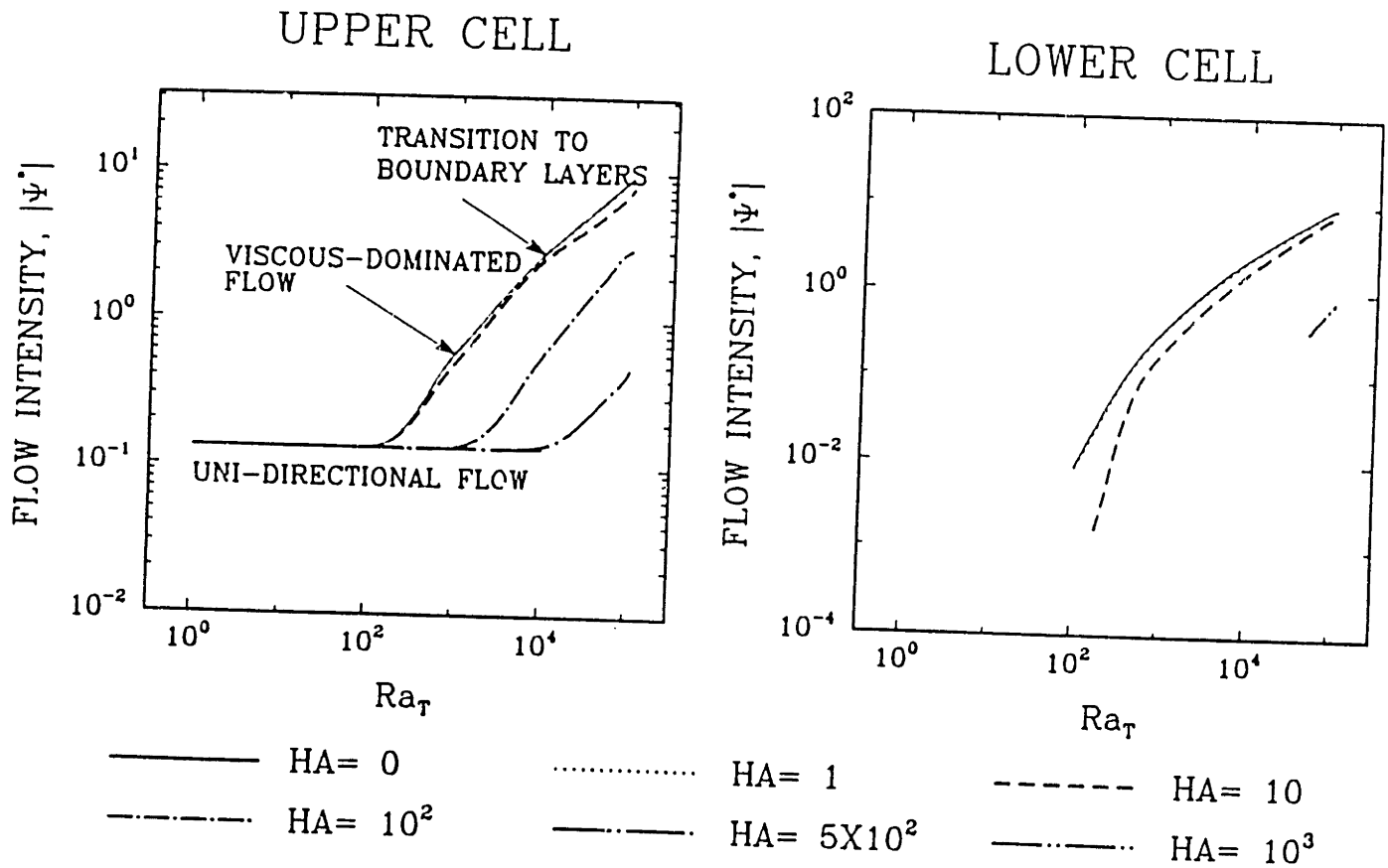


Figure 4.7: Maximum values of stream function in the upper and lower flow cells as a function of Ra_τ and Ha for growth of GaGe in the vertical Bridgman furnace.

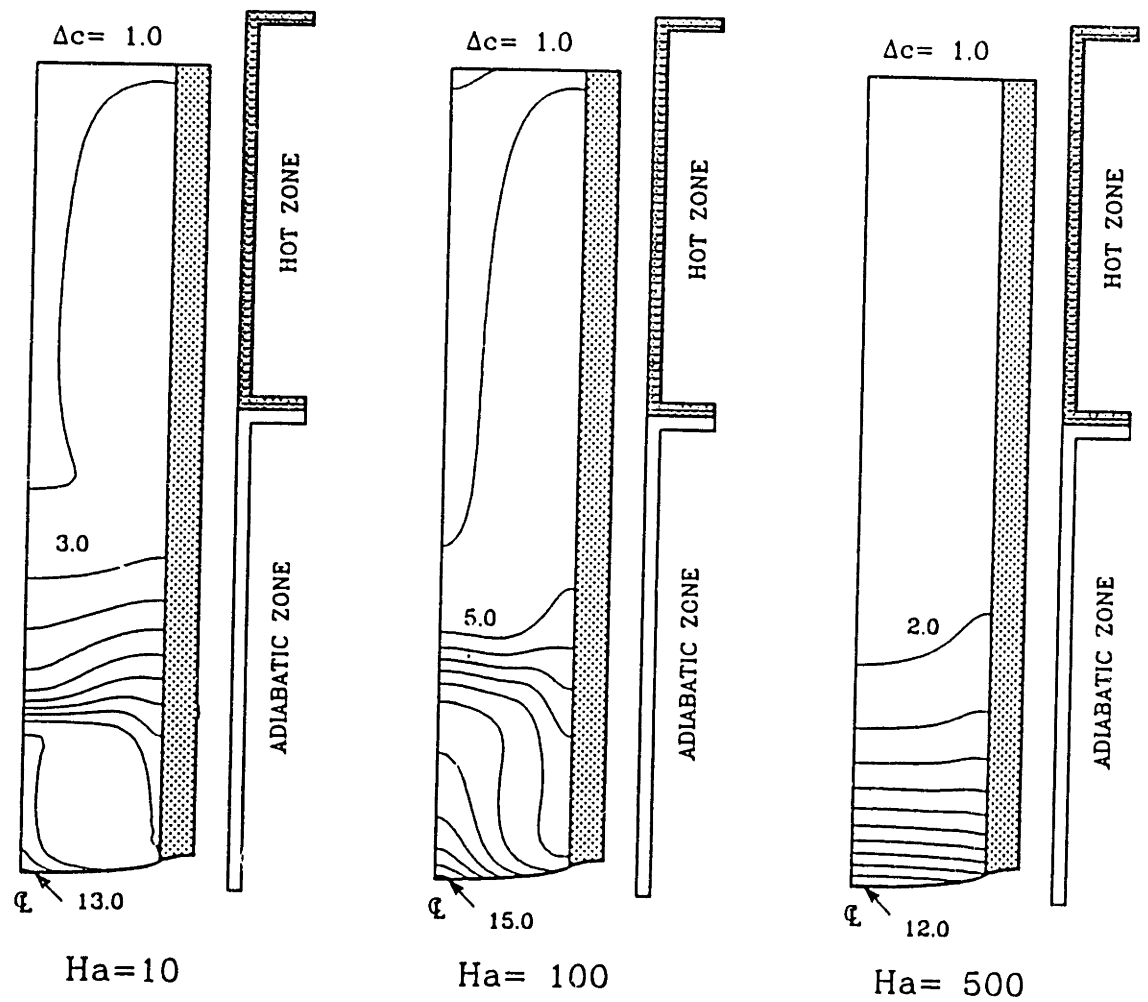


Figure 4.8: Sample concentration fields for gallium solute in the vertical Bridgman system; results are for different values of Ha and $Ra_c = 1 \times 10^5$.

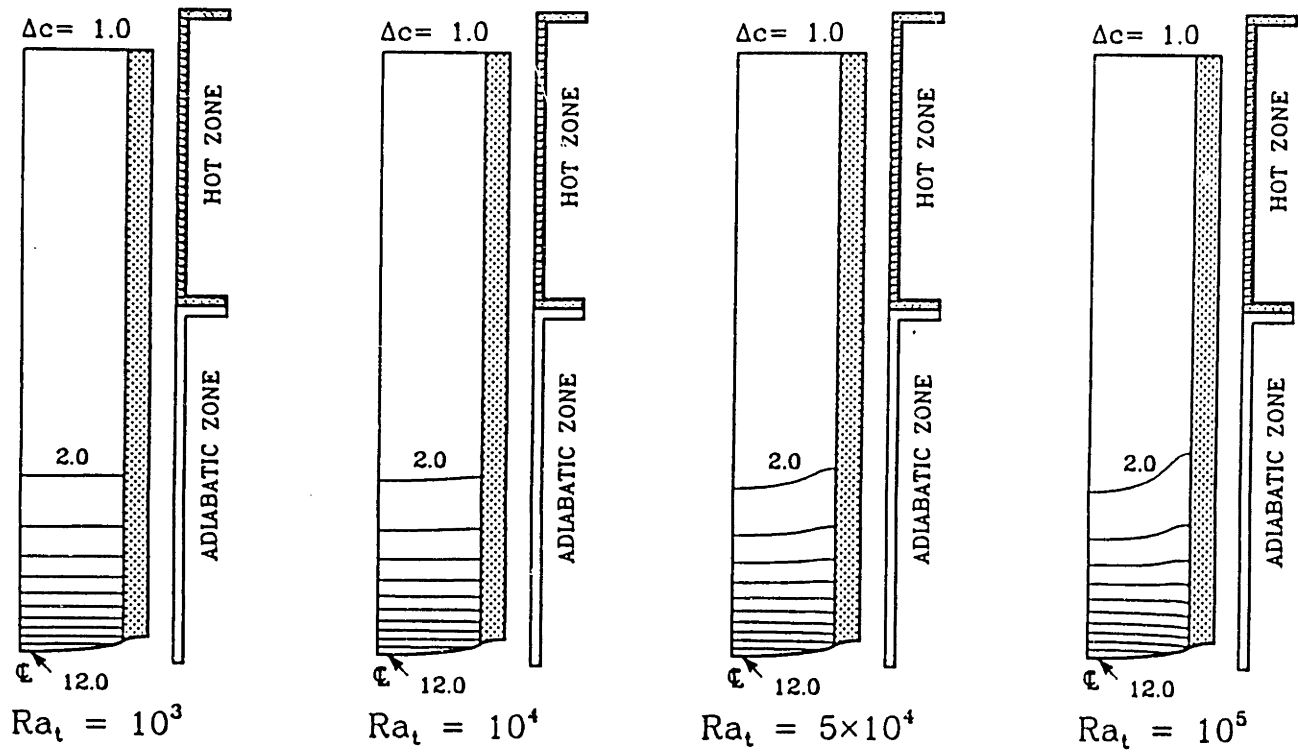


Figure 4.9: Sample concentration fields for gallium solute in the vertical Bridgman system; results are for different values of Ra_t and $Ha = 500$.

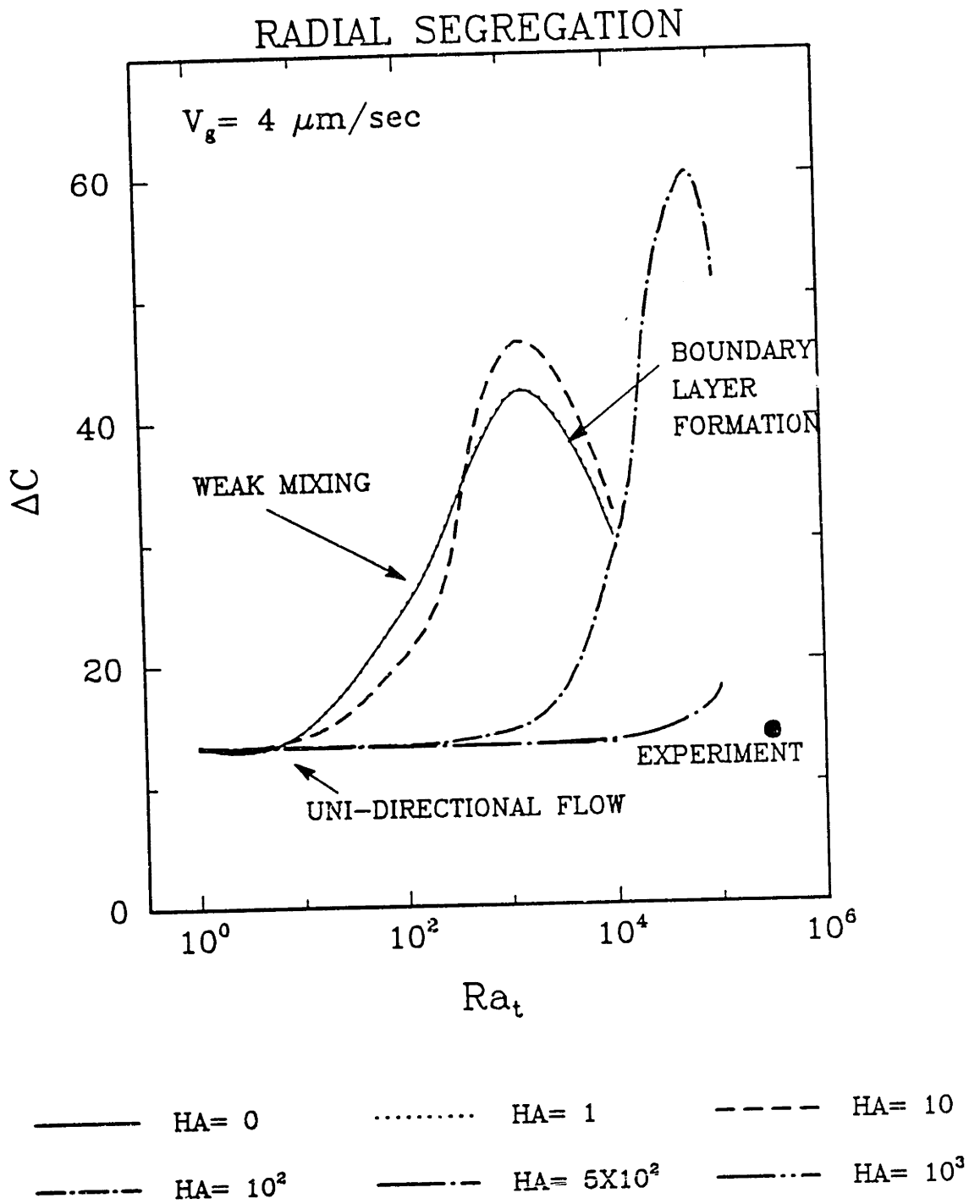


Figure 4.10: Percentage radial segregation as a function of thermal Rayleigh number and Hartmann numbers for growth of GaGe in the vertical Bridgman system. The solid dot (•) corresponds to experimental measurement of Wang (1984).

field is increased. For $Ha \geq 500$, Δc is caused only by the curvature of the melt/solid interface up to $Ra_t = 1 \times 10^4$. Calculations at higher values of Ra_t were not possible with the finite element mesh used here because of the formation of boundary layers along the ampoule wall, as explained in Section 4.5. The experimental measurement of Wang (1984) also is shown; Adornato and Brown (1987a) explain how to extrapolate the numerical calculations to get reasonable agreement with measurement by using boundary-layer theory for describing the dependence of Δc on Ra_t .

The variation of the axial segregation of solute with Ha and Ra_t is estimated from the calculations with the PSSM by computing the effective segregation coefficient defined by Eq. (4.1). These values are plotted in Figure 4.11 as a function of Ra_t and Ha . The value of k_{eff} for no convection ($Ra_t = 0$) is not unity because the ampoule is not long enough so that the variation in concentration caused by the diffusion layer is small relative to the portion of the melt which is at the bulk concentration ($c = 1$). The increased mixing caused by convection and the decrease in k_{eff} towards the equilibrium value ($k = 0.087$) are obvious. Increasing the magnetic field strength increases the effective segregation coefficient, shifting the critical value of Ra_t for the beginning of the decrease in k_{eff} with Ra_t to higher values of Ra_t . The experimental measurement of Wang (1984) without a magnetic field is shown again for reference.

4.4.2 Constant Gradient Furnace

The temperature field in the ampoule is established by a surrounding heater that imposes a nearly constant axial temperature gradient. The resulting axial temperature gradient in the melt is nearly linear over the entire length, compared to the vertical Bridgman furnace where it is interrupted by the discontinuity introduced by the junction of the adiabatic and hot zones. The calculations with the axial magnetic field reported here are based on the ampoule design for the constant gradient furnace introduced by Rouzaud *et al.* (1985), where a quartz sleeve is enclosed in a graphite liner. The dimensions of the ampoule are listed in Table 4.3. Again the crystal growth velocity was set as $V_g = 4 \mu m/s$.

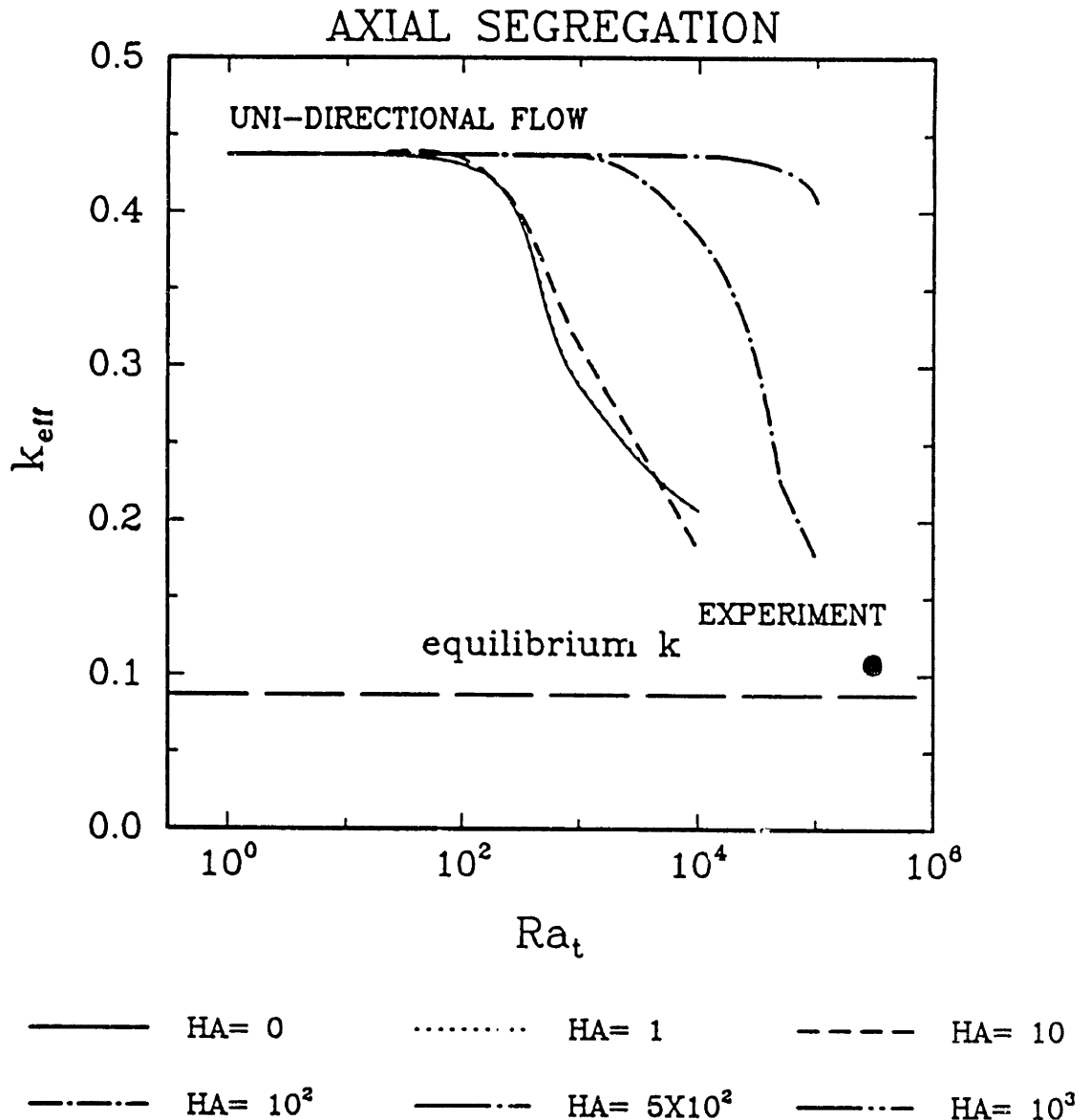


Figure 4.11: Effective segregation coefficient computed from Eq. (4.1) in the vertical Bridgman system; The solid dot (•) corresponds to experimental measurement of Wang (1984).

Contours of the temperature, stream function (velocity) and concentration fields are shown in Figure 4.12 for $Ra_t = 1.25 \times 10^4$ and $Ha = 0$. The radial temperature gradients are caused primarily by the differences in the thermal conductivities of melt, crystal and ampoule material and are largest adjacent to the convex melt/crystal interface. The temperature field and interface shape are essentially unaffected by the flow.

The radial temperature gradient drives a flow cell centered near the interface that moves down the ampoule wall and up along the centerlines of the ampoule as shown in Figure 4.12. No upper cell is present, because the mechanism has been removed for the inversion in the radial temperature gradients. The solute concentration field shows a well-mixed region near the interface. However, the radial temperature gradients are weaker and mixing is less efficient than in the vertical Bridgman system.

The effects of the axial magnetic field on the flow field is shown in Figure 4.13. Very weak fields, e.g. $Ha = 5$, decrease the strength of the flow, but leave the flow pattern unchanged. Increasing the magnetic field strength further causes the flow cell to stretch to fill most of the ampoule, so that more of the flow is aligned with the field and unaffected by it. At $Ha = 500$ the cell has almost disappeared and only the unidirectional motion due to crystal growth remains. But, the action of magnetic field compresses the streamlines near the wall indicating the formation of a Hartmann boundary layer.

The variation of the flow intensity, as measured by Ψ_{max} , is plotted in Figure 4.14 as a function of Ra_t and Ha . These intensities are approximately an order-of-magnitude weaker than are shown in Figure 4.7 for the vertical Bridgman furnace. With no magnetic field and low field levels, Ψ_{max} is approximately linear with Ra_t for given Ha . The value of $|\Psi_{min}|$ is constant for the range of Ha and Ra_t considered here, since only one flow cell exists, at most.

The solute fields computed for dilute gallium in germanium are shown in Figure 4.15 with increasing Ha for the constant gradient furnace. The transition toward the diffusion layer that corresponds to unidirectional growth is obvious. The percentage radial

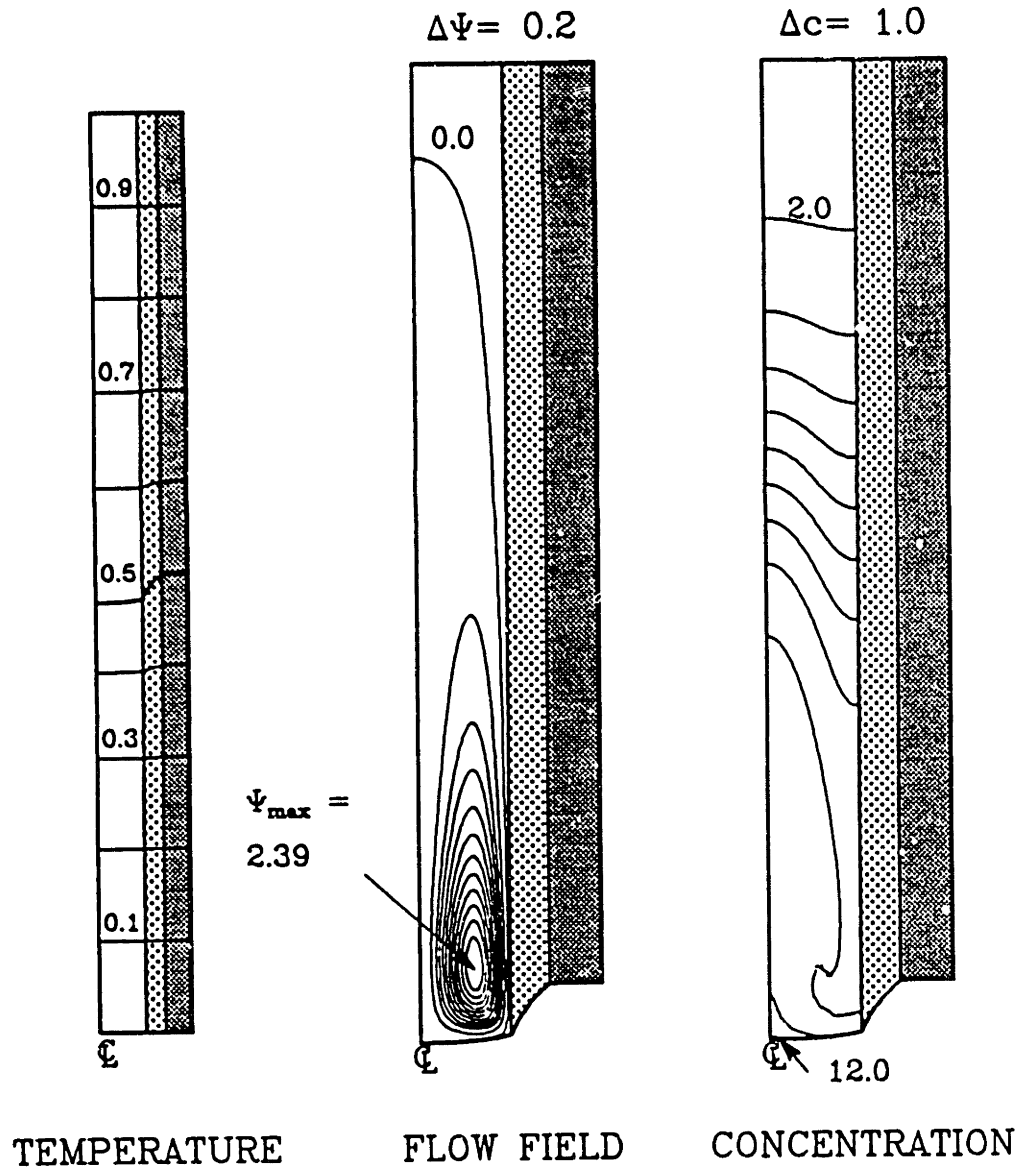


Figure 4.12: Contours of temperatures, stream function and concentration for growth in the constant gradient furnace with $Ra_t = 1.25 \times 10^4$. Streamlines are spaced at equal intervals between the maximum, and minimum, values for the cells and zero.

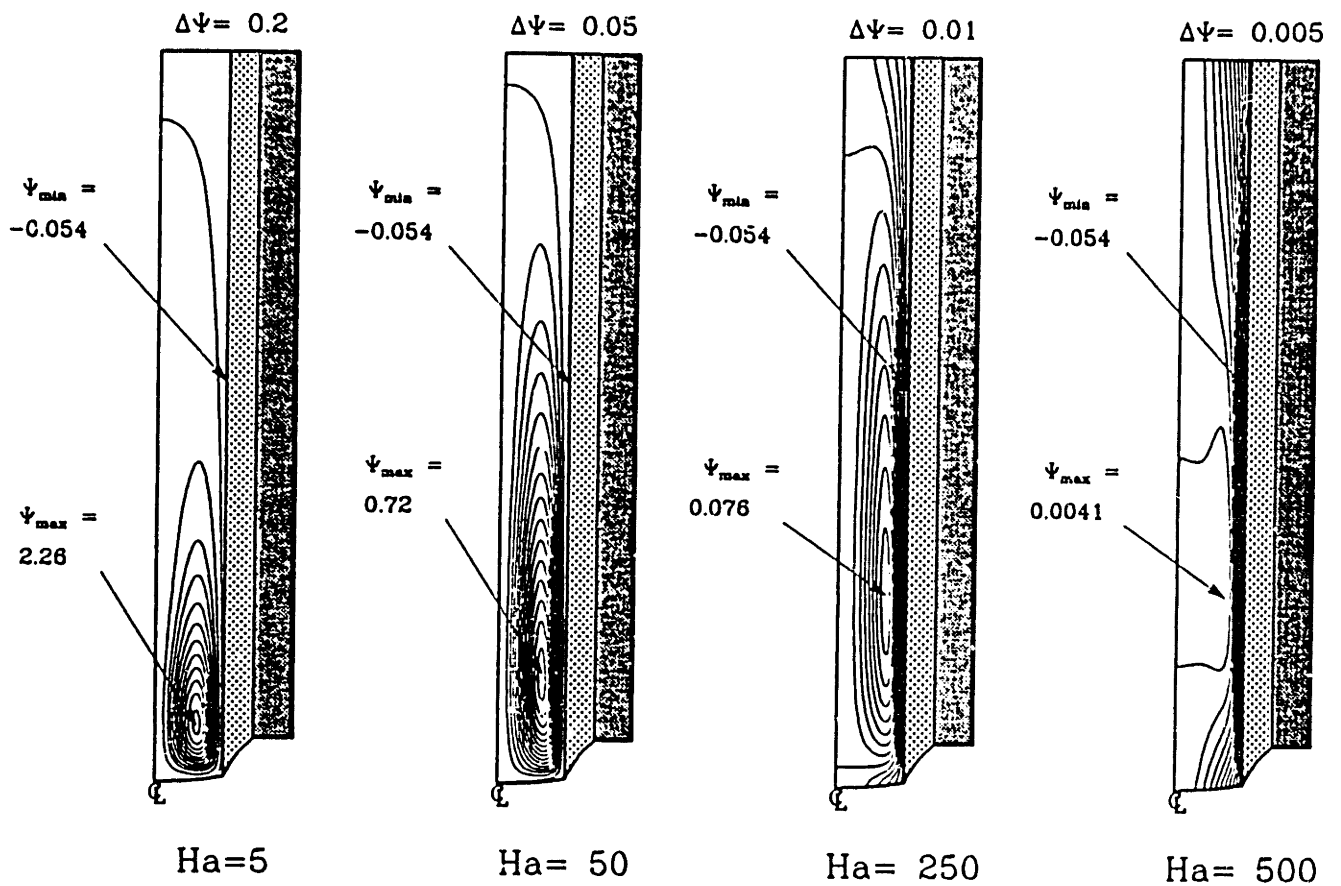


Figure 4.13: Sample melt flow fields for growth in vertical Bridgman system; results are for different values of Ha and $Ra_t = 1.25 \times 10^4$.

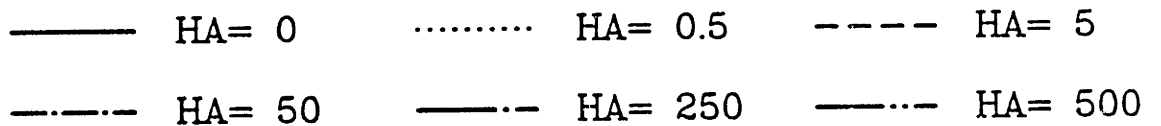
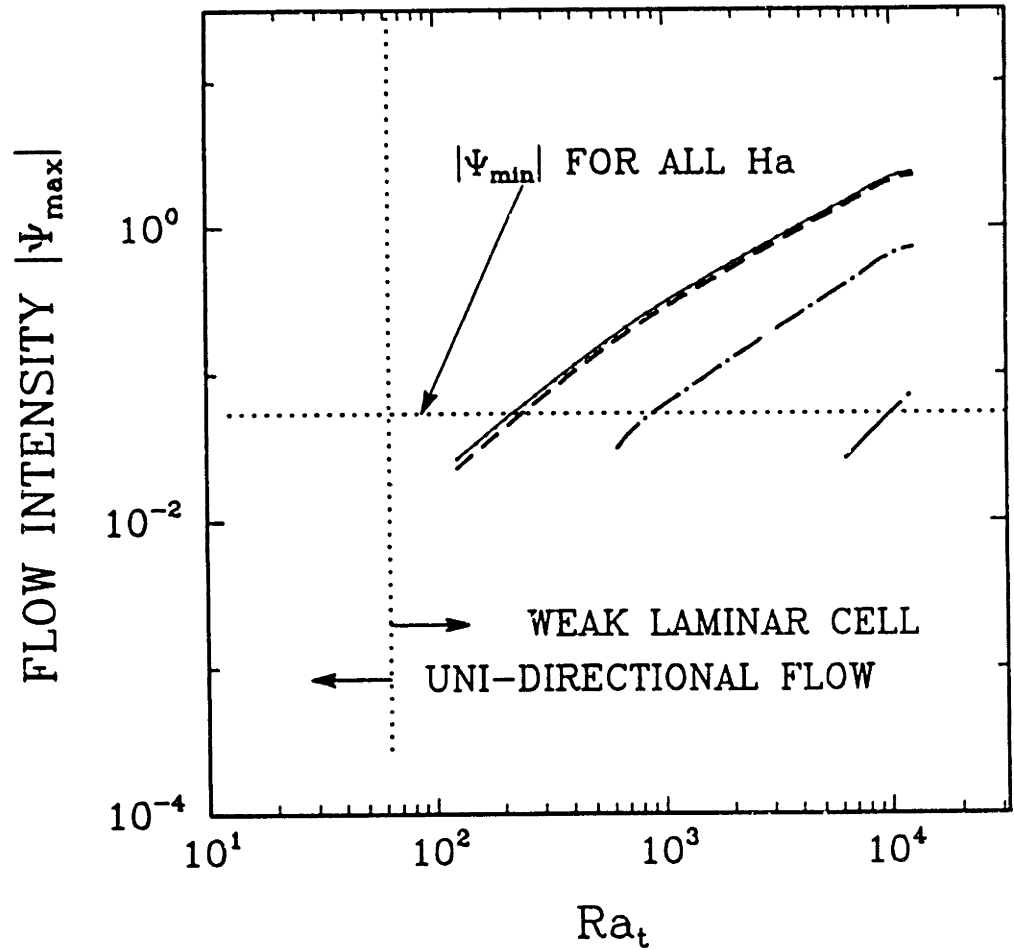


Figure 4.14: Maximum values of stream function in the single toroidal cell plotted as a function of Ra_t and Ha for growth of GaGe in the constant gradient furnace.

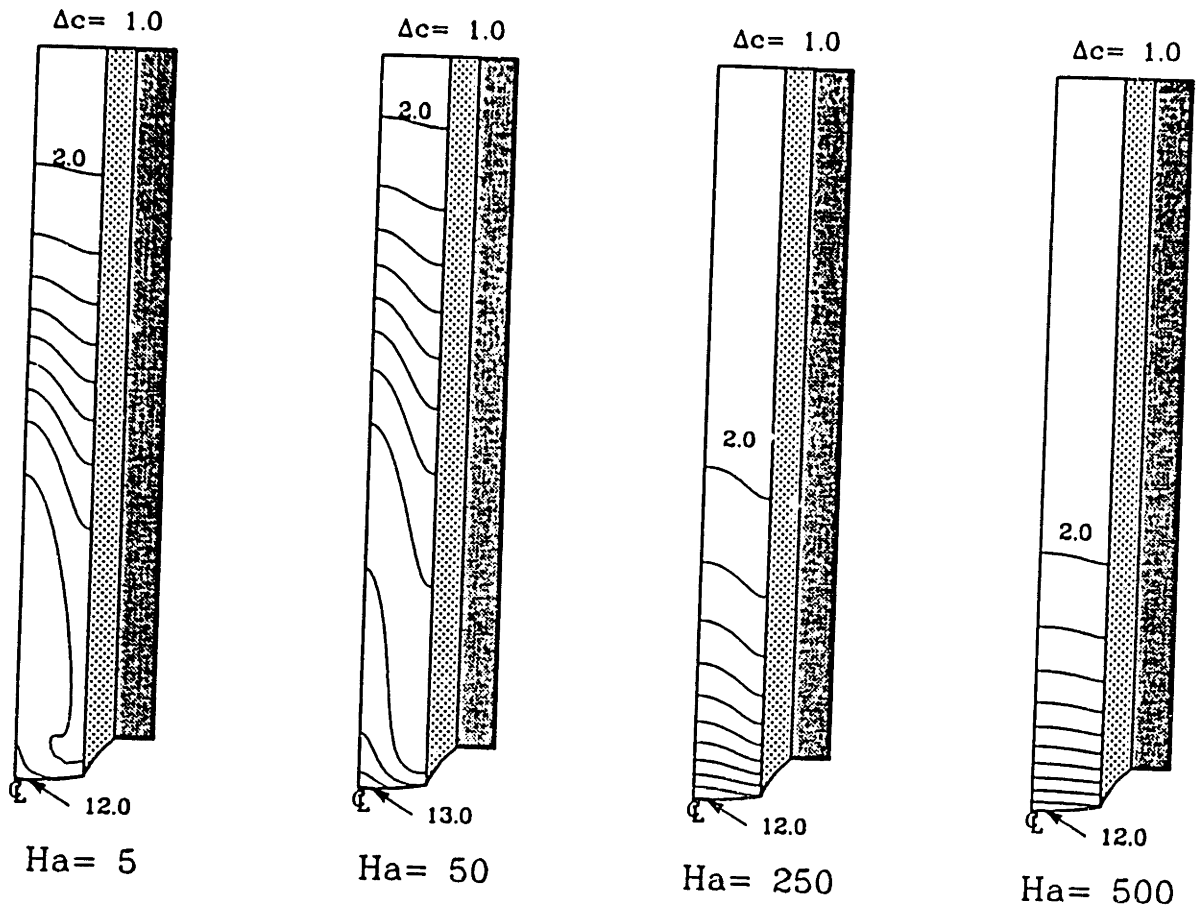


Figure 4.15: Sample concentration fields for gallium solute in constant gradient furnace; results are for different values of Ha and $Ra_t = 1.25 \times 10^4$.

segregation Δc is displayed in Figure 4.16 as a function of Ra_t and Ha . The characteristics of these results are the same as for the vertical Bridgman system, with two exceptions. First, the position of the maximum in Δc for $Ha = 0$ is shifted toward larger values of Ra_t because of the weaker convection in the constant gradient furnace. Second, the level of segregation at this maximum is less than half the values for the vertical Bridgman system, because of the flatter melt/crystal interface in the constant gradient furnace.

The effective segregation coefficient defined by Eq. (4.1) is plotted in Figure 4.17 and a function of Ha and Ra_t . The thermal Rayleigh number where k_{eff} begins to deviate from the value for diffusion-controlled growth increases with increasing Ha and is an order-of-magnitude higher than in the vertical Bridgman furnace.

4.5 Asymptotic Analysis for High Magnetic Fields

The action of the magnetic field on the form and intensity of the flow field is easily understood from an asymptotic analysis designed for a simple limit of an almost perfect directional solidification system. In this limit the effect of the ampoule is neglected and a temperature field is imposed directly on the boundary of the melt, as shown in Figure 4.18. The system is *almost perfect* in the sense that the gradient of the wall temperature is assumed to deviate only slightly from the constant value associated with a perfect unidirectional growth system. Much of the analysis parallels the results of Hjellming and Walker (1987) for Czochralski growth in the presence of a strong field.

The goal of the analysis described here is to determine the structure and intensity of the flow in the limit of a strong imposed magnetic field. We assume the melt/crystal interface to be planar and neglect the motion of the melt introduced by growth of the crystal. The analysis is performed in terms of the cylindrical coordinate system shown in Figure 4.18. The dimensionless wall temperature is defined as

$$\theta_w(z) = 1 - \epsilon z - \epsilon z \kappa (1 - \epsilon z) \quad (4.23)$$

RADIAL SEGREGATION

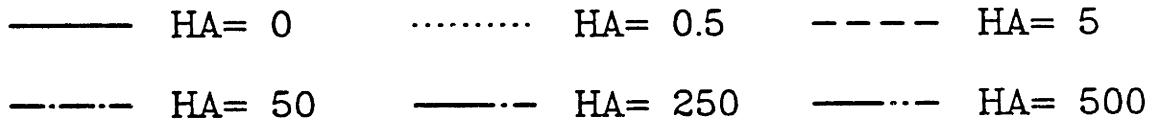
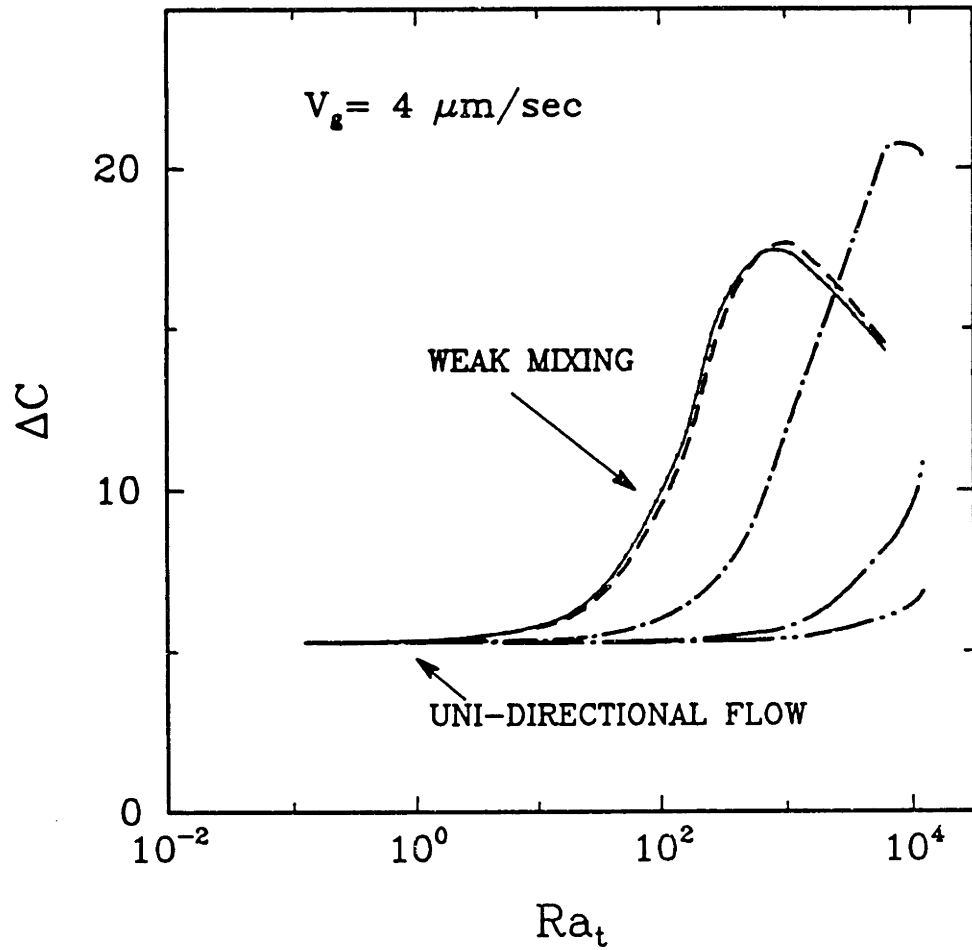


Figure 4.16: Percentage radial segregation as a function of thermal Rayleigh number and Hartmann number for growth of GaGe in the constant gradient system.

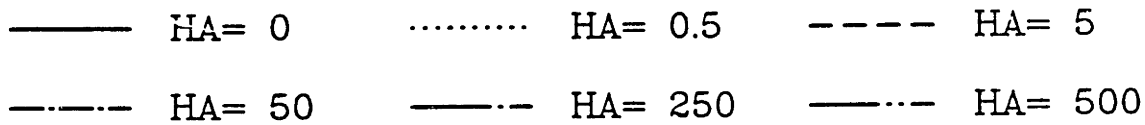
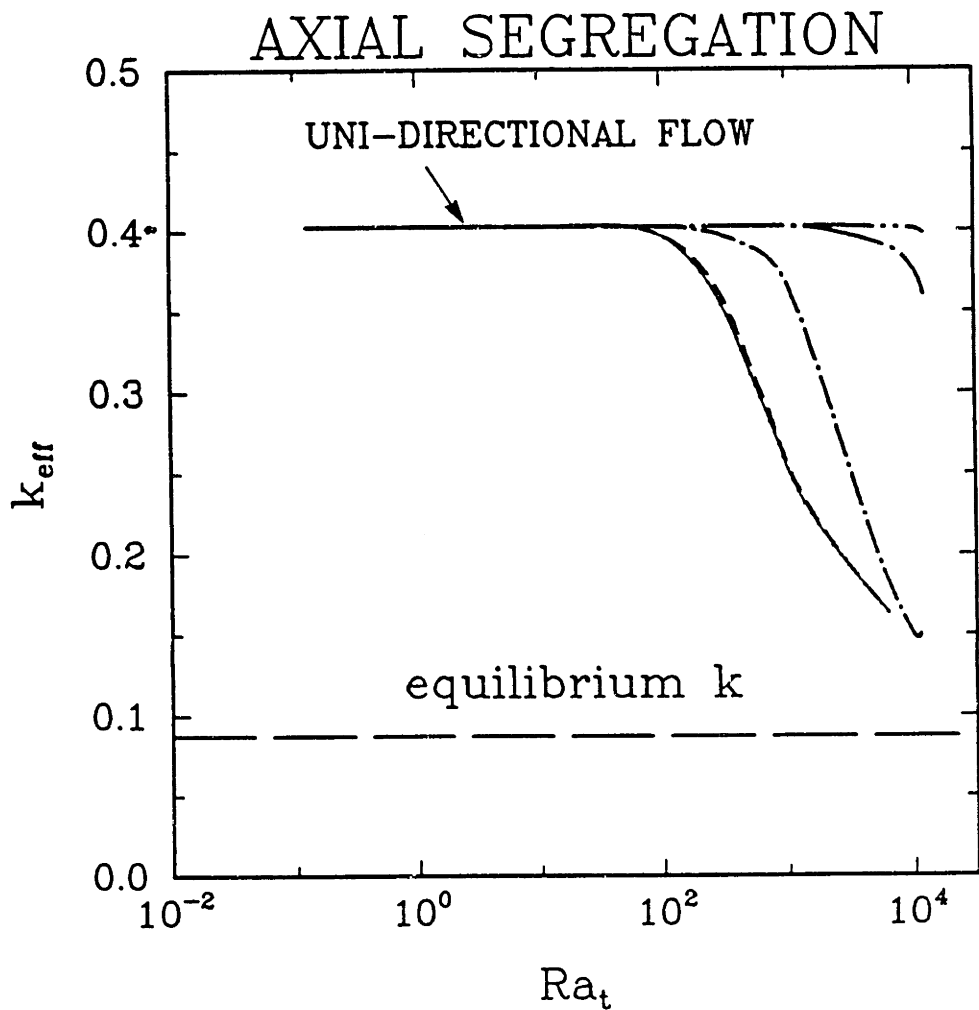


Figure 4.17: Effective segregation coefficient computed from Eq. (4.1) plotted as a function of Ra_t and Ha for growth of GaGe in the constant gradient furnace.

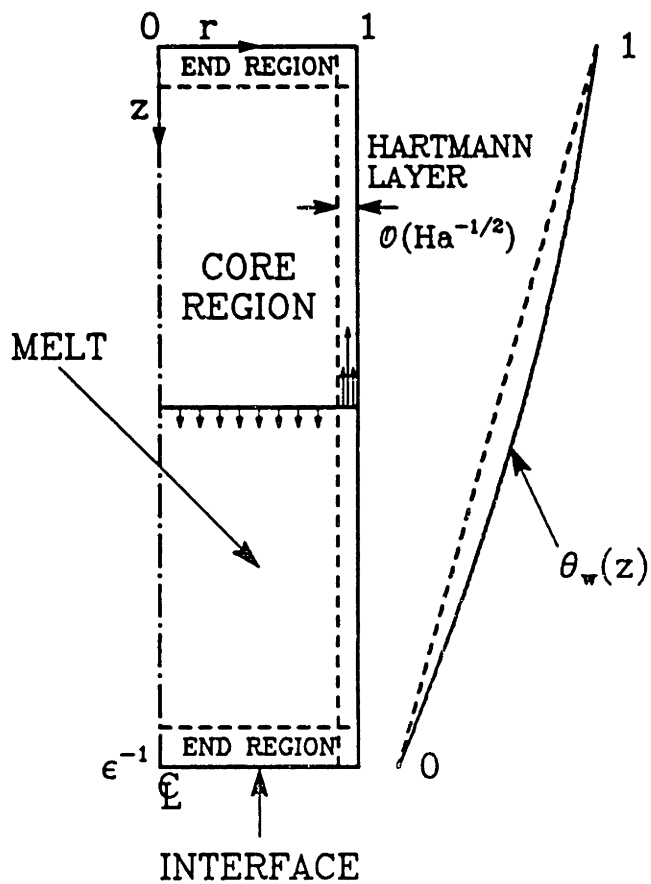


Figure 4.18: The simplified directional solidification system considered in the asymptotic analysis of flow with large magnetic fields. A qualitative picture of regions of the flow as expected for high Ha is included.

where the dimensionless temperature is

$$\theta(r, z) \equiv \frac{T(r, z) - T_m}{T_h - T_m}. \quad (4.24)$$

The coordinates (r, z) are scaled with the radius of the crystal R_c , and $\epsilon^{-1} \equiv L/R_c$ is the dimensionless length of the ampoule. The constant κ scales the magnitude of the deviation of the wall temperature from the constant gradient; κ must be in the range $0 \leq \kappa \leq 1$ to give a monotonic temperature decrease along the ampoule wall.

The momentum, continuity and energy equations for the melt are rescaled in terms of new characteristic dimensions; for the velocity $V^* \equiv \rho_o g \beta_t \Delta T / \sigma B_o^2$, the temperature $\Delta T \equiv T_h - T_m$, and the pressure $p^* \equiv \rho_o g \beta \Delta T R_c$.

These new scales are appropriate when a balance of buoyancy and Lorentz forces control the momentum equation in the limit of a large field strength (Hjellming and Walker, 1987). The new dimensionless field equations in the melt become

$$\nabla \cdot \mathbf{v} = 0 \quad (4.25)$$

$$N^{-1} \mathbf{v} \cdot \nabla \mathbf{v} = -\nabla p + Ha^{-2} \nabla^2 \mathbf{v} - v_r \mathbf{e}_r - \theta \mathbf{e}_z \quad (4.26)$$

$$Pe_h \mathbf{v} \cdot \nabla \theta = \nabla^2 \theta \quad (4.27)$$

where the Magnetic Interaction parameter N , the Hartmann number Ha and the thermal Peclet number Pe_h are defined in Table 4.4. Typical values of these parameters for small-scale directional solidification systems are listed there. As noted by Hjellming and Walker (1987), Eqs. (4.26) and (4.27) can be simplified by neglecting convective contributions to momentum and heat transport, because $N \gg 1$ and $Pe_h \ll 1$ for intense magnetic fields.

Moreover, eliminating the viscous term in Eq. (4.26) by neglecting the term proportional to Ha leaves only the balance of buoyancy and Lorentz forces in the momentum equation:

$$\frac{\partial v_r}{\partial z} = \frac{\partial \theta}{\partial r} \quad (4.28)$$

B_o (kG)	Interaction parameter ^{a)} $N =$ $\sigma B_o^2 R_c / \rho_o V^*$	Hartmann number $Ha =$ $B_o R_c (\sigma / \mu)^{1/2}$	Peclet number ^{a)} $Pe_h =$ $V^* R_c / \alpha_m$
2.4	0.350	35.1	25.2
24	3.5×10^3	351	0.252
120	2.2×10^6	1760	0.0101

^{a)} $V^* = \rho_o g \beta \Delta T / \sigma B_o^2$.

Table 4.4: Dimensionless groups and characteristic values for gallium-doped germanium crystal growth in constant gradient furnace for asymptotic analysis.

Because this last step eliminates the highest derivatives in the equation, the no-slip condition along the ampoule wall and at the melt/crystal interface can no longer be satisfied and the equations are only valid in the core of the flow, *i.e.* away from these boundaries. Boundary layers adjacent to the ampoule and the interface must be present in order to satisfy the no-slip condition.

Analysis of the core equations and the boundary layer proceeds only after the conduction equation (Eq. (4.27) with $Pe_h = 0$) is solved for the imposed thermal boundary conditions. We simplify this step by assuming that the ampoule is long ($\epsilon \ll 1$) so that a slender body analysis (Cormack *et al.*, 1974a) can be used for solution of (4.27). This assumption is introduced by rescaling the axial coordinate as $\zeta = \epsilon z$ valid away from the melt/crystal interface. The energy equation reduces to

$$\frac{1}{r} \frac{\partial}{\partial r} \left(r \frac{\partial \theta}{\partial r} \right) + \epsilon^2 \frac{\partial^2 \theta}{\partial \zeta^2} = 0 \quad (4.29)$$

The temperature field in the core of the melt away from the melt/crystal interface and the ampoule wall is computed as a Taylor series expansion in ϵ from Eq. (4.29) using the boundary conditions of the specified temperature along the wall (Eq. (4.23)) and axial symmetry about $r = 0$. The first two terms in this expansion are

$$\begin{aligned} \theta(r, z) = & [1 - \zeta - \kappa\zeta(1 - \zeta)] \\ & + \frac{\epsilon^2 \kappa(1 - r^2)}{4} + \mathcal{O}(\epsilon^4) \end{aligned} \quad (4.30)$$

Substituting Eq. (4.30) into Eq. (4.28) and introducing the stream function in the core $\hat{\Psi}_c(r, z)$ defined by

$$v_r^\epsilon = \frac{1}{r} \frac{\partial \hat{\Psi}_c}{\partial z}, \quad v_z^\epsilon = -\frac{1}{r} \frac{\partial \hat{\Psi}_c}{\partial r}, \quad (4.31)$$

gives the leading order term for the stream function as

$$\hat{\Psi}_c(r, z) = \frac{\kappa}{4} r^2 \zeta (1 - \zeta) \quad (4.32)$$

In the limit of a long ampoule with the wall temperature profile given by Eq. (4.23), the core flow is a nearly uniform buoyancy-driven motion driven downward toward

the melt/crystal interface. This convective flow returns in the boundary layer along the ampoule wall so that mass is conserved by the total motion. In this scaling, the maximum value of the stream function in the core is the constant $\hat{\Psi}_{c,max} = \kappa/16$, indicating the validity of scaling of velocity with respect to the magnetic field strength.

Converting the result (Eq. (4.32)) to the dimensionless variables used to scale the numerical calculations leads to the relationship

$$\Psi_{max} \sim \hat{\Psi}_{c,max} Ha^{-2}, \quad (4.33)$$

as the appropriate scaling of the flow intensity with the field strength. This result is compared below to the finite element calculations.

The rigorous solution of the entire flow problem in the limit $Ha \gg 1$ is not complete without the analysis of the Hartmann boundary-layer along the ampoule wall necessary to satisfy the no-slip condition. The analysis of the Hartmann layer closely follows the procedure introduced by Hjellming and Walker (1987). The definitions of the rescaled radial coordinate η , pressure $p_w(\eta, z)$ and stream function $\Psi_w(\eta, z)$ in the boundary layer that leads to a balance of viscous buoyancy, and Lorentz forces in this region are

$$\begin{aligned} r &= 1 - Ha^{-1/2} \eta \\ p &= p_c(1, z) + Ha^{-1/2} p_w(\eta, z) \\ v_{r,w} &= \frac{\partial \Psi_w}{\partial z} \\ v_{z,w} &= -Ha^{1/2} \frac{\partial \Psi_w}{\partial \eta} \end{aligned} \quad (4.34)$$

where $p_c(1, z)$ is the pressure distribution in the core evaluated at the wall, $r = 1$. Note that the stream function in the boundary layer, and hence the velocity, increase with increasing Ha . This increase is necessary to conserve mass because the thickness of the Hartmann layer decreases with increasing field strength.

The reduced momentum and energy balances that describe the fields in the boundary

layer are

$$\frac{\partial \Psi_w}{\partial z} = \frac{\partial \theta_w}{\partial \eta} + \frac{\partial^4 \Psi_w}{\partial \eta^4} \quad (4.35)$$

$$\frac{\partial \theta_w}{\partial \eta} = \frac{\partial \theta_c}{\partial r}(1, z) \quad (4.36)$$

These equations can be solved by the procedure described by Hjellming and Walker (1987) and matched to the expressions for the stream function and temperature in the core. We do not complete the analysis here because the analytical results are of little value for the idealized temperature profile (Eq. (4.23)) proposed along the ampoule wall. The asymptotic scalings for the variation of the core flow (Eq. (4.33)) and for the thickness of the Hartmann layer (Eq. (4.34)) are important and should be invariant to changes in the thermal boundary conditions; these are summarized in Figure 4.18.

The scaling predicted for the intensity of the core flow (Eq. (4.33)) is compared in Figure 4.19 to calculations for the constant temperature gradient furnace with $V_g = 0$. The slope of Ψ_{max} agrees with (Eq. (4.33)) for values of Ra_t shown and for Hartmann numbers between 100 and 1×10^4 . The decrease of the slope of the flow intensity computed for higher values of Ha is a numerical artifact caused by the failure of the finite element approximations to resolve the Hartmann layer adjacent to the ampoule wall for large values of Ha . Since the thickness of this layer is proportional to $Ha^{-1/2}$, this layer has decreased in thickness for $Ha = 500$ to less than element size, which is one-twentieth of the inner radius of the ampoule.

4.6 Discussion

The calculations reported here show important interactions between the flow field and axial and radial segregation in directional solidification. Radial segregation is set by the flow structure near the crystal/melt interface, whereas axial segregation is influenced by solute mixing throughout the melt and therefore is affected by flow cells isolated from the interface. These differences are brought out by the calculations in the vertical

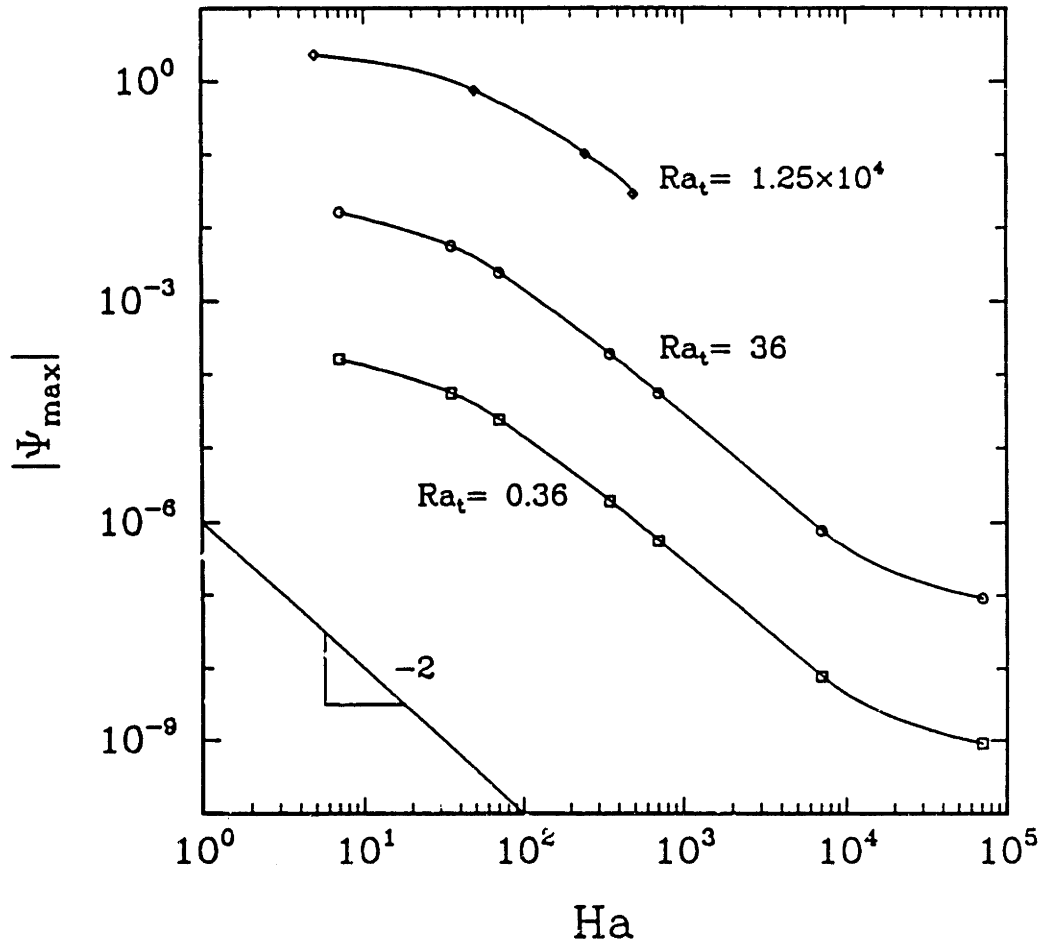


Figure 4.19: Variation of flow intensity with increasing Hartmann number predicted by finite element analysis rescaled as $\Psi_{\max} \sim Ha^{-2}$, as determined from asymptotic analysis in the limit $Ha \gg 1$.

Bridgman crystal growth system.

For example, the maximum in radial segregation in this system corresponds to the value of thermal Rayleigh number where the flow intensity of the cell closest to the interface changes slope as a momentum boundary layer begins to develop. The correspondence between the maximum in segregation and this flow transition also occurs in the constant gradient furnace. By contrast, transitions in the effective segregation coefficient in the heat-pipe system correspond more closely to changes in the intensity of the upper flow cell, instead of the lower cell. The lack of the upper flow cell in the constant gradient furnace makes this difference immaterial.

The predicted quality of the crystals described by these simulations is characterized by the curves in Figures 4.10 and 4.16 as a function of Ra_t and Ha . The radial segregation is lowest when either convection is unidirectional (Ra_t small or Ha large) or when the laminar mixing is intense enough to homogenize the melt adjacent to the interface. Growth with unidirectional convection is most desirable because of the axial uniformity of the crystal that results when no mixing is present. These conditions are not easily achieved in practice and careful analysis of growth conditions is necessary for optimum design of growth systems with moderate convection levels. On earth, unidirectional growth conditions can be reached for growth of small diameter crystals and magnetic fields, but these growth conditions are difficult to duplicate for larger crystals because of the excessively large fields involved. Then the strength of the magnetic field should be tuned to eliminate unwanted temporal fluctuations in the convection, but to leave intense laminar convection to mix solutes and modulate radial segregation.

Crystal growth in a low gravity environment is more promising. Here unidirectional growth conditions are achieved in small scale samples without an imposed magnetic field. The more intense convection caused by increasing sample size ($Ra_t \sim R_c^3$) can be eliminated by including a reasonably sized magnetic field in the microgravity experiment.

Chapter 5

Convection and Segregation in Vertical Bridgman Growth of Nondilute Alloy Semiconductors

5.1 Introduction

Crystal growth from the melt of $\text{Hg}_{1-x}\text{Cd}_x\text{Te}$ and other nondilute alloy materials is extremely challenging because of the myriad of transport processes that must be controlled for growth of crystallographically perfect and compositionally uniform crystals. Directional solidification in a closed ampoule has been the most developed technique, because the high vapor pressure of the HgCdTe melt (Schmit, 1983; Capper *et al.*, 1983; Jones *et al.*, 1983; Szofran and Lehoczky, 1984; Szofran *et al.*, 1984) requires extraordinary measures for confinement.

The vertical Bridgman crystal growth system used by Lehoczky and coworkers (Szofran and Lehoczky, 1984; Szofran *et al.*, 1984) is one of the best characterized experiments for growth of HgCdTe single crystals and is the focus of the analysis presented here. These researchers have grown small diameter (5 mm), long (~ 200 mm)

crystals from a thick quartz ampoule at extremely low growth rates ($\sim 0.1\mu\text{m/s}$). Measurements of the axial composition of CdTe along the boule correlate well with the profile for diffusion-controlled species transport in a pseudobinary alloy with the correct phase diagram (Szofran and Lehoczky, 1984).

Simultaneously with the diffusion controlled axial segregation, Szofran and Lehoczky (1984) reported large compositional nonuniformities of CdTe across the radius of the crystal. These two observations are in apparent contradiction; the diffusion-controlled axial redistribution of the alloy suggests convection in the melt is unimportant in species transport, whereas the large radial variations in composition are too large to be explained by the interaction of the interface shape with diffusion-controlled growth (Coriell and Sekerka, 1979; Coriell *et al.*, 1981).

The analysis of transport processes in vertical Bridgman growth of $\text{Hg}_{1-x}\text{Cd}_x\text{Te}$ presented here is directed at an explanation for the radial and axial segregation data presented in the works by Lehoczky and coworkers (Szofran and Lehoczky, 1984; Szofran *et al.*, 1984). We show that both data sets are explained by a detailed analysis of heat transfer, convection and species transport which accounts for thermosolutal convection in the melt and for the heat transfer mechanisms that dominate in the HgCdTe alloy system. The analysis presented here is a direct extension of our earlier calculations (Chang and Brown, 1983b; Adornato and Brown, 1987a; Kim *et al.*, 1988) of thermosolutal convection and solute transport in directional solidification to a prototype system for growth of HgCdTe alloys.

The analysis presented here is also useful in the experiments of Capper *et al.* (1983) for the growth of HgCdTe alloys in directional solidification systems with either a vertically stabilizing temperature field or an axial temperature profile that has a maximum in the melt. For larger radius ($R = 7.5 \text{ mm}$) crystals, Capper *et al.* reported axial segregation that was intermediate between diffusion-controlled growth and complete mixing. The extent of the mixing was a function of both the growth rate and the percent CdTe in the alloy. For the vertically stabilized temperature profile, decreased mixing in the melt is expected from either increasing the growth rate or increasing

the CdTe composition because of the effect of these variables on the magnitude of the diffusion-controlled solute gradient. Capper *et al.* reported that the radial composition variation decreased with decreasing growth rate, but increased with increasing CdTe composition. We will demonstrate that these responses to growth rate and composition can be explained entirely in terms of the degree of mixing in the melt caused by radial temperature gradients and the solutal damping of this flow caused by preferential incorporation of CdTe at the interface.

The details of heat, momentum and species transport important in design and control of vertical Bridgman crystal growth systems have been the subject of intense research over the last decade; most of the important concepts are reviewed by Brown (1988). For small-scale systems and pure melts with high thermal conductivities, conduction governs the heat transport in the melt and the shape of the melt/crystal interface. Then the shape of the interface and the temperature field in the melt is influenced primarily by changing the heat transfer from the furnace to the ampoule.

Control of the temperature field and melt/crystal interface shape in $\text{Hg}_{1-x}\text{Cd}_x\text{Te}$ is much more difficult because of the variation in the thermophysical properties with composition and because of the large difference in thermal conductivities between melt and crystal. The most important variation in the thermophysical properties with composition is the extremely large variation in melting temperature as the composition of the alloy changes (Kelly *et al.*, 1982), which is shown in Figure 5.1. The large separation between the liquidus and solidus curves leads to coupling between the interface shape and the local composition of the melt, so that the melting temperature and interface shape vary as the composition of the melt changes during growth.

The change in the location of the melting point of the alloy within the ampoule and the variation in the local crystal growth rate has been simulated numerically using one-dimensional, diffusion-controlled models for solute and heat transport (Clayton *et al.*, 1982; Bourret *et al.*, 1985; Derby and Brown, 1986). The inherently transient location of the melt/crystal interface and of the local solidification rate make the design of the heat transfer system much more difficult in nondilute alloy systems than in the growth

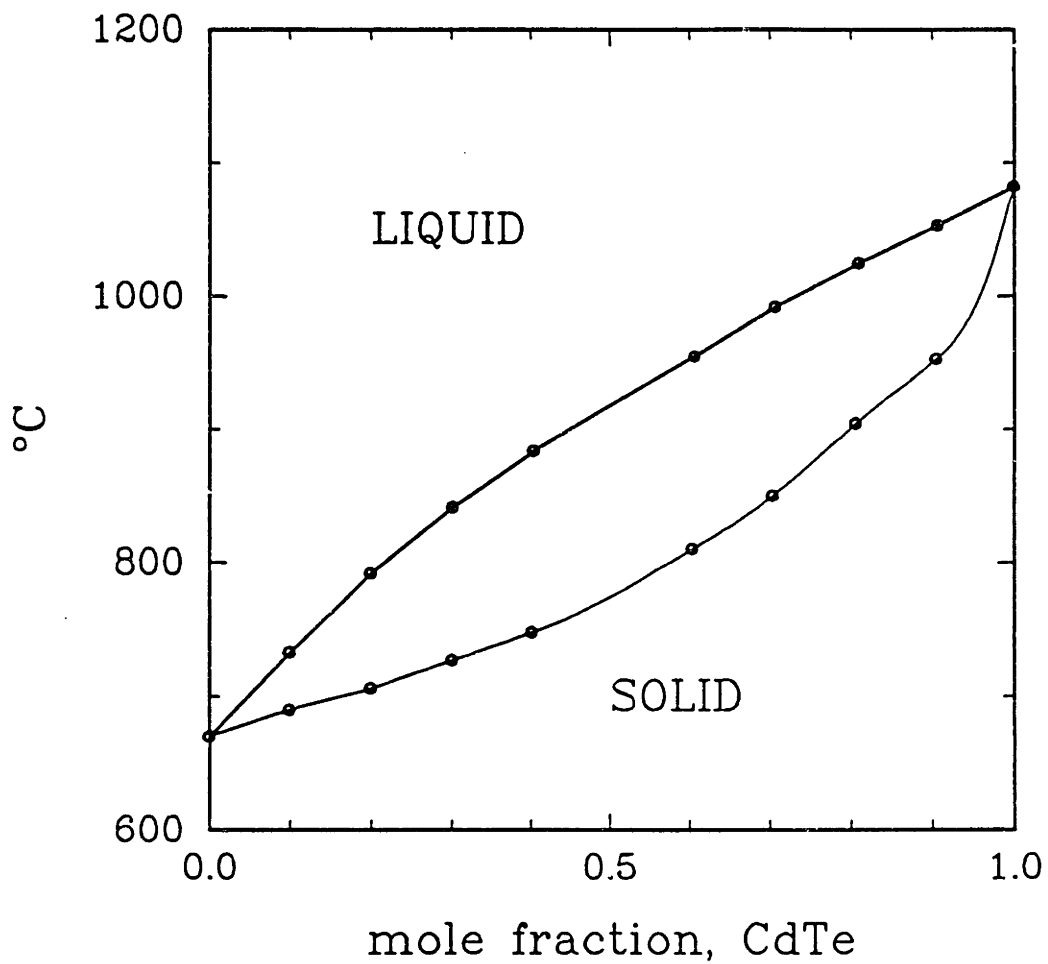


Figure 5.1: Phase diagram of pseudobinary HgCdTe (Szofran and Lehoczky, 1981).

of pure materials where the temperature field alone fixes the location of the interface.

In the pseudobinary representation of HgCdTe, the less dense component CdTe is preferentially partitioned into the crystal so that the axial density gradient is stably stratified when the crystal is below the melt. The diffusion-controlled solute transport observed along the growth axis is consistent with the idea that this density profile retards buoyancy-driven convection. Indeed, similar axial segregation profiles were reported by Rouzard *et al.* (1985) for the growth of a GeSi alloy which also has a vertically stabilized density profile. The dampening of buoyancy-driven convection by the solute profile in the GeSi system was clearly demonstrated in the calculations presented by Adornato and Brown (1987a) for thermosolutal convection with heat transfer boundary conditions set to model the same vertical Bridgman system.

Heat transfer in the HgCdTe system is far from one-dimensional near the melt/crystal interface, because of the factor of seven decrease in the thermal conductivity between the melt and crystal. This difference coupled with the very thick quartz ampoules that are used to withstand the high vapor pressure of the melt forces heat to flow from the melt into the ampoule and leads to highly curved melt/crystal interfaces. Naumann and Lehoczky (1983) and Jasinski *et al.* (1983) presented approximate two-dimensional conduction heat transfer calculations that demonstrated the large melt/crystal interface deflections expected because of the mismatch in thermal conductivities. More recently, Dakhoul *et al.* (1988) presented numerical calculations of conduction heat transfer that account more realistically for thermophysical properties of HgCdTe alloys.

The radial temperature gradients caused by this thermal conductivity difference and by other thermal imperfections in the crystal growth system are extremely important to understanding convection and species transport in the growth of nondilute alloys. This is especially true in systems such as HgCdTe and GeSi where the average density gradient is vertically stabilizing and convection must be initiated solely by thermal imperfections and radial gradients that result.

The calculations of Chang and Brown (1983b) demonstrated the strong effect of

the difference in thermal conductivities between melt and crystal on the direction and intensity of thermal convection in the melt. The analysis of convection and segregation in the vertical Bridgman system by Adornato and Brown (1987a) included heat transfer through the ampoule in calculations of the temperature and showed the generic structure for the axisymmetric flow driven by radial temperature gradients in the melt.

Two distinct toroidal roll cells stacked axially in the ampoule were computed and were driven by different sets of radial temperature gradients. Near the melt/crystal interface, the mismatch in the thermal conductivities of the melt, crystal and ampoule drives flow which is up along the center of the ampoule when the solidification interface is convex with respect to the melt, as it is drawn in Figure 5.2. Large radial temperature gradients are also caused by the mismatch in thermal boundary conditions at the junction of the hot zone with the insulation region (see Figure 5.2). These gradients lead to an upper toroidal cell in which melt moves upward along the sidewall and down along the axis of the ampoule. This flow cell is not present in directional solidification systems where the axial temperature gradient is established by tailoring the heater design in such a way that the radial temperature gradient has the same sign all along the melt; this is the case for the furnace used by Rouzaud *et al.* (1985) to grow GeSi. In either case, adding an axial magnetic field damps these convective flows and leads to diffusion-controlled crystal growth, albeit at high field levels (Kim *et al.*, 1988) for realistic crystal sizes.

The calculations described here show that the diffusion-controlled axial segregation and large radial nonuniformities seen in HgCdTe growth can be explained by the unique combination of radial temperature gradients and thermosolutal convection in this system. Here the large difference in the thermal conductivities between melt and crystal leads to large radial temperature gradients at the interface and drives a flow there that is so intense that it is not damped by the solute rejected during solidification. However, the extent of the buoyancy-driven convection is confined to the melt near the interface and convection higher in the ampoule is damped by the very long axial solute profile caused by the low growth rate. Then the solute field near the interface and the degree

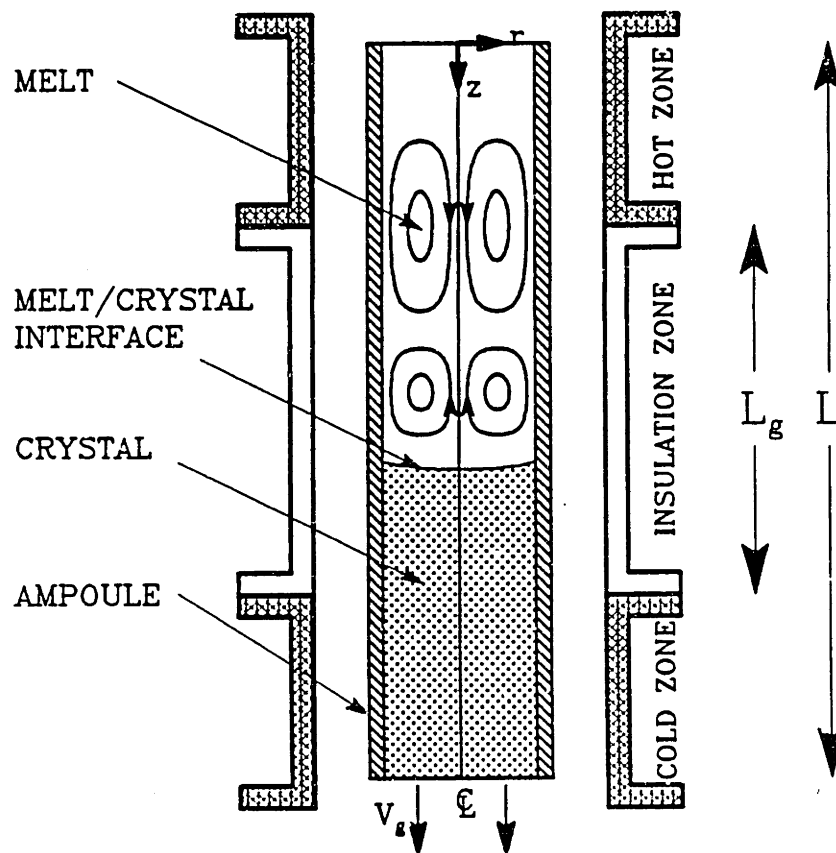


Figure 5.2: Schematic of prototypical vertical Bridgman crystal growth system.

of radial segregation is controlled by the poor mixing caused by the thermally-driven convection there and the axial segregation along the length of the crystal is governed by the nearly diffusive profile that exists over the length of the melt.

Interestingly, the flow in the region damped by the solute profile has the boundary-layer structure predicted by Hart's (1971) one-dimensional model for thermal convection driven by lateral temperature gradients in the presence of a linear, stabilizing solute field; this comparison is discussed in Section 5.3.2. Moreover, additional axial roll cells develop with increasing solute concentration as suggested by the sideways diffusive flow instability predicted by a linear stability analysis of the one-dimensional motion (Hart, 1971). Similar roll-cells were seen in calculations of thermosolutal convection in directional solidification (Adornato and Brown, 1987b) and in the analysis of the GeSi system by Adornato and Brown (1987a). We show in Section 5.3.1 that this instability causes multiple steady-states in the HgCdTe and leads to hysteresis in the radial segregation profiles in experiments.

The interaction between buoyancy-driven convection caused by radial temperature gradients and damping due to the vertically stabilizing solute field suggests a more complex dependence of radial and axial segregation on the crystal growth rate than is predicted by simple segregation models that neglect the interdependence of the intensity of convection on the solute profile caused by solute segregation. Higher growth rates should lead to increased axial solute gradients and more effective damping of thermal convection; therefore the intensity of the motion should be decreased. In addition, the higher growth rates decrease the residence time of solute in the melt adjacent to the interface, again decreasing the effectiveness of the mixing. This leads to lower axial segregation at higher growth rates, in agreement with the observation of Capper *et al.* (1983).

The response of radial segregation to the increase in growth rate depends on whether the system is closer to the diffusion-controlled or well-mixed limits; see Brown (1988) for a lengthy discussion of solute mixing and radial segregation. When good mixing is present near the interface, increasing the growth rate decreases the mixing and leads

to increased radial segregation, as is seen in the experiments of Capper *et al.* (1983). Damping weak convection by increasing the growth rate decreases radial segregation toward the diffusion-controlled limit, where radial segregation is caused solely by interface curvature.

The finite element calculations of solute segregation suggest a one-dimensional model for axial segregation of dopants that is an alternative to the diffusion-controlled and well mixed-limits used traditionally. We propose in Section 5.4 an alternate model that couples a well-mixed region limited to a region next to the interface to a diffusion-controlled bulk away from it.

5.2 Pseudo-Steady-State Model of Vertical Bridgman Growth of HgCdTe

The analysis presented here is for the prototypical model of the vertical Bridgman crystal growth system shown schematically in Figure 5.2. The model includes a cylindrical ampoule filled with melt and crystal positioned along the axis of a furnace which is composed of hot and cold regions separated by an insulated region. In the pseudo-steady-state model (PSSM) the translation of the ampoule is modelled by melt entering the top of the cylinder with uniform velocity V_g and composition c_0 and by removing the crystal from the ampoule bottom at a rate that conserves the mass of the material.

Modelling of the vertical Bridgman crystal growth system with the PSSM neglects the evolution of the system caused by the batchwise transient caused by the shrinking of the melt. Then the calculations discussed here cannot approximate changes in the location of the melt/crystal interface and the flow caused by the changing composition of the melt, except as a sequence of steady-state calculations with varying bulk solute concentrations.

The mathematical description of the equations and boundary conditions for convection and species transport of a nondilute binary alloy used here are identical to those

presented in Chapter 4. The field variables and interface shape are described in terms of the stationary axisymmetric cylindrical polar coordinate system (r, z) shown in Figure 5.2. The interface is represented by the shape function $z = H(r)$ and has the unit normal vector \mathbf{N} . Crystal growth is in the negative z -direction, which is represented by the unit vector \mathbf{e}_z .

Variables are put in dimensionless form by scaling lengths with the radius of the crystal R_c , velocity components with the momentum diffusion velocity ν/R_c , pressure with $\rho\nu^2/R_c$ and composition with c_o . Dimensionless concentration and temperature fields are defined as

$$S(r, z) \equiv c(r, z) - 1 \quad (5.1)$$

$$\theta(r, z) \equiv \frac{T(r, z) - T_{cold}}{T_{hot} - T_{cold}} \quad (5.2)$$

where T_{hot} and T_{cold} are the values of the hot and cold isothermal zones in the Bridgman furnace. The location of the melt/crystal interface is described by the function $H(r)$ and is computed with the field variables so that the energy balance along the interface and the condition for the melting point isotherm are satisfied. Axisymmetric convection in the melt is modelled by the Boussinesq equations which are written in dimensionless form as

$$\nabla \cdot \mathbf{v} = 0 \quad (5.3)$$

$$\mathbf{v} \cdot \nabla \mathbf{v} = -\nabla p + \nabla^2 \mathbf{v} + \frac{1}{Pr} \{Ra_t S - Ra_t(\theta - 1)\} \mathbf{e}_z \quad (5.4)$$

$$Pr \mathbf{v} \cdot \nabla \theta = \nabla^2 \theta \quad (5.5)$$

$$Sc \mathbf{v} \cdot \nabla S = \nabla^2 S \quad (5.6)$$

where ∇ is the gradient operator in cylindrical coordinates and the Schmidt (Sc) and Prandtl (Pr) numbers are defined in Table 5.1. The definitions of the thermal and solutal Rayleigh numbers are given in Table 5.1 and scale the magnitudes of the thermal and solutal components of the buoyancy driving force, respectively.

The energy equations in the crystal and ampoule are identical to Eqs. (4.17) and

Name	Symbol	Definition	Value
Thermal Rayleigh number	Ra_t	$g\beta_t\Delta TR_c^3/(\alpha_m\nu)$	2.1×10^4
Solutal Rayleigh number	Ra_s	$g\beta_s c_o R_c^3/(\alpha_m\nu)$	-4.4×10^4
Modified			
Solutal Rayleigh number	Ra_s^*	$Ra_s Pe_s(1 - k)/k$	2.5×10^3
Thermal Peclet number	Pe	$V_g R_c/\alpha$	5×10^{-4}
Solutal Peclet number	Pe_s	$V_g R_c/D$	0.092
Prandtl number	Pr	ν/α_m	0.11
Schmidt number	Sc	ν/D	19.6
Stefan number	St	$\Delta H_s/C_{p,m}\Delta T$	1.4
Thermal diffusivity ratio	γ	α_s/α_m	0.27
Density ratio	σ	ρ_s/ρ_m	1.0

Table 5.1: Definitions of dimensionless groups that appear in analysis of thermosolutal convection of HgCdTe crystal growth; characteristic values computed from the thermo-physical properties of HgCdTe are also shown.

(4.18) in Chapter 4. The condition for the interface to correspond to the slope of the liquidus curve for a binary mixture and the energy balance at the melt/crystal interface are given by:

$$\theta(r, H(r)) = \theta_m(S) = \theta_m^o + m(S + 1 - 1/k) \quad (5.7)$$

$$[\mathbf{N} \cdot \nabla \theta]_m - K_c [\mathbf{N} \cdot \nabla \theta]_c = St Pe (\mathbf{N} \cdot \mathbf{e}_z) \quad (5.8)$$

where the liquidus curve has been approximated by a straight line with dimensionless slope m and θ_m^o is the melting point of the alloy with concentration c_o/k . We assume that m and the segregation coefficient k are independent of concentration. Parameters appearing in the interfacial energy balance, Eq. (5.8), are the ratio of thermal conductivities $K_c \equiv k_s/k_m$, the Stefan Number St and the thermal Peclet number Pe based on the solidification rate V_g ; these parameters are defined in Table 5.1. The capillary correction to the melting temperature has been ignored in Eq. (5.7). This is justified as long as the length scale associated with the interface shape is not comparable to the scale for morphological instability.

The interfacial balance for the dilute solute is written as

$$[\mathbf{N} \cdot \nabla S] = \frac{Pe Sc}{Pr} (\mathbf{N} \cdot \mathbf{e}_z) (1 - k)(S + 1) \quad (5.9)$$

where Sc is the Schmidt number. The specification of the thermal boundary conditions between the ampoule and the surrounding furnace is also discussed in Chapter 4 and are identical for the calculations presented here.

The free-boundary problem with convection is solved by the same finite element/Newton analysis discussed in Chapter 3. A mesh of 20 radial elements in the melt and 4 in the ampoule with an axial approximation using 48 elements in the melt and 16 in the crystal was used in most of the calculations described here. This discretization leads to set of 24,085 equations that are solved by Newton's method. Accurate calculations at high values of Ra_s require resolution of the thin boundary-layers described in Section 5.3.2. A second discretization with ten extra radial elements (33,945 total unknowns) distributed close to the ampoule wall was used for calculations with

| Ra , $> 1 \times 10^3$. Arc length continuation methods (Yamaguchi *et al.*, 1984) based on the thermal and solutal Rayleigh numbers are used to increment the calculations from one parameter set to another; details are found in Chapter 3.

The calculations presented here are much simplified by assuming that $Hg_{1-x}Cd_xTe$ alloys can be modelled as a dilute pseudobinary materials and that the thermophysical properties and equilibrium constants have constant values that are independent of composition and temperature. This is an extreme simplification. Measurements of the phase diagram (Kelly *et al.*, 1982; Szofran and Lehoczký, 1981, 1983), thermal diffusivity (Holland and Taylor, 1983), and heat capacity (Su, 1986) show very strong dependencies on composition and temperature. These variations will need to be accounted for a quantitative analysis of the alloy redistribution during a batchwise growth experiment, but can be neglected in the more phenomenological analysis presented here.

The properties used in this analysis were compiled by Professor B. Antar (1988) and are listed in Table 5.2, along with the characteristic values for the dimensionless groups that appear in the field equations. The values of the properties have been estimated as those of a $x = 0.20$ mole fraction CdTe in alloy composition. The knowledge of the thermophysical properties is incomplete; for example, the viscosity of HgCdTe melts is unknown and the value of kinematic viscosity listed in Table 5.2 is only an approximation.

The crystal growth rate for the simulations is taken as $0.25 \mu\text{m/s}$ and is representative of the value used in the experiments (Szofran *et al.*, 1984). For diffusion-controlled crystal growth, this value leads to an exponential solute concentration layer that extends over ten crystal radii from the interface, and thus well into the hot zone of the furnace. The axial solute gradient is approximately constant for a distance of two crystal radii above the interface; this fact will be used in the discussion of the flow structure in Section 5.3.2.

The calculations presented here are modelled after the vertical Bridgman system of Szofran *et al.* (1984). The dimensions of the ampoule and the thermophysical properties

Quantity	Symbol (units)	Value
Thermal conductivity of the melt	k_m (W/°C·cm)	2.0×10^{-2}
Thermal conductivity of the solid	k_s (W/°C·cm)	2.9×10^{-3}
Density of the melt	ρ_m (g/cm ³)	7.6
Density of the solid	ρ_s (g/cm ³)	7.6
Specific heat of the melt	$C_{p,m}$ (J/°C·g)	0.26
Specific heat of the solid	$C_{p,s}$ (J/°C·g)	0.18
Melting temperature	T_m (°C)	800
Slope of the liquidus curve	\bar{m} (°C/mole frac. CdTe)	505
Kinematic viscosity	ν (cm ² /sec)	0.0011
Heat of solidification	ΔH_s (J/g)	130
Thermal expansion coefficient	β_t (°C ⁻¹)	8.0×10^{-5}
Solutal expansion coefficient	β_s ((mole frac. CdTe) ⁻¹)	-0.31
Diffusion coefficient of CdTe in HgCdTe	D (cm ² /sec)	5.5×10^{-5}
Equilibrium distribution coefficient of CdTe	k	2.6

Table 5.2: Thermophysical property data used in analysis of HgCdTe growth.

used in the simulation to model it are described in Table 5.3. We include only conduction in the quartz ampoule in the analysis and assume that heat transfer between the ampoule and the furnace is by radiation and convection. The effective heat transfer coefficients used to transport heat between these elements are computed in the same way described in Chapter 4.

5.3 Analysis of Flow Structure and Radial Segregation

5.3.1 Effect of Solutal Field on Flow

The interaction of the solute field with thermosolutal convection driven by the radial temperature gradients is best exemplified by calculations at fixed thermal Rayleigh number, Ra_t , and decreasing solutal Rayleigh number, Ra_s . Because the dimensionless liquidus slope, m , is held fixed, this sequence of calculations does not correspond to varying the solute concentration, but is strictly equivalent to examining alloys with different values of the coefficient of solutal expansion β_s .

The temperature, solute concentration, melt density and stream function fields are shown in Figure 5.3 for the reference case of an alloy without solutal convection, but in the same ampoule and furnace; $Ra_t = -2 \times 10^4$ and $Ra_s = 0$. The isotherms have extremely large deflections near the melt/crystal interface caused by the difference in the thermal conductivities; the interface deflection is a half of the crystal radius. The radial temperature gradients caused by the mismatch in thermal boundary conditions at the junction of the hot and insulation zones is barely noticeable from these contours because this discontinuity is almost completely modulated by heat transfer through the thick ampoule. The temperature field shown in Figure 5.3 is almost identical to the field for conduction-dominated transport computed for $Ra_t = Ra_s = 0$. No other temperature fields are shown in the analysis presented here because there is very little variation from the result in Figure 5.3.

The flow driven by these two sets of temperature gradients has the two cell structure

Parameter	Value
Ampoule length, L (cm)	2.0
Crystal radius, R_c (cm)	0.2
Ampoule outer radius, R_a (cm)	0.4
Gradient zone length, L_g (cm)	0.56
Temperature difference, $T_h - T_c$ (°C)	375
Growth velocity, V_g ($\mu\text{m}/\text{sec}$)	0.25
Ampoule material	fused silica
Thermal conductivity of ampoule, K_a (W/°C·cm)	0.025
Density of ampoule, ρ_a (g/cm ³)	2.2
Specific heat of ampoule, $C_{p,a}$ (J/°C·g)	0.77

Table 5.3: Thermophysical data for ampoule and system geometry.

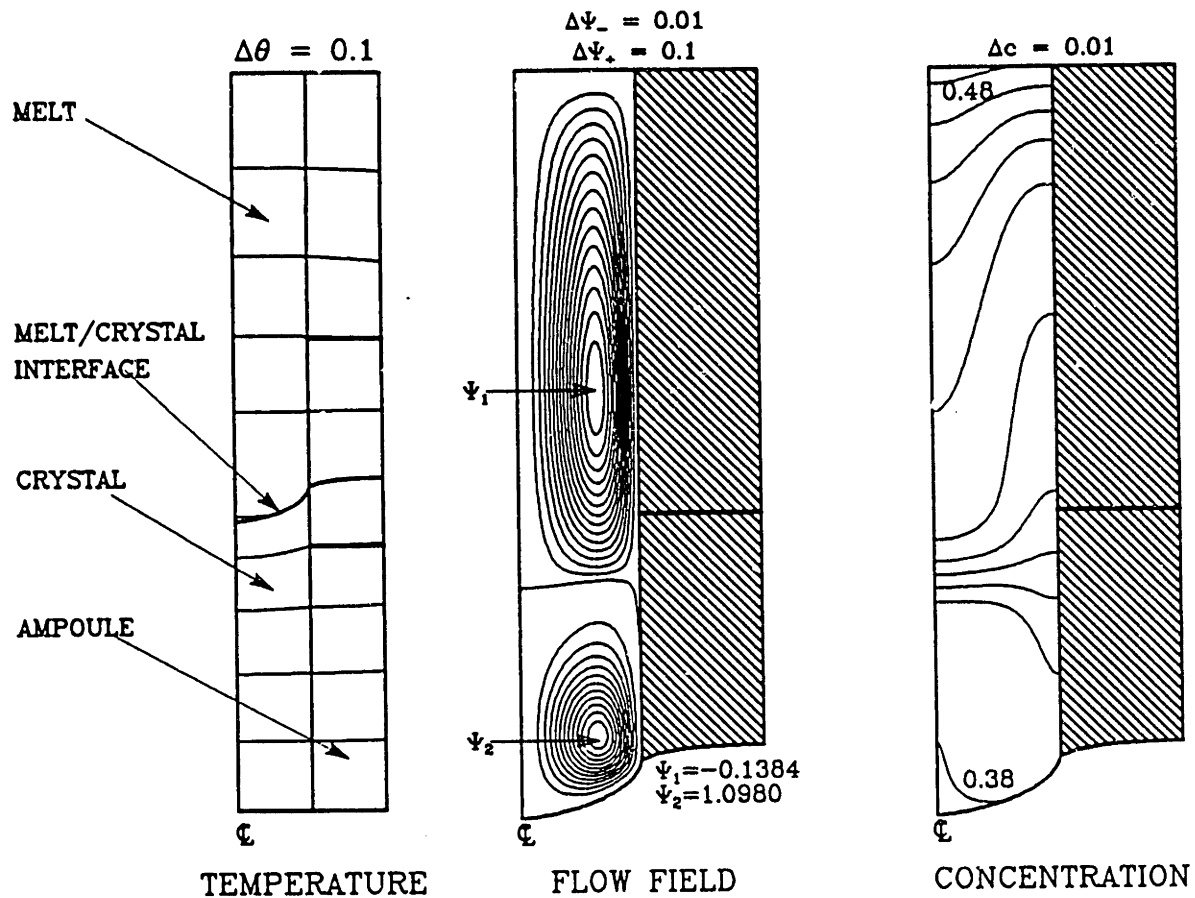


Figure 5.3: Sample isotherms, stream function and solute contours for thermophysical properties of HgCdTe listed in Tables 5.1 and 5.2, except that $Ra_s = 0$. Streamlines are spaced at equal intervals between maximum (or minimum) for flow cells and zero.

that we have shown to be generic for vertical Bridgman systems, although the lower flow cell is much more intense than the upper one. The concentration field shows the distorted contours that are characteristic of incomplete mixing by convection in small-scale growth systems. Higher convection levels, e.g. larger values of Ra_t , would lead to two almost totally mixed concentration regions separated by a thin diffusion layer at the junction of the two cells, as reported by Adornato and Brown (1987b).

Decreasing the solutal Rayleigh number Ra_s from zero leads to damping of convection by the composition field. Calculations to demonstrate this effect have been performed for decreasing Ra_s and are summarized by the plots of the flow intensity and the percentage of radial segregation Δc shown in Figures 5.4 and 5.5, respectively. In Figure 5.4, the points denoted by the symbols (\bullet), (\times) and (\square) show the positions of the solutions shown in Figures 5.6, 5.7 and 5.8, respectively. The intensity of the flow is documented by the circulation rates of the lower and upper flow cells. The measure of radial segregation Δc is defined as the difference between the percentage of the maximum and minimum concentration levels at the interface divided by the average interfacial value.

Several phenomena are important. First the decrease in the intensity of the flow is most pronounced in the upper cell where the radial temperature gradients are lower. The lower cell is affected by the solutal damping only at high values of Ra_s which are closest to the values appropriate for the system with $x = 0.2$ listed in Table 5.2. At very high values of Ra_s diffusion-controlled solute segregation is expected because of solutal damping of convection throughout the flow. This state is difficult to compute because of the formation of thin boundary-layers along all solid surfaces in the system. The structure of these layers is discussed in Section 5.3.2.

The amount of radial segregation in the diffusion-controlled growth state is estimated from the computation for $Ra_t = Ra_s = 0$ as $\Delta c = 7.62\%$. This value agrees well with the approximate solution of Coriell and Sekerka (1979) for a slightly deformed interface. This asymptotic analysis leads to an approximation for the dimensionless

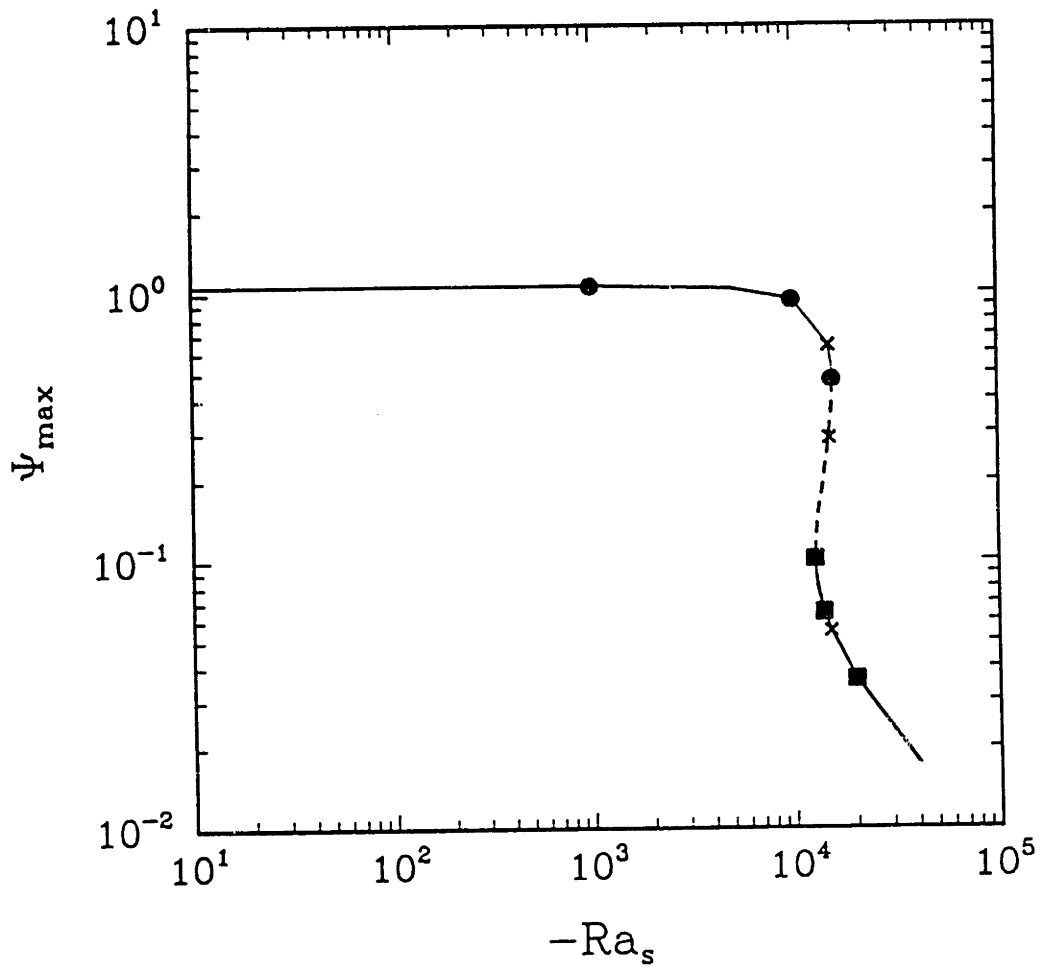


Figure 5.4: Flow intensity for lower flow cell (Ψ_{max}) as a function of solutal Rayleigh number Ra_s . All other parameters are fixed at the values listed in Tables 5.1 and 5.2.

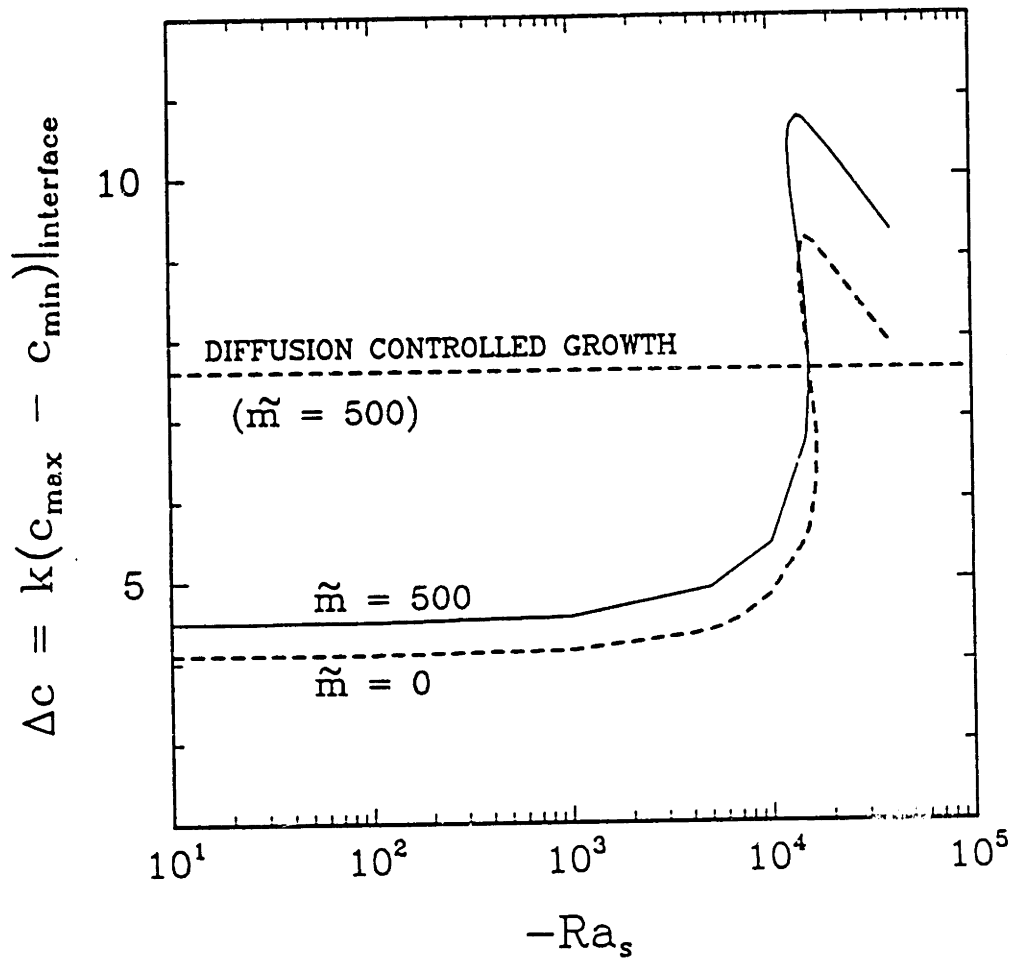


Figure 5.5: Radial segregation Δc as a function of solutal Rayleigh number Ra_s . All other parameters are fixed at the values listed in Tables 5.1 and 5.2.

radial segregation across the interface given by

$$\Delta c = \left[-\frac{Pe Sc}{Pr}(1 - k)\Delta H + \mathcal{O}(\Delta H^2) \right] \times 100\% \approx 8\% \quad (5.10)$$

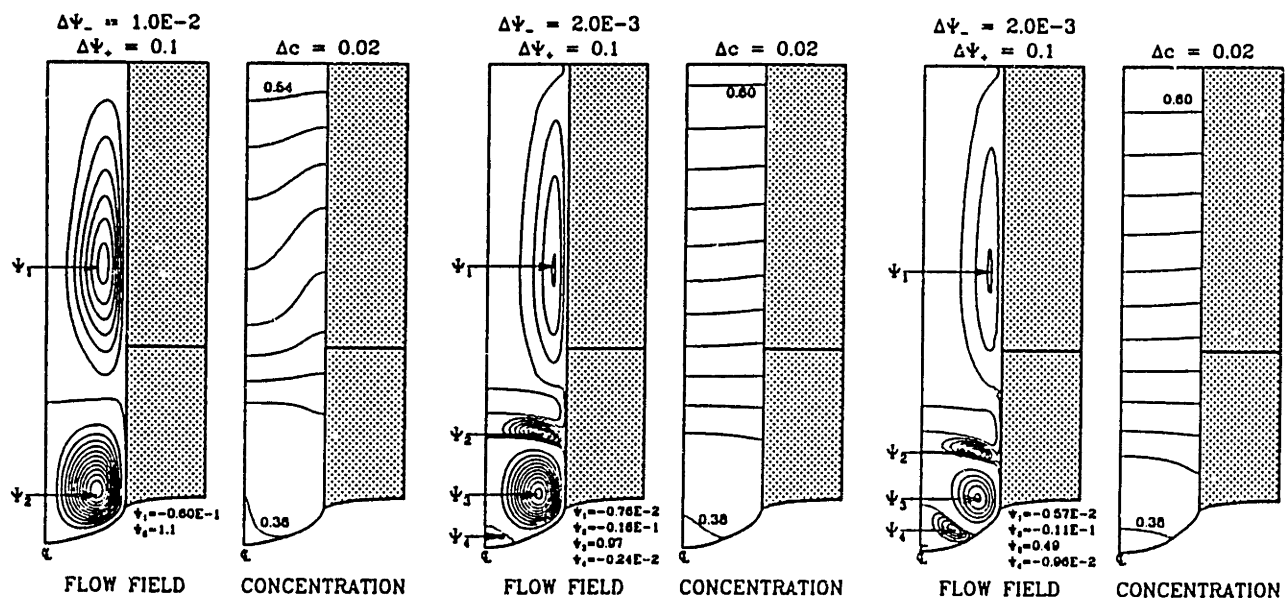
where $\Delta H \simeq 0.5$ is the dimensionless deflection of the melt/solid interface.

An important observation is that there is not a unique set of flow states computed with decreasing Ra_s , *i.e.* increasing solute stabilization. As shown in Figure 5.4, flow hysteresis is predicted, as exemplified by the existence of the two limit points. For a range of Ra_s , three flow states are predicted to exist. From elementary ideas about the link between flow stability and bifurcation of steady-state solutions the flows between the two limit points (dashed portion of the curve in Figure 5.4) are shown to be unstable and the other two states are stable (Yamaguchi *et al.*, 1984). The cause of the hysteresis is evident from the flow fields and is discussed below.

Sample flow states leading to the first limit point with decreasing Ra_s , are shown in Figure 5.6. Several features deserve mentioning. The damping of the flow by solute field is first apparent in the upper flow cell for $Ra_s = -1 \times 10^3$ by the tendency of the composition field to approach the diffusion-controlled state. The formation of an exponential profile that is almost radially uniform is complete by $Ra_s = -5 \times 10^3$ everywhere except in the region occupied by the lower flow cell. The flow and solute segregation in the region adjacent to the interface remains unchanged down to $Ra_s = -1 \times 10^4$, beyond which the flow begins to be damped.

The upper flow cell becomes weaker and the center moves toward the ampoule wall as Ra_s is decreased. The movement of the center of the cell and the flattening of the streamlines adjacent to the wall denote the formation of a thin boundary-layer there; this layer is discussed in Section 5.3.2.

For $Ra_s < -1 \times 10^3$ secondary flow cells form between the upper and lower flow cells. Similar cells have been seen in the calculations reported by Adornato and Brown (1987a) for the GeSi system and have been attributed to the sideways diffusive instability discussed by Hart (1971). Here an almost parallel flow driven by lateral temperature



(a) $Ra_s = -1 \times 10^3$

(b) $Ra_s = -1 \times 10^4$

(c) $Ra_s = -1.57 \times 10^4$

Figure 5.6: Streamlines and isoconcentration contours for calculations with decreasing Ra_s , up to the first limiting value $Ra_s^{(1)} \approx -1.57 \times 10^4$; $Ra_t = 2 \times 10^4$.

gradients and counter-balanced by a vertically stabilizing solute gradient becomes unstable to the tendency of vertically-stacked secondary cells to form composition layers in the flow. In a perfect parallel flow these cells form as abrupt transitions at bifurcations from the base state as Ra_s is decreased. We postulate the imperfections of our flow from a perfectly parallel motion lead to the breaking of these bifurcations as described by imperfect bifurcation theory and to the continuous evolution of the flow to one with secondary cells.

The limit points in the family of states found at $Ra_s \approx -1.5 \times 10^4$ can be interpreted in terms of this imperfection as an indication that the bifurcation from the parallel flow is subcritical in terms of Ra_s , *i.e.* the flows with secondary cells evolve to higher values of Ra_s until a second critical point, such as $Ra_s = Ra_s^{(2)}$ is reached where the states turn back to decreasing values of the parameter. The three flow states that co-exist for $Ra_s^{(1)} \leq Ra_s \leq Ra_s^{(2)}$ are shown in Figure 5.7. The states differ only in the number and intensity of the small flow cells that are stacked near the interface. The intensity of all these cells decreases along the transition from the lower to the upper branches. Moreover, the small region of well-mixed melt adjacent to the interface disappears along this transition. By comparison, the flow state on the lower branch in Figure 5.7 has this well-mixed core, whereas the one on the upper branch does not.

Flow fields and concentration fields computed for $Ra_s \leq Ra_s^{(2)}$ are shown in Figure 5.8. The two-cell structure of these flows is relatively unchanged with increasing solutal damping, although both cells are damped with decreasing Ra_s . We return to the asymptotic analysis of the structure of these flows in the next sub-section.

The evolution of the flow structure with varying concentration (Ra_s) has a profound effect on the radial segregation in the crystal, as shown by the plots of $c(r, H(r))$ in Figure 5.9. A *gull-wing* shaped segregation profile results for weak solutal damping ($|Ra_s| \leq 1 \times 10^3$) and becomes more pronounced as the first secondary flow cell forms adjacent to the interface and along the centerline (*e.g.*, $Ra_s = -1.5 \times 10^4$). Increased solutal damping decreases the influence of the flow structure on solute transport and

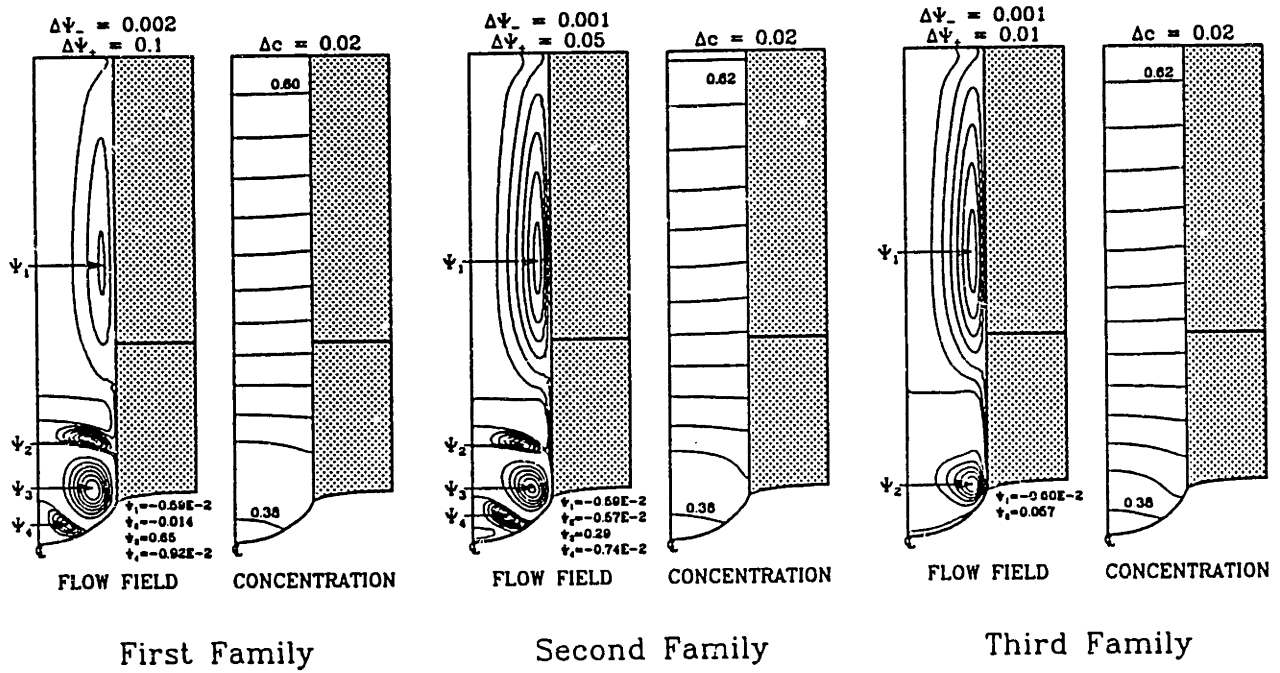


Figure 5.7: Streamlines and isoconcentration contours for three flow states that co-exist at $Ra_s = -1.5 \times 10^4$ with all other parameters held fixed.

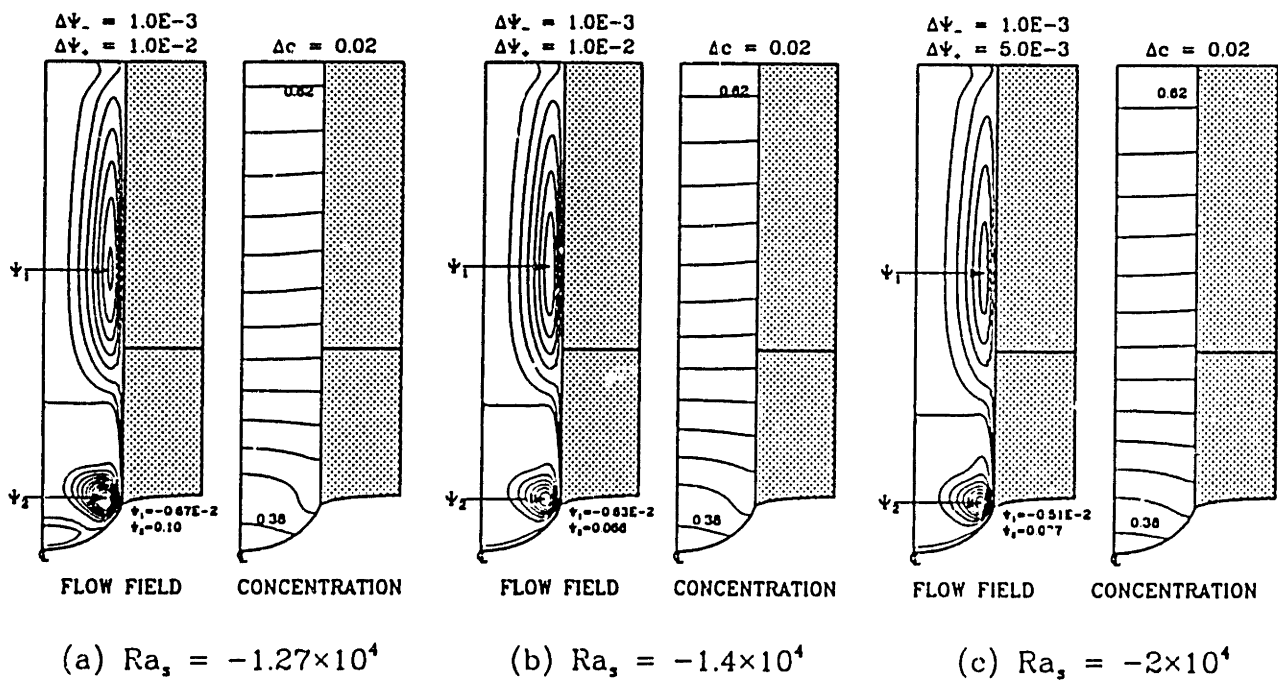


Figure 5.8: Streamlines and isoconcentration contours for calculations with decreasing Ra_s , from the second limiting value $Ra_s^{(2)} \approx -1.27 \times 10^4$; $Ra_t = 2 \times 10^4$.

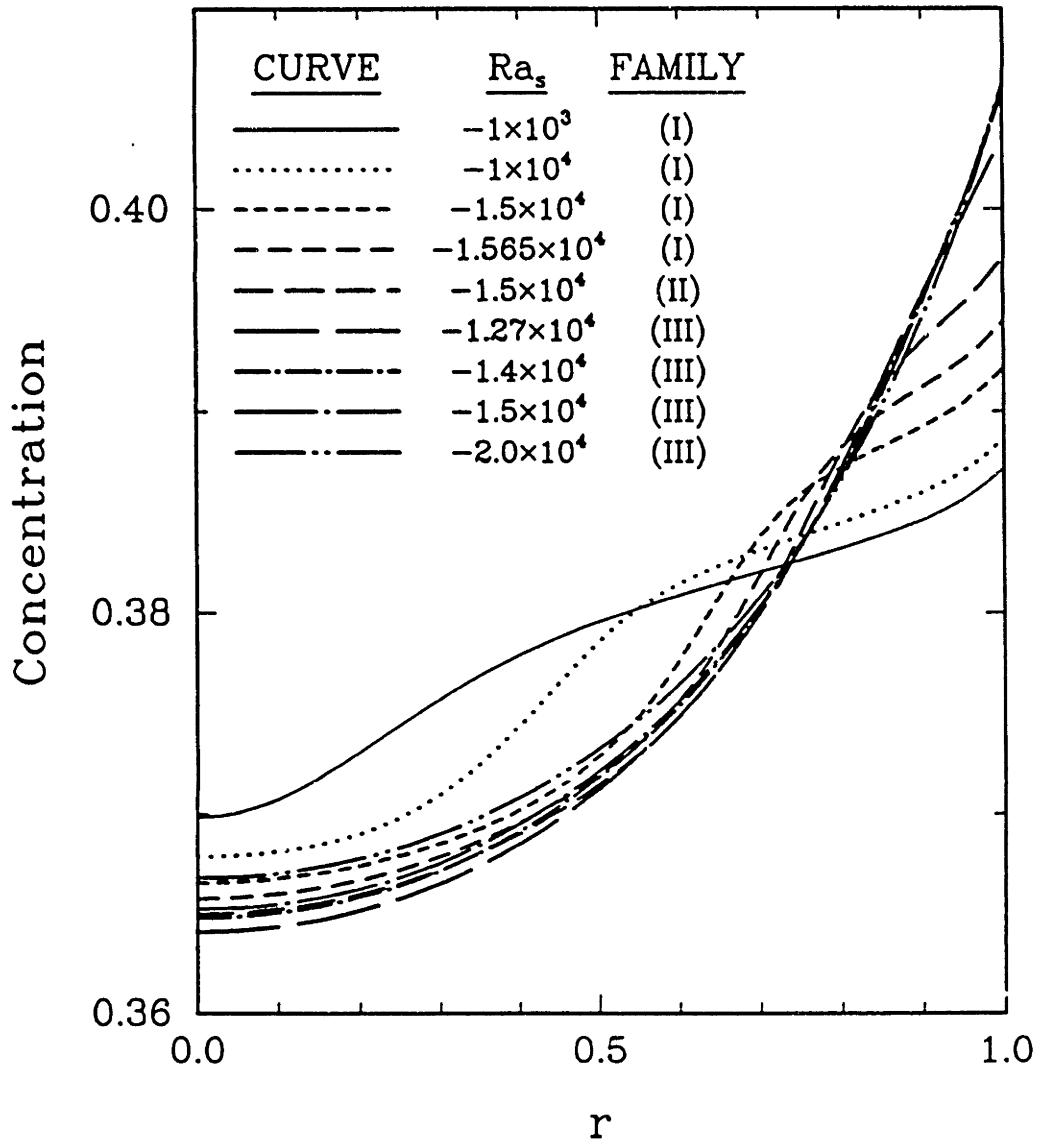


Figure 5.9: Variation of dimensionless concentration of CdTe along the melt/crystal interface for varying Ra_s , with $Ra_t = 2 \times 10^4$.

leads to convex radial segregation profiles that have the same form as the diffusion-controlled result. The increased radial segregation with decreasing Ra_s is very evident in these profiles.

The effect of the flow structure on the segregation profile is not mimicked by the interface morphology, as is demonstrated by the plots of the interface shape for varying Ra_s in Figure 5.10. Changes in the interface shape caused solely by the flow and solute field are only found for the most intense convection levels, corresponding to the lowest magnitudes of Ra_s . The interface shape is approximately constant when the solutal damping becomes significant.

5.3.2 Flow Structure with Solute Damping

The damping of convection in the upper flow cell and the formation of the boundary-layer in the axial component of the velocity along the ampoule surface can best be understood by comparison of the calculations in Section 5.3.1 with a simple, boundary-layer analysis first described by Hart (1971). The discussion here focusses on the fluid mechanics of the boundary-layer and on the scalings implied for the flow.

The flow in the region of the melt with the almost constant solute gradient is divided into a core and a boundary-layer near the ampoule wall. In the core, the momentum balance, Eq. (5.4), is assumed to be controlled by a balance of the solutal and thermal components of the buoyancy force. Then the temperature field is essentially the conduction field and the solute field is the radially constant solution for diffusion-controlled growth. Near the wall the momentum balance must include viscous forces so that the no-slip condition on the solid surface is satisfied. Assuming that this layer is thin for $|Ra_s| \gg 1$ and $Ra_t = \mathcal{O}(|Ra_s|)$ leads to equations for the local variation in the solute and velocity fields.

Forcing the viscous and buoyancy terms in the momentum equation and the axial convective and radial diffusive fluxes of solute in the solute balance to be of equal magnitude leads to a boundary-layer thickness that scales as $Ra_s^{-1/4}$ and to axial and

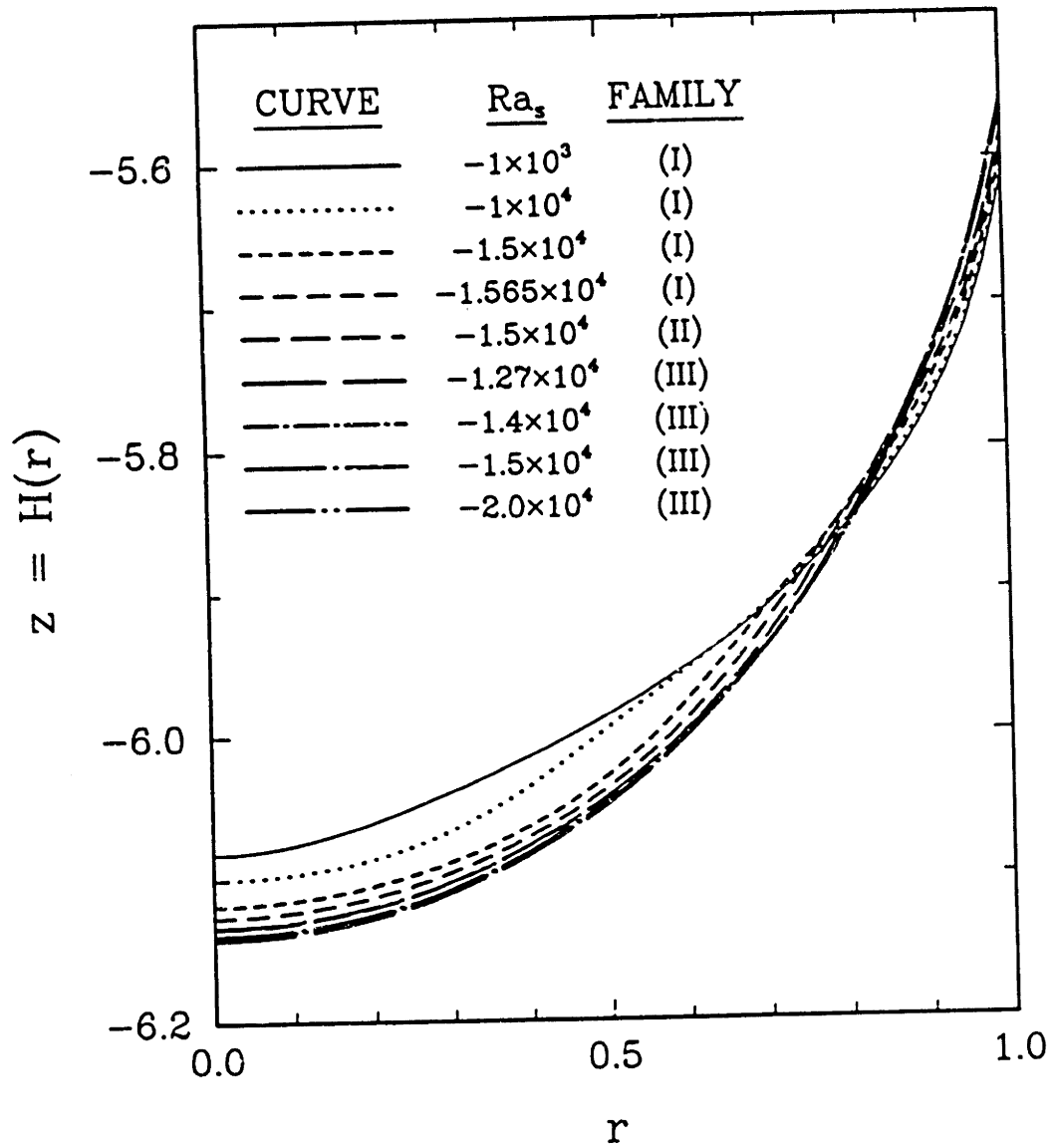


Figure 5.10: Variation of melt/crystal interface shapes for varying Ra_s , with $Ra_t = 2 \times 10^4$.

radial velocity components that vary as $Ra_s^{-1/2}$. This boundary-layer feeds the upper circulation in the melt and implies that the circulation rate in this cell scales as $Ra_s^{-3/4}$.

The scalings predicted for the thermosolutal boundary-layer analysis were compared to the finite element simulations with extra elements added to resolve the radial variations close to the ampoule wall. The comparison between the magnitude of the recirculation in the upper flow cell $\Psi_{min} = \Psi_{min}(Ra_s)$ and the scaling $Ra_s^{-3/4}$ predicted by the asymptotic analysis is shown in Figure 5.11 for $Ra_t = 2 \times 10^4$. The comparison is extremely good for large $|Ra_s|$.

A direct comparison of the axial velocity profile near the ampoule wall for fixed z is a more demanding test of the boundary-layer theory and calculations. The profile of the scaled axial velocity $v_z^* = [v_z(\eta, z) - Pe/Pr] |Ra_s|^{1/2}$ is shown in Figure 5.12 as a function of the stretched radial coordinate $\eta = (1 - r) |Ra_s|^{1/4}$ near the wall and the axial location parallel with the center of the upper flow cell. Note that the uniform component of the velocity caused by growth has been subtracted from v_z before rescaling Ψ_{min}^* in Figure 5.11 and v_z^* in Figure 5.12 because this portion of the motion is unaffected by the solutal damping. The profiles superimpose for the largest values of $|Ra_s|$, thereby indicating that the scales for v_z and r are determined correctly from the boundary-layer analysis.

5.3.3 Effect of Growth Rate

The magnitude of the solute gradient in the melt that leads to damping of convection is coupled to the solidification rate Pe through the dependence on Pe of the diffusion-controlled profile. Accordingly, the effective solutal Rayleigh number Ra_s^* that is a better measure of this driving force is

$$Ra_s^* = Ra_s \left| \frac{\partial S}{\partial z} \right| \approx Ra_s Pe_s \frac{1 - k}{k} = \frac{g\beta_s c_o R_c^4 V_g}{\alpha \nu D} \frac{1 - k}{k} \quad (5.11)$$

The damping of the flow expected because of modest increases in the growth rate

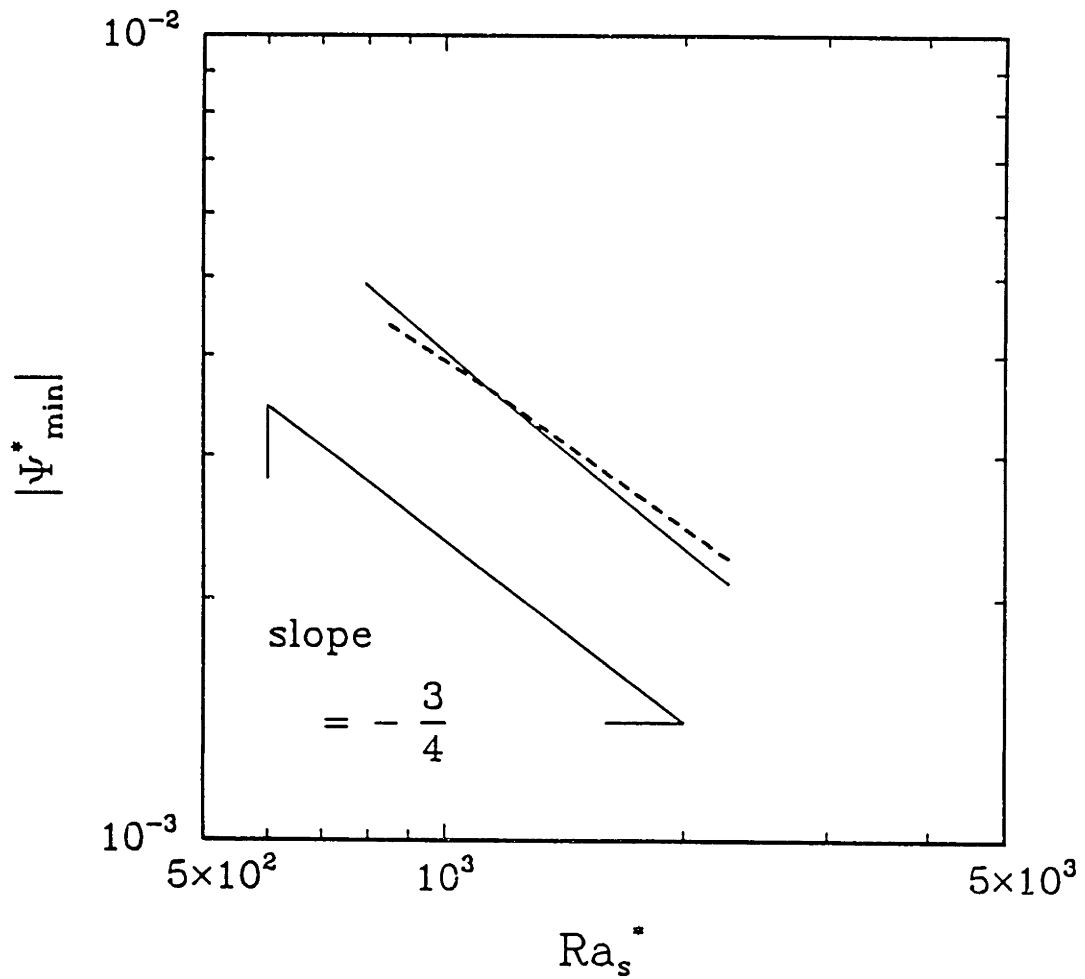


Figure 5.11: Dependence of the circulation rate in the upper flow cell on the modified solutal Rayleigh number Ra_s^* . Results are shown that were obtained with increasing Ra_s , (—) and with increasing the dimensionless crystal growth rate Pe (- - -).

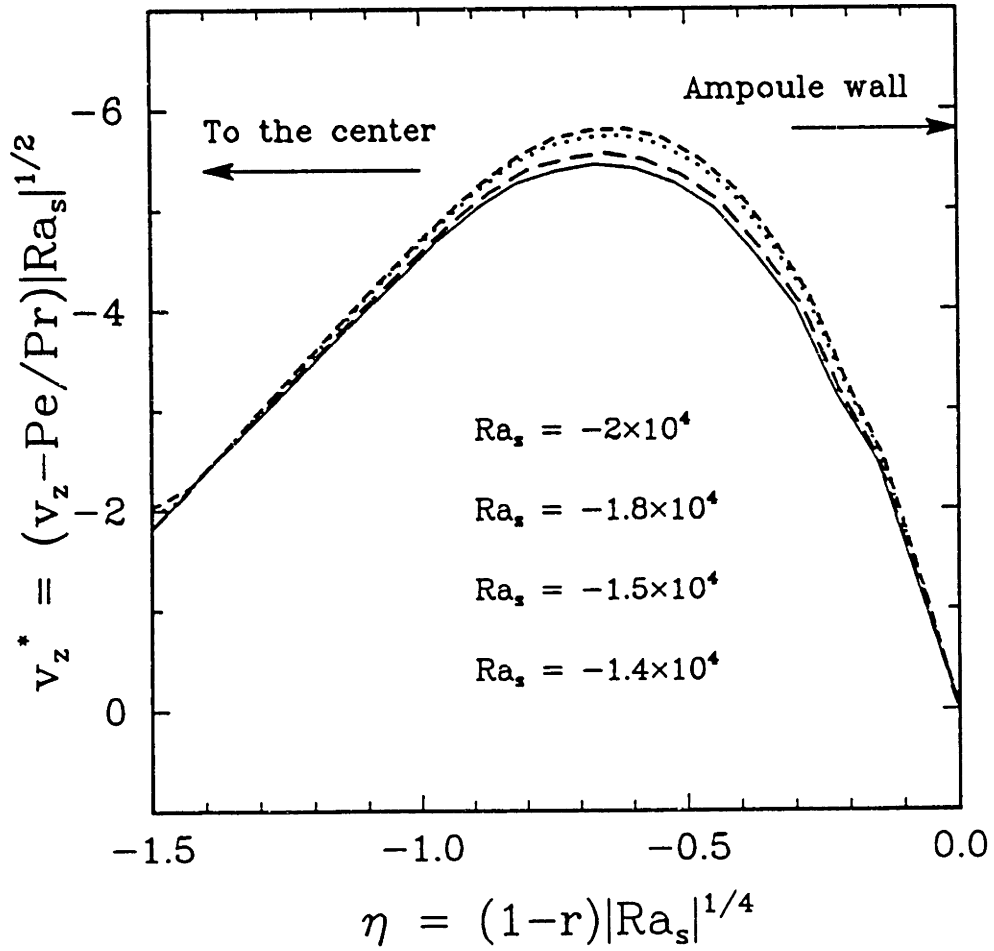


Figure 5.12: Radial variation of the axial velocity near the ampoule wall in the scaled variables predicted by the analysis of the thermosolutal boundary-layer. Results for increasing Ra_s show convergence to the boundary-layer scaling.

Pe is demonstrated in Figure 5.13. The intensity of the motion in both the top and bottom cells is decreased by simply increasing the growth rate. The top cell conforms more to the boundary-layer structure for the higher value of Pe , where Ra_s^* is highest. The flow intensities for the upper cell predicted for varying Pe are plotted on Figure 5.11 as a test of whether Ra_s^* represents the correct scaling for the solute damping. The agreement between these results and the scaling predicted from the asymptotic analysis verifies this hypothesis.

5.3.4 Effect of Microgravity

The undesirable radial segregation and flow hysteresis demonstrated in Section 5.3.1 can be removed by crystal growth in a microgravity environment. However, the benefit of a moderate reduction in the magnitude of the gravitational acceleration on thermal convection is modulated by a corresponding decrease in the role of solute damping of this motion. This effect is demonstrated by calculations presented in Figure 5.14 for an order-of-magnitude lower value of Ra_t (2×10^3) and a range of Ra_s .

The intensity of the circulation decreases nearly an order-of-magnitude over the result for $Ra_t = 2 \times 10^4$; however, the asymptotic region where $|Ra_s|$ is large enough that the flow has the boundary-layer structure described in Section 5.3.2 still occurs only when $|Ra_s| > Ra_t$. Because decreasing gravity affects each mechanism identically, there is no increased role of solute damping.

As we have demonstrated several times (Chang and Brown, 1983b; Adornato and Brown, 1987a; Kim *et al.*, 1988), environments with only slight reductions in gravity may not lead to improved compositional uniformity for the crystal. This is demonstrated here by the dependence of the radial segregation for $Ra_t = 2 \times 10^3$ and 2×10^4 for a range of values of Ra_s , shown in Figure 5.15. Both systems show peaks in Δc for $|Ra_s| \approx Ra_t$ that are larger than the values for diffusion-controlled growth ($Ra_t = Ra_s = 0$). These peaks correspond to the loss of mixing of solute in the flow cell adjacent to the interface. Because this interface is extremely curved, mixing in this cell is essential for low radial

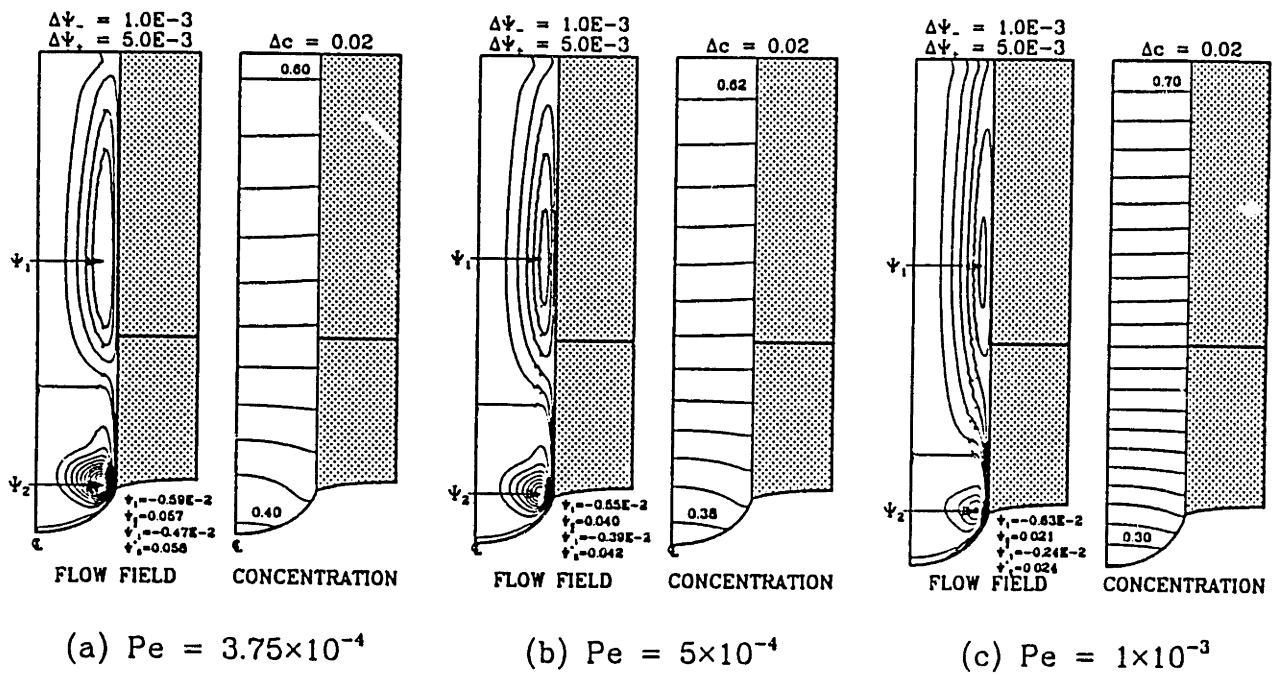


Figure 5.13: Streamlines and isoconcentration contours for calculations with varying crystal growth rate Pe ; $Ra_t = 2 \times 10^4$ and $Ra_s = -2 \times 10^4$.

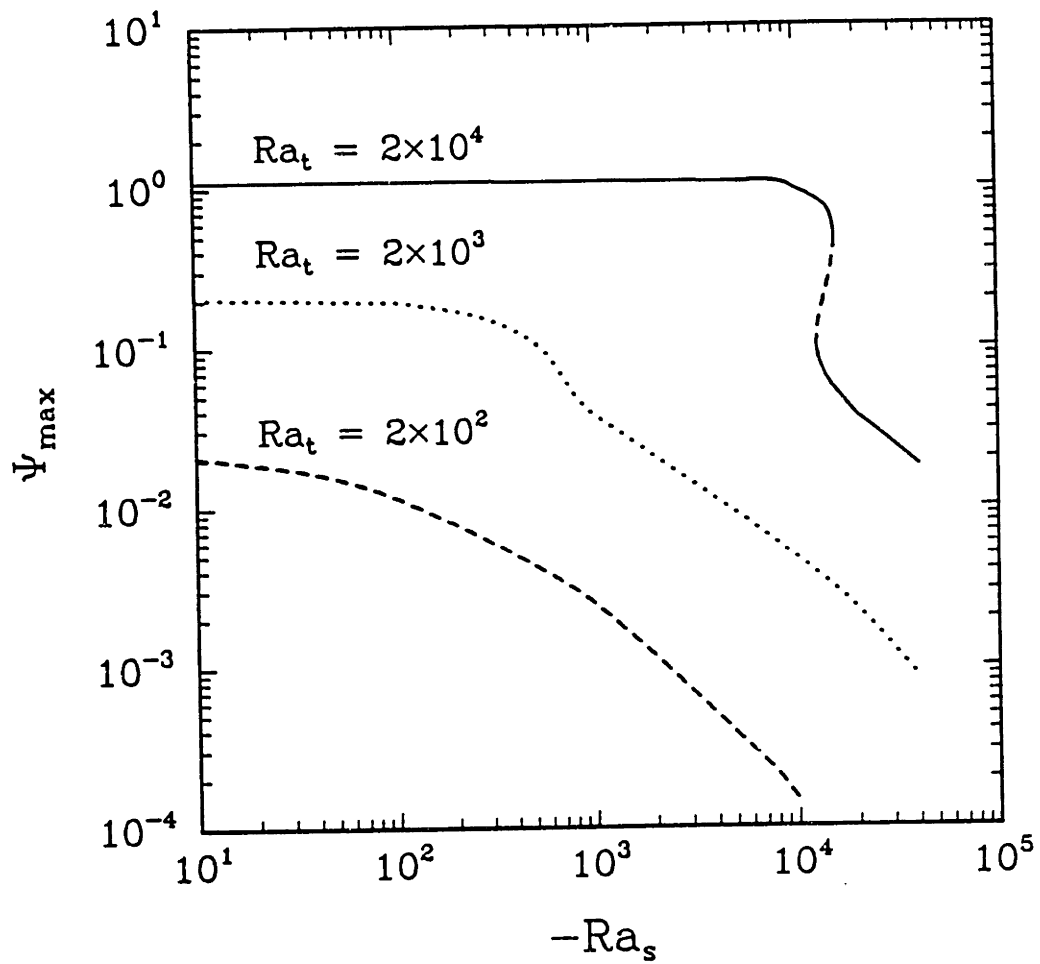


Figure 5.14: Flow intensity for lower flow cell Ψ_{\max} as a function of solutal Rayleigh number Ra_s , for varying values of Ra_t . All parameters are fixed at the values listed in Tables 5.1 and 5.2.

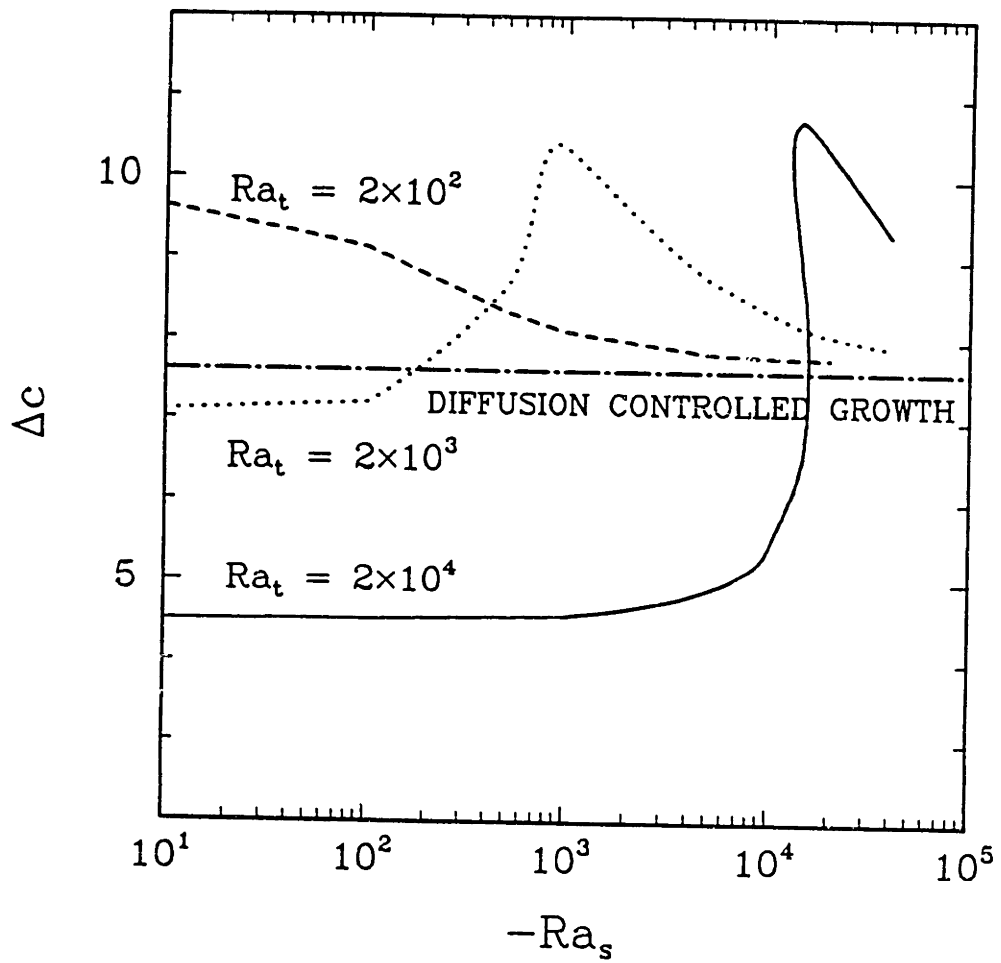


Figure 5.15: Radial segregation Δc as a function of sclutal Rayleigh number Ra_s , for varying values of Ra_t . All parameters are fixed at the values listed in Tables 5.1 and 5.2.

segregation.

Decreasing Ra_t leads to diffusion-like segregation at low $|Ra_s|$ and to more undesirable solute segregation. For $Ra_t = 2 \times 10^2$, the amount of radial segregation for small values of solute damping is above the level for diffusion controlled growth, thereby implying that the maxima in the Δc with Ra_t is near this value. Smaller values of thermal Rayleigh number should lead to radial composition levels that are close to the diffusion limit ($\Delta c \sim 7.6\%$) for all values of Ra_s .

5.4 Axial Segregation Model

The flow structure of an intense cell adjacent to the interface and damped convection away from it leads to an interesting picture of axial segregation that is different from either the diffusion-controlled case analyzed by Smith *et al.* (1955) or the perfectly mixed limit of Scheil (1942). In this section a simple one-dimensional model for solute transport in this idealized flow structure is presented to explain qualitatively the axial segregation results seen in the HgCdTe system (Capper *et al.*, 1983). The analysis accounts for the transients in the axial solute segregation and for the motion of the melt/crystal interface caused by the changes in the melting temperature with composition.

Because our intent is for the model to give a qualitative description of the axial transport, we remove the complication of the evolution of the temperature field with time by assuming that the melt/crystal interface experiences a constant temperature gradient at any location in the ampoule. This assumption also was made by Clayton *et al.* (1982).

We assume that for distance δ above the interface a strong flow exists which guarantees complete mixing of the solute. Solute transport in the remainder of the melt is assumed to be controlled by diffusion and by convection caused by ampoule motion. This situation is shown schematically in Figure 5.16.

The position of the melt/crystal interface is given in a stationary coordinate system

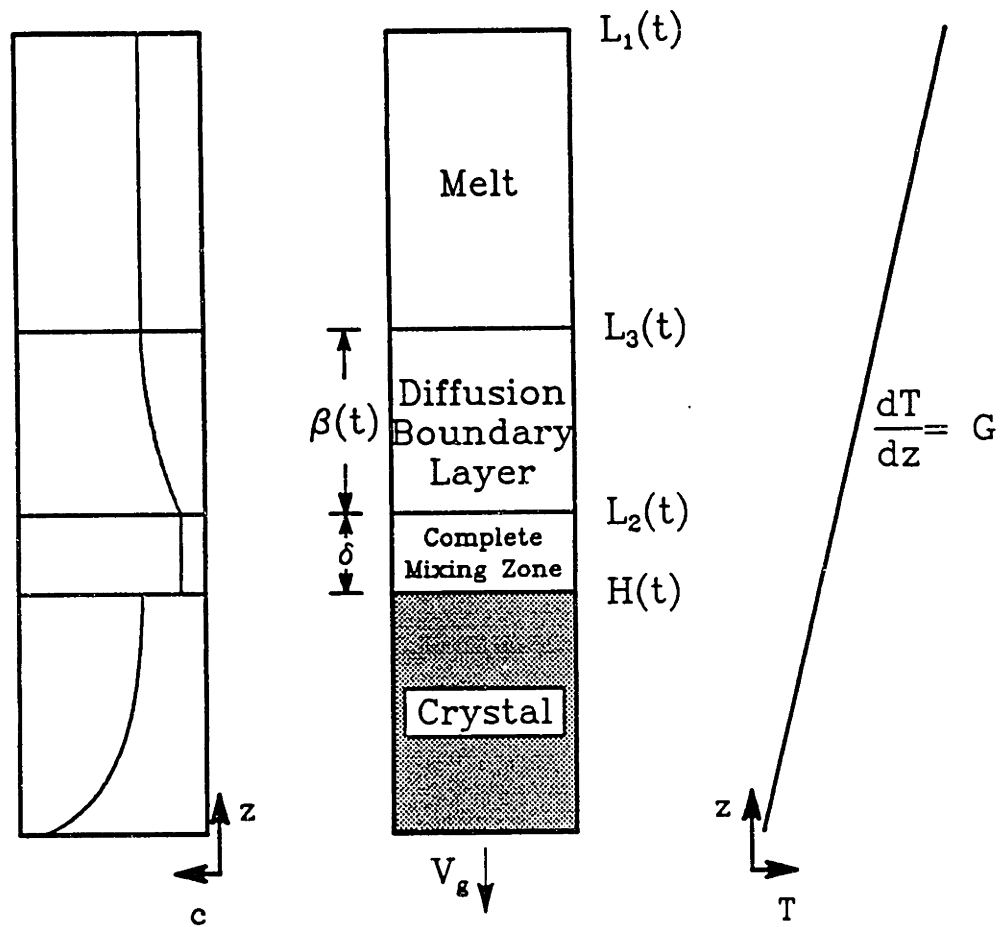


Figure 5.16: Schematic of one-dimensional model of axial segregation. The crystal is assumed to be separated from a bulk of diffusion-controlled melt by a region of thickness δ with intense convection.

as $H(t)$. This location and other lengths are scaled with the length of the ampoule L . Concentrations are scaled with an initial bulk value and time is made dimensionless with L^2/D .

The length of the melt $L_1(t) = H_o + 1 - Pe_m t$, where $Pe_m = V_g L/D$ is the dimensionless pull rate and D is the diffusivity of the solute. The location of the transition between complete mixing and diffusion controlled control transport is $L_2(t) = H(t) + \delta$.

The mathematical statement of one-dimensional solute transport in this *two-region* model is

$$C(z, t) = C_b(t), \quad H(t) \leq z \leq L_2(t) \quad (5.12)$$

$$\frac{\partial C}{\partial t} = \frac{\partial^2 C}{\partial z^2} + Pe_m \frac{\partial C}{\partial z}, \quad L_2(t) \leq z \leq L_1(t) \quad (5.13)$$

where $C(z, t)$ is a radially averaged concentration field. These equations are subject to boundary and initial conditions, as well as constraints. The boundary and initial conditions are

$$H(0) = H_o, \quad (5.14)$$

$$L_2(0) = \delta + H_o, \quad (5.15)$$

$$L_1(0) = H_o + 1, \quad (5.16)$$

$$C_b(0) = 1, \quad (5.17)$$

$$\frac{\partial C}{\partial z}(L_1(t), t) = 0, \quad (5.18)$$

$$C(L_2(t), t) = C_b(t), \quad (5.19)$$

where the condition (5.18) specifies no penetration of the solute at the end of the ampoule and (5.19) guarantees continuity of concentration between the two regions.

The location of the interface is given by the melting temperature according to the phase diagram:

$$m(C_b - 1) = G(H - H_o) \quad (5.20)$$

where m is an appropriately dimensionless liquidus slope and G is the dimensionless temperature gradient. The location of the ampoule end $L_1(t)$ is given by

$$L_1(t) = L_1(0) - Pe_m t \quad (5.21)$$

The concentrations fields in the well-mixed and diffusion controlled regions are coupled together by the integral constraint for total solute

$$\frac{\partial}{\partial t} \int_{H(t)}^{L_1(t)} C(z, t) dz = -kC_b(t) \left(\frac{\partial H}{\partial t} + Pe_m \right) \quad (5.22)$$

where k is the partition coefficient. This equation sets the bulk concentration $C_b(t)$.

To determine the dependence of the qualitative features of the axial segregation profile predicted by this model on the size of the well-mixed region relative to the melt length, we have analyzed the moving-boundary problem described by Eqs. (5.12) – (5.22) by an approximate integral analysis similar to that described by Crank (1984) for a simpler Stefan problem.

We assume that the concentration field in the diffusion controlled region $L_2(t) < z < L_1(t)$, can be approximated by a penetration region $L_2(t) < z < L_3(t)$, in which the composition varies from the initial value and a constant composition region $L_3(t) < z < L_1(t)$, that extends over the remainder of the melt. This penetration layer is shown schematically in Figure 5.16. The concentration profile $C(t)$ in the penetration region is modelled by a quadratic polynomial with time varying coefficients:

$$C(z, t) = C_b(t) - 2[C_b(t) - 1]\eta + [C_b(t) - 1]\eta^2 \quad (5.23)$$

where $\eta = [z - L_2(t)]/\beta(t)$. The polynomial (5.23) already satisfies the boundary conditions (5.18) and (5.19). The unknown bulk penetration thickness $\beta(t)$ is determined so that the solute balance equation (5.13) is satisfied in an integral sense over the appropriate region, or

$$\int_{L_2(t)}^{L_1(t)} \left(\frac{\partial C}{\partial t} - \frac{\partial^2 C}{\partial z^2} - Pe_m \frac{\partial C}{\partial z} \right) dz = 0 \quad (5.24)$$

Substituting the approximate concentration field (5.23) into (5.24) and the overall solute balance (5.22) leads to coupled differential equations for the evolution of the penetration thickness $\beta(t)$ and the bulk concentration $C_b(t)$ as

$$\begin{aligned} & \begin{bmatrix} \beta/3 + (C_b - 1)m/G & (C_b - 1)/3 \\ \delta + \beta/3 - (1 - kC_b)m/G & (C_b - 1)/3 \end{bmatrix} \begin{bmatrix} \partial C_b / \partial t \\ \partial \beta / \partial t \end{bmatrix} \\ & = \begin{bmatrix} 2(C_b - 1)(1/\beta - Pe_m/2) \\ Pe_m(1 - kC_b) \end{bmatrix} \end{aligned} \quad (5.25)$$

The interface velocity $\partial H / \partial t$ is recovered from Eq. (5.20) as

$$\frac{\partial H}{\partial t} = \left(\frac{m}{G} \right) \frac{\partial C_b}{\partial t} \quad (5.26)$$

The steady-state solution of the model is obtained by setting the left side of Eq. (5.25) to be zero and is

$$C_b = \frac{1}{k}, \quad \beta = \frac{2}{Pe_m} \quad (5.27)$$

so that the concentration in the well mixed region is exactly that which compensates for the preferential incorporation of solute into the crystal and the penetration thickness is given by the dimensionless growth rate $Pe_m = V_g L / D$.

Equations (5.25) were integrated numerically starting from the initial conditions of a penetration layer of zero thickness and a uniformly distributed solute concentration. The accuracy of the penetration model for the solute field in the diffusion-controlled region was verified by reducing the model to the case of dilute alloy without the mixing zone adjacent to the interface; this limit is recovered by setting the liquidus slope m and mixing length δ to be zero. Then the crystal growth rate corresponds to the pull rate and only the composition field evolves in time. The analysis of Smith *et al.* (1955) describes this evolution. The calculations for the initial transient in the axial solute profile in the crystal are compared in Figure 5.17 to the short-time result of Smith

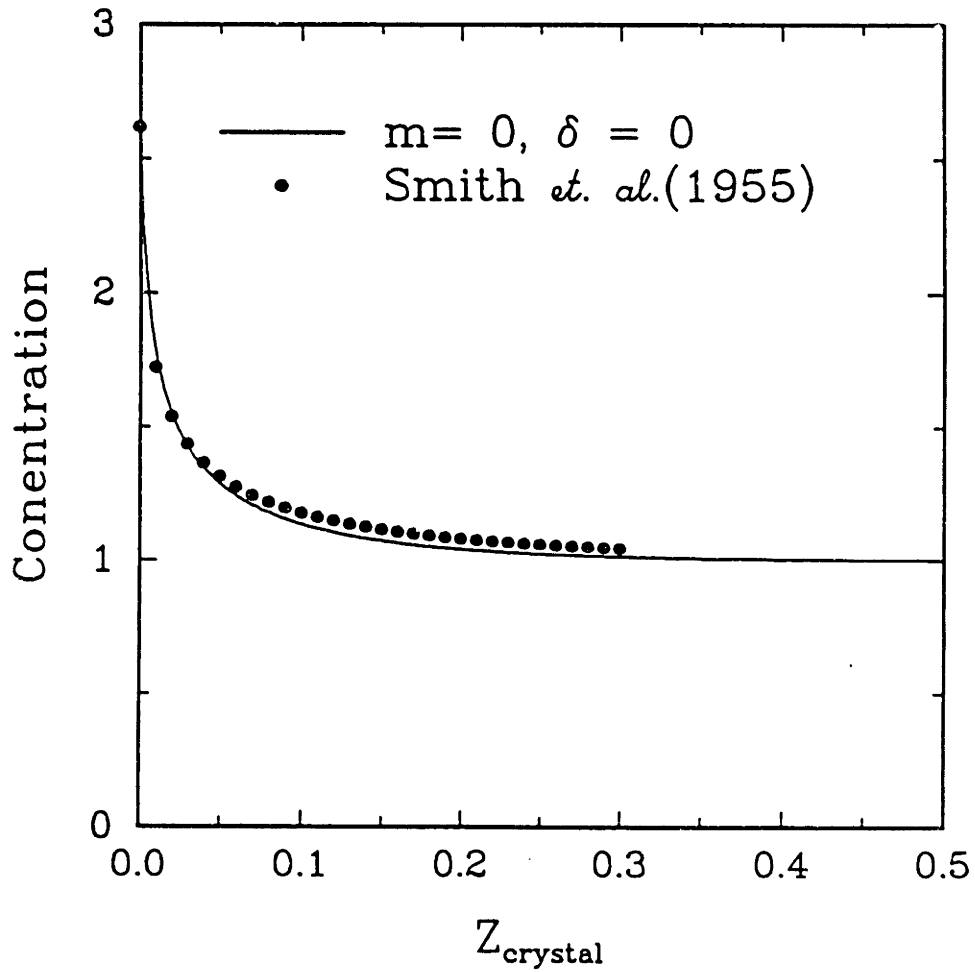


Figure 5.17: Comparison of predictions for the axial composition variation in the crystal for the approximate solution with the complete solution of Smith *et al.* (1955) for $\delta = 0$ and a dilute alloy ($m = 0$).

et al.. The agreement is extremely good considering the very approximate nature of the concentration profile used in our analysis.

The effect of the mixing zone adjacent to the melt/crystal interface on the axial segregation profile is demonstrated in Figure 5.18 by calculations with values of δ varying from the diffusion limit ($\delta = 0$) to an entirely well-mixed melt ($\delta = 1$). When the mixing region corresponds to over 10 % of the ampoule length, the axial segregation behavior begins to show the transition between profiles that look like diffusion-controlled growth and the complete mixing limit. Our analysis models the well-mixed melt in the limit of $\delta = 1$, as shown by the comparison of the calculation in this limit to the result of Scheil (1942).

On the basis of axial segregation data alone it is probably impossible to distinguish these profiles, especially in experiments using ampoules with large aspect ratios, without very precise knowledge of the diffusion coefficient. This is demonstrated in Figure 5.19 by comparing the axial composition profiles predicted for $\delta = 0$ and 0.1 for a specific diffusion coefficient ($Pe_m = 9.2$) with the diffusion-controlled results for a diffusion coefficient twice as high ($\delta = 0, Pe_m = 4.6$). In most experiments data cannot be deconvoluted to distinguish between the last two curves especially if the dependence of the diffusion coefficient on concentration is taken into account.

5.5 Discussion

More than anything else the calculations and analysis presented here have demonstrated that convection and solute segregation in nondilute alloys results from a complex interaction of heat transfer in the furnace and material and convection and species transport in the melt. Numerical simulations of the coupled flow, heat and species transport problems leads to mechanistic interpretations of both radial and axial segregation measurements.

We have demonstrated that the segregation behavior in the HgCdTe system is a

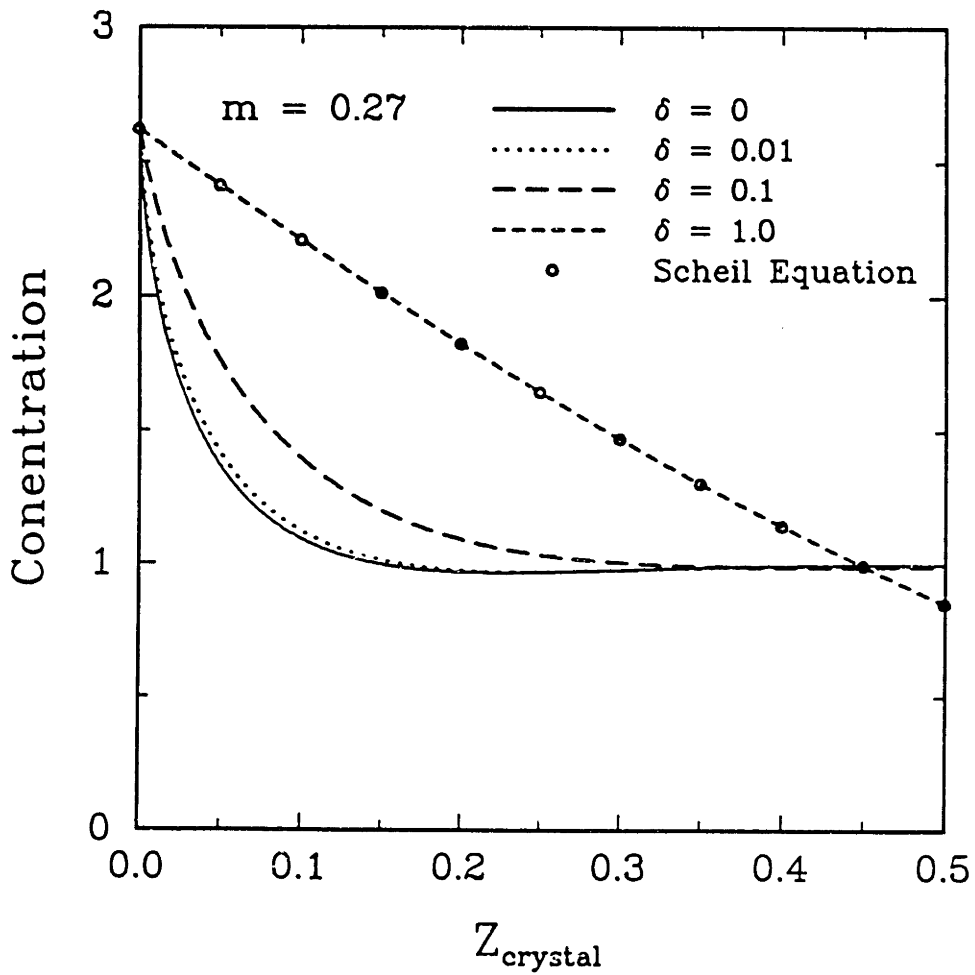


Figure 5.18: Variation of the axial composition in the crystal predicted by the one-dimensional model with the extent of the mixing zone adjacent to the interface. The profiles vary between diffusion-controlled growth for $\delta \ll 1$ to growth from a well-mixed melt for $\delta \sim 1$; $m = 0.27$.

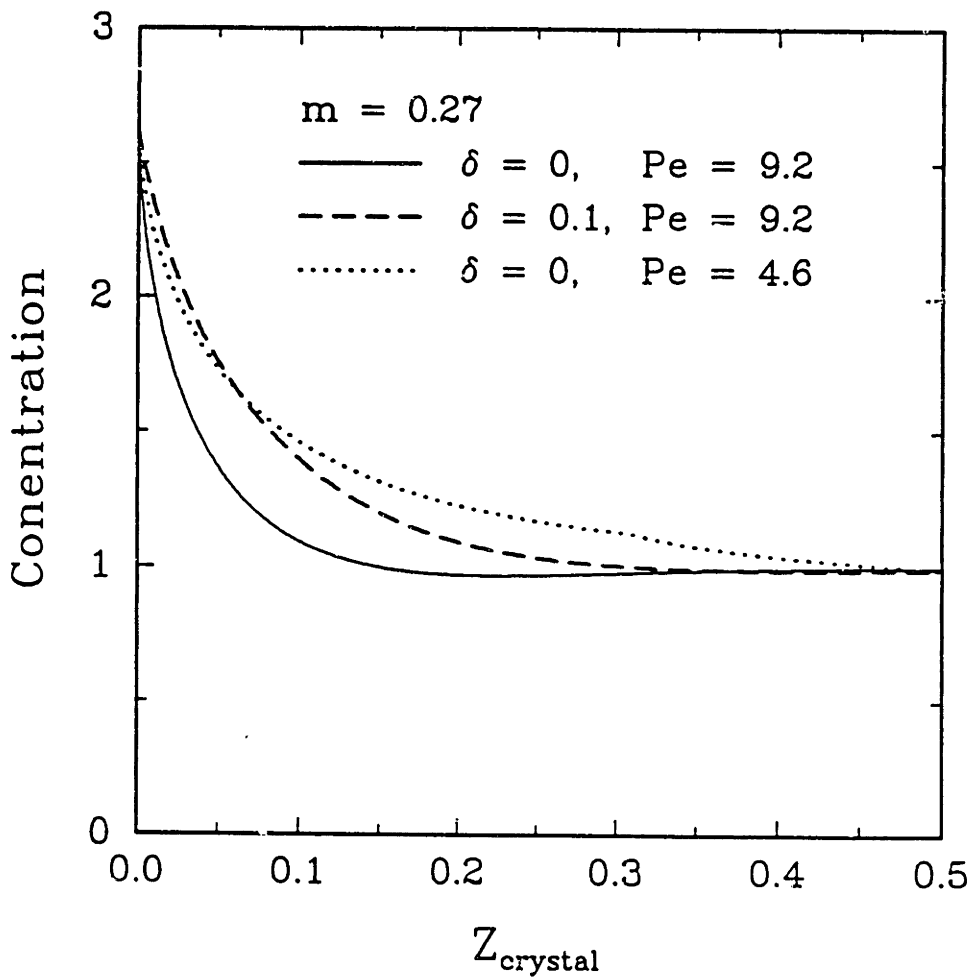


Figure 5.19: Comparison of the axial composition variation in the crystal predicted with increasing the extent of the mixing zone ($\delta = 0.1, Pe_m = 9.2$) or increasing the diffusion coefficient of the solute by a factor of two ($\delta = 0, Pe_m = 4.6$); the result for diffusion-controlled growth corresponds to $\delta = 0$ and $Pe_m = 9.2$.

result of the combined actions of thermally-driven convection caused by the large radial temperature gradients near the interface and solutally-driven damping of buoyancy flow by the gradient of CdTe in the melt. Quantitative determination of the relative importance of the two mechanisms can only be determined by precise numerical simulations that account of correct thermophysical properties and for the curvature of the melt/solid interface.

The radial and axial segregation patterns seen in HgCdTe crystal growth experiments by Szofran *et al.* (1984) and by Capper *et al.* (1983) are explained by the calculations. The large radial temperature gradients caused by the difference in the thermal conductivities between the melt, crystal and ampoule lead to strong convection adjacent to the interface. The solutal damping of this motion caused by the alloy concentration profile partially damps this motion.

For the small ampoules used by Szofran *et al.* (1984), solutal damping almost suppresses convection entirely in the upper portion of the ampoule, but a relatively intense flow cell still exists near the melt/crystal interface. The damping of convection over the length of the ampoule is responsible for the diffusion-like axial segregation profile observed in these experiments. The large radial nonuniformity seen on the crystals results from incomplete mixing in the flow cell adjacent to the interface.

The effect of solute damping on buoyancy-driven convection in the core is described well by the asymptotic analysis of Hart (1971). Moreover, the linear scaling of the effective solutal Rayleigh number Ra_s^* with the axial concentration gradient caused by solidification explains the decreasing axial segregation with increasing growth rate that was observed in the experiments of Capper *et al.* (1983) with larger ampoules.

There appears to be an important distinction between the two sets of experiments described here. Those of Szofran *et al.* (1984) were performed in small enough ampoules that the radial segregation operates closer to the diffusion-controlled limit, while the larger system of Capper *et al.* (1983) operates closer to the limit of a well-mixed melt. This difference is clear from the response of the radial segregation to increases in the

crystal growth where the Δc decreases in the small system, but increases in the larger one. These results are possible only if the systems are operating on opposite sides of the maxima in Δc with convection intensity, as defined for each system.

The one-dimensional model proposed in Section 5.4 for axial solute transport from a melt with a well-mixed cell separating convectionless melt from the solidification interface gives a good phenomenological picture of axial segregation in this system. The apparent diffusion-like profile is explained and the effective diffusion coefficient is shown to be a function of the size of the well-mixed region. The predictions from this analysis are appealing for the growth of many materials because they suggest that the growth of radially-uniform crystals with nearly constant axial composition profiles is possible if these conditions can be met.

Chapter 6

Transient Analysis of the Growth of Dilute Binary Alloy in a Vertical Bridgman Process and Gradient Freeze Furnace

The time-dependent finite element formulation developed in Chapter 3 is applied to investigate the transient transport processes in confined crystal growth systems. Calculations are presented for growth of a dilute gallium-doped germanium alloy in a vertically stabilized Bridgman-Stockbarger system and for growth of a dilute selenium-doped gallium arsenide in a gradient freeze furnace.

6.1 Introduction

Solidification in a confined crystal growth system is time-dependent through the translation of the imposed temperature profile relative to the materials in the ampoule, either by furnace or ampoule motion. Transport processes such as convection and solute seg-

regation in this system are also transient, because of the steady decrease of the melt volume in a finite length ampoule.

Most theoretical research for the Bridgman growth system has been limited to the steady-state analysis, which is based on several assumptions (see Section 2.2) valid for the region of steady solidification in a sufficiently long ampoule. One or more aspects of the transport processes, such as heat transfer, convective flow and solute segregation, in the Bridgman growth system have been previously analyzed using the steady-state assumption.

In the simplest thermal modelling, only the conductive heat transfer is accounted for, taking advantage of the low Prandtl numbers that are characteristic of semiconductor materials. One-dimensional analyses of heat transfer (Chang and Wilcox, 1974; Naumann, 1982a; Jasinski *et al.*, 1983; Jasinski and Naumann, 1984) have focussed on determining the criteria necessary for neglecting the thermal end effects. One example is the infinite length criterion for the necessary aspect ratio (Jasinski *et al.*, 1983), written as

$$\frac{L}{D} > \frac{2.5}{(Bi^*)^{1/2}}$$

where Bi^* is the effective Biot number defined by them. Two-dimensional thermal models (Chang and Wilcox, 1974; Sen and Wilcox, 1975; Fu and Wilcox, 1980; Borisov *et al.*, 1982; Naumann, 1982b; Chin and Carlson, 1983; Naumann and Lehoczky, 1983; Ravishankar and Fu, 1983; Huang *et al.*, 1983; Jasinski *et al.*, 1984; Jasinski and Witt, 1985; Taghavi and Duval, 1989) have analyzed the effect of various process conditions on the curvature of melt/solid interface.

The uniformity of the dopant concentration in the semiconductor crystal is one of the major concerns for the quality of crystal (Gatos, 1982). The convective flow structure in the melt is important in setting the solute segregation in the crystal because the motion of the flow governs the solute transport mechanism in the semiconductor melt of high Schmidt number. Steady-state analyses of flow in the melt (Chang and Brown, 1983a, 1984; Müller *et al.*, 1984; Carlson *et al.*, 1984) have revealed that the

radial temperature gradients in the melt are large enough to drive thermally buoyant convection even in the system of thermally stabilizing configuration, i.e. melt above crystal. But, the effect of convection on the solute distribution has not been investigated in their analysis.

The effect of convection on the solute segregation has been studied (Chang and Brown, 1983b; Adornato and Brown, 1987a,b) by steady-state finite element analysis up to the convection level comparable to that in small scale experimental systems. An important observation was made in their analyses that the mixing caused by intense convection near the melt/solid interface reduces the radial segregation and the imperfect suppression of convection can actually increase the radial nonuniformity in the solute distribution. Studies of the effect of vertical magnetic field on the convection and segregation has led to the similar observations, as discussed by Chapter 4.

The behaviour of field variables in the initial and final transient period is completely ignored in the steady-state analysis. In some cases the length of the ampoule used for crystal growth is not long enough to allow the steady-state transport processes, e.g., $L/D = 4$ for the pyrolytic boron nitride ampoule in the growth of gallium arsenide (Arnold, *et al.*, 1989), and the solidification process is completed before steady-state heat transfer is reached. Only transient analysis can provide the complete picture of the batchwise solidification process in the confined crystal growth system.

The dynamics of the solidification process involves multiple time scales, including the time scales for the dynamics of heat transfer, for ampoule translation, for viscous diffusion of momentum and for solute transfer. This complex dynamics in the system makes transient numerical analysis of the complete system a formidable task. Simple models have been used by a number of investigators to answer particular questions.

One-dimensional transient analysis of heat transfer (Favier, 1980; Fu and Wilcox, 1981; Sukanek, 1982a,b) has been used to investigate the deviation of the solidification rate from the translation rate of ampoule when the translation rate is subject to a step change, as in the beginning of the solidification process. Time-dependent models of

solute diffusion equation without convection have been solved analytically (Pohl, 1954; Smith *et al.*, 1955; Hulme, 1955; Memelink, 1956) for the solute redistribution during directional solidification of a dilute component with constant segregation coefficient. In these analyses, the solidification rate is assumed to be constant throughout the process and this rate is imposed on the interface as soon as solidification begins. Although thermal transients are neglected, this solution is frequently used as a good approximation in the limiting case of diffusion-controlled solute transport in the melt, as opposed to the Scheil equation (Scheil, 1942) for which complete mixing in the melt is assumed. The same time-dependent diffusion equation has been solved numerically (Clayton *et al.*, 1982) for the case where no steady solidification is present and the alloy is nondilute. With transient finite difference analysis, Verhoeven *et al.* (1988) established the region in the parameter space composed of equilibrium distribution coefficient k and solutal Peclet number Pe , where the transient solution of Smith *et al.* and Scheil are valid, respectively. The effect of diffusion in the solid phase on the solute segregation also has been investigated analytically (Bourret *et al.*, 1983; Kobayashi, 1988).

The transient in the microscopic growth rate caused by the imperfect heat transfer was accounted for in the one-dimensional numerical analysis of both heat and solute transfer in the Bridgman growth of nondilute binary alloy (Bourret *et al.*, 1985). The coupling between concentration and temperature at the melt/solid interface contributed to the longer transients observed in the nondilute system than in the dilute system where heat and solute transfer are decoupled.

The purpose of this chapter is to present detailed transient calculations for the complete description of the directional solidification process in a confined growth system. Heat transfer in the melt, crystal and ampoule is coupled to convection in the melt, which is a key factor to the solute transport in the melt and ultimately to the solute segregation in the growing crystal. In this chapter, a dilute binary alloy is considered and convection driven by temperature is incorporated. The temperature variations important in directional solidification are the axial gradient imposed for solidification and the radial gradients caused by imperfections in the heat transfer between the charge,

ampoule and furnace. In the axially stabilizing thermal configuration, convection is caused by the radial temperature gradients alone.

Two furnace designs previously used in the experiment are of particular interest in this study and are shown schematically in Figure 6.1. The crucibles shown in Figure 6.1 are the prototypes of the ones used in the experimental systems shown in Figure 6.2. These are the classical Bridgman-Stockbarger furnace constructed by Wang (1984) at the Massachusetts Institute of Technology and the gradient freeze furnace constructed at the GTE Laboratories (Kafalas and Bellows, 1988; Arnold *et al.*, 1989) for the space experiments. The MIT furnace has been built using two heat pipes for forming isothermal hot and cold regions separated by a nearly adiabatic zone. The isothermal zones are long enough so that the solidification rate equilibrates with the ampoule displacement rate after initial transient period. The GTE gradient freeze furnace uses multizone resistance heating elements to establish a desired temperature profile over a length of ampoule. Instead of moving the ampoule through furnace, this temperature profile is translating upward to give axial temperature gradient necessary for solidification. In the multizone gradient freeze method, temperature gradients near the interface can be minimized, which reduces the thermal stress level in the crystal (Parsey and Thiel, 1985, 1987).

The transient model for the vertical Bridgman growth system and finite-element/time-integration method developed in Chapter 2 and Chapter 3, respectively, are applied to the calculations for both MIT and GTE furnace systems. Results are presented for the growth of gallium-doped germanium in the MIT furnace and selenium-doped gallium arsenide in the GTE furnace system. The growth of the gallium-doped germanium in the MIT furnace has been studied experimentally by Wang (1984) and the GTE space experiment to grow selenium-doped gallium arsenide is expected aboard STS in 1990 (Arnold *et al.*, 1989).

Transient calculations for growth of gallium-doped germanium in the boron nitride ampoule show the development of flow structure in time. The impact of convection on the solute concentration in the crystal is demonstrated by the radial and axial segrega-

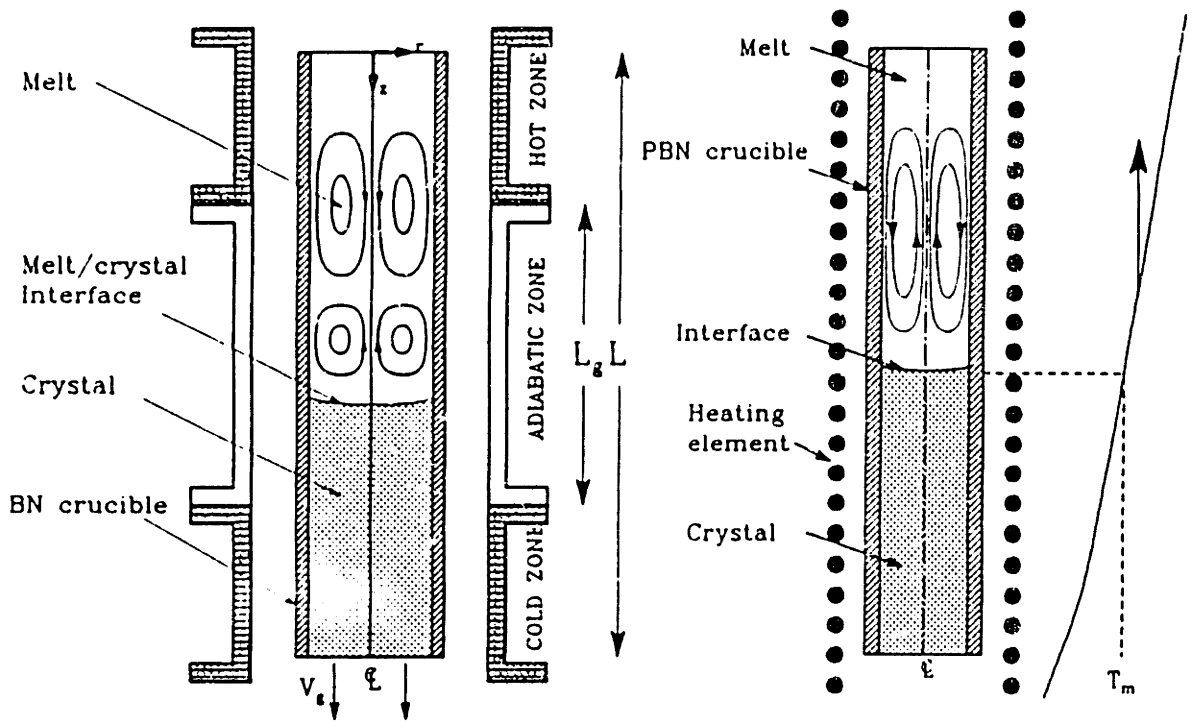


Figure 6.1: Schematic diagrams of the prototypical models for the (a) MIT vertical Bridgman crystal growth system and (b) GTE gradient freeze growth system.

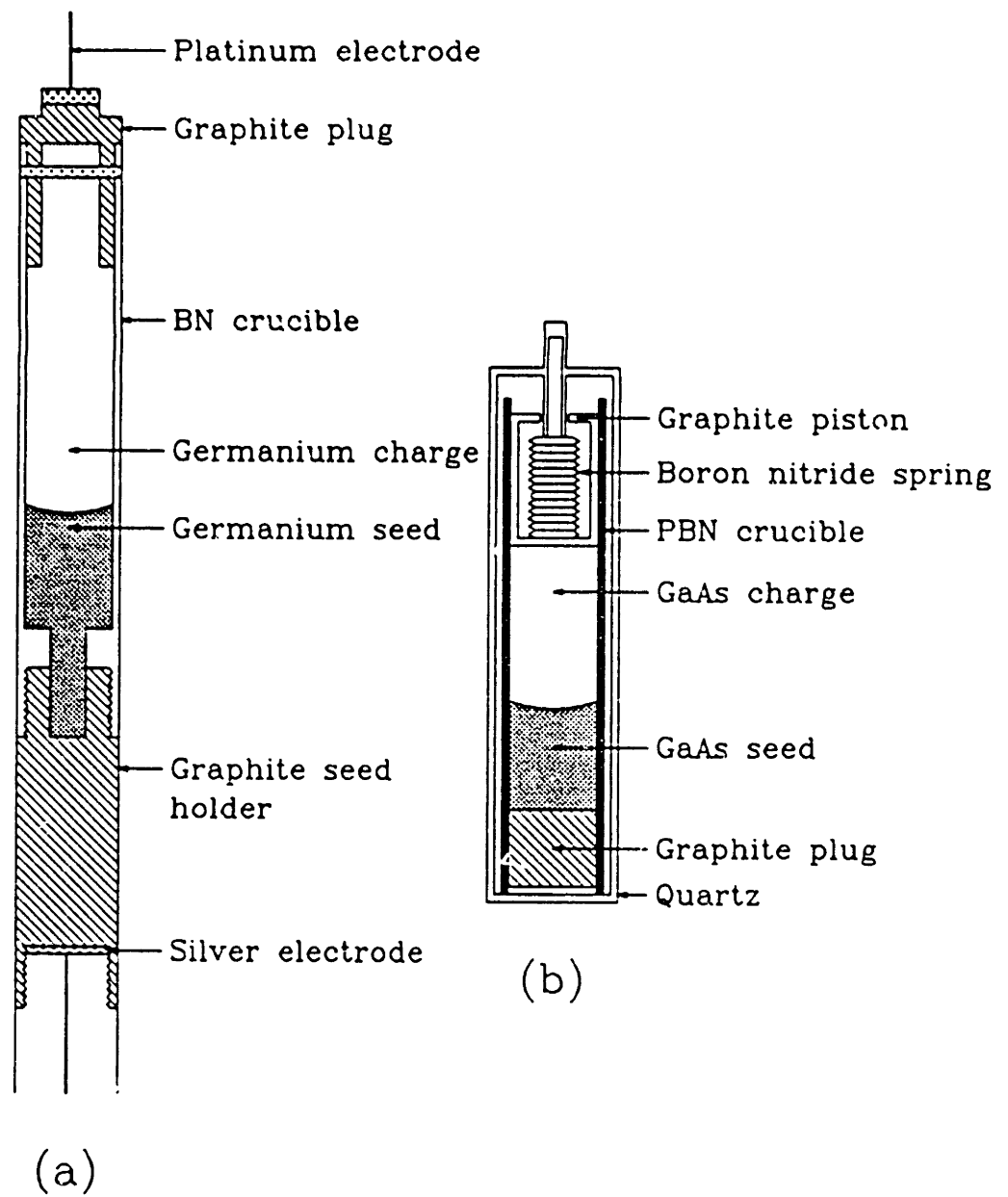


Figure 6.2: Schematic diagrams of the crucibles used for growth in (a) MIT vertical Bridgman growth system and (b) GTE gradient freeze growth system.

tion calculations for the dilute gallium-germanium alloy. The predicted values of radial segregation and effective segregation coefficient for gallium are compared to values obtained by Wang(1984). These are the first quantitative comparisons with experiments of solute segregation predicted from detailed transient analysis of melt flow. The effect of the step change in ampoule translation rate is also investigated for this calculation.

Results for growth of selenium-doped gallium arsenide in a PBN (pyrolytic boron nitride) ampoule show the effect of large latent heat of solidification on temperature field and interface shape in time. The geometry of the melt region is determined by the interface shape and location and influences the structure of flow and solute distribution in the crystal. These consequences are presented for the dilute selenium-doped gallium arsenide alloy.

6.2 Transient Model for Vertical Bridgman Growth Process and Gradient Freeze Growth Process

The transient model for the vertical Bridgman crystal growth process has been presented in detail in Chapter 2. In this Section, basic differences between the vertical Bridgman and gradient freeze processes are examined. It is shown that the transient model developed for vertical Bridgman process can be used for gradient freeze process without modifications.

In the MIT furnace, two heat pipes provide nearly isothermal hot and cold zones and the temperature gradient near the interface is controlled by the length and material used for the adiabatic zone. Typical furnace temperature and heat transfer coefficient profiles are shown in Figure 6.3(a). The temperature profile along the axis of the cylindrical ampoule shows the effect of imperfect heat transfer between the furnace, ampoule and charge.

Multi-zone heating elements in the gradient freeze furnace make it easier to tailor the desired furnace temperature profile in time, by controlling the power to each heating elements in the furnace. With the increase of the number of independent heating zones, more sophisticated shape of the temperature profile is possible. Figure 6.3(b) shows typical time change of the temperature profile in GTE furnace system. In the gradient freeze furnace, the absence of the adiabatic zone yields almost uniform heat transfer coefficient over the length of the ampoule, except for the temperature dependence of radiative heat transfer.

The most distinguished difference between the crystal growth processes in MIT furnace and GTE furnaces lies in the dynamics of heat supply to the ampoule. In the MIT furnace, the furnace temperature profile is stationary in the fixed laboratory frame and the ampoule is pulled down so that it sees the changing furnace temperature in time. On the contrary, the ampoule is stationary and the furnace temperature profile is changed in time in the GTE gradient freeze furnace system. These differences disappear with the proper choice of the coordinate reference frame. In our model, we fix the

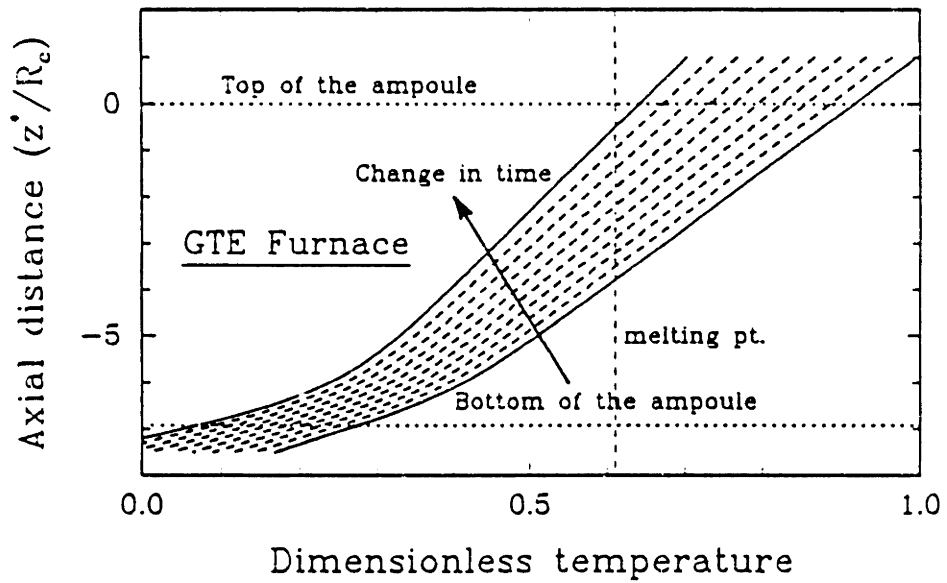
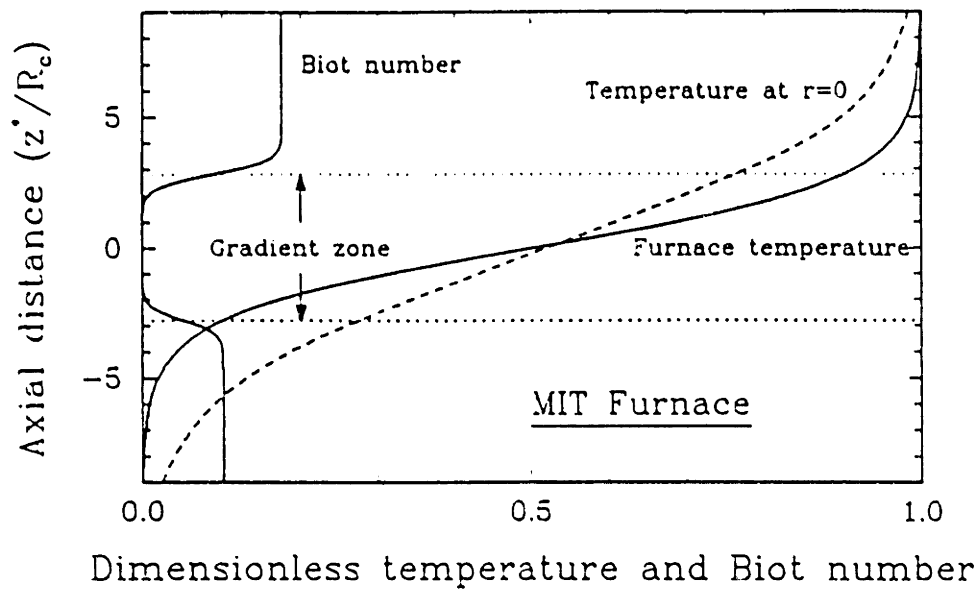


Figure 6.3: Typical furnace temperature profiles for (a) MIT vertical Bridgman furnace system and (b) GTE gradient freeze furnace system.

coordinate reference to the top of the ampoule and the furnace temperature profile translates or changes shape in time for both systems. These time-dependent profiles of furnace temperature and heat transfer coefficient are incorporated into the model in analytical forms.

Another feature which should be accounted in the modelling of the GTE gradient freeze furnace is that the pyrolytic boron nitride used as a ampoule material is a strongly anisotropic material. Its thermal conductivities vary as 1:25 for the radial and axial directions, respectively, as shown in Table 6.5. Chait (1988) accounted for this anisotropy in his model by dividing the ampoule into two isotropic layers of different conductivity. We incorporate the anisotropy into the model by assuming pyrolytic boron nitride as a *orthotropic solid* (Carslaw and Jaeger, 1959). For orthotropic solids, off-diagonal components of the second-order conductivity tensor are zero and heat fluxes are expressed for the axisymmetric cylindrical system as

$$\begin{bmatrix} q_r \\ q_z \end{bmatrix} = \begin{bmatrix} K_{rr} & 0 \\ 0 & K_{zz} \end{bmatrix} \begin{bmatrix} -\partial T / \partial r \\ -\partial T / \partial z \end{bmatrix} \quad (6.1)$$

The Laplacian of temperature in the axisymmetric cylindrical system is written for constant K_{rr} and K_{zz} as

$$\begin{aligned} \nabla^2 T &= -\frac{1}{r} \frac{\partial}{\partial r} (r q_r) - \frac{\partial q_z}{\partial z} \\ &= K_{rr} \frac{1}{r} \frac{\partial}{\partial r} \left(r \frac{\partial T}{\partial r} \right) + K_{zz} \frac{\partial^2 T}{\partial z^2} \end{aligned} \quad (6.2)$$

This formulation is used for the modelling of heat conduction in the anisotropic PBN ampoule.

6.3 Growth of Gallium-doped Germanium in MIT Vertical Bridgman Heat-pipe Furnace

The thermophysical properties used in this study for gallium-doped germanium were compiled from results of Crouch *et al.* (1982) and Wang (1984) and are listed in Table 6.1. All properties were assumed to be independent of temperature. The small degree of temperature dependence of germanium properties reported by Crouch *et al.* (1982) partially support this assumption. We assume that the small concentrations of gallium (10^{14} – 10^{19} atoms/cm³ or 10^{-9} – 10^{-4} mole fractions) of experiments by Wang (1984) do not drive solutal convection, as discussed by Adornato and Brown (1987a).

The calculations for germanium growth are presented for the MIT furnace. Parameters corresponding to the design of this system (Wang, 1984) and thermophysical properties of boron nitride ampoule (Touloukian, 1967) are tabulated in Table 6.2. Dimensionless groups appropriate for the terrestrial growth of germanium with this furnace design parameters are listed in Table 6.3, where V_g is a ampoule translation rate through furnace.

6.3.1 Thermal Boundary Conditions

Comparisons between the predictions of calculations and small-scale growth experiments is only possible when the thermal boundary conditions for the experiment are well established and these boundary conditions are incorporated into the model precisely.

Equations describing the transient heat transfer in the system have been developed in Section 2.3. Equation (2.29) dictates the thermal boundary conditions between the ampoule and the surrounding furnace and rewritten here as

$$\left[\frac{\partial \theta}{\partial \tau} \right]_a = Bi(z, \tau) [\theta_\infty(z, \tau) - \theta(r, z, \tau)] \quad (6.3)$$

where $Bi(z, \tau)$ is a time-dependent, dimensionless heat transfer coefficient ($Bi(z, \tau) \equiv h_a(z, \tau)R_c/k_a$) defined to include radiative, conductive, and convective transport be-

Quantity	Symbol (units)	Value
Thermal conductivity of the melt	K_m (W/°C·cm)	0.39
Thermal conductivity of the solid	K_s (W/°C·cm)	0.18
Density of the melt	ρ_m (g/cm ³)	5.5
Density of the solid	ρ_s (g/cm ³)	5.5
Specific heat of the melt	$C_{p,m}$ (J/°C·g)	0.35
Specific heat of the solid	$C_{p,s}$ (J/°C·g)	0.38
Melting temperature	T_m (°C)	937.4
Kinematic viscosity	ν (cm ² /sec)	0.0013
Heat of solidification	ΔH_s (J/g)	460
Thermal expansion coefficient	β_t (°C ⁻¹)	5.0×10^{-4}
Diffusion coefficient of Ga in Ge	D (cm ² /sec)	2.1×10^{-4}
Equilibrium distribution coefficient of Ga	k	0.087

Table 6.1: Thermophysical properties of germanium.

Ampoule length, L (cm)	15.2
Crystal radius, R_c (cm)	0.68
Ampoule outer radius, R_a (cm)	0.95
Gradient zone length, L_g (cm)	3.8
Temperature difference, $T_h - T_c$ (°C)	340
Ampoule translation rate, V_g ($\mu\text{m}/\text{sec}$)	4.0
Initial location of the center of the gradient zone, $z_{c,0}^*$ (cm)	9.91
Ampoule material	Boron nitride
Thermal conductivity of ampoule, K_a (W/°C·cm)	0.26
Density of ampoule, ρ_a (g/cm ³)	2.3
Specific heat of ampoule, $C_{p,a}$ (J/°C·g)	1.9

Table 6.2: Design parameters for MIT vertical Bridgman furnace

Name	Symbol	Definition	Value
Thermal Rayleigh number	Ra_t	$g\beta_t\Delta T R_c^3/(\alpha_m\nu)$	2×10^5
Solutal Rayleigh number	Ra_s	$g\beta_s c_o R_c^3/(\alpha_m\nu)$	0
Peclet number	Pe	$V_g R_c/\alpha$	1.3×10^{-3}
Prandtl number	Pr	ν/α_m	6.4×10^{-3}
Schmidt number	Sc	ν/D	6.2
Stefan number	St	$\Delta H_s/C_{p,m}\Delta T$	3.9

Table 6.3: Dimensionless groups and characteristic values appropriate for gallium-doped germanium crystal growth in MIT furnace.

tween the ampoule and the furnace, and $\theta_\infty(z, \tau)$ is the temperature distribution at the furnace wall.

The changes in the heat transfer coefficient between the three zones of the MIT vertical Bridgman furnace are modelled by the function

$$Bi(z, \tau) = \frac{bi_0}{2} (bi_3 \{1 + \tanh[bi_1(z_c(\tau) - bi_2 - z)]\} + 1 + \tanh[-bi_1(z_c(\tau) + bi_2 - z)]) \quad (6.4)$$

where $z_c(\tau)$ is the time-dependent location of the mid-plane of gradient zone in coordinate system fixed to the ampoule and is linear in time as

$$z_c(\tau) = z_{c,0} - \frac{Pe}{Pr} \tau \quad (6.5)$$

for which $z_{c,0}$ is a initial location of z_c and translation Peclet number of ampoule is constant throughout the run. The coefficients $\{bi_i\}$ are constant in time and have the following significance: $bi_0 = h_{cold}R_c/k_a$ is the value of Biot number in the cold zone; bi_1 sets the slope of the transition in $Bi(z)$ between the isothermal zones and the adiabatic region; $bi_2 = (L_g/R_c)/2$ is the half of the dimensionless length of the adiabatic zone; $bi_3 = h_{hot}/h_{cold}$ sets the ratio between the Biot numbers in the hot and cold zone. The furnace wall temperature is modelled by the function

$$\theta_\infty(z, \tau) = \frac{1}{2} \{1 + \tanh[\theta_0(z_c(\tau) - z + \Delta z)]\} \quad (6.6)$$

where θ_0 determines the sharpness of the transition in $\theta_\infty(z, \tau)$ between the hot and cold zones and Δz accounts for the degree of asymmetry in dimensionless furnace temperature.

These formulations for the heat transfer coefficient and furnace temperature profile is tested by performing numerical simulation of heat transfer for the experiment of thermal characterization by Wang (1984). In this experiment, a graphite rod was used instead of an ampoule. Axial temperature fields along the furnace wall and in the graphite rod were measured in a helium atmosphere.

The heat transfer coefficients in the hot and cold isothermal zones were estimated from the contribution of conduction through the ambient gas phase and radiation between the furnace wall and the charge, i.e. $h = h_{cond} + h_{rad}$. The heat transfer coefficient due to conduction in the gas is given by

$$h_{cond} = \frac{k_g}{r_f \ln(r_f/r_{ch})} \quad (6.7)$$

where k_g is thermal conductivity of the gas in the gap and r_f and r_{ch} are outer radii of the furnace and the charge, respectively. The contribution of radiative heat transfer is summed up as

$$h_{rad} = 4\mathcal{F}\sigma \left[\frac{T_f + T_{ch}}{2} \right]^3 \quad (6.8)$$

where T_f and T_{ch} are temperature of the furnace wall and the charge, respectively and σ is Stefan-Boltzmann constant (5.67×10^{-12} W/cm²·K⁴). Overall interchange factor \mathcal{F} is a function of emissivities of furnace wall (ε_f) and charge (ε_{ch}), given by (Siegel and Howell, 1972)

$$\mathcal{F} = \left[\frac{1}{\varepsilon_{ch}} + \left(\frac{r_{ch}}{r_f} \right)^2 \left(\frac{1}{\varepsilon_f} - 1 \right) \right]^{-1} \quad (6.9)$$

The coefficients bi_0 and bi_3 in Eq. (6.4) are determined from these heat transfer coefficients and bi_2 is obtained from the length of adiabatic zone. Coefficients for the slope, bi_2 and θ_0 , are obtained by best fitting to the experimental measurements of temperature.

The predicted and measured temperature are shown in Figure 6.4. No solidification is involved with the graphite rod and temperature has been predicted from steady-state finite element analysis, with coefficients $\{\theta_0, \Delta z\} = \{0.39, 0.38\}$, $\{bi_i\} = \{0.10, 2., 2.8, 1.7\}$. The average error in the predicted temperature was only 0.011 in dimensionless temperature or about 4 °C. This comparison validates the thermal model and boundary conditions.

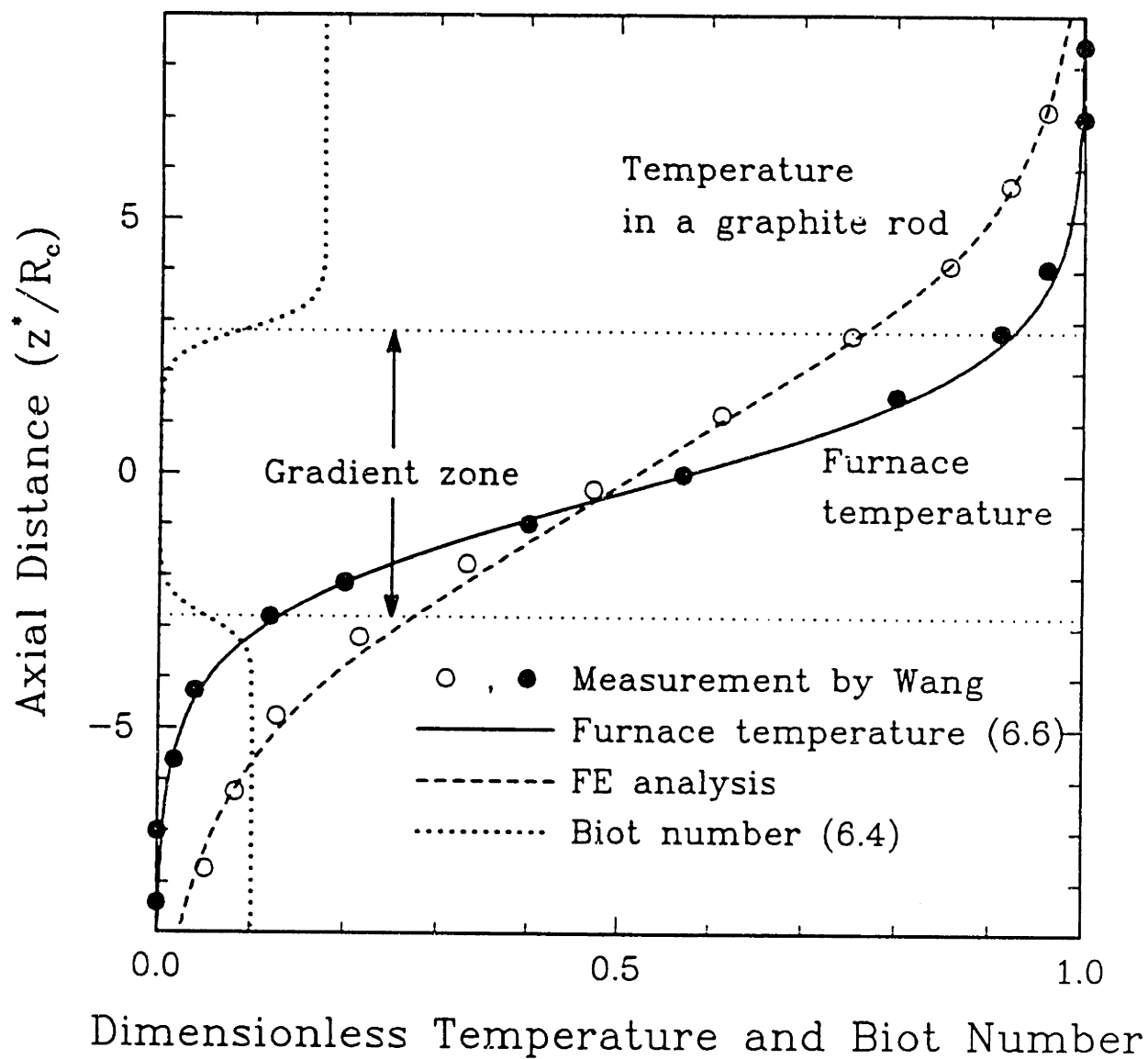


Figure 6.4: Comparison of axial temperature profiles along the center of a graphite rod predicted by finite element analysis and measured by Wang (1984).

6.3.2 Temperature Fields and Growth Velocity

Transient calculations for the growth of gallium-doped germanium alloy in a boron nitride ampoule are performed with an initial condition for which the center plane of the gradient zone is placed at 0.65 of the ampoule length from the top and ampoule translation rate is set to zero. Initial concentration of gallium dopant is uniform throughout the melt because of the zero growth rate. The temperature field is equilibrated with the surrounding furnace and steady thermal convection due to this temperature field is used as an initial state before the translation of the ampoule is begun. The calculations are continued until about 0.65 of the charge is solidified. Sample meshes shown in Figure 6.5 are used for the transient calculation and display the deformation and translation of the individual element during the run.

Heat transfer in the crystal and ampoule is caused by conduction only and conductive heat transfer dominates in the melt because of the low Prandtl number of semiconductor material. The high level of convection in the system does not deform the shape of isotherm appreciably as shown in Figure 6.6. Almost the same temperature field was computed for $Ra_t = 0$ and 2×10^5 . This confirms the dominance of conductive heat transfer in the melt. Only close scrutiny of the temperature field reveals a little flattening of the isotherm in the melt at $Ra_t = 2 \times 10^5$ due to convective heat transfer. The effect of convective heat transfer is more evident in Figure 6.8, where the interface deflection is plotted as a function of Ra_t . The melt/crystal interface becomes somewhat flatter with the more intense convection associated with the higher Ra_t .

In the MIT vertical Bridgman system, the furnace temperature in the hot and cold zones is nearly constant and temperature change is confined to the gradient zone. This is reflected by the temperature field inside the ampoule, where the temperature gradient is steepest near the interface and becomes lower with distance away from it. The large length of the hot and cold zones, compared to the size of the adiabatic zone, enables the temperature field around the interface to be independent of the position inside the ampoule and thus results in a steady-state growth rate as solidification proceeds.

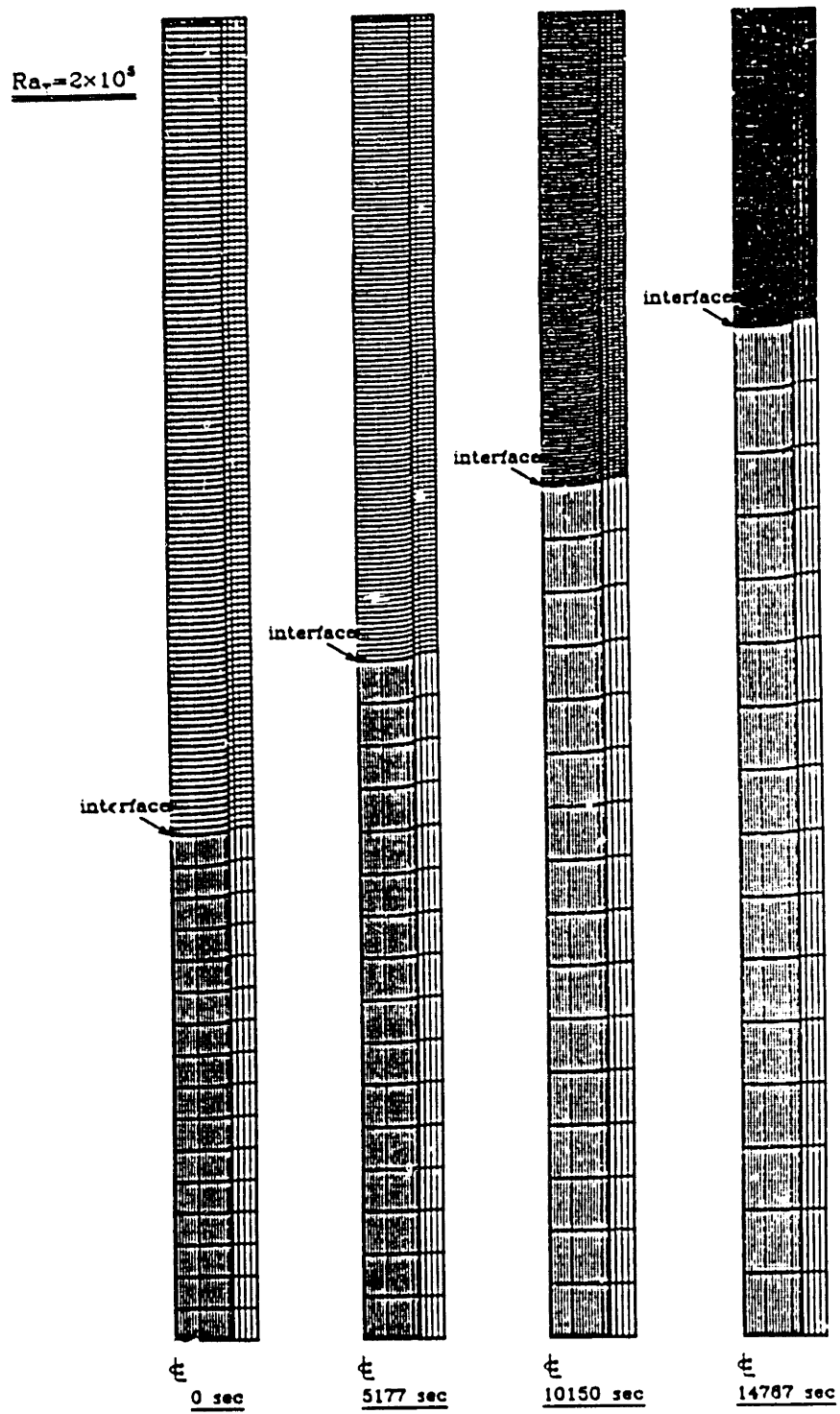


Figure 6.5: Sample finite element mesh used for the transient calculations for the MIT vertical Bridgman system.

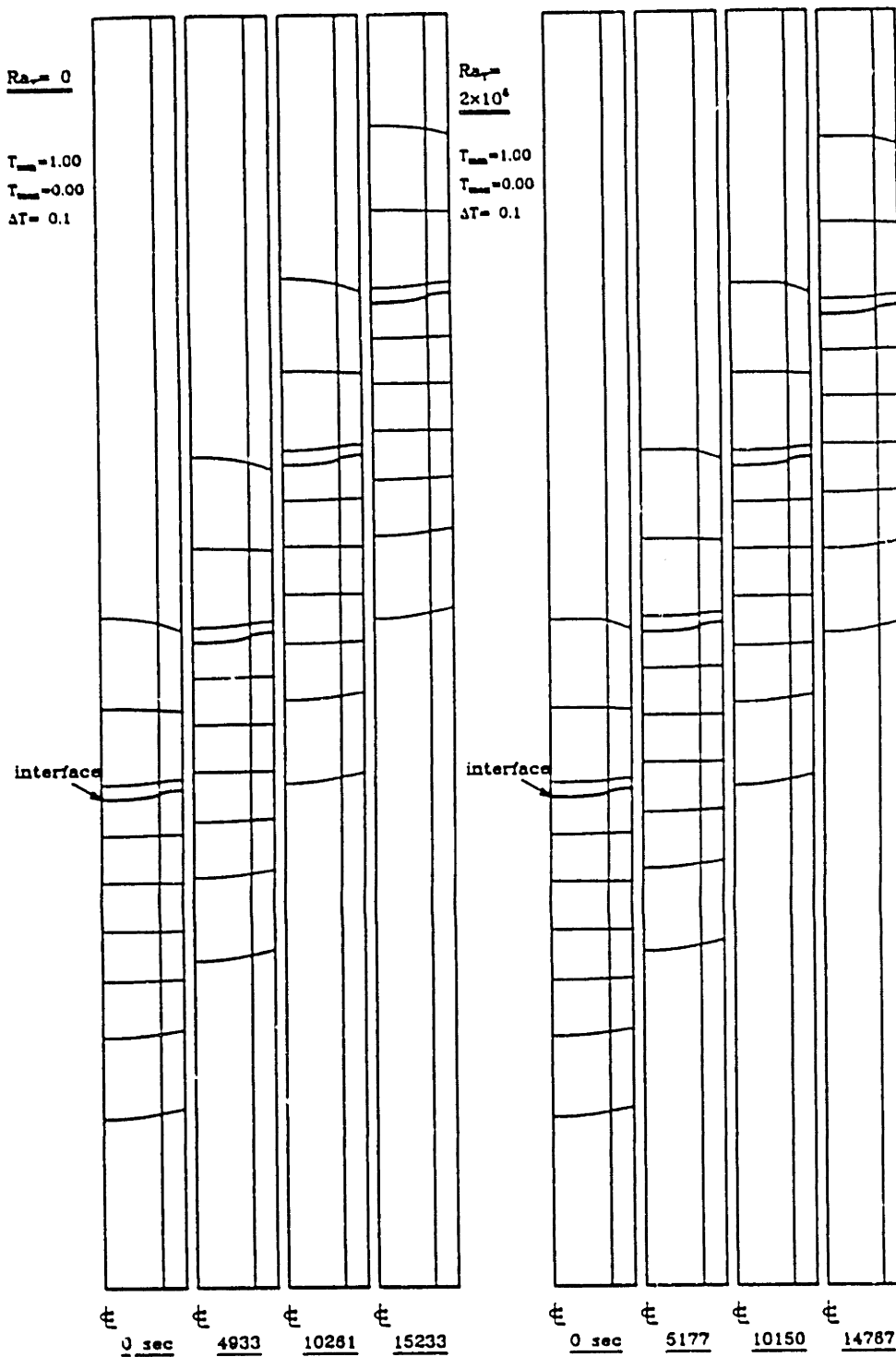


Figure 6.6: Sample temperature fields for growth of GaGe in MIT furnace with thermal Rayleigh number of (a) $Ra_t = 0$ and (b) $Ra_t = 2 \times 10^5$.

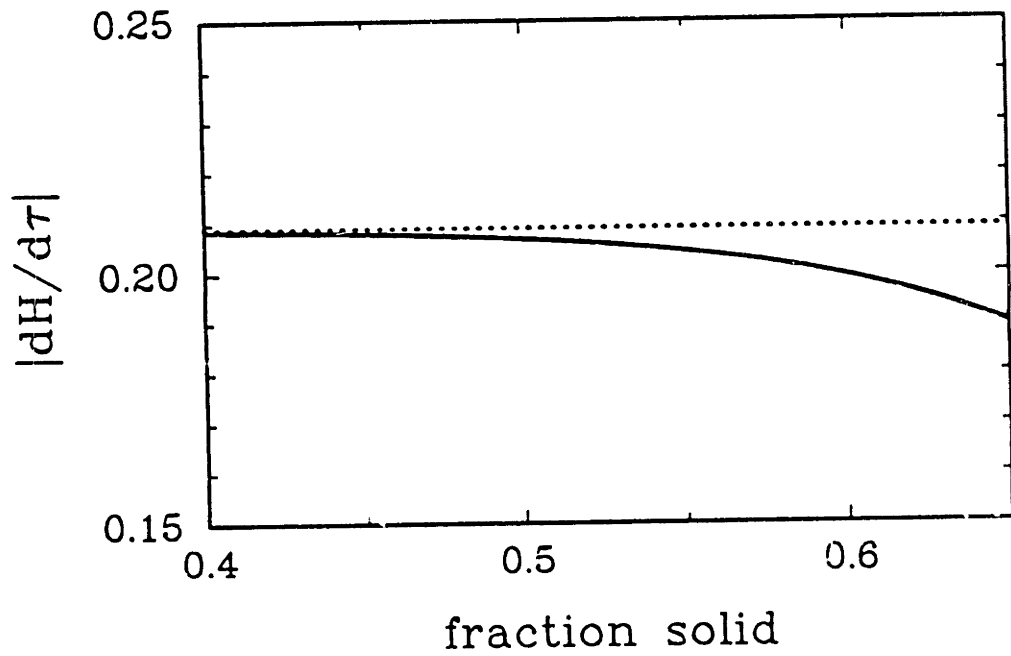
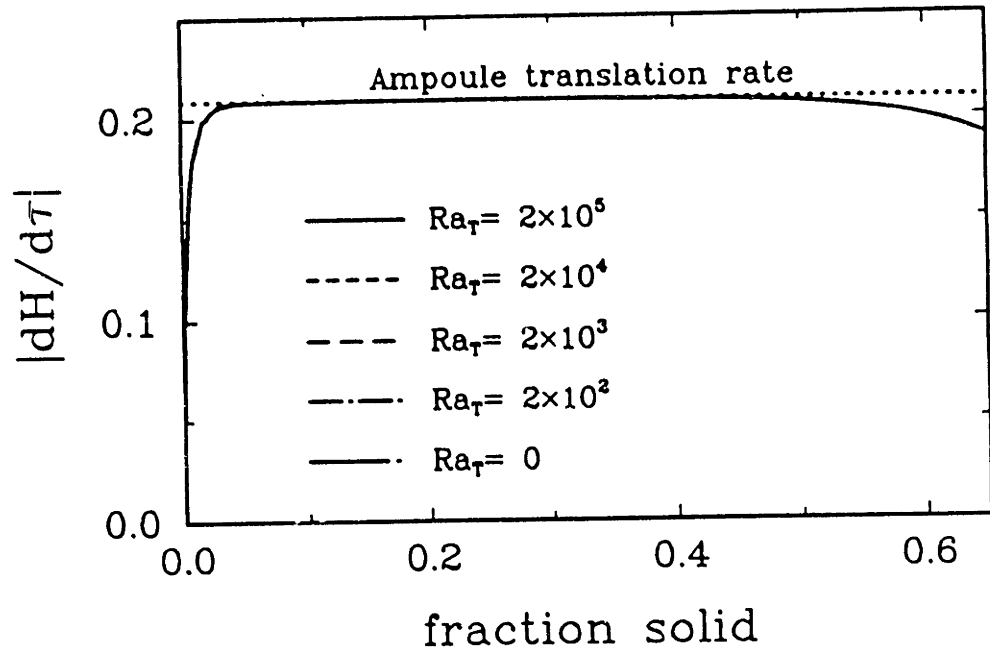


Figure 6.7: Transient growth rate of GaGe crystal for several values of thermal Rayleigh numbers, Ra_τ .

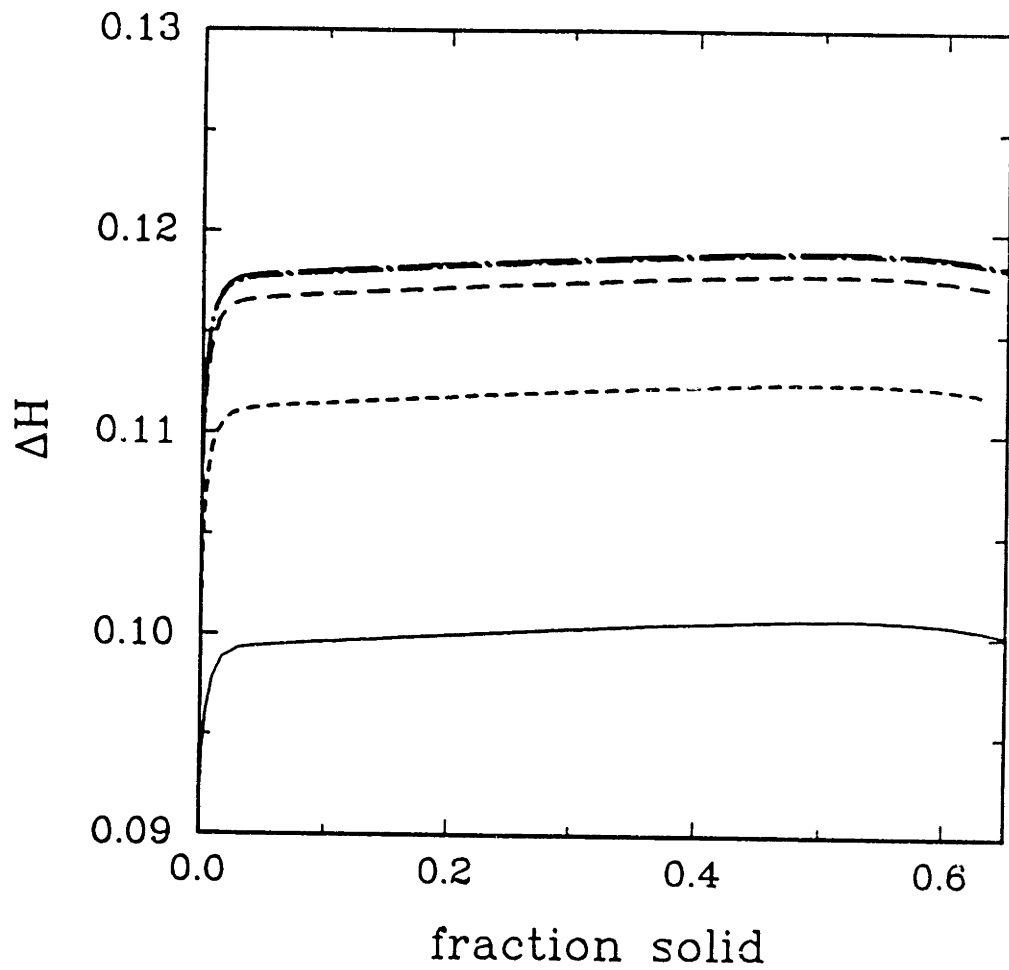


Figure 6.8: Transient interface deflection for several values of thermal Rayleigh numbers, Ra_t .

The growth rate of the crystal was computed from the transient location of the interface, which is determined solely from the temperature field for a dilute binary alloy. Since the temperature field in the melt is affected little by the convection level, the growth rate histories for several values of Ra_t superpose on one another and are nearly indistinguishable in Figure 6.7. These growth rate profiles show the initial transients caused by the step change of ampoule translation rate (from 0 to 4 $\mu\text{m}/\text{sec}$) and the deviation of growth rate from the ampoule translation rate in later time is caused by changes in the temperature field as the interface senses the approaching end of the ampoule.

The initial transient represents the adaptation of the crystal growth rate $|\partial H/\partial\tau(\tau)|$ to the translation rate of the ampoule V_g upon sudden change in the translation rate. This change is caused by unsteady heat transfer which is coupled with the transient crystal growth rate through the latent heat release at the melt/crystal interface. Fu and Wilcox (1981) obtained the correlation for the transient growth rate from a one-dimensional heat transfer model as

$$\left| \frac{\partial H}{\partial \tau} \right| = V_g [1 - \exp(-\tau/A)] \quad (6.10)$$

where A is a time constant of thermal response in the growth system and mostly depends on the heat transfer coefficient between the furnace and ampoule and the magnitude of latent heat release at the interface. The computed growth rate in the initial transient is plotted as a function of fraction solidified in Figure 6.9 for thermal Rayleigh number of 0 and 2×10^5 . In the initial transient, the growth rate is well correlated with the functional form suggested by Fu and Wilcox (1981). Figure 6.9 also shows the effect of convection on the thermal response in the system. Comparison of the slopes of two curves shows that a slightly faster thermal response is obtained with the high level of convection $Ra_t = 2 \times 10^5$.

The differences between the thermal conductivities of melt, crystal and ampoule cause the characteristic thermal field near the interface. In this region, the melt near the centerline is hotter than near the ampoule wall and a concave interface shape to the

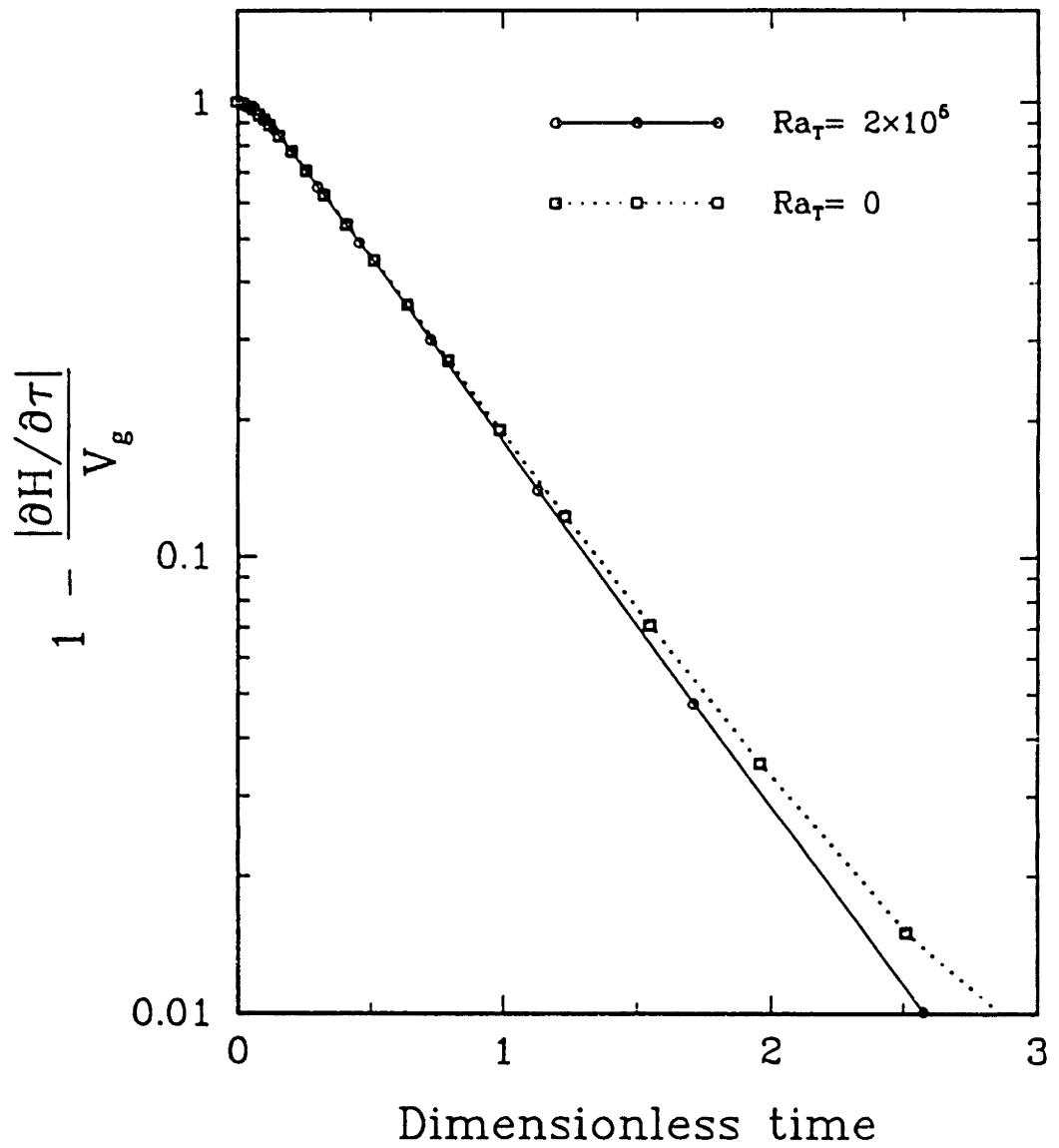


Figure 6.9: Growth rate transients for step change in ampoule translation rate; comparison is shown to the correlation of Fu and Wilcox (1981).

solid is obtained. The concavity of the interface increases with the release of latent heat at the interface. The amount of concavity is proportional to the growth rate of crystal. A sudden change of the ampoule translation rate leads to the transient behaviour in both growth rate and interface deflection, as shown in Figures 6.7 and 6.8. Interface deflection ΔH is much more sensitive to convection level. This is important for matching the computed results with experiments in Section 6.3.5.

6.3.3 Flow Fields

The axial temperature gradient in stabilizing vertical Bridgman system does not drive the flow in the melt. The temperature field near the interface provides a negative radial temperature gradient adjacent to the interface and the large change of thermal environment at the junction of the hot zone and adiabatic zone results in the positive radial temperature gradients in that region. These two radial temperature gradients play the role of driving forces for thermal buoyant flow in the melt and lead to the characteristic two-cell structured flow first seen by Chang and Brown (1984). The upper toroidal cell moves melt upward along the ampoule wall and down at the centerline. Lower toroidal cell near the interface rotates in the opposite direction.

Sample flow fields in the melt are presented in Figure 6.10–6.13 for thermal Rayleigh numbers of $Ra_t = 2 \times 10^2, 2 \times 10^3, 2 \times 10^4$ and 2×10^5 . These flow fields occur at the elapsed time of approximately 0, 5,000, 10,000, and 15,000 seconds for each thermal Rayleigh number and show the relative locations of the ampoule with respect to the furnace.

The initial structure of the two axially stacked counter-rotating cells is unchanged in time, as shown in Figure 6.10. The intensity of each flow cell, as measured by the maximum absolute values of the stream function Ψ , is almost constant. As the interface approaches the end of ampoule, the upper flow cell suffers the resistance of the solid end wall and the flow intensity decreases.

The two-cell structure of flow is not affected by increasing the thermal Rayleigh

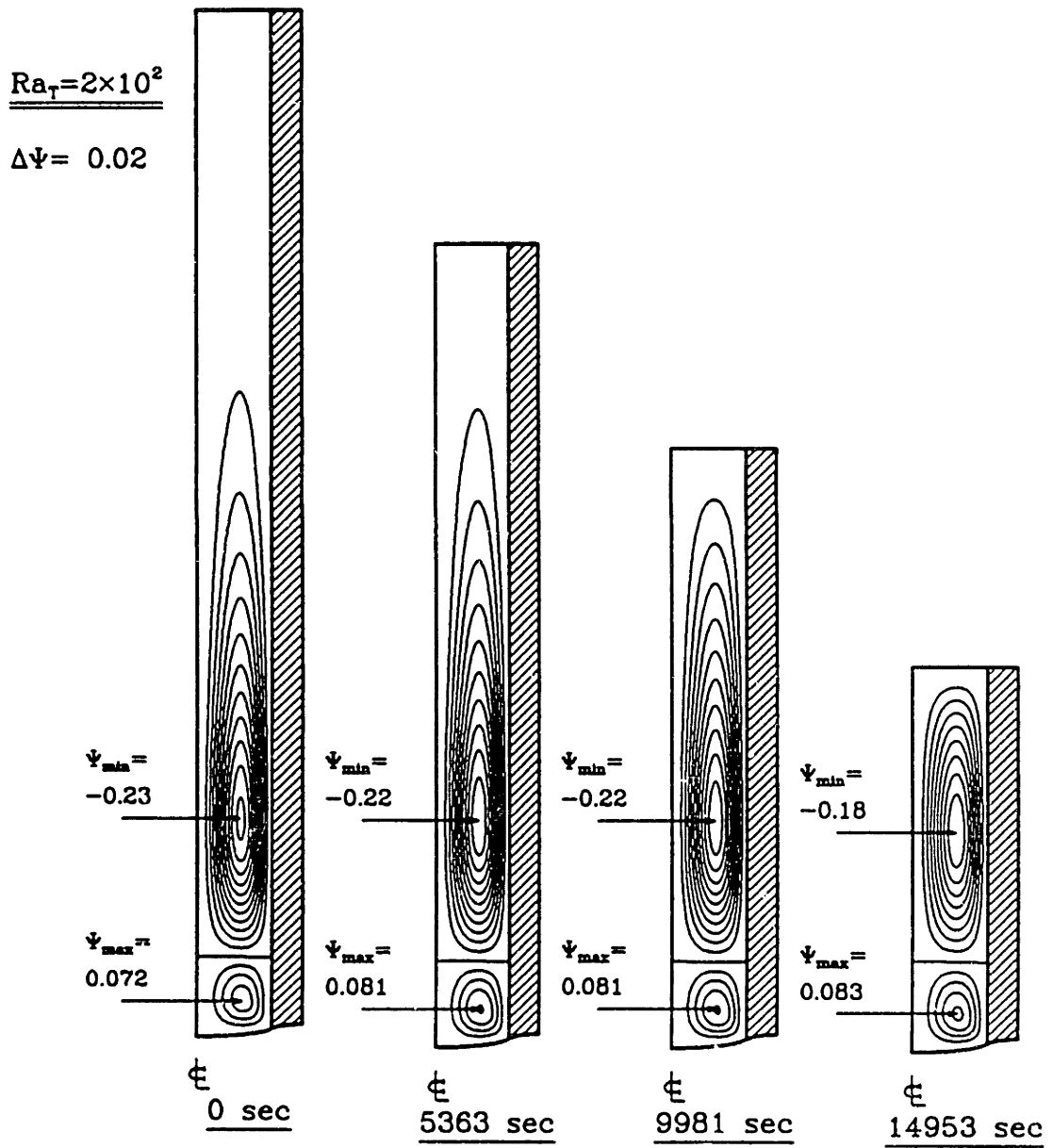


Figure 6.10: Sample flow fields for growth of GaGe in MIT system with boron nitride ampoule: $Ra_t = 2 \times 10^2$.

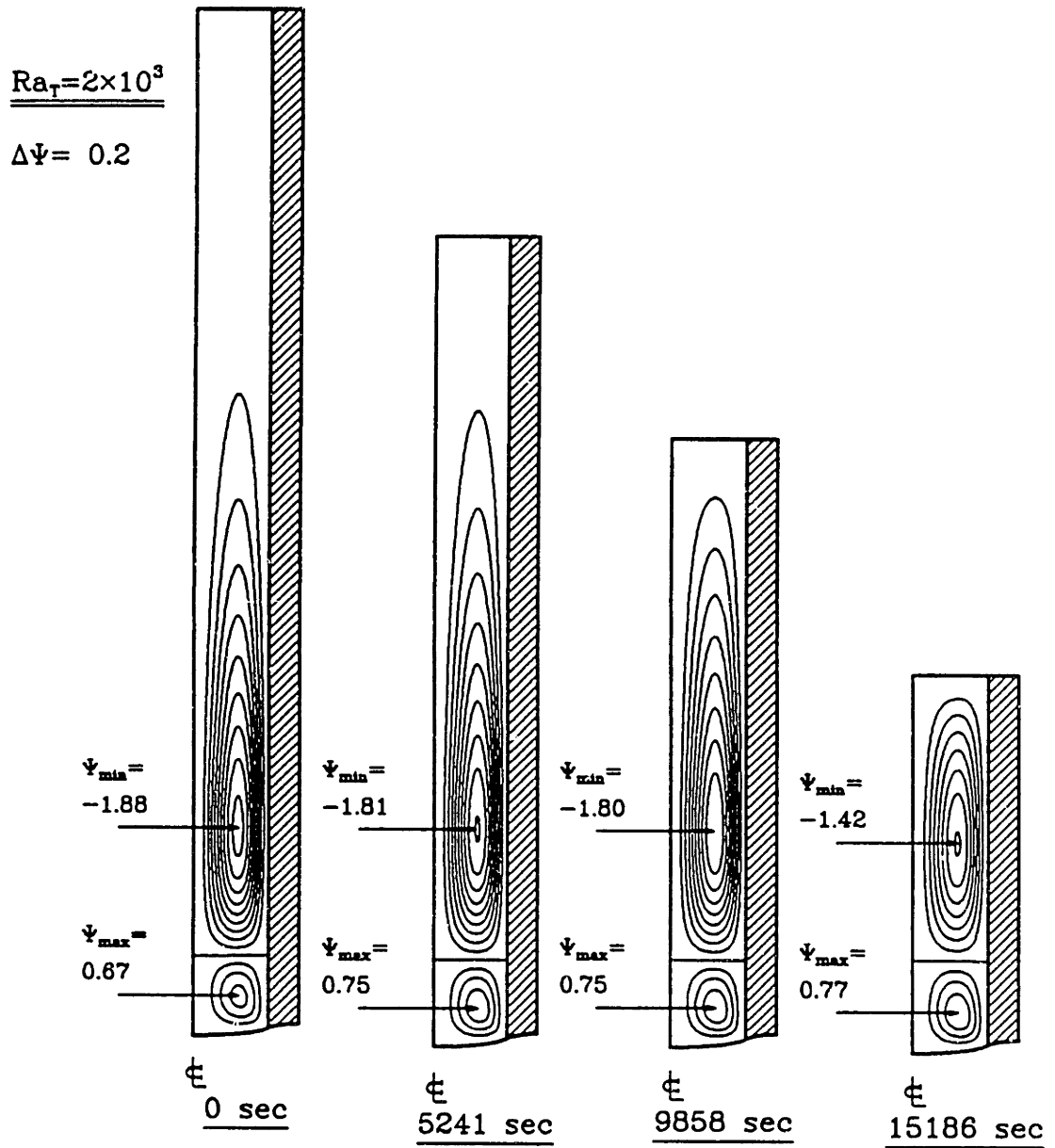


Figure 6.11: Sample flow fields for growth of GaGe in MIT system with boron nitride ampoule: $Ra_t = 2 \times 10^3$.

$$\underline{Ra_T = 2 \times 10^4}$$

$$\Delta\psi = 1.0$$

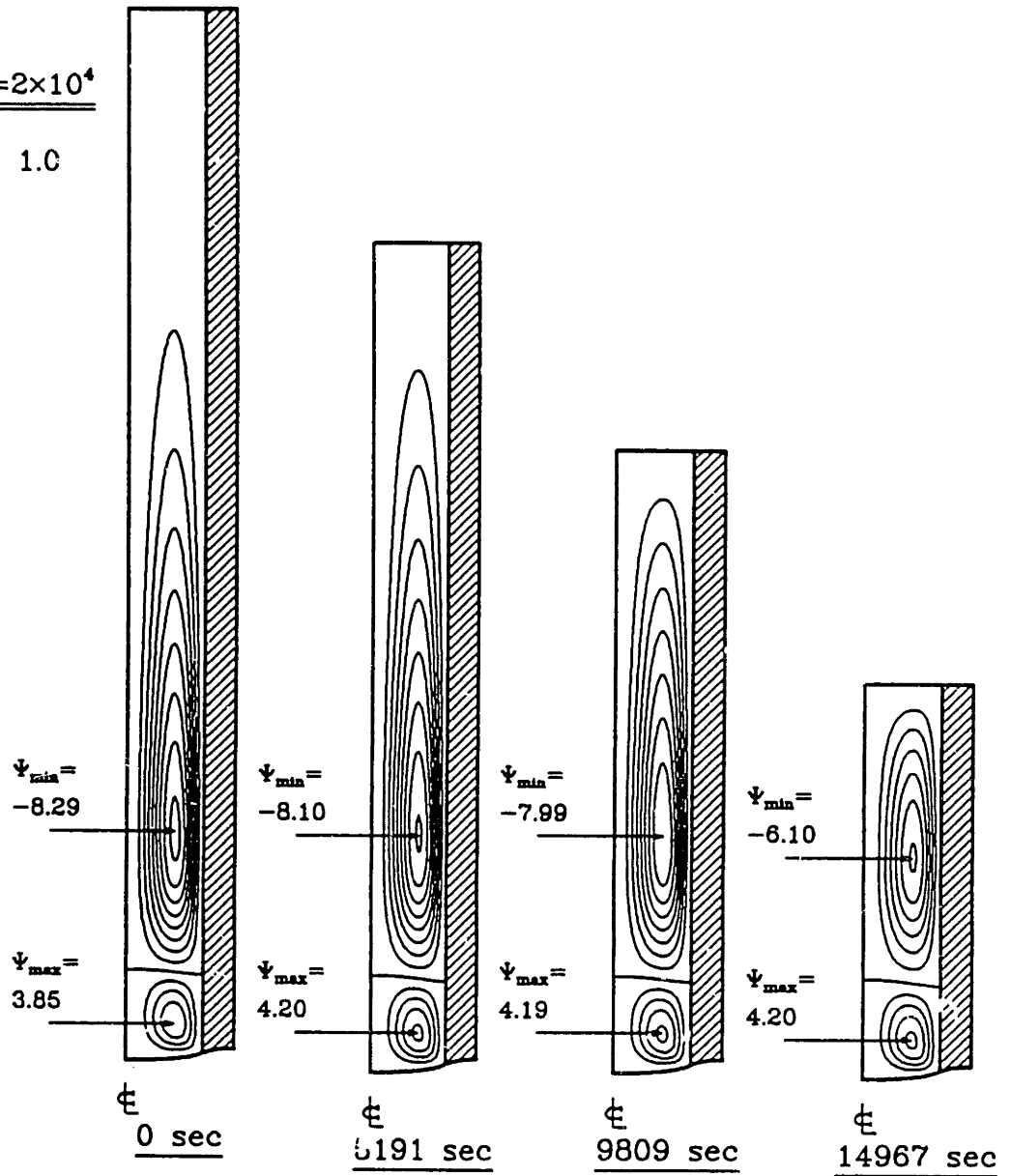


Figure 6.12: Sample flow fields for growth of GaGe in MIT system with boron nitride ampoule: $Ra_t = 2 \times 10^4$.

$$\underline{Ra_T = 2 \times 10^5}$$

$$\Delta\Psi = 2.0$$

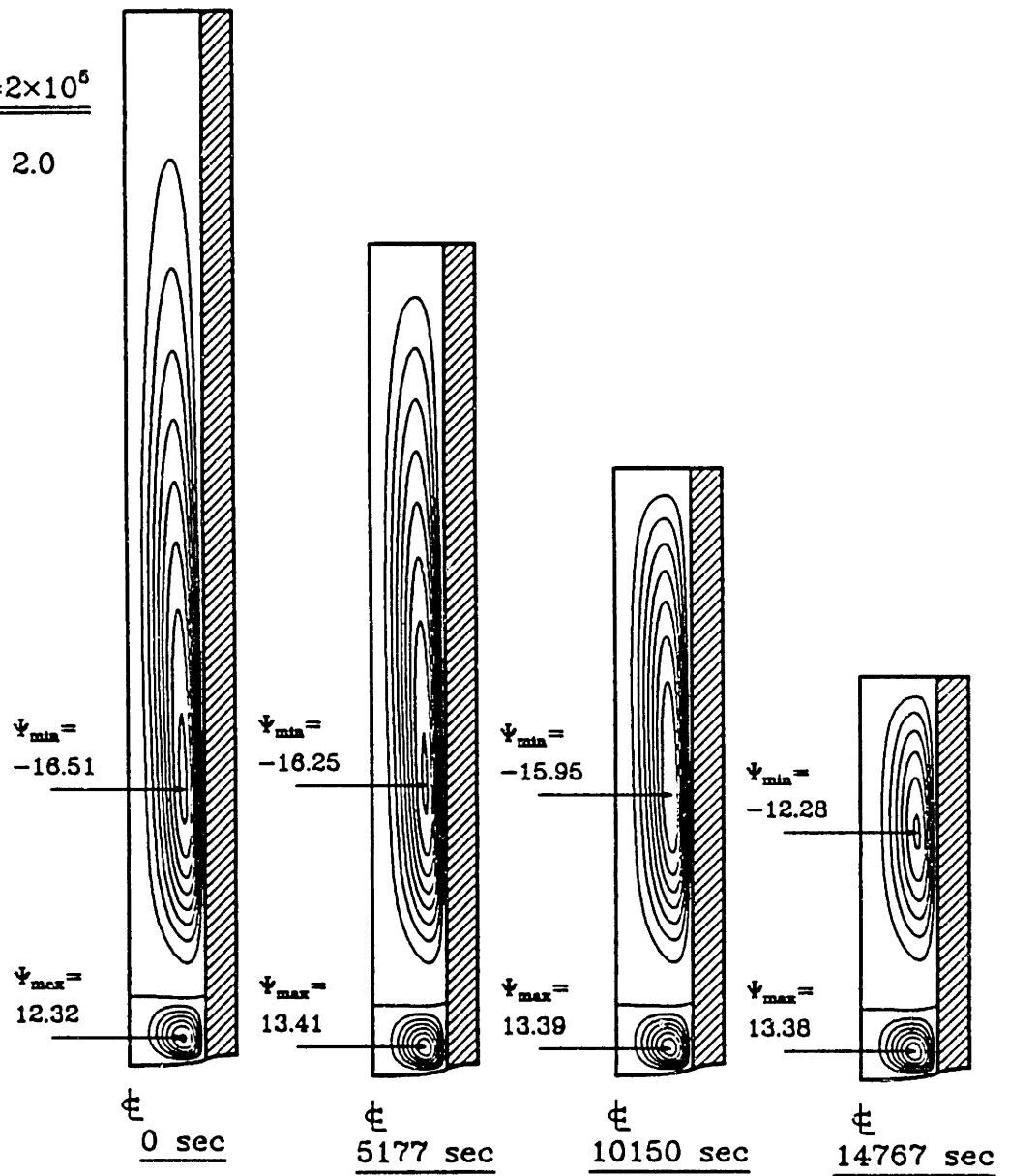


Figure 6.13: Sample flow fields for growth of GaGe in MIT system with boron nitride ampoule: $Ra_t = 2 \times 10^5$.

number. Only the intensities of the cells in terms of the stream function values Ψ increase with the thermal Rayleigh number. As the intensity of flow increases, thin boundary layers form along the ampoule wall, as exemplified by the shift of the center of the flow cell to the wall. This is more evident in the upper flow cell than in the lower cell, because the flow in the lower cell is much more restricted by the geometry near the interface. The time histories of the intensities of the flow cells are presented in Figure 6.14; the intensities of the upper and lower flow cells are Ψ_{min} and Ψ_{max} , respectively. The intensities of the lower flow cell are almost constant during the run, but, the upper flow cell experiences the decrease of flow intensity due to the reason discussed above.

The effect of increasing thermal Rayleigh number on the intensity of the flow is presented in Figure 6.15 for $f = 0$ and $f = 0.6$, where f is the fraction of the melt that has been solidified. The increase of the flow intensity with thermal Rayleigh number is approximately linear up to $Ra_t = 2 \times 10^4$, indicating that inertia and thermal convection are not important. When the thermal Rayleigh number is large enough, inertial effect becomes important in the momentum equation and convection in the energy transfer reduces the radial temperature gradient in the melt. These combined effect leads to the slower increase in the circulation rate with high Ra_t .

The results for the flow fields by transient analysis are very similar to the pseudo-steady-state results with varying melt depths. In the MIT system, the radial temperature gradients, which drive the melt flow, are almost constant in time because the steady-state temperature field near the interface is set shortly after the beginning of ampoule translation. The combined effect of long ampoule and steady-state temperature field near the interface leads to the steady-state flow structure as viewed from the interface.

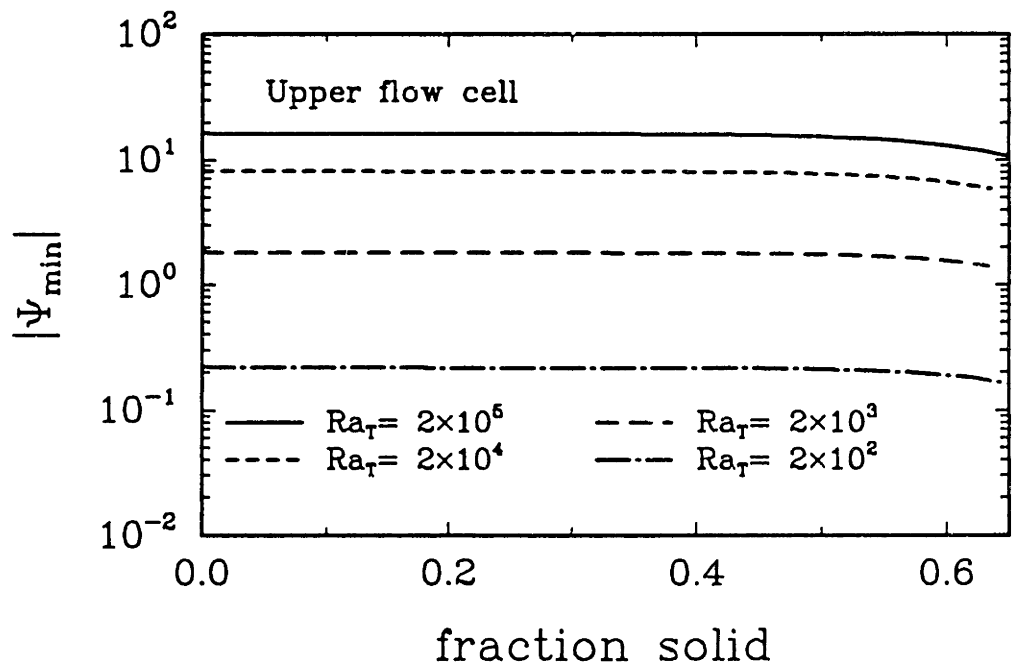
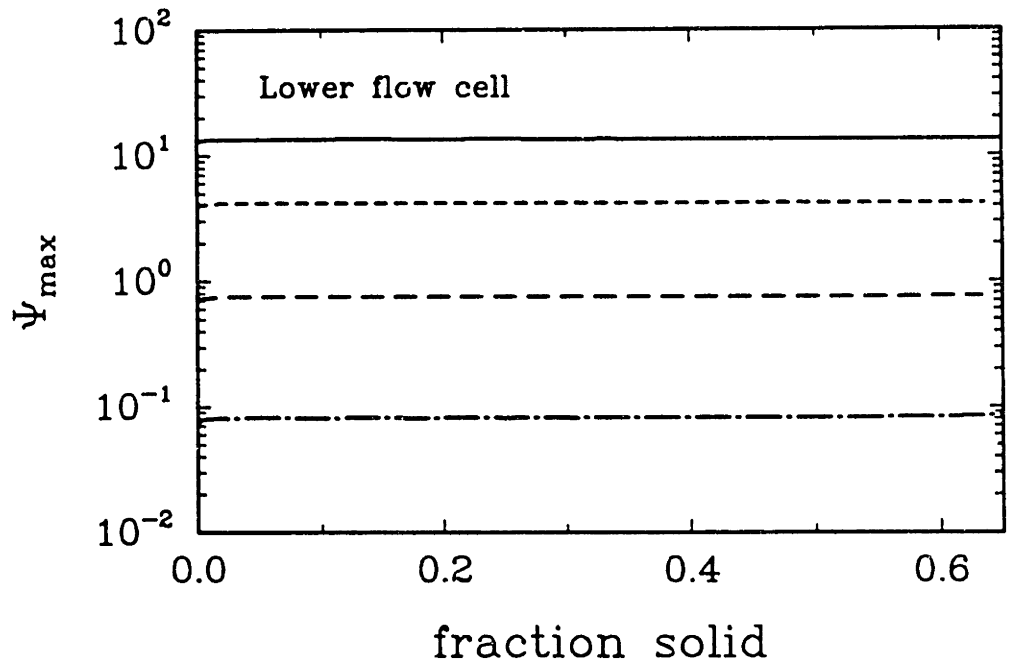


Figure 6.14: Time histories of the maximum values of the stream function in the upper and lower flow cells as a function of Ra_t for growth of GaGe in MIT system.

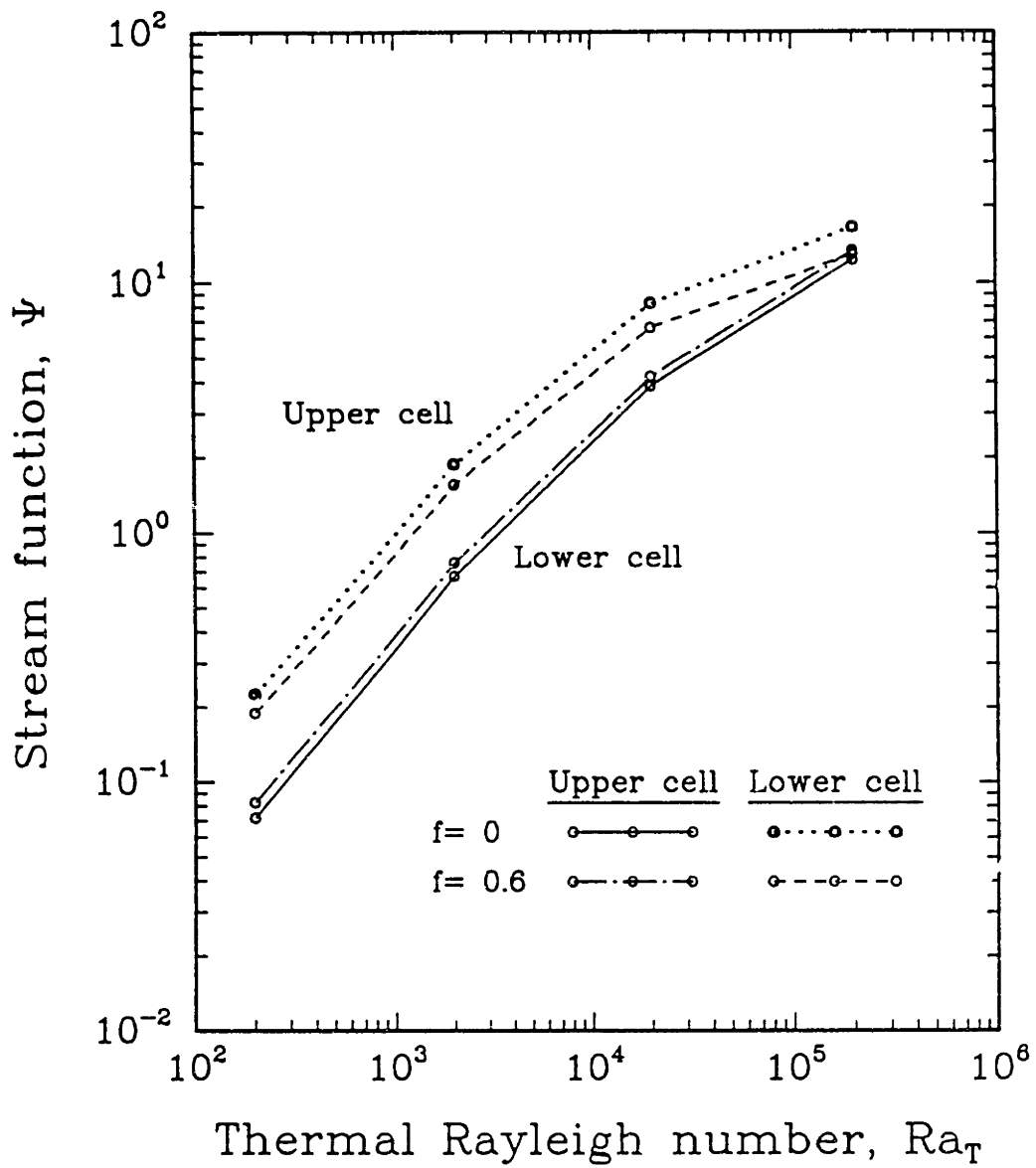


Figure 6.15: Maximum values of the stream function in the upper and lower flow cells as a function of Ra_t for fraction solidified $f = 0$ and 0.6 .

6.3.4 Solute Fields

The diffusion coefficient of gallium in germanium is 2.1×10^{-4} cm²/sec and the Schmidt number Sc is between 1 and 10. As a result of relatively high Schmidt number, convection dominates solute transfer and the solute distribution is highly dependent on the flow pattern in the melt. Transient solute profiles for dilute gallium in germanium are shown in Figure 6.16–6.20, as calculated for the flows shown in Figure 6.10–6.13 and the ampoule translation rate of $4\mu\text{m}/\text{sec}$. At time zero, solute concentration is uniform throughout the melt, as denoted by the lack of isoconcentration contours in these figures.

When $Ra_t = 0$, solute distribution is almost one-dimensional in the axial direction and the solute diffusion layer develops in time due to the rejection of solute at the interface, as shown in Figure 6.16. The only deviation from a perfectly one-dimensional profile is caused by the curvature of the melt/crystal interface. Slight increase of the convection level deforms the iso-concentration contour lines to resemble the direction of flow in each cell, as shown in Figure 6.17. The influence of the flow structure on the solute distribution is more evident in Figure 6.18, where flow near the interface transports solute from the ampoule wall to the centerline of the melt, resulting in the higher dopant concentration near the center of the crystal. Above $Ra_t = 2 \times 10^4$ (Figure 6.19,6.20), convection is intense enough to form the well mixed regions within the core of each cell, where the solute concentration is almost uniform respectively. The gradients of solute concentration are present only in the region of weak flow, forming an internal solute boundary layer between the two flow cells, which prevents the exchange of solute between two regions.

Result of dopant concentration profile in the crystal are presented in Figure 6.21, in terms of the radially-averaged concentration $\langle C \rangle$, the radial segregation Δc and effective segregation coefficient k_{eff} , each defined as

$$\langle C \rangle = \int_0^1 c \sqrt{1 + H_r^2} r dr / \int_0^1 \sqrt{1 + H_r^2} r dr \quad (6.11)$$

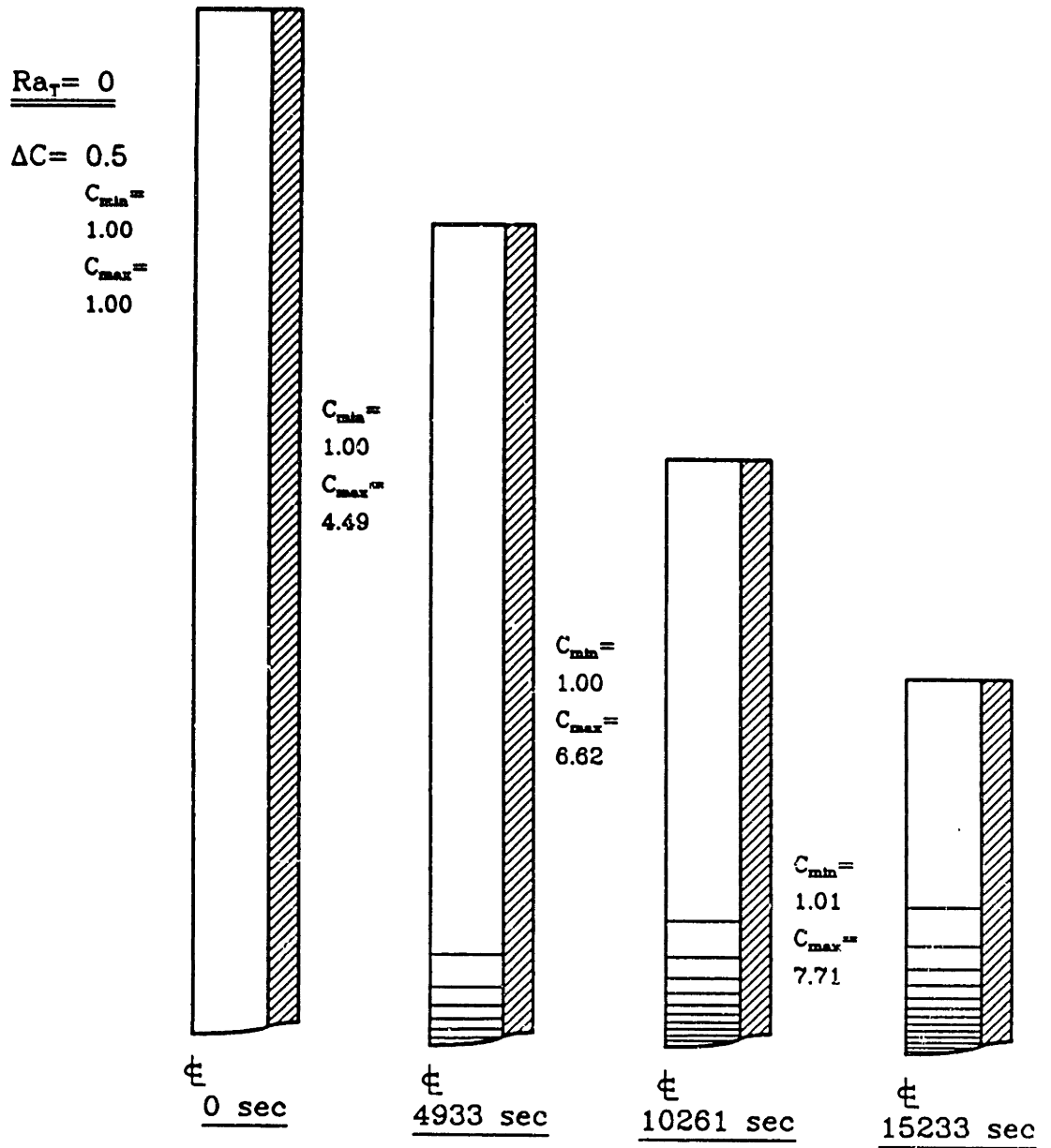


Figure 6.16: Sample gallium concentration fields for growth of GaGe in MIT system.
 $Ra_T = 0$ and $V_g = 4\mu\text{m}/\text{sec}$.

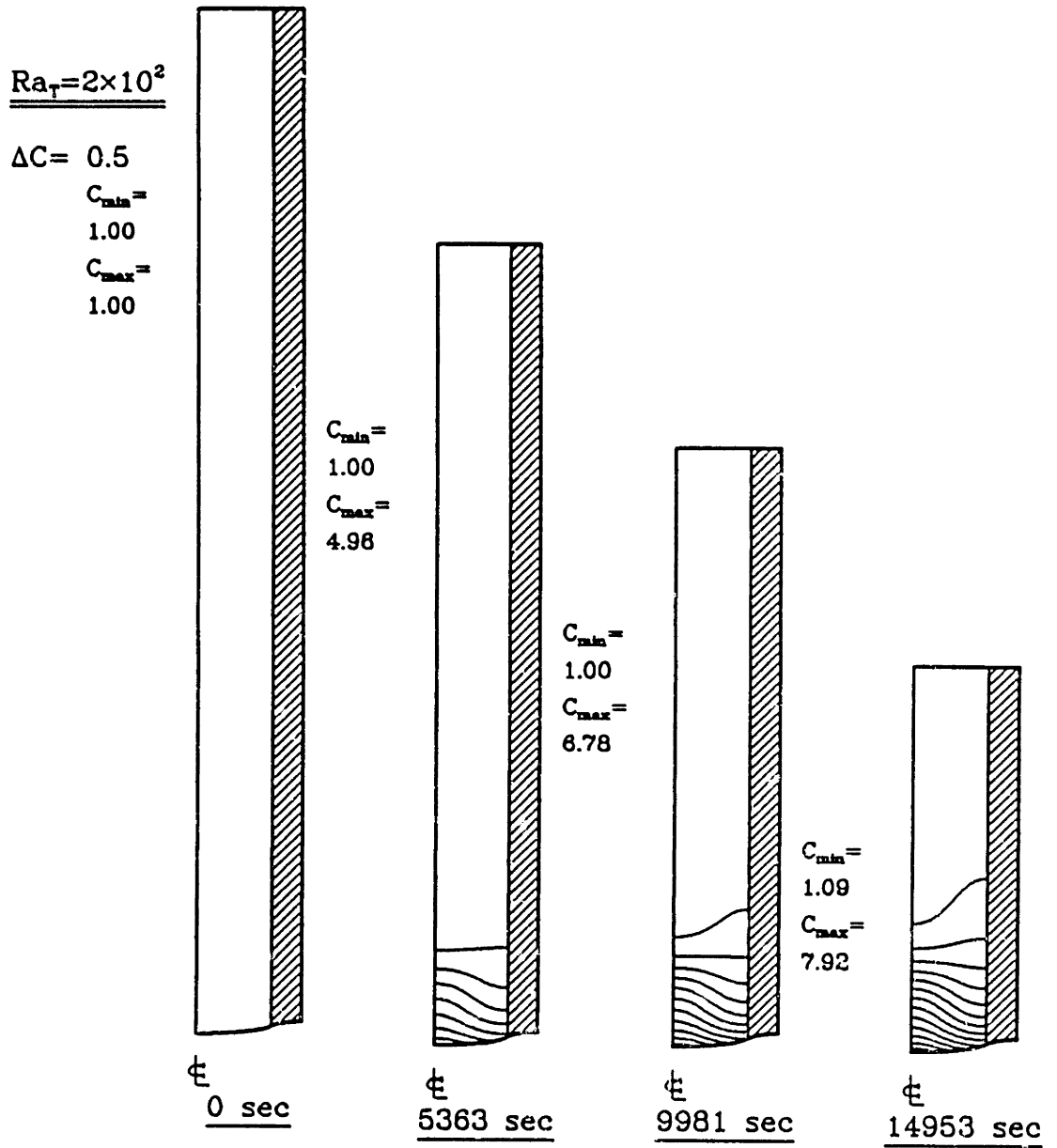


Figure 6.17: Sample gallium concentration fields for growth of GaGe in MIT system.
 $Ra_t = 2 \times 10^2$ and $V_g = 4 \mu\text{m}/\text{sec}$.

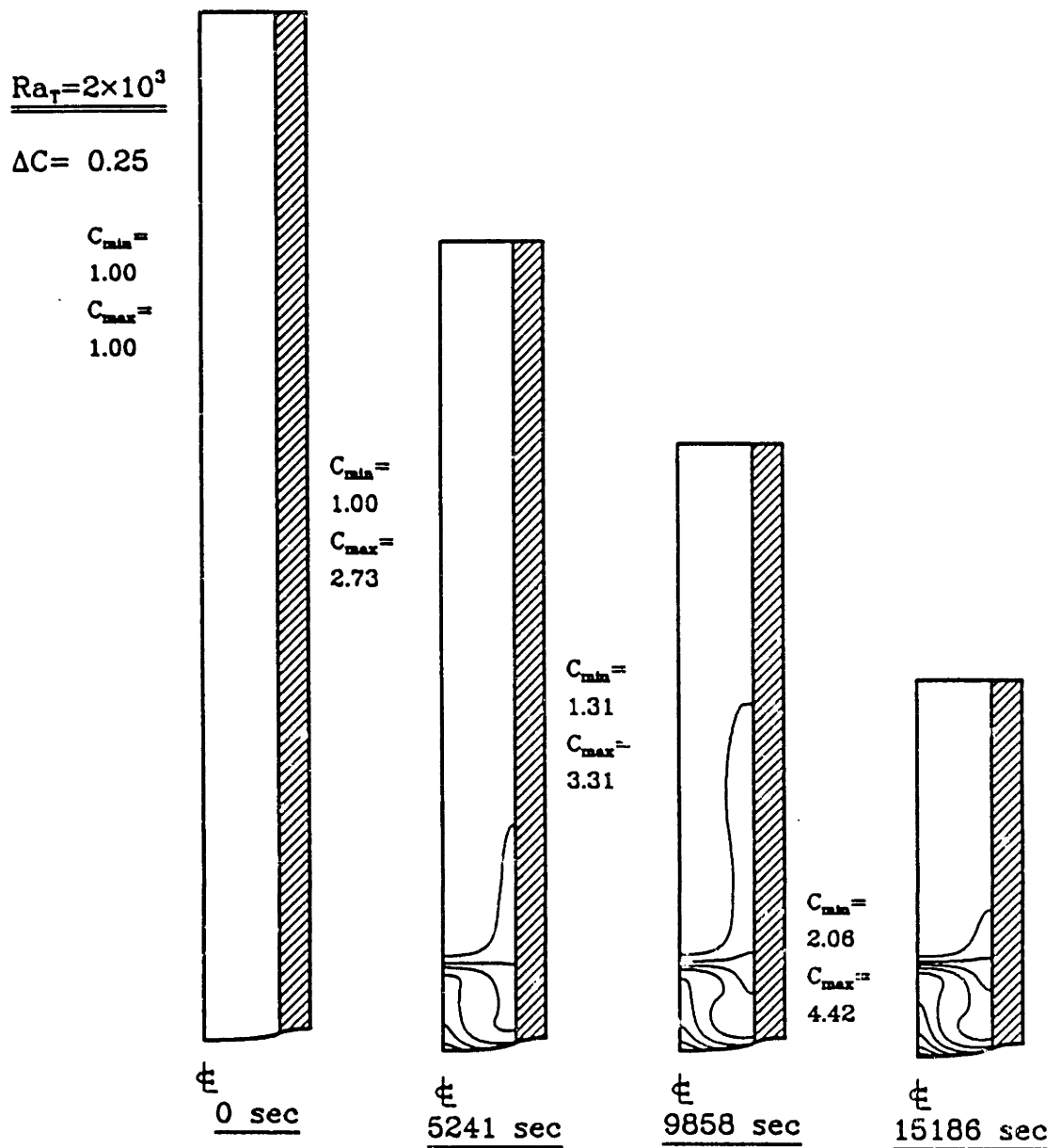


Figure 6.18: Sample gallium concentration fields for growth of GaGe in MIT system.
 $Ra_t = 2 \times 10^3$ and $V_g = 4 \mu\text{m}/\text{sec}$.

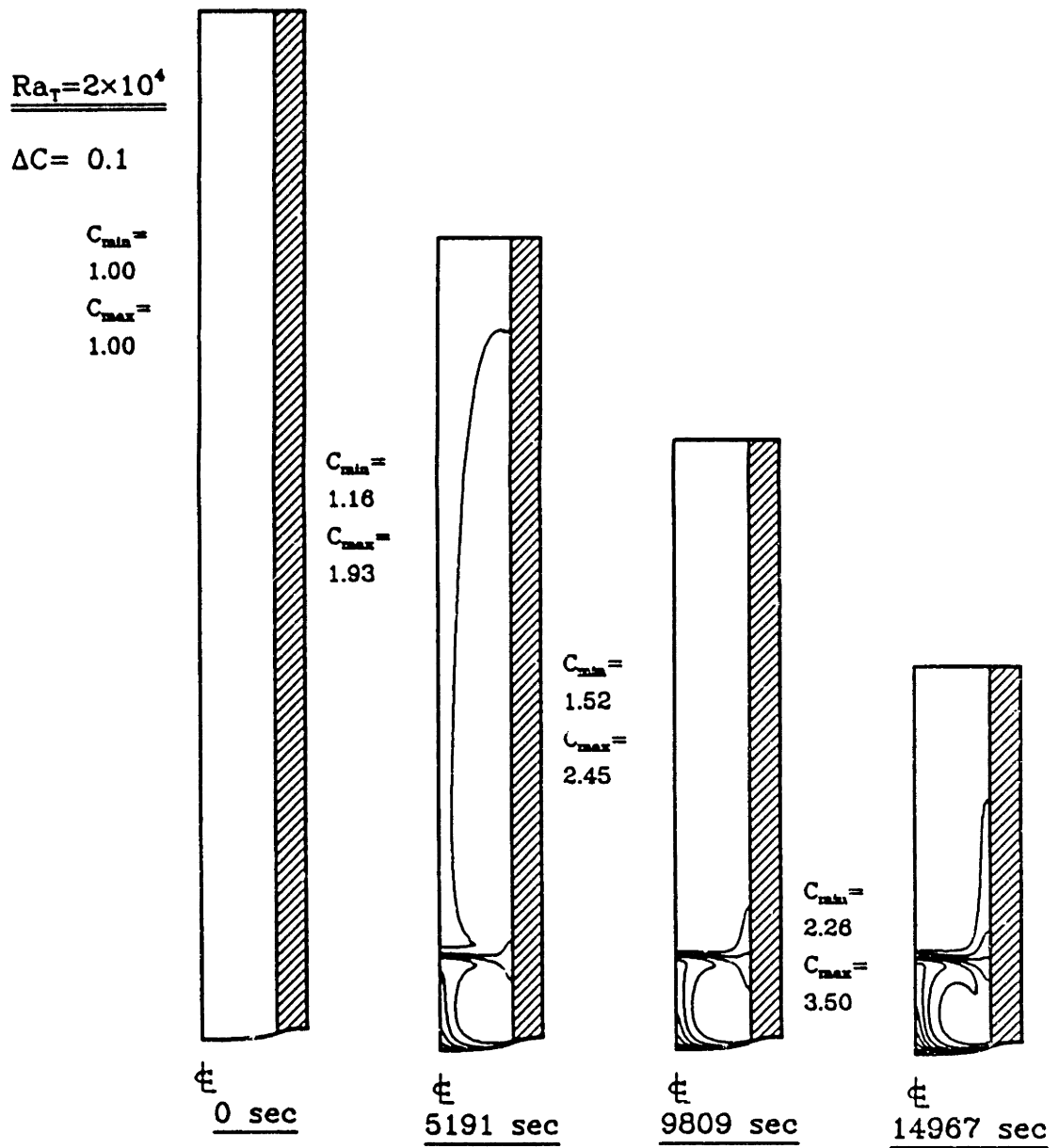


Figure 6.19: Sample gallium concentration fields for growth of GaGe in MIT system.
 $Ra_t = 2 \times 10^4$ and $V_g = 4 \mu\text{m}/\text{sec}$.

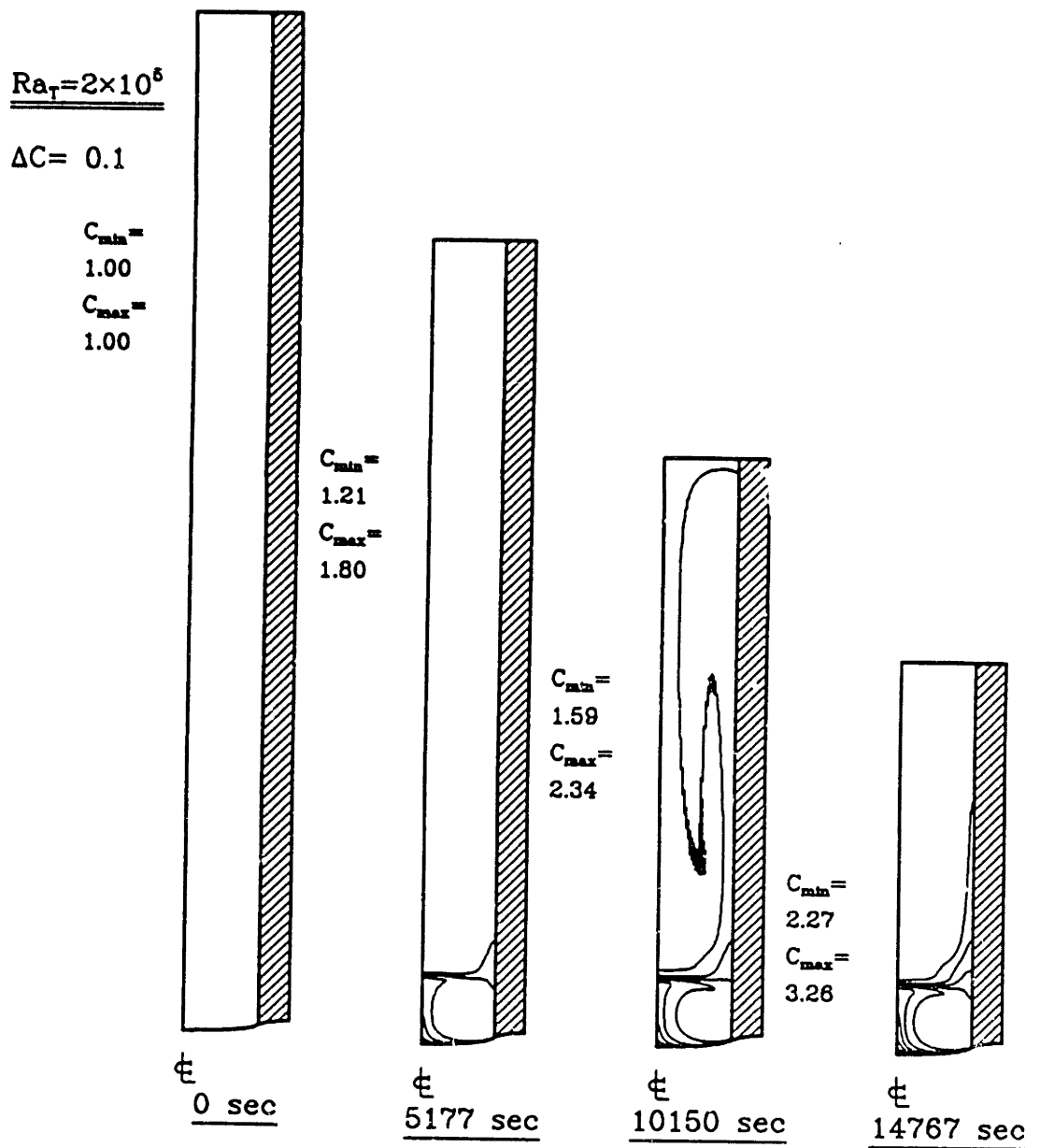


Figure 6.20: Sample gallium concentration fields for growth of GaGe in MIT system.
 $Ra_t = 2 \times 10^5$ and $V_g = 4 \mu\text{m}/\text{sec}$.

$$\Delta C(\%) = \left[\max_{0 \leq r \leq 1} C(r, H(r)) - \min_{0 \leq r \leq 1} C(r, H(r)) \right] / \langle C \rangle \times 100\% \quad (6.12)$$

$$k_{eff} = k \frac{\langle C \rangle}{\langle\langle C \rangle\rangle} \quad (6.13)$$

where $\langle\langle C \rangle\rangle$ is the bulk-averaged concentration in the melt and k is the equilibrium distribution coefficient for the solute.

The solute concentration profile in the crystal computed for $Ra_t = 0$ agrees well with the one-dimensional concentration profile derived by Smith *et al.* (1955) in the absence of convection. Even if the initial growth rate transient is neglected in their solution, the effect of growth rate transient is not distinct in the comparison because of the short transient period of growth rate. The deviation of growth rate from the ampoule translation rate in later time (Figure 6.7) leads to the deviation of the calculated one-dimensional solute profile at $Ra_t = 0$ from the solution by Smith *et al.* (1955). Increasing convection in the melt by increasing the thermal Rayleigh number shifts the solute profile to the solution of Scheil equation (1942), which is written as

$$c_s(z) = k(1 - f)^{(k-1)} \quad (6.14)$$

where k is a equilibrium distribution coefficient and $f = \bar{z}/L$ is a fraction solidified. It is somewhat surprising that calculated solute profiles in the crystal approach the solution of the Scheil equation, because the convection pattern has two well-mixed regions and the exchange of solute between these two regions is by diffusion alone.

The computed radial segregation shown in Figure 6.21(b) has a maximum at intermediate thermal Rayleigh numbers, as observed previously in the steady-state analysis of the same system (Adornato and Brown, 1987a,b). The intensity of convection during terrestrial growth ($Ra_t = 2 \times 10^5$) is not considered to be high enough to reduce the radial segregation to the level of convectionless growth ($Ra_t = 0$). It is interesting that the solute fields for $Ra_t = 2 \times 10^2$ and 2×10^3 lead to very different solute profiles in the crystal; one for $Ra_t = 2 \times 10^2$ is close to the solution of Smith *et al.* for diffusion-controlled growth and the other for $Ra_t = 2 \times 10^3$ is close to the solution of Scheil; however, both fields have nearly the same values of radial segregation ΔC .

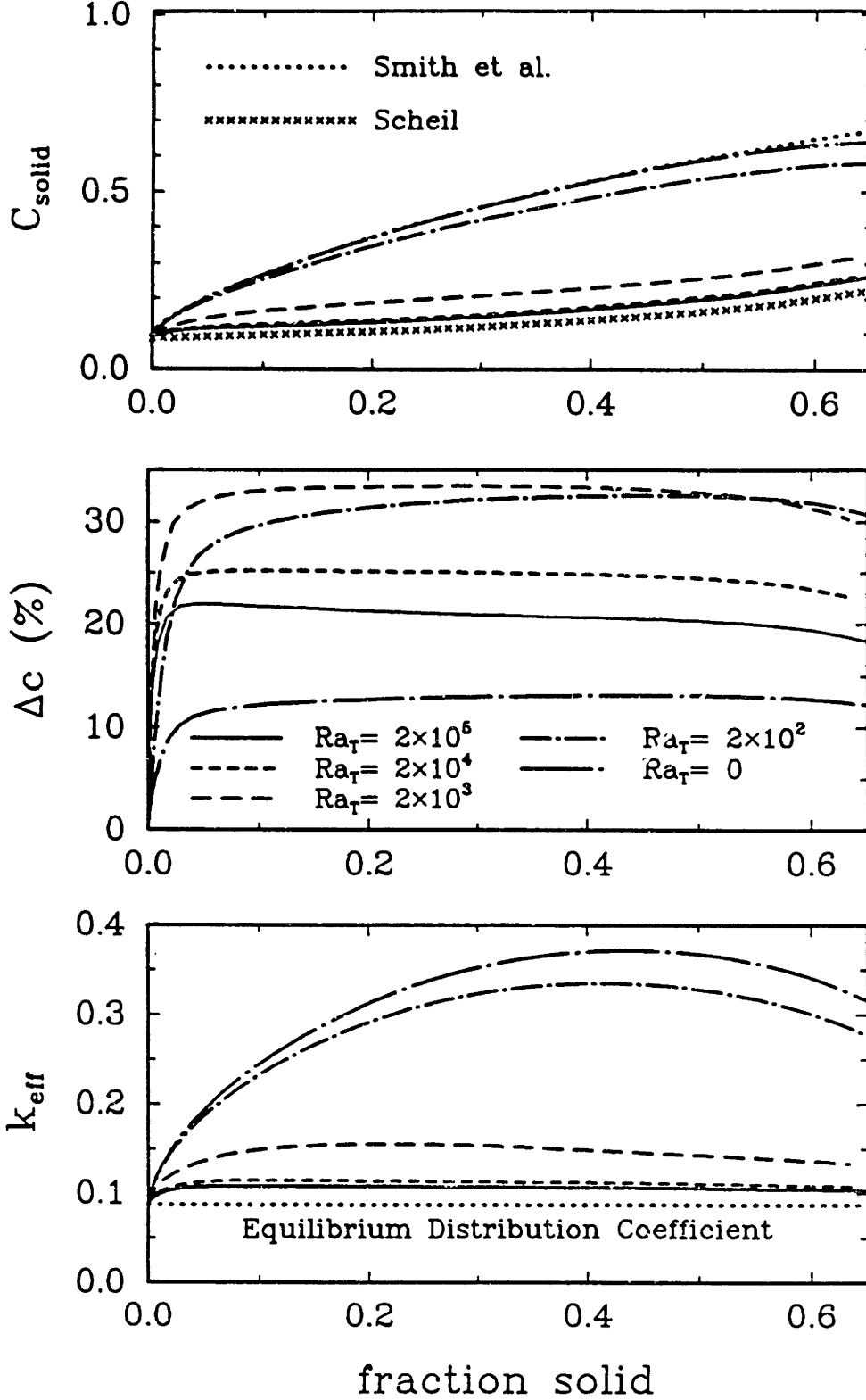


Figure 6.21: Simulations of GaGe crystal growth at the ampoule translation rate of $4 \mu\text{m}/\text{sec}$ and several values of thermal Rayleigh numbers; (a) axial segregation profile, (b) radial segregation, and (c) effective segregation coefficient in the crystal.

From the definition of effective segregation coefficient k_{eff} (6.13), it is easily deduced that k_{eff} approaches the equilibrium distribution coefficient k for complete mixing, where the solute concentration is uniform everywhere along interface and in the bulk. Calculated values of the effective segregation coefficients k_{eff} are very close to k above $Ra_t = 2 \times 10^4$ as shown in Figure 6.21. This indicates that convection under terrestrial growth conditions is intense in terms of axial segregation. For low values of Ra_t , k_{eff} increases initially as the solute diffusion layer is developed and the interface concentration increases; however, it tends to decrease, when the solute diffusion layer fills the melt.

6.3.5 Comparison with Experimental Measurements

The results of the transient numerical calculations are compared with the experimental measurements of Wang (1984) to quantify the accuracy of our model. For the purpose of comparison, calculations are done for the case where the ampoule translation rate is increased from $2 \mu\text{m}/\text{sec}$ to $4 \mu\text{m}/\text{sec}$ after 0.3 of the charge has been solidified. Every measurement obtained from the experiment can be calculated from the transient model, including the transient growth rate, the interface deflection, the radially-averaged solute concentration profile in the crystal, the radial segregation of gallium across the crystal and the effective segregation coefficient of gallium as a function of fraction of the melt that has been solidified.

Comparisons between the calculated and experimentally measured growth rates are presented in Figure 6.22(a) and (b). Part of Figure 6.22(a) is redrawn in Figure 6.22(b) to show detail in the initial transient. The initial transient and the transient caused by the step change in ampoule translation rate are well reproduced by simulation calculation, without any adjustments of thermophysical parameters or any accounting for the errors involved in the experimental measurement.

Experimental data of interface deflection are available only in terms of focal lengths for each ampoule translation rate. Interface deflection calculated from this data are

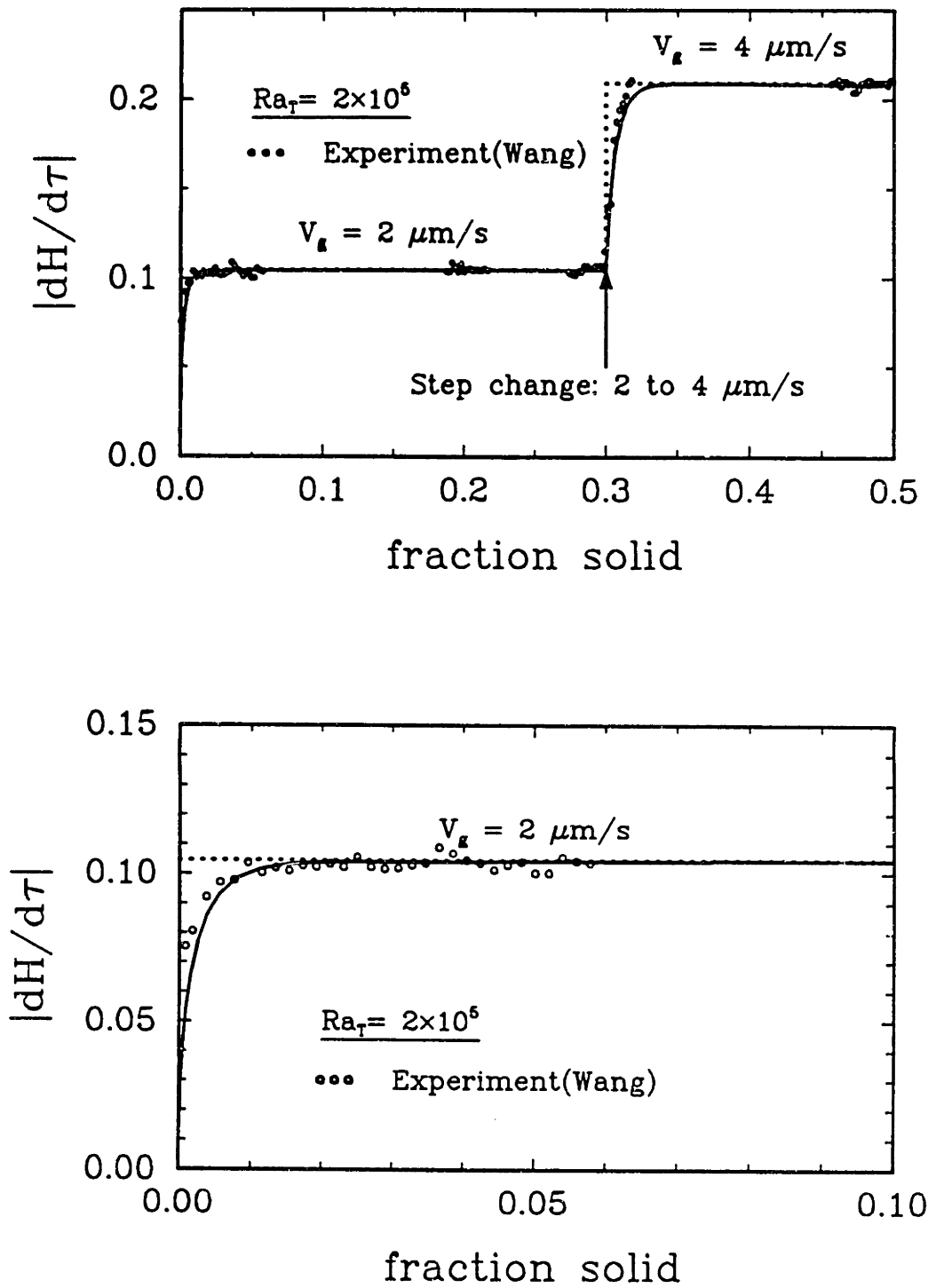


Figure 6.22: Comparison of computed transient growth rate of GaGe crystal with experimental data by Wang (1984) for the case of a step change in ampoule translation rate from $2 \mu\text{m/sec}$ to $4 \mu\text{m/sec}$: $Ra_\tau = 2 \times 10^5$.

plotted in Figure 6.23 with the results from transient numerical calculation. The numerical result has a tendency to overestimate the interface deflection, as in the work by Adornato and Brown (1987a), because of the weak singularity in the temperature field at the trijunction of melt, crystal and ampoule. However, the changes in the interface deflection caused by the increase of the ampoule translation rate follows the same trends of the experimental measurement.

The gallium concentration profile in the crystal measure experimentally is shown in Figure 6.24 with the comparison to the calculated profile. The profiles are in good agreement everywhere, except in the the initial stages of growth. Interestingly, the experimental data follows the solution of Scheil equation exactly in this region; this can be explained only by more intense mixing in the melt. Otherwise, the discrepancy in the initial region may be attributed to the dilution of the crystal by remelting of seed crystal on initiation of growth.

The overestimate of the numerically calculated interface deflection leads to the overestimation in radial segregation, as shown in Figure 6.25(a). The effective segregation coefficient obtained from the experiment are drawn as dots in Figure 6.25(b) and compared with the calculated values of k_{eff} . The agreement is good, except in the initial stage of growth, which coincides the region of discrepancy in Figure 6.24. The possible reasons for the discrepancy are the same.

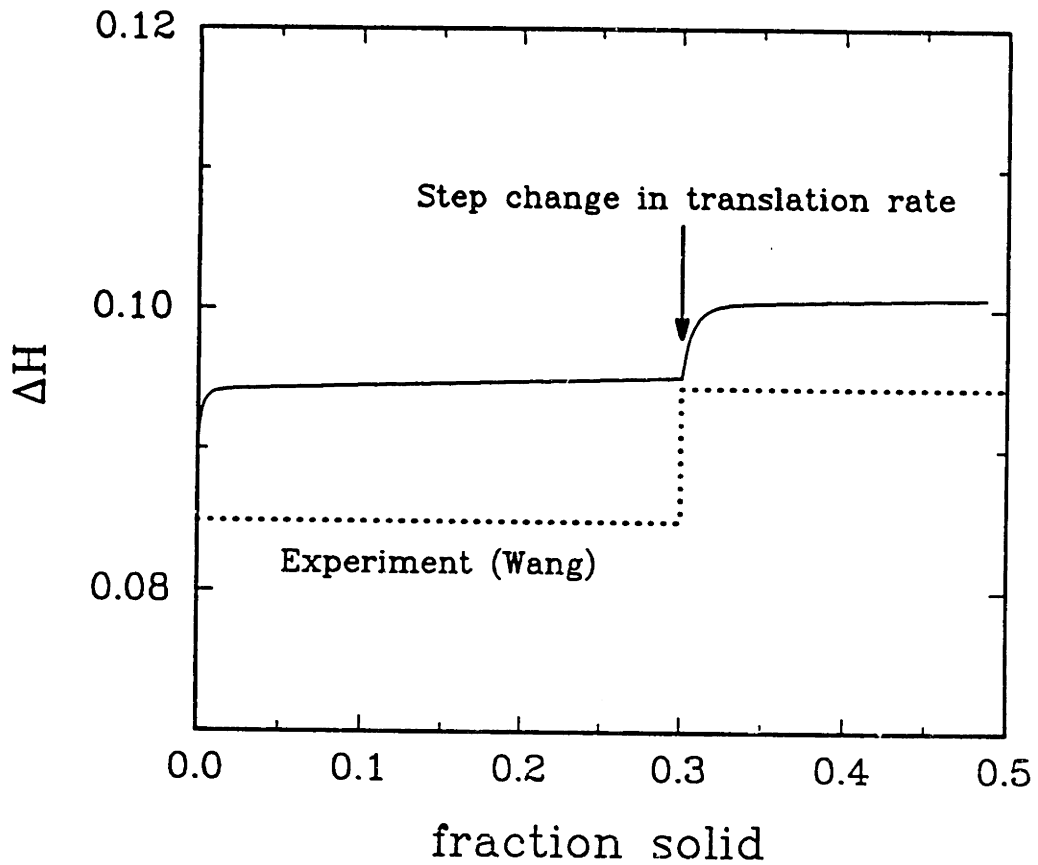


Figure 6.23: Comparison of computed transient interface deflection during the growth of GaGe crystal with experimental data by Wang (1984) for the case of step change in ampoule translation rate from $2 \mu\text{m}/\text{sec}$ to $4 \mu\text{m}/\text{sec}$; $Ra_t = 2 \times 10^5$.

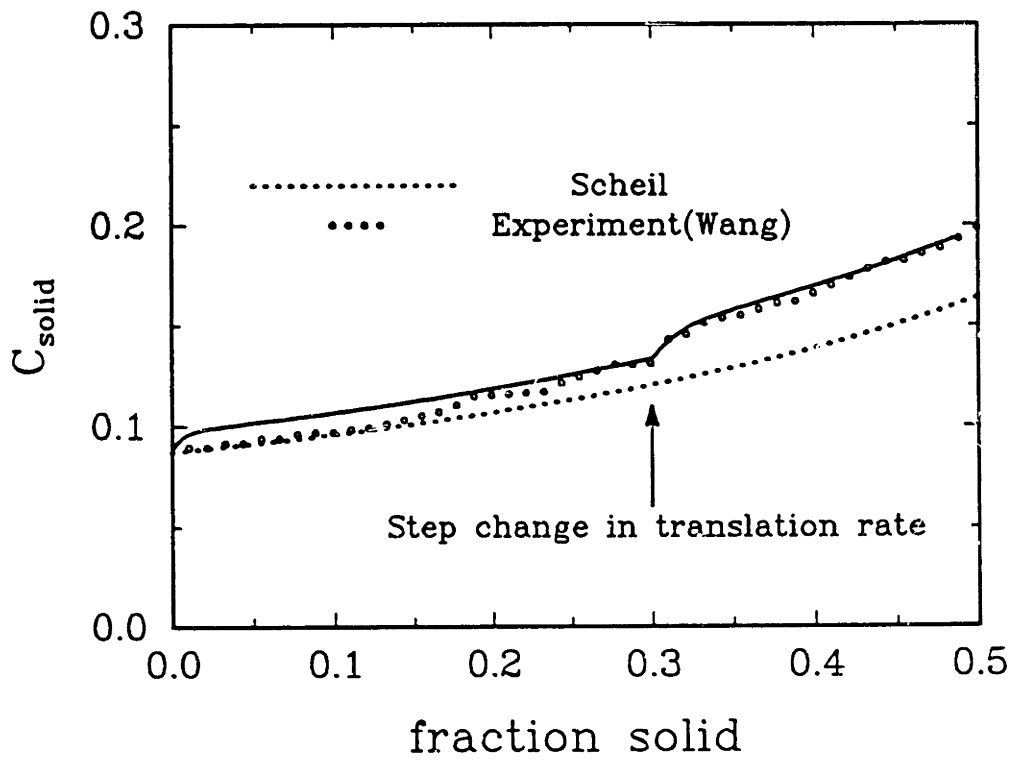


Figure 6.24: Comparison of computed axial segregation profile in GaGe crystal with experimental data by Wang (1984) for the case of step change in ampoule translation rate from $2 \mu\text{m}/\text{sec}$ to $4 \mu\text{m}/\text{sec}$: $Ra_t = 2 \times 10^5$.

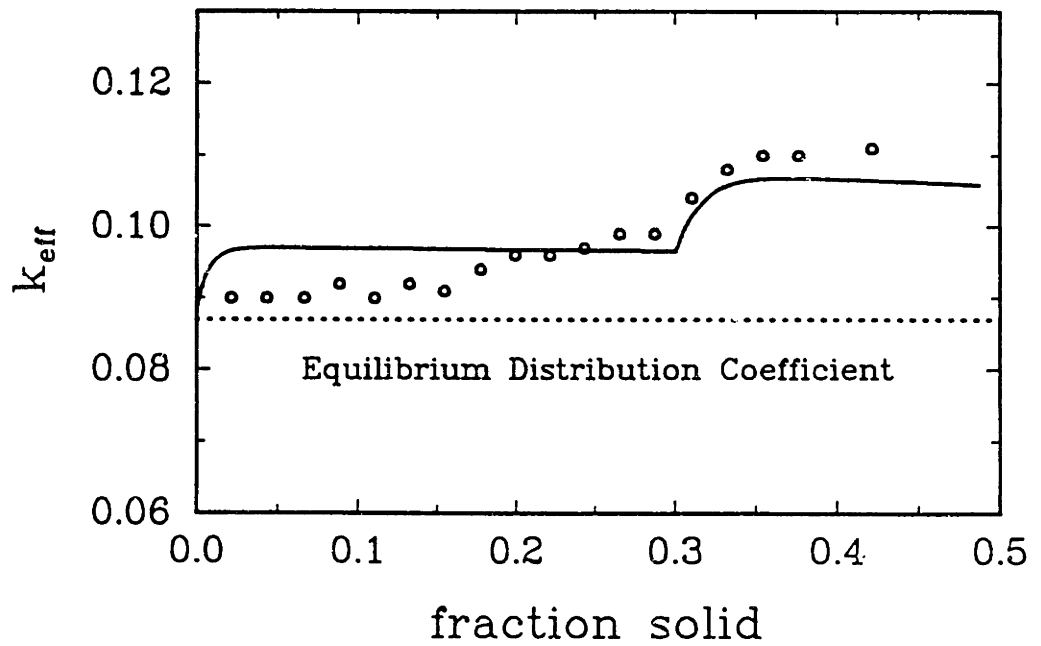
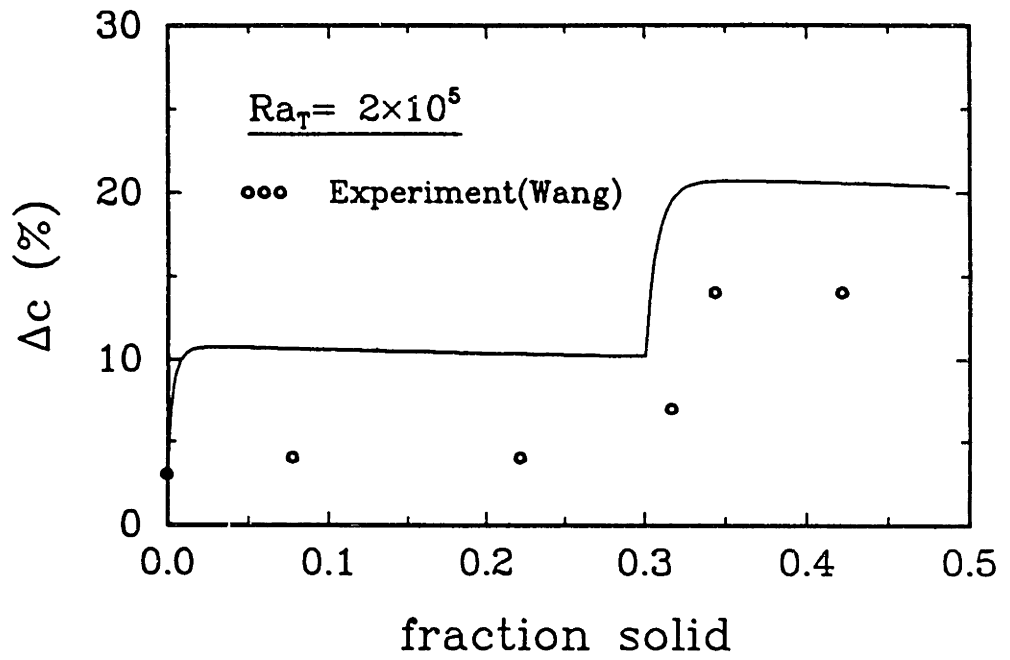


Figure 6.25: Comparison of computed transient (a) radial segregation and (b) effective segregation coefficient during the growth of GaGe crystal with experimental data by Wang (1984) for the case of step change in ampoule translation rate from $2 \mu\text{m}/\text{sec}$ to $4 \mu\text{m}/\text{sec}$: $Ra_t = 2 \times 10^5$.

6.4 Growth of Selenium-doped Gallium Arsenide in GTE Gradient Freeze Furnace

Gallium arsenide, a compound semiconductor of *congruent transformation* (Ghandi, 1983), is treated as a single material in this study. The thermophysical properties used for simulating the growth of selenium-doped gallium arsenide are compiled from Touloukian (1967,1970), Glazov *et al.*(1969), Neuberger (1971), Jordan (1980,1985) and Chait (1988). All properties are assumed to be independent of temperature and are listed in Table 6.4. This assumption is appropriate for the growth in the GTE gradient freeze furnace, because of the small range of temperature in the furnace. The only exception is for the viscosity which varies about 30 percent in the temperature range of interest (Jordan, 1985; Kakimoto and Hibiya,1987). The mean value of viscosity in the temperature range is used to mimic the effect of the variable viscosity. The concentration of selenium in gallium arsenide ($2 - 6 \times 10^{17}$ atoms/cm³ or $8 \times 10^{-6} - 3 \times 10^{-5}$ mole fraction) is considered to be small enough not to drive solutal convection during the growth.

The calculations are presented for the growth of gallium arsenide in GTE gradient freeze furnace. Design parameters corresponding to this system are listed in Table 6.5. Dimensionless groups appropriate for the growth of gallium arsenide in this furnace design are tabulated in Table 6.6 for growth under earthbound conditions.

6.4.1 Furnace Temperature Profile

Data on the furnace temperature profile were measured in the experiment "Run M" by the group at GTE (Chait, 1988). We model this furnace temperature profile by an analytical form to incorporate it into the model. In the experiment, temperatures outside the ampoule were measured at five axial locations with a time interval of 600 seconds. Temperature data from the experiment are shown in Figure 6.26 and show some irregularities, such as the same values of temperature at two instances of time for

Quantity	Symbol (units)	Value
Thermal conductivity of the melt	K_m (W/°C·cm)	0.18
Thermal conductivity of the solid	K_s (W/°C·cm)	0.071
Density of the melt	ρ_m (g/cm ³)	5.7
Density of the solid	ρ_s (g/cm ³)	5.2
Specific heat of the melt	$C_{p,m}$ (J/°C·g)	0.44
Specific heat of the solid	$C_{p,s}$ (J/°C·g)	0.42
Melting temperature	T_m (°C)	1238.0
Kinematic viscosity	ν (cm ² /sec)	0.0042
Heat of solidification	ΔH_s (J/g)	726
Thermal expansion coefficient	β_t (°C ⁻¹)	1.9×10^{-4}
Diffusion coefficient of Se in GaAs	D (cm ² /sec)	1×10^{-4}
Equilibrium distribution coefficient of Se	k	0.1

Table 6.4: Thermophysical properties of gallium arsenide.

Ampoule length, L (cm)	8.8
Crystal radius, R_c (cm)	1.27
Ampoule outer radius, R_a (cm)	1.45
Maximum temperature in space and time, T_h (°C)	1277
Minimum temperature in space and time, T_c (°C)	1177
Temperature difference, $T_h - T_c$ (°C)	100
Ampoule material	pyrolytic boron nitride
Thermal conductivity of ampoule, K_a (W/°C·cm)	
(Axial direction)	0.628
(Radial direction)	0.025
Density of ampoule, ρ_a (g/cm ³)	1.90
Specific heat of ampoule, $C_{p,a}$ (J/°C·g)	1.97

Table 6.5: Design parameters for GTE gradient freeze furnace.

Name	Symbol	Definition	Value
Thermal Rayleigh number	Ra_t	$g\beta_t\Delta T R_c^3/(\alpha_m\nu)$	1.2×10^5
Solutal Rayleigh number	Ra_s	$g\beta_s c_o R_c^3/(\alpha_m\nu)$	0
Prandtl number	Pr	ν/α_m	5.9×10^{-2}
Schmidt number	Sc	ν/D	42
Stefan number	St	$\Delta H_s/C_{p,m}\Delta T$	16.7

Table 6.6: Dimensionless groups and characteristic values appropriate for selenium-doped gallium arsenide crystal growth in GTE furnace.

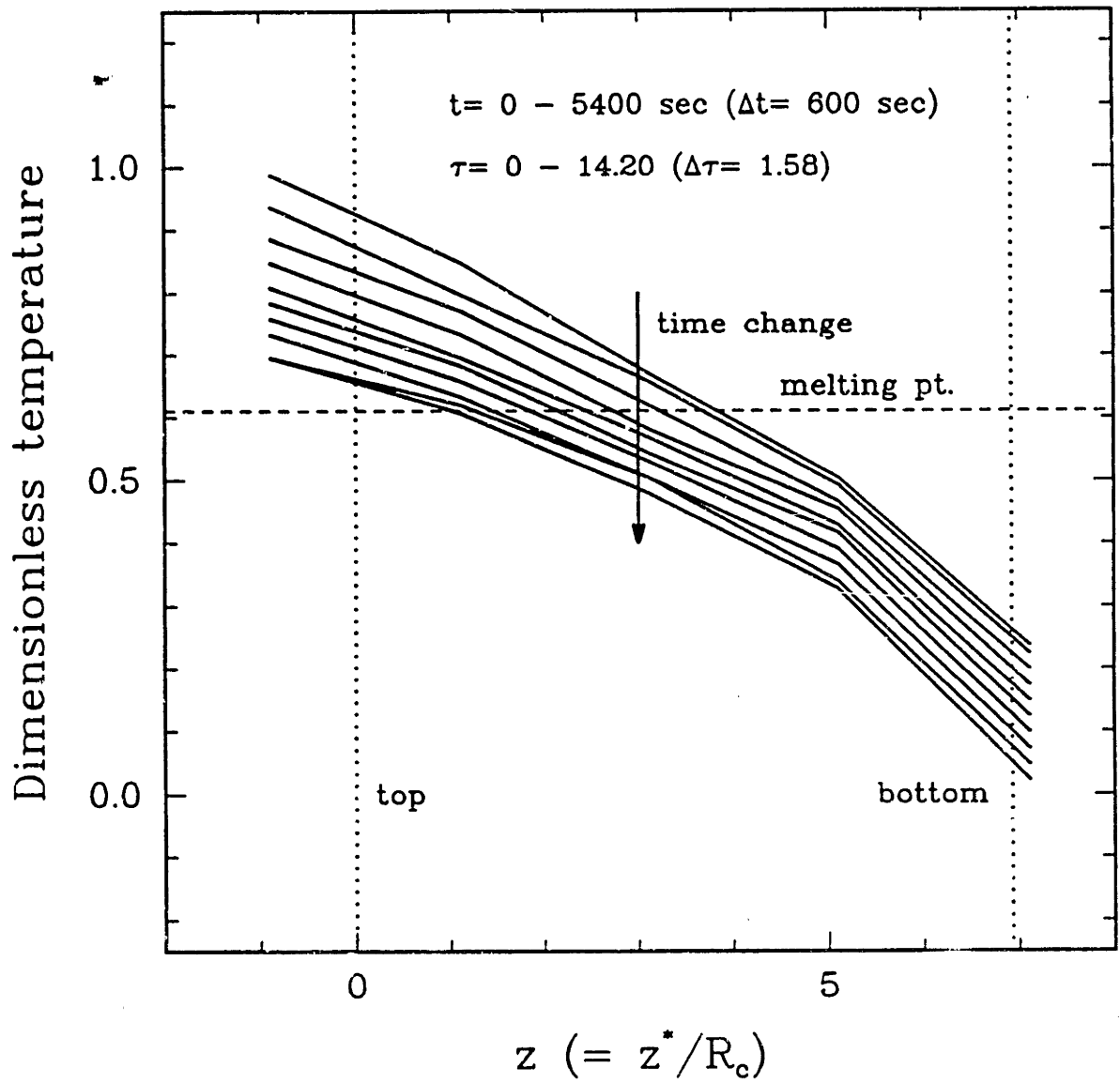


Figure 6.26: Furnace temperature data from GTE experiment.

the same location or a nonuniform rate of temperature decrease in time. We refined these temperature profiles by taking the initial and final temperature profiles and interpolating between them for the intermediate times. The smoothed temperature profiles are presented in Figure 6.27.

Analytical forms of the furnace temperature profile have been devised to approximate the experimental data by

$$\theta_{\infty}(z, \tau) = a(\tau) \cdot z + b(\tau) + c(\tau) \tanh(d - z) \quad (6.15)$$

where $a(\tau)$, $b(\tau)$ and $c(\tau)$ are time-dependent coefficients determined from the transient temperature profile and the constant d is determined from the axial location of the data points. The result are shown in Figure 6.28, where the solid lines represent initial and final temperature profiles and dashed lines are for the intermediate time. Experimental data for the initial and final temperature profile is shown as blank circles for comparison. These furnace temperature profiles are used throughout the analysis in this Section.

Actually, the furnace temperature profile measured in the experiment is the temperature profile outside the ampoule wall. Because heat transfer between the furnace and the ampoule is approximated by Newton's cooling law in our model, we use very high heat transfer coefficient of $10 \text{ W/cm}^2\cdot\text{K}$ ($Bi = 500$) to equilibrate the temperatures in the furnace and outside the ampoule wall at the same axial location.

6.4.2 Temperature Fields and Growth Velocity

The growth of selenium-doped gallium arsenide in a pyrolytic boron nitride ampoule is numerically simulated with an initial condition obtained from steady-state calculation. An initial furnace temperature profile is used with the melting point (0.61 in dimensionless unit) located at approximately 0.55 of the ampoule length from the top. For this initial condition, the steady equilibrium temperature profile and corresponding flow field are calculated with the selenium concentration uniform throughout the melt. Beginning with this initial state, transient calculations are performed until the position of furnace temperature corresponding to the melting point is located at approximately

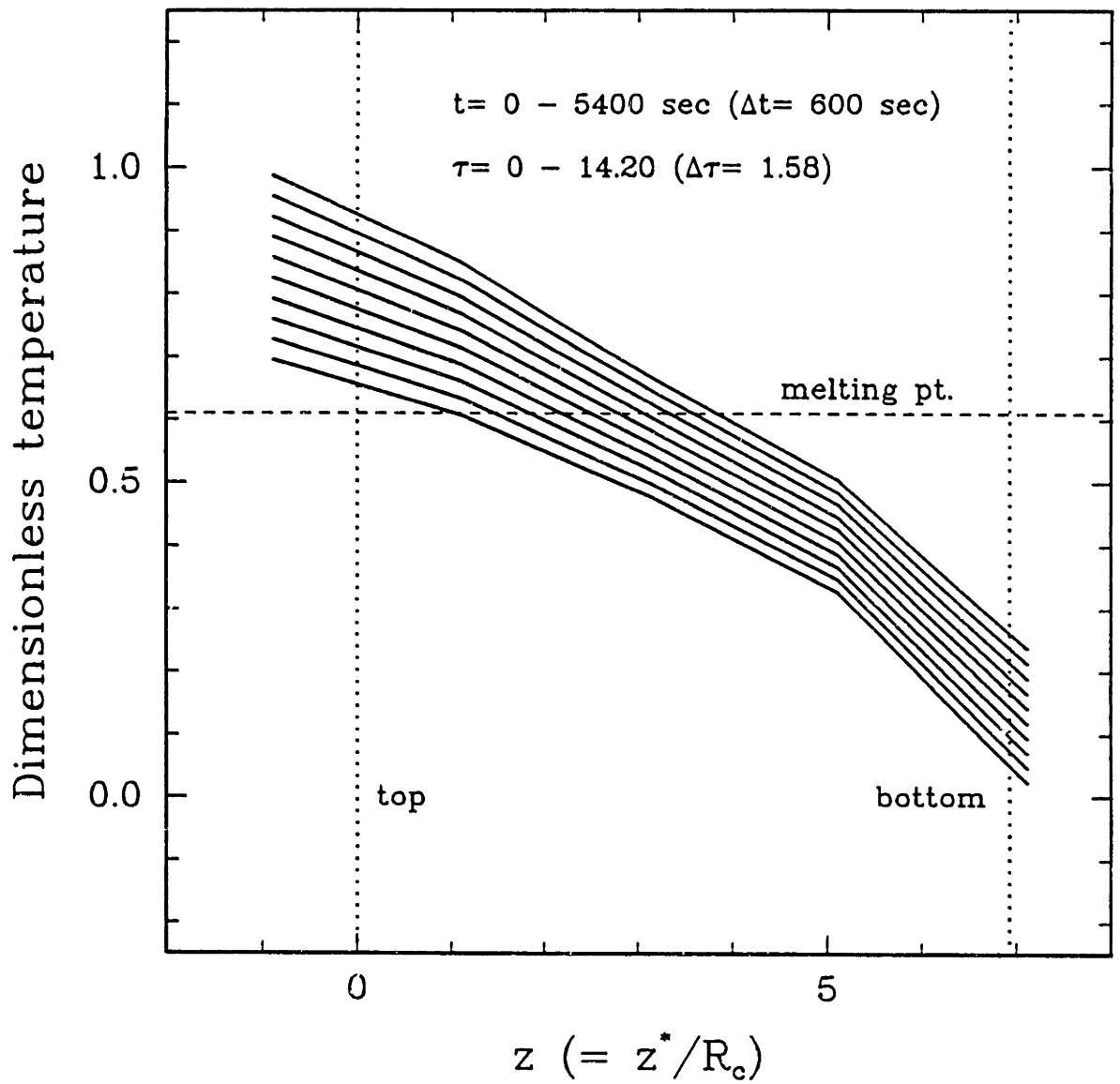


Figure 6.27: Refined transient furnace temperature profiles based on initial and final temperature profiles.

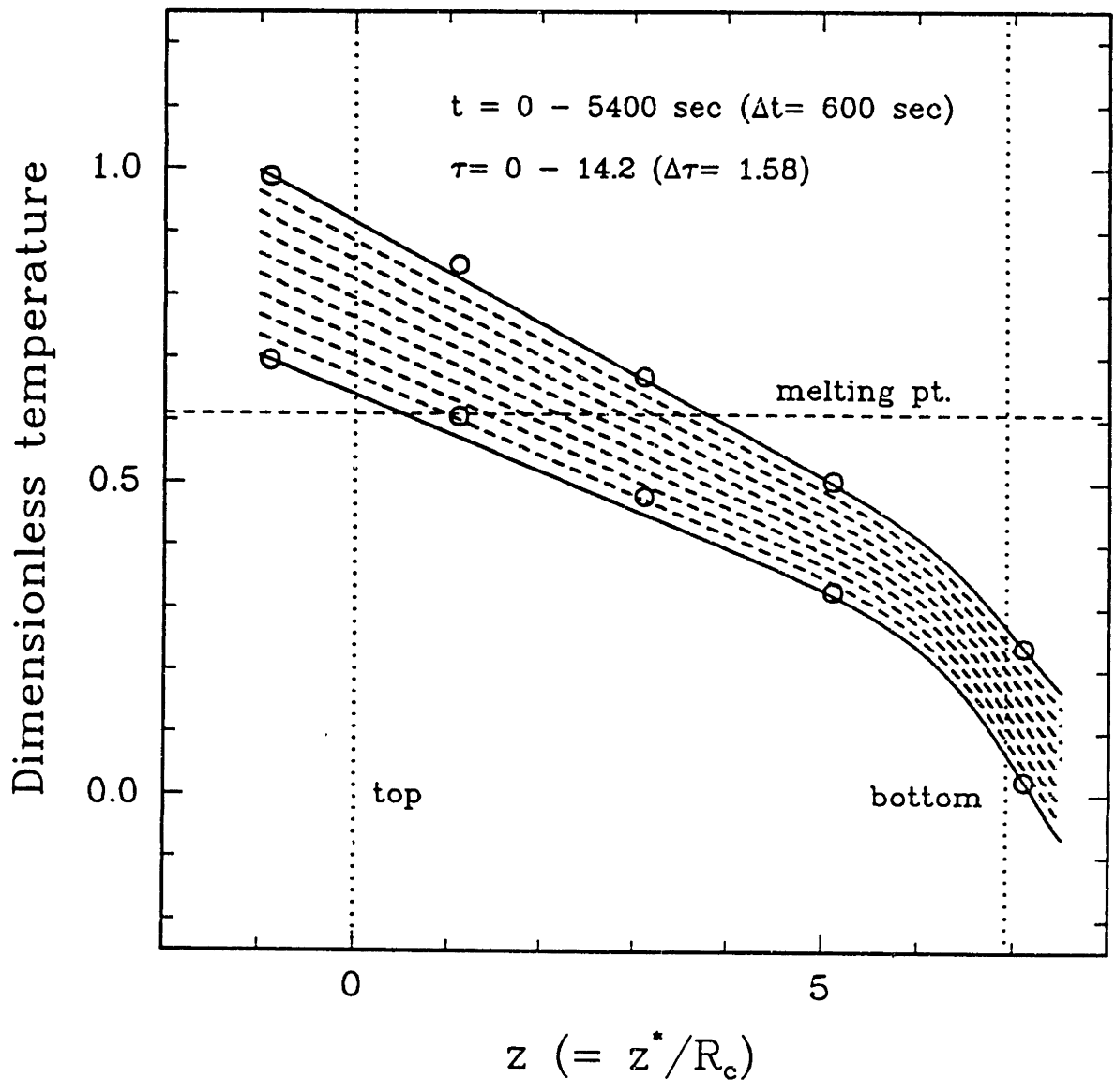


Figure 6.28: Furnace temperature profiles used in the numerical model created by analytical expressions.

0.1 of the ampoule length from the top. Sample meshes during the transient simulation are shown in Figure 6.29 and display the translation and extreme deformation of the individual elements.

Heat transfer in the GTE gradient freeze system shows several important differences from the MIT vertical Bridgman system described in Section 6.3. The large amount of latent heat release ($St = 16.7$) and the low thermal conductivity ratio between melt and crystal results in dramatic changes in the curvature of melt/crystal interface during the run, as shown in Figure 6.30 for $Ra_t = 0$ and 1.2×10^5 . As solidification proceeds, latent heat is released at the interface. If the resulting latent heat is not extracted properly, it heats up the material around the interface and the system adjusts itself to this situation by lowering the temperature gradient in the melt and raising the gradient in the crystal in the vicinity of interface. Subsequently, the interface tends to not move near the centerline of the ampoule leading to the low growth rate in that region. This phenomenon becomes more severe in the GTE gradient freeze growth system, because the furnace temperature profile results in the reverse flow of heat from the furnace to the crystal near the bottom of the ampoule and reduces efficiency of heat removal from the interface.

The role of latent heat in the interface deflection becomes more evident, from a comparison of the temperature fields obtained from the transient calculation and from the steady-state calculation for the furnace temperature profile at rest with the same furnace temperature profile, as shown in Figure 6.31. The temperature field for the stationary furnace temperature profile does not exhibit the extreme interface deflection seen in the transient solution, because the effect of latent heat is completely eliminated for the stationary furnace.

The level of convection associated with the high thermal Rayleigh number Ra_t does not affect the shape of the isotherms, indicating that conductive heat transfer is dominant in the melt. Only a slight tendency toward flatter isotherms in the melt is observed for $Ra_t = 2 \times 10^5$ in Figure 6.30.

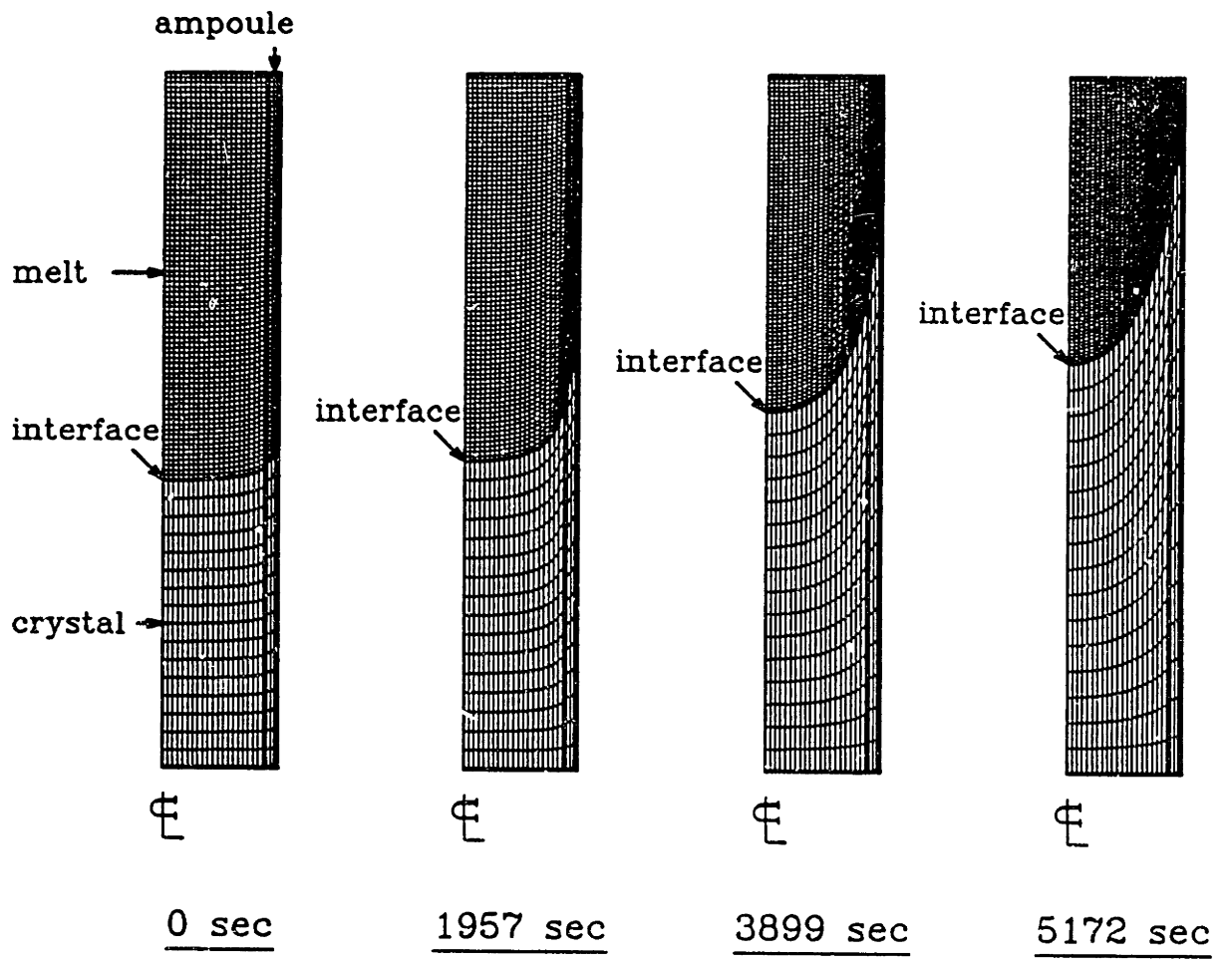


Figure 6.29: Sample mesh used for the analysis of GaAs growth in GTE furnace.

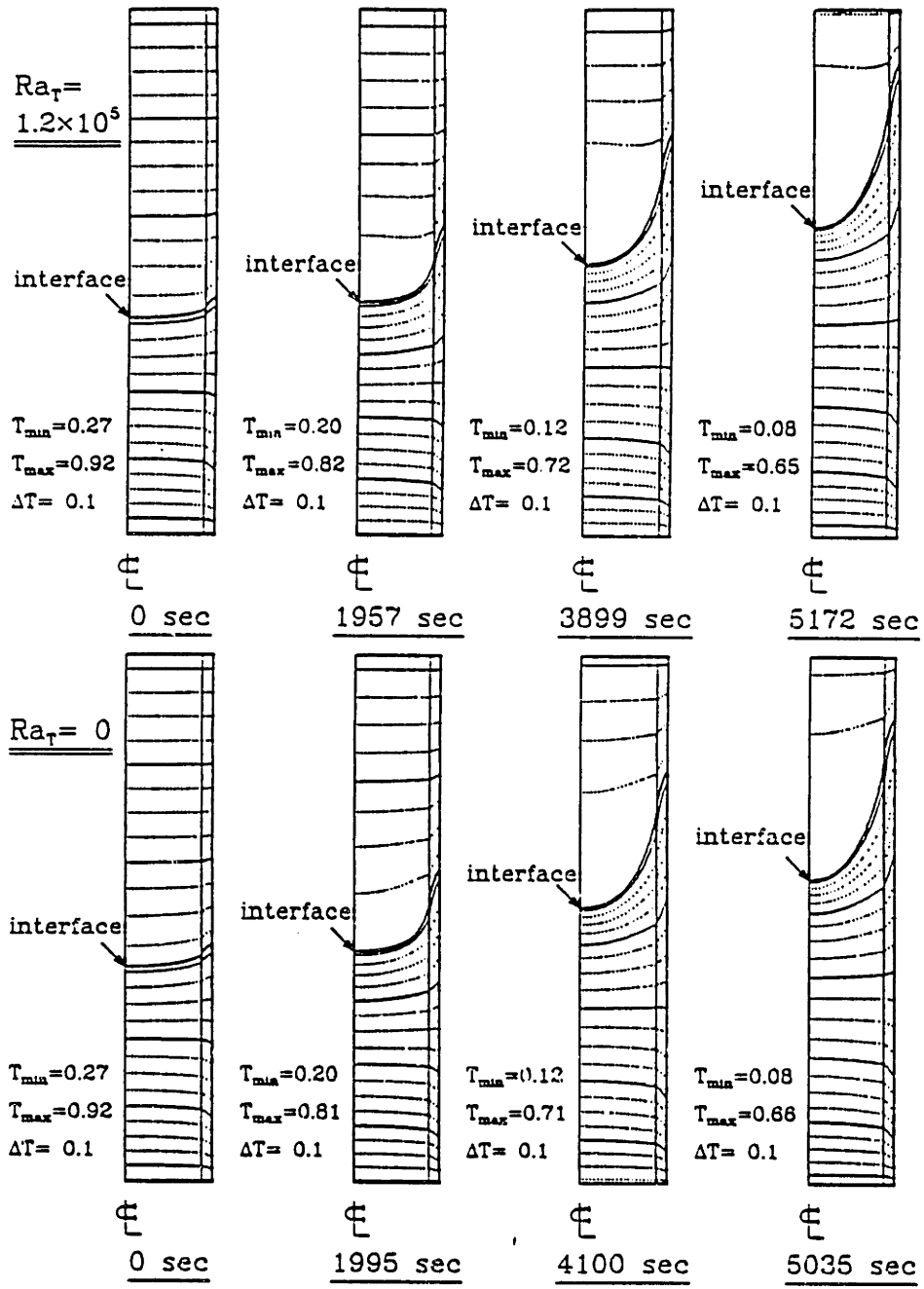


Figure 6.30: Sample transient temperature fields for growth of GaAs in GTE furnace:
 $Ra_t = 0$ and $Ra_t = 1.2 \times 10^5$.

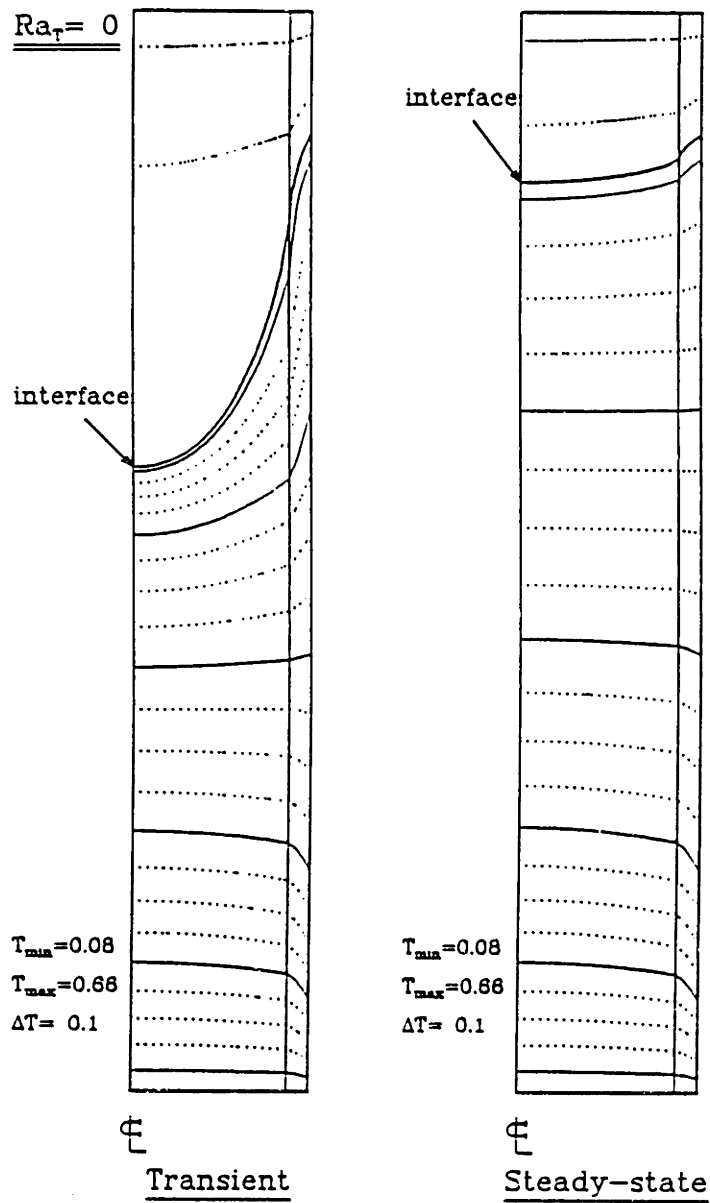


Figure 6.31: Comparison of temperature fields obtained from the transient calculation and steady-state calculation for the stationary furnace temperature profile.

In the gradient freeze system, the temperature field around the interface varies continuously in time due to the effect of latent heat release, thereby preventing the crystal growth rate from attaining a constant value. The crystal growth rate is computed from the transient location of the interface at the midpoint between the centerline and ampoule wall; these results are presented in Figure 6.32 for several values of Ra_t . As discussed above, the level of convection has little influence on the temperature field which determines the interface shape and growth rate for the dilute binary alloy system; the growth rate history corresponding to each Ra_t follows the single curve.

In the initial state at $\tau = 0$, the interface deflection is less than 15 percent of the charge radius. The thermal characteristics in the growth system lead to interface deflections of more than 1.5 times the charge radius at later stage of the growth process.

Observations made in this Section lead to the suggestion that a flatter interface and a steady growth rate can be achieved only by incorporating lower translation rates for the furnace temperature profile, which will result in lower growth rates and a reduction of the effect of latent heat. Also, the furnace temperature profile needs to be tailored so that the latent heat released at the interface is extracted more effectively.

6.4.3 Flow Fields

In the GTE gradient freeze growth system, the smooth change of the furnace temperature profile and the almost uniform heat transfer coefficient between the furnace and ampoule over the ampoule length lead to the formation of one toroidal cell in the melt, which moves upward near the centerline and downward along the ampoule wall. This flow is shown in Figure 6.33 for $Ra_t = 1.2 \times 10^5$ and 1.2×10^3 by stream functions at the elapsed times of approximately 0, 1900, 3900 and 5200 seconds for each Ra_t .

The flow structure is strongly dependent on the interface shape which changes with the progress of solidification. However, the intensity of the flow cell, measured in terms of the maximum value of stream function Ψ_{max} , is nearly constant until the length of the melt is comparable to the size of flow cell. This effect is shown separately in

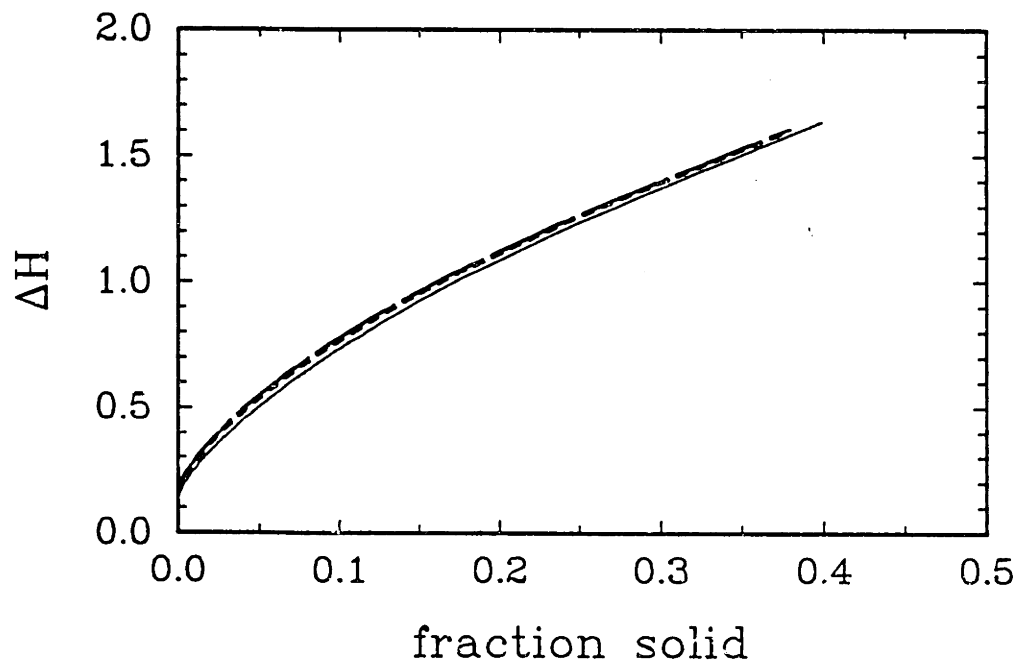
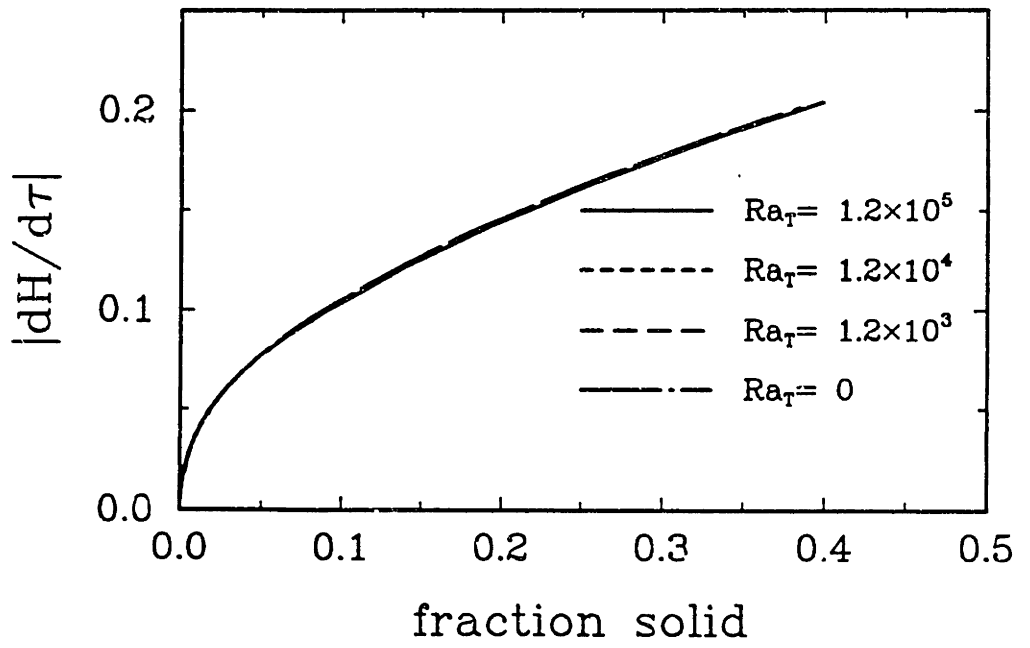


Figure 6.32: Transient growth rate of selenium-doped GaAs crystal and interface deflection as predicted for several values of thermal Rayleigh numbers.

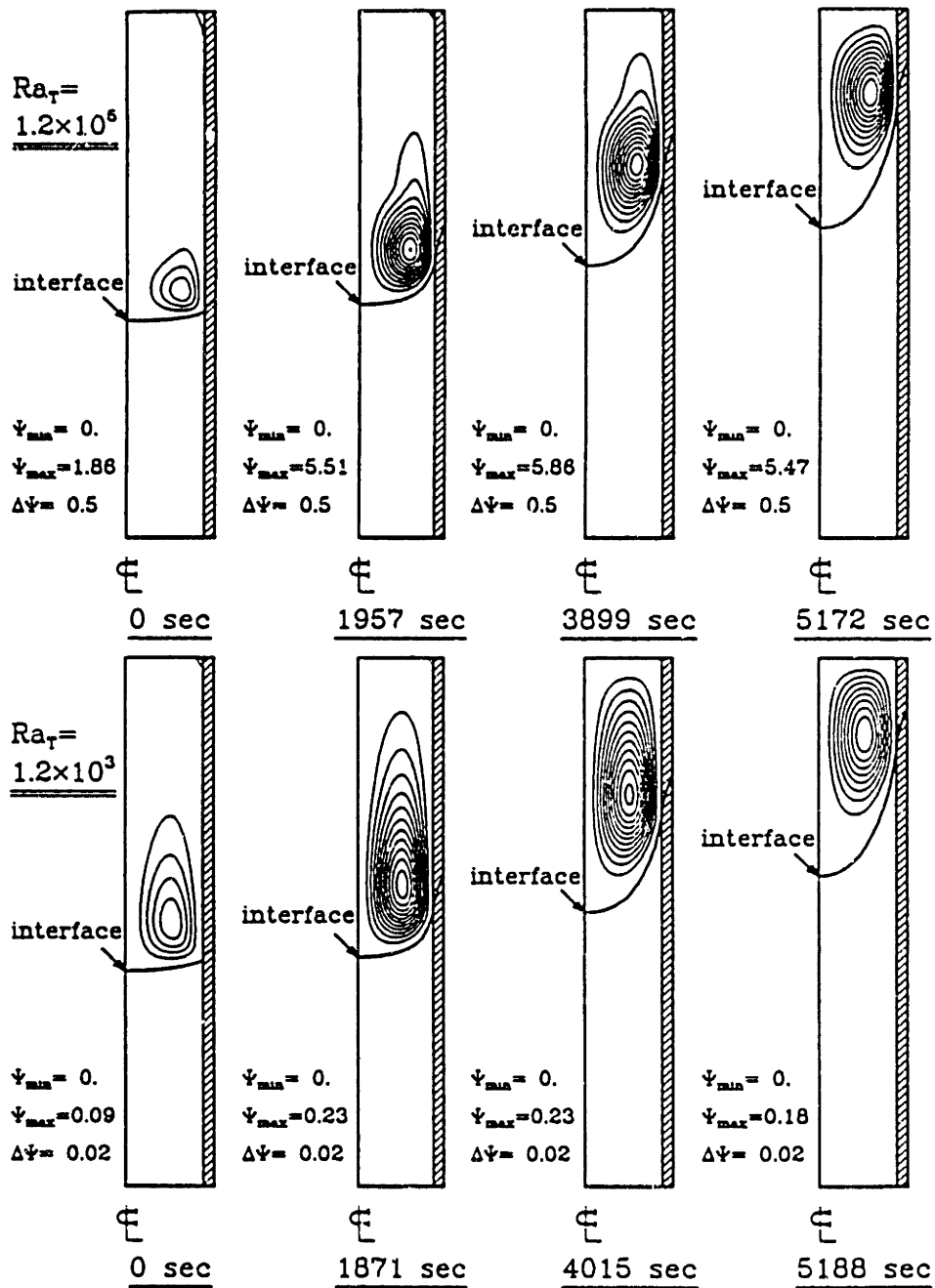


Figure 6.33: Sample flow fields for growth of GaAs in GTE system with pyrolytic boron nitride ampoule: $Ra_t = 1.2 \times 10^3$ and $Ra_t = 1.2 \times 10^5$.

Figure 6.34(a). When the intensity of the flow cell is high ($Ra_t = 1.2 \times 10^5$), convective heat transfer in the melt reduces the radial temperature gradient. As a result, the flow cell with higher convection level is confined to the narrower region near the interface in the initial period of growth. As the length of melt decreases with the solidification, the flow cell occupies almost the entire length of the melt, regardless of the convection level. The intensities of the flow cell when 0.2 of the melt has been solidified is shown in Figure 6.34 and display linear dependence on Ra_t , indicating no boundary layer formation in the melt.

6.4.4 Solute Fields

The diffusion coefficient of selenium in gallium arsenide melt (1×10^{-4} cm²/sec) and equilibrium distribution coefficient ($k = 0.1$) are order-of-magnitude estimates based on the data compiled by Ghandi (1983). With this value of the diffusion coefficient, the Schmidt number is much greater than unity ($Sc = 42$) and the solute distribution in the melt is strongly affected by the flow structure.

Solute concentration fields in the melt are represented in Figure 6.35 at four times for the thermal Rayleigh numbers of $Ra_t = 1.2 \times 10^5$ and 1.2×10^3 . The solute fields are calculated simultaneously with the corresponding flow fields shown in Figure 6.33 and for the furnace temperature profiles shown in Figure 6.28. At the initiation of growth, the solute concentration is uniform everywhere in the melt and no contours are shown in the field. In Figure 6.35, the spacings of the solid curves are indicated as Δc and the concentration differences between the dotted lines are $0.2 \Delta C$'s. The exception is that the dotted curves are spaced at the interval of 0.2 in the fourth plot for $Ra_t = 1.2 \times 10^3$. For example, the solid curves correspond to the dimensionless concentrations of 1.2, 1.4 and 1.6 and dotted curves are for 1.04, 1.08, 1.12 and 1.16 in the second plot for $Ra_t = 1.2 \times 10^5$.

Because of the high value of Schmidt number, the solute concentration is uniform in most of the melt even for $Ra_t = 1.2 \times 10^3$ and concentration gradients are confined to the

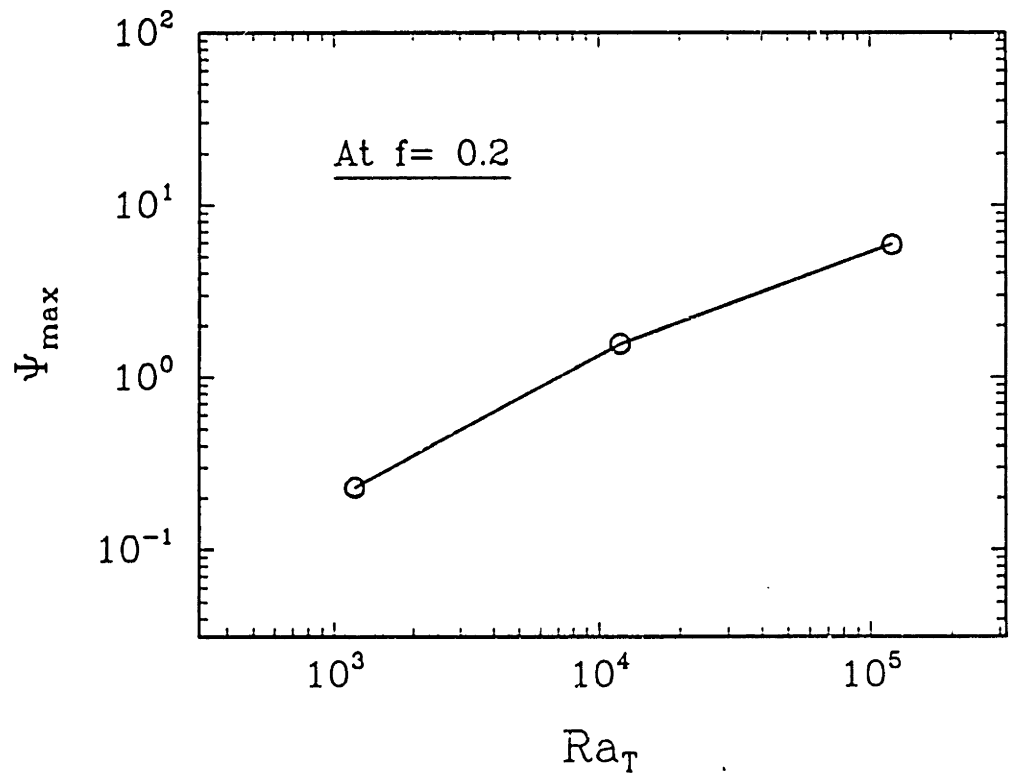
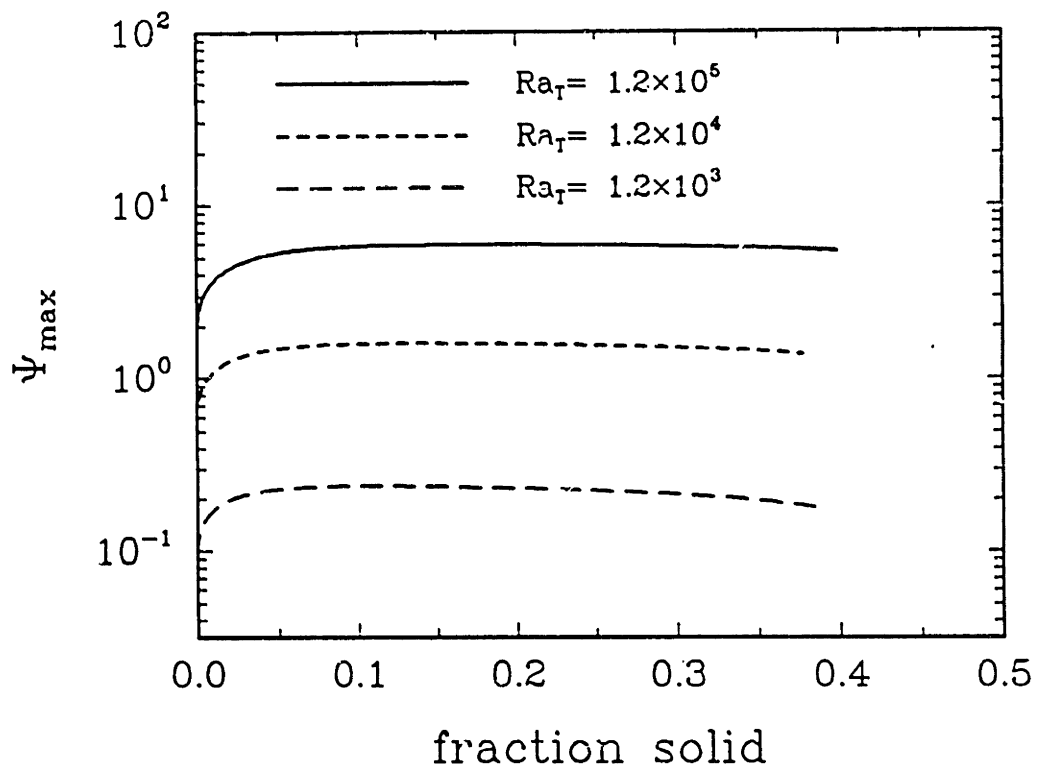


Figure 6.34: History of the maximum values of the stream function in the flow cell for the growth of selenium-doped GaAs in GTE system for $1.2 \times 10^3 < Ra_t < 1.2 \times 10^5$.

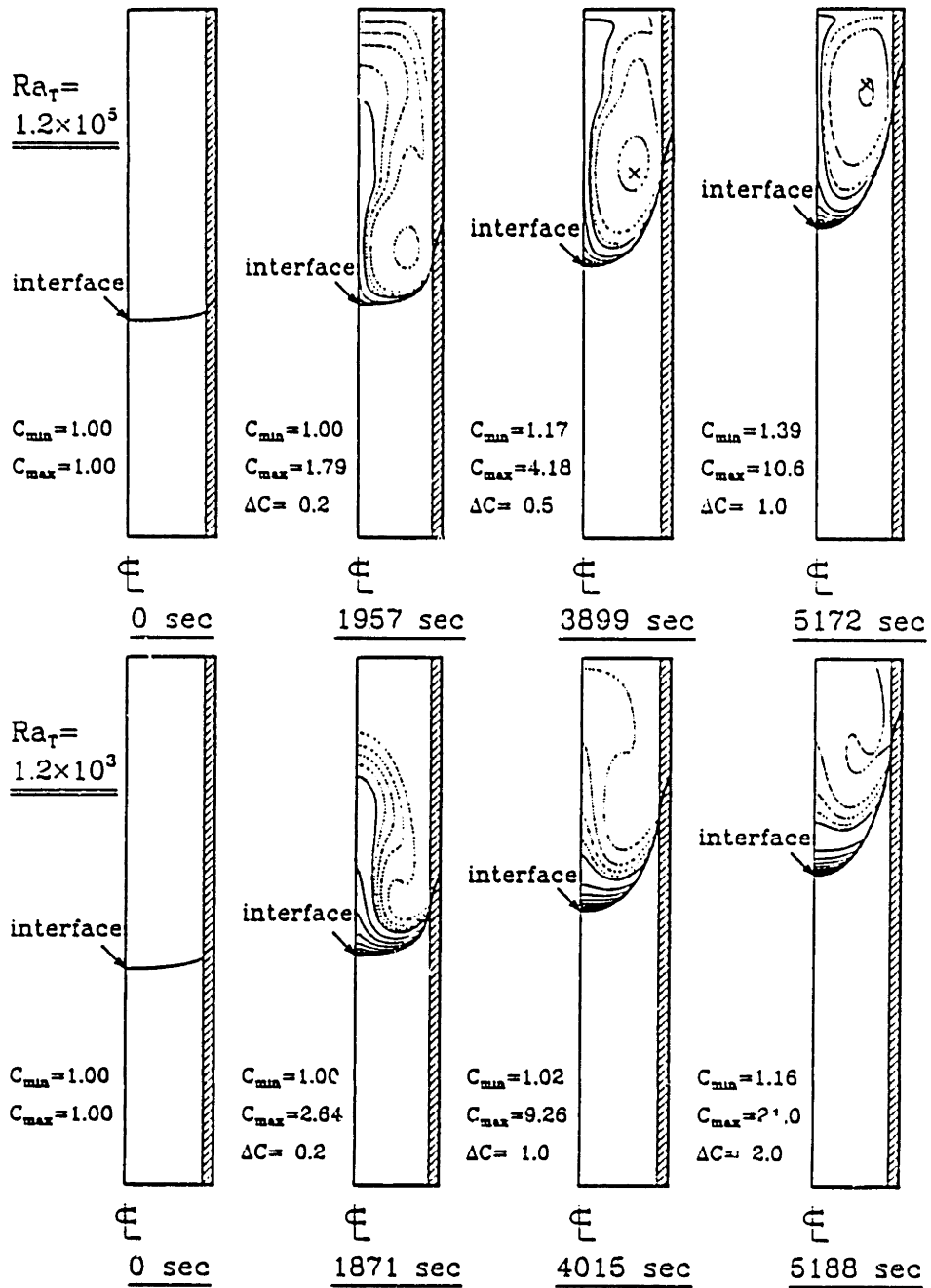


Figure 6.35: Sample selenium concentration fields computed for growth of GaAs in GTE system: $Ra_t = 1.2 \times 10^3$ and $Ra_t = 1.2 \times 10^5$.

centerline near the interface where convection is weak. For $Ra_t = 1.2 \times 10^3$, the isoconcentration contour curves are relatively flat near the interface, but the radial variation of concentration along the interface is very severe due to the large interface deflection. Most of the radial variations in composition are confined near the centerline and become more centralized with an increase in the convection level. The high convection levels associated with increased Ra_t leads to the formation of closed isoconcentration curves, for which the position of minimum concentration is located inside the curve as denoted by the symbol (\times) in Figure 6.35.

The radially-averaged axial segregation of solute in the crystal is presented in Figure 6.36(a) as a function of the fraction solidified for several values of Ra_t . These curves approach the Scheil's solution Eq. 6.14 with increasing Ra_t . For growth under terrestrial conditions ($Ra_t = 1.2 \times 10^5$), the profile deviates from Scheil's solution at later stage of solidification because the convection is weak near the interface at the centerline, as interface deflection becomes extreme. Mixing is then incomplete near the centerline.

The large interface deflections observed in this system have most remarkable effect on the radial variation of solute concentration in the crystal, measured in terms of radial segregation, defined by Eq. (6.12). The radial segregation shown in Figure 6.36(b) amounts to several hundred percent, that is, the radial variation of concentration along the interface is several times of average interfacial concentration. The radial segregation increases in time following the behaviour of the interface deflection but shows a maximum value for the intermediate Ra_t as expected.

The effective segregation coefficient k_{eff} is a means of quantifying axial segregation in the crystal and its transient behaviour shows the same trends as observed in the axial segregation profile in the crystal. As the axial solute distribution in the crystal approaches the solution of Scheil equation, k_{eff} become closer to the equilibrium distribution coefficient. Transient values of k_{eff} for $Ra_t = 1.2 \times 10^5$ are shown in Figure 6.36(c) and deviate from the equilibrium distribution coefficient during the later period, for the same reasons described for the axial segregation profile.

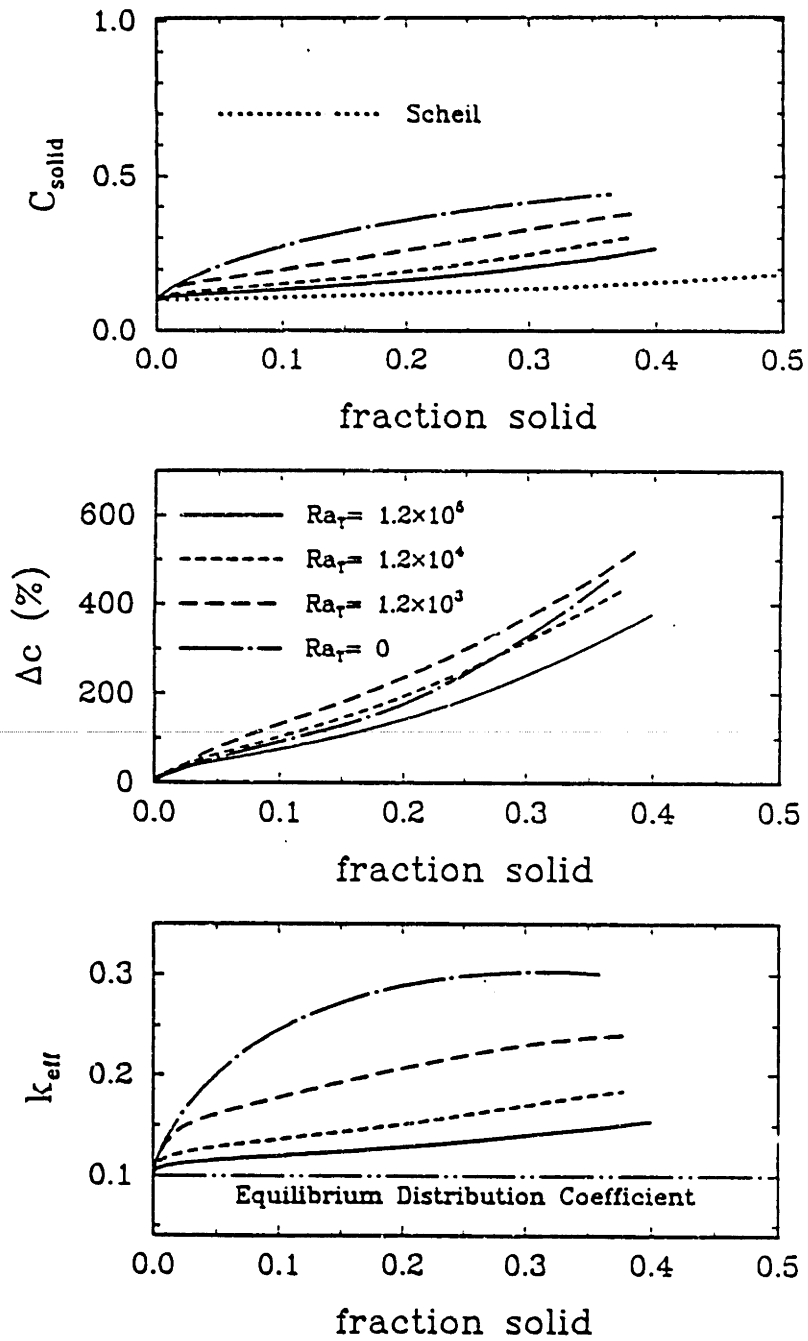


Figure 6.36: Simulation of selenium-doped GaAs crystal growth in the GTE growth system; (a) axial segregation profile, (b) radial segregation, and (c) effective segregation coefficient in the crystal for several values of thermal Rayleigh numbers.

6.4.5 Effect of Ampoule

The pyrolytic boron nitride used as a ampoule material in GTE growth system has a severe anisotropy in the thermal conductivity: the ratio of the radial and axial components of thermal conductivity reaches 1:25. In order to investigate the effect of this anisotropy, comparisons are made in this Section between the growth in the isotropic ampoule and in the anisotropic ampoule of three thicknesses. The isotropic ampoule assumes an increased thermal conductivity of ampoule in radial direction by 25 times, thus equal to the thermal conductivity in axial direction. The *thick* ampoule and *thin* ampoule in this Section denote the ampoules with the wall thickness doubled and halved, respectively.

Temperature Fields

The change of ampoule design was expected to change considerably on the temperature field. However, the large amount of latent heat of solidification in the present system overwhelms the effect of ampoule design. Temperature fields calculated for the four cases listed above and at $Ra_t = 1.2 \times 10^5$ are presented in Figures 6.37(a)-(b) and in Figures 6.38(a)-(b). The temperature fields do not vary much between the four cases, one another at every times. The overall axial temperature gradient between the top and bottom of the ampoule is set by the temperatures at both ends, which are assumed uniform and are equal to the furnace temperature at the same axial location. Radial temperature gradient between the melt at the centerline and furnace remains nearly same for all cases at each time. Only the temperature field in the melt near the ampoule wall and inside the ampoule wall adjusts with the ampoule design.

Radial thermal communication between the melt and furnace decreases in the order of (i) isotropic ampoule, (ii) thin ampoule, (iii) mean ampoule thickness, and (iv) thick ampoule. The growth rate $|\partial H/\partial \tau|$ and interface deflection ΔH seen in Figure 6.39 show this effect clearly. The interface location at the ampoule wall moves closer to the top of the ampoule for the same furnace temperature profile with an increase in thermal

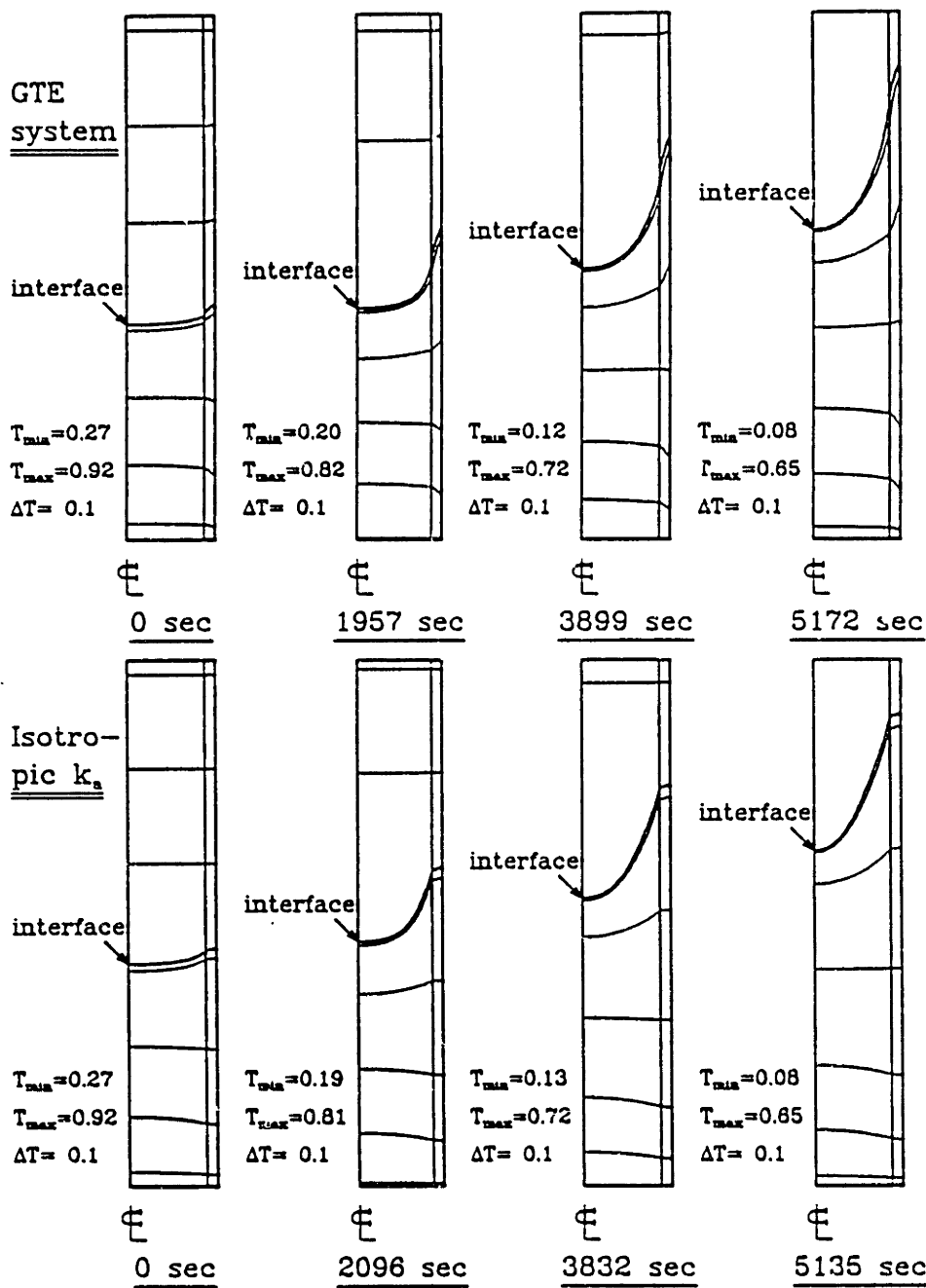


Figure 6.37: Sample transient temperature fields for growth of GaAs in GTE furnace for the cases of (a) anisotropic and (b) isotropic thermal conductivity of ampoule material: $Ra_t = 1.2 \times 10^5$.

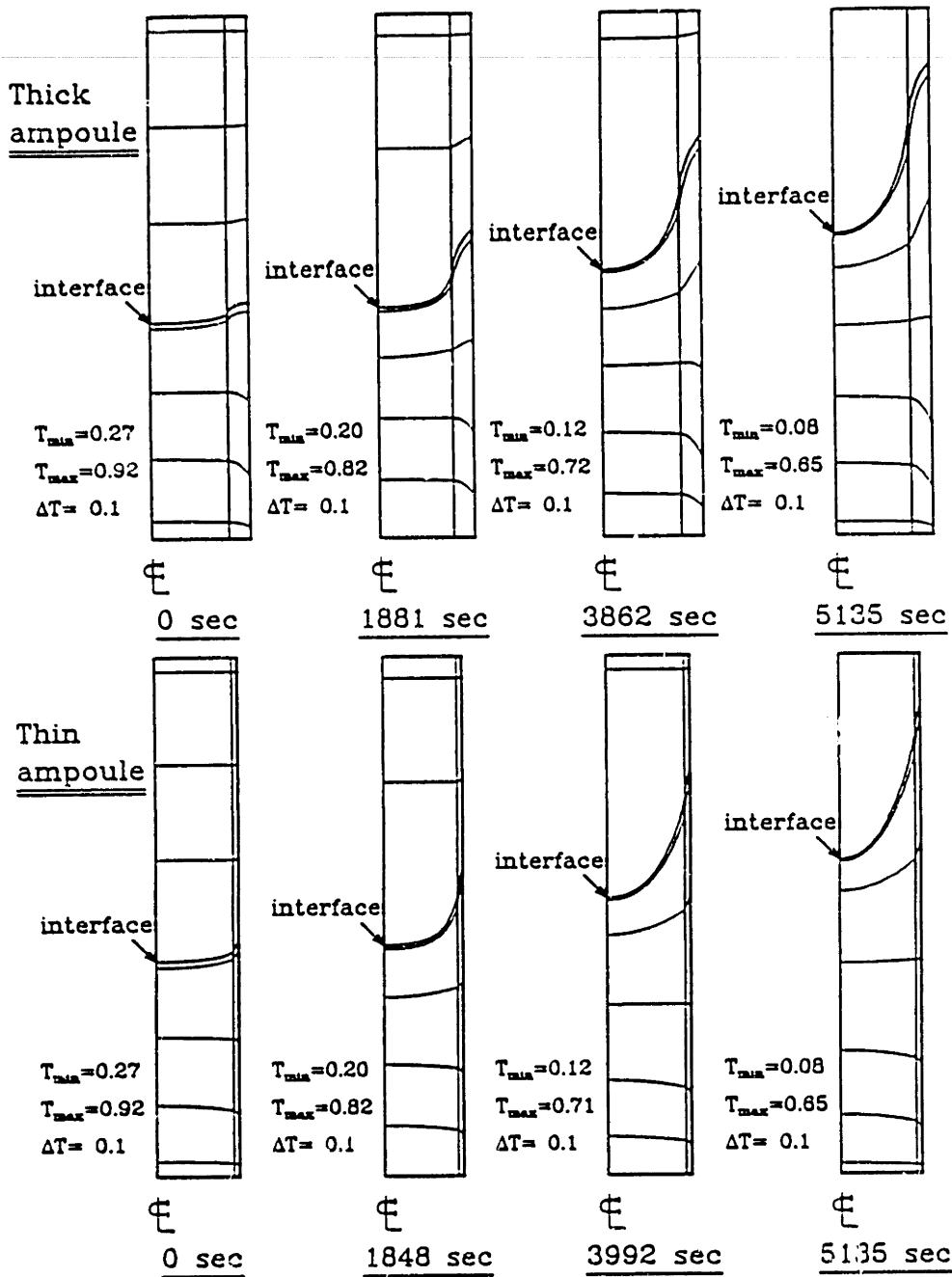


Figure 6.38: Sample transient temperature fields for growth of GaAs in GTE furnace for the cases of (a) thick and (b) thin ampoule wall: $Ra_t = 1.2 \times 10^5$.

communication between the charge and the furnace.

Flow Fields

In the GTE growth system, the structure of flow is determined by the distribution of radial temperature gradient in the melt and the interface shape. Since the temperature field does not vary much for the different ampoule designs, the transient structure of the flow are similar in the shape and location of the flow cell for each of the cases. These flow fields are displayed in Figures 6.40(a)-(b) and in Figures 6.41(a)-(b).

The changes in the radial temperature gradient distribution in the melt for different ampoule designs cause differences in intensity of flow cell in these systems. Because the radial temperature gradient has a linear relationship with the deflection of an isotherm, the intensity of the flow cell descends in the same order as the interface deflection, as shown by Figure 6.42.

Solute Fields

The slight change in growth rate and interface shape between variants of ampoule design has considerable effect on the time-dependent behaviour of solute field; these effects are shown in Figures 6.43(a)-(b) and in 6.44(a)-(b). The symbol (\times) denotes the location of minimum concentration in the melt. The difference between the minimum and maximum concentrations for each case is strongly influenced by the ampoule design. These differences follow the same order as in the order of better thermal communication between the furnace and ampoule. However, if the difference in growth rates caused by changes in the ampoules are accounted for in the solute distribution in crystal is plotted as a function of fraction solidified, the distinctions almost disappear as shown in Figure 6.45.

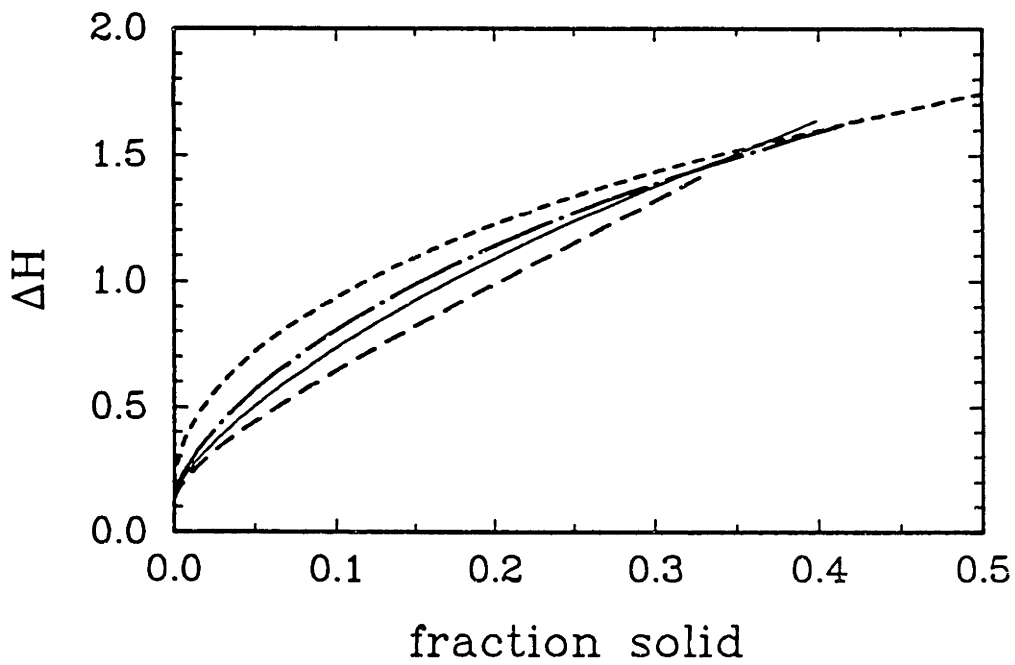
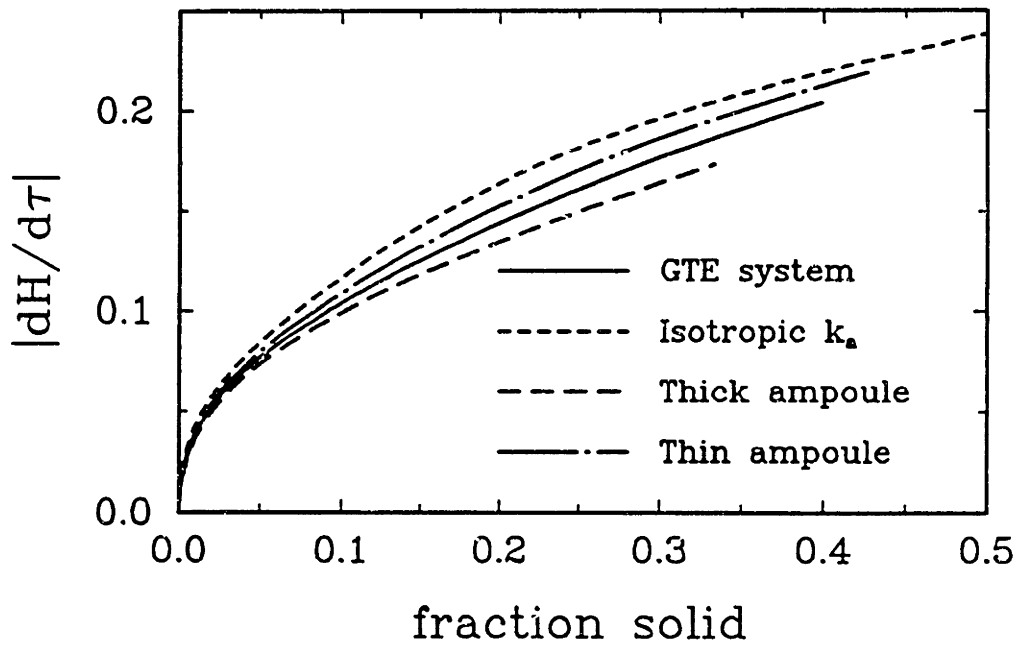


Figure 6.39: Transient growth rate of GaAs crystal and interface deflection for the isotropic ampoule and three thicknesses of the anisotropic ampoule.

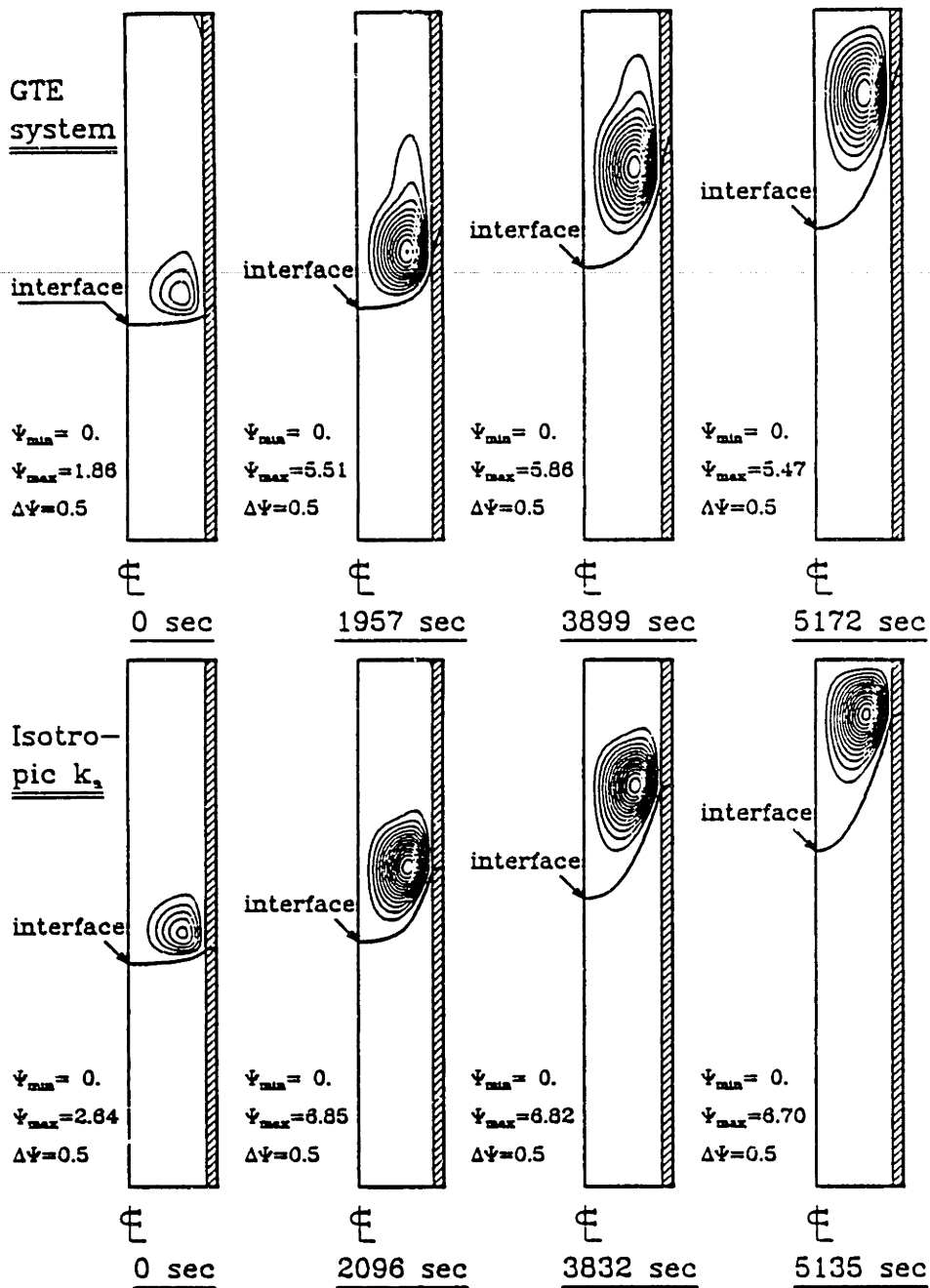


Figure 6.40: Sample flow fields for growth of GaAs in GTE furnace system for the cases of (a) anisotropic and (b) isotropic thermal conductivity of ampoule material: $Ra_t = 1.2 \times 10^5$.

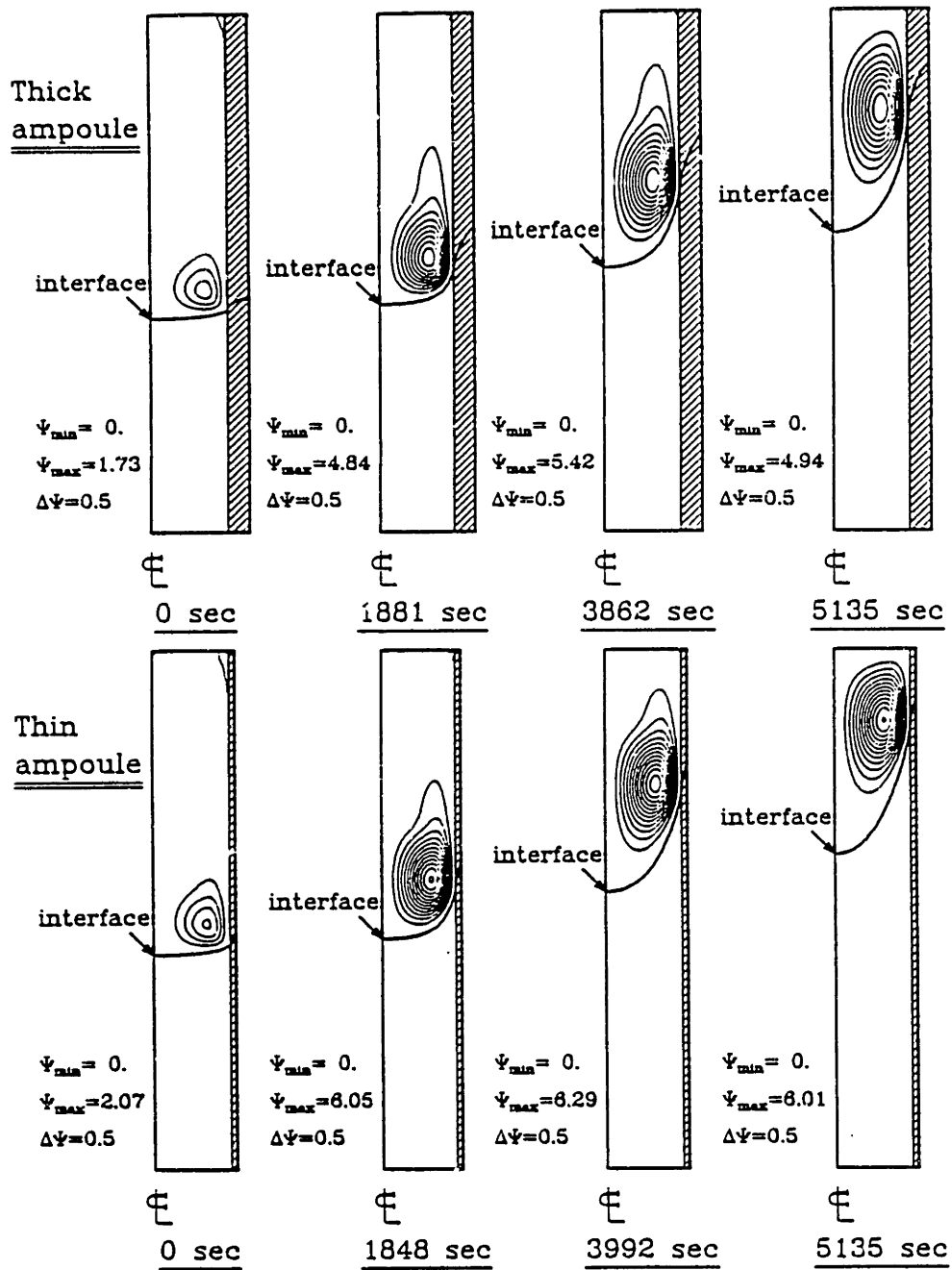


Figure 6.41: Sample flow fields for growth of GaAs in GTE furnace system for the cases of (a) thick and (b) thin ampoule wall: $Ra_t = 1.2 \times 10^5$.

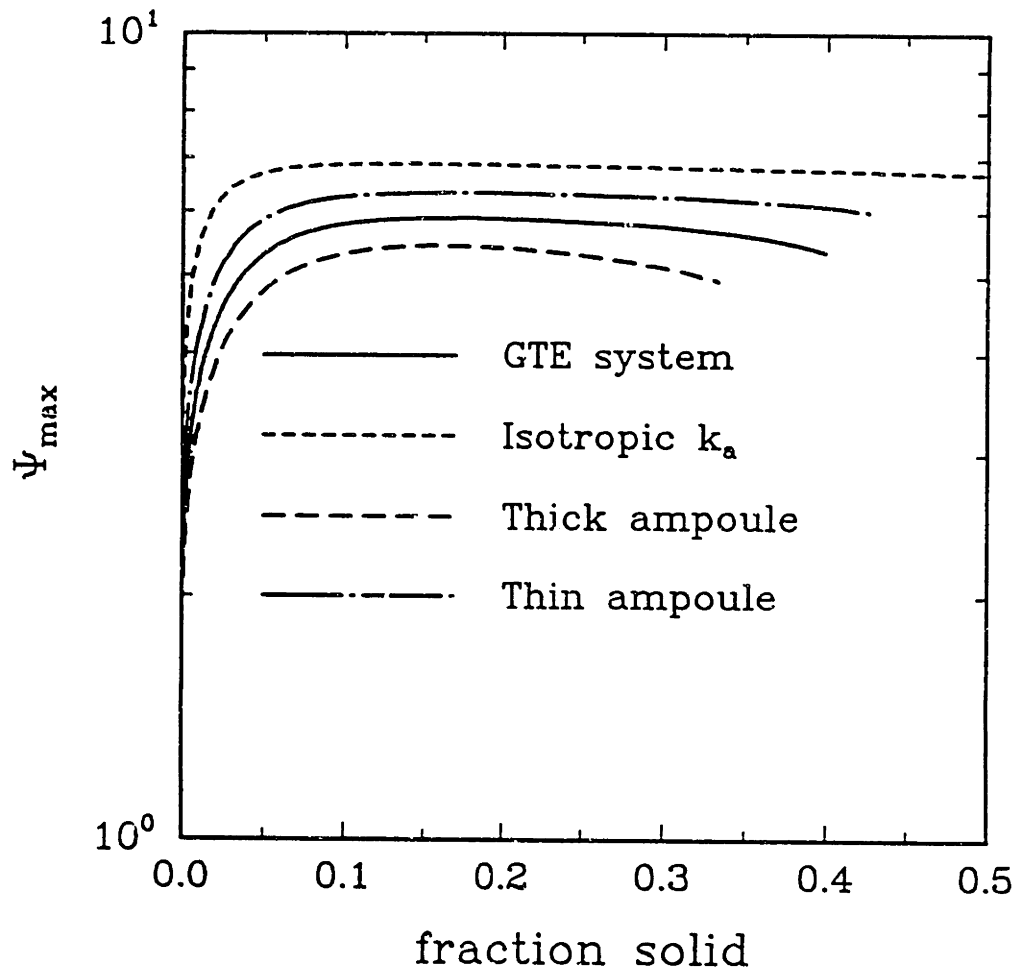


Figure 6.42: History of the maximum value of the stream function in the flow cell for the growth of selenium-doped GaAs in GTE system for different ampoule designs: $Ra_t = 1.2 \times 10^5$.

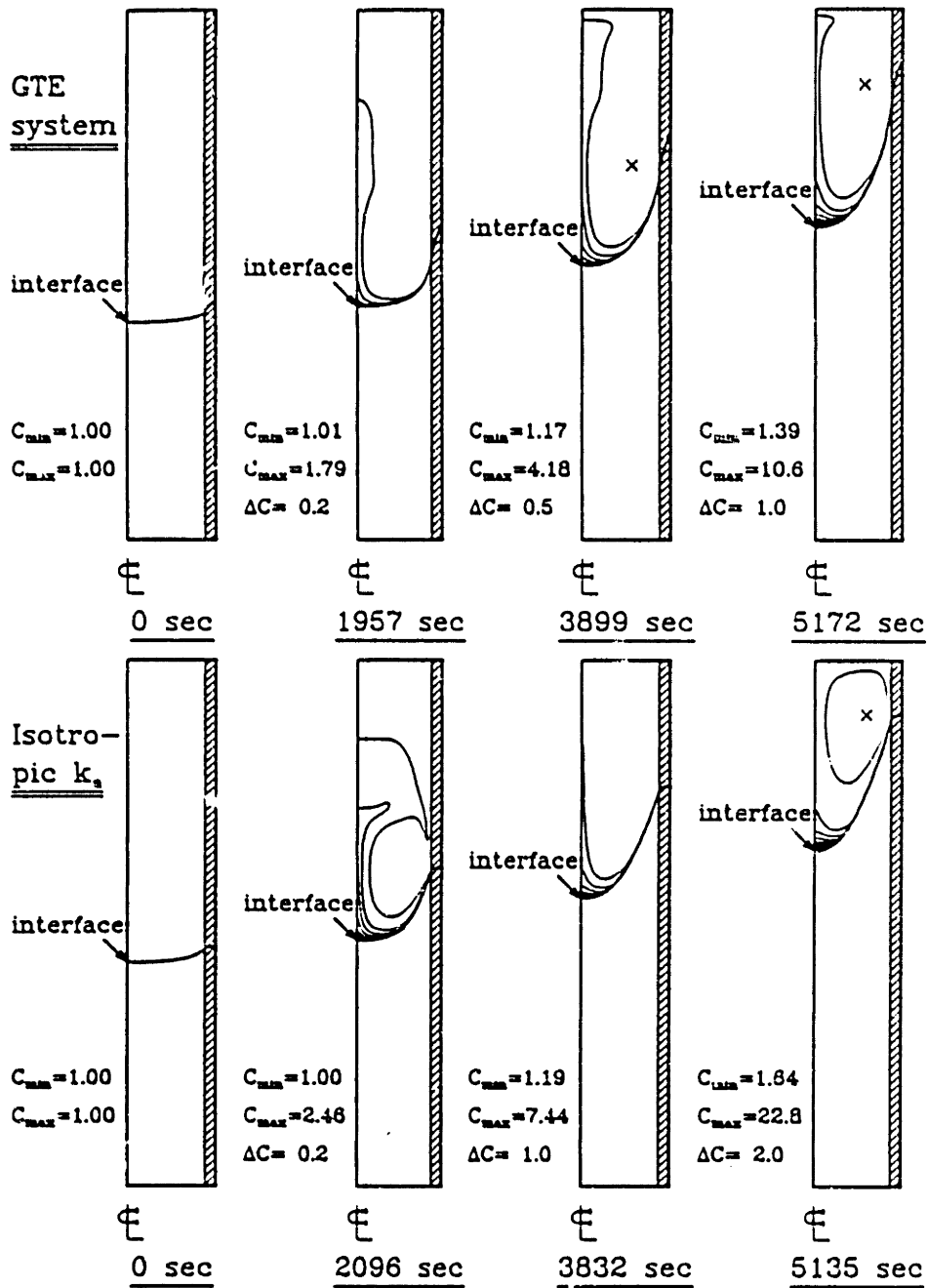


Figure 6.43: Sample selenium concentration distributions computed for growth of selenium-doped GaAs in GTE furnace system for the cases of (a) anisotropic and (b) isotropic thermal conductivity of ampoule material: $Ra_t = 1.2 \times 10^5$.

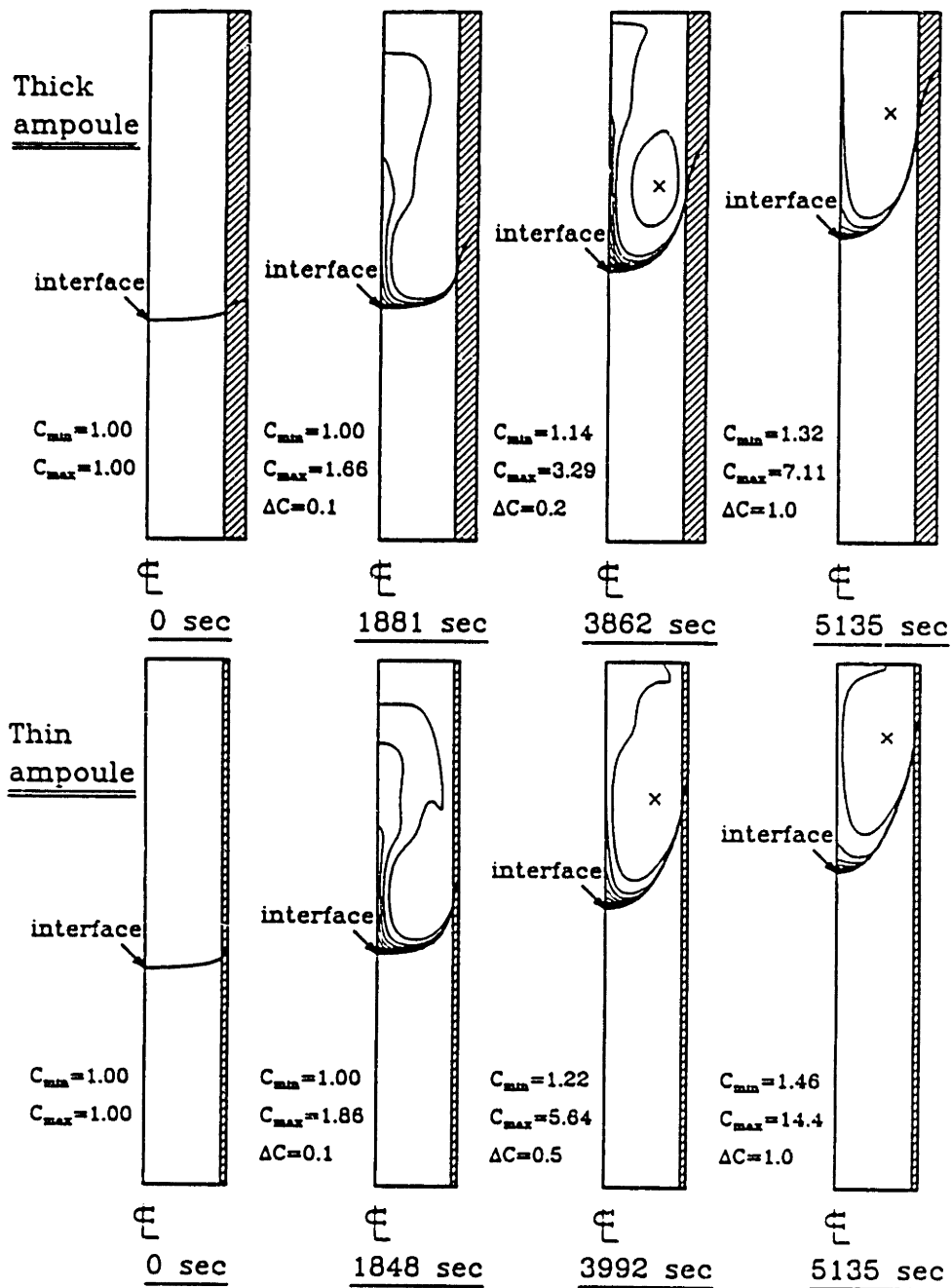


Figure 6.44: Sample selenium concentration distributions computed for growth of selenium-doped GaAs in GTE furnace system for the cases of (a) thick and (b) thin ampoule wall: $Ra_t = 1.2 \times 10^5$.

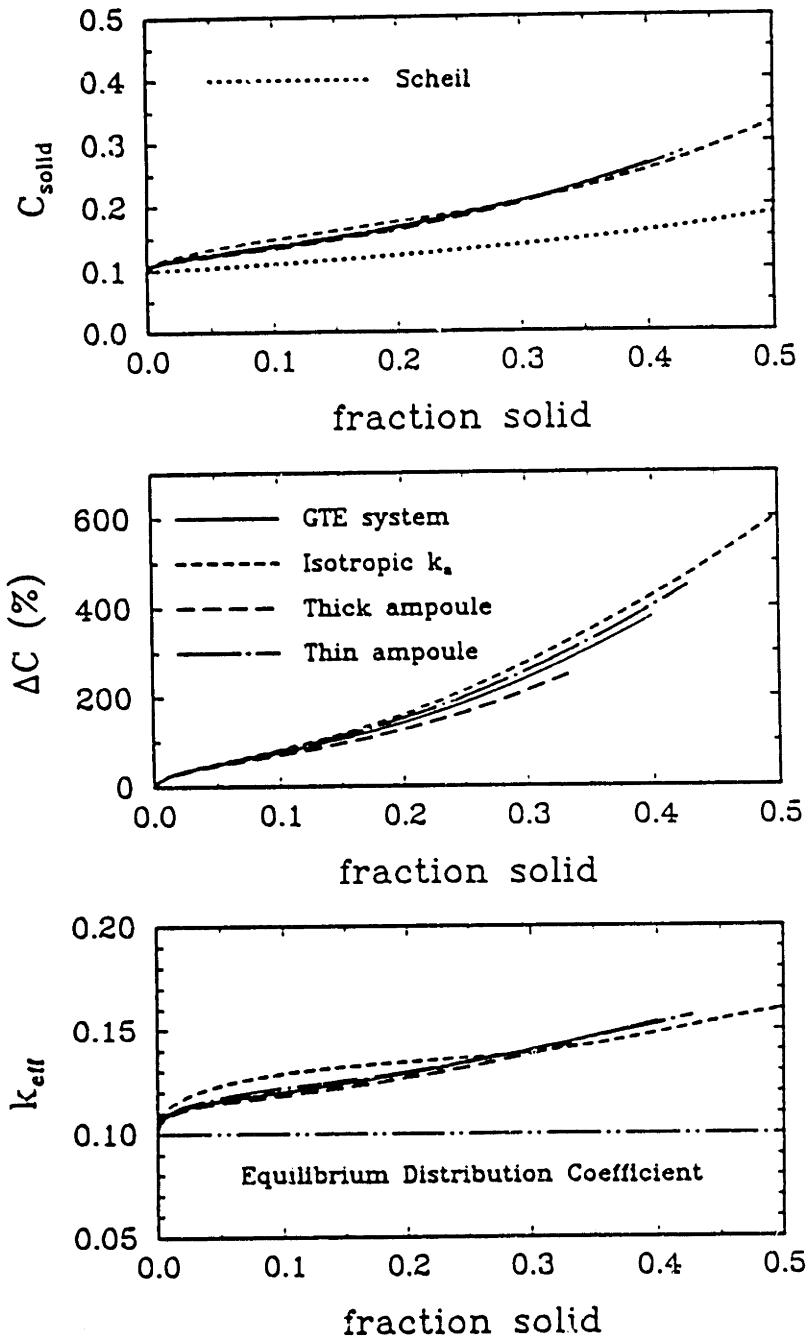


Figure 6.45: Simulation of selenium-doped GaAs crystal growth in the GTE growth system; (a) axial segregation profile, (b) radial segregation, and (c) effective segregation coefficient in the crystal for different ampoule design: $Ra_t = 1.2 \times 10^5$.

6.5 Discussion

The detailed transient simulation of the directional crystal growth process shown here for the experimental systems at MIT and GTE, emphasizes the importance of furnace design and operation for accomplishing optimized steady-state growth.

In the well designed MIT system, the temperature field around the interface is set shortly after the beginning of the ampoule translation, leading to the constant growth rate during most of the run, except in the initial transient period. As a result, the flow field maintains the two-cell structure with almost constant intensity of each flow cell. After the top of the ampoule begins to restrict the upper flow cell, only the intensity of upper flow decreases. The solute concentration in the crystal keeps increasing without attaining the steady value even for the diffusion-controlled growth with the present ampoule length. Nevertheless, the radial segregation and effective segregation coefficient reaches the steady value after the initial transient period which is a little longer than the transient for the growth rate or maximum stream function value. These observations justify the use of pseudo-steady-state analysis previously done (Adornato and Brown, 1987a,b) for the study of temperature field, flow structure, convection and solute segregation during the crystal growth process in the same MIT system. An axial concentration profile in the crystal is not directly obtained from the steady-state analysis. However, it can be approximated by the following equation that is similar to Scheil's results for a well-mixed melt

$$c_s(z) = k_{eff} (1 - f)^{(k_{eff}-1)}, \quad (6.16)$$

where f is a fraction solidified and k_{eff} is obtained from the steady value of effective segregation coefficient. Comparison of the axial segregation profile calculated from transient numerical analysis and from Eq. (6.16) are shown in Figure 6.46, showing good agreement, except in the initial transient period.

The large latent heat of solidification associated with gallium arsenide growth prevents the growth process in GTE system from reaching either a steady-state interface or growth rate. Most quantities observed in the transport process, such as growth rate, in-

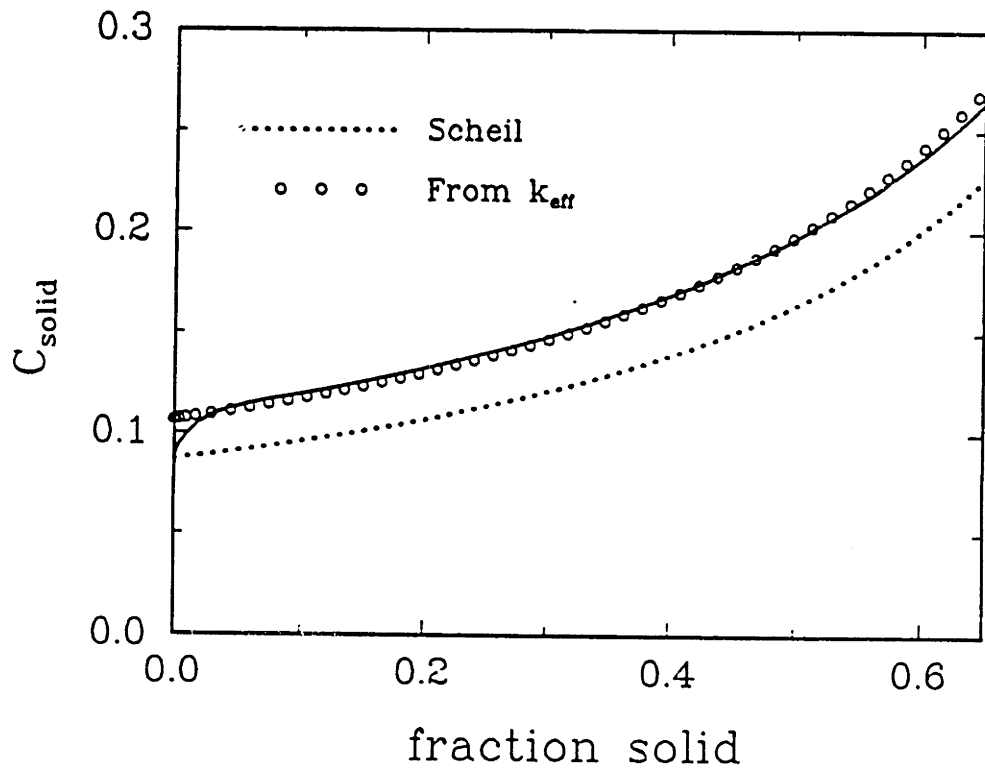


Figure 6.46: Comparison of axial segregation profiles in the crystal obtained from transient analysis and modified Scheil equation for $Ra_t = 1.2 \times 10^5$.

terface deflection, axial segregation and radial segregation, changed throughout the run. Pseudo-steady-state analysis cannot be applied to the system like this, because steady-state results do not describe the continuously transient process. Only by complete transient analysis like the calculations presented here, meaningful results are obtained.

Comparison between the calculated results and experiments by Wang (1984) in the MIT system demonstrate the usefulness of our model in predicting transport processes during the crystal growth. If the boundary conditions are well defined and thermophysical properties of the material are reasonably well known, this model can be utilized in designing new processes for growing crystals.

Chapter 7

Transient Analysis of the Growth of Nondilute Binary Alloy Crystal in a Vertical Bridgman Growth System.

The growth of pseudobinary HgTe–CdTe alloy crystal in the vertical Bridgman furnace system has been studied with the transient model described in Chapter 2. The development of flow structure due to the thermosolutal convection driven by both temperature and concentration gradients, time-dependent melt/crystal interface morphology and solute segregation in the crystal have been calculated by the time-integration/finite-element formulation developed in Chapter 3.

7.1 Introduction

Mercury cadmium telluride (MCT; $\text{Hg}_{1-x}\text{Cd}_x\text{Te}$) is one of the most important semiconductor material at present because of its unique electronic and electro-optical properties.

This compound semiconductor material can have a direct energy band gap anywhere between zero and 1.6 eV by selecting the alloy composition. It is mainly used for the fabrication of infrared detectors that operate in the range from 3 to 13 μm , which covers the range of the important atmospheric transmission windows of 3 to 5 and 8 to 13 μm . The fundamental properties of MCT suitable for the fabrication of infrared detectors promote the development of many different types of infrared devices made from MCT, including photoconductive detectors, photovoltaic detectors, photodiodes and charge transfer devices (Schmit, 1983; Elliot, 1985).

Solidification in a sealed ampoule has been the most widely used technique for the growth of single crystal mercury cadmium telluride, because the high vapor pressure of mercury can cause the explosion and the precise stoichiometry control is required (Micklethwaite, 1981). Methods used for the growth of mercury cadmium telluride in a closed ampoule are classified as *quench-anneal* technique (Parker and Kraus, 1969; Johnson, 1971; Brau, 1972; Kruse and Schmit, 1973; Brau and Reynolds, 1974; Dietl and Jarosch, 1976; Bartlett *et al.*, 1979b; Su *et al.*, 1988; Bollong and Proux, 1989), *Bridgman growth* method (Blair and Newnham, 1961; Capper *et al.*, 1979; Lehoczky *et al.*, 1980; Lehoczky and Szofran, 1982; Capper *et al.*, 1983; Szofran *et al.*, 1984; Szofran and Lehoczky, 1984; Andrews *et al.*, 1988) and *zone melting* method (Dziuba, 1969; Ueda *et al.*, 1972; Takase, 1974; Nishizawa *et al.*, 1976; Gallet *et al.*, 1976; Triboulet, 1977; Itoh *et al.*, 1980; Triboulet *et al.*, 1985; Colombo *et al.*, 1988).

The quench-anneal method is the most commonly used method at present for preparing bulk crystals of mercury cadmium telluride (Schmit, 1983). Here the melt is cast to form a polycrystalline solid ingot, which is then recrystallized in the solid state by annealing the sample below the solidus temperature. Recrystallization by annealing is an extremely slow process (typically 5 to 15 days) and often results in high densities of microstructural defects in crystal, such as dislocations, small-angle grain boundaries, and second-phase precipitates, that can limit the device performance and future applications (Lehoczky and Szofran, 1982).

The vertical Bridgman process was among the first methods used for the crystal

growth of mercury cadmium telluride. The crystals grown by this method have shown high dislocation density (Bornykh *et al.*, 1974) and large amount of radial and axial segregation (Dittmar, 1978; Bartlett *et al.*, 1979a), limiting the use of this material for detector devices. Axial segregation can be advantageous because the material suitable for both the atmospheric windows can be obtained from the same crystal ingot. The Bridgman process and casting step in quench-anneal method can share the same furnace system, differing only in the solidification or growth rate.

The effects of growth conditions on the solute segregations and the relative importance of the various mechanisms involved in the solute redistribution have been studied intensively in recent years to overcome the difficulties in growing compositionally homogeneous bulk MCT crystals with low defect densities in the Bridgman furnace. Most of these studies are based on experiments for the growth of mercury cadmium telluride in a carefully designed Bridgman furnace system and have been carried out by Capper's group at Mullard, UK and Lehoczky's group at NASA. The detailed description of the furnaces used in these studies is found in the works by those two groups (Capper *et al.*, 1979; Lehoczky *et al.*; 1980; Lehoczky and Szofran, 1982).

Heat transfer in the small-scale Bridgman system for the growth of semiconductor crystal is governed by conduction in the charge and ampoule. Temperature field of the furnace provides the axial temperature gradient necessary for solidification, where local heat transfer is complicated by the different thermal conductivities of melt, crystal and ampoule material and by the latent heat release coupled to the growth rate. For a pure component or dilute binary alloy system, the interface shape and location are determined by the isotherm corresponding to the melting point.

The curvature of the interface has been considered as a major factor in radial segregation of mercury cadmium telluride crystal grown in the Bridgman system (Bartlett *et al.*, 1979; Jones *et al.*, 1983; Capper *et al.*, 1983). Many efforts have been made to yield the flat interface or minimize the interface curvature by controlling the temperature field. Jones *et al.* (1982,1983,1984) investigated the possible improvement of melt/solid interface shape by changing the shape of ampoule, increasing the ampoule

stem conductance or forced cooling of the base of the ampoule. These changes were designed by numerical analysis of conductive temperature field in the system, using the concept of electrical analogues. Szofran and Lehoczky (1984) proposed the method for interface shape control using heat-pipes in a two-zone Bridgman growth system by adjusting the circular opening and thickness of the heat barrier between heat pipes and controlling the radiative heat transfer. However, the large change of thermal conductivity upon solidification (Naumann and Lehoczky, 1983), inherent to the HgCdTe system, and the large amount of heat carried by the thick quartz ampoule have limited the success of the heat pipe system. Naumann and Lehoczky (1983) demonstrated the large interface deflections due to the mismatch of thermal conductivities between two phases by analytical solution of two-dimensional conduction equations.

The variation of the thermophysical properties with temperature and composition adds to the difficulty in the control of temperature field and melt/solid interface shape (Holland and Taylor, 1983; Chandra and Holland, 1983). The large change of melting point temperature with the composition (Brice *et al.*, 1986) leads to the coupling between the interface shape and local solute concentration in the melt, thus to the variation of the interface shape and location during the growth. Dakhoul *et al.* (1988) studied the effect of cold zone temperature on the interface curvature by numerical calculation of conductive heat transfer accounting the variations of some thermophysical properties. Their result shows the coupling of interface shape with local concentration significantly increases the interface curvature.

During the growth of HgCdTe crystal, the lighter component of the pseudobinary CdTe is preferentially incorporated into the crystal and the heavier component HgTe is more rejected at the interface, which results in the stabilizing axial solute gradient in the melt when the melt is above crystal. The density profile with this stable solute gradient tends to retard the buoyancy-driven convection caused by the radial temperature gradient in the stabilizing configuration of Bridgman growth system (Adornato and Brown, 1987a,b). This idea is supported by the fact that axial segregation profile in the crystal, observed in the experiments (Lehoczky and Szofran, 1982; Szofran *et al.*,

1984), can be approximated by the profile for diffusion-controlled growth corrected for the variable equilibrium distribution coefficient.

The large separation between the liquidus and solidus curves in the pseudobinary HgCdTe phase diagram causes the partitioning of solute at the interface and results in large axial segregation of solute in the crystal. Axial segregation in the crystal has been analyzed numerically by one-dimensional transient models for diffusion-controlled growth (Clayton *et al.*, 1982; Bourret *et al.*, 1985; Derby and Brown, 1986). The transient growth rate and mean interface location were also calculated in their analyses by the solution of one-dimensional conduction and solute diffusion equations in the melt and crystal with the assumed furnace temperature profiles.

The effect of density-driven thermosolutal convection on the interface shape and radial segregation across the crystal has been recognized earlier, at least in concept (Bartlett *et al.*, 1979; Lehoczky and Szofran; 1982). When a slightly concave interface is present as a result of a radial temperature gradient, the density-driven convective flow near the interface yields a higher HgTe concentration in the center of the melt. This enhances the deflection of interface because the lower melting HgTe near the center shifts the interface into the crystal. The analysis of thermosolutal convection in HgCdTe growth system is indispensable in understanding the large compositional nonuniformities across the crystal, observed by Szofran and Lehoczky (1984), despite the diffusion-controlled axial segregation profile.

In Chapter 3, steady-state analysis was performed to investigate the interaction of convection and segregation in this directional solidification of HgCdTe. These results resolved the apparent contradiction between diffusion-controlled axial segregation measurement and larger radial segregations than expected for diffusion-controlled growth, as were observed in the experiments by Lehoczky and Szofran (1982). For the system with thermosolutal convection, convection and solute segregations are dependent on the growth rate through the coupling of convection and solute field. The effect of growth rate was also discussed in Chapter 3, along with an interpretation to the experimental data by Capper *et al.* (1983).

The calculations described here show the effect of thermosolutal convection and the temperature field on the transient growth rate and axial and radial segregation profile in the crystal. The convection level is high in the beginning, because the solute field is initially uniform and cannot provide the necessary gradient for the solutal convection, which will stabilize the thermal convection caused by the imperfect heat transfer between charge and furnace. As the solute diffusion layer develops, the convection level in the melt decreases and the solute concentration field resembles the results for nearly diffusion-controlled growth. The radial segregation approaches the steady value after the initial transient, but the variation of the solute concentration across the crystal decreases with the decrease of radially-averaged concentration along the axis of crystal.

The pseudobinary alloy $\text{Hg}_{1-x}\text{Cd}_x\text{Te}$ is known to have a maximum density in the liquid state slightly above the melting point for $x \leq 0.1$ (Chandra and Holland, 1983). The region of density increase with temperature is thermally unstable and provides an additional driving force for convection. During the growth of HgCdTe , this region always appears near the interface some time after the beginning of growth as the interface concentration in the melt drops below 0.1 due to the equilibrium partitioning. This type of convection is called *penetrative convection* and commonly occurs in geophysical and astrophysical flows (Veronis, 1963). Antar (1987) performed the linear stability analysis for the simplified HgCdTe growth system for the combined penetrative and solutal convection. We included this effect in our analysis by representing the volumetric expansion coefficient (β_t) as a function of temperature and concentration. Comparisons are made in Section 7.4 between the calculated results with constant β_t and variable β_t .

The analysis presented here is for the vertical growth system used by Lehoczky's group (Szofran and Lehoczky, 1984), illustrated in Figure 7.1. We simplified this furnace configuration with several assumptions: the melt is assumed to fill the ampoule and there is no free volume above the melt. The heat barrier in Lehoczky's system is modelled as a insulation zone, where the heat transfer communication between the furnace and ampoule is negligible. Heat transfer coefficients in the hot zone and cold zone are estimated from Wang's system (Wang, 1984). Profiles for the furnace temperature and

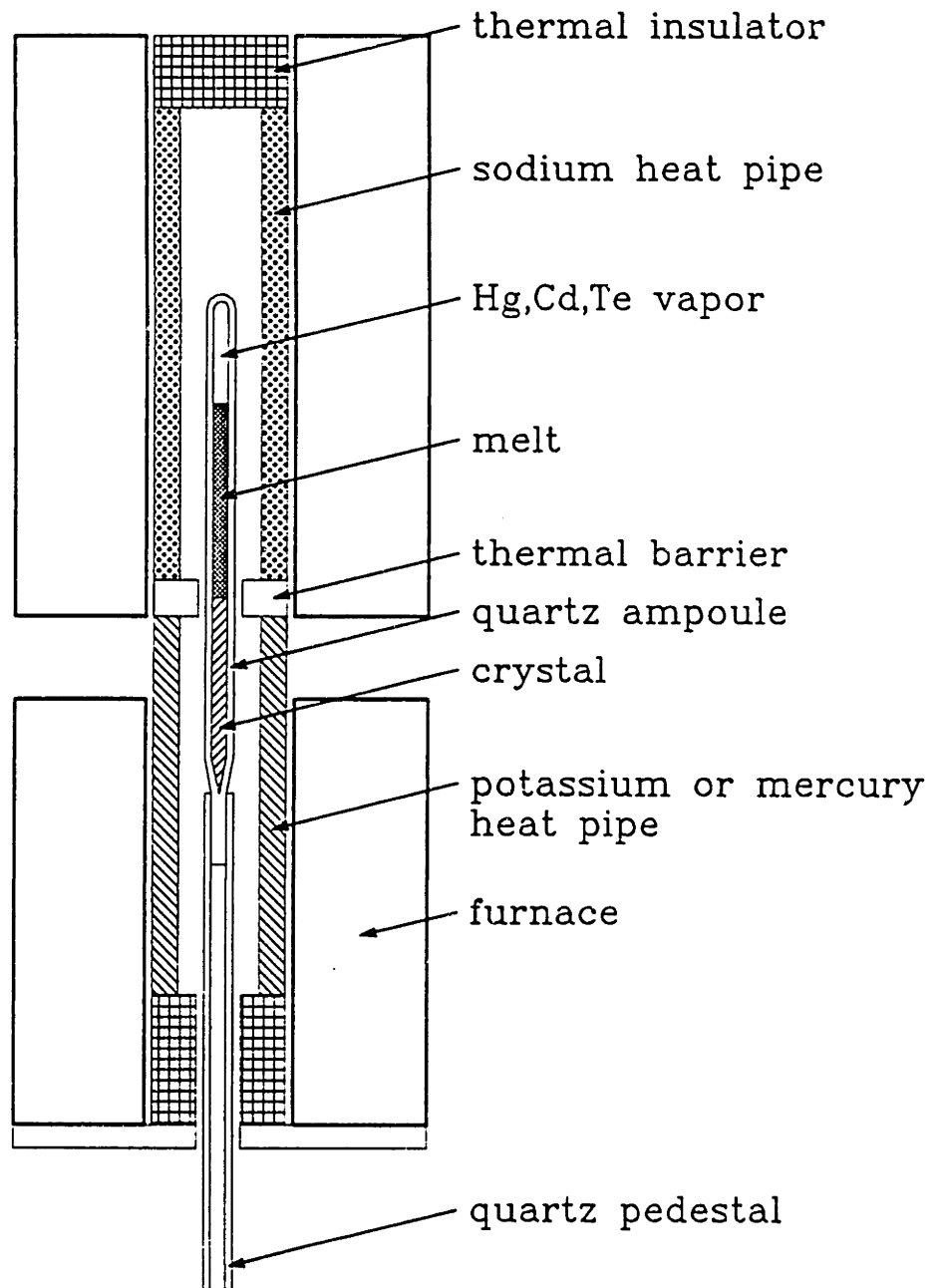


Figure 7.1: Bridgman-Stockbarger crystal growth furnace assembly (Szofran and Lehoczky, 1984).

Biot number used here are shown in Figure 7.2.

Schematic diagram of vertical Bridgman growth system used for the modelling is shown in Figure 7.3. The model system includes a quartz cylindrical ampoule filled with melt and crystal located along the axis of furnace which is composed of hot and cold zone separated by the insulation zone.

We focus on the initial transient behaviour in several aspects of the transport phenomena during the growth. The mathematical description of the equations and boundary conditions for convection and species transport of nondilute binary alloy used here are described in Chapter 2. The only exception is the employment of phase diagram for the melting point T_m and equilibrium distribution coefficient k . These properties are described in Section 7.2. The moving boundary value problem with convection is solved by the same finite element formulation developed in Chapter 3. A mesh of 20 radial elements in the melt and 4 in the ampoule with an axial approximation using 120 elements in the melt and 16 in the crystal was used for the calculations described here. This discretization leads to set of 57,493 equations for each time step that are solved by the modified Newton's method.

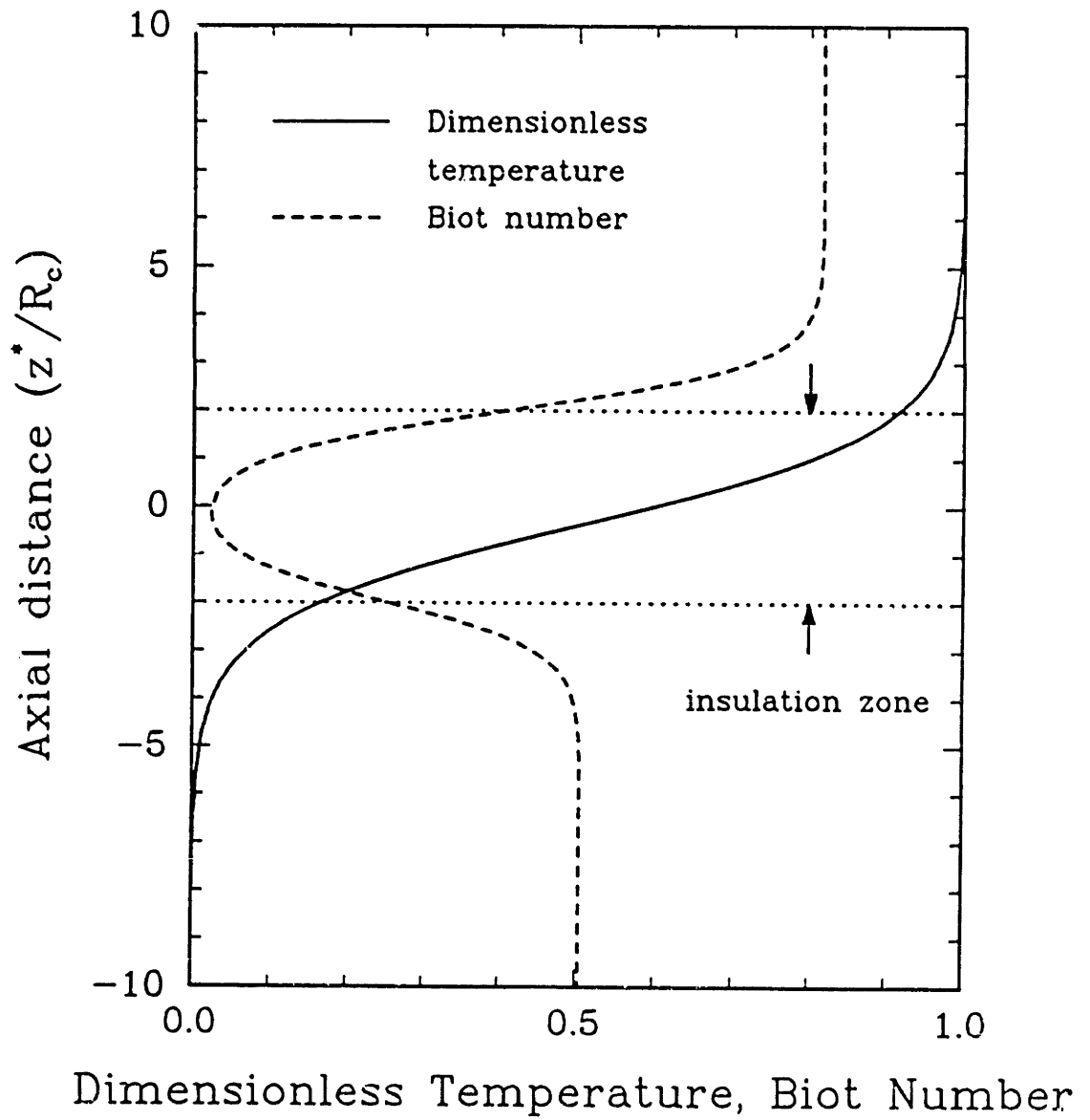


Figure 7.2: Profiles for furnace temperature and Biot number used in the modelling of Bridgman growth system.

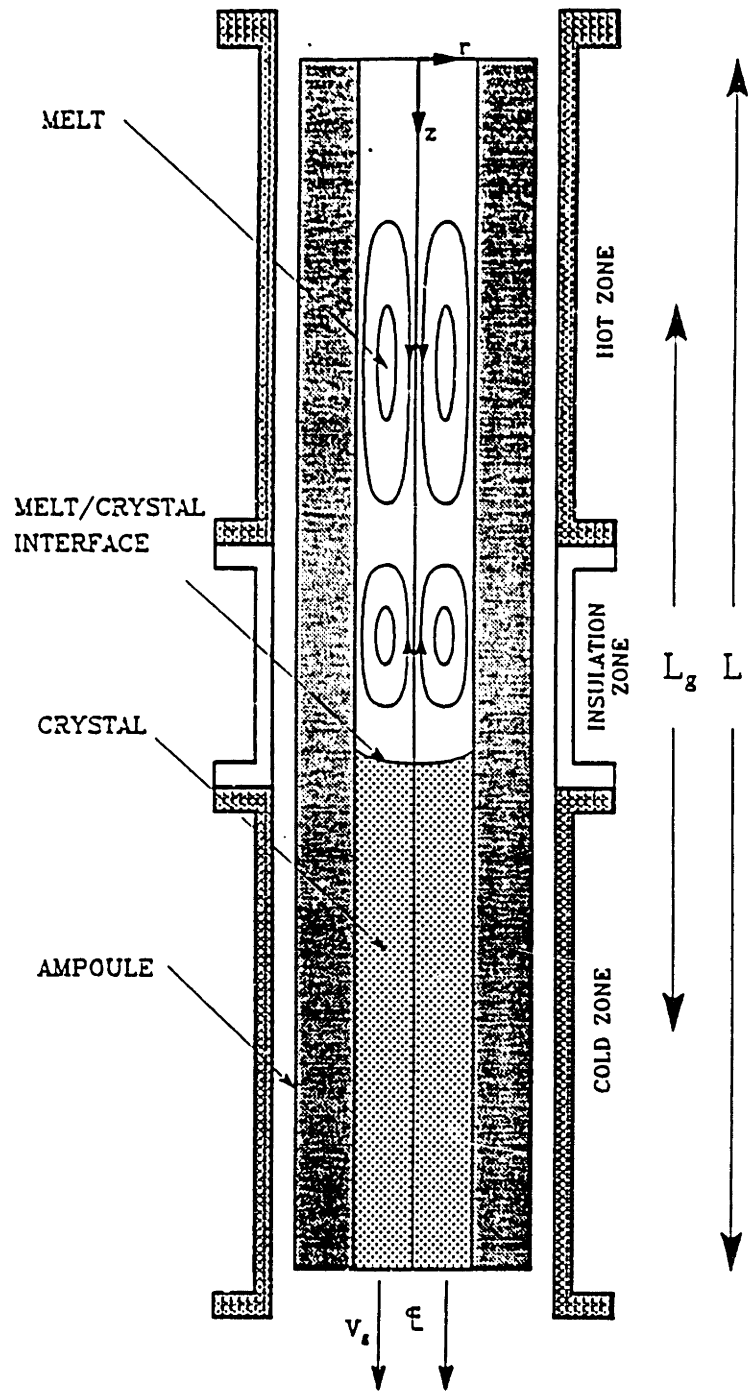


Figure 7.3: Schematic diagram of vertical Bridgman crystal growth system used in model calculation.

7.2 Thermophysical Properties

7.2.1 Phase Diagram

The accuracy of calculations of the solute field and interface shape for a nondilute binary alloy system hinges on the correct phase diagram, especially when the separation between liquidus and solidus curves are large as for $\text{Hg}_{1-x}\text{Cd}_x\text{Te}$. There have been data published for the phase diagram of pseudobinary HgTe-CdTe. Szofran and Lehoczky (1981) paid particular attention to the accurate measurement of temperature and their phase diagram is sufficiently reliable. Recently, Brice *et al.* (1986) synthesized the HgTe-CdTe pseudobinary phase diagram from all the published data. It is considered the most accurate phase diagram and employed in the present study.

The correct phase diagram is most useful for the determination of the melting point temperature T_m and the equilibrium distribution coefficient k . Micklethwaite (1981) and Brice *et al.* (1986) gave the formulae for T_m and k , respectively as a function of CdTe mole fraction x as

$$T_m(^{\circ}\text{C}) = \frac{1000x}{1.37 + 0.97x} + 668 \quad (7.1)$$

$$k = \frac{1}{0.210 + 0.790x} \quad (7.2)$$

Analysis by Brice *et al.* (1986) of the previously published phase data showed significant disagreement with the formula proposed by Micklethwaite (1981). New formula for the liquidus curve based on the data suggested by Brice *et al.* (1986) was developed in this thesis. For the convenience in differentiation, it is represented in terms of a polynomial in the mole fraction of CdTe x as

$$T_m(^{\circ}\text{C}) = a_0 + a_1x + a_2x^2 + a_3x^3 \quad (7.3)$$

where the $\{a_i\}$ take the values of

$$a_0 = 670.9445$$

$$a_1 = 671.4593$$

$$a_2 = -375.0729$$

$$a_3 = 110.5424$$

The phase diagram of pseudobinary CdTe–HgTe alloy system is shown in Figure 7.4, with these formulae for the liquidus curve. In Figure 7.4, the symbols (o) indicate the median values of data within 90% confidence limits, as suggested by Brice *et al.* (1986).

The dimensionless melting point temperature is used in the calculation. It is represented as a polynomial in the dimensionless concentration at the interface in the form of

$$\theta_m = \theta_{m,0} + \theta_{m,1}(S + 1) + \theta_{m,2}(S + 1)^2 + \theta_{m,3}(S + 1)^3 \quad (7.4)$$

where the dimensionless concentration S is defined in Section 2.2 and the $\{\theta_{m,i}\}$ are defined as

$$\theta_{m,0} = \frac{a_0 - T_c}{\Delta T}$$

$$\theta_{m,1} = \frac{a_1 c_o}{\Delta T}$$

$$\theta_{m,2} = \frac{a_2 c_o^2}{\Delta T}$$

$$\theta_{m,3} = \frac{a_3 c_o^3}{\Delta T}$$

The formula proposed by Brice *et al.* (1986) for the equilibrium distribution coefficient showed good agreement with experimental data. We fit the data to the fifth-order polynomial in x , written as

$$k = \sum_{i=0}^5 b_i x^i, \quad (7.5)$$

where the $\{b_i\}$ have the values

$$b_0 = 4.72607$$

$$b_1 = -15.93513$$

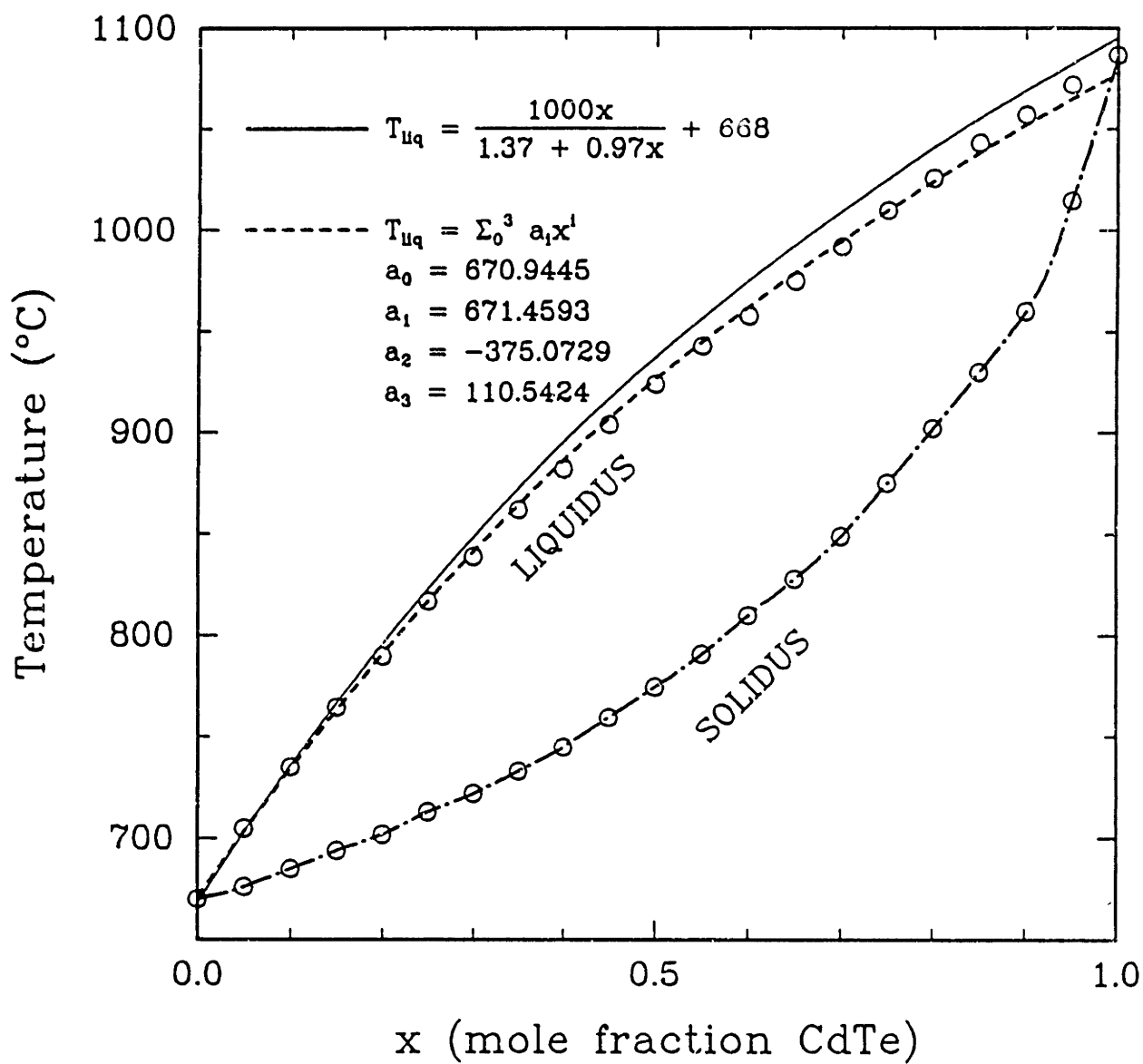


Figure 7.4: The pseudobinary phase diagram for CdTe-HgTe alloy system. Symbols (o) denote median values within 90 % confidence limits, as suggested by Brice *et al.* (1986).

$$\begin{aligned}
b_2 &= 39.33464 \\
b_3 &= -59.15100 \\
b_4 &= 46.75216 \\
b_5 &= -14.74259
\end{aligned}$$

These correlations are compared in Figure 7.5 with the data obtained from the phase diagram of Brice *et al.* (1986).

The representation of k in dimensionless concentration at the interface is written as

$$k = \sum_{i=0}^5 k_i (S + 1)^i, \quad (7.6)$$

where the $\{k_i\}$ are defined as

$$k_i = b_i c_o^i \quad i = 0, 1, 2, 3, 4, 5$$

7.2.2 Variation of Thermophysical Properties

Measurements of thermal diffusivity (Holland and Taylor, 1983) and estimations of the heat capacity and thermal conductivity (Su, 1986) for HgCdTe show strong dependencies on temperature and composition. The density of HgCdTe melt (Chandra and Holland, 1983) depends on composition, more than on temperature, because of the large density differences between HgTe and CdTe. The example of variation of thermal diffusivity is shown in Figure 7.6, based on the data by Holland and Taylor (1983).

Most variations in thermophysical properties for HgCdTe are larger for the melt than for the crystal so that properties of crystal may be assumed to be constant. Even for the melt, the use of constant thermophysical properties is not considered to yield significant errors in the result, because of the narrow range of temperature and composition in the system. Representative values for the thermophysical properties have been compiled by Antar (1988) and are listed in Table 7.1. These values are used in most of our calculations.

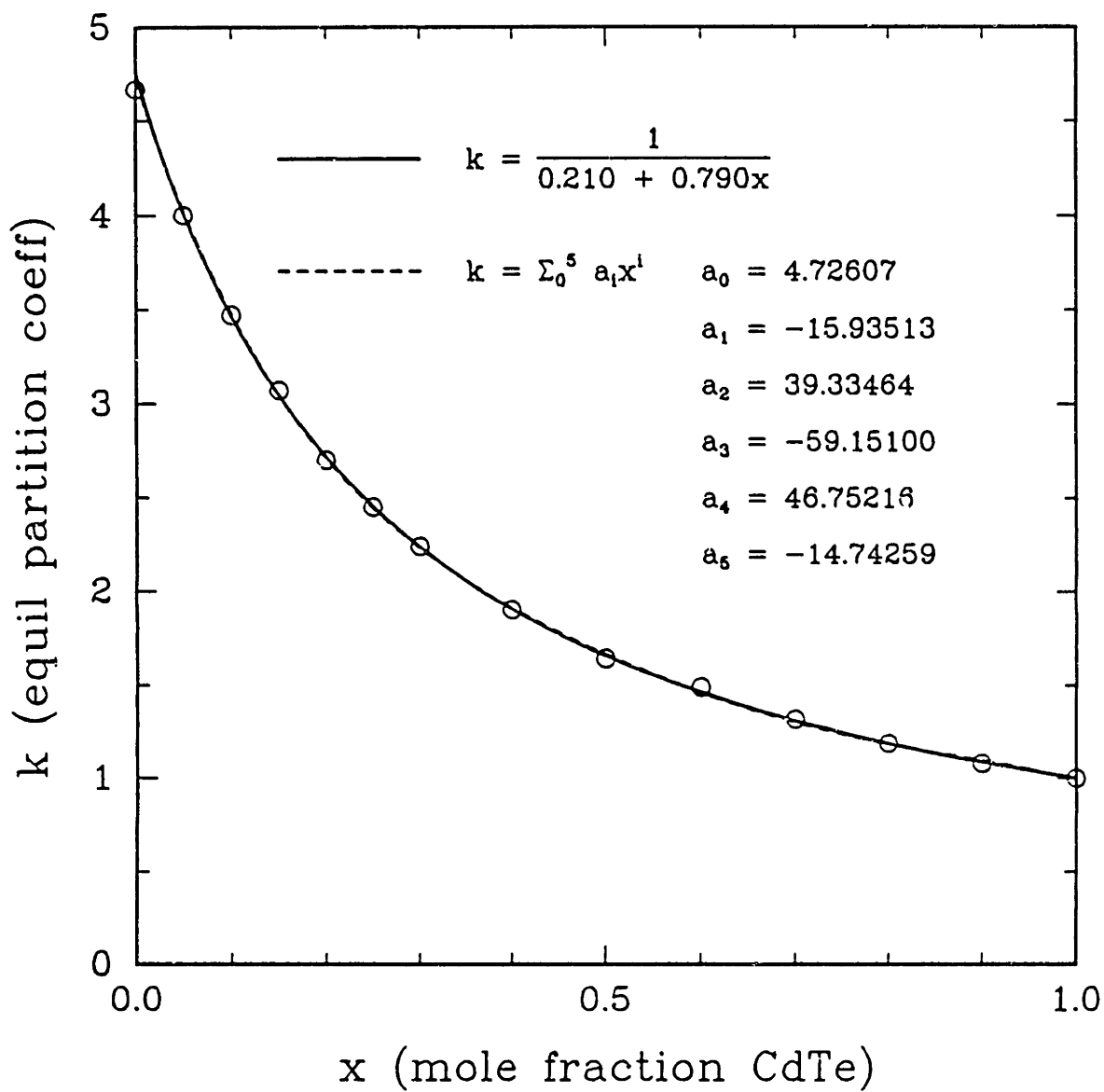


Figure 7.5: Comparison of equilibrium distribution coefficient values from the diagram and the formulae. Symbols (o) denote values of k from the phase diagram of Brice *et al.* (1986).

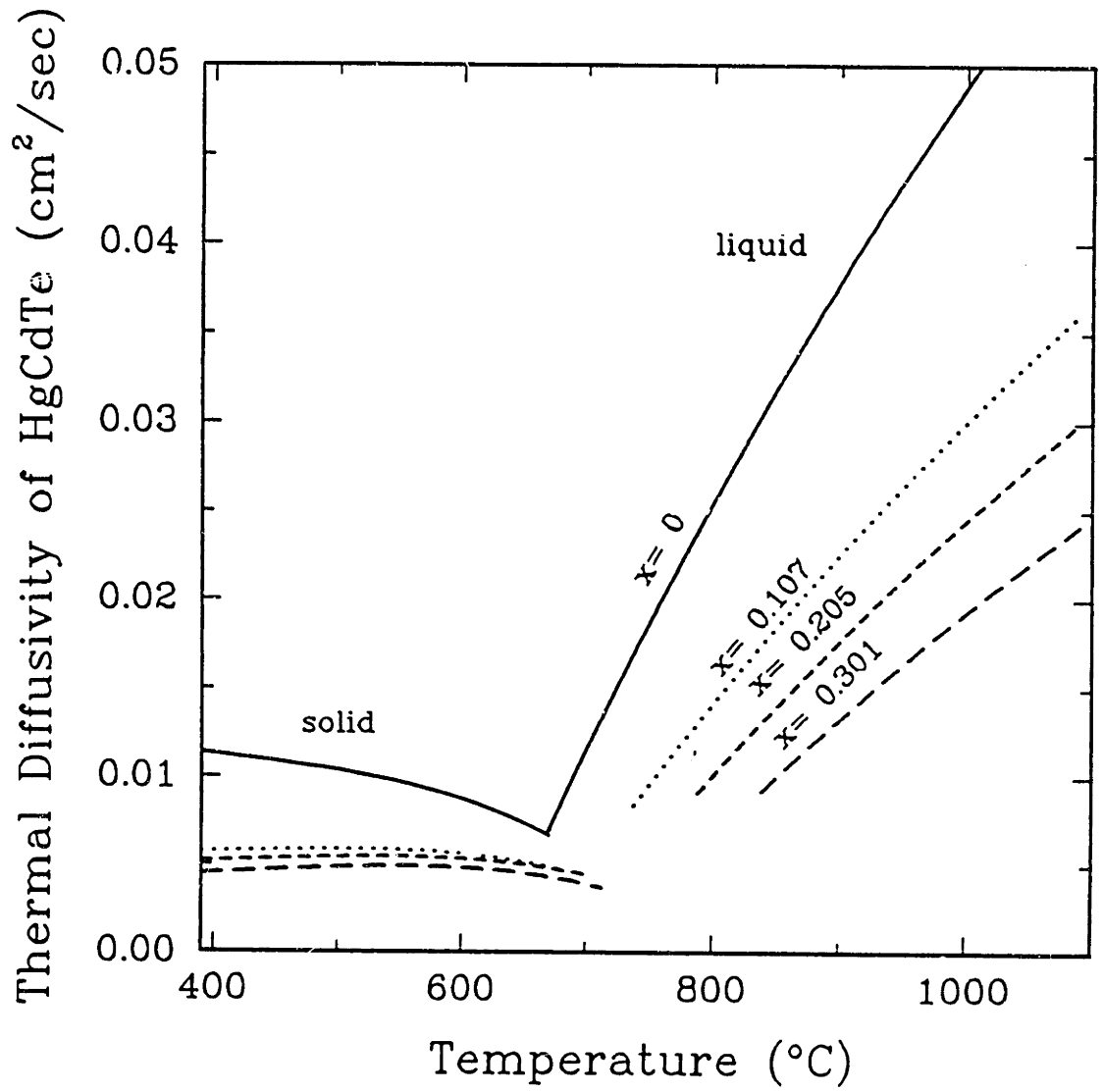


Figure 7.6: Thermal diffusivity of $\text{Hg}_{1-x}\text{Cd}_x\text{Te}$ (Holland and Taylor, 1983).

In the vertical Bridgman growth system, density gradients are the main driving forces for convection in the presence of gravity. Those gradients are related to the gradient of temperature or composition through the coefficients of thermal expansion (β_t) and solutal expansion (β_s). The sign of these coefficients are important in understanding the mechanism of fluid motion, because they are one of the key factors determining the stability of flow in a given configuration. The density of the HgCdTe melt is known (Chandra and Holland, 1983) to have a maximum with temperature for a certain range of composition, leading to the change of sign of β_t at that maximum.

For the precise estimation of β_t , we fit the experimental measurements of HgCdTe melt density by Chandra and Holland (1983) to the second order polynomial of T and x , as

$$\rho_{liq}(\text{g/cm}^3) = c_0 + c_1x + c_2T + c_3xT + c_4x^2 + c_5T^2 \quad (7.7)$$

where x is a mole fraction CdTe and T is a temperature in Celcius. The coefficients $\{c_i\}$ have been estimated as

$$\begin{aligned} c_0 &= 2.25085 \\ c_1 &= -4.47815 \\ c_2 &= 1.54035 \times 10^{-2} \\ c_3 &= 2.54384 \times 10^{-3} \\ c_4 &= 3.60881 \times 10^{-1} \\ c_5 &= -1.02193 \times 10^{-5} \end{aligned}$$

The correlations are shown in Figure 7.7 with experimental data by Chandra and Holland (1983) and show the maximum in density for $x \leq 0.1$. Contour plots of isodensity lines are constructed in Figure 7.8 from the correlation formula for melt density. These curves clearly show the density maximum in a range of temperature and composition that occurs in typical crystal growth systems.

Coefficients of thermal and solutal expansion are displayed in Figure 7.9 and 7.10 for selected compositions. They are obtained by differentiation of Eq. (7.7) with respect to temperature and composition. Thermal expansion coefficients cross the line for $\beta_t = 0$

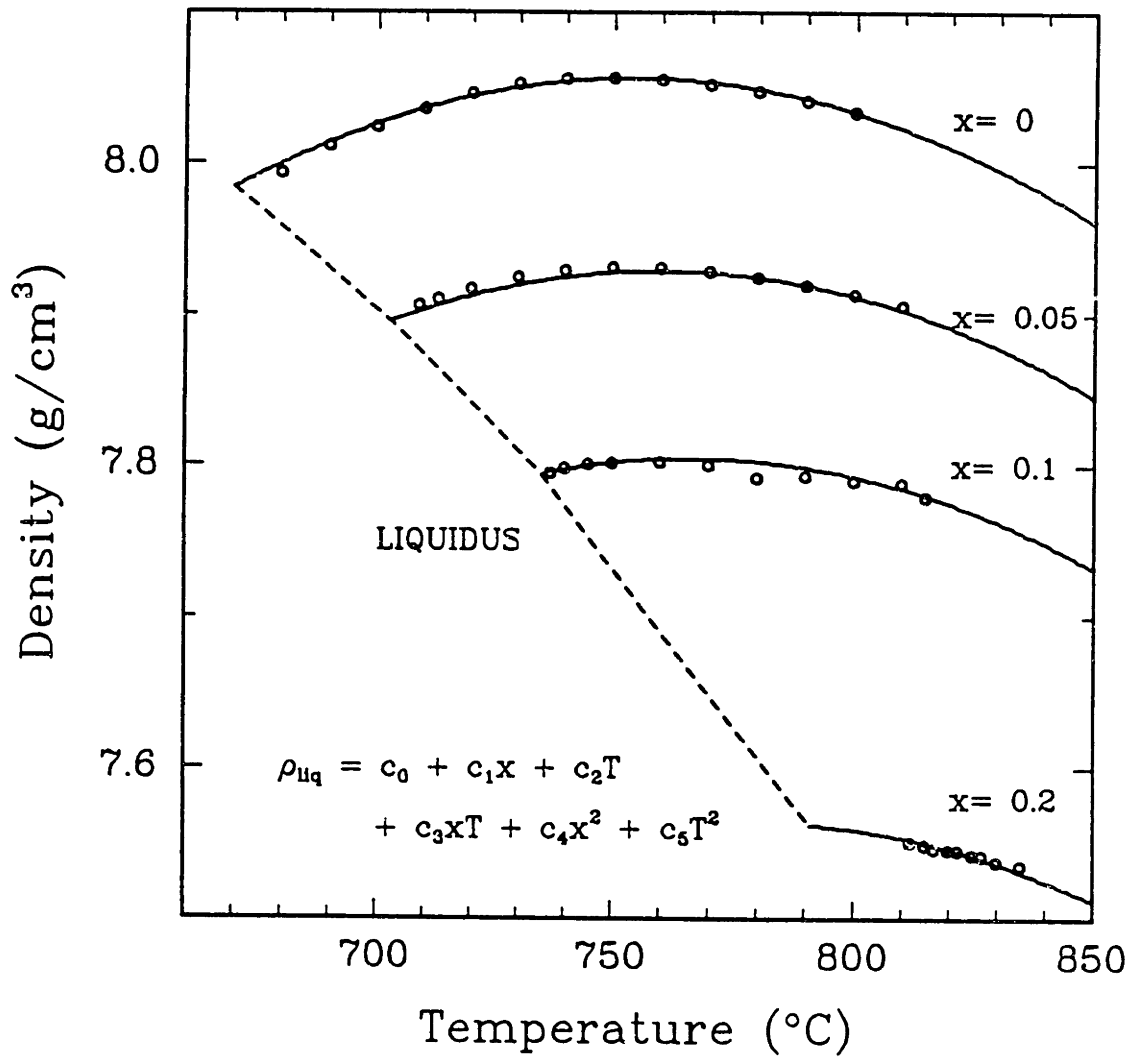


Figure 7.7: Density for liquid Hg_{1-x}Cd_xTe. Circles (o) denote experimental measurements by Chandra and Holland (1983).

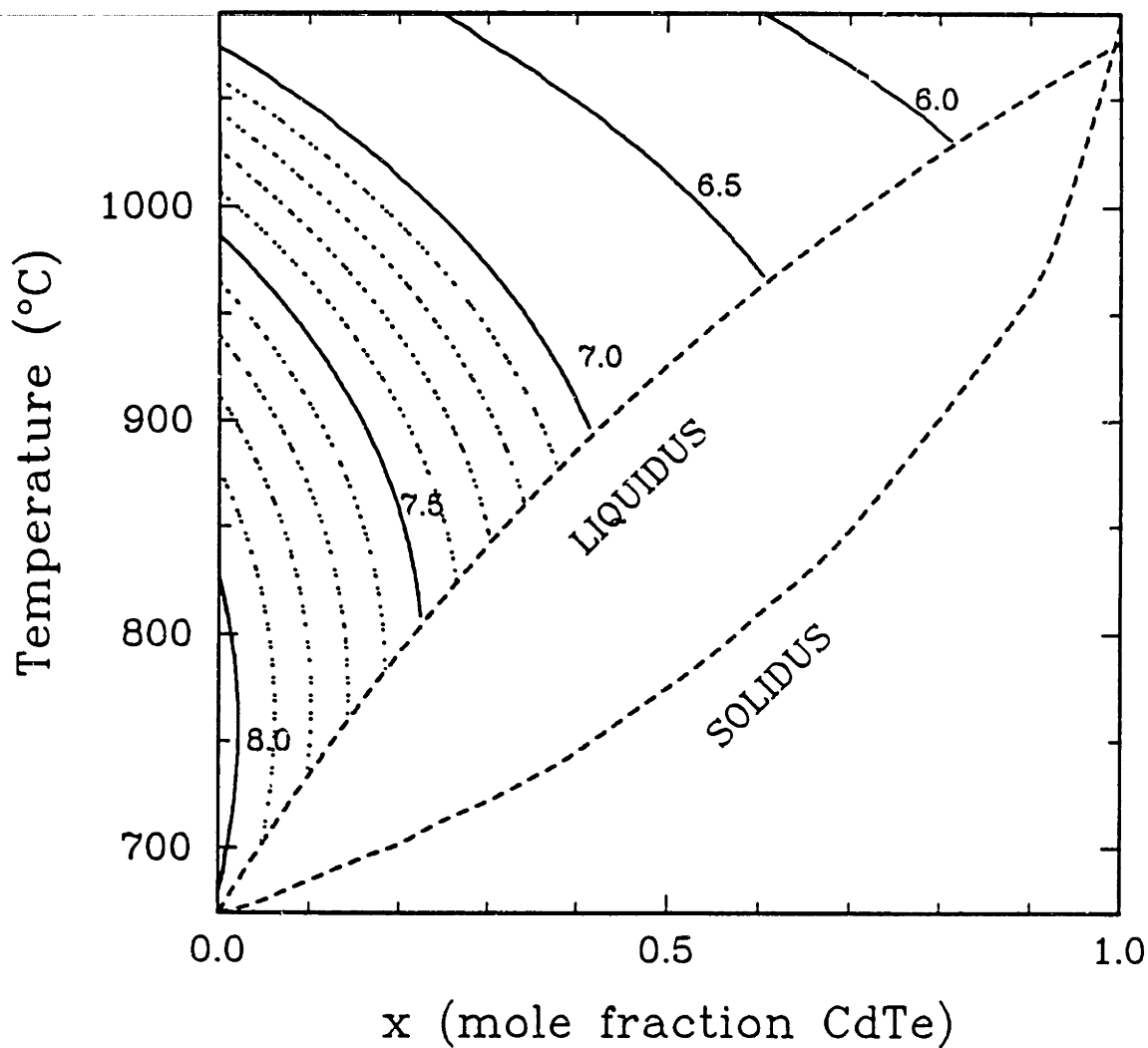


Figure 7.8: Contours of $\text{Hg}_{1-x}\text{Cd}_x\text{Te}$ melt density in the possible ranges of temperature and composition in the crystal growth system.

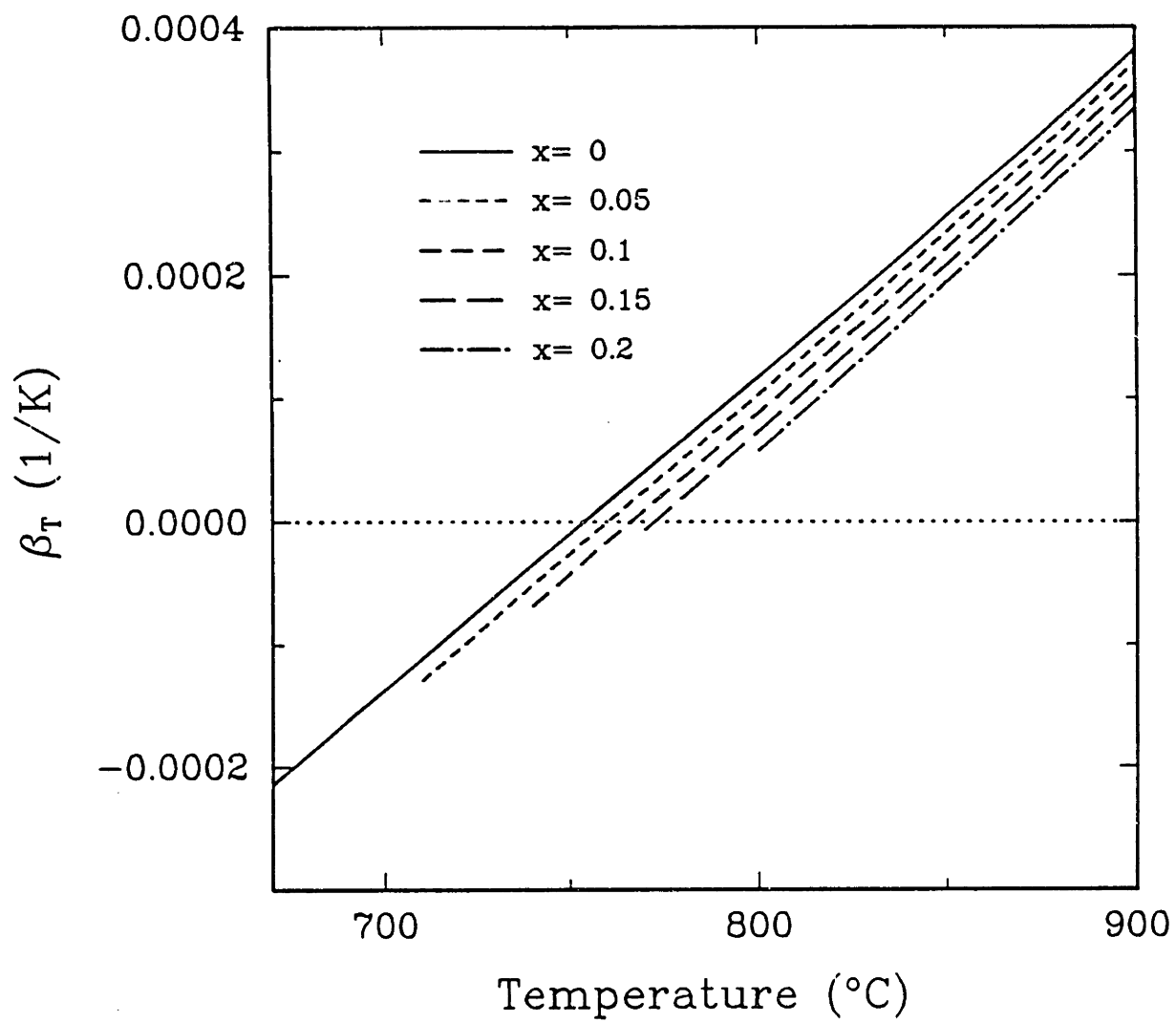
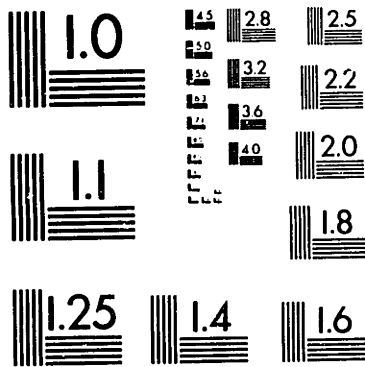


Figure 7.9: Coefficients of thermal expansion for $\text{Hg}_{1-x}\text{Cd}_x\text{Te}$ for selected compositions.

THIS COPY MAY NOT BE FURTHER REPRODUCED OR DISTRIBUTED
IN ANY WAY WITHOUT SPECIFIC AUTHORIZATION IN EACH IN-
STANCE, PROCURED THROUGH THE DIRECTOR OF LIBRARIES,
MASSACHUSETTS INSTITUTE OF TECHNOLOGY.



MICROCOPY RESOLUTION TEST CHART
NATIONAL BUREAU OF STANDARDS
STANDARD REFERENCE MATERIAL 1010a
(ANSI and ISO TEST CHART No. 2)

24 : 1

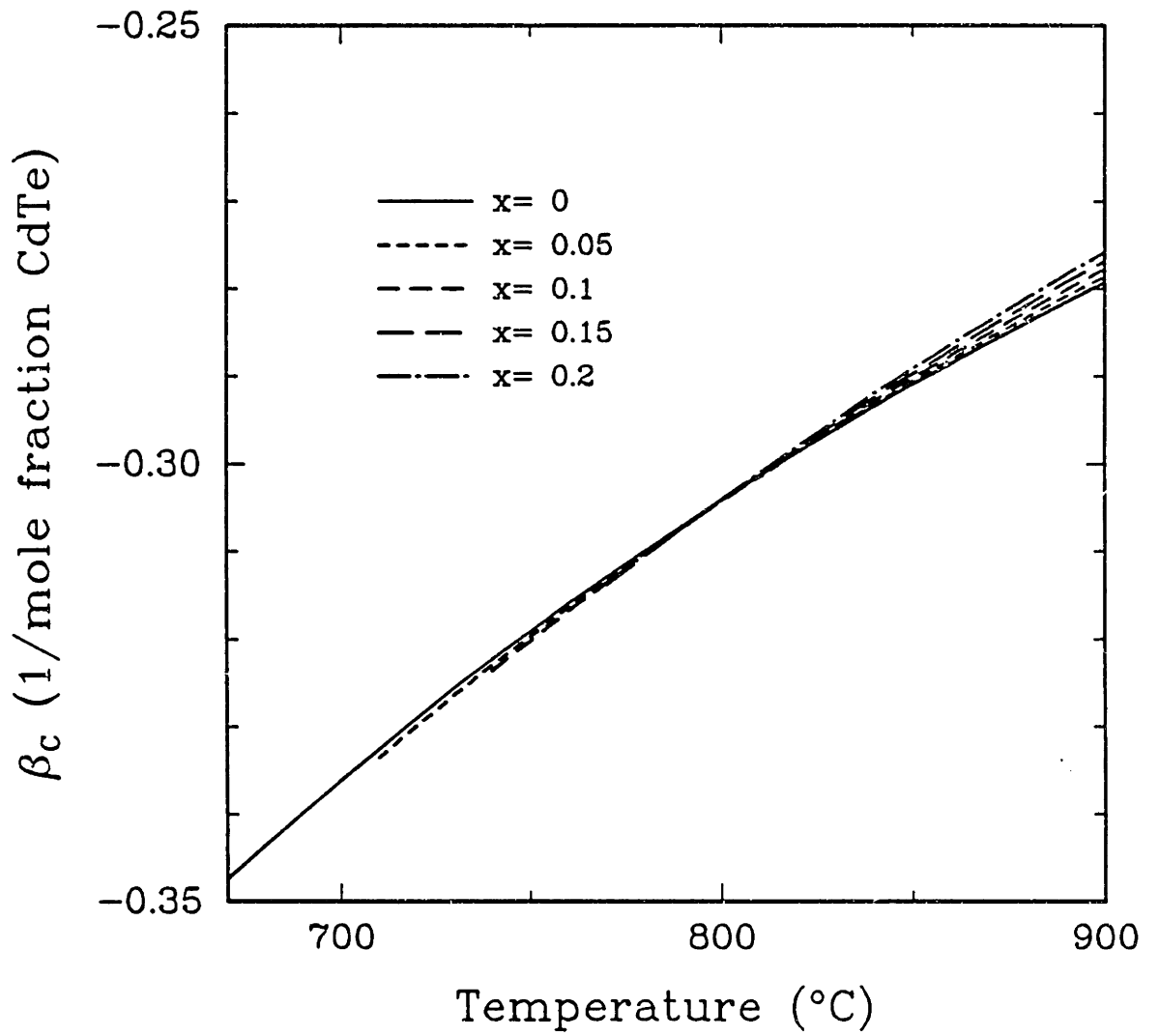


Figure 7.10: Coefficients of solutal expansion for $\text{Hg}_{1-x}\text{Cd}_x\text{Te}$ for selected compositions.

when x is less than 0.15. Because the range of β_l includes zero, β_l can vary by orders-of-magnitude in a small range. On the other hand, coefficients of solutal expansion are almost independent of the composition in the melt and show the variations with temperature only. The maximum variations are about 10 percent in the temperature range for our model and can be assumed to be constant.

The range of thermal Rayleigh number (Ra_t) are generated by calculating β_l under the condition imposed in our model. It is presented in Figure 7.11 with $c_o = 0.2$. The upper curve represents the condition at the top of the melt, that is, only composition changes while temperature is maintained at hot zone temperature. The lower curve follows the temperature and composition of the liquidus curve so that the equilibrium relationship at the interface is satisfied. The area bounded by these two curves and by $x = 0$ and c_o covers the range of possible Ra_t . If we further assume that the composition at the top of the melt remains at c_o , Ra_t changes only inside the shaded area. This assumption is valid when the mixing effect is negligible as in the diffusion-controlled growth. Almost diffusion-controlled axial segregation observed previously (Lehoczky and Szofran, 1982; Szofran *et al.*, 1984) supports this assumption.

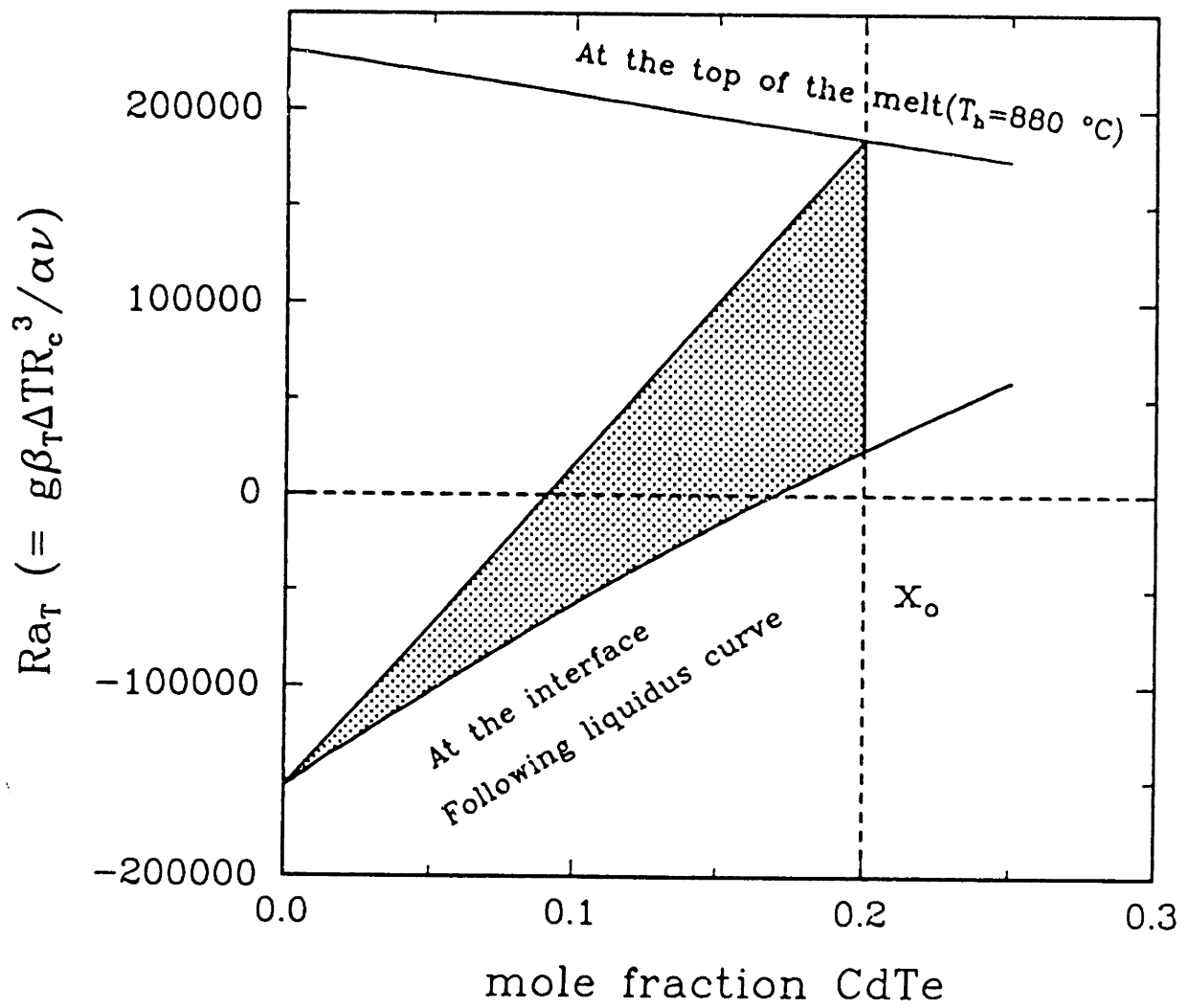


Figure 7.11: Range of Ra_T under the condition imposed in the model.

7.3 Flow Structure and Solute Segregation

The thermophysical properties used in this study for HgCdTe were compiled by Professor Antar (1988) and are listed in Table 7.1. The values of the properties have been estimated for the alloy with $x = 0.20$ mole fraction CdTe. The melting point temperature and equilibrium distribution coefficient are obtained from the phase diagram and calculated from Eq. (7.3) and (7.5), respectively. All other properties were assumed to be independent of temperature and composition, except for specific calculation with variable β .

The calculations for HgCdTe growth are presented simulating the vertical Bridgman system of Szofran and Lehoczky (1984). Parameters and the thermophysical properties of quartz used in the simulation are tabulated in Table 7.2. The effective heat transfer coefficients between the ampoule and the furnace are computed in the same way described in Chapter 6. Dimensionless groups appropriate for the terrestrial growth of HgCdTe with this furnace design parameters are listed in Table 7.3, with their definitions.

Transient calculations for the growth of nondilute pseudobinary HgCdTe alloy in a quartz ampoule were conducted using the stationary state as an initial condition. For this a stationary ampoule was positioned with the center plane of the gradient zone at 0.65 of the ampoule length from the top. The initial temperature field reached a steady-state with the surrounding furnace and the composition was uniform throughout the melt in the absence of incorporation or rejection of solute at the interface due to solidification. The initial condition for the flow calculation corresponds to steady thermal buoyancy-driven fluid motion. The transient calculation was continued until about 0.2 of the charge was solidified to focus on the initial transients in the transport processes. Sample meshes used in the transient finite element discretizations are shown in Figure 7.12, displaying the deformation and translation of the individual elements in time.

Quantity	Symbol (units)	Value
Thermal conductivity of the melt	k_m (W/°C·cm)	1.96×10^{-2}
Thermal conductivity of the solid	k_s (W/°C·cm)	2.91×10^{-3}
Density of the melt	ρ_m (g/cm ³)	7.55
Density of the solid	ρ_s (g/cm ³)	7.63
Specific heat of the melt	$C_{p,m}$ (J/°C·g)	0.257
Specific heat of the solid	$C_{p,s}$ (J/°C·g)	0.177
Melting temperature	T_m (°C)	Eq. (7.3)
Kinematic viscosity	ν (cm ² /sec)	1.08×10^{-3}
Heat of solidification	ΔH_s (J/g)	130
Thermal expansion coefficient	β_t (°C ⁻¹)	1.5×10^{-4}
Solutal expansion coefficient	β_s ((mole frac. CdTe) ⁻¹)	-0.30
Diffusion coefficient of CdTe in HgCdTe	D (cm ² ·sec)	5.5×10^{-5}
Equilibrium distribution coefficient of CdTe	k	Eq. (7.5)

Table 7.1: Thermophysical property data used in analysis of HgCdTe growth.

Parameter	Value
Ampoule length, L (cm)	5.0
Crystal radius, R_c (cm)	0.25
Ampoule outer radius, R_a (cm)	0.50
Gradient zone length, L_g (cm)	1.00
Temperature difference, $T_h - T_c$ (°C)	480
Temperature in hot zone, T_h (°C)	880
Temperature in cold zone, T_c (°C)	400
Initial concentration, c_o (mole fraction CdTe)	0.20
Ampoule translation rate, V_g ($\mu\text{m}/\text{sec}$)	1.12
Ampoule material	quartz
Thermal conductivity of ampoule, K_a (W/°C·cm)	0.025
Density of ampoule, ρ_a (g/cm ³)	2.2
Specific heat of ampoule, $C_{p,a}$ (J/°C·g)	1.05

Table 7.2: Thermophysical data for ampoule and system geometry.

Name	Symbol	Definition	Value
Thermal Rayleigh number	Ra_t	$g\beta_t\Delta TR_c^3/(\alpha_m\nu)$	1.0×10^5
Solutal Rayleigh number	Ra_s	$g\beta_s c_o R_c^3/(\alpha_m\nu)$	-8.5×10^4
Thermal Peclet number	Pe	$V_g R_c/\alpha$	2.8×10^{-3}
Solutal Peclet number	Pe_s	$V_g R_c/D$	0.51
Prandtl number	Pr	ν/α_m	0.11
Schmidt number	Sc	ν/D	19.6
Stefan number	St	$\Delta H_s/C_{p,m}\Delta T$	1.05
Thermal diffusivity ratio	γ	α_s/α_m	0.21
Density ratio	σ	ρ_s/ρ_m	1.0

Table 7.3: Definitions of dimensionless groups that appear in analysis of thermosolutal convection of HgCdTe crystal growth; characteristic values computed from the thermo-physical properties of HgCdTe are also shown.

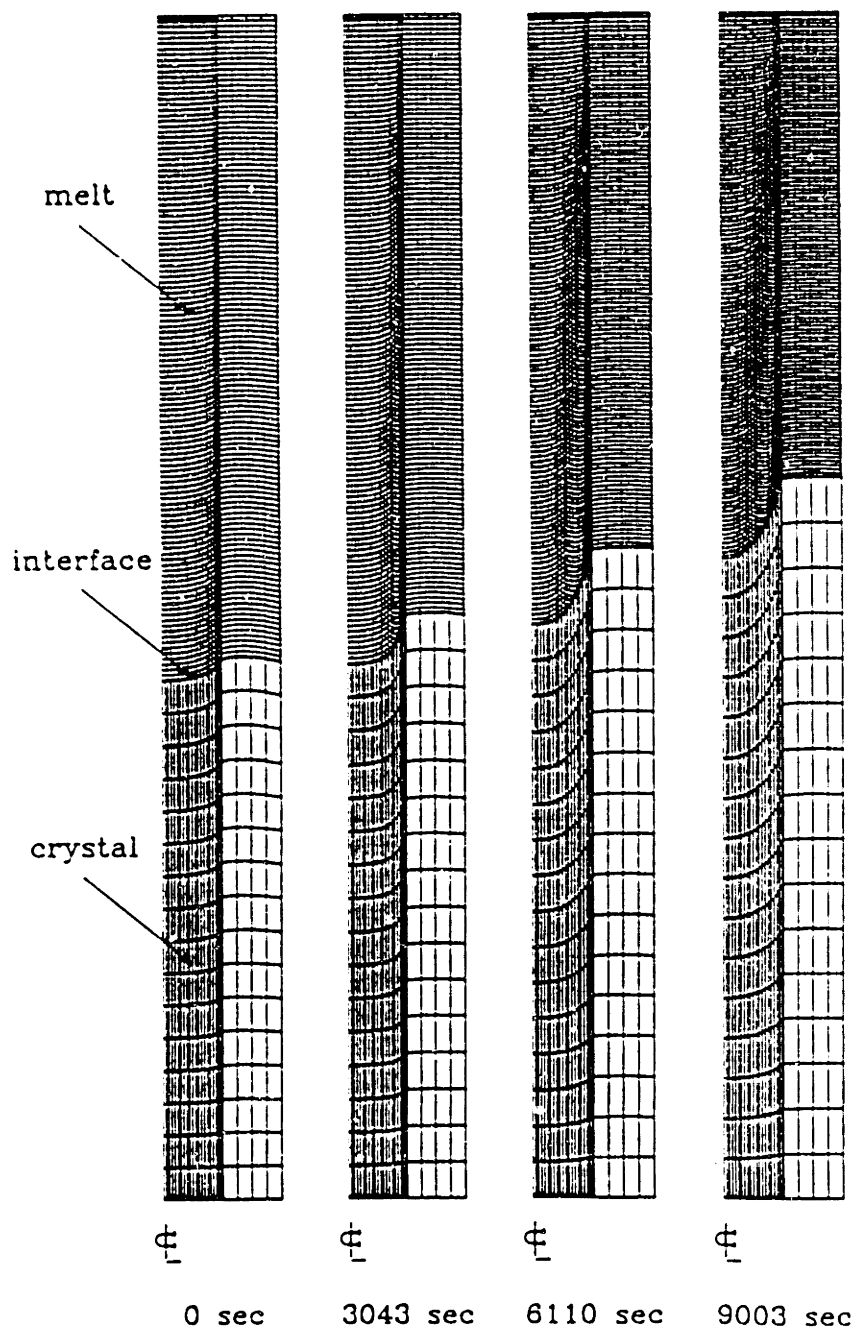


Figure 7.12: Sample finite element meshes used for the transient calculations for the growth of HgCdTe in vertical Bridgman system.

7.3.1 Temperature Fields and Growth Velocity

Conduction dominates the heat transfer in the melt because of the low Prandtl number (0.11 for $x = 0.2$) of $\text{Hg}_{1-x}\text{Cd}_x\text{Te}$ melt, while conduction is the only mechanism for heat transfer in the solid materials. Effective heat transfer coefficients between the furnace and ampoule account for the effects of conduction and radiation.

Sample temperature fields for $Ra_t = 0$ are shown in Figure 7.13 as isotherm contours. They are spaced at equal spacings of $0.1\Delta T$, where ΔT is the overall temperature difference in the furnace. The constant temperature in the hot zone and cold zone, and relatively small length of insulation zone cause the axial temperature gradient to be confined to the insulation zone. Temperature field in this region keep the same relative shape regardless of the location of ampoule in the furnace.

The most distinct feature of the temperature field for the growth of the nondilute alloy is observed in the change of the interface shape and location during growth. This is attributed to the dependence of the melting point temperature on the local composition at the interface. The initial interface shape follows the isotherm, as shown in Figure 7.13(a), because the composition is uniform along the interface. As the solute diffusion layer develops due to the preferential incorporation of CdTe at the interface, interfacial concentration of CdTe decreases gradually until it reaches the steady value. The change in interface concentration leads to the decrease in melting point temperature, following the liquidus curve in the pseudobinary phase diagram (Figure 7.4). Comparison of the interface location at $r = 0$ between Figure 7.13(a) and (d) shows the melting point temperature changes about $0.2\Delta T$ or 98°C during the crystal growth process. Histories of the melting point temperature at the midpoint of interface are presented in Figure 7.14. It shows melting point temperature or the concentration at that point by which it is determined is hardly affected by the gravitational level, because the convection itself is weak and competing thermal and solutal effects are influenced by gravity to the same degree.

Another consequence of the coupling of interface shape and interface concentration

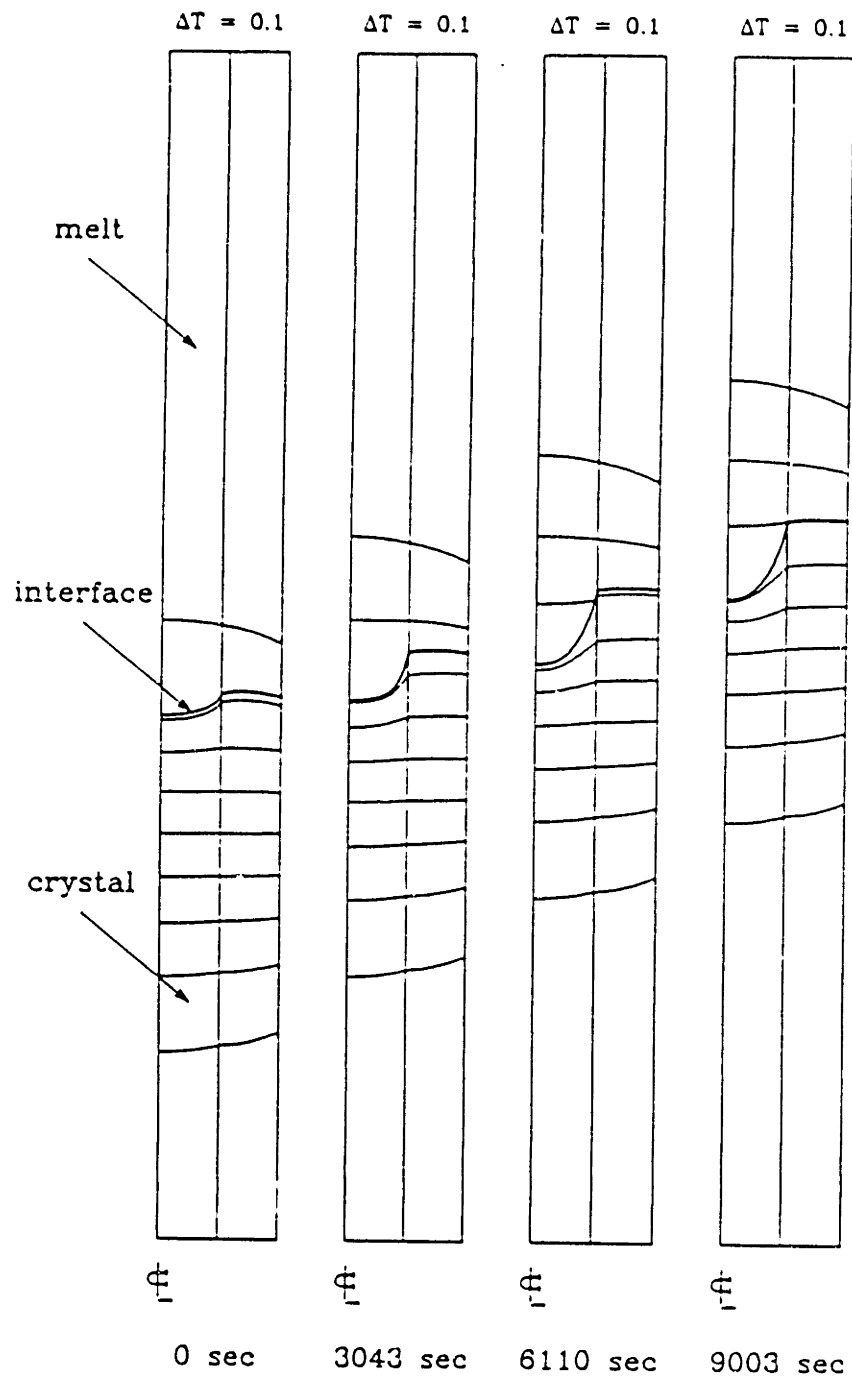


Figure 7.13: Sample temperature fields for growth of HgCdTe in vertical Bridgman growth: with $Ra_t = 0$.

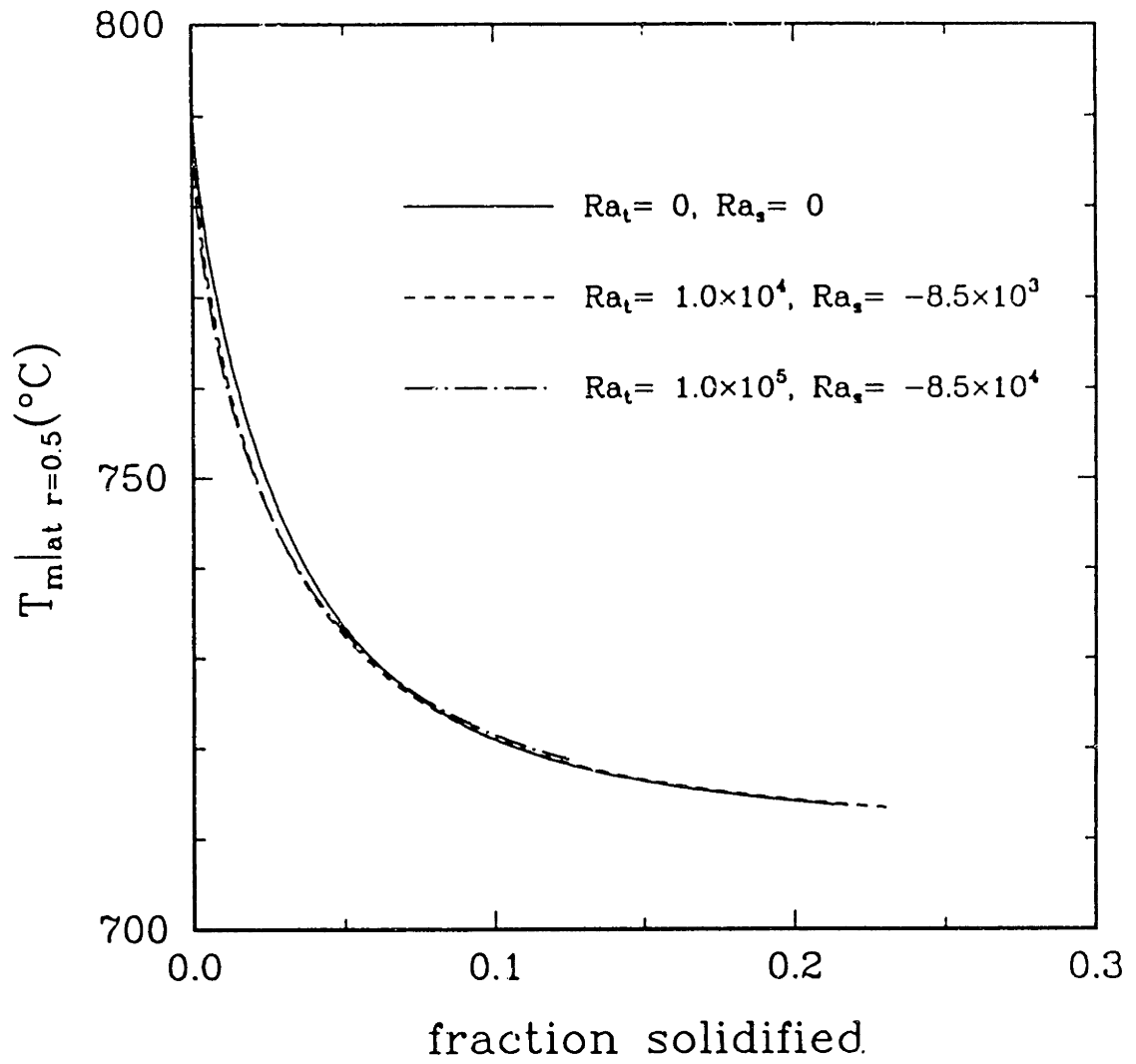


Figure 7.14: Time histories of the melting point temperature at the midpoint of interface for several gravitational force level.

is that the interface coincides with neither an isotherm or an isoconcentration line. The initial curvature of the interface is caused by the imperfections in heat transfer and by the different thermal conductivities between melt, crystal and ampoule. Once the ampoule starts to move and crystal begins to grow, the effects of latent heat release and radial segregation in composition across the interface complicates the mechanism determining the interface shape in the growth of nondilute alloy crystal. The variation of composition across the interface results in the variation in melting point temperature. In Figure 7.13(d), melting point temperature changes about $0.1\Delta T$ or 48°C across the interface.

Comparison of the temperature fields from the calculations for $Ra_t = 0$ and 1.0×10^4 supports the conduction-dominated heat transfer in the melt. Temperature fields at $Ra_t = 1.0 \times 10^4$ are shown in Figure 7.15 for nearly the same time instances as in Figure 7.13. These fields show almost the same isotherm shape and location, suggesting convection hardly alters the temperature fields.

The growth rate of the crystal has been computed from the transient location of the interface. The coupling of the interface composition and melting point temperature causes a variation of growth rate across the crystal. The transient history of growth rates for several Ra_t , shown in Figure 7.16, were computed at the midpoint of interface. The growth rate approaches the ampoule translation rate and show little dependence on Ra_t . As growth rate attains the steady value after the initial transient period, interface shape and its location with respect to the furnace becomes steady, as shown in Figure 7.18 more clearly.

The interface deflection in the growth of the nondilute alloy is the product of complex interactions between the temperature and solute fields near the interface, through thermosolutal convection and the dependence of melting point temperature on interface concentration. The history of interface deflection displayed in Figure 7.17 shows that the convection near the interface slightly enhances the interface deflection. When the interface shape is concave, thermosolutal convection near the interface carries more HgTe to the center and higher concentration of HgTe in that region lowers the melting point

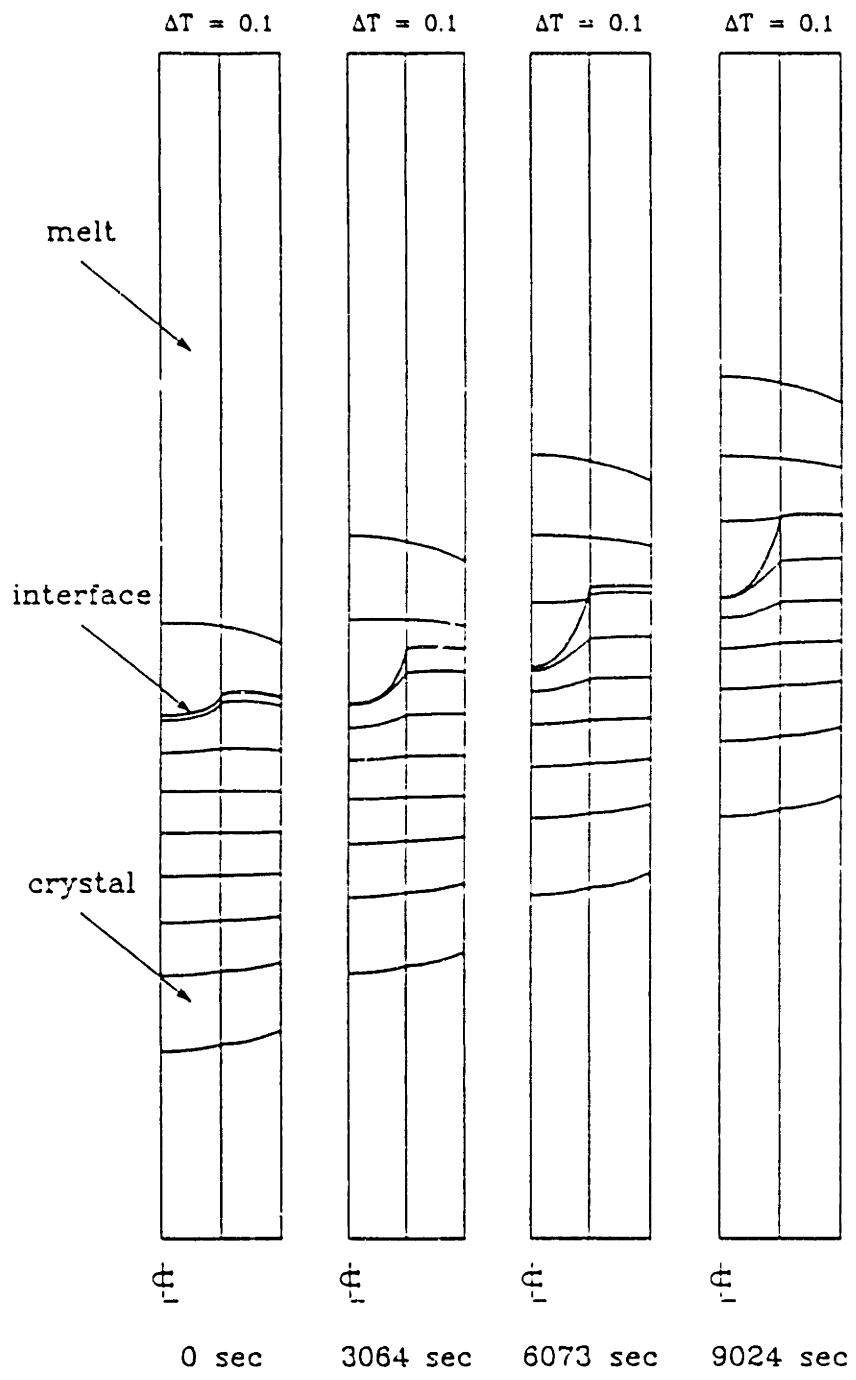


Figure 7.15: Sample temperature fields for growth of HgCdTe in vertical Bridgman growth: $Ra_t = 1 \times 10^4$.

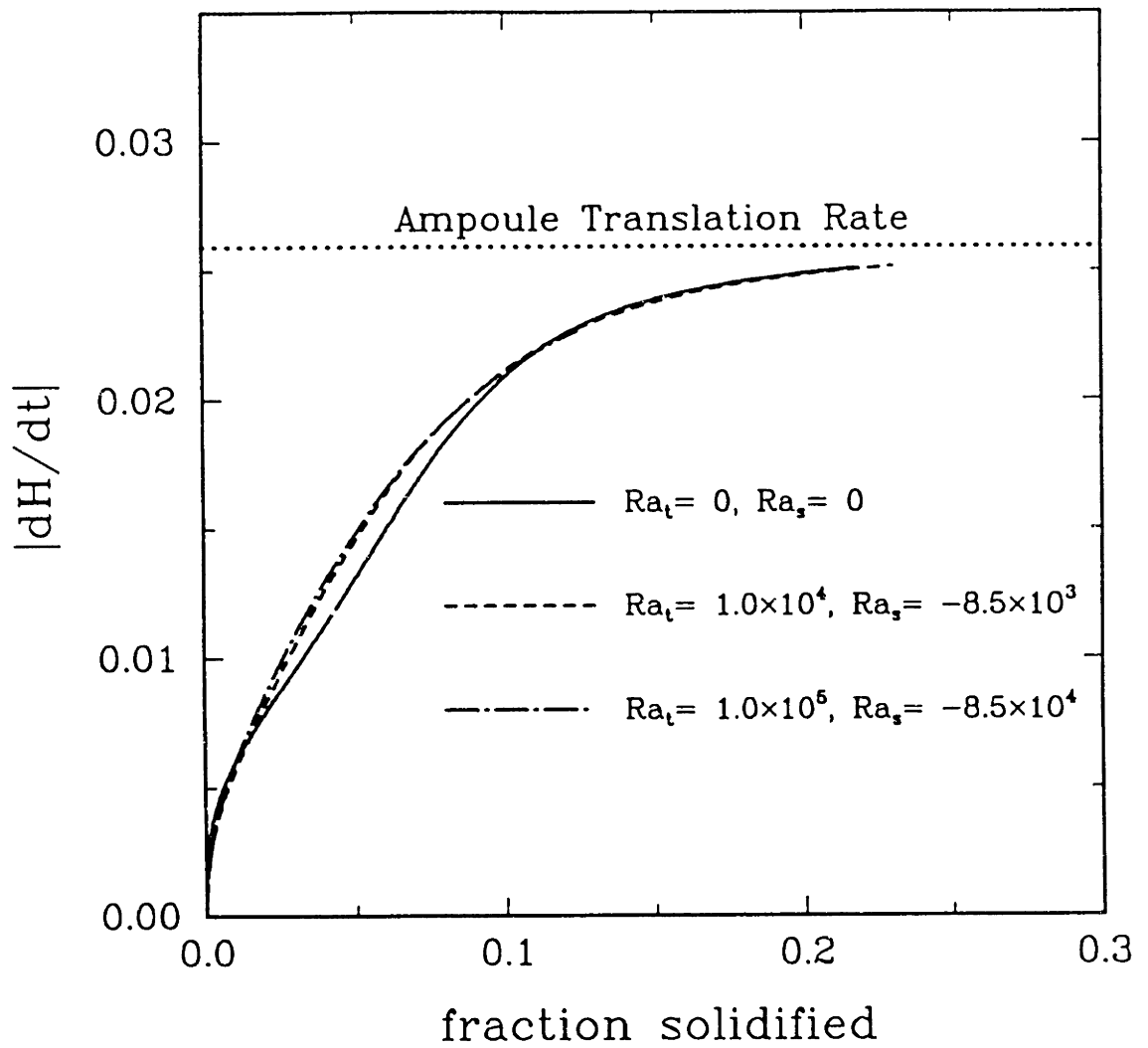


Figure 7.16: Transient growth rate of HgCdTe crystal for several pairs of the thermal Rayleigh number, Ra_t and solutal Rayleigh number, Ra_s .

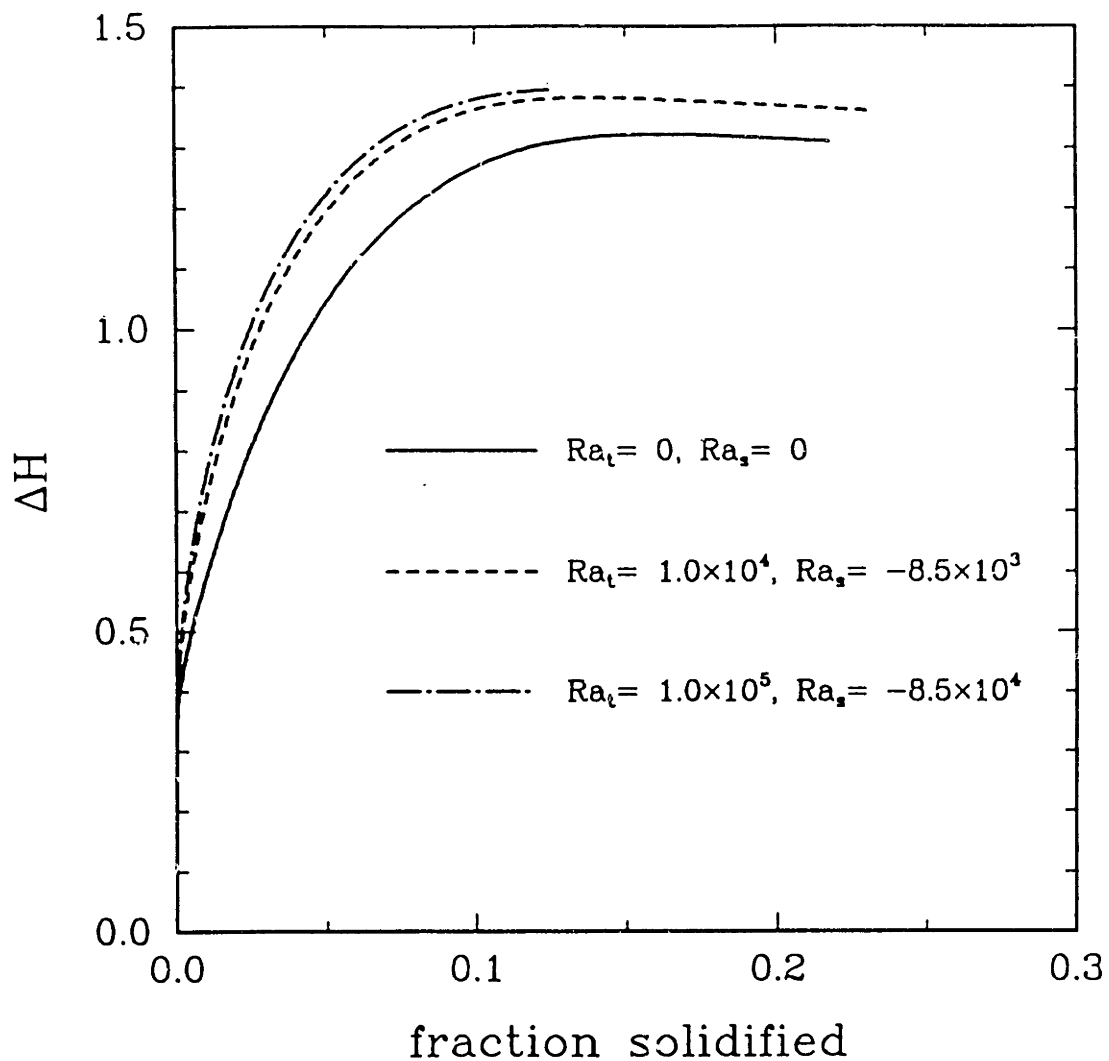


Figure 7.17: Transient interface deflections of HgCdTe crystal in vertical Bridgman growth system for several pairs of the thermal Rayleigh number, Ra_t and solutal Rayleigh number, Ra_s .

temperature and shifts the interface to the direction of bottom. This effect causes more interface deflection in the presence of weak convection.

7.3.2 Flow Fields

The analysis of fluid motion in the melt of the crystal growth system is important to understanding the convection and solute distribution in the crystal. For the growth of dilute binary alloy or pure material in the stabilizing vertical Bridgman growth system, it is well known that radial temperature gradients caused by the thermal conductivity differences and by other thermal imperfections drive the flow in the melt (Chang and Brown, 1983b; Adornato and Brown, 1987a). Two distinct toroidal cells stacked axially in the ampoule are present for the Bridgman furnace with insulation or gradient zone. The mismatch in the thermal conductivities of the melt, crystal and ampoule near the interface region causes one set of radial temperature gradients, which drive the flow up along the centerline. Heat transfer from the furnace to the charge in the upper part of the ampoule sets the radial temperature gradients which are opposite in sign to the radial temperature gradients near the interface. This second region of radial temperature gradient drives the upper toroidal cell which rotates in the counter direction of the flow cell near the interface.

In the growth of nondilute HgCdTe growth, the lighter component CdTe is preferentially incorporated into the crystal and the accumulation of the heavier component HgTe near the interface leads to the stably stratified axial density gradient. This density profile damps the thermal buoyancy-driven convection as demonstrated by Adornato and Brown (1987a) for the GeSi system of similar nature.

The sequence of snap shots of flow fields at approximately 0, 3,000, 6,000, and 9,000 seconds are described in Figure 7.18 for $Ra_t = 1.0 \times 10^4$, $Ra_s = -8.5 \times 10^3$. These plots show the relative position of the ampoule with respect to the furnace during the growth. Before the solidification starts, the composition in the melt is uniform and the solute field does not participate in the mechanism for convection. The corresponding flow field

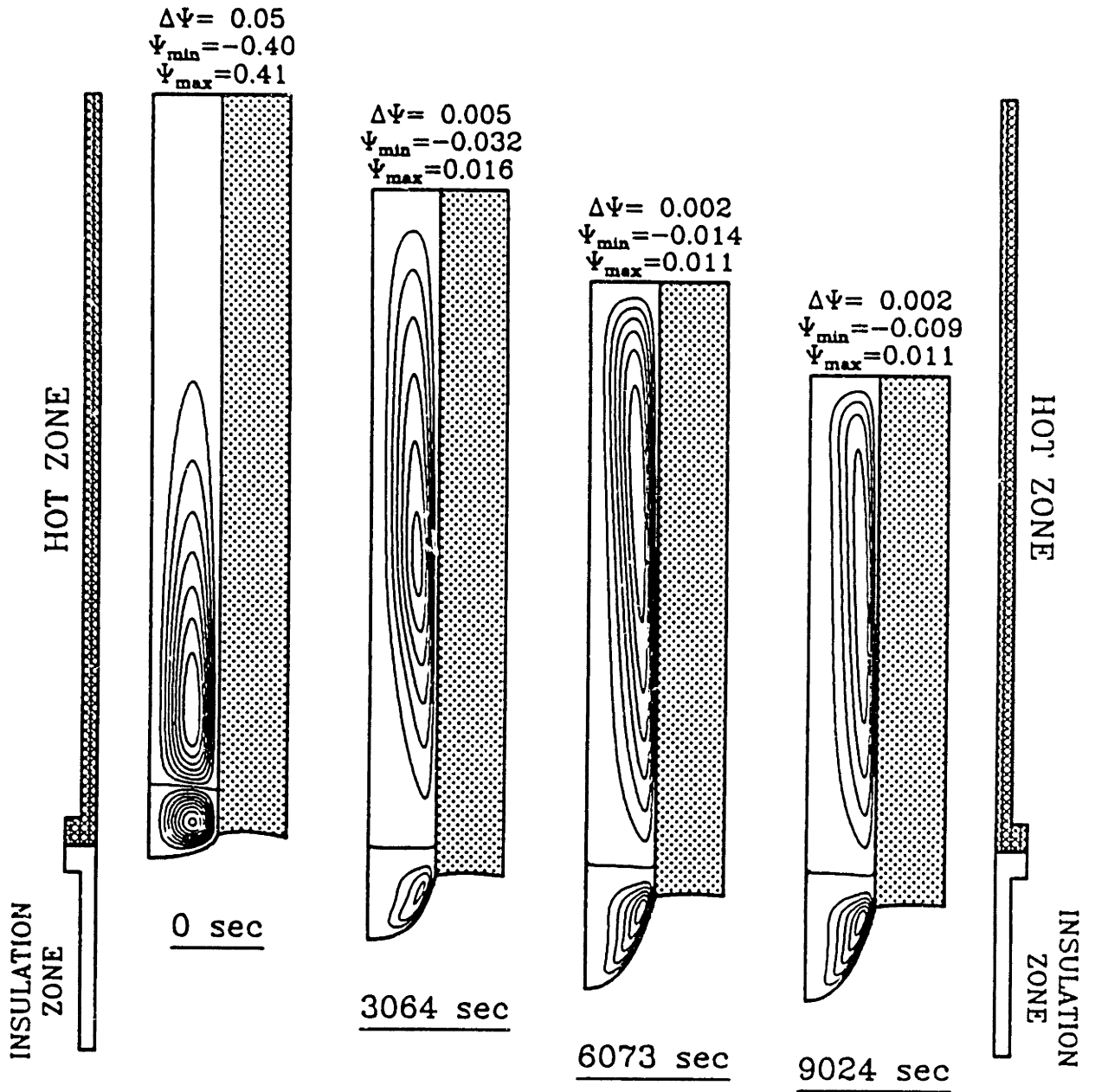


Figure 7.18: Sample flow fields for growth of HgCdTe crystal in the vertical Bridgman furnace: $(Ra_t, Ra_s) = (1.0 \times 10^4, -8.5 \times 10^3)$.

(Figure 7.18(a)) shows the typical structure of flow driven by the radial temperature gradients in the vertical Bridgman growth system.

As the solute diffusion layer develops and penetrates into the melt, the flow intensities of both the upper and lower flow cell decreases by more than an order. The lower flow cell is damped more readily in the early stage because of the high axial solute gradient near the interface. The flow intensity of this cell is lower than in the upper cell, although they are comparable initially. With the extension of solute diffusion layer, the upper cell is damped continuously, while the large radial temperature gradient near the interface prevents the further weakening of the lower cell.

With the decrease of flow intensity, the centers of the flow cells move toward the ampoule wall. The movement of the center of the cell and the flattening of the streamlines adjacent to the wall suggests the formation of a thin boundary layer, which was discussed in Chapter 5 by steady-state analysis.

Calculations for $Ra_t = 1.0 \times 10^5$ and $Ra_s = -8.5 \times 10^4$, which corresponds to the condition of terrestrial growth, show the similar flow structure with higher flow intensities, as presented in Figure 7.19. The intermediate flow structure between initial thermal buoyancy-driven flow and flow field damped by the solute field is shown in Figure 7.19(b). The lower flow cell is already damped by the solute field, but the upper flow cell still maintains the initial flow intensity. The detailed transition of flow structure is described in Figure 7.20 and 7.21 with shorter time intervals. The upper flow cell initially driven by thermal buoyancy gradually reduces in size and finally disappears to give way to the flow cell damped by the solute field. The flow intensity of the upper flow cell shows a maximum during this transition period.

The intensities of the flow fields are summarized by the history of stream function of the each flow cell shown in Figure 7.22 for $(Ra_t, Ra_s) = (1.0 \times 10^4, -8.5 \times 10^3)$ and $(1.0 \times 10^5, -8.5 \times 10^4)$. The lower flow cell behaves in the same manner at both cases. However, the upper flow cell demonstrates significant differences in the early stages of growth. The large driving force for thermal buoyancy-driven convection at

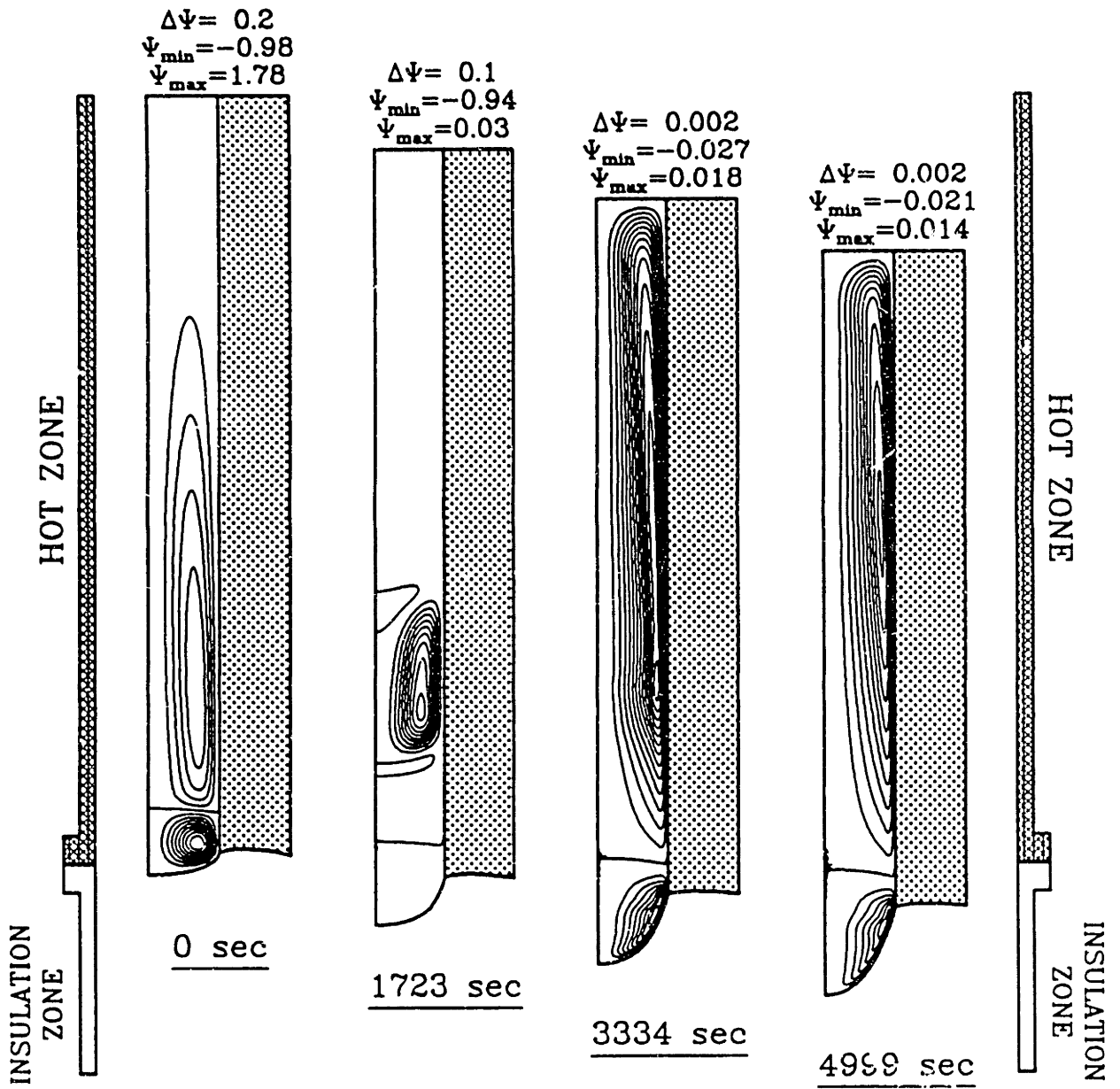


Figure 7.19: Sample flow fields for growth of HgCdTe crystal in the vertical Bridgman furnace: $(Ra_t, Ra_s) = (1.0 \times 10^5, -8.5 \times 10^4)$.

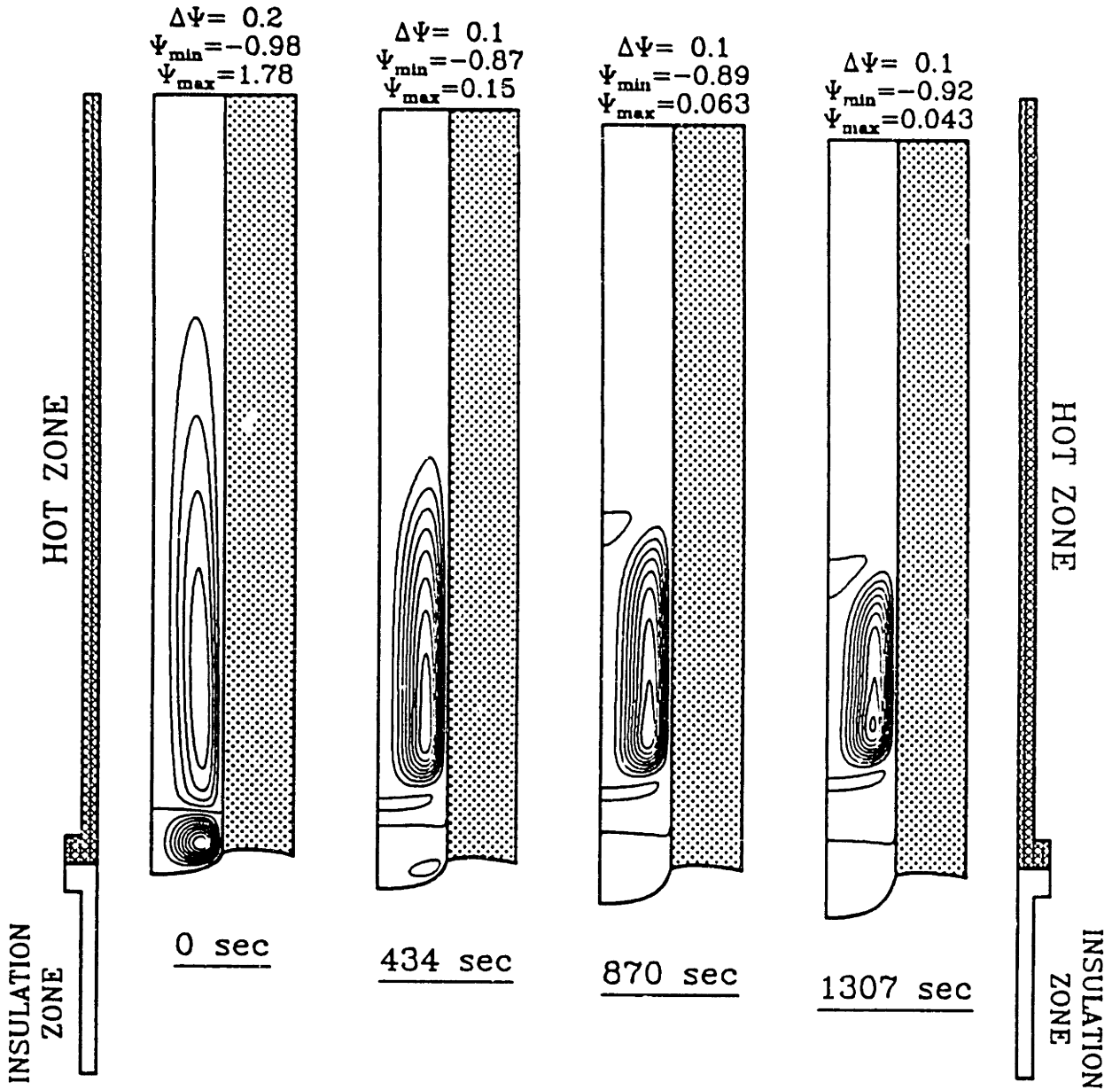


Figure 7.20: (I) Sample flow fields for growth of HgCdTe crystal showing the transition in flow structure: $(Ra_t, Ra_s) = (1.0 \times 10^5, -8.5 \times 10^4)$.

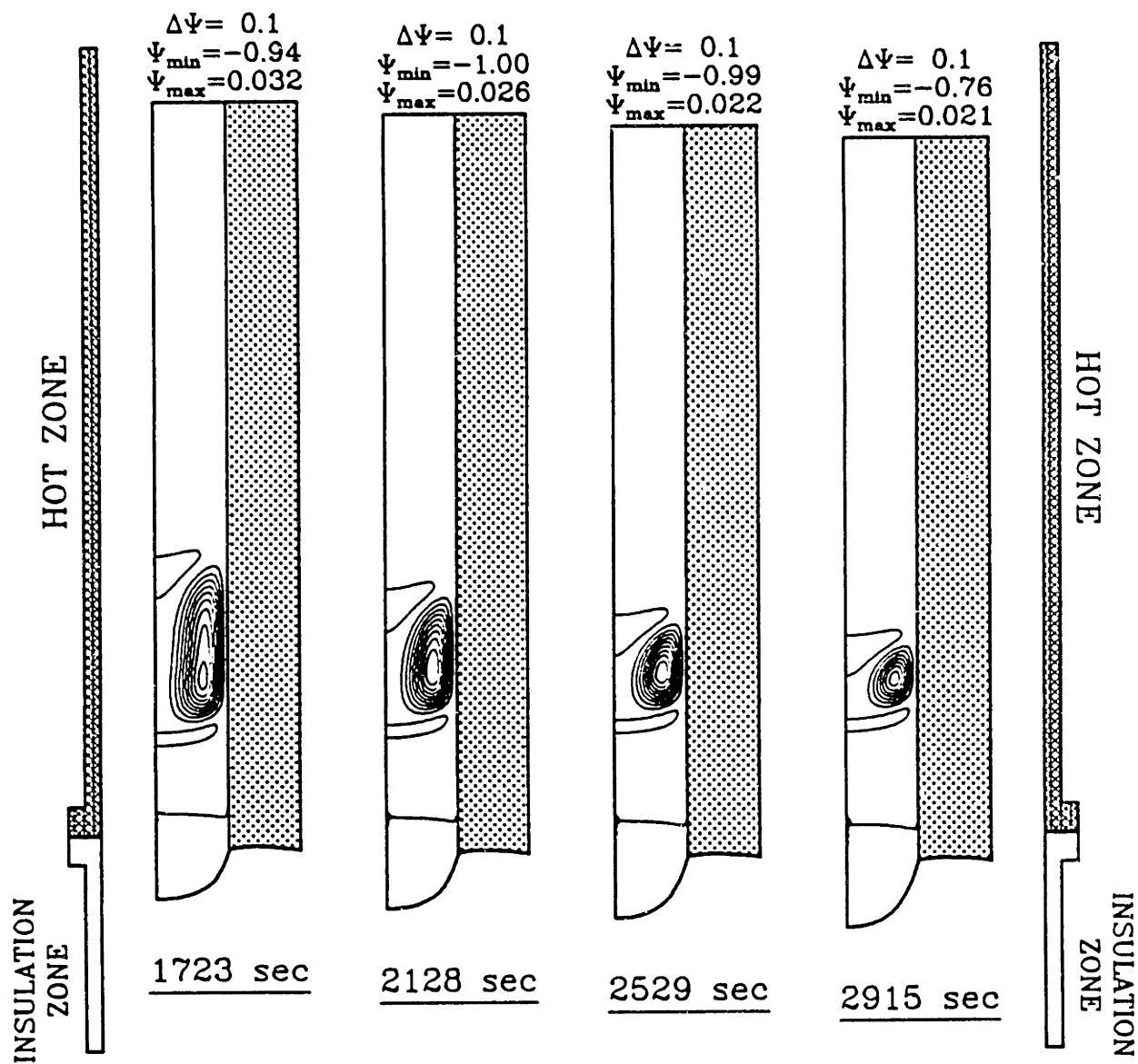


Figure 7.21: (II) Sample flow fields for growth of HgCdTe crystal showing the transition in flow structure: $(Ra_t, Ra_s) = (1.0 \times 10^5, -8.5 \times 10^4)$.

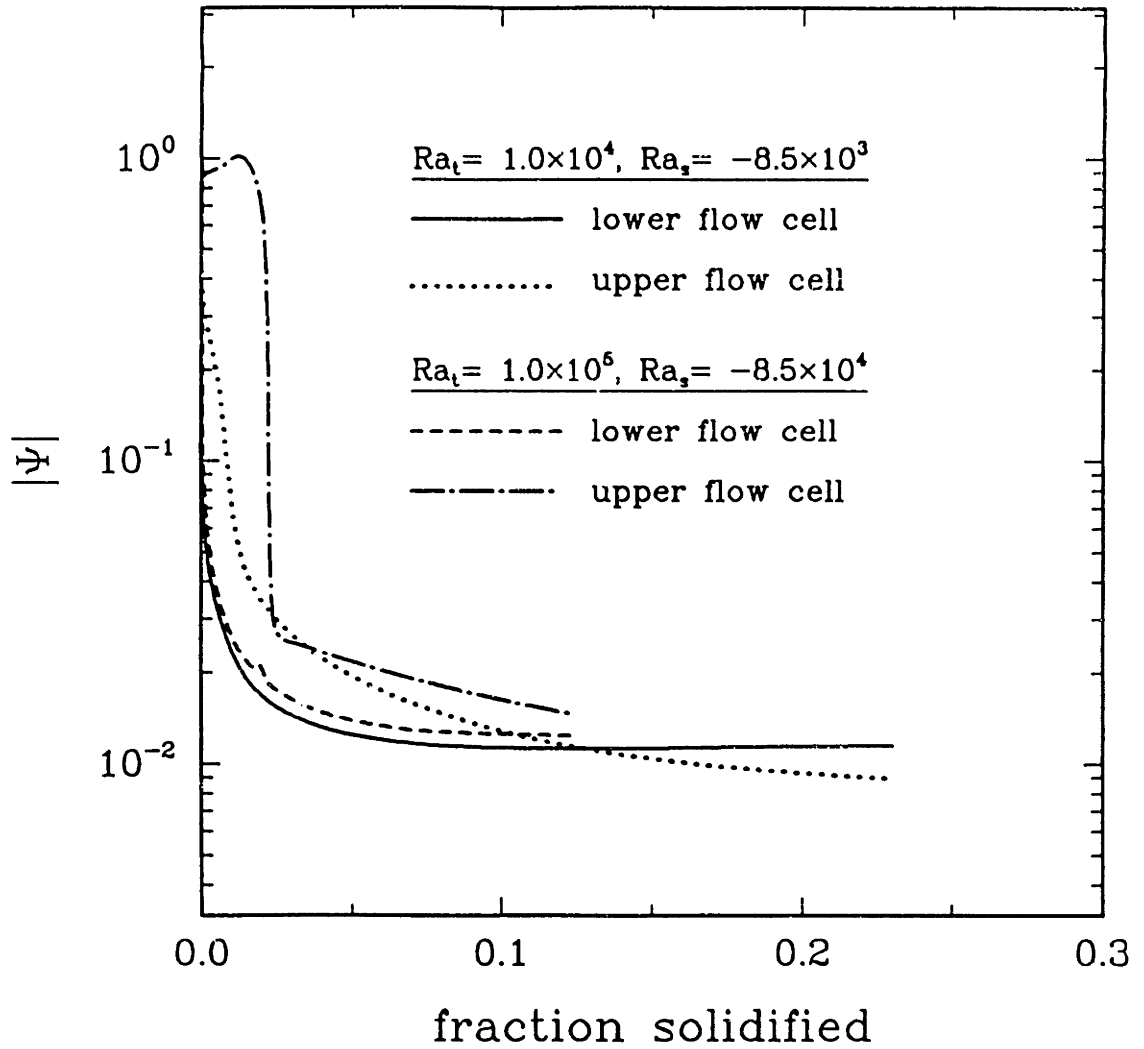


Figure 7.22: Time histories of the maximum absolute stream function values in each flow cell for growth of HgCdTe crystal at the conditions of $(Ra_t, Ra_s) = (1.0 \times 10^4, -8.5 \times 10^3)$ and $(1.0 \times 10^5, -8.5 \times 10^4)$.

$Ra_t = 1.0 \times 10^5$ causes a very abrupt change in flow structure and almost a step change is observed in the stream function. These changes require a small time step size in the numerical integration.

7.3.3 Solute Fields

During the growth of HgCdTe alloy, CdTe is preferentially partitioned into the crystal and it is depleted in the region of melt near the interface. It is replaced by the transport of solute from the bulk melt by convection and diffusion. When the level of convection is negligible, solute transport is limited by diffusion and solute diffusion layer develops beginning from the interface. Sample solute fields for $Ra_t = Ra_s = 0$ in Figure 7.23 display the process of solute diffusion layer development in time. The solute profile is expected to be perfectly one-dimensional for flat interface. The curvature of the melt/crystal interface leads to the variation in composition along the interface. For the growth of nondilute alloy with variable equilibrium distribution coefficient, these variations of composition results in the nonuniform equilibrium distribution coefficients along the interface. The rate of incorporation of solute into the crystal is subsequently nonuniform and the isoconcentration lines are a little distorted near the interface, as shown in Figure 7.23.

The stably stratified density gradient in the growth HgCdTe alloy suppresses the thermal buoyancy-driven convection almost entirely. The structure of two toroidal cells stacked axially in the ampoule is still maintained, but their intensities are too weak to convect the solute. The solute profile in the presence of convection shows the characteristics of diffusion-controlled growth, despite the high Schmidt number for HgCdTe. Sample solute fields at $Ra_t = 1.0 \times 10^4$, $Ra_s = -8.5 \times 10^3$ and $Ra_t = 1.0 \times 10^5$, $Ra_s = -8.5 \times 10^4$ are presented in Figure 7.24 and 7.25, showing these features. The presence of weak convection leads to the flatter isoconcentration lines near the interface and slightly distorts the isoconcentration lines in the upper part of the ampoule. The change of curvature in isoconcentration lines from concave to flat predicts slightly more radial segregation in the presence of convection. Solute fields in

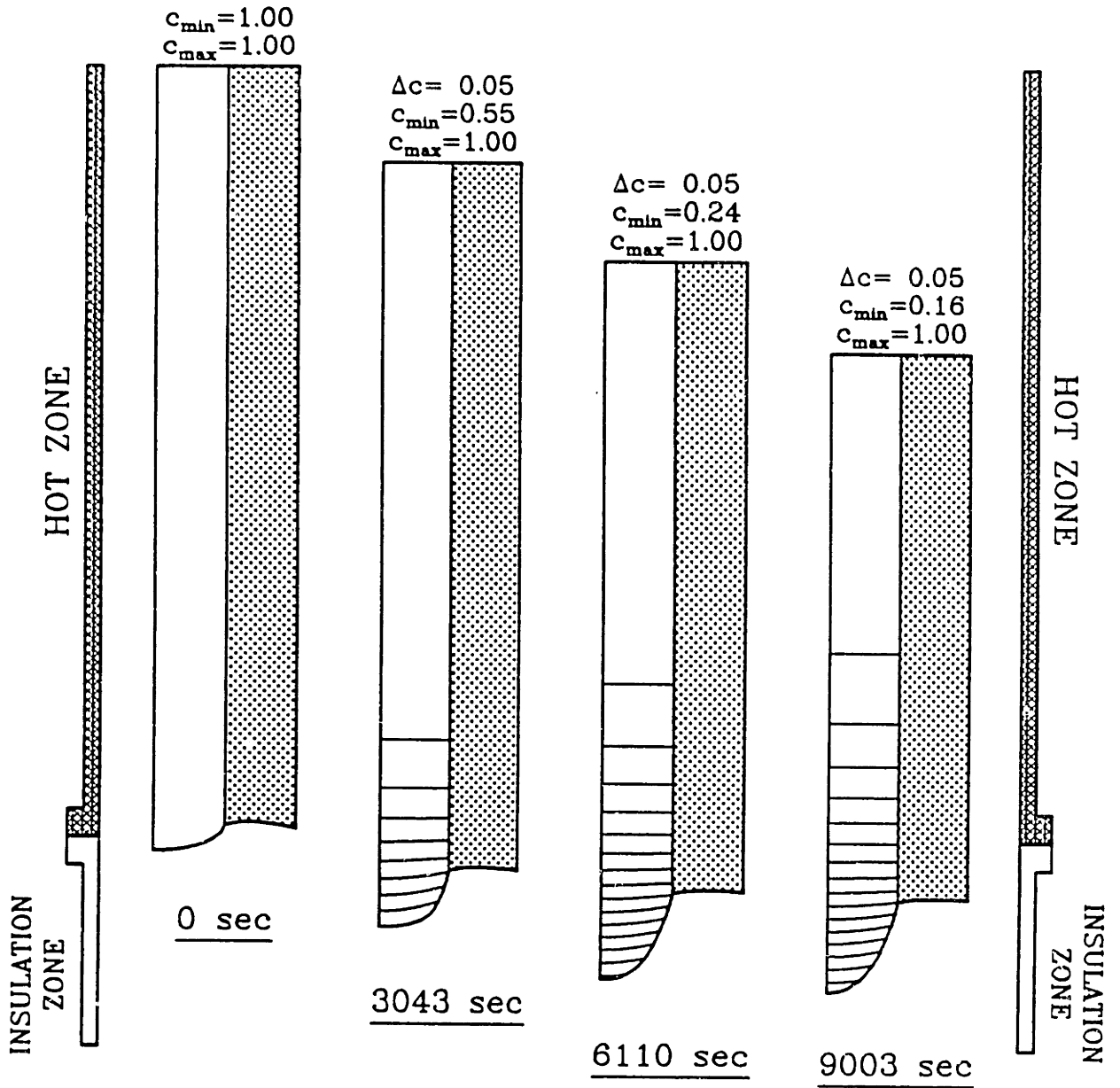


Figure 7.23: Sample CdTe concentration fields for growth of HgCdTe in vertical Bridgman growth system: $Ra_t = Ra_s = 0$.

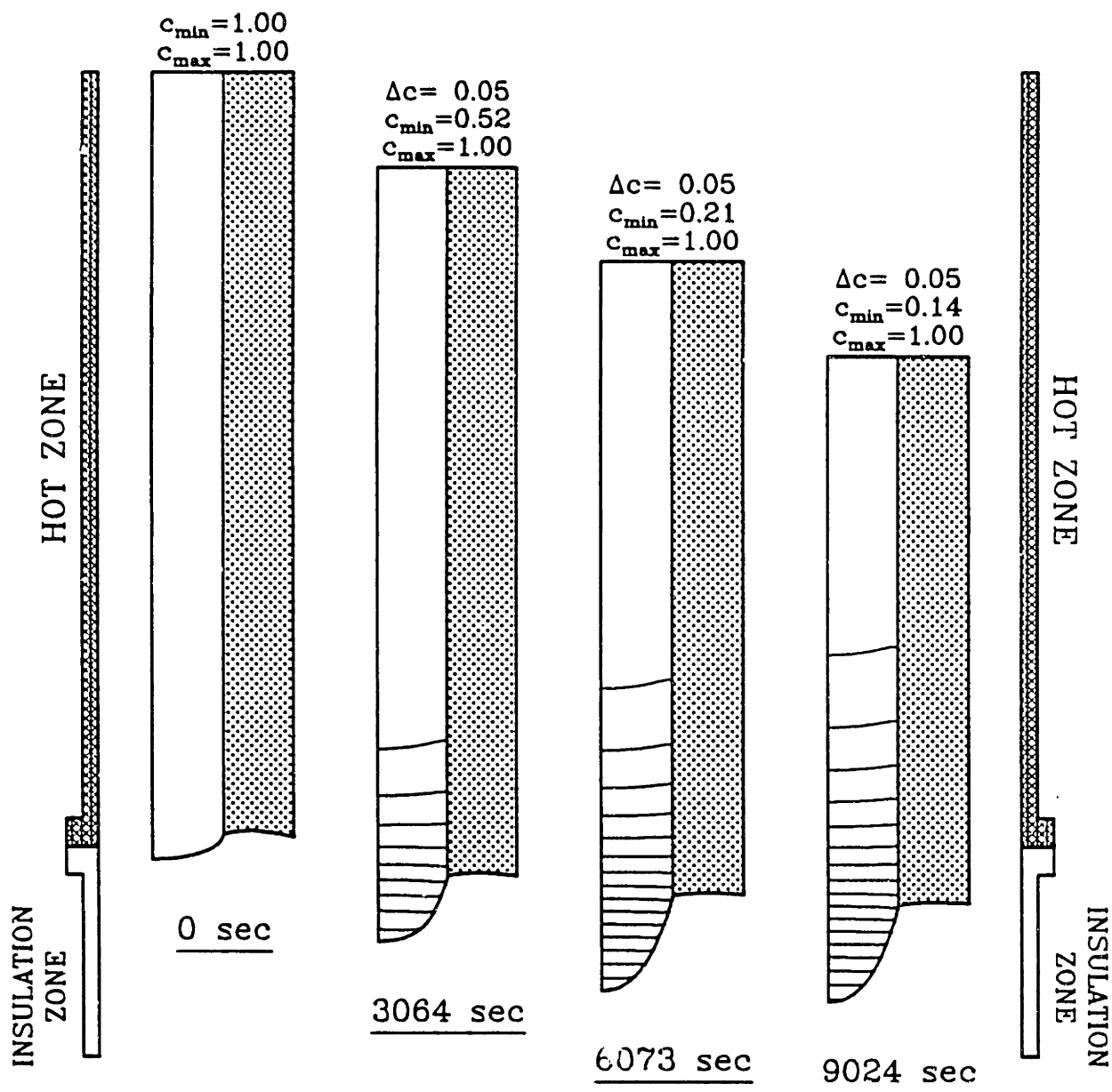


Figure 7.24: Sample CdTe concentration fields for growth of HgCdTe in vertical Bridgman growth system: $(Ra_t, Ra_s) = (1.0 \times 10^4, -8.5 \times 10^3)$.

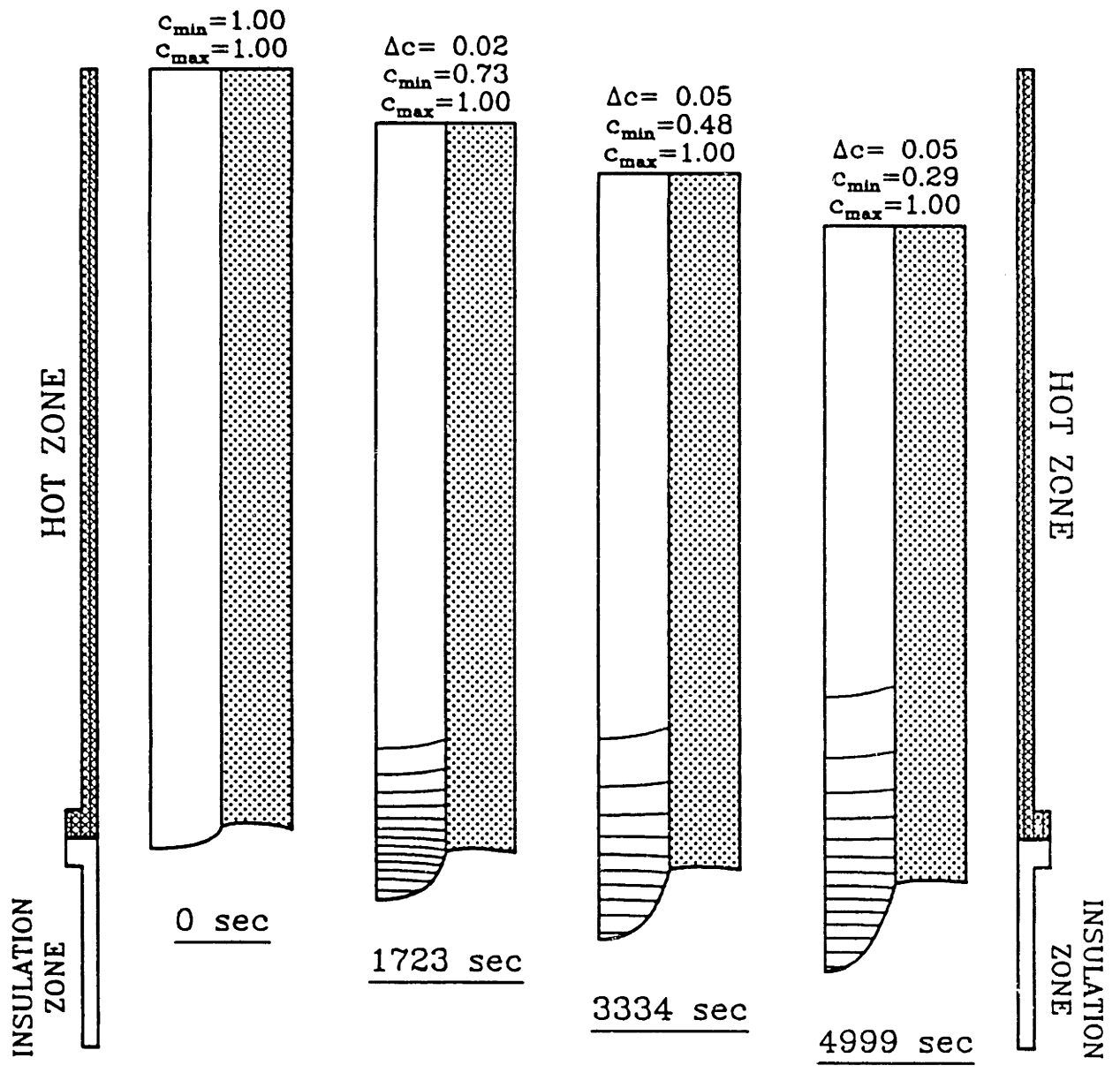


Figure 7.25: Sample CdTe concentration fields for growth of HgCdTe in vertical Bridgman growth system: $(Ra_t, Ra_s) = (1.0 \times 10^5, -8.5 \times 10^4)$.

earlier period are described in Figure 7.26 to show the effect of convection, when the lower flow cell still undergoes a transition. The distorted isoconcentration lines near the interface indicate the effect of mixing by convection.

Solute concentration profiles in the crystal has been calculated by multiplying the equilibrium distribution coefficient by the average melt concentration over the interface at each instant of time. The results are shown in Figure 7.27 and compared with the exact solutions of Smith *et al.* (1955) and Scheil (1942).

The diffusion-controlled axial solute segregation in the crystal was obtained from the solution of Smith *et al.* (1955), which assumes constant growth rate and constant equilibrium distribution coefficient. The other one accounts for the changing growth rate and variable equilibrium distribution coefficients from the phase diagram. It was calculated using our model while the interface was forced to be flat by assuming high and equal thermal conductivities in all materials and neglecting the latent heat.

Scheil's equation is the solution of the solute conservation in the melt and crystal assuming complete mixing in the melt and no diffusion in the crystal. The differential equation for bulk solute conservation is written as

$$\frac{df}{1-f} = \frac{dC}{C-C_s} \quad (7.8)$$

where f is a fraction solidified, C is a uniform concentration in the melt and C_s is a concentration in the crystal at the interface at f . The equilibrium relationship, $C_s = kC$, holds at the interface. With constant k , Eq. (7.8) is easily solved for to give the solution as

$$C_s = kc_o(1-f)^{k-1} \quad (7.9)$$

where c_o is the initial concentration in the melt. When k is not constant, no closed-form solution of Eq. 7.8 exist. We solved Eq. (7.8) with k from Eq. (7.2) using a fourth-order Runge-Kutta numerical integration method.

The calculations indicate that the level of gravity is not important in determining the axial segregation in the crystal. The calculated axial segregation profiles show an almost

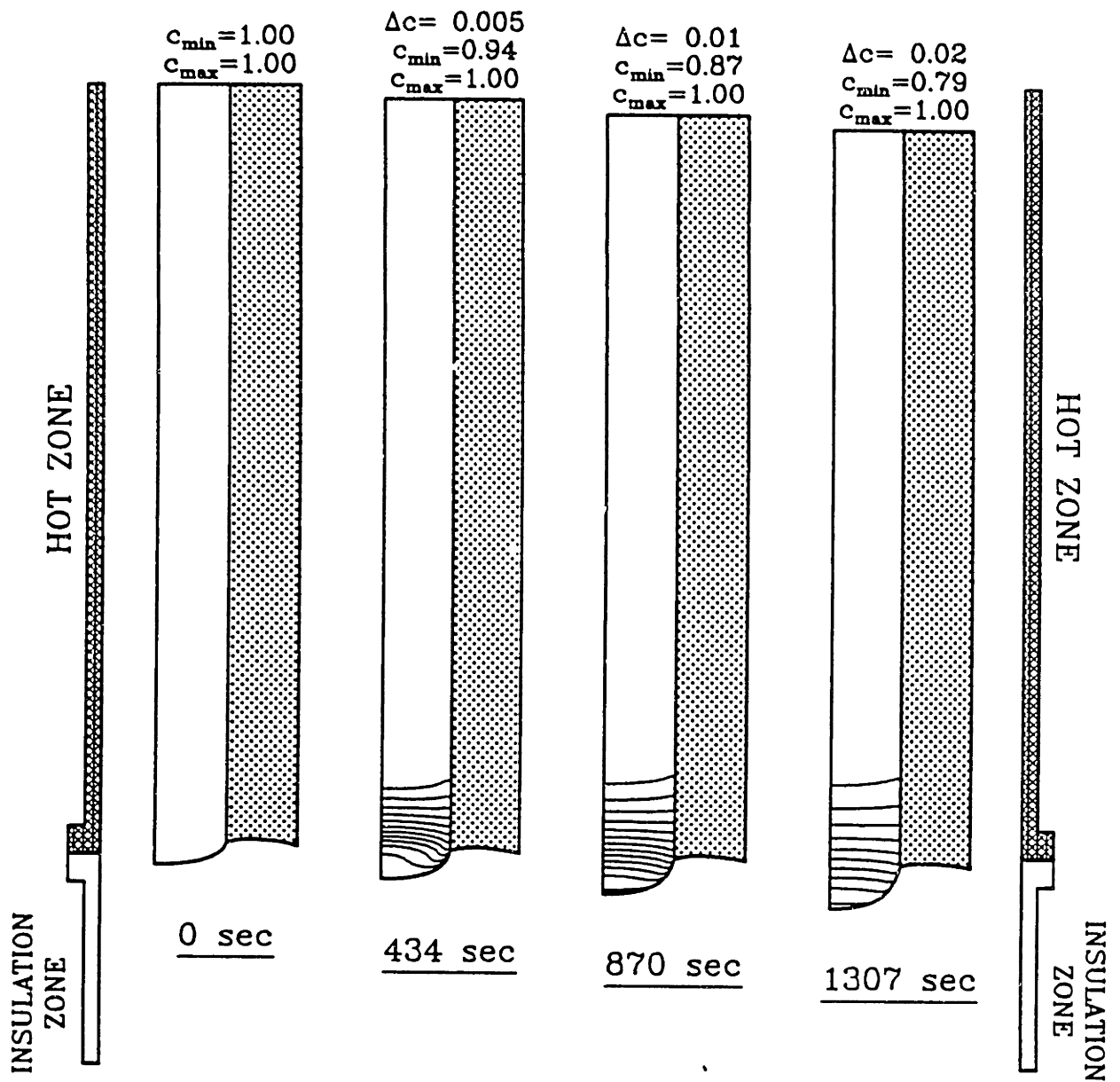


Figure 7.26: Sample CdTe concentration fields for growth of HgCdTe in vertical Bridgman growth system during the early period: $(Ra_t, Ra_s) = (1.0 \times 10^5, -8.5 \times 10^4)$.

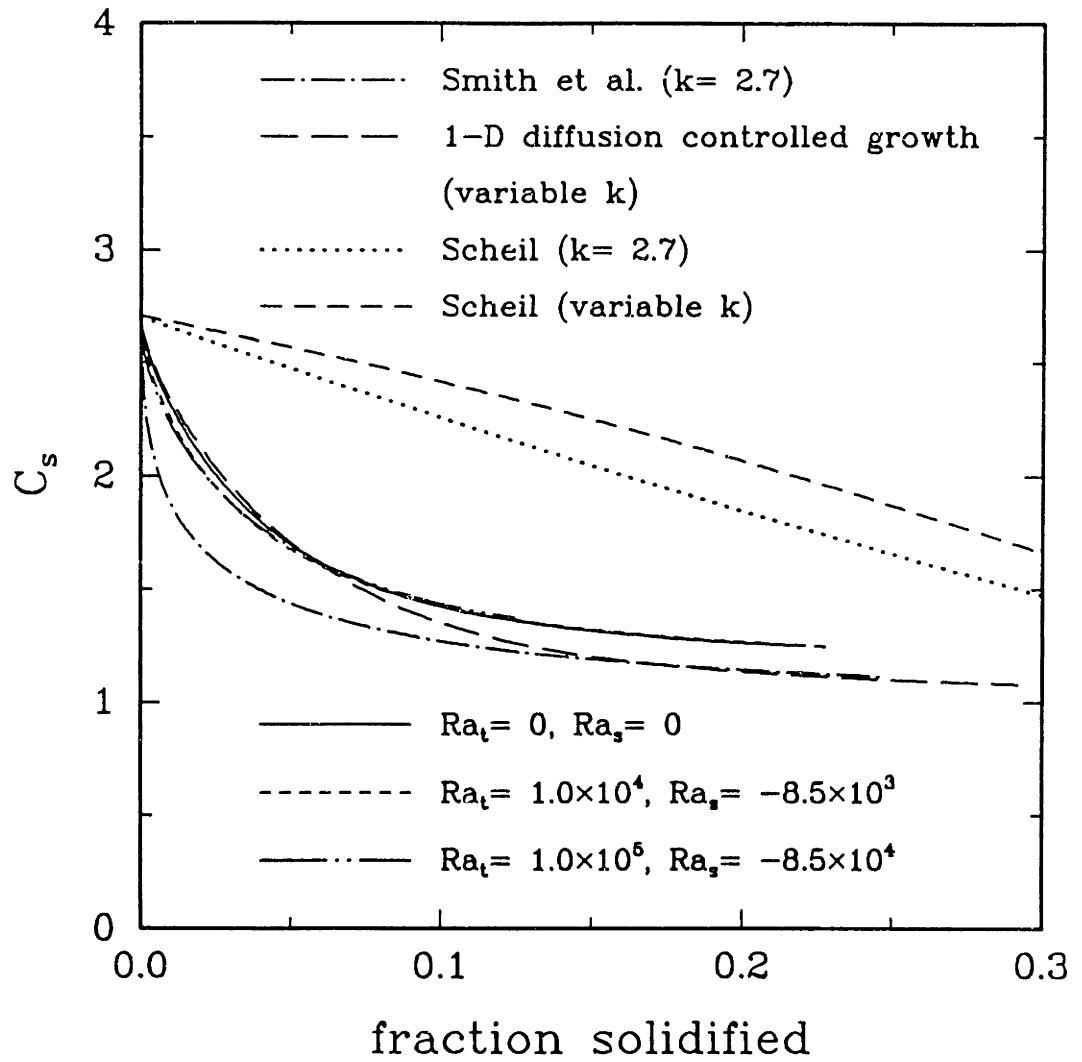


Figure 7.27: Axial segregation profile of CdTe in the crystal. Comparison is made with the cases of diffusion-controlled growth and complete mixing in the melt.

constant difference from the solution of Smith *et al.* (1955) with constant k . At short times, the numerical calculations are in good agreement with the diffusion-controlled profile with flat interface and variable k . As the profile approaches its steady-state value, the deviation between these profiles becomes constant, as is the comparison with the solution of Smith *et al.* (1955). These observations lead to the argument that the later deviations are caused by the high curvature of the interface and the average concentration at the highly curved interface does not coincide with the interfacial concentration calculated by the one-dimensional analysis. Despite these deviations, the calculated axial segregation is much more closer to the diffusion-controlled case and far from the segregation profile predicted by Scheil's equation with either constant or variable k .

Hence, the weak convection does not alter appreciably the solute field near the interface and the radial segregation is mainly governed by the interface curvature during the growth of HgCdTe. The radial segregation is defined as a measure of the nonuniformity in composition along the interface as

$$\Delta C(\%) = \left[\max_{0 \leq r \leq 1} C(r, H(r)) - \min_{0 \leq r \leq 1} C(r, H(r)) \right] / \langle C \rangle \times 100\% \quad (7.10)$$

$$\langle C \rangle = \int_0^1 c \sqrt{1 + H_r^2 r} \, dr / \int_0^1 \sqrt{1 + H_r^2 r} \, dr$$

where $\langle C \rangle$ is the radially-averaged value of solute concentration in the melt. As discussed previously, the presence of weak convection near the interface flattens the isoconcentration lines and causes slightly increased radial segregation, as shown in Figure 7.28. The small average concentration at the interface amplifies the radial segregation, which is more than 100 per cent at steady-state.

The effective segregation coefficient k_{eff} is used as a measure of the relative resemblance of the crystal growth process to the diffusion-controlled growth or growth with complete mixing in the melt. It is defined as

$$k_{eff} = k \frac{\langle C \rangle}{\langle\langle C \rangle\rangle} \quad (7.11)$$

where $\langle C \rangle$ is the radially-averaged value of solute concentration in the melt, $\langle\langle C \rangle\rangle$ is the

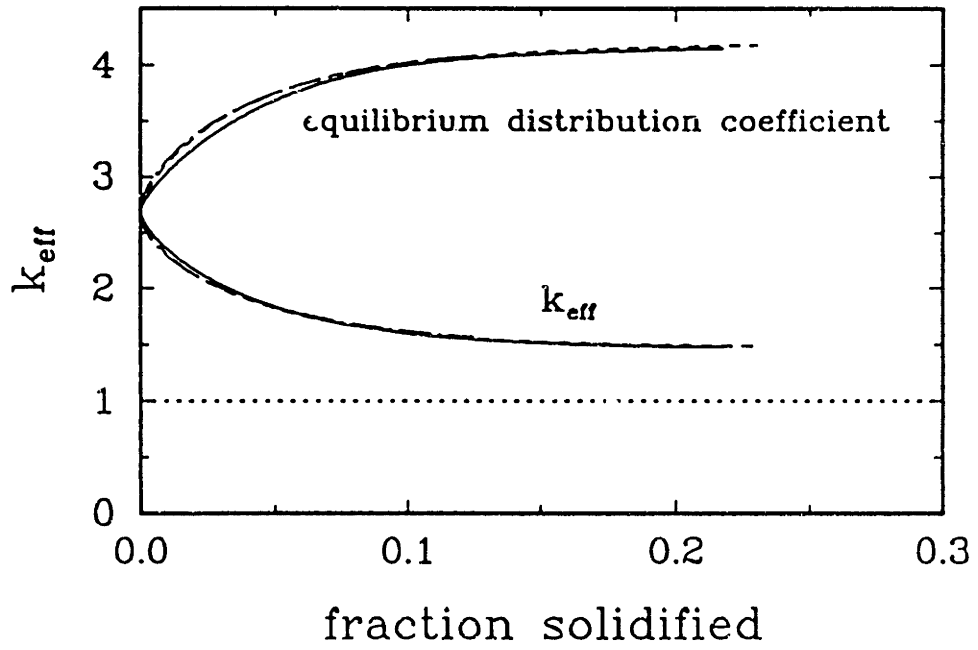
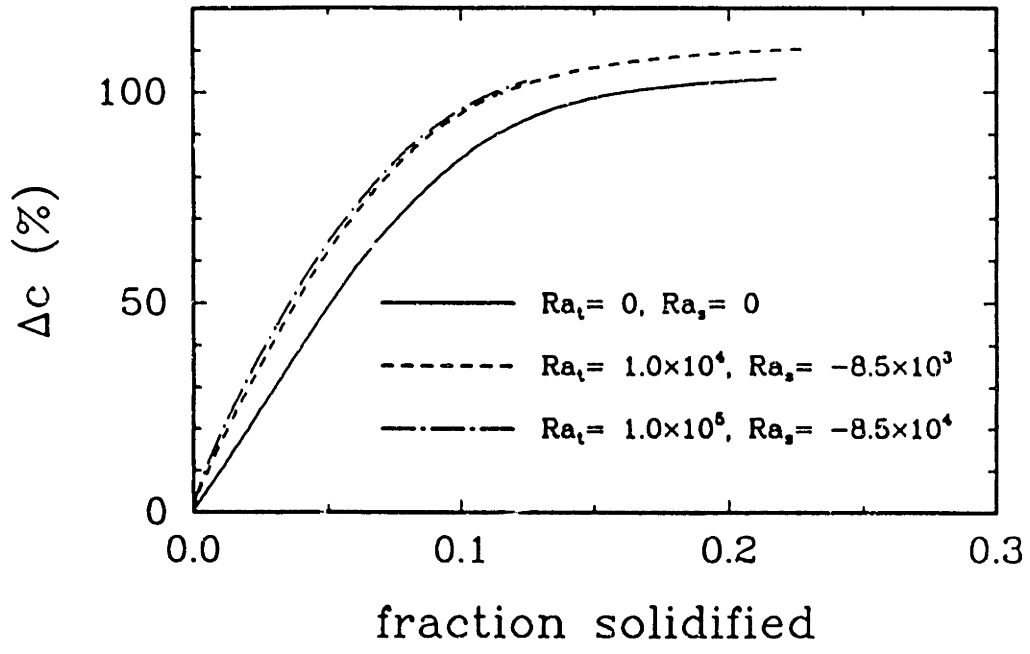


Figure 7.28: Time histories of the radial segregation and effective segregation coefficient for growth of HgCdTe in vertical Bridgman growth system.

bulk-averaged concentration in the melt, H_r is a derivative of the interface location with respect to r and k is the equilibrium segregation coefficient for the solute. When mixing is complete, $\langle C \rangle$ and $\langle\langle C \rangle\rangle$ become equal and k_{eff} approaches k . For steady diffusion-controlled growth, solute concentration in the crystal just solidified and in the bulk are c_0 when the whole length of melt is infinite so that the length of solute diffusion layer is negligible. In this situation, k_{eff} becomes unity. Calculated k_{eff} from numerical analysis approaches one but it is not exactly one because of the finite melt length.

7.4 The Effect of Variable Coefficient of Thermal Expansion

The melt density of HgCdTe has a strong dependence on temperature and composition (Chandra and Holland, 1983). This dependence affects the flow structure in the melt through variable coefficients of thermal expansion (β_t) and solutal expansion (β_s). The range of magnitude of solutal expansion coefficient in the present growth system leads to the assumption of constant β_s . In this Section, we will demonstrate only the effect of variable β_t on the flow structure.

The analytical form of the dependence of β_t on x and T is obtained from the density function, Eq. (7.7), by differentiation with respect to temperature. From Eq. (7.7), β_t is determined as

$$\begin{aligned}\beta_t &= -\frac{1}{\rho_m} \left(\frac{d\rho}{dT} \right) \\ &= -\frac{1}{\rho_m} (c_2 + c_3x + 2c_5T) \\ &= \beta_0 + \beta_1x + \beta_2T\end{aligned}$$

where $\beta_0 = -c_2/\rho_m$, $\beta_1 = -c_3/\rho_m$ and $\beta_2 = -2c_5/\rho_m$. The thermal Rayleigh number Ra_t is defined as

$$\begin{aligned}Ra_t &= \frac{g\beta_t\Delta TR_c^3}{\alpha\nu} \\ &= Ra_0 + Ra_1(S+1) + Ra_2\theta\end{aligned}$$

where the $\{Ra_i\}$ are defined as

$$\begin{aligned}Ra_0 &= \frac{g(\beta_0 + \beta_2T_c)\Delta TR_c^3}{\alpha\nu} \\ Ra_1 &= \frac{g\beta_1c_0\Delta TR_c^3}{\alpha\nu} \\ Ra_2 &= \frac{g\beta_2(\Delta T)^2R_c^3}{\alpha\nu}\end{aligned}$$

where g is the gravitational acceleration and $\alpha \equiv k/\rho c_p$ is the thermal diffusivity. The definitions of other variables are found in Table 7.1 and 7.2.

The calculations for the variable β_t has been done for the conditions corresponding to $Ra_t = 1.0 \times 10^4$ and $Ra_s = -8.5 \times 10^3$ with constant β_t . The most significant change appears in the flow field, as shown in Figure 7.29. In the initial state, the upper and lower flow cell typically observed in the flow field with constant β_t are connected together and rotate in the same direction, whereas they rotate in opposite direction when β_t is constant. This reversal of flow direction near the interface is caused by the presence of quadratic on temperature in the buoyancy force of the momentum equation. As the solute diffusion layer develops and the solute concentration participates in the convection mechanism, secondary flow cells form between the upper and lower flow cells. Similar cells were observed in the calculations by Adornato and Brown (1987a) for the GeSi system and in the first family of the steady-state solutions described in Chapter 3 for HgCdTe system. These flow structures can be attributed to the sideways diffusive instability discussed by Hart (1971)

In the present system, the maximum density is present at a short distance from the interface because of the characteristic dependency of HgCdTe melt density on temperature. Below the location of maximum density, both the axial and radial temperature gradients provide the driving force for convective flow near the interface. This type of convection is called *penetrative convection* and occurs when the density variation with temperature is not monotonic (Antar, 1987). The instability due to the axial temperature gradient near the interface combined with sideways diffusive instability tends to form vertically-stacked secondary cells in this region.

Comparisons between the constant and variable β_t are made in Figure 7.30 in terms of stream function values in upper and lower flow cells. The difference in stream function values between upper and lower flow cells becomes larger with variable β_t . The flow cell in the upper region of the ampoule becomes more intense with variable β_t , while the opposite is true in the region near the interface. The amount of increase in the stream function value of upper flow cell is almost the same amount as the decrease

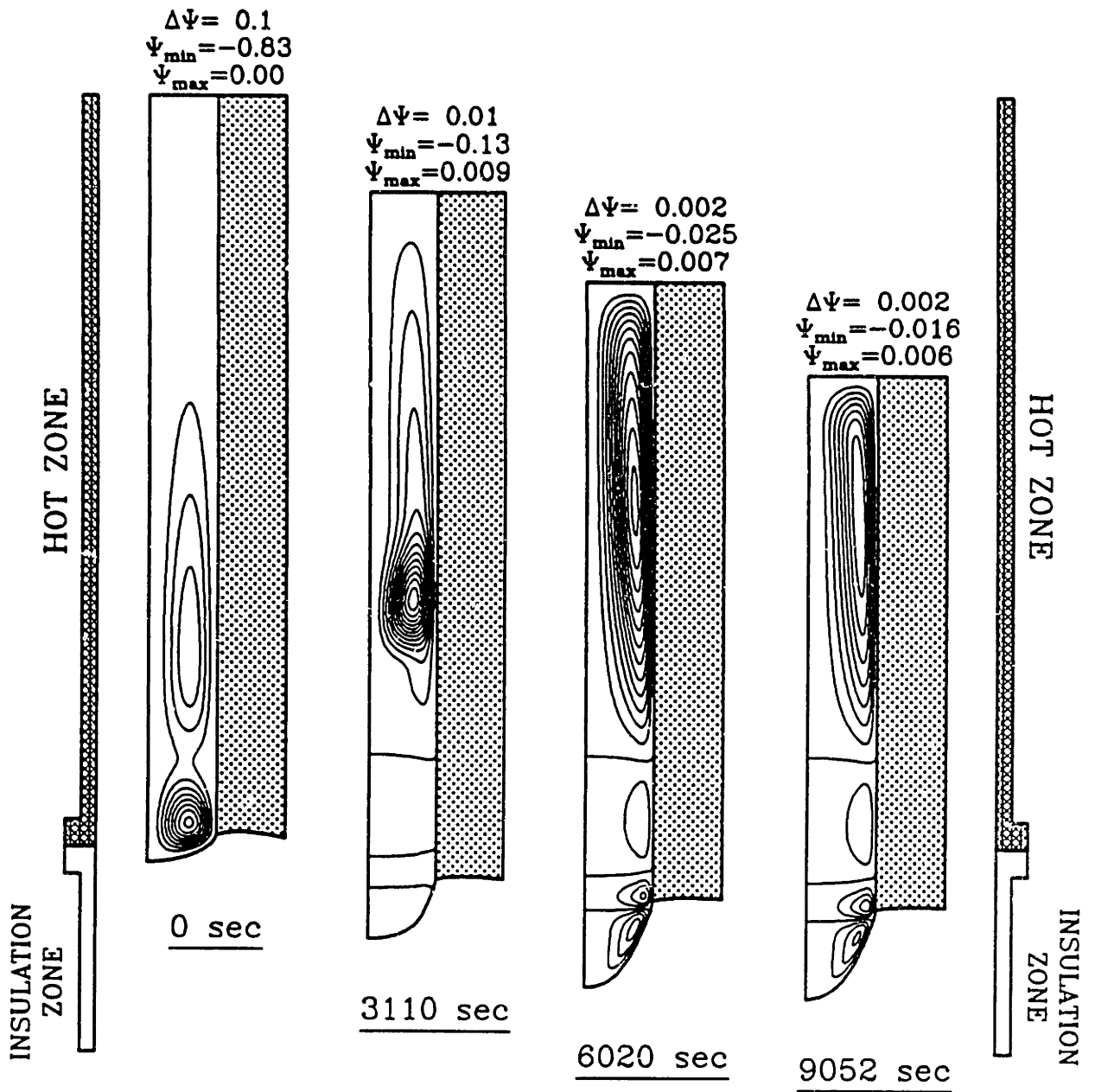


Figure 7.29: Sample flow fields for growth of HgCdTe crystal in the vertical Bridgman furnace calculated with variable β_r . Gravity acceleration is 0.1 of terrestrial condition.

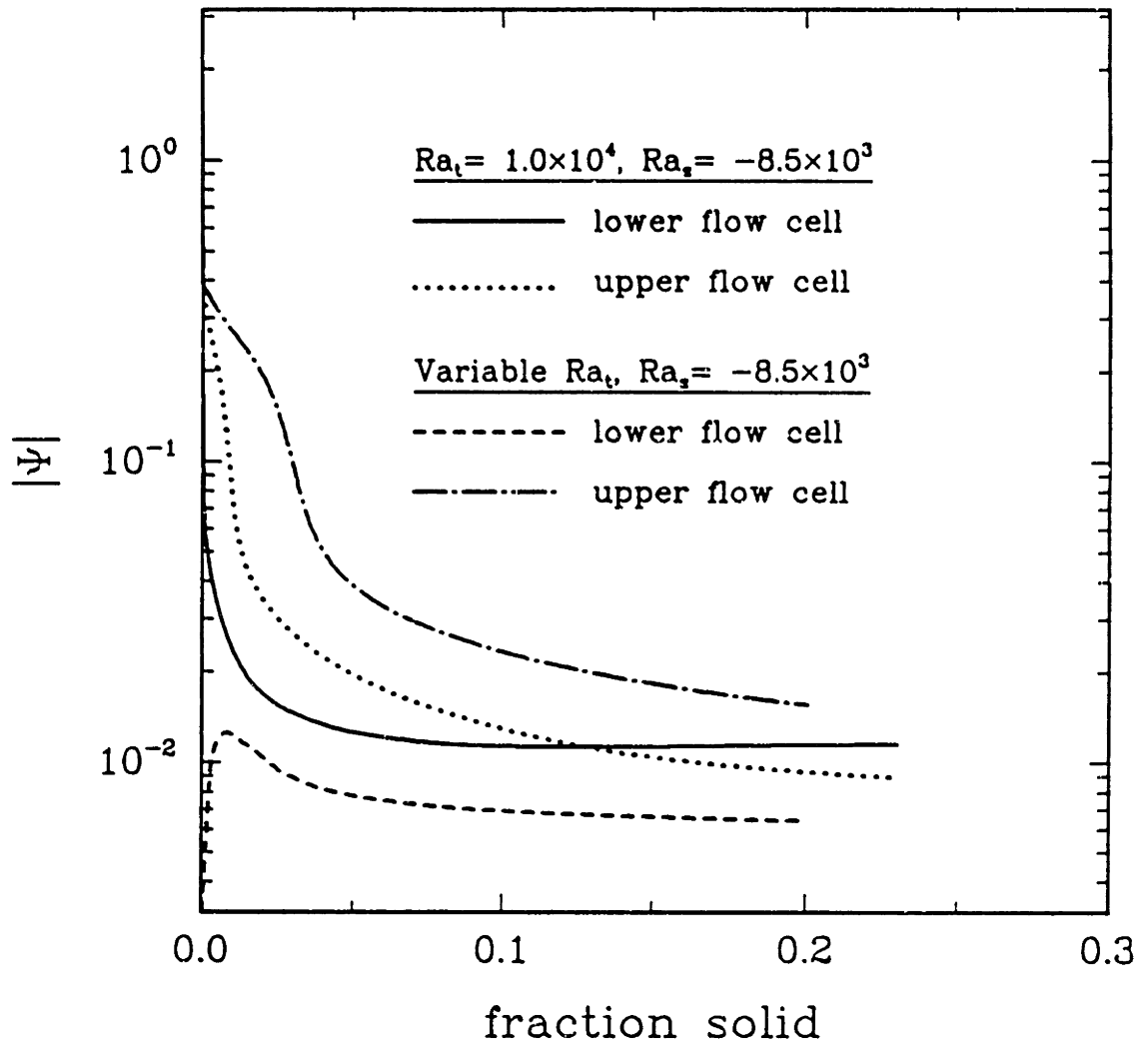


Figure 7.30: Time histories of the maximum absolute stream function values in each flow cell for growth of HgCdTe crystal at $Ra_s = -8.5 \times 10^3$; $Ra_t = 1.0 \times 10^4$ for constant β_t and Ra_t does not have a single value for variable β_t .

of the lower flow cell. This suggests that the value of constant β_t well represents the mean β_t . In the initial stages of growth, where the lower cells show greater difference in stream function value, the secondary flow cell of the variable β_t case assumes the stream function value which show the similar trend as the constant β_t case with the difference in stream function value mentioned above.

The weaker convection in the variable β_t case has the effect of reducing interface deflection, as shown in Figure 7.31. Interface deflection has been decreased almost to the level of convectionless state, which will lead to the reduction in radial segregation.

Solute concentration profiles corresponding to these flow fields are described in Figure 7.32. Solute fields displays the development of solute diffusion layer with concentration profiles that are almost one-dimensional profiles characteristic of diffusion-controlled growth. The deviation from the perfectly one-dimensional profile shows the effect of flow structure with secondary flow cells. Closer examination at the isoconcentration lines indicates that the radial solute gradient changes sign several times along the axial direction.

The decreased level of convection near the interface and interface deflection for the case of variable β_t results in the slight reduction of radial segregation to the level of diffusion-controlled growth, as shown in Figure 7.33. The increased convection level in the upper region of the ampoule does not affect the concentration field considerably because concentration in that region is nearly constant in the early stage of growth. The history of the effective axial segregation coefficient for variable β_t is almost indistinguishable from that for constant β_t .

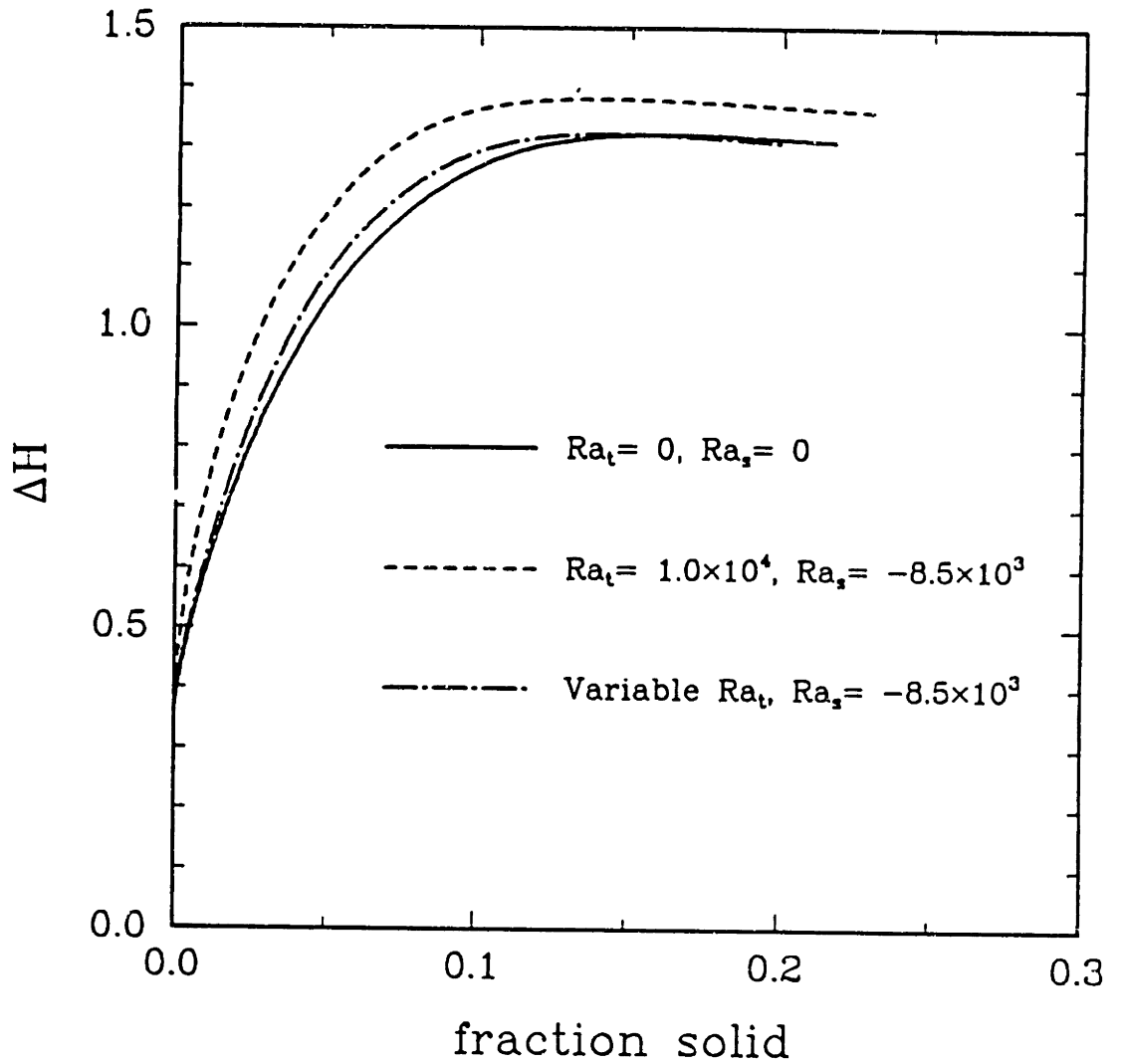


Figure 7.31: Transient interface deflections for growth of HgCdTe in vertical Bridgman growth system at $Ra_s = -8.5 \times 10^3$: $Ra_t = 1.0 \times 10^4$ for constant β_t and Ra_t does not have a single value for variable β_t .

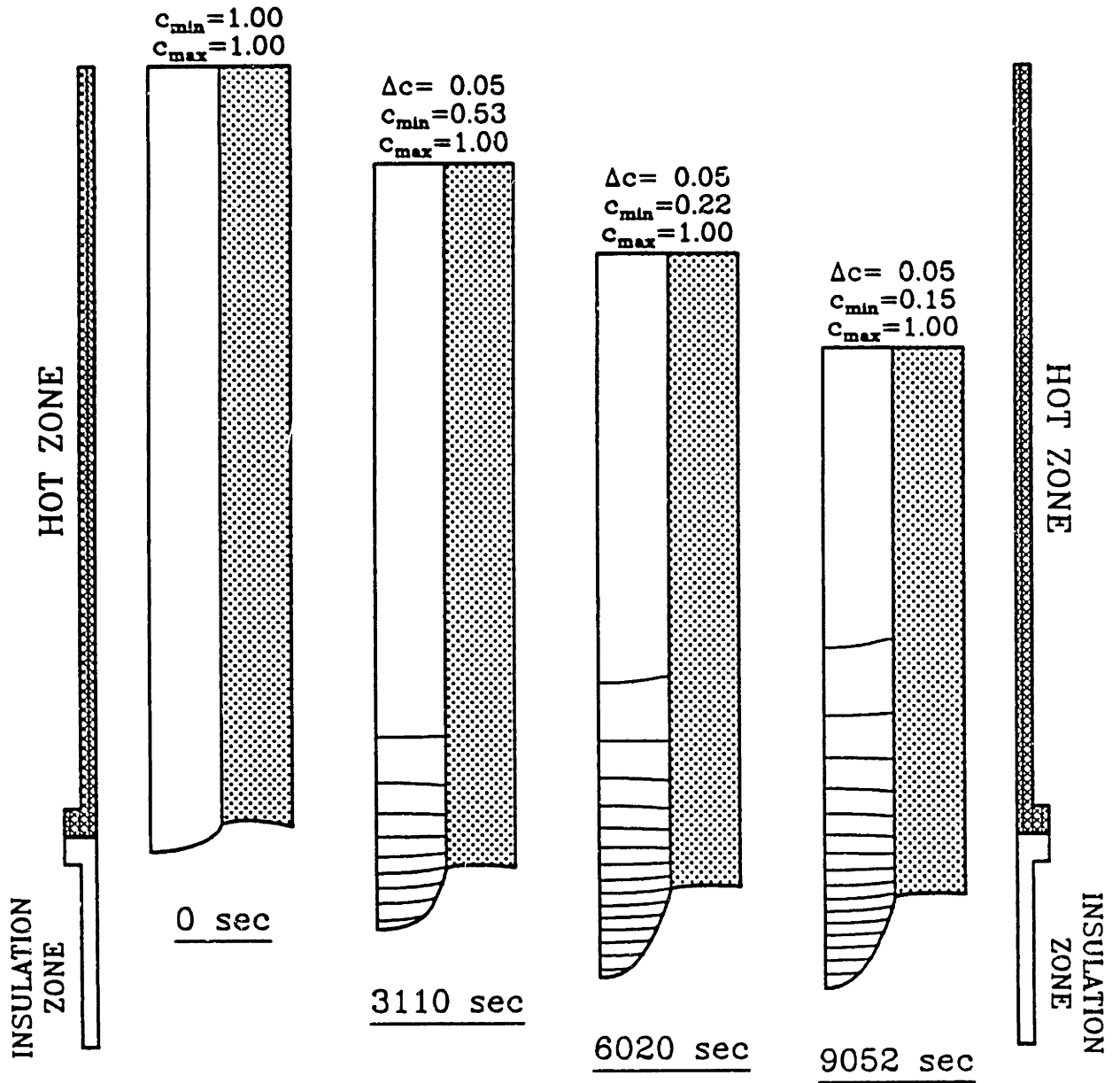


Figure 7.32: Sample CdTe concentration fields for growth of HgCdTe in vertical Bridgman growth system calculated with variable β_t . Gravity acceleration is 0.1 of terrestrial conditions.

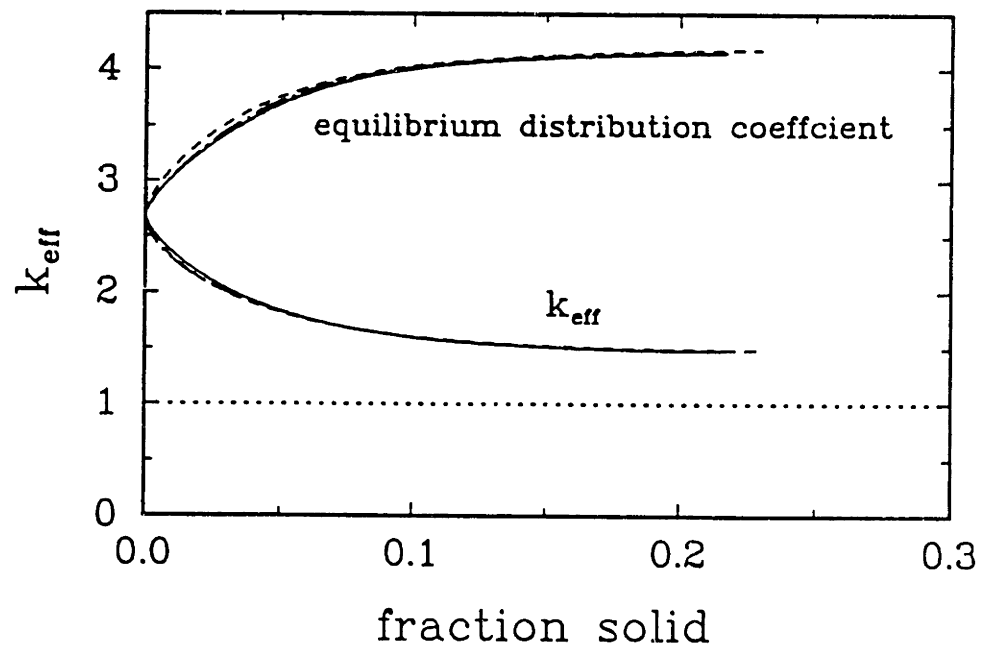
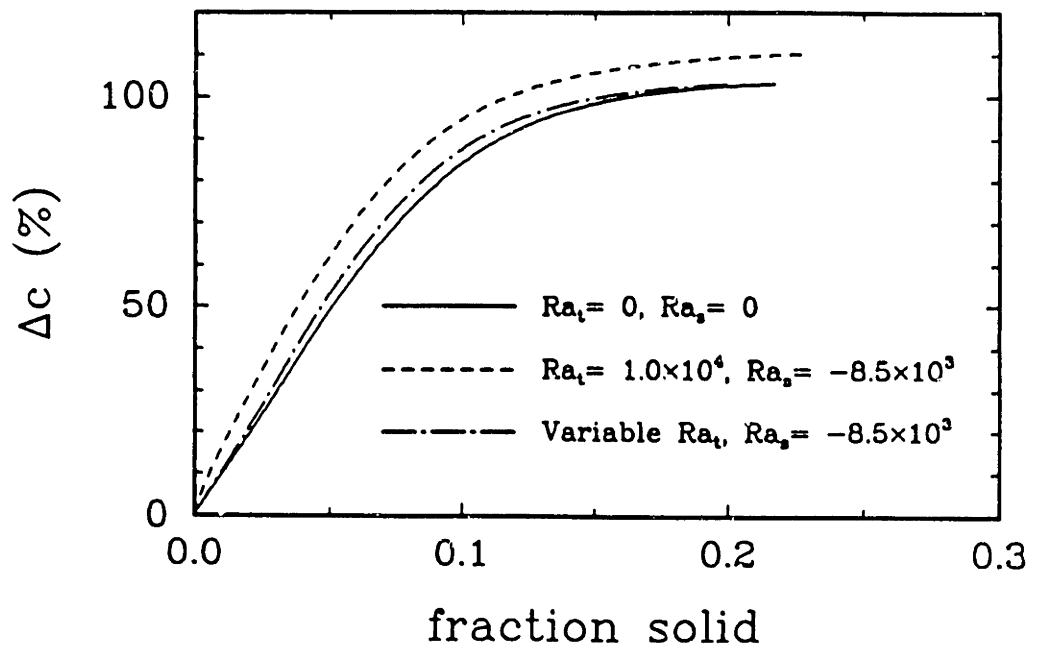


Figure 7.33: Histories of radial segregation and effective segregation coefficient for growth of HgCdTe in vertical Bridgman growth system at $Ra_s = -8.5 \times 10^3$: $Ra_t = 1.0 \times 10^4$ for constant β_t and Ra_t does not have a single value for variable β_t .

7.5 Conclusions

Thermosolutal convection during the growth of nondilute HgCdTe alloy in vertical Bridgman growth system is governed by the interactions of driving forces determined by the alloy's thermophysical properties, the design of ampoule and furnace, and operating conditions for growth. The flow patterns are coupled with the temperature and solute concentration fields to give a rich structure. The lighter component CdTe is preferentially partitioned into the crystal and the remaining HgTe components are accumulated near the interface to help form the stably stratified axial density gradient in the melt. The resulting solute field retards the thermal convection driven by the large radial temperature gradient near the interface. The analysis presented in this Chapter is meaningful in that it is the first transient numerical calculations for the growth of nondilute alloy in the vertical Bridgman growth system accounting for the convection, heat transfer and solute transport with interface shape and location determined simultaneously. The complete phase diagram was included in the calculation through the dependency of the melting point temperature and equilibrium distribution coefficient on the composition.

Concentration gradient is set up first near the interface to form the solute diffusion layer, which is more effective in damping the flow cell near the interface. As the solute diffusion layer penetrates into the melt, transient calculations showed the transition of a flow structure that was governed by the temperature field to motion suppressed by the solute field. The damped flow structure consisted of two toroidal cells stacked axially in the ampoule, as is typically observed in the thermal driven convection in the Bridgman growth system; however, the intensity of this motion, expressed in terms of stream function values, is much lower than for a thermally-driven flow cells.

Transient analysis of the growth of HgCdTe alloy in the vertical Bridgman growth system has demonstrated that the previous experimentally obtained axial segregation profiles (Lehoczky and Szofran, 1982; Szofran *et al.*, 1984) are the result of the effective damping of the thermal convection by the solute field. The calculated solute segregation

is almost one-dimensional, characteristic of diffusion-controlled growth.

In addition to the large radial temperature gradient, the coupling of the melting point temperature with the interfacial concentration leads to the large interface deflections, which are mainly responsible for the large radial segregation observed in the growth of HgCdTe. This observation is not contradictory to the result from steady-state analysis, where ampoule translation rate was lower and imperfect mixing near the interface is more important to large radial segregation. The intensity of the flow cell near the interface was not high enough to provide the sufficient mixing to reduce the concentration variations along the interface, except for the short time period in the beginning when the solute concentration gradient is small.

Thermophysical properties of HgCdTe melt is strongly dependent on temperature and composition. Among others, the dependency of the density of HgCdTe melt are most influential to the flow structure in the melt. Density shows maximum with temperature in some range of concentration, which fall into the range of present operating conditions. The variation of density with temperature and composition was implied in the expression of the coefficient of thermal expansion (β_t) as a function of temperature and composition. The variable β_t introduced additional instability caused by the axial temperature gradient near the interface. This instability, combined with the sideways diffusive instability, resulted in the secondary flow cells between the upper and lower flow cells typically observed in the Bridgman growth system. As a result of variable β_t , the upper flow cell showed an increase in intensity of approximately the same amount as the decrease in intensity of lower flow cell. The concentration field displayed little effect by the variable β_t because of weak convection level.

Chapter 8

Conclusions

The goal of the research in this thesis was to extend the understanding of the physics involved in the directional solidification of semiconductor and optoelectronic crystals grown in vertical Bridgman and gradient freeze systems. The specific objectives focused on the investigation of convection in the melt during growth of dilute or nondilute binary alloys and its effect on species transport and axial and radial segregation of impurities and dopants. These objectives have been met by constructing detailed pseudo-steady-state and transient models describing the crystal growth process; the models include the shape of the melt/crystal interface, convection, heat and solute transfer in the melt, heat conduction in the crystal and ampoule, and radiative exchange between the furnace and the ampoule. The transient analyses that have been presented in this study are meaningful because these are the first time-dependent simulations of crystals growth in the closed ampoule of the vertical Bridgman growth system, which account for these effects simultaneously.

8.1 Steady State Analysis

In the pseudo-steady-state model (PSSM), the translation of the ampoule is modelled by supplying melt at the top of the ampoule with a uniform velocity and composition and

removing crystal from the bottom of the ampoule at the same average concentration. Transients in the field variables caused by the steady decrease of the melt length with crystal growth and by the displacement of the ampoule in the furnace was neglected in this model.

The complete set of partial differential equations and boundary conditions for field variables and interface location defines a nonlinear free boundary problem. We solved this equation set using an efficient finite element/Newton method based on the works by Chang and Brown (1983a,b) and Adornato and Brown (1987a,b). A mesh of bi-quadratic isoparametric finite elements was used to spatially discretize the melt, crystal and ampoule with the melt/crystal interface taken as boundaries in the mesh. The components of the velocity, temperature and solute fields are approximated by a set of two-dimensional biquadratic Lagrangian basis functions defined on this mesh. The pressure field is approximated by a set of linear, discontinuous basis function, which is compatible with basis functions for velocity. The melt/crystal interface shape is interpolated by one-dimensional quadratic Lagrangian polynomials defined on the same finite element mesh. A Newton's method was used to solve the large set of nonlinear algebraic equations that arise from finite element discretization.

The pseudo-steady-state model was used to investigate the effect of a axially aligned magnetic field on the convection in the melt and solute segregation in the crystal, assuming the limit of zero magnetic Reynolds number. The steady-state calculations for the growth of dilute gallium-germanium alloy showed important interactions between the flow field and axial and radial segregation for a vertical Bridgman furnace and for a furnace with a uniform temperature gradient. Radial segregation is set by the flow structure near the crystal/melt interface, whereas axial segregation is influenced by solute mixing throughout the melt and therefore is affected by flow cells isolated from the interface. These differences are brought out by the calculations in the vertical Bridgman crystal growth system.

The radial segregation is lowest when either convection is unidirectional (Ra_t small or Ha large) or when the laminar mixing is intense enough to homogenize the melt adja-

cent to the interface. Growth with unidirectional convection is most desirable because of the axial uniformity of the crystal that results when no mixing is present. These conditions are not easily achieved in practice and careful analysis of growth conditions is necessary for optimum design of growth systems with moderate convection levels. On earth, unidirectional growth conditions can be reached for growth of small diameter crystals and magnetic fields, but these growth conditions are difficult to duplicate for larger crystals because of the excessively large magnetic fields involved. It is practical to tune the strength of the magnetic field to eliminate unwanted temporal fluctuations in the convection, but to leave intense laminar convection to mix solutes and modulate radial segregation.

The second application of the steady-state model was to the growth of nondilute HgCdTe alloy in a vertical Bridgman growth system. The calculations demonstrated that convection and solute segregation in nondilute alloys results from a complex interaction of heat transfer in the furnace and material and convection and species transport in the melt. Numerical simulations of the coupled flow, heat and species transport problems led to mechanistic interpretation of both radial and axial segregation measurements made in several laboratories.

The calculations demonstrated that the segregation behavior in the HgCdTe system results from the combined actions of thermally-driven convection caused by the large radial temperature gradients near the interface and solutally-driven damping of buoyancy flow by the gradient in CdTe composition in the melt. Quantitative determination of the relative importance of the two mechanisms can only be determined by precise numerical simulations that account of correct thermophysical properties and for the curvature of the melt/solid interface.

The radial and axial segregation patterns seen in HgCdTe crystal growth experiments by Szofran *et al.* (1984) and by Capper *et al.* (1983) were explained by the calculations. The large radial temperature gradients caused by the difference in the thermal conductivities between the melt, crystal and ampoule lead to strong convection adjacent to the interface. The solutal damping of this motion caused by the alloy concentration profile

partially damps this motion. For the small ampoules used by Szofran *et al.* (1984), solutal damping almost suppresses convection entirely in the upper portion of the ampoule, but a relatively intense flow cell still exists near the melt/crystal interface. The damping of convection over the length of the ampoule is responsible for the diffusion-like axial segregation profile observed in these experiments. The large radial nonuniformity seen in the crystals results from incomplete mixing in the flow cell adjacent to the interface.

The effect of solute damping on buoyancy-driven convection in the bulk of the flow is described well by the asymptotic analysis of Hart (1971). Moreover, the linear scaling of the effective solutal Rayleigh number Ra_s^* with the axial concentration gradient caused by solidification explains the decreasing axial segregation with increasing growth rate that was observed in the experiments of Capper *et al.* (1983) with larger ampoules.

A one-dimensional model is proposed for describing axial solute transport from a melt with a well-mixed cell separating convectionless melt from the solidification interface. This model gives a good phenomenological picture of axial segregation in the HgCdTe system. The apparent diffusion-like axial segregation profile is explained and the effective diffusion coefficient is shown to be a function of the size of the well-mixed region. The predictions from this analysis are appealing for the growth of many materials because they suggest that the growth of radially-uniform crystals with nearly constant axial composition profiles is possible if these conditions can be met.

8.2 Transient Analysis

A transient model for crystal growth in closed vertically oriented cylindrical ampoules was developed to account for the inherent transient behaviour of the transport phenomena in these growth systems. The time-dependence in these systems is caused by the steady decrease of the melt volume in a finite length of ampoule and by the time-dependence of the furnace temperature profile with respect to the ampoule during growth. A robust algorithm for numerical integration of the resulting complex moving-boundary problem was constructed by systematic implementation of finite element

discretizations and by implicit time integration methods for the resulting differential-algebraic set of equations. Modified Newton's method implemented using frontal elimination techniques was effective for solving the large set of nonlinear algebraic equations that arise at each time step.

The transient analysis was applied to the simulation of directional solidification systems for the growth of dilute gallium-doped germanium and selenium-doped gallium arsenide crystal in the vertical Bridgman growth system at MIT and gradient freeze growth system at GTE, respectively, and for the growth of nondilute HgCdTe crystal in the vertical Bridgman growth system at NASA in Huntsville, AL. The most distinguished difference between the crystal growth processes in the vertical Bridgman system and the gradient freeze furnace lies in the dynamics of heat supply to the ampoule. In the vertical Bridgman furnace, the furnace temperature profile is stationary in the fixed laboratory frame and the ampoule is pulled down so that it sees the changing furnace temperature in time. On the contrary, the ampoule is stationary and the furnace temperature profile is changed in time in the gradient freeze furnace system. These differences disappear in transient model using the coordinate frame fixed to the ampoule.

The well designed MIT furnace lead to temperature and flow fields around the interface that were in approximately steady-state shortly after the beginning of the ampoule translation. The solute concentration in the crystal kept increasing without attaining a constant value even for the diffusion-controlled growth because of the finite ampoule length. Nevertheless, the radial segregation and effective segregation coefficient reaches steady-state values after the initial transient which is a little longer than the transients for the temperature field and flow field. These observations justify the use of pseudo-steady-state analysis (Adornato and Brown, 1987a) for the study of temperature field, flow structure, convection and solute segregation during the crystal growth process in the same MIT system. Comparisons between the calculated results and experiments by Wang (1984) in MIT system demonstrated the robustness and accuracy of our model and algorithm in transient description of the crystal growth process.

The large latent heat of solidification associated with the gallium arsenide alloy prevented the attainment of steady growth in the gradient freeze system. Most quantities observed in the transport process, such as growth velocity, interface deflection, axial segregation and radial segregation, exhibited transients throughout the growth in GTE gradient freeze system. The pseudo-steady-state approach is not valid for modelling this system. Only complete transient analysis, like the one presented here, gives meaningful results.

Thermosolutal convection during the growth of nondilute HgCdTe alloy in vertical Bridgman growth system is governed by the interactions of driving forces determined by the alloy's thermophysical properties, the design of ampoule and furnace, and operating conditions for growth. A stably stratified axial density gradient develops in the melt because the lighter component CdTe is preferentially partitioned into the crystal and the remaining HgTe is accumulated near the interface. The resulting solute field retards the thermal convection driven by the large radial temperature gradient near the interface. The flow patterns are coupled with the temperature and solute concentration fields and change in time as the solute diffusion layer develops. This picture of the coupling between convection and segregation was confirmed by finite element analysis using the pseudo-steady-state model.

The transient analysis of the growth of HgCdTe alloy in the vertical Bridgman growth system has demonstrated the transition of flow structure caused by the development of the solute diffusion layer next to the interface. The solute concentration is uniform in the melt at time zero because no solidification occurs in the system. As the melt is solidified with the translation of ampoule, solute diffusion layer develops near the melt/crystal interface in the melt. The flow cell near the interface was damped earlier by the solute gradient which exist only in the region near the interface initially. As the solute diffusion layer penetrates into the melt, the flow field initially driven by the temperature field is suppressed entirely by the solute field. The flow structure damped by the solute field still consists of two toroidal cells stacked axially in the ampoule, as is typically observed in the thermal driven convection in the Bridgman growth system,

but, the intensities of the cells, expressed in terms of stream function values, are much lower than those of thermally-driven flow cells.

For the transient analysis of HgCdTe growth in the vertical Bridgman growth system, the complete phase diagram was included in the calculation through the dependence of the melting point temperature and equilibrium distribution coefficient on the composition. The time-dependent calculations show that the previous experimentally obtained axial segregation profiles (Lehoczky and Szofran, 1982; Szofran *et al.*, 1984) are the result of the effective damping of the thermal convection by the solute field. The calculated solute segregation is almost one-dimensional, characteristic of diffusion-controlled growth. The deviation from perfectly one-dimensional composition profile was caused by the large interface deflections due to the mismatch of the thermal conductivities of melt, crystal and ampoule and due to the coupling of the melting point temperature with the interfacial concentration. The intensity of the flow cell near the interface was too small to provide the sufficient mixing to reduce the concentration variations along the interface, except for the short time period in the beginning when the solute concentration gradient is small.

The dependence of β_t of HgCdTe melt on temperature and composition introduced additional instability caused by the density inversion near the interface. This instability, combined with sideways diffusive instability in the bulk, resulted in the secondary flow cells between the upper and lower flow cells. By including the dependence of β_t on temperature and composition, the upper flow cell showed the increase in the intensity of flow by the approximately same amount as the intensity of lower flow cell decreased. The concentration field displayed little effect by the variable β_t because of weak convection level.

8.3 Suggestions for the Future Work

The transient analysis reported here was successful at quantitatively modelling crystal growth in confined vertical ampoule systems. The expression of the real crystal growth

system to the mathematical model is in most cases accompanied by some simplifications. In this Section, some suggestions are made which are expected to increase the accuracy of the model.

Free Volume above the Melt

For most semiconductor materials, the expansion of material upon solidification (For example, germanium, silicon or gallium arsenide) requires the free volume space above melt to avoid the excessive stress. The free volume naturally occurs in the confined growth system during the preparation of the melt charge. The porosity of the solid constituents charged into the ampoule leaves the free volume above the melt.

The presence of the free volume above the melt changes the temperature field near the top of the melt because of the different thermal conductivities of the vapor phase, leading to the possible change in flow field driven by the temperature gradients. The present study has focused on the initial period of solidification when no more than sixty percent of the melt volume has been solidified. If there is a interest is in the final transient, the free volume above the melt should be included in the model.

Thermal Boundary Condition at the Ends of Ampoule

The thermal boundary conditions at the top and bottom of the ampoule were assumed in this study that the temperatures there are equal to the furnace temperatures at the same axial locations. Because we were interested in the initial transients, the both ends of the relatively long ampoule were in the constant temperature zones during the period of interest and above assumptions were justified. However, if we are dealing with the short ampoule or interested in the final transient, these boundary conditions do not faithfully represent reality. This is also true when the ends of the ampoule are not free from other parts of the furnace system, such as the pedestal, plug, or plunger. The thermal boundary conditions in these cases should be more carefully defined and applied in the model calculation.

Variable Viscosity

Gallium arsenide melt is known to have a viscosity which are very strongly dependent on the temperature upto 70 °C above the melting point (Kakimoto and Hibiya, 1987). This temperature range covers most of the melt region in a gradient freeze furnace system where axial temperature gradient is smaller than conventional Bridgman growth system. Although the viscosity data for HgCdTe is not available, it is expected to show the significant dependence on temperature and composition.

The variation of viscosity has a great impact on the flow structure in the melt by facilitating the convection in the region of low viscosity and suppressing it in the region of high viscosity (Hyun and Lee, 1988). As we have shown throughout this study that the nonuniformity of composition in the crystal is closely coupled to the flow field, the variation of the viscosity also influences the solute segregation in the crystal. The stability of the flow with variable viscosity has been discussed recently by Smith (1988) for the directional solidification system and by Chen and Pearlstein (1989) for the free convective flow. The inclusion of the dependence of the viscosity on temperature is expected to improve the accuracy of the model.

Remelting

The accumulation of the heavier component HgTe at the interface due to the rejection lead to the lowering the melting point temperature and there is a chance that just solidified crystal can remelt during the growth of HgCdTe crystal. The present transient model is not capable of describing remelting or backmelting except for the pure material. The description of the remelting for the binary alloy can be possible by including the solute transport equations in the crystal.

Three-dimensional Calculations

When the instability of the system drives the flow to be time-dependent or periodic as in the case of destabilizing vertical Bridgman growth system (melt below crystal), our transient model is able to capture the time-dependency of the flow field using a small time step. But, in most cases these flows are no more axisymmetric and become three dimensional. Although it requires an enormous amount of work, the accurate description of time fluctuations of the flow field should be preceded by the construction of the three-dimensional model.

Traveling Heater Method

The traveling heater method is one of the confined solution growth techniques, where part of the charge enclosed in the ampoule is melted as it passes by the heater. It has received recent attention in growing high quality HgCdTe crystals (Triboulet *et al.*, 1985; Colombo *et al.*, 1988) for the infrared detectors. The present transient model can readily be modified to be applied to the traveling heater method by adding another melt/crystal interface and solid phase into the model.

Control of Interface

The interface curvature or deflections can be controlled using a side heater or booster heater near the interface (Jasinski and Witt, 1985). Control strategy to couple the interface deflection and the power of the side heater can be devised so that the interface deflection should be minimized. The implementation of the control algorithm to the transient model is not formidable task, as it was done similarly for the Czochralski growth method (Derby *et al.*, 1987). These control schemes can also be applied in the experiment with the aid of the development of *in-situ* observation technique of the interface (Barber *et al.*, 1986; Kakimoto *et al.*, 1988). Combined with the image processing technology, *in-situ* observation of the interface shape can be easily linked to

the heater power through controller.

Bibliography

1. Adornato, P. M. (1986), *Thermosolutal Convection in Directional Solidification of Dilute and Non-Dilute Binary Alloys*, Ph. D. Thesis, Mass. Inst. Technol., Cambridge.
2. Adornato, P. M. and R. A. Brown (1987a), 'Convection and segregation in directional solidification of dilute and non-dilute binary alloys: Effects of ampoule and furnace design,' *J. Crystal Growth*, **80**, 155–190.
3. Adornato, P. M. and R. A. Brown (1987b), 'Petrov-Galerkin methods for natural convection in directional solidification of binary alloys,' *Int. J. Num. Meth. Fluids*, **7**, 761–791.
4. Adams, L. M. (1982), *Iterative Algorithms for Large Sparse Linear Systems on Parallel Computers*, NASA CR-166027, NASA Langley Research Center, Hampton, VA.
5. Andrews, R. N., F. R. Szofran and S. L. Lehoczky (1988), 'Internal temperature gradient of alloy semiconductor melts from interrupted growth experiments,' *J. Crystal Growth*, **86**, 100–105.
6. Antar, B. N. (1987), 'Penetrative double-diffusive convection,' *Phys. Fluid*, **30**, 322–330.
7. Antar, B. (1988), University of Tennessee Space Institute, private communication.

8. Arakawa, A. (1966), 'Computational design for long-term numerical integration of the equations of fluid motion; two-dimensional incompressible flow, Part I,' *J. Comput. Phys.*, **1**, 119–143.
9. Arnold, W. A., D. A. Jacqmin, R. L. Gaug and A. Chait (1989), 'Convection phenomena in low-gravity processing: the GTE GaAs space experiment,' Manuscript prepared for the 28th AIAA Aerospace Sciences Meeting, Reno, NV, January 1990.
10. Babuška, I. (1971), 'Error bounds for finite element method,' *Numer. Math.*, **16**, 322–333.
11. Babuška, I. (1973), 'The finite element method with Lagrange multipliers,' *Numer. Math.*, **20**, 179–192.
12. Babuška, I. and A. K. Aziz (1972), 'Survey lectures on the mathematical foundations of the finite element method,' in *The Mathematical Foundations of the Finite Element Method with Applications to Partial Differential Equations*, A. K. Aziz, ed., Academic Press, New York.
13. Barber, P. G., R. K. Crouch, A. L. Fripp, Jr., W. L. Debnam, Jr., R. F. Berry, Jr., and R. Simchick (1986), 'A procedure to visualize the melt-solid interface in Bridgman grown germanium and lead tin telluride,' *J. Crystal Growth*, **74**, 228–230.
14. Bartholomew, D. M. L. and A. Hellawell (1980), 'Changes of growth conditions in the vertical Bridgman-Stockbarger method for the solidification of aluminum,' *J. Crystal Growth*, **50**, 453–460.
15. Bartlett, B. E., P. Capper, J. E. Harris and M. J. T. Quelch (1979a), 'The effects of growth speed on the compositional variations in crystals of cadmium mercury telluride,' *J. Crystal Growth*, **46**, 623–629.
16. Bartlett, B. E., P. Capper, J. E. Harris and M. J. T. Quelch (1979b), 'A study of casting in the $\text{Cd}_x\text{Hg}_{1-x}\text{Te}$ system,' *J. Crystal Growth*, **47**, 341–350.

17. Bathe, K. J. and E. L. Wilson (1976), *Numerical Methods in Finite Element Analysis*, Prentice-Hall, Englewood Cliffs, NJ.
18. Bazeley, G. P., Y. K. Cheung, B. M. Irons and O. C. Zienkiewicz (1965), 'Triangular elements in bending - Conforming and non-conforming solutions,' in *Proceedings of the Conference on Matrix Methods in Structural Mechanics*, Wright-Patterson Air Force Base, Ohio.
19. Bennon, W. D. and F. P. Incropera (1988), 'Numerical simulation of binary solidification in a vertical channel with thermal and solutal mixed convection,' *Int. J. Heat Mass Transfer*, **31**, 2147-2160.
20. Bercovier, M. and O. Pironneau (1979), 'Error estimates for finite element method solution of the Stokes problem in the primitive variables,' *Numer. Math.*, **33**, 211-224.
21. Bird, R. B., W. E. Stewart and E. N. Lightfoot (1960), *Transport Phenomena*, Wiley, New York.
22. Bixler, N. E. and R. E. Benner (1985), 'Finite element analysis of axisymmetric oscillations of sessile liquid drops,' in *Numerical Methods in Laminar and Turbulent Flow*, Pineridge Press, Swansea, C. Taylor, M. D. Olson, P. M. Gresho and W. G. Habashi, eds., 1336-1347.
23. Blair, J. and R. Newnham (1961), 'Preparation and physical properties of crystals in the HgTe-CdTe solid solution series,' in *Metallurgy of Elemental and compound Semiconductors*, R. O. Grubel, ed., 393-402, Interscience Pub., New York.
24. Bollong, A. B. and G. T. Proux (1989), 'Analysis of $\text{Cd}_{0.21}\text{Hg}_{0.79}\text{Te}$ quenched in 10^{-4}g ,' *J. Crystal Growth*, **94**, 475-480.
25. Bonnerot, R. and P. Jamet (1974), 'A second order finite element method for the one-dimensional Stefan problem,' *Int. J. Numer. Eng.*, **8**, 811-820.
26. Borisov, W. T., A. Modrzejewski and S. Warchol(1982), 'Numerical calculation of the isotherms in metallic plates during crystal growth by the Bridgman method,'

- J. Crystal Growth*, **56**, 206–212.
27. Bornykh, N. M., A. M. Sokolov, G. V. Indenbaum and A. V. Vanyukov (1974), 'The structure of crystals of solid solutions of $Cd_xHg_{1-x}Te$ grown from the melt,' *Russ. Metall.*, No. 5, 195–198.
 28. Bourret, E. D., J. J. Favier and A. F. Witt (1983), 'Segregation during directional melting and its implications on seeded crystal growth: A theoretical analysis,' *J. Crystal Growth*, **61**, 681–688.
 29. Bourret, E. D., J. J. Derby, R. A. Brown and A. F. Witt (1984), 'Segregation effects during growth of pseudo-binary systems with large liquidus-solidus separation,' *Acta Astronautica*, **11**, 163–171.
 30. Bourret, E. D., J. J. Derby and R. A. Brown (1985), 'Dynamics of Bridgman-Stockbarger growth of non-dilute binary alloys,' *J. Crystal Growth*, **71**, 587–596.
 31. Brattkus, K. and S. H. Davis (1988), 'Directional solidification with heat losses,' *J. Crystal Growth*, **91**, 538–556.
 32. Brau, M. J. (1972), 'Method of producing homogeneous ingots of a metallic alloy,' *US Patent*, No. 3,656,944.
 33. Brau, M. J. and R. A. Reynolds (1974), 'Enhancement of solid state recrystallization by induced nucleation,' *US Patent*, 3,849,205.
 34. Brent, R. P. (1973), 'Some efficient algorithms for solving systems of nonlinear equations,' *SIAM J. Numer. Anal.*, **10**, 327–344.
 35. Brezzi, F. (1974), 'On the existence, uniqueness and approximation of saddle point problems arising from Lagrangian multipliers,' *RAIRO. Anal. Num.*, **8**, R2, 129–151.
 36. Brice, J. C. (1986), *Crystal Growth Processes*, John Wiley & Sons, New York.

37. Brice, J. C., P. Capper and C. L. Jones (1986), 'The phase diagram of the pseudo-binary system CdTe-HgTe and the segregation of CdTe,' *J. Crystal Growth*, **75**, 395-399.
38. Bridgman, P. W. (1925), 'Certain physical properties of single crystals of tungsten, antimony, bismuth, tellurium, cadmium, zinc, and tin,' *Proc. Amer. Acad. Arts Science*, **60**, 305-383.
39. Brooks A. and T. J. R. Hughes (1982), 'Streamline upwind/Petrov-Galerkin formulation for convection dominated flows with particular emphasis on the incompressible Navier-Stokes equations,' *Comp. Meth. Appl. Mech. Eng.*, **32**, 199-259.
40. Brown, R. A. (1979), 'Finite-element methods for the calculation of capillary surfaces,' *J. Comput. Phys.*, **33**, 217-235.
41. Brown, R. A. (1987), 'Convection and solidification in melt crystal growth,' in *Advanced Crystal Growth*, P. Dryburgh, ed., 41, Prentice Hall, New York.
42. Brown, R. A. (1988), 'Theory of transport processes in single crystal growth from the melt,' *AIChE J.*, **34**, 881-911.
43. Brown, R. A., L. E. Scriven and W. J. Silliman (1980), 'Computer-aided analysis of nonlinear problems in transport phenomena,' in *New Approaches in Nonlinear dynamics*, P. J. Holmes, ed., SIAM, Philadelphia.
44. Burden, M. H., D. J. Hebditch and J. D. Hunt (1973), 'Macroscopic stability of planar, cellular or dendritic interface during directional freezing,' *J. Crystal Growth*, **20**, 121-124.
45. Burton, J. A., R. C. Prim and W. P. Slichter (1953), 'The distribution of solute in crystals grown from the melt. part I. theoretical,' *J. Chem. Phys.*, **21**, 1987-1991.
46. Camel, D., and J. J. Favier (1986), 'Scaling analysis of convective solute transport and segregation in Bridgman crystal growth from the doped melt,' *J. Physique*, **47**, 1001-1004.

47. Capper, P., J. E. Harris, D. Nicholson and D. Cole (1979), 'An improved system for the Bridgman growth of crystals with toxic and/or highly volatile components,' *J. Crystal Growth*, **46**, 575-581.
48. Capper, P., C. L. Jones, E. J. Pearce and M. J. T. Quelch (1983), 'Growth of $\text{Cd}_x\text{Hg}_{1-x}\text{Te}$: Comparison of some properties with the predictions of two melt growth models,' *J. Crystal Growth*, **62**, 487-497.
49. Carey, G. F. and Oden, J. T. (1983), *Finite Elements: A Second Course*, Vol. 2, Prentice Hall, New York.
50. Carlson, F. M., L.-Y. Chin, A. L. Fripp and R. K. Crouch (1982), 'Finite element analysis of the effect of a non-planar solid-liquid interface on the lateral solute segregation during unidirectional solidification,' in *Materials Processing in the Reduced Gravity Environment of Space*, G. E. Rindone, ed., Vol. 9, 629-638, North Holland, New York.
51. Carlson, F. M., A. L. Fripp and R. K. Crouch (1984), 'Thermal convection during Bridgman crystal growth,' *J. Crystal Growth*, **68**, 747-756.
52. Carslaw, H. S. and J. C. Jaeger (1959), *Conduction of Heat in Solids*, second ed., Oxford University Press, Oxford.
53. Carruthers, J. R. (1977), 'Thermal convection instabilities relevant to crystal growth from liquids,' in *Preparation and Properties of Solid State Materials*, Vol. 3, W. R. Wilcox and R. A. Lefever, 1-121, Marcel Dekker, New York.
54. Carruthers, J. R. and A. F. Witt (1975), 'Transient Segregation Effects in Czochralski Growth,' in *Crystal Growth and Characterization*, R. Ueda and J. B. Mullins, eds., North-Holland, Amsterdam.
55. Chait, A. (1988), Private communications.
56. Chandra, D. and L. R. Holland (1983), 'Density of liquid $\text{Hg}_{1-x}\text{Cd}_x\text{Te}$,' *J. Vac. Sci. Technol.*, **A1**, 1620-1624.

57. Chandrasekhar, S. (1961), *Hydrodynamic and Hydromagnetic Stability*, Oxford Univ. Press, Oxford.
58. Chang, C. J. (1983), *A Study of Natural Convection and Its Effects on Melt Crystal Growth*, Ph. D. Thesis, Mass. Inst. Technol., Cambridge.
59. Chang, C. J. and R. A. Brown (1983a), 'Radial segregation induced by natural convection and melt/solid interface shape in vertical Bridgman growth,' *J. Crystal Growth*, **63**, 343-364.
60. Chang, C. J. and R. A. Brown (1983b), 'Finite element calculation of buoyancy-driven convection near a melt/solid phase boundary,' in *Numerical Properties and Methodologies in Heat Transfer*, T. M. Shih, ed., Hemisphere, Washington.
61. Chang, C. J. and R. A. Brown (1984), 'Natural convection in steady solidification: finite element analysis of a two-phase Rayleigh-Bénard problem,' *J. Comput. Phys.*, **53**, 1-27.
62. Chang, E. C. and W. R. Wilcox (1974a), 'Control of interface shape in the vertical Bridgman-Stockbarger technique,' *J. Crystal Growth*, **21**, 135-140.
63. Chang, E. C. and W. R. Wilcox (1974b), 'Localized interface breakdown in zone melting and the travelling heater method,' *J. Crystal Growth*, **21**, 182-186.
64. Charlson, G. S. and R. L. Sani (1971), 'On thermoconvective instability in a bounded cylindrical fluid layer,' *Int. J. Heat Mass Transfer*, **14**, 2157-2160.
65. Chedzey, H. A. and D. T. J. Hurle (1966), 'Avoidance of growth-striae in semiconductor and metal crystals grown by a zone-melting techniques,' *Nature*, **210**, 933-934.
66. Chen, Y.-M. and A. J. Pearlstein (1989), 'Stability of free-convection flows of variable-viscosity fluids in vertical and inclined slots,' *J. Fluid Mech.*, **198**, 513-541.
67. Cheng, G. C., D. Elwell, R. S. Feigelson and C. E. Huang (1985), 'Interface shape during Bridgman growth of CsCdCl₃,' *J. Crystal Growth*, **73**, 417-424.

68. Chi, J. Y. and H. C. Gatos (1979), 'Determination of dopant-concentration diffusion length and lifetime variations in silicon by scanning electron microscopy,' *J. Appl. Phys.*, **50**, 3433-3440.
69. Chin, L.-Y. and F. M. Carlson (1983), 'Finite element analysis of the control of interface shape in Bridgman crystal growth,' *J. Crystal Growth*, **62**, 561-567.
70. Christie, I., D. F. Griffiths, A. R. Mitchell and O. C. Zienkiewicz (1976), 'Finite element methods for second-order differential equations with significant first derivatives,' *Int. J. Numer. Methods Eng.*, **10**, 1389-1396.
71. Chung, T. J. (1978), *Finite Element Analysis in Fluid Dynamics*, McGraw-Hill, New York.
72. Clayton, J. C., M. C. Davidson, D. C. Gillies and S.L. Lehoczky (1982), 'One-dimensional analysis of segregation in directionally solidified HgCdTe,' *J. Crystal Growth*, **60**, 374-380.
73. Clemans, J. E. and J. H. Conway (1988), 'Vertical gradient freeze growth of 75 mm diameter semi-insulating GaAs,' in *Semi-insulating III-V Materials, Malmö 1988*, G. Grossmann and L. Ledebø, eds., 423-428, Adam Hilger, Bristol.
74. Clyne, T. W. (1980a), 'Heat flow controlled directional solidification of metals: I. Experimental investigation,' *J. Crystal Growth*, **50**, 684-690.
75. Clyne, T. W. (1980b), 'Heat flow controlled directional solidification of metals: II. Mathematical model,' *J. Crystal Growth*, **50**, 691-700.
76. Cockayne, B. and M. P. Gates (1967), 'Growth striations in vertically pulled oxide and fluoride single crystals,' *J. Mat. Sci.*, **2**, 118-123.
77. Colombo, L., R. R. Chang, C. J. Chang and B. A. Baird (1988), 'Growth of Hg-based alloys by the traveling heater method,' *J. Vac. Sci. Technol. A*, **6**, 2795-2799.

78. Coriell, S. R., R. F. Boisvert, R. G. Rehm and R. F. Sekerka (1981), 'Lateral solute segregation during unidirectional solidification of a binary alloy with a curved solid-liquid interface: II. Large departures from planarity,' *J. Crystal Growth*, **54**, 167-175.
79. Coriell, S. R., G. B. McFadden, R. F. Boisvert, M. E. Glicksman and Q. T. Fang (1984), 'Coupled convective instabilities at crystal-melt interface,' *J. Crystal Growth*, **66**, 514-524.
80. Coriell, S. R. and R. F. Sekerka (1979), 'Lateral solute segregation during unidirectional solidification of a binary alloy with a curved solid-liquid interface,' *J. Crystal Growth*, **46**, 479-482.
81. Coriell, S. R. and R. F. Sekerka (1981), 'Effect of convective flow on morphological stability,' *PhysicoChem. Hydrodyn.*, **2**, 281-293.
82. Cormack, D. E., L. G. Leal and J. Inberger (1974a), 'Natural convection in a shallow cavity with differentially heated end walls. Part 1. Asymptotic theory,' *J. Fluid Mech.*, **65**, 209-229.
83. Cormack, D. E., L. G. Leal and J. H. Seinfeld (1974b), 'Natural convection in a shallow cavity with differentially heated end walls. Part 2. Numerical solutions,' *J. Fluid Mech.*, **65**, 231-246.
84. Courant, R. (1943), 'Variational methods for the solution of problems of equilibrium and vibration,' *Bull. Am. Math. Soc.*, **49**, 1-23.
85. Crandall, S. H. (1956), *Engineering Analysis*, McGraw-Hill, New York.
86. Crank, J. (1984), *Free and Moving Boundary Problems*, Oxford Press, Oxford.
87. Crochet, M. J., F. T. Geyling and J. J. Van Schaftingen (1983), 'Numerical simulation of the horizontal Bridgman growth of a gallium arsenide crystal,' *J. Crystal Growth*, **65**, 166-172.

88. Crochet, M. J., F. T. Geyling and J. J. Van Schaftingen (1985), 'finite element method for calculating the horizontal Bridgman growth of semiconductor crystals,' in *Finite Elements in Fluids*, R. H. Gallagher, G. F. Carey, J. T. Oden and O. C. Zienkiewicz, eds., 321–337, John Wiley, Chichester.
89. Crochet, M. J., F. T. Geyling and J. J. Van Schaftingen (1987), 'Numerical simulation of the horizontal Bridgman growth. part I: two-dimensional flow,' *Int. J. Num. Meth. Fluids*, **7**, 29–47.
90. Crouch, R. K., A. L. Fripp, W. J. Debnam, R. E. Taylor and H. Groot (1982), 'Thermophysical properties of germanium for thermal analysis of growth from the melt,' in *Materials Processing in the Reduced Gravity Environment of Space*, G. E. Rindone, ed., Vol. 9, 657–663, North Holland, New York.
91. Cuvelier, C., A. Segal and A. A. van Steenhoven (1986), *Finite Element Methods and Navier-Stokes Equations*, D. Reidel Publishing Co., Dordrecht.
92. Danckwerts, P. V. (1955), 'Continuous flow systems: Distribution of residence time,' *Chem. Eng. Sci.*, **2**, 1–13.
93. Dakhoul, Y. M., R. Farmer, S. L. Lehoczky and F. R. Sofran (1988), 'Numerical simulation of heat transfer during the crystal growth of HgCdTe alloys,' *J. Crystal Growth*, **86**, 49–55.
94. Davis, K. G. (1972), 'Calculation of the steady-state temperature profile in a rod during directional solidification,' *Can. Met. Quart.*, **11**, 317–322.
95. Dennis, J. E. and J. J. Moré (1977), 'Quasi-Newton methods, motivation and theory,' *SIAM Review*, **19**, 46–89.
96. Derby, J. J. (1986), *Analysis of Heat Transfer. Stability and Dynamics of Czochralski and Liquid Encapsulated Czochralski Growth of Semiconductor Materials*, Ph. D. Thesis, Mass. Inst. Technol., Cambridge.
97. Derby, J. J. and R. A. Brown (1986), 'A fully implicit method for simulation of the one-dimensional solidification of a binary alloy,' *Chem. Eng. Sci.*, **41**, 37–46.

98. Derby, J. J., L. J. Atherton, P. D. Thomas and R. A. Brown (1987), 'Finite-element methods for analysis of the dynamics and control of Czochralski crystal growth,' *J. Sci. Comp.*, **2**, 297-343.
99. Derby, J. J., R. A. Brown, F. T. Geyling, A. S. Jordan and G. A. Nikolakopoulou (1985), 'Finite element analysis of a thermal-capillary model for liquid encapsulated Czochralski growth,' *J. Electrochem. Soc.*, **132**, 470-482.
100. Dietl, J. and J. Jarosch (1976), 'Process for preparing a homogeneous alloy,' *US Patent*, **4,011,074**.
101. Dilorenzo, J. V. (1978), 'FET development - Low noise and high power,' *Microwave J.*, **21(2)**, 39-44.
102. Dittmar, G. (1978), 'Die Züchtung homogener Mischkristalle mit großer Segregationsneigung nach dem Bridgman-Verfahren am Beispiel des pseudobinären Systems $Cd_xHg_{1-x}Te$,' *Krist. Tech.*, **13**, 639-643.
103. Donea, J., T. Belytschko and P. Smolinski (1985), 'A generalized Galerkin method for steady convection-diffusion problems with application to quadratic shape function elements,' *Comp. Meth. Appl. Mech. Eng.*, **48**, 25-43.
104. Drazin, P. G. and W. H. Reid (1981), *Hydrodynamic Stability*, Cambridge Univ. Press, Cambridge.
105. Duda, J. L., N. F. Malone, R. H. Notter and J. S. Vrentas (1975), 'Analysis of two-dimensional diffusion-controlled moving boundary problems,' *Int. J. Heat Mass Transfer*, **18**, 901-910.
106. Dupont, S., J. M. Marchal, M. J. Crochet and F. T. Geyling (1987), 'Numerical simulation of the horizontal Bridgman growth. part II: three-dimensional flow,' *Int. J. Num. Meth. Fluids*, **7**, 49-67.
107. Dussan V., E. B. (1979), 'On the spreading of liquids on solid surfaces: static and dynamic contact lines,' *Ann. Rev. Fluid Mech.*, **11**, 371-400.

108. Dziuba, E. Z. (1969), 'Preparation of Cd_xHg_{1-x} Te crystals by the vertical-zone melting method,' *J. Electrochem. Soc.*, **116**, 104–106.
109. Elliot, C. T. (1985), 'Cadmium mercury telluride infrared detectors,' *J. Crystal Growth*, **72**, 453–461.
110. Engelman, M. S., R. L. Sani, P. M. Gresho and M. Bercovier (1982), 'Consistent vs. Reduced integration penalty methods for incompressible media using several old and new elements,' *Int. J. Num. Meth. Fluids*, **2**, 25–42.
111. Ettouney, H. M. (1983), *Heat, Mass and Momentum Transfer in Edge-Defined Film-Fed Crystal Growth*, Ph. D. Thesis, Mass. Inst. Technol., Cambridge.
112. Ettouney, H. M. and R. A. Brown (1983), 'Finite-element methods for steady solidification problems,' *J. Comput. Phys.*, **49**, 118–150.
113. Favier, J-J (1980), 'Initial transient segregation during unidirectional solidification of a binary alloy in a furnace with thermal damping,' *J. Crystal Growth*, **49**, 373–380.
114. Finlayson, B. A. (1972), *The Method of Weighted Residuals and Variational Principles*, Academic Press, New York.
115. Flemings, M. C. (1974), *Solidification Processing*, McGraw-Hill, New York.
116. Fletcher, C. A. J. (1984), *Computational Galerkin Methods*, Springer-Verlag, New York.
117. Fortin, M. (1981), 'Old and new finite elements for incompressible flows,' *Int. J. Num. Meth. Fluids*, **1**, 347–364.
118. Fortin, M. and A. Fortin (1985a), 'Newer and newer elements for incompressible flow,' in *Finite Elements in Fluids*, Vol. 6, R. H. Gallagher, R. H., G. F. Carey, J. T. Oden and O. C. Zienkiewicz ,eds., John Wiley, Chichester.
119. Fortin, M. and A. Fortin (1985b), 'Experiments with several elements for viscous incompressible flows,' *Int. J. Num. Meth. Fluids*, **5**, 911–928.

120. Fu, T.-W. and W. R. Wilcox (1980), 'Influence of insulation on stability of interface shape and position in the vertical Bridgman-Stockbarger technique,' *J. Crystal Growth*, **48**, 416-424.
121. Fu, T.-W. and W. R. Wilcox (1981), 'Rate change transients in Bridgman-Stockbarger growth,' *J. Crystal Growth*, **51**, 557-567.
122. Fu, T.-W. and W. R. Wilcox (1982), 'Programmed and oscillatory motion in Bridgman-Stockbarger growth,' *J. Crystal Growth*, **57**, 91-93.
123. Fu, T.-W., W. R. Wilcox and D. J. Larson (1982), 'Rate change transients in Bridgman-Stockbarger growth of MnBi/Bi eutectic,' *J. Crystal Growth*, **57**, 189-193.
124. Galerkin, B. G. (1915), 'Series solution of some problems of elastic equilibrium of rods and plates,' *Vestn. Inzh. Tech.*, **19**, 897-908.
125. Gallagher, R. H., J. T. Oden, C. Taylor and O. C. Zienkiewicz (eds.) (1975a), *Finite Elements in Fluids: Viscous Flows and Hydrodynamics*, Vol. 1, John Wiley, London.
126. Gallagher, R. H., J. T. Oden, C. Taylor and O. C. Zienkiewicz (eds.) (1975b), *Finite Elements in Fluids: Mathematical Foundations, Aerodynamics and Lubrication*, Vol. 2, John Wiley, London.
127. Gallagher, R. H., O. C. Zienkiewicz, J. T. Oden, M. M. Cecchi and C. Taylor (eds.) (1978), *Finite Elements in Fluids*, Vol. 3, John Wiley, London.
128. Gallagher, R. H., D. Norrie, J. T. Oden and O. C. Zienkiewicz, (eds.) (1982), *Finite Elements in Fluids*, Vol. 4, John Wiley, Chichester.
129. Gallagher, R. H., J. T. Oden, O. C. Zienkiewicz, T. Kawai and M. Kawahara (eds.) (1984), *Finite Elements in Fluids*, Vol. 5, John Wiley, Chichester.
130. Gallagher, R. H., G. F. Carey, J. T. Oden and O. C. Zienkiewicz (eds.) (1985), *Finite Elements in Fluids*, Vol. 6, John Wiley, Chichester.

131. Gallagher, R. H., R. Glowinski, P. M. Gresho, J. T. Oden and O. C. Zienkiewicz (eds.) (1988), *Finite Elements in Fluids*, Vol. 7, John Wiley, Chichester.
132. Gallet, J., J. Marine, B. Pelliciani and B. Schaub (1976), 'Preparation of group IIA-IIB chalcogenides by travelling-solvent zone melting,' *US Patent*, **4,003,741**.
133. Gartling, D. K. and E. B. Becker (1976), 'Finite element analysis of viscous, incompressible fluid flow : I and II,' *Comp. Meth. Appl. Mech. Eng.*, **8**, 51-60, 127-138.
134. Gatos, H. C. (1982), 'Semiconductor crystal growth and segregation problems on earth and in space', in *Materials Processing in the Reduced Gravity Environment of Space*, G. E. Rindone, ed., Vol. 9, 355-371, North Holland, New York.
135. Gault, W. A., E. M. Monberg and J. E. Clemans (1986), 'A novel application of the vertical gradient freeze method to the growth of high quality III-V crystals,' *J. Crystal Growth*, **74**, 491-506.
136. Gear, C. W. (1971), 'Simultaneous numerical solution of differential-algebraic equations,' *IEEE Trans. Circuit Theory*, **Ct-18**, 89-95.
137. Gebhart, B., Y. Jaluria, R. L. Mahajan and B. Sammakia (1988), *Buoyancy-Induced Flows and Transport*, Hemisphere, Washington.
138. Ghandhi, S. K. (1983), *VLSI Fabrication Principles: Silicon and Gallium Arsenide*, John Wiley, New York.
139. Gill, A. E. (1974), 'A theory of thermal oscillations in liquid metals,' *J. Fluid Mech.*, **64**, 577-588.
140. Girault, V. and P.-A. Raviart (1986), *Finite Element Methods for Navier-Stokes Equations*, Springer-Verlag, Berlin.
141. Glazov, V. M., S. N. Chizhevskaya and N. N. Glagoleva (1969), *Liquid Semiconductors*, Plenum Press, New York.

142. Glicksman, M. E., S. R. Coriell and G. B. McFadden (1986), 'Interaction of flows with the crystal-melt interface,' *Ann. Rev. Fluid Mech.*, **18**, 307–335.
143. Gresho, P. M. and R. L. Lee (1979), 'Don't suppress the wiggles—they're telling you something!' in *Finite Element Methods for Convection Dominated Flows*, T. J. R. Hughes, ed., AMD Vol. 34, ASME, New York.
144. Gresho, P. M., R. L. Lee, S. T. Chan and R. L. Sani (1980a), 'Solution of the time-dependent incompressible Navier-Stokes and Boussinesq equations using the Galerkin finite element method,' in *Approximation Methods for Navier-Stokes Problems*, Springer Verlag Lecture Notes in Math., No. 771, 203–222, New York.
145. Gresho, P. M., R. L. Lee and R. L. Sani (1980b), 'On the time-dependent solution of the incompressible Navier-Stokes equations in two and three dimensions,' in *Recent Advances in Numerical Methods in Fluids*, Vol. 1, C. Taylor and K. Morgan, eds., 27–79, Pineridge, Swansea.
146. Gulliver, G. H. (1922), *Metallic alloys*, Charles Griffin, London.
147. Gustafson, J., A. Bellows and J. Kafalas (1986), 'The comparative study of the influence of convection on gallium arsenide growth,' *Proc. 2nd Pathways to Space Exp. Workshop*, Orlando, FL (June, 1986).
148. Harriot, G. M. and R. A. Brown (1984), 'Steady solute fields induced by differential rotation in a small floating zone,' *J. Crystal Growth*, **69**, 589–604.
149. Hart, J. E. (1971). 'On sideways diffusive instability,' *J. Fluid Mech.*, **49**, 279–288.
150. Heinrich, J. C. (1988), 'Numerical simulations of thermosolutal instability during directional solidification of a binary alloy,' *Comput. Meths. Appl. Mech. Engrg.*, **69**, 65–88.
151. Heinrich, J. C. and O. C. Zienkiewicz (1977), 'Quadratic finite element schemes for two-dimensional convective transport problems,' *Int. J. Numer. Methods Eng.*, **11**, 1831–1844.

152. Hicks, T. W., A. E. Organ and N. Riley (1989), 'Oxygen transport in magnetic Czochralski growth of silicon with a non-uniform magnetic field,' *J. Crystal Growth*, **94**, 213-228.
153. Hirata, H., K. Hoshikawa and N. Inoue (1984), 'Improvement of thermal symmetry in CZ silicon melts by the application of a vertical magnetic field,' *J. Crystal Growth*, **70**, 330-334.
154. Hirata, H. and N. Inoue (1985), 'Macroscopic axial dopant distribution in Czochralski silicon crystals grown in a vertical magnetic field,' *Japan. J. Appl. Phys.*, **24**, 1399-1403.
155. Hjellming, L. N. and J. S. Walker (1986), 'Melt motion in a Czochralski crystal puller with an axial magnetic field: isothermal motion,' *J. Fluid Mech.*, **164**, 237-273.
156. Hjellming, L. N. and J. S. Walker (1987), 'Melt motion in a Czochralski crystal puller with an axial magnetic field: motion due to buoyancy and thermocapillarity,' *J. Fluid Mech.*, **182**, 335-370.
157. Hofmann, D., F. Mosel and G. Müller (1988), 'Influence of a vertical magnetic field on the LEC-growth and properties of 3-inch s.i. InP crystals,' *Semi-insulating III-V Materials, Malmö 1988*, G. Grossmann and L. Ledebø, eds., 429-434, Adam Hilger, Bristol.
158. Holland, L. R. (1989), 'Crucible surface, thermal refraction, boundaries, and interface shape in melt growth,' *J. Crystal Growth*, **96**, 577-583.
159. Holland, L. R. and R. E. Taylor (1983), 'Measured thermal diffusivity of $\text{Hg}_{1-x}\text{Cd}_x\text{Te}$ solids and melts,' *J. Vac. Sci. Technol.*, **A1**, 1615-1619.
160. Holmes, D. E. and H. C. Gatos (1981a), 'Morphological stability of the planar solid-liquid interface,' *J. Appl. Phys.*, **52**, 2971-2982.
161. Holmes, D. E. and H. C. Gatos (1981b), 'Convective interference and "effective" diffusion-controlled segregation during directional solidification under stabilizing

- vertical thermal gradients; Ge,' *J. Electrochem. Soc.*, **128**, 429–437.
162. Hood, P. (1976), 'Frontal solution program for unsymmetric matrices,' *Int. J. Num. Meth. Eng.*, **10**, 379–399.
163. Hood, P. (1977), 'Note on frontal solution program for unsymmetric matrices,' *Int. J. Num. meth. Eng.*, **11**, 1055.
164. Hood, P. and C. Taylor (1974), 'Navier-Stokes equation using mixed interpolation,' in *Finite Element Methods in Flow Problems*, J. T. Oden, O. C. Zienkiewicz, R. H. Gallagher and C. Taylor, eds., 57–66, UAH Press, Huntsville.
165. Horowitz, A. and Y. S. Horowitz (1989), 'The growth of semiconductors in confined vertical crucibles,' *AA CG Newsletter*, **19**(1), 3–4.
166. Hoselitz, K. (1968), 'The crystals we need,' *J. Crystal Growth*, **3/4**, 5–12.
167. Hoshikawa, K. (1982), 'Czochralski silicon crystal growth in the vertical magnetic field,' *Japan. J. Appl. Phys.*, **21**, L545–L547.
168. Hoshikawa, K., H. Kohda, H. Hirata and H. Nakanishi (1980), 'Low oxygen content Czochralski silicon crystal growth,' *Japan. J. Appl. Phys.*, **19**, L33–L36.
169. Huang, C. E., D. Elwell and R. S. Feigelson (1983), 'Influence of thermal conductivity on interface shape during Bridgman growth,' *J. Crystal Growth*, **64**, 441–447.
170. Huebner, K. H. and E. A. Thornton (1982), *The Finite Element Method for Engineers*, John Wiley, New York.
171. Hughes, T. J. R. (1978), 'A simple scheme for developing upwind finite elements,' *Int. J. Numer. Methods Eng.*, **12**, 1359–1365.
172. Hughes, T. J. R. (1987), *The Finite Element Method: Linear Static and Dynamic Finite Element Analysis*, Prentice-Hall, Englewood Cliffs.

173. Hughes, T. J. R. and A. Brooks (1980), 'A multidimensional upwind scheme with no crosswind diffusion,' in *Finite Element Methods for Convection Dominated Flows*, AMD Vol. 34, T. J. R. Hughes, ed., ASME, New York.
174. Hughes, T. J. R. and A. Brooks (1982), 'A theoretical framework for Petrov-Galerkin methods with discontinuous weighting functions: application to the streamline-upwind procedure,' in *Finite Elements in Fluids*, Vol. 4, R. H. Gallagher, D. Norrie, J. T. Oden and O. C. Zienkiewicz, eds., John Wiley, Chichester.
175. Huh, C. and L. E. Scriven (1971), 'Hydrodynamic model of steady movement of a solid/liquid/fluid contact line,' *J. Colloid Interface Sci.*, **35**, 85–101.
176. Hulme, K. F. (1955), 'On the distribution of impurity in crystals grown from impure unstirred melts,' *Proc. Phys. Soc. B*, **68**, 393–399.
177. Hurle, D. T. J. (1966), 'Temperature oscillations in molten metal and their relationship to growth striae in melt-grown crystals,' *Phil. Mag., Ser. 8*, **13**, 305–310.
178. Hurle, D. T. J. (1967), 'Thermo-hydrodynamic oscillations in liquid metals: The cause of impurity striations in melt-grown crystals,' in *Crystal Growth*, H. S. Peiser, ed., 659–663, Pergamon, Oxford.
179. Hurle, D. T. J. (1972), 'Hydrodynamics, convection and crystal growth,' *J. Crystal Growth*, **13/14**, 39–43.
180. Hurle, D. T. J. (1983), 'Convective Transport in melt growth systems,' *J. Crystal Growth*, **65**, 124–132.
181. Hurle, D. T. J., E. Jakeman and C. P. Johnson (1974), 'Convective temperature oscillations in molten gallium,' *J. Fluid Mech.*, **64**, 565–576.
182. Hurle, D. T. J., E. Jakeman and E. R. Pike (1968), 'Striated solute distributions produced by temperature oscillations during crystal growth from the melt,' *J. Crystal Growth*, **3/4**, 633–640.
183. Hurle, D. T. J., E. Jakeman and A. A. Wheeler (1982), 'Effect of solutal convection on the morphological stability of a binary alloy,' *J. Crystal Growth*, **58**, 163–179

184. Huyakorn, P. S., C. Taylor, R. L. Lee and P. M. Gresho (1978), 'A comparison of various mixed-interpolation finite elements in the velocity-pressure formulation of the Navier-Stokes equations,' *Computers and Fluids*, **6**, 25–35.
185. Hyun, J. M. and J. W. Lee (1988), 'Transient natural convection in a square cavity of a fluid with temperature-dependent viscosity,' *Int. J. Heat Fluid Flow*, **9**, 278–285.
186. Irons, B. M. (1970), 'A frontal solution program for finite element analysis,' *Int. J. Num. Meth. Eng.*, **2**, 5–32.
187. Irons, B. M. (1971), 'Quadrature rules for brick based finite elements,' *AIAA J.*, **9**, 293–294.
188. Irons, B. M. and S. Ahmad (1980), *Techniques of Finite Elements*, John Wiley, New York.
189. Irons, B. M., O. C. Zienkiewicz and E. R. de Arantes Oliveira (1970), 'Comments on the paper: Theoretical foundations of the finite element method,' *Int. J. Solids Structure*, **6**, 695–697.
190. Itoh, M., H. Takigawa and R. Ueda (1980), 'Mercury cadmium telluride photoconductive detector array,' *IEEE Tran. Electron Devices*, **ED-27**, 150–154.
191. Jamet, P. and P. A. Raviart (1974), 'Numerical solution of the stationary Navier-Stokes equation by finite element method,' in *Lecture Notes in Computer Science*, Vol. 10, 193–223, Berlin, Springer.
192. Jasinski, T. and R. J. Naumann (1984), 'One-dimensional thermal modeling of vertical Bridgman-type crystal growth,' *J. Crystal Growth*, **66**, 469–471.
193. Jasinski, T., W. M. Rohsenow and A. F. Witt (1983), 'Heat transfer analysis of the Bridgman-Stockbarger configuration for crystal growth: I. Analytical treatment of the axial temperature profile,' *J. Crystal Growth*, **61**, 339–354.

194. Jasinski, T. and A. F. Witt (1985), 'On control of the crystal-melt interface shape during growth in a vertical Bridgman configuration,' *J. Crystal Growth*, **71**, 295–304.
195. Jasinski, T., A. F. Witt and W. M. Rohsenow (1984), 'Heat transfer analysis of the Bridgman-Stockbarger configuration for crystal growth: II. Analytical treatment of radial temperature variations,' *J. Crystal Growth*, **67**, 173–184.
196. Jenkins, D. R. (1985), 'Non-linear interaction of morphological and convective instabilities during solidification of a dilute binary alloy,' *IMA J. Appl. Math.*, **35**, 145–157.
197. Jespersen, D. C. (1974), 'Arakawa's method is a finite element method,' *J. Comput. Phys.*, **16**, 383–390.
198. Jiang, H. D., S. Ostrach and Y. Kamotani (1988), 'Thermosolutal convection flow regimes with opposed buoyancy forces in shallow enclosures,' *PhysicoChem. Hydrodyn.*, **10**, 599–613.
199. Johnson, R. E. (1971), 'Method for preparing single crystal pseudobinary alloys,' *US Patent, No. 3,622,399*.
200. Jones, R. E. (1964), 'A generalization of the direct-stiffness method of structural analysis,' *J.A.I.A.A.*, **2**, 821–826.
201. Jones, C. L., P. Capper and J. J. Gosney (1982), 'Thermal Modelling of Bridgman crystal growth,' *J. Crystal Growth*, **56**, 581–590.
202. Jones, C. L., P. Capper, B. W. Straughan and A. W. Vere (1983), 'Thermal modelling of the casting of $Cd_xHg_{1-x}Te$,' *J. Crystal Growth*, **63**, 145–153.
203. Jones, C. L., P. Capper, J. J. Gosney, G. Ard and I. Kenworthy (1983), 'Comments on segregation during Bridgman growth of $Cd_xHg_{1-x}Te$,' *J. Crystal Growth*, **64**, 403–406.
204. Jones, C. L., P. Capper, J. J. Gosney and I. Kenworthy (1984), 'Factors affecting isotherm shape during Bridgman crystal growth,' *J. Crystal Growth*, **69**, 281–290.

205. Jordan, A. S. (1980), 'An evaluation of the thermal and elastic constants affecting GaAs crystal growth,' *J. Crystal Growth*, **49**, 631-642.
206. Jordan, A., S. (1985), 'Estimated thermal diffusivity, Prandtl number and Grashof number of molten GaAs, InP and GaSb,' *J. Crystal Growth*, **71**, 551-558.
207. Kafalas, J. A. and A. H. Bellows (1988), 'A comparative study of the influence of buoyancy driven flow on GaAs crystal growth,' *Proceedings of 1988 AIAA conference*.
208. Kakimoto, K. and T. Hibiya (1987), 'Temperature dependence of viscosity of molten GaAs by an oscillating cup method,' *Appl. Phys. Lett.*, **50**, 1249-1250.
209. Kakimoto, K., M. Eguchi, H. Watanabe and T. Hibiya (1988), 'In-situ observation of solid-liquid interface shape by X-ray radiography during silicon single crystal growth,' *J. Crystal Growth*, **91**, 509-514.
210. Kawahara, M., N. Yoshimura, K. Nakagawa and H. Ohsaka (1976), 'Steady and unsteady finite element analysis of incompressible viscous flow,' *Int. J. Num. Meth. Eng.*, **10**, 437-456.
211. Keller, H. B. (1977), 'Numerical solution of bifurcation and nonlinear eigenvalue problems,' in *Application of Bifurcation Theory*, Academic Press, New York.
212. Kelly, D. W., S. Nakazawa, C. C. Zienkiewicz and J. C. Heinrich (1980), 'A note on upwinding and anisotropic balancing dissipation in finite element approximations to convective diffusion problems,' *Int. J. Numer. Methods Eng.*, **15**, 1705-1711.
213. Kelly, J. D., B. G. Martin, F. R. Szofran and S. L. Lehoczky (1982), 'Application of the regular associated solution model to the Cd-Te and Hg-Te binary systems,' *J. Electrochem. Soc.*, **129**, 2360-2365.
214. Keunings, R. (1986), 'An algorithm for the simulation of transient viscoelastic flows with free surfaces,' *J. Comput. Phys.*, **62**, 199-220.

215. Kheshgi, H. S. and L. E. Scriven (1984), 'Penalty finite element analysis of unsteady free surface flows,' in *Finite Elements in Fluids*, Vol. 5, R. H. Gallagher, J. T. Oden, O. C. Zienkiewicz, T. Kawai and M. Kawahara ,eds., John Wiley, Chichester.
216. Kim, D. H., P. M. Adornato and R. A. Brown (1988), 'Effect of vertical magnetic field on convection and segregation in vertical Bridgman crystal growth', *J. Crystal Growth*, **89**, 339-356.
217. Kim, D. H. and R. A. Brown (1989), 'Models for convection and segregation in the growth of HgCdTe by the vertical Bridgman method,' *J. Crystal Growth*, **96**, 609-627.
218. Kim, K. M. (1982), 'Suppression of thermal convection by transverse magnetic field,' *J. Electrochem. Soc.*, **129**, 427-429.
219. Kim, K. M. and P. Smetana (1985), 'Striations in CZ silicon crystals grown under various axial magnetic field strengths,' *J. Appl. Phys.*, **58**, 2731-2735.
220. Kim, K. M., A. F. Witt and H. C. Gatos (1972), 'Crystal growth from the melt under destabilizing thermal gradients,' *J. Electrochem. Soc.*, **119**, 1218-1226.
221. Kim, K. M., A. F. Witt, M. Lichtensteiger and H. C. Gatos (1978), 'Quantitative analysis of the effects of destabilizing vertical thermal gradients on crystal growth and segregation: Ga-doped Ge,' *J. Electrochem. Soc.*, **125**, 475-480.
222. Kobayashi, S. (1988), 'Solute redistribution during solidification with diffusion in solid phase: A theoretical analysis,' *J. Crystal Growth*, **88**, 87-96.
223. Kreith, F. (1958), *Principles of Heat Transfer*. Harper, New York.
224. Krishnamurti, R. (1973), 'Some further studies on the transition to turbulent convection,' *J. Fluid Mech.*, **60**, 285-303.
225. Kroeger, P. G. and S. Ostrach (1974), 'The solution of a two dimensional freezing problem including convection effects in the liquid region,' *Int. J. Heat Mass Transfer*, **17**, 1191-1207.

226. Kruse, P. W. and J. L. Schmit (1973), 'Mercury cadmium telluride,' *US Patent*, No. 3,723,190.
227. Kubiček, M. (1976), 'Dependence of solution of nonlinear equations on a parameter,' *ACM Trans. Math. Software*, 2, 98-107.
228. Kuiken, H. K. (1988), 'A note on the wall singularity of a solid-liquid interface caused by a difference between the thermal conductivities of the solid and the liquid phases,' *SIAM J. Appl. Math.*, 48, 921-924.
229. Kurz, W. and D. J. Fisher (1984), *Fundamentals of Solidification*, Trans Tech, Switzerland.
230. Ladyzhenskaya, O. A. (1969), *The Mathematical Theory of Viscous Incompressible Flows*, 2nd ed., Gordon and Breach, New York.
231. Landau, H. G. (1950), 'Heat conduction in a melting solid,' *Quart. Appl. Math.*, 8, 81-94.
232. Langlois, W. E. (1984), 'Computer simulation of Chochralski melt convection in a magnetic field,' *J. Crystal Growth*, 70, 73-77.
233. Langlois, W. E. (1985), 'Buoyancy-driven flows in crystal-growth melts,' *Ann. Rev. Fluid Mech.*, 17, 191-215.
234. Langlois, W. E. and J. S. Walker (1982), 'Czochralski crystal growth in an axial magnetic field,' in *Computational and Asymptotic Methods for Boundary and Interior Layers*, J. J. H. Miller, ed., 299-304.
235. Larrabee, G. B. (1985), 'Microelectronics,' *Chemical Engineering*, June 10, 51-59.
236. Laudise, R. A. (1974), 'Future needs and opportunities in crystal growth - crystal growth toward the year 2000,' *J. Crystal Growth*, 24/25, 32-42.
237. Lawrence, J. E. and H. R. Huff (1982), 'Silicon material properties for VLSI circuitry,' in *VLSI Electronic Microstructure Science*, N. G. Einspruch, ed., Vol. 5, 51-102, Academic Press, New York.

238. Lee, J., M. T. Hyun and K. W. Kim (1988), 'Natural convection in confined fluids with combined horizontal temperature and concentration gradients,' *Int. J. Heat Mass Transfer*, **31**, 1969–1977.
239. Lee, K.-J., W. E. Langlois and K. M. Kim (1984), 'Digital simulation of oxygen transfer and oxygen segregation in magnetic Czochralski growth of silicon,' *PhysicoChem. Hydrodyn.*, **5**, 135–141.
240. Lehoczky, S. L. and F. R. Szofran (1982), 'Directional solidification and characterization of $\text{Hg}_{1-x}\text{Cd}_x\text{Te}$ alloys,' in *Materials Processing in the Reduced Gravity Environment of Space*, G. E. Rindone, ed., Vol. 9, 409–420, North Holland, New York.
241. Lehoczky, S. l., F. R. Szofran and B. G. Martin (1980), *Advanced Methods for Preparation and Characterization of Infrared Detector Materials*, NASA CR-161598.
242. Leonard, B. P. (1979), 'A survey of finite differences of opinion in numerical muddling of the incomprehensible defective confusion equation,' in *Finite Element Methods for Convection Dominated Flows*, T. J. R. Hughes, ed., AMD Vol. 34, ASME, New York.
243. Lesaint, P. and R. Touzani (1989), 'Approximation of the heat equation in a variable domain with application to the Stefan problem,' *SIAM J. Numer. Anal.*, **26**, 366–379.
244. Lin, C. C. and L. A. Segel (1974), *Mathematics Applied to Deterministic Problems in the Natural Sciences*, Macmillan Publishing, New York.
245. Lin, W. and K. E. Benson (1987), 'The science and engineering of large-diameter Czochralski silicon crystal growth,' *Ann. Rev. Mater. Sci.*, **17**, 273–298.
246. Long, D. (1968), *Energy Bands in Semiconductors*, Wiley, New York.
247. Lynch, D. R. (1982), 'Unified approach to simulation on deforming elements with application to phase change problems,' *J. Comput. Phys.*, **47**, 387–411.

248. Lynch, D. R. and W. G. Gray (1980), 'Finite element simulation of flow in deforming regions,' *J. Comput. Phys.*, **36**, 135-153.
249. Marti, J. T. (1986), *Introduction to Sobolev Spaces and Finite Element Solution of Elliptic Boundary Value Problems*, Academic Press, London.
250. Mase, G. E. (1970), *Continuum Mechanics*, McGraw-Hill, New York.
251. Matsushima, H. and R. Viskanta (1988), 'Effects of internal radiation on temperature distribution and natural convection in a vertical crystal growth configuration,' in *Collected Papers in Heat Transfer 1988*, K. T. Yang, ed., 151-160, ASME, New York.
252. Matthiesen, D. H. (1988), Ph. D. Thesis, *A Comparative Analysis of Magnetic Fields and Reduced Gravity for Melt Stabilization: Dopant Segregation during Vertical Bridgman Growth*, Mass. Inst. Technol..
253. Matthiesen, D. H., M. J. Wargo, S. Motakef, D. J. Carlson, J. S. Nakos and A. F. Witt (1987), 'Dopant segregation during vertical Bridgman-Stockbarger growth with melt stabilization by strong axial magnetic fields,' *J. Crystal Growth*, **85**, 557-560.
254. McCartney, D. G. and J. D. Hunt (1981), 'Measurement of cell and primary dendrite arm spacings in directionally solidified aluminum alloys,' *Acta Metal.*, **29**, 1851-1863.
255. Melosh, R. J. (1963), 'Basis of derivation of matrices for the direct stiffness method,' *J.A.I.A.A.*, **1** 1631-1637.
256. Memelink, O. W. (1956), 'The distribution of impurity in a semi-infinite solidified melt,' *Proc. Phys. Soc. B*, **69**, 119-120.
257. Micklethwaite, W. F. H. (1981), 'The crystal growth of cadmium mercury telluride,' in *Semiconductors and Semimetals*, Vol. 18, 47-119, R. K. Willardson and A. C. Beer, eds., Academic Press, New York.

258. Mihelčić, M. and K. Wingerath (1985), 'Numerical simulation of the Czochralski bulk flow in an axial magnetic field: effects on the flow and temperature oscillations in the melt,' *J. Crystal Growth*, **71**, 163–168.
259. Miller, D. C., A. J. Valentino and L. K. Shick (1978), 'The effect of melt flow phenomena on the perfection of Czochralski grown gadolinium gallium garnet,' *J. Crystal Growth*, **44**, 121–134.
260. Monberg, E. M., W. A. Gault, F. Simchock and F. Dominguez (1987), 'Vertical gradient freeze growth of large diameter, low defect density indium phosphide,' *J. Crystal Growth*, **83**, 174–183.
261. Monberg, E. M., H. Brown, S. N. G. Chu and J. M. Parsey (1988), 'The growth of low defect density semi-insulating InP,' in *Semi-insulating III-V Materials, Malmö 1988*, G. Grossmann and L. Ledebø, eds., 459–464, Adam Hilger, Bristol.
262. Morizane, K., A. F. Witt and H. C. Gatos (1966), 'Impurity distributions in single crystals: I. Impurity striations in nonrotated InSb crystals,' *J. Electrochem. Soc.*, **113**, 51–54.
263. Müller, G. (1984), *Tiegel zum Herstellen von Kristallen und Verwendung des Tiegels*, German Patent, P3,441,707.9, filed Nov. 15, 1984.
264. Müller, G. (1988), *Crystals: Crystal Growth from the Melt*, **12**, Springer-Verlag, New York.
265. Müller, G., G. Neumann and H. Matz (1987), 'A Two-Rayleigh-Model of buoyancy convection in vertical melt growth configurations,' *J. Crystal Growth*, **84**, 36–49.
266. Müller, G., G. Neumann and W. Weber (1984), 'Natural convection in vertical Bridgman configurations,' *J. Crystal Growth*, **70**, 78–93.
267. Mullins, W. W. and R. F. Sekerka (1963), 'Morphological stability of a particle growing by diffusion or heat flow,' *J. Appl. Phys.*, **34**, 323–329.
268. Mullins, W. W. and R. F. Sekerka (1964), 'Stability of a planar interface during solidification of a dilute binary alloy,' *J. Appl. Phys.*, **35**, 444–451.

269. Murgai, A., H. C. Gatos and A. F. Witt (1976), 'Quantitative analysis of microsegregation in silicon grown by the Czochralski method,' *J. Electrochem. Soc.*, **123**, 224-229.
270. Naumann, R. J. (1982a), 'An analytical approach to thermal modeling of Bridgman-type crystal growth:I. One-dimensional analysis,' *J. Crystal Growth*, **58**, 554-568.
271. Naumann, R. J. (1982b), 'An analytical approach to thermal modeling of Bridgman-type crystal growth:I. Two-dimensional analysis,' *J. Crystal Growth*, **58**, 569-584.
272. Naumann, R. J. and S. L. Lehoczky (1983), 'Effect of variable thermal conductivity on isotherms in Bridgman growth,' *J. Crystal Growth*, **61**, 707-710.
273. Neuberger, M. (ed.) (1971), *Handbook of Electronic Materials: III-V Semiconducting Compounds*, Vol. 2, IFI/Plenum Press, New York.
274. Neugebauer, G. T. and W. R. Wilcox (1988), 'Convection in the vertical Bridgman-Stockbarger technique,' *J. Crystal Growth*, **89**, 143-154.
275. Nernst, W. (1904), 'Theorie der Reaktionsgeschwindigkeit in heterogenen Systemen,' *Z. Phys. Chem.*, **47**, 52-55.
276. Nickell, R. E., R. I. Tanner and B. Caswell (1974), 'The solution of viscous incompressible jet and free surface flow using finite element methods,' *J. Fluid Mech.*, **65**, 189-206.
277. Nishizawa, J., K. Suto, M. Kitamura, M. Sato, Y. Takase and A. Ito (1976), 'Electrons and holes in HgTe and $\text{Hg}_{0.82}\text{Cd}_{0.18}\text{Te}$ with controlled deviations from stoichiometry,' *J. Phys. Chem. Solids*, **37**, 33-42.
278. Noor, A. K., O. O. Storaasli and R. E. Fulton (1983), 'Impact of new computing systems on finite element computations,' in *State-of-the-Art Surveys on Finite Element Technology*, A. K. Noor and W. D. Pilkey, eds., ASME, New York.

279. Oden, J. T. and G. F. Carey (1983), *Finite Elements: Mathematical Aspects*, Vol. 4, Prentice Hall, New York.
280. Oden, J. T. and J. N. Reddy (1976), *An Introduction to the Mathematical Theory of Finite Elements*, John Wiley, New York.
281. Ogawa, O. (1988), 'Effects of composition and thermal history on crystal properties of LEC GaAs,' in *Semi-insulating III-V Materials, Malmö 1988*, G. Grossmann and L. Ledebø, eds., 477-482, Adam Hilger, Bristol.
282. Oreper, G. M. and J. Szekely (1983), 'The effect of an externally imposed magnetic field on buoyancy driven flow in a rectangular cavity,' *J. Crystal Growth*, **64**, 505-515.
283. Oreper, G. M. and J. Szekely (1984), 'The effect of a magnetic field on transport phenomena in a Bridgman-Stockbarger crystal growth,' *J. Crystal Growth*, **67**, 405-419.
284. Ortega, J. M. and W. C. Rheinboldt (1970), *Iterative Solution of Nonlinear Equations in Several Variables*, Academic Press, New York.
285. Osaka, J. and K. Hoshikawa (1984), 'Homogeneous GaAs grown by vertical magnetic field applied LEC method,' in *Semi-Insulating III-V Materials: Kahneta 1984*, Shiva, 126-133.
286. Ostrach, S. (1983), 'Fluid mechanics in crystal growth-the 1982 Freeman Schoar lecture,' *J. Fluid Engng.*, **105**, 5-20.
287. Ozawa, S., T. Kimura, J. Kobayashi and T. Fukuda (1987). 'Programmed magnetic field applied liquid encapsulated Czochralski crystal growth.' *Appl. Phys. Lett.*, **50**, 329-331.
288. Parker, S. G. and H. Kraus (1969), 'Method of producing homogeneous ingots of mercury cadmium telluride,' *US Patent*, No. **3,468,363**.

289. Parsey, J. M. and F. A. Thiel (1985), 'A new apparatus for the controlled growth of single crystals by horizontal Bridgman techniques,' *J. Crystal Growth*, **73**, 211–220.
290. Parsey, J. M. and F. A. Thiel (1987), 'Microscale phenomena in bulk GaAs crystals: the effect of thermal gradients,' *J. Crystal Growth*, **85**, 327–334.
291. Pelletier, D., A. Fortin and R. Camarero (1989), 'Are FEM solutions of incompressible flows really incompressible? (of how simple flows can cause headaches!),' *Int. J. Num. Meth. Fluids*, **9**, 99–112.
292. Petzold, L. R. (1982), 'Differential-algebraic equations are not ODEs,' *SIAM J. Stat. Comput.*, **3**, 367–384.
293. Phann, W. G. (1952), 'Principles of zone-melting,' *Trans. AIME*, **194**, 747–753.
294. Pimputkar, S. M. and S. Ostrach (1981), 'Convective effects in crystals grown from melt,' *J. Crystal Growth*, **55**, 614–646.
295. Pohl, R. G. (1954), 'Solute redistribution by recrystallization,' *J. Appl. Phys.*, **25**, 1170–1178.
296. Potts, H. and W. R. Wilcox (1986), 'Chaotic asymmetric convection in the Bridgman-Stockbarger technique,' *J. Crystal Growth*, **74**, 443–445.
297. Poulikakos, D. and W.-Z. Cao (1989), 'Solidification of a binary alloy from a cold wire or pipe: modeling of the mixed-phase region,' *Num. Heat Transfer part A*, **15**, 197–219.
298. Powell, M. J. D. (1970), 'A hybrid method for nonlinear equations.' in *Numerical Methods for Non-linear Algebraic Equations*, P. Rabinowitz, ed., Gordon and Breach, London.
299. Prager, W. and J. L. Synge (1947), 'Approximation in elasticity based on the concepts of functional space,' *Q. J. Appl. Math.*, **5**, 241–269.

300. Ramachandran, N. R., J. P. Gupta and Y. Jaluria (1982), 'Thermal and fluid flow effects during solidification in a rectangular enclosure,' *Int. J. Heat Mass Transfer*, **25**, 187–194.
301. Rao, S. S. (1982), *The Finite Element Method in Engineering*, Pergamon, Oxford.
302. Ravishankar, P. S. and T. W. Fu (1983), 'Mathematical modeling and parametric study of heat transfer in Bridgman-Stockbarger growth of crystals,' *J. Crystal Growth*, **62**, 425–432.
303. Rheinboldt, W. C. (1978), 'Numerical methods for a class of finite dimensional bifurcation problems,' *SIAM J. Numer. Anal.*, **15**, 1–11.
304. Rhines, P. and W. R. Young (1983), 'How rapidly is a passive scalar mixed within closed streamlines?' *J. Fluid Mech.*, **133**, 133–145.
305. Richardson, L. F. (1910), 'The approximate arithmetical solution by finite differences of physical problems involving differential equations with an application to the stresses in masonry dam,' *Trans. Roy. Soc. Lond., Ser. A*, **210**, 307–357.
306. Roache, P. J. (1976), *Computational Fluid Dynamics*, Hermosa Publishers, Albuquerque, NM.
307. Rouzaud, A., D. Camel and J. J. Favier (1985), 'A comparative study of thermal and thermosolutal convective effects in vertical Bridgman crystal growth,' *J. Crystal Growth*, **73**, 149–166.
308. Rutter, J. W. and B. Chalmers (1953), 'A prismatic substructure formed during solidification of metals,' *Can. J. Phys.*, **31**, 15–39.
309. Sackinger, P. A. (1989), *Flows and Transitions during Solidification: (I) Mode Expansion Calculations of Rayleigh-Bénard Convection in a Cylinder (II) Simulation of Hydrodynamics, Heat Transfer, and Free Boundaries in Czochralski Growth*, Ph. D. Thesis, Mass. Inst. Technol., Cambridge.

310. Sackinger, P. A., R. A. Brown and J. J. Derby (1989), 'A finite element method for analysis of fluid flow, heat transfer and free interfaces in Czochralski crystal growth,' *Int. J. Num. meth. Fluids*, **9**, 453–492.
311. Saito, H. L. and L. E. Scriven (1981), 'Study of coating flow by the finite element method,' *J. Comput. Phys.*, **42**, 53–76.
312. Saitoh, T. (1978), 'Numerical method for multi dimensional freezing problems in arbitrary domain,' *Trans. ASME J. Heat Transfer*, **100**, 294–299.
313. Salcudean, M. and Z. Abdullah (1988), 'On the numerical modelling of heat transfer during solidification processes,' *Int. J. Numer. Meth. Eng.*, **25**, 445–473.
314. Sani, R. L., P. M. Gresho, R. L. Lee, D. F. Griffiths and M. Engelman (1981), 'The cause and cure (!) of the spurious pressures generated by certain FEM solutions of the incompressible Navier-Stokes equations: part 2,' *Int. J. Num. Meth. Fluids*, **1**, 171–204.
315. Schaefer, R. J. and S. R. Coriell (1984), 'Convection-induced distortion of a solid-liquid interface,' *Met. Trans. A*, **15A**, 2109–2115.
316. Scheil, E. (1942), 'Bemerkungen zur Schichtkristallbildung,' *Z. Metallkde.*, **34**, 70–72.
317. Schmit, J. L. (1983), 'Growth, properties and applications of HgCdTe,' *J. Crystal Growth*, **65**, 249–261.
318. Schwarz, H. R. (1988), *Finite Element Methods*, Academic Press, London.
319. Sekerka, R. F. (1965), 'A stability function for explicit evaluation of the Mullins-Sekerka interface stability criterion,' *J. Appl. Phys.*, **36**, 264–268.
320. Sekerka, R. F. (1967), 'Application of the time-dependent theory of interface stability to an isothermal phase transformation,' *J. Phys. Chem. Solids*, **28**, 983–994.
321. Sekerka, R. F. (1968), 'Morphological stability,' *J. Crystal Growth*, **3/4**, 71–81.

322. Sen, S., and W. R. Wilcox (1975), 'Influence of crucible on interface shape, position and sensitivity in the vertical Bridgman-Stockbarger technique,' *J. Crystal Growth*, **28**, 36–40.
323. Series, R. W. (1989a), 'Cz growth of silicon under an axial magnetic field,' *First NATO Workshop on Comput. Model. Crystal Growth from the Melt*, Parma, Italy.
324. Series, R. W. (1989b), 'Effect of shaped magnetic field on Cz silicon growth,' *First NATO Workshop on Comput. Model. Crystal Growth from the Melt*, Parma, Italy.
325. Series, R. W., D. T. J. Hurle and K. G. Barraclough (1985), 'Effective distribution coefficient of silicon dopants during magnetic Czochralski growth,' *IMA J. Appl. Math.*, **35**, 195–203.
326. Shercliff, J. A. (1965), *A Textbook of Magnetohydrodynamics*, Pergamon, Oxford.
327. Shimura, F. (1989), *Semiconductor silicon crystal technology*, Academic Press, San Diego.
328. Siegel, R. and J. R. Howell (1972), *Thermal Radiation Heat Transfer*, McGraw Hill, New York.
329. Silliman, W. J. and L. E. Scriven (1980), 'Separating flow near a static contact line: slip at a wall and shape of a free surface,' *J. Comput. Phys.*, **34**, 287–313.
330. Simpson, R. B. (1975), 'A method for the numerical determination of bifurcation states of nonlinear systems of equations,' *SIAM J. Numer. Anal.*, **12**, 439–451.
331. Smith, M. K. (1988), 'Thermal convection during the directional solidification of a pure liquid with variable viscosity,' *J. Fluid Mech.*, **188**, 547–570.
332. Smith, V. G., W. A. Tiller and J. W. Rutter (1955), 'A mathematical analysis of solute redistribution during solidification,' *Can. J. Phys.*, **33**, 723–745.

333. Spaid, F. W., A. F. Charwat, J. G. Redekopp and R. Rosen (1971), 'Shape evolution of a subliming surface subject to unsteady spatially nonuniform heat flux,' *Int. J. Heat Mass Transfer*, **14**, 673-687.
334. Spalding, D. B. (1972), 'A novel finite difference formulation for differential equations involving both first and second derivatives,' *Int. J. Num. Meth. Eng.*, **4**, 551-559.
335. Sparrow, E. M., S. V. Patankar and S. Ramadhyani (1977), 'Analysis of melting in the presence of natural convection in the melt region,' *Trans. ASME C: J. Heat Transfer*, **99**, 520-526.
336. Stern, M. E. (1960), 'The salt fountain and thermohaline convection,' *Tellus*, **12**, 172-175.
337. Storaasli, O. O., S. W. Peebles, T. W. Crockett, J. D. Knott and L. Adams (1982), *The Finite Element Machine: An Experiment in Parallel Processing*, NASA TM-84514, NASA Langley Research Center, Hampton, VA.
338. Strang, G. and G. J. Fix (1973), *An Analysis of the Finite Element Method*, Prentice Hall, Englewood Cliffs.
339. Stroud, A. H. and D. Secrest (1966), *Gaussian Quadrature Formulas*, Prentice-Hall, Englewood Cliffs, NJ.
340. Su, C.-H. (1986), 'Heat capacity, enthalpy of mixing, and thermal conductivity of $\text{Hg}_{1-x}\text{Cd}_x\text{Te}$ pseudobinary melts,' *J. Crystal Growth*, **78**, 51-57.
341. Su, C.-H., G. L. E. Perry, F. R. Szofran and S. L. Lehoczky (1988), 'Compositional redistribution during casting of $\text{Hg}_{0.8}\text{Cd}_{0.2}\text{Te}$ alloys,' *J. Crystal Growth*, **91**, 20-26.
342. Sukanek, P. C. (1982a), 'Deviation of freezing rate from translation rate in the Bridgman-Stockbarger technique: I. very low translation rates,' *J. Crystal Growth*, **58**, 208-218.

343. Sukanek, P. C. (1982b), 'Deviation of freezing rate from translation rate in the Bridgman-Stockbarger technique: II. moderate translation rates,' *J. Crystal Growth*, **58**, 219–228.
344. Szabo, B. A. and G. C. Lee (1969), 'Derivation of stiffness matrices for problems in plane elasticity by Galerkin's method,' *Int. J. Numer. Methods Eng.*, **1**, 301–310.
345. Szofran, F. R. and S. L. Lehoczky (1981), 'The pseudobinary HgTe-CdTe phase diagram,' *J. Electron. Mater.* **10**, 1131–1150.
346. Szofran, F. R. and S. L. Lehoczky (1983), 'Liquidus temperatures of Hg-rich Hg-Cd-Te alloys,' *J. Elect. Mat.*, **12**, 713–717.
347. Szofran, F. R. and S. L. Lehoczky (1984), 'A method for interface shape control during Bridgman type crystal growth of HgCdTe alloys,' *J. Crystal Growth*, **70**, 349–355.
348. Szofran, F. R., D. Chandra, J.-C. Wang, E. K. Cothran and S. L. Lehoczky (1984), 'Effect of growth parameters on compositional variations in directionally solidified HgCdTe alloys,' *J. Crystal Growth*, **70**, 343–348.
349. Taghavi, K. and W. M. B. Duval (1989), 'Inverse heat transfer analysis of Bridgman crystal growth,' *Int. J. Heat Mass Transfer*, **32**, 1741–1750.
350. Takase, Y. (1974), 'Freezing interface and anomalous diffusion layer of $\text{Hg}_{1-x}\text{Cd}_x\text{Te}$ growing by zone leveling,' *Japan J. Appl. Phys.*, **13**, 539–540.
351. Teal, G. K. (1976), 'Single crystals of germanium and silicon – Basic to the transistor and integrated circuit,' *IEEE Trans. Electron Devices*, **ED-23**, 621–639.
352. Thomas, P. D., H. M. Ettouney and R. A. Brown (1986), 'A thermal-capillary mechanism for a growth rate limit in Edge-Defined Film-fed growth of silicon sheets,' *J. Crystal Growth*, **76**, 339–351.
353. Thomasset, F. (1981), *Implementation of Finite Element Methods for Navier-Stokes Equations*, Springer-Verlag, New York.

354. Thompson, J. F., F. L. Thames and C. W. Mastin (1974), 'Automatic numerical generation of body-fitted curvilinear coordinate system for field containing any number of arbitrary two-dimensional bodies,' *J. Comput. Phys.*, **15**, 299-319.
355. Thompson, M. E. and J. Szekely (1988), 'Mathematical and physical modelling of double-diffusive convection of aqueous solutions crystallizing at a vertical wall,' *J. Fluid Mech.*, **187**, 409-433.
356. Tiller, W. A., K. A. Jackson, J. W. Rutter, and B. Chalmers (1953), 'The redistribution of solute atoms during the solidification of metals,' *Acta Metal.*, **1**, 428-437.
357. Touloukian, Y. S. (ed.) (1967), *Thermophysical Properties of High Temperature Solid Materials: Intermetallics, Cermets, Polymers, and Composite Systems*, Vol. 6, Macmillan Co., New York.
358. Touloukian, Y. S. and C. Y. Ho (eds.) (1970), *Thermophysical Properties of Matter*, IFI/Plenum, New York.
359. Triboulet, R. (1977), 'CdTe and CdTe:Hg alloys crystal growth using stoichiometric and off-stoichiometric zone passing techniques,' *Rev. Phys. Appl.*, **12**, 123-128.
360. Triboulet, R., T. N. Duy and A. Durand (1985), 'THM, a breakthrough in $\text{Hg}_{1-x}\text{Cd}_x\text{Te}$ bulk metallurgy,' *J. Vac. Sci. Technol. A*, **3**, 95-99.
361. Tsivinsky, S. V. (1979), 'Dislocation density in pure crystals grown from melts,' *Kristall. Tech.*, **10**, 5-35.
362. Turner, J. S. (1973), *Buoyancy Effects in Fluids*, Cambridge Univ. Press, Cambridge.
363. Turner, J. S. (1985), 'Multicomponent convection,' *Ann. Rev. Fluid Mech.*, **17**, 11-44.
364. Ueda, H. (1961), 'Resistivity striations in germanium single crystals,' *J. Phys. Soc. Japan*, **16**, 61-66.

365. Ueda, R., O. Ohtsuki, K. Shinohara and Y. Ueda (1972), 'Crystal growth of $\text{Hg}_{1-x}\text{Cd}_x\text{Te}$ using Te as a solvent,' *J. Crystal Growth*, **13/14**, 668-671.
366. Ungar, L. H. (1984), *Directional solidification from a Bifurcation Viewpoint*, Ph. D. Thesis, Mass. Inst. Technol., Cambridge.
367. Ungar, L. H. and R. A. Brown (1982), 'The dependence of the shape and stability of captive rotating drops on multiple parameters,' *Phil. Trans. Roy. Soc. Lond.*, **A306**, 347-370.
368. Ungar, L. H., N. Ramprasad and R. A. Brown (1988), 'Finite element methods for unsteady solidification problems arising in prediction of morphological structure,' *J. Sci. Comput.*, **3**, 77-108.
369. Utech, H. P. and M. C. Flemings (1966), 'Elimination of solute banding in indium antimonide crystal by growth in a magnetic field,' *J. Appl. Phys.*, **37**, 2021-2024.
370. Utech, H. P. and M. C. Flemings (1967), 'Thermal convection in metal-crystal growth: effect of magnetic field,' in *Crystal Growth*, H. S. Peiser, ed., 651-658, Pergamon, Oxford.
371. Verhoeven, J. D., W. N. Gill, J. A. Puszynski and R. M. Gindé (1988), 'Macrosegregation during convection-free plane front solidification: I. rectilinear geometry,' *J. Crystal Growth*, **89**, 189-201.
372. Veronis, G. (1963), 'Penetrative convection,' *Astrophys. J.*, **137**, 641-643.
373. Wacker, H. (1978), *Continuation Methods*, Academic Press, New York.
374. Wang, C. A. (1984), *Crystal Growth and Segregation in Vertical Bridgman Configuration*, Ph. D. Thesis, Mass. Inst. Technol., Cambridge.
375. Wang, C. A., A. F. Witt and J. R. Carruthers (1984), 'Analysis of crystal growth characteristics in a conventional vertical Bridgman configuration,' *J. Crystal Growth*, **66**, 299-308.

376. Warchol, S. and A. Modrzejewski (1986), 'Computer calculation of the temperature at the interface under disturbed Bridgman growth,' *J. Crystal Growth*, **79**, 99-104.
377. Weatherburn, C. E. (1927), *Differential Geometry of Three Dimensions*, Cambridge University Press, Cambridge.
378. Wen, C. Y. and L. T. Fan (1975), *Models for Flow Systems and Chemical Reactors*, Marcel Dekker, New York.
379. Whitaker, S. (1968), *Introduction to Fluid Mechanics*, Prentice Hall, Englewood Cliffs.
380. Whiteman, J. R. (ed.) (1973), *The Mathematics of Finite Elements and Applications*, Academic Press, London.
381. Whiteman, J. R. (ed.) (1977), *The Mathematics of Finite Elements and Applications*, Vol. 2, Academic Press, London.
382. Whiteman, J. R. (ed.) (1979), *The Mathematics of Finite Elements and Applications*, Vol. 3, Academic Press, London.
383. Whiteman, J. R. (ed.) (1982), *The Mathematics of Finite Elements and Applications*, Vol. 4, Academic Press, London.
384. Whiteman, J. R. (ed.) (1984), *The Mathematics of Finite Elements and Applications*, Vol. 5, Academic Press, London.
385. Whiteman, J. R. (ed.) (1987), *The Mathematics of Finite Elements and Applications*, Vol. 6, Academic Press, London.
386. Wilcox, W. R. (1969), 'Validity of the stagnant film approximation for mass transfer in crystal growth and dissolution,' *Mat. Res. Bull.*, **4**, 265-274.
387. Witt, A. F. and H. C. Gatos (1966), 'Impurity distribution in single crystals: II. Impurity striations in InSb as revealed by interference contrast microscopy,' *J. Electrochem. Soc.*, **113**, 808-813.

388. Witt, A. F., H. C. Gatos, M. Lichtensteiger, M. C. Lavine, and C. J. Herman (1975), 'Crystal growth and steady-state segregation under zero gravity: InSb,' *J. Electrochem. Soc.*, **122**, 276-283.
389. Witt, A. F., H. C. Gatos, M. Lichtensteiger, and C. J. Herman (1978), 'Crystal growth and segregation under zero gravity: Ge,' *J. Electrochem. Soc.*, **125**, 1832-1840.
390. Witt, A. F., C. J. Herman and H. C. Gatos (1970), Czochralski-type crystal growth in transverse magnetic fields,' *J. Mat. Sci*, **5**, 822-824.
391. Witt, A. F., M. Lichtensteiger and H. C. Gatos (1973), 'Experimental approach to the quantitative determination of dopant segregation during crystal growth on a microscale: Ga doped Ge,' *J. Electrochem. Soc.*, **120**, 1119-1123.
392. Wolf, S. and R. N. Tauber (1986), *Silicon Processing for the VLSI Era*, Vol. 1, Lattice Press, Sunset Beach.
393. Woods, A W. and H. E. Huppert (1988), 'The growth of compositionally stratified solid above a horizontal boundary,' *J. Fluid Mech.*, **199**, 29-53.
394. Wouters, P., J. J. Van Schaftingen, M. J. Crochet and F. T. Geyling (1987), 'Numerical simulation of the horizontal Bridgman growth. part III: calculation of the interface,' *Int. J. Num. Meth. Fluids*, **7**, 131-153.
395. Yamada, Y., K. Ito, Y. Yokouchi, T. Tamano and T. Ohtsubo (1975), 'Finite element analysis of steady fluid and metal flow,' in *Finite Elements in Fluids: Viscous Flows and Hydrodynamics*, Vol. 1, R. H. Gallagher, J. T. Oden, C. Taylor and O. C. Zienkiewicz ,eds.,John Wiley, London.
396. Yamaguchi, Y., C. J. Chang and R. A. Brown (1984), 'Multiple buoyancy-driven flows in a cylinder heated from below,' *Phil. Trans. Roy. Soc. Lond.*, **A312**, 519-552.
397. Zienkiewicz, O. C. (1971), *The Finite Element Method in Engineering and Science*, McGraw-Hill, New York.

398. Zienkiewicz, O. C. (1977), *The Finite Element Method*, 3rd ed., McGraw-Hill, London.
399. Zienkiewicz, O. C. and Y. K. Cheung (1965), 'Finite elements in the solution of field problems,' *The Engineer*, Sept. 1965, 507-510,.
400. Zienkiewicz, O. C., B. M. Irons, J. Ergatoudis, S. Ahmad and F. C. Scott (1969), 'Iso-parametric and associate elements families for two and three dimensional analysis,' Chapter 13, in *Finite Element Methods in Stress Analysis*, I. Holand and K. Bell, eds., Tapir Press, Trondheim, Norway.
401. Zienkiewicz, O. C. and C. J. Parekh (1970), 'Transient field problems: two dimensional and three dimensional analysis by isoparametric finite elements,' *Int. J. Num. Methods Eng.*, 2, 61-71.
402. Zienkiewicz, O. C., R. L. Taylor and J. M. Too (1971), 'Reduced integration techniques in general analysis of plates and shells,' *Int. J. Num. Methods Eng.*, 3, 275-290.

Biographical Note

DO HYUN KIM

김도현

Date of Birth: June 17, 1956

Place of Birth: Seoul, Korea

EDUCATION

MASSACHUSETTS INSTITUTE OF TECHNOLOGY, Cambridge, MA

Sc.D. in Chemical Engineering, Fluid Mechanics Minor, February 1990. Thesis under the supervision of Professor Robert A. Brown on "Dynamic Analysis of Transport Phenomena in Directional Solidification of Binary Alloys".

KOREA ADVANCED INSTITUTE OF SCIENCE, Seoul, KOREA

M.S. in Chemical Engineering, February 1981. Thesis under the supervision of Professor Ho Nam Chang on "Mass Transfer Study around a Turbulence Promoter by Electrochemical Method".

SEOUL NATIONAL UNIVERSITY, Seoul, KOREA

B.S. in Chemical Engineering, February, 1979. Thesis under the supervision of Professor Hyun-Ku Rhee on "The Existence of the Asymmetric Composition and Temperature Profile in Catalyst Slab". Graduated with *Summa Cum Laude*.

EXPERIENCE

1981 - 1984

KOREA ADVANCED INSTITUTE OF SCIENCE AND TECHNOLOGY Seoul, KOREA

Research Engineer in Chemical Process Laboratory headed by Dr. Chang K. Yun.

PUBLICATION

1. D. H. Kim and R. A. Brown, "Models for Convection and Segregation in the Growth of HgCdTe by the Vertical Bridgman Method," *J. Crystal Growth*, **96**, 609-627, (1989).
2. D. H. Kim, P. M. Adornato, and R. A. Brown, "Effect of Vertical Magnetic Field on Convection and Segregation in Vertical Bridgman Crystal Growth," *J. Crystal Growth*, **89**, 339-356, (1988).
3. D. H. Kim, I. H. Kim, and H. N. Chang, "Experimental Study of Mass Transfer around a Turbulence Promoter by the Limiting Current Method," *Int. J. Heat Mass Transfer*, **26**, 1007-1016 (1983).

PATENT

1. "Process for High Conductive Carbon Production," Korean Patent (KP 21441, July 16, 1986) (with C. K. Yun and S. H. Han).
2. "A Method for Upgrading Paratosyl Chloride," Korean Patent (KP 18858, February 27, 1985), Japanese Patent (JP 59-32641, August 9, 1984) (with C. K. Yun and S. H. Han).